Liquefaction-Targeted Ground Motions and Lateral Spreading Driving Stresses

Ryan A Rasanen

A thesis

submitted in partial fulfillment of the

requirements for the degree of

Master of Science in Civil Engineering

University of Washington

2019

Reading Committee:

Steve Kramer, Chair

Pedro Arduino

Brett Maurer

Program Authorized to Offer Degree:

Civil and Environmental Engineering

University of Washington

Abstract

Liquefaction-Targeted Ground Motions and Lateral Spreading Driving Stresses

Ryan A Rasanen

Chair of the Supervisory Committee:
Steve Kramer
Civil and Environmental Engineering

Earthquake induced soil liquefaction has been one of the most studied topics in geotechnical engineering over the past 60 years due to its severe impacts on natural and man-made structures. Improving the prediction of liquefaction triggering has already been undertaken for many years, however, in ways that can produce inconsistent, and inaccurate, results in different seismic environments. The first focal point of this thesis is the introduction of a liquefaction-targeted intensity measure that would allow practicing engineers to obtain the benefits of a full probabilistic liquefaction hazard analysis with the same, or less, effort than required by current conventional liquefaction hazard analyses.

Lateral spreading is one of the most common, and most severe, effects of liquefaction. Up to three mechanisms are believed to drive lateral spreading. Each of these potential deformation mechanisms is influenced by static shear stresses yet both empirical and semi-empirical procedures for prediction of lateral spreading displacements currently characterize static shear stresses in a crude and incomplete manner. The second focal point of this research was directed toward developing an improved framework for characterizing the initial static shear stresses over a continuous range of site conditions commonly encountered at lateral spreading sites. This framework is intended to lay the foundation for an improved lateral spreading displacement procedure. To accomplish this, numerical analyses were performed to develop a function that can predict the initial static shear stress at depths of lateral spreading interest.

TABLE OF CONTENTS

LIST OF FIGURES

LIST OF TABLES

ACKNOWLEDGEMENTS

First, and foremost, I want to highlight the efforts of my research advisor, Dr. Steve Kramer, for going above and beyond in helping me grow in critical areas for my success in the future. Whether that was helping me understand the key concepts of the research, showing me the importance of probability in geotechnical earthquake engineering, or working hard to develop me into a better technical writer. Dr. Kramer is a great mentor and truly cares about his students. I would like to acknowledge my two other committee members, Dr. Pedro Arduino and Dr. Brett Maurer, who always made time to chat along with keeping me company in the office while working long hours into the dark of the night. I also would like to thank Mertcan Geyin, a fellow graduate student who helped me more times than I can count when getting stuck coding and for inspiring me to keep pushing on while finishing this thesis.

Lastly, I would like to thank my family and friends for all of their support throughout grad school and my life. Specifically, I would like to thank my mom Laurie, for showing me what true work ethic is, along with always being able to talk when I needed it the most. My mom is without a doubt the hardest worker I know and she still inspires me to this day. I want to thank my dad for passing along his humor to me and always being there to talk about sports when I needed a fun conversation to take a break from research. There are many others to thank as well, for all of those not mentioned here, thank you.

DEDICATION

To the past, present, and future grad students of More Hall.

Chapter 1. **INTRODUCTION**

Soil liquefaction has become one of the most studied topics in geotechnical engineering due to its severe impacts on natural and man-made structures which have been thrust to light over the past 60 years. Soil liquefaction typically occurs in loose granular materials and/or coarse silts that are saturated and subjected to strong ground motions that typically originate from large earthquake events. The cyclic shear stresses imposed by the ground motions applied to an undrained soil cause the loose soil particles to have the tendency to contract, thus, causing pore pressure to build up. If the ground motions are strong enough, and last for a long enough period of time, the soil can undergo large amount of shear strain as the soil fabric is degraded. Because the three general components of soil liquefaction: (1) loose granular material and/or coarse silts, (2) shallow ground water, and (3) strong ground motions, are typically encountered along coastlines, and because a major portion of the world's population lives in such areas, soil liquefaction is a severe threat to the welfare of human life.

The first focus of this thesis is the introduction of a new mapped liquefaction-targeted ground motion parameter that a practicing engineer in the future will be able to obtain by entering the latitude and longitude coordinates of their site of interest on a website. The engineer could then input the mapped parameter into their conventional liquefaction hazard analysis and obtain the liquefaction triggering results that would have been obtained from a full probabilistic liquefaction hazard analysis. This would allow practicing engineers to evaluate liquefaction potential in a more accurate and consistent manner while requiring the same, or less, work than currently needed to perform conventional liquefaction hazard analysis procedures. This thesis will describe the process of obtaining this conventional liquefaction-targeted ground motion parameter value that

corresponds to an event with a return period of a full probabilistic liquefaction hazard analysis and will discuss how the liquefaction-targeted ground motion parameter values obtained by two common liquefaction triggering procedures are influenced by various site conditions.

The second focus of this thesis is the development of a unified approach to characterizing the initial static shear stress for any geometry (free-face or ground slope) anywhere within lateral spreading regions of interest. The initial static shear stress is a key component in predicting the lateral deformations that occur when a soil liquefies. Current commonly used procedures for the prediction of lateral spread displacement, however, characterize the initial static shear stress crudely and incompletely, which contributes to uncertainty in current procedures for prediction of lateral spreading displacements. A more complete characterization of the initial static shear stress has the potential to improve agreement between the predicted and observed lateral displacements and, therefore, reduce uncertainty in lateral spreading hazard evaluation.

1.1 OBJECTIVES

The research described in this thesis is oriented towards improving existing procedures for evaluation of liquefaction hazards, specifically triggering of liquefaction and prediction of lateral spreading displacement. The primary objectives of the work included:

- Discussion of the current state of probabilistic liquefaction hazard analysis, the tools for it, and its current role in design.

- Introduction of a liquefaction-targeted ground motion parameter, PGA_M, and discuss the influences of various site conditions on the PGA_M for two common liquefaction triggering procedures.

- Discussion of the current state of lateral spreading procedures today including empirical, semi-empirical, and numerical analysis.

- Development of a unified framework to characterizing the static stress state for any slope geometry (free-face or ground slope) using numerical analysis to develop a function that can predict the initial static shear stress at any point within the slope.

1.2 ORGANIZATION OF THESIS

This thesis is partitioned into six chapters to facilitate the review of background information and research presented herein. Chapter 2 provides an in-depth literature review of liquefaction susceptibility, initiation, and effects. Chapter 3 discusses the current state of probabilistic liquefaction hazard analysis to quantify liquefaction hazards, the current tools available for probabilistic liquefaction hazard analysis, the relatively new method of mapped parameters, introduces a new liquefaction-targeted intensity measure that can be mapped, and the current role of probabilistic liquefaction hazard analysis in design. Chapter 4 then discusses the effects of various site conditions on two commonly used liquefaction triggering procedures for the proposed liquefaction-targeted ground motion parameter. Chapter 5 reviews the current state of lateral spreading procedures today and then introduces a framework to characterize the initial static shear stress for a wide array of lateral spreading geometries within lateral spreading regions of interest. During the process of developing this framework, a transformed coordinate system is introduced, the slope geometries investigated are shown, the numerical results discussed and then mapped to a regular grid, and the stress function and then the calibration process of it discussed. A summary of the findings of the proposed research, and the future research that can built upon these findings, are discussed in Chapter 6.

Chapter 2. **LIQUEFACTION**

2.1 INTRODUCTION

Soil liquefaction is among one of the most critical phenomena pertaining to geotechnical engineering and the hazards that arise from earthquake shaking. Knowledge of the principle concepts of soil liquefaction is key to understanding the effects of this ground failure mechanism. The effects of soil liquefaction on natural and man-made structures became prevalent to geotechnical engineers following the 1964 Good Friday earthquake (M_w = 9.2) in Alaska and the 1964 Niigata, Japan earthquake (M_s = 7.5) occurring a few months later. "Liquefaction" typically occurs in loosely packed sand and/or coarse silts that are located beneath the water table (saturated) and subjected to earthquake loading. More broadly, liquefaction can occur in cohesionless soils that are undrained and subjected to monotonic or transient loading. Although there are two primary categories of liquefaction, flow liquefaction and cyclic liquefaction, the general term "liquefaction" has typically been used to refer to both even though both have clear differences in the initiation of liquefaction. It should also be noted a liquefaction related phenomena termed "cyclic softening" can also take place in fine-grained plastic soils.

2.1.1 **Flow Liquefaction**

Flow liquefaction, the more severe of the two liquefaction categories, can cause tremendous amounts of destruction upon initiation. Flow liquefaction occurs when the shear strength of the soil drops below the static shear stresses present in the soil due to the reduction of shear strength from loading (seismic or non-seismic) that causes pore pressure generation to reduce the effective stress of the soil. The shear stresses acting on the soil (typically increased on a slope or near/beneath a building) immediately prior to loading are what drive the failure of the soil upon the reduction of the shear strength. Soil deformations caused by flow liquefaction occur quickly

and the deformed soil can travel large distances. Figure 2.1 shows the dramatic effects of flow liquefaction causing a bearing capacity failure of the Kawagishi-cho apartments buildings during the 1964 Niigata, Japan earthquake.

Figure 2.1. Bearing capacity failure of the Kawagishi-cho apartment buildings due to flow liquefaction (USGS).

2.1.2 Cyclic Liquefaction

Cyclic liquefaction occurs when the in-situ static shear stress of the soil is less than the shear strength of the liquefied soil due to cyclic loading. Prior to shaking, the ground is in an at rest state where the shear strength of the soil counteracts the static shear stresses acting on it. During earthquake shaking, the cyclic nature of the ground motion causes deformations to develop incrementally and cause lateral spreading when the combination of the initial static stresses and the cyclic stress exceed the shear strength of the soil for a brief period of time. These brief occurrences of exceeding the shear strength of the soil can continually take place over the duration of earthquake shaking, and in some cases can lead to several meters of permanent displacement. These permanent displacements due to cyclic liquefaction are markedly less than those of flow liquefaction, however, are significantly more common and can also cause severe damage to natural

and man-made structures. Lateral spreading caused by cyclic liquefaction can occur on sloped and level ground with deformations ranging from a few centimeters (cm) to several meters (m). Figure 2.2 shows the severe effects of liquefaction induced lateral spreading of artificial fill during the January 12th, 2010 Haiti earthquake (Mw = 7.0) causing damage to the pile-supported North Wharf at the Port de Port-au-Prince (Green et al. 2011).

Figure 2.2. Liquefaction-induced lateral spreading at the North Wharf of the Port de Port-au-Prince (photo from DesRoches et al., 2011).

2.1.3 Cyclic Softening

Cyclic softening occurs in saturated, fine grained plastic soils subjected to vibrations (e.g., earthquake ground motions). Unlike flow liquefaction and cyclic liquefaction, cyclic softening is considered separately because the effective stress does not reach a value of zero as the ability to generate pore pressure in fine-grained plastic soils lacks behind that of non-plastic soils (i.e., the pore pressure generation in plastic soils tends to stall out prior to an effective stress of zero).

Although liquefaction is not reached, the clayey (plastic) soil does soften as the soil is subjected to cyclic loading because the loading induces pore pressure generation, reducing the effective stress, which causes a drop in the soils shear modulus, ultimately resulting in increasing shear strains. Although not as severe as liquefaction, cyclic softening can still result in slope instabilities and damage to building foundations.

2.2 PROCEDURE FOR EVALUATING LIQUEFACTION HAZARDS

In order for a geotechnical earthquake engineer to evaluate liquefaction hazards today, one needs to address the susceptibility, initiation, and effects of liquefaction. The latter elements of liquefaction should be evaluated by addressing each of these elements individually. The first step in any liquefaction evaluation is whether the soil is susceptible to liquefaction. Second, if the soil is susceptible, is the anticipated earthquake shaking strong enough to initiate liquefaction? Third, if the anticipated earthquake shaking is strong enough to initiate liquefaction, will damage occur (Kramer, 1996). Liquefaction susceptibility, initiation, and effects are thoroughly explained in the following sections.

2.3 LIQUEFACTION SUSCEPTIBILITY

The first part of assessing the potential for liquefaction is susceptibility. A soil is susceptible to liquefaction if it can exist in a state where liquefaction can occur. Susceptibility does not require that liquefaction take place, however, does require that the soil has the potential to liquefy. Multiple factors can be considered in order to evaluate the susceptibility of a soil to liquefaction including a soils historical, geological, and compositional characteristics (Kramer, 1996).

Historical

Historical factors are evidence that liquefaction has occurred in a given soil at some time in the past. The basis of historical factors is that if a soil liquefied in the past, it is susceptible to liquefaction in the future. Evidence that liquefaction has occurred in the past may be ejecta present from sand boils, sand ejecta that did not reach the ground surface forming sand dikes, or the remnants of lateral spreading. In other words, if there is evidence of paleoliquefaction, this is a historical indicator that the soil is susceptible to liquefaction. Figure 2.3 shows paleoliquefaction where the remnants of a sand boil remain between two layers of silt. The liquefied sand penetrated through the non-liquefiable lower silt and formed a sand boil at the surface which was then covered by the deposition of the upper silt.

Figure 2.3 Paleoliquefaction. Remnants of sand ejecta from a sand boil along the Duwamish River in Seattle, Washington. Liquefied sand penetrated the non-liquefiable lower silt followed by deposition of the upper silt.

Geological

Youd and Hoose (1977) found that a soil's age along with its hydrogeological and depositional environment can play a role in determining a soils susceptibility to liquefaction. Liquefaction most often occurs in saturated poorly graded loose soils, therefore, it should be expected that geological processes that create this type of environment are more likely to be susceptible to liquefaction. Examples of geological processes that deposit soil in a loose state may include fluvial (rivers) or aeolian (wind blown) deposits. Youd and Hoose (1977) also noted that alluvial-fan, alluvial-plain, beach, terra, and playa deposits are susceptible, however, less susceptible than the former depositional environments. Geologic processes are not the only way a soil can be placed in a loose state. Human related processes such as hydraulic filling (similar to a fluvial process) also can leave soil in a loose, poorly graded state that is susceptible to liquefaction.

Along with depositional and hydrological processes, age can be an important factor to the susceptibility of a soil. As a soils age increases, the susceptibility of the soil typically decreases. Generally, older soils are less susceptible to liquefaction compared to younger soils. For example, Holocene age soils are more susceptible than Pleistocene age soils. (Kramer, 1996).

Compositional

Soil susceptibility to liquefaction is also analyzed on the basis of compositional factors. Perhaps the most important compositional factors are grain size, fines content, and the plasticity of these fines. High plasticity soils are not able to generate enough pore pressure to cause the effective stress to reduce to zero, whereas, coarse grained soils such as gravel are typically not susceptible to liquefaction due to the inability of gravels to generate enough pore pressure due to their inherently high permeability. It should be noted however, that a saturated gravel layer can be susceptible to liquefaction if it is between two impermeable layers (e.g., clay) because if the pore

water has nowhere to go, then pore pressures may be large enough to cause the soil to liquefy. Therefore, gravels with a low fines content (clean gravels) should be considered susceptible to liquefaction (Kramer, 1996).

In order to address the plasticity of the fines that result in a soil not being susceptible to liquefaction, researchers have relied on the plasticity index. Boulanger and Idriss (2006) developed guidelines for determining whether a soil is susceptible to liquefaction based on the whether the soil is considered "sand-like" or "clay-like." Whether a soil is considered "sand-like" or "clay-like" is determined based on the plasticity index (PI) of the soil. Boulanger and Idriss determined that soils with a PI $\geq$ 8 have "clay-like" behavior, whereas, soils with a PI $\leq$ 3 have "sand-like" behavior. Soils with a plasticity index between the range of 3 and 8 are considered a transition zone from sand to clay like behavior where soils can exhibit both sand and clay like behavior. Boulanger and Idriss recommended that a PI $\geq$ 7 be used as a guideline to determine whether a soil is susceptible to liquefaction or not. Figure 2.4 shows an illustration of "sand-like" and "clay-like" behavior based on the plasticity index.

Bray and Sancio (2006) also developed a procedure to evaluate whether a soil is susceptible to liquefaction based on the plasticity index (PI) and ratio of water content (w_c) to the liquid limit of the soil. The guidelines developed by Bray and Sancio were that if a soil has a PI > 18 or a w_c < 80% then the soil is not susceptible to liquefaction. If the soil has a PI < 12 and w_c > 85% then the soil is susceptible to liquefaction. Soils falling between this range with 12 < PI < 20 and 80% < w_c < 85% are considered potentially susceptible to liquefaction. It can be noted that by using water content, which is linked to density and therefore to liquefaction resistance, as one of the factors in their assessment of liquefaction susceptibility, that it appears the latter procedure mixes liquefaction susceptibility and triggering (Kramer and Stewart, unpublished manuscript).

Although soil liquefaction susceptibility is slightly different between the Boulanger and Idriss (2006) and Bray and Sancio (2006), one can see both procedures have transition zones between soils considered susceptible and not susceptible to liquefaction. However, both transition zones occur at a high enough plasticity index that may allow for sampling and lab testing in order to better determine the susceptibility of the soil to liquefaction.

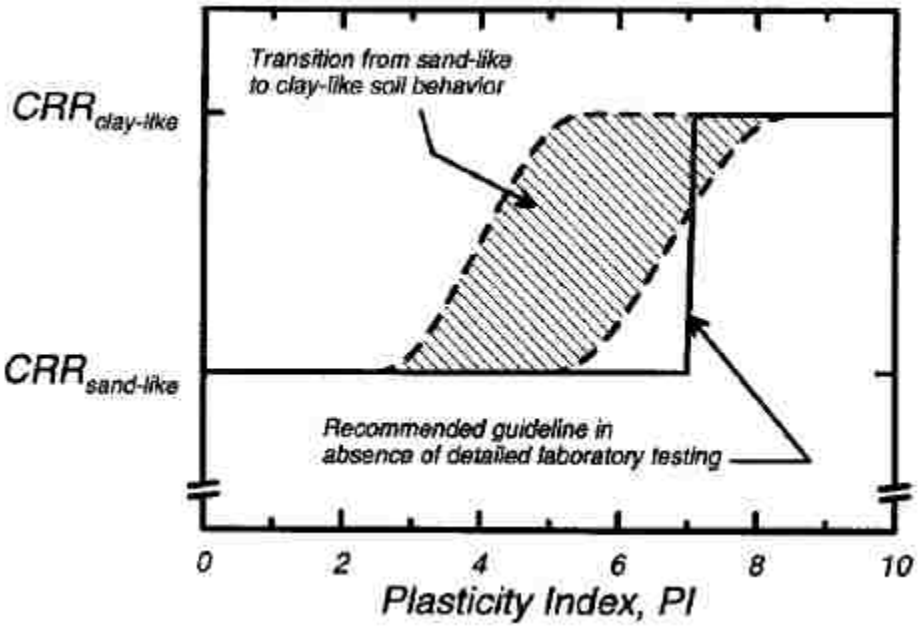

Figure 2.4. Illustration showing the boundaries of "sand-like" and "clay-like" soil based on the plasticity index (Boulanger and Idriss, 2006)

2.4 LIQUEFACTION INITIATION

Liquefaction is the incremental build-up of pore pressure due to static or transient loading of undrained sands/coarse silts that leads to the collapse of the soil skeleton (effective stress reduces to zero). Liquefaction is considered to be initiated at the moment the effective stress reduces to zero (Seed and Lee, 1966). For one to grasp the phenomenon of liquefaction, one must understand when, and how, pore pressure is generated. In order to do so, one must recognize the importance of soil behavior and the mechanics of liquefaction. Whether pore pressure builds up,

and in turn reduces the effective stress, depends on the state of the soil. For undrained conditions, positive pore pressure develops when a soil contracts (decreasing effective stress), and negative pore pressure occurs when a soil dilates (increasing effective stress). Therefore, the state of the soil is important in the consideration of liquefaction initiation.

2.4.1 **Soil Behavior**

The behavior of a soil to loading depends on the initial state that a soil is at prior to loading, i.e. the initial void ratio (density) and initial effective stress. How a soil behaves is related to its initial position relative to the critical state line of the soil. How a soil behaves in the process of approaching the critical state line depends on whether a soil is drained or undrained and whether it is loaded monotonically or cyclically. The latter is important for design considerations and can determine whether short term or long is the critical condition for design.

2.4.1.1 The Critical State

In order to define the critical state of a soil one must know the shearing characteristics of that soil. Carrying out tests on a rubber bag filled with buckshot and sand, while attached to a water filled graduated cylinder to measure volume change, Reynolds (1885) discovered that the volume of a soil changes when being sheared. More specifically, Reynolds found that when sheared, granular materials in a dense state would increase in volume (i.e., the height of water in the graduated cylinder would fall). Reynolds coined this increase in volume due to the shearing of dense granular material as dilatancy (Castro, 1969). More than 50 years later in 1936 Casagrande performed several drained (shear stresses applied slowly allowing water to move in or out of the voids), strain-controlled triaxial tests on both initially loose and initially dense sands (Kramer, 1996). Ultimately, this led Casagrande to discover what he called the critical state line.

2.4.1.1.1 Monotonic Loading Behavior of Sands – Drained

Casagrande's series of drained triaxial tests were monumental in understanding the shearing behavior of sands. Kramer (1996) developed Figure 2.5 in order to illustrate the product of these drained triaxial tests where dense sand behaves like a brittle material undergoing strain softening behavior, while the loose sand exhibits strain hardening behavior. The dense sand undergoes a relatively small initial contraction followed by dilation, whereas the loose sand is purely contractive. The main takeaway from Figure 2.5 is that at large strains a soil approaches the same void ratio (the critical void ratio) whether the soil was initially loose or initially dense, and at this critical void ratio the sample will no longer change in volume upon additional loading. Casagrande (1936) realized that the critical void ratio was unique to the effective confining stress the sand specimen was subjected to. By carrying out drained tests at several different effective confining stresses, Casagrande was able to create what he termed as the critical state line (CSL), also known as the critical void ratio line (CVR), which is shown in Figure 2.6 from Kramer (1996). Figure 2.6 shows a clear visualization of how a soil will behave based upon its initial state (initial void ratio and initial effective confining stress). Soil specimens plotting below the CVR line representing a dense state (point 1) will undergo an initial contraction (slightly moves down along the void ratio axis) followed by dilation (moves up the void ratio axis) until reaching the CVR line. Soil specimens plotting above the CVR line representing a loose state (point 2) will behave purely contractive in nature moving down the void ratio axis until reaching the CVR line. It should be noted that in this case, points 1 and 2 represent sand specimens at different effective confining pressures, however, if each sample had the same effective confining pressure the specimens would approach the same critical void ratio at large strains.

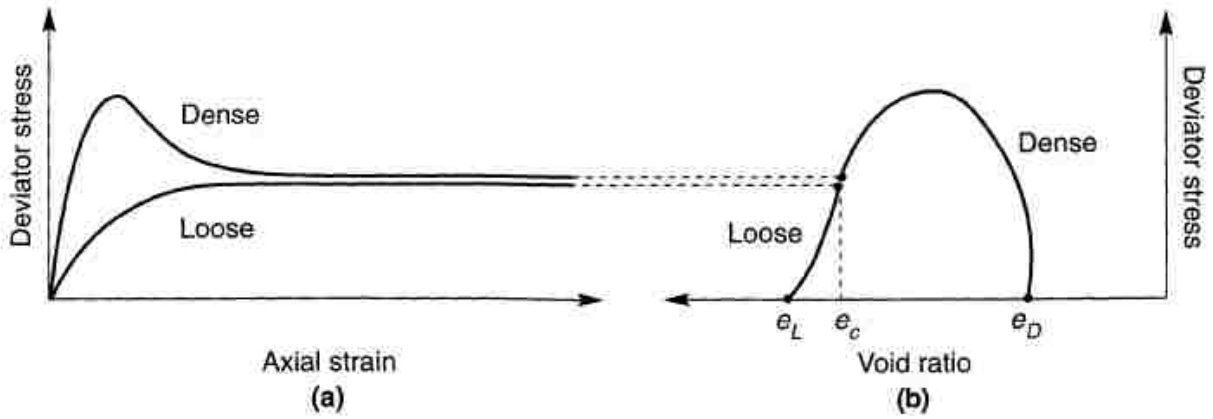

Figure 2.5. Representation from Kramer (1996) depicting the drained triaxial (strain-controlled) behavior of loose and dense sands. (a) Shows the stress-strain behavior of the sands. (b) Illustrates the stress-void ratio curves from the initial state to the critical void ratio at large strains.

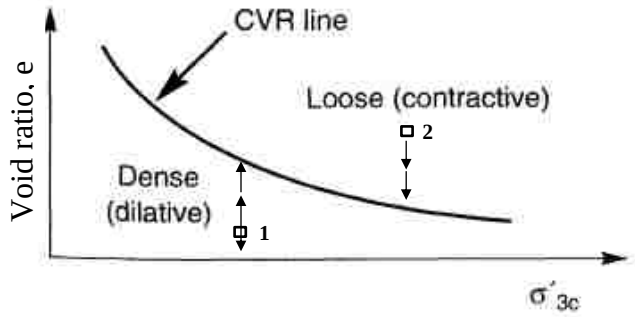

Figure 2.6. Representation of the critical void ratio line modified from Kramer (1996) illustrating how the critical void ratio changes dependent upon the effective confining stress for drained loading.

At the time Casagrande performed the drained triaxial stress, the means were not yet available to perform undrained strain-controlled triaxial tests. Although limited by equipment in 1936, Casagrande was able to qualitatively analyze what would happen for undrained soils based upon his knowledge of soil behavior and the CSL. He predicted that undrained monotonic loading would cause changes in pore pressure based on a soils initial state with respect to the CSL. In other words, Casagrande predicted that soils would remain at a constant volume (void ratio) and the soils effective confining pressure would move to the CSL based upon whether the soil was contractive (positive excess pore pressures) causing a decrease in effective confining stress, or dilative

(negative excess pore pressure) resulting in an increase in effective confining pressure. This prediction was not verified experimentally until Seed and Lee (1967) performed monotonic undrained strain-controlled tests (Kramer, 1996).

2.4.1.1.2 Monotonic Loading Behavior of Sands – Undrained

For many cases in nature, saturated sandy soils can be considered to be in drained conditions because loading is typically applied slowly compared to the rate at which the pore water drains from the voids due to the relatively high permeability of sandy soils. For example, consider a building being constructed on a sandy soil with a water table at the base of the foundation. The rate at which the load is applied (the construction of the building) is much slower than the rate the pore water leaves the voids. Now consider the latter situation, but with the sand trapped between two low permeability confining clay layers. The clay has such a low permeability the pore water cannot escape during the loading of the building. In order to evaluate this type of loading in the laboratory, the engineer would require the need to perform an undrained triaxial test in which the volume of the soil is considered constant due to pore water unable to escape prior to the rapid loading. The characteristics of sandy soils subjected to undrained loading is also important for earthquakes which apply a load rapid enough that most or all of the pore water cannot escape.

In order to study the behavior of sandy soils subjected to undrained loading, Seed and Lee (1967) performed several monotonic undrained strain-controlled triaxial tests and verified Casagrande's predictions experimentally. Undrained tests have the characteristic of a shear stress being applied rapidly prior to the pore water escaping the voids (no volume change). Therefore, because the volume of the soil is constant, undrained loading causes positive or negative pore pressures to develop due to the tendency of the soil to contract or dilate when being sheared. An undrained soil in a loose state (plotting above the CVR line in Figure 2.6) would have the tendency

to contract when subjected to loading thus causing positive excess pore pressure which in turn cause a reduction in effective confining stress. The same sandy soil subjected to undrained loading conditions in a dense state (plotting below the CVR line) would have the tendency to dilate thus causing negative excess pore pressure which in turn leads to the increase in effective confining stress.

Figure 2.7 (after Kramer and Stewart, unpublished manuscript) shows the idealized behavior of sands subjected to an undrained triaxial test at a constant void ratio (density), but different initial effective stresses. Specimen 1 is above the CVR line and has a high initial effective confining pressure (thus is considered loose) and has an inherent tendency to contract when sheared. Because undrained tests are constant volume tests this tendency for the soil specimen to contract induces a positive pore pressure as shown in (c). This positive pore pressure causes specimen 1 to move left on the e – p' plot shown in (d) as the effective stress is reduced. Soils considered loose (above the CVR line) exhibit strain softening behavior when undrained shearing takes place where the soil specimen reaches a maximum strength at a relatively low shear strain and then undergoes softening behavior as the shear strain increases quickly once passing the peak shear strength of the soil until reaching a constant state. Therefore, the stress path for specimen 1 in (b) reaches a peak deviator stress and then quickly decreases to the steady state point. In other words specimen 1 exhibits flow liquefaction behavior (Section 2.1.1). Specimen 3 has a low confining pressure and because it lies below the CVR line in (d) it is considered to be dense. Dense soils subjected to undrained shearing undergo an initial contraction followed by dilation until reaching the CVR line. Therefore, specimen 3 in (c) initially has a small positive excess pore pressure followed by negative pore pressure as the soil continuously dilates as the shear strain increases until reaching a steady state. The negative excess pore pressure causes the effective

confining stress to increase and thus specimen 3 moves to the right in (d) until reaching the CVR line. Soils considered dense (specimen 3) subjected to undrained shearing exhibit strain hardening behavior where the strength of the soil increases as the shear strain increases. Specimen 2 is slightly above the CVR line and thus is considered loose although here (since it is so close to the CVR line) can be considered to be at an intermediate density. Initially, specimen 2 behaves similar to that of specimen 1 as they both are above the CVR line and will have a tendency to contract. Specimen 2 has an initial increase in positive pore pressure, however, it is lower in magnitude than that of specimen 1 because specimen 1 is more contractive than specimen 2. Specimen 2 behaves similar to specimen 1 initially undergoing strain softening behavior until reaching a point of phase transformation where the soil changes from being contractive to dilative and thus transitions from strain softening to strain hardening behavior until reaching the steady state point. This point of phase transformation is the transition point between contractive and dilative tendency where the soil for an instant in time is neither contractive nor dilative. The phase transformation point was first characterized by Ishihara, Tatsuoka, and Yasuda (1975) and Ishihara (1993). It should be noted that because specimens 1, 2, and 3 in Figure 2.7 are undrained and at the same initial void ratio, the samples will all have the same strength and effective confining pressure at large strains as can be seen from the overlapping paths of each specimen at large strains in (a) and the single black dot shown in (d). It is important to note that samples initially at the same effective confining pressure that undergo undrained shearing will not end at the same void ratio as can be viewed in Figure 2.8. On the other hand, if initial sample locations shown in Figure 2.8 (d) were to go undergo drained shearing, then the samples would move vertically in e – p’ space similar to Figure 2.6 and would therefore would approach the same final void ratio reaching the CVR line at the same point.

Figure 2.9 developed by Kramer (1996) is an excellent representation of soil behavior due to drained and undrained shearing.

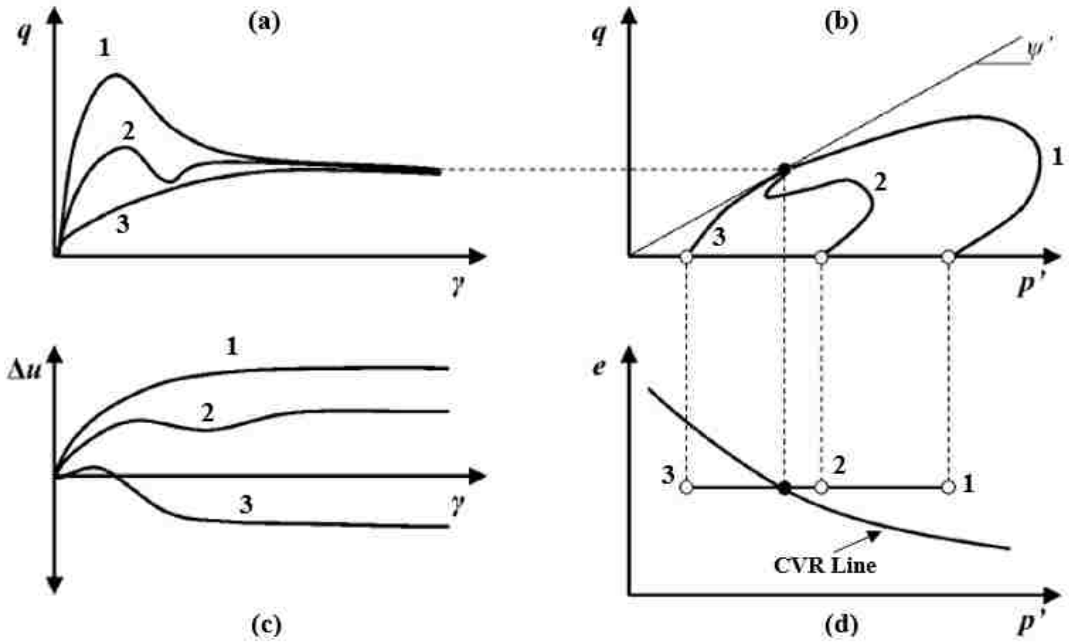

Figure 2.7. Representation of ideal soil behavior for three specimens undergoing undrained triaxial testing at the same initial void ratio (after Kramer and Stewart, unpublished manuscript).

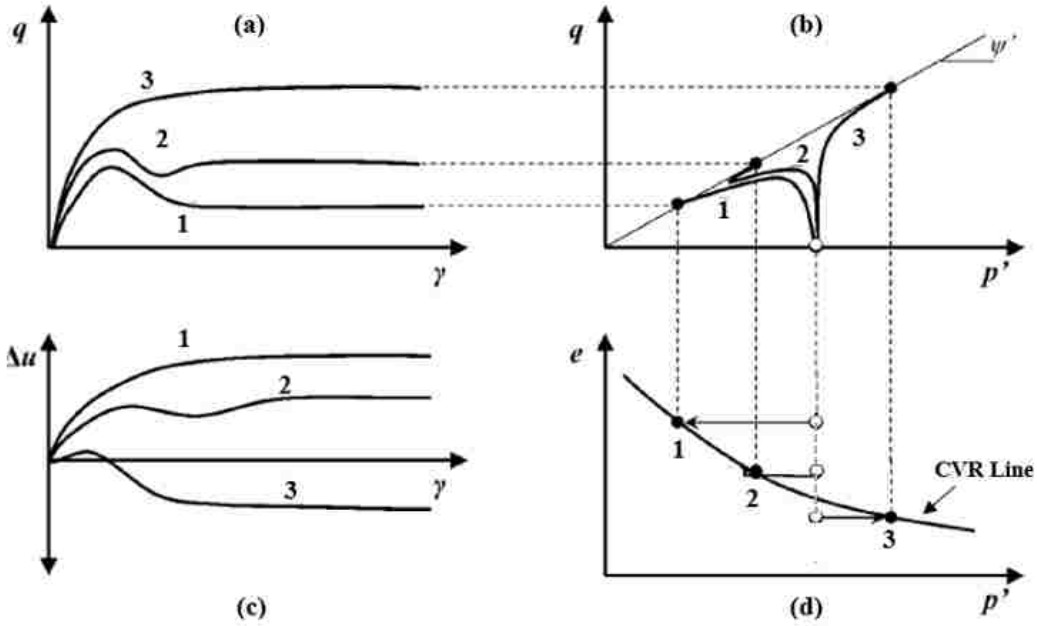

Figure 2.8. Representation of ideal soil behavior for three specimens undergoing undrained triaxial testing at the same initial effective confining pressure (after Kramer and Stewart, unpublished manuscript).

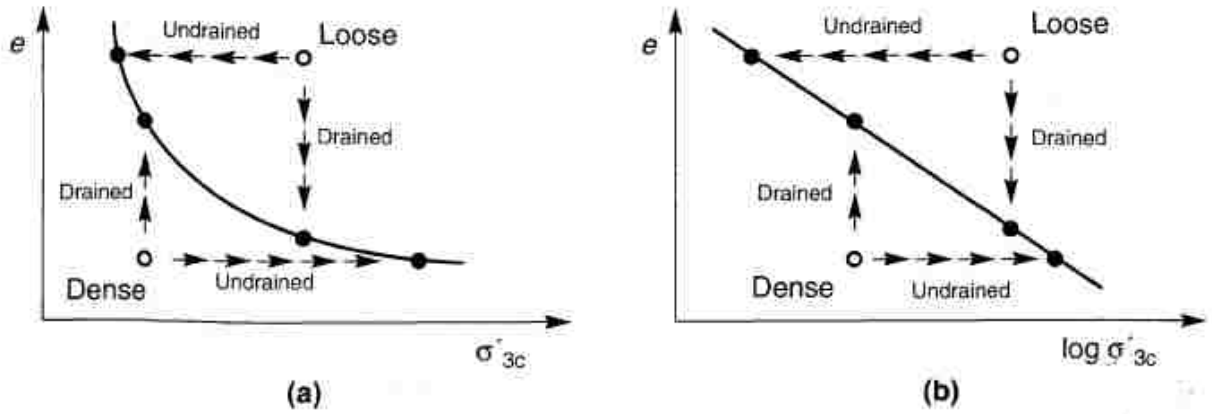

Figure 2.9. Representation of drained and undrained soil behavior based on the initial state of the soil with respect to the CVR line for (a) arithmetic and (b) logarithmic effective confining pressure abscissas from Kramer (1996).

After performing undrained triaxial tests on the Toyoura sand prepared by the moist deposition method, Ishihara (1993) emphasized that a phase transformation point occurs typically in loose sands with a high effective confining stress similar to the position of specimen 2 in Figure 2.7 (d). Ishihara also found that soils that were not at an intermediate density, considerably loose (specimen 1) or considerably dense (specimen 3), did not undergo a phase transformation point at intermediate strains and instead the state of phase transformation does not occur until reaching the steady state point. The steady state that all of the latter specimens reach at large shear strain levels represents the point where the specimens are at a constant shearing resistance, constant effective stress, constant void ratio (volume), and constant strain rate which was described as the steady state of deformation by Poulos (1981).

Upon examining several case histories of liquefaction induced by earthquake shaking or monotonic loading, Castro and Poulos (1977) emphasized that, for loose sands such as specimen 1 in Figure 2.7, the loss in shear strength is not accompanied by regaining that strength, but instead by a permanent loss in shear strength. One of the case histories Castro and Poulos examined was

the failure of Fort Peck dam in Montana in 1938 which exhibited a static liquefaction flow failure during the placement of rip-rap along the upstream face of the dam.

Fort Peck dam was created via hydraulic filling. Hydraulic filling placement of the dam material led to the core of the dam consisting of fine-grained particles that transition to larger particles at the extent of the dam due to the nature of hydraulic filling. On September 22, 1938 the upstream face of Fort Peck dam underwent a static liquefaction flow failure during the placement of rip rap. A two-dimensional schematic illustration of the dam is shown in Figure 2.10. The static liquefaction flow failure was not accounted for in the design of the dam because there were only drained triaxial tests available to perform at the time and based on these drained tests the soil states relative to the CVR line exhibit dilative behavior as the sample specimens were considered dense (below the CVR line in Figure 2.11). The latter was detrimental because soil initial states plotting above the CVR line were considered to be susceptible to liquefaction and soil initial states plotting below the CVR line were considered to not be susceptible to liquefaction. Therefore, because drained triaxial tests were performed, designers prior to the construction of Fort Peck dam likely thought the soil would exhibit dilative behavior as a result to loading. The conditions at the site were actually undrained during the filling of the dam and thus the undrained CVR line would have been below the drained CVR line as shown in Figure 2.11. Based on the hypothetical sample specimen locations on the $e - \log\sigma'_{3c}$ plot shown in Figure 2.11, one can see the soil would actually exhibit contractive behavior because the soils initial states were loose (above the undrained CVR line). The weight from the upstream slope caused a large enough shear stress on the soil in the dam and thus when the static shear stress on the upstream face of the dam surpassed the shearing resistance of the soil the dam exhibited a static liquefaction flow failure. The equipment/resources necessary to perform undrained tests had not been developed at the time of the construction of Fort

Peck dam. Had the resources been available, the engineers may have recognized this problem and designed the dam with flatter slopes (thus reducing the static shear stress). Therefore, distinguishing between drained and undrained behavior is essential in design.

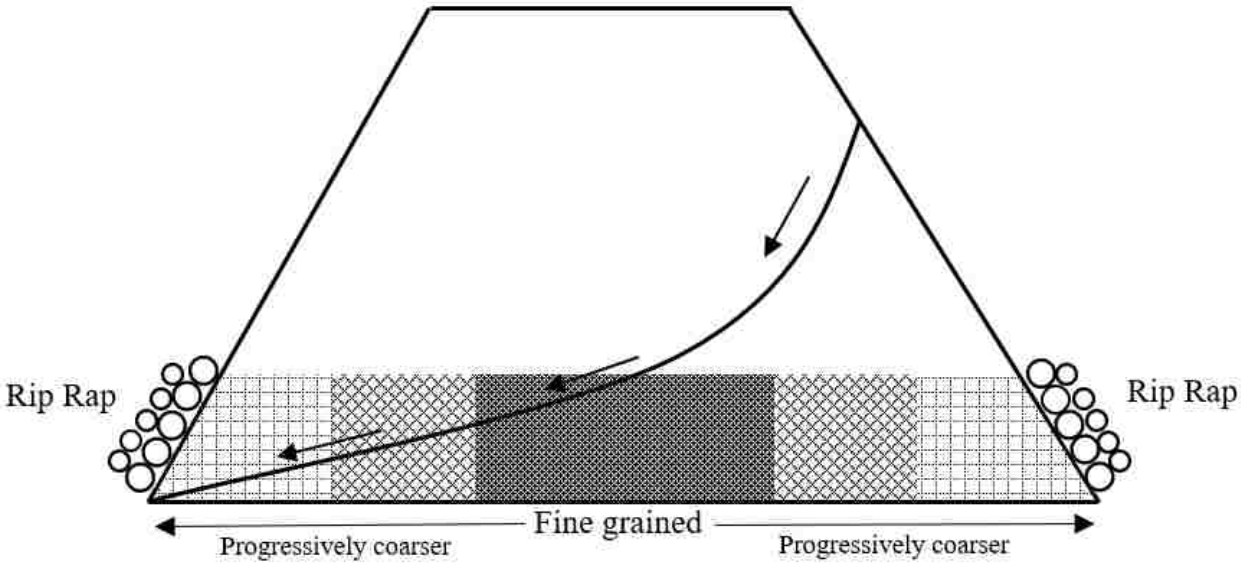

Figure 2.10. Two-Dimensional schematic representation of Fort Peck dam showing finer material at the center of the dam and getting progressively coarser towards the slopes (hydraulic filling) along with the rip rap on the slopes of the dam and an example of the failure surface.

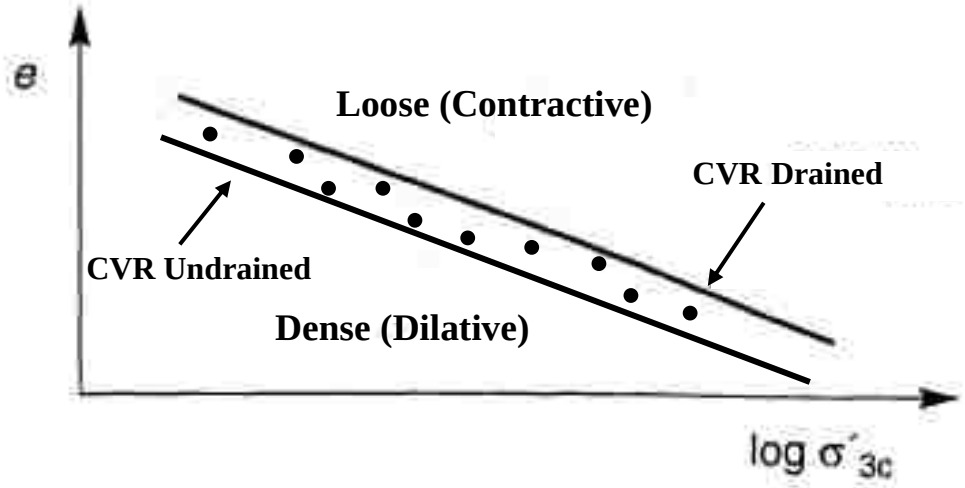

Figure 2.11. Semi-log plot of CVR line for drained and undrained triaxial testing modified from Kramer (1996). The black dots represent soils specimens tested.

2.4.1.1.3 State Parameter

Upon going through the monotonic drained and undrained behavior of sands, one can see that the soil behavior depends not only on the density (void ratio) of the soil, but also the effective confining pressure the soil specimen is subjected to. Therefore, the state of a soil depends on both the void ratio and the effective confining pressure. Been and Jefferies (1985) created the state parameter attempting to better characterize soil behavior. Where the state parameter represents the distance a certain state of soil is vertically from the steady-state line as shown in Equation 2.1

$$\psi = e - e_{ss} \tag{2.1}$$

where ψ is the state parameter, e is the void ratio of the soil, and e_{ss} is the void ratio at the steady state. Therefore, when the value of the state parameter is positive the soil is in a loose state (contractive) and when negative the soil is in a dense state (dilative) as shown in Figure 2.12**.**

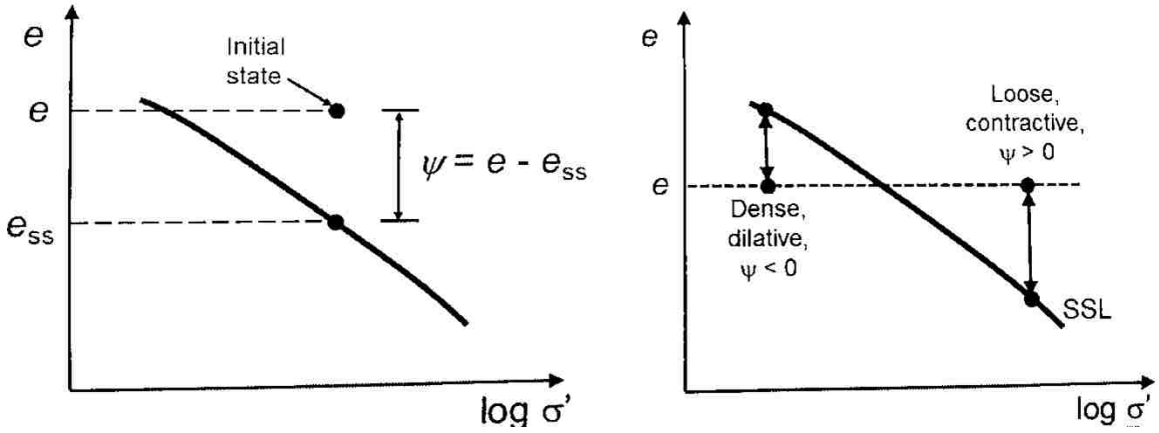

Figure 2.12. e – log σ' plot describing state parameter values with respect to the steady state line (after Kramer, unpublished manuscript).

Been and Jefferies predicted that soils with the same state parameter value would have similar behavior. Due to the steady-state not occurring until large strains (which may not be attainable or feasible) the state parameter is difficult to measure in practice. As an alternative to the state parameter that is easier to calculate, Boulanger (2003) developed the relative state parameter index based primarily on the work of Been and Jefferies (1985), Bolton (1986) and Konrad (1998). The

relative state parameter index conforms with the steady state and state parameter concepts and can be used to determine the potential volume change of soils. The relative state parameter index is shown in Equation 2.2

$$\xi_R = \frac{R}{Q - \ln(\frac{100p'}{p_a})} - D_R \quad (2.2)$$

where ξ_R is the relative state parameter index, Q and R are empirical constants, p' is the mean effective stress in kPa, p_a is the atmospheric pressure in kPa, and D_R is the relative density of the soil. Q and R can be found from laboratory testing, however, Bolton (1986) performed a series of laboratory tests and found values of Q = 10 and R = 1 represent the data well for different types of clean silica sands (Salgado, 2008). Table 2.1 from Salgado (2008) shows values of Q and R for Ottawa sand with differing percent of fines content. Because D_R is related to the void ratio, and p' changes based on pore pressure generation, the relative state parameter index can provide insight into soil behavior for both drained and undrained conditions. Therefore, one could conduct laboratory tests on soil specimens in order to measure potential volume changes and pore pressure generation that a soil specimen would undergo when subjected to drained and undrained loading respectively.

Table 2.1. Values of empirical constants Q and R for Ottawa sand with differing fines contents and soil type (after Salgado, 2008).

Fines (%)	Best fit		
	Q	R	coefficient of correlation (r^2)
0	9.9	0.86	0.95
5 (silt)	9.1	-0.33	0.99
10 (silt)	9.3	-0.30	0.98
2 (clay)	12.1	2.78	0.96
5 (clay)	11.7	3.17	0.95
10 (clay)	10.9	3.43	0.80

2.4.1.1.4 Cyclic Loading Behavior of Sands

Cyclic loading typically occurs at a rate that does not allow pore pressure to dissipate when soils are subjected to it. For the remainder of this thesis, cyclic loading (such as the nature of earthquake loading) will be assumed to be applied at a rate that does not allow a saturated soil to dissipate water during loading. In order to understand the nature of cyclic loading, one can first consider the case of harmonic loading using a cyclic simple shear test. Figure 2.13 **(**Kramer and Stewart, unpublished manuscript) shows the shear stress-shear strain and shear stress-vertical effective stress plots obtained when using a cyclic simple shear device to subject a sand specimen to a harmonic horizontal shear stress (to idealize harmonic cyclic loading) where the soil is dry (therefore no change in effective stress) and assumed to not undergo degradation during each loading cycle. The loading reaches a constant maximum shear stress at each ¼ and ¾ cycle represented by points A through H. At small strains the soil can be considered to have linear behavior (where the shear modulus is at its maximum), however, soils behave non-linear as the shear stress increases causing the tangent shear modulus to decrease as the shear strain increases at a faster rate than the shear stress. Figure 2.13 (a) shows the latter behavior of the soil during the first ¼ cycle of loading. Upon reaching the maximum shear stress at point A, the loading is reversed in the other direction. At this point of stress reversal, the shear strain also reverses direction (from positive towards negative). Because the soil is behaving non-linear the soil does not follow the same path as initially and once again as the shear stress reaches point B the rate of shear strain to shear stress increases (the shear modulus reduces up until the point of stress reversal). Because the soil in this idealized case does not degrade, point C will be in the same location as point A. The soil will continue to follow this path so points A, C, E, and G will correspond to the same positive maximum shear strain, and points B, D, F, and H will correspond

to the same negative maximum shear strain. The latter points of maximum positive/negative shear strain will also occur at the same vertical effective stress for a dry soil.

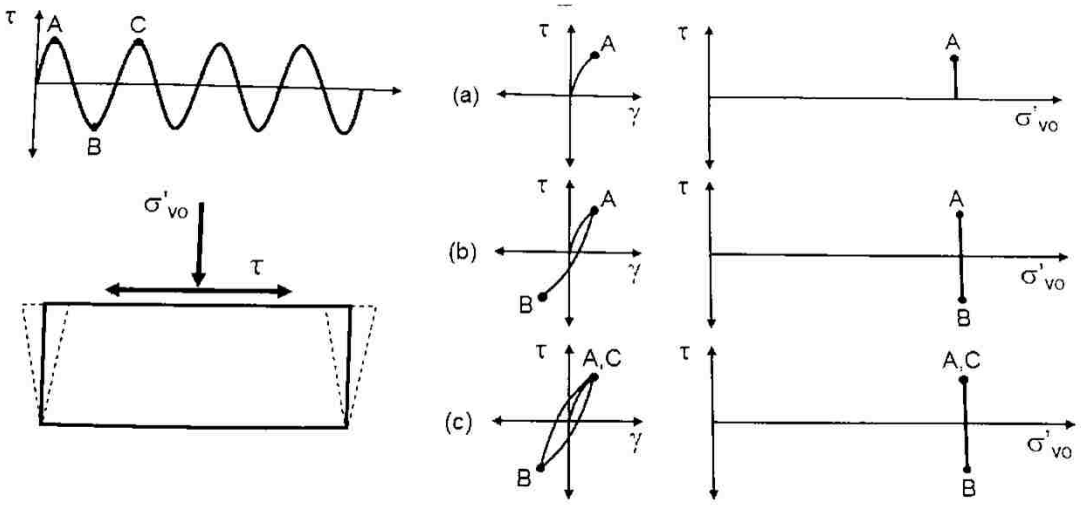

Figure 2.13. Non-degrading soil behavior to a harmonically applied horizontal shear stress using a cyclic simple shear device where (a) is at ¼ cycle, (b) ¾ cycle, and (c) 1 and ¼ cycle (Kramer and Stewart, unpublished manuscript).

If the soil were to degrade during each cycle of loading points A, C, E, and G would not correspond to the same positive maximum shear strain, point C would be at a higher shear strain than point C, point E at a higher shear strain than point C, and point G at a higher shear strain than point E. The same would be true for points B, D, F, and H where point B would have the lowest shear strain and point H would have the highest shear strain. The latter is shown in Figure 2.14 (Kramer and Stewart, unpublished manuscript) where (a) shows the response of a dry soil (no change in effective stress) and (b) shows the response of an undrained soil developing pore pressure thus reducing the vertical effective stress.

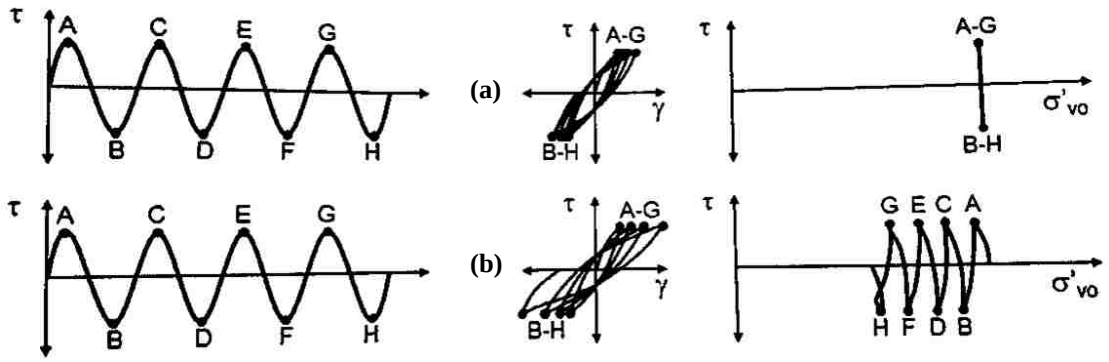

Figure 2.14. Degradation soil behavior to a harmonically applied horizontal shear stress using a cyclic simple shear device where the soil is drained and at a constant effective stress in (a) and (b) is undrained and therefore pore pressure generation takes places and reduced the vertical effective stress (Kramer and Stewart, unpublished manuscript).

2.4.1.1.4.1 Cyclic Loading Behavior of Sands – Drained

Drained cyclic loading of sands will not alter the effective stress because there is no pore pressure generation, however, there is volume change. Similar to drained monotonic loading of sands, whether a soil is loose or dense it will undergo initial contraction as depicted in Figure 2.6. Figure 2.15 (after Gao and Zhao, 2015) shows the drained cyclic loading behavior of Toyoura sand initially in a loose state subjected to constant amplitude and stress controlled cyclic shear loading. First, one can note that the contractiveness of the sand during each quarter cycle of loading progressively decreases as the load nears stress reversal. The latter is similar to pulling a rubber band, when you initially stretch the rubber band it's relatively easy, but progressively becomes harder to pull and requires more force to move the same distance (assuming the rubber band does not rupture) as it is stretched. Much like the rubber band, the soil becomes progressively less contractive from the start to the end of each quarter cycle of loading. The contraction of the soil causes the volume to decrease (void space to reduce) as the sand particles re-align as they are sheared. The rate the sand particles re-align and fill void space during shearing decreases during each loading cycle (as shown by the large changes in volumetric strain during the early loading cycles followed by smaller changes in volumetric strain in the subsequent cycles). One will also

notice as contraction continues, and the sand particles fill more of the available void space, the shear strain decreases with each subsequent cycle. The latter makes sense conceptually because "there is less room" for shear strains to develop (i.e., the resisting forces of the surrounding particles prevent further shear strain). Upon approaching the critical state of the sand, the soil begins to experience phase transformation behavior and undergoes episodes of dilation (as the resisting forces surrounding particles start to give way). Dilation begins to occur after approximately three cycles of loading, where the soil now begins to increase in volume when nearing stress reversal, however the soil specimen continues to have an increase in volumetric strain per cycle. Volumetric strain increases with each cycle until reaching a limiting point where the soil will follow the same path of contraction and dilation continuously for each cycle. Although unsaturated sands cannot liquefy, the highly contractive nature of loose sands (depending on their position relative to the steady state line) can cause severe damage to structures via settlement of the ground surface.

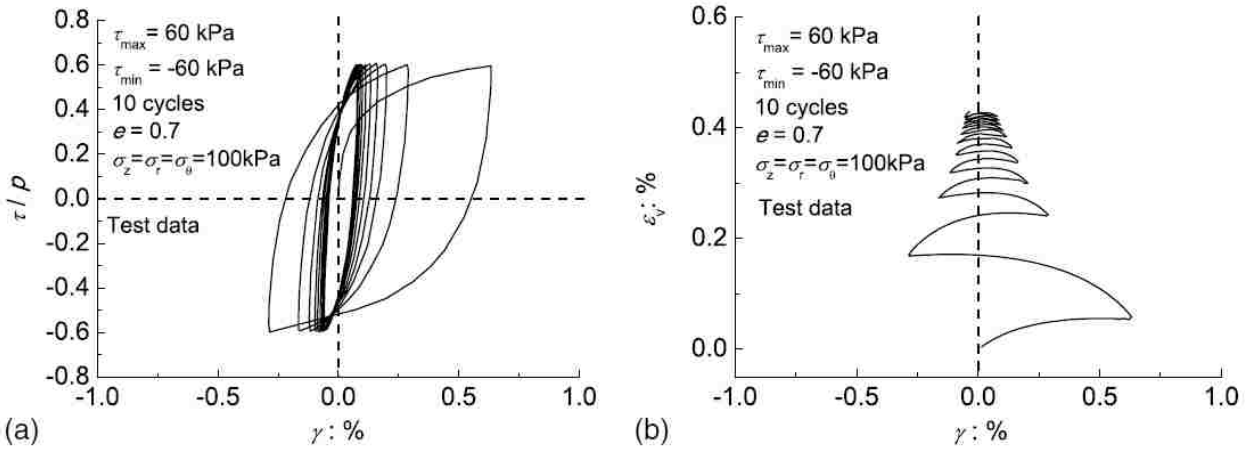

Figure 2.15. Drained cyclic loading behavior of the Toyoura sand initially in a loose state subjected to constant amplitude and stress controlled cyclic shear loading (after Gao and Zhao, 2015).

2.4.1.1.4.2 Cyclic Loading Behavior of Sands – Undrained

Similar to drained cyclic loading, undrained cyclic loading causes the sand to contract or dilate, however, because the soil is undrained (pore water cannot escape during loading) the volume of the soil does not change. Because the volume of the soil does not change stress applied is taken by the pore water instead of the soil grains, therefore, the pore pressure increases and applies a pressure to the surrounding soil skeleton thus causing the effective stress to reduce. Idriss and Boulanger (2008) created Figure 2.16 which explains this concept well. Before describing this figure, one should note that the curve shown is the compression curve and not the critical state line. Drained loading allows for volume change as indicated from points A to B in Figure 2.16, however, this volume change cannot occur when the void space is completely filled with water. Therefore, instead of changing in volume, the tendency of this idealized loose sand to contract instead applies the load to the pore water causing the generation of pore pressure, and thus, the reduction in effective stress as is shown from point A to C. Idriss and Boulanger (2008) describe this process as the cyclic loading causing plastic volumetric contraction of the sand from point A to B if the soil were drained, although it's undrained, therefore, they show the dashed line from point B to C to represent the plastic volumetric strain being countered by expansion due to elastic rebound of the sand skeleton from the pore pressure causing the reduction in effective stress. It should be noted that if the cyclic loading were to bring the soil to point C, liquefaction would not occur as the effective stress has not been reduced to zero (the origin on this plot).

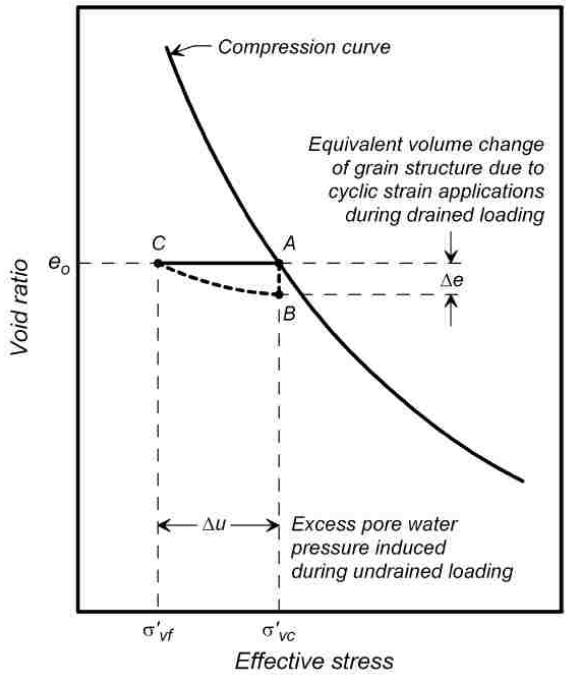

Figure 2.16. Illustration of pore pressure generation occurring during undrained cyclic loading of an idealized loose sand (Idriss and Boulanger, 2008).

In order to clearly show the behavior of a saturated sand to undrained loading throughout each cycle of loading, Kramer and Stewart (unpublished manuscript) created Figure 2.17 illustrating undrained constant-amplitude stress controlled simple cyclic shear loading on a sand. Figure 2.17 shows (a) the shear stress versus shear strain, (b) the shear stress versus the normalized vertical effective stress, (c) the number of cycles versus shear strain, and (d) the number of cycles versus normalized vertical effective stress. Note (a) through (d) all show the number of cycles with the black dots and associated number. First, one should note that the first 20 cycles of loading cause minimal shear strain as shown in (a) and (c). Although the shear strain for the first 20 cycles stays relatively small, the increments of pore pressure generated each cycle add up to a large change in the normalized vertical effective stress which is 40% of the value prior to loading as shown in (b) and (d). Because the strength of the soil is directly related to the vertical effective stress, one can note that the strength of the soil continually decreases at a rate much different than

the soil stiffness. The soil is relatively stiff during the first 20 cycles of loading as given by the shear strain in (a) and (c), however, after the 20th cycle the soil begins to lose its stiffness relatively quickly (as the shear strain increases the soil stiffness decreases) as the soil approaches the phase transformation line during the 21st cycle. Upon reaching the phase transformation line as shown in (b), the soil dilates as the stress path moves up along the phase transformation line followed by rather large contractions until reaching the phase transformation line after another ½ cycle of loading. After the 22nd cycle of loading, the soil appears to reach zero vertical effective stress and then continually follows the same stress path where the soil strongly contracts and then dilates reaching zero vertical effective stress twice during each loading cycle. Seed and Lee (1966) referred to this point of zero effective stress as initial liquefaction. It should be noted once reaching initial liquefaction the soil stress path as shown in (b) continues to repeat, however, (a) and (c) clearly shows the shear strain of the soil continuing to increase during each cycle of loading. Therefore, the soil reaches a state of initial liquefaction twice during each loading cycle which causes continuous increases in the shear strain. In other words, the cyclic shear stress (loading) exceeds the steady-state strength of the soil momentarily causing deformation, hence this is termed cyclic liquefaction.

Initial liquefaction is also often determined via the pore pressure ratio given in Equation 2.3 as

$$r_u = \frac{\Delta u}{\sigma'_{vo}} \tag{2.3}$$

where r_u is the pore pressure ratio, Δu the change in pore pressure, and σ'_{vo} the initial effective vertical stress. As can be noted in (d) of Figure 2.17 the normalized vertical effective stress is equal to one minus the value of the pore pressure ratio. Therefore, initial liquefaction occurs when r_u is equal to one, which is shown where the normalized vertical effective stress is zero in (d). Because

understanding the soil mechanics point of view is critical to understanding liquefaction, it will be noted again that the stiffness of the soil behaves differently than the strength. Figure 2.17 (b) shows that the strength of the soil decreases fairly consistently, whereas, the stiffness degrades relatively little until approaching initial liquefaction (r_u is equal to one) where the stiffness rapidly decreases as shown in (a) with the large increases in shear strain and the elongated (flattening) of the stress strain curve. For example, the soil beneath a building may undergo a large loss in shear strength during an earthquake, however, have little to no displacement (thus little damage) because the stiffness of the soil does not decrease quickly until nearing initial liquefaction. Therefore, assuming the soil was subjected to the conditions shown in Figure 2.17, but with a loading only lasting 19 cycles, the soil beneath the building would have lost a good portion of its shear strength, but only little displacement would have occurred. Once the cyclic loading stopped after 19 cycles, the pore pressure would then start to dissipate and the soil would begin to regain its strength.

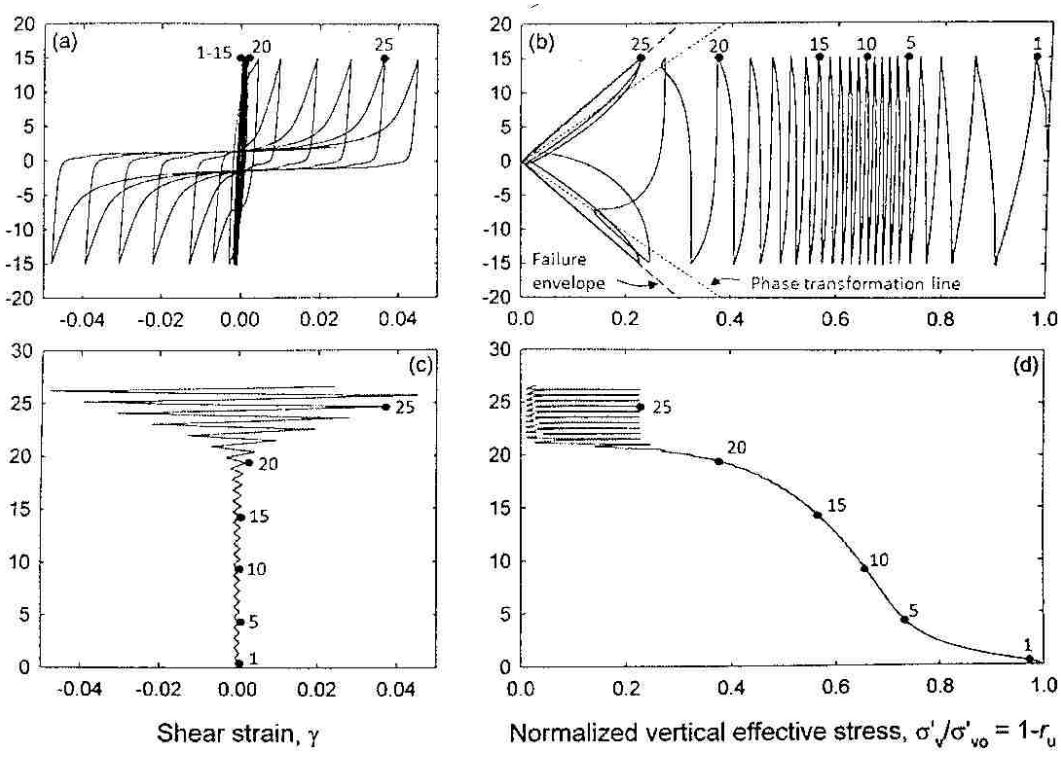

Figure 2.17. Undrained behavior of a saturated sand undergoing constant-amplitude cyclic simple shear testing (after Kramer, unpublished manuscript).

2.4.2 Analysis of Liquefaction Potential

After considering the undrained monotonic and cyclic behavior of sands, the potential of the development of liquefaction should be considered for flow liquefaction and cyclic liquefaction. Although there are key differences between the two, both can cause severe damage to natural and man-made structures. The development of a soil undergoing flow liquefaction and cyclic liquefaction will be discussed followed by the factors affecting liquefaction potential.

2.4.2.1 Flow Liquefaction

Flow liquefaction occurs when the initial shear stress on a soil exceeds the steady state shear strength. Flow liquefaction can occur due to monotonic or cyclic loading and the initiation of flow liquefaction can be defined by the three-dimensional flow liquefaction surface (FLS). Figure 2.18 from Kramer (1996) shows examples of stress path behavior for stress controlled triaxial tests of anisotropically consolidated loose saturated sand specimens reaching the FLS by monotonic and cyclic loading. Both loading regimes start at point A, however, the stress path taken to the FLS differs. Monotonic loading behaves as a strain-softening material where the soil contracts (causing pore pressure generation and the reduction in effective stress), reaches a peak shear strength (point B), and then undergoes a large amount of strain as the soil quickly fails to the steady state point C. Similarly, cyclic loading causes pore pressure generation reducing the effective stress, however, the stress path moves in a more horizontal overall fashion towards the FLS until reaching point D where the soil begins to undergo a large amount of strain at a fast rate to the steady state. Therefore, the same soil with different loading behavior may reach the FLS surface at different locations along this surface depending on the soils initial state and the stress path induced by undrained loading. One should also keep in mind that soils under different initial conditions (e.g. soils subjected to different initial shear stresses), would require different

magnitude undrained loading to reach the FLS (Kramer and Seed, 1988). Therefore, if two soils were subjected to the same loading, but one had a higher initial shear stress, one may encounter only one of the soils reaching the FLS and failing, whereas, the other soil subjected to the same loading may have only experienced a relatively small strain compared to the soil at a high initial shear stress.

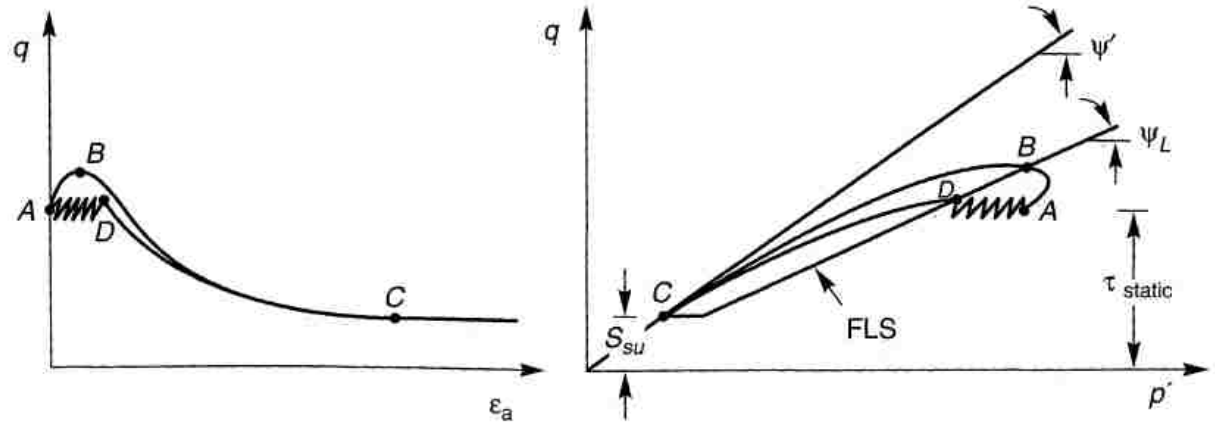

Figure 2.18. Monotonic and cyclic loading stress path behavior of anisotropically saturated loose sand specimens subjected to stress controlled triaxial tests (Kramer, 1996).

The FLS was first called the "CSR plane" by Vaid, Chern, & Tumi (1985) which was defined as the intersection of the critical consolidation stress in a 3-dimensional sand behavior diagram (e-σ'-τ space) with the "CSR line," where the CSR line was the line (q'-p' stress space) where CSR values above the CSR line would cause flow liquefaction to occur and CSR values below this line would not cause flow liquefaction to occur (unless an undrained response brought the state of the soil to the CSR line). Vaid et al. further discussed that the lower bound of the CSR plane, which they termed the "critical consolidation stress" marks the surface where if the state of a soil lies below this surface, cyclic loading cannot cause flow liquefaction. Current terminology generally represents the latter description by Vaid et al. as the FLS where initial soil states below

the steady state point will not undergo flow liquefaction due to monotonic or cyclic loading. If the state of a soil reaches the FLS (the state of soil in which the shear strength is less than the static shear stress applied to the soil) the soil will have reached the "point of no return" where flow liquefaction will occur. Figure 2.19, modified from Kramer (1996), shows the flow liquefaction surface in (q'-p' stress space) with the area of soils susceptible to flow liquefaction shaded. Below the stress at the steady state the soil is susceptible to cyclic liquefaction.

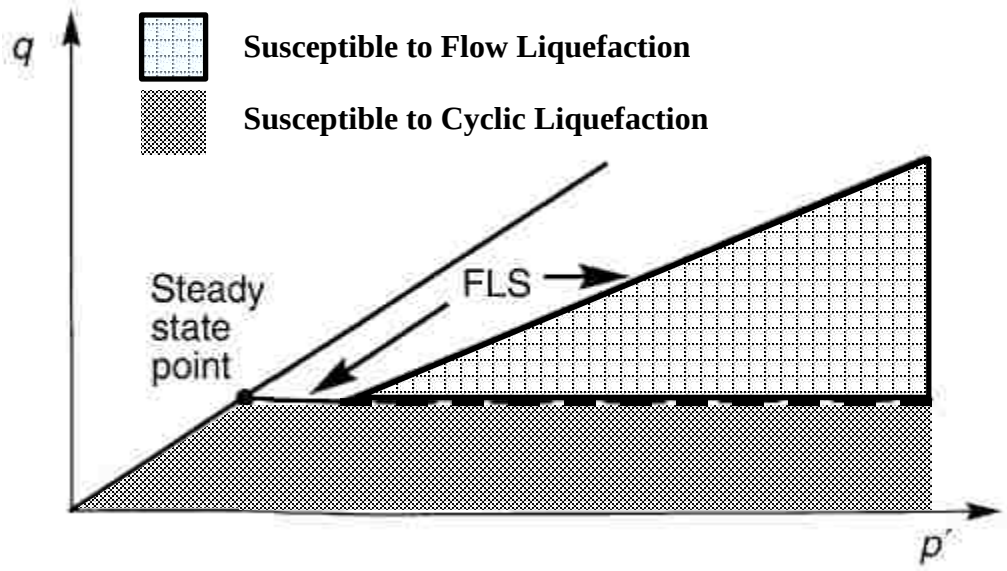

Figure 2.19. Liquefaction susceptibility for flow liquefaction and cyclic liquefaction (Modified from Kramer, 1996).

2.4.2.2 Cyclic Liquefaction

Cyclic liquefaction occurs when a soils steady state strength (shear strength of the liquefied soil) is greater than the initial static shear stress. Therefore, a soil is susceptible to flow liquefaction below the steady state point shown in Figure 2.19. Cyclic liquefaction causes deformations that occur incrementally as the shear strength of the soil is momentarily exceeded over multiple cycles of loading. It is important to note that cyclic loading does not necessarily mean cyclic liquefaction, monotonic and cyclic loading can cause flow liquefaction, however, only cyclic loading can cause cyclic liquefaction. It is also important to note that the initiation of liquefaction has been defined

in multiple ways. Generally, the initiation of liquefaction is taken to be when the effective stress is reduced to zero (Seed and Lee, 1966), i.e., when the pore pressure ratio (see Equation 2.3) reaches a value of one, however, other methods are based on a threshold shear strain value such as Ishihara (1993). In this thesis, the initiation of liquefaction will be taken as when the pore pressure ratio reaches a value of one, and soils experiencing shear strains/deformations, but not reaching a pore pressure ratio of one, will be termed cyclic mobility. For example, Figure 2.20 from Kramer (1996) shows three stress paths of soils under different initial shear stress and different cyclic shear stresses where two of the cases are exhibiting cyclic mobility and one cyclic liquefaction.

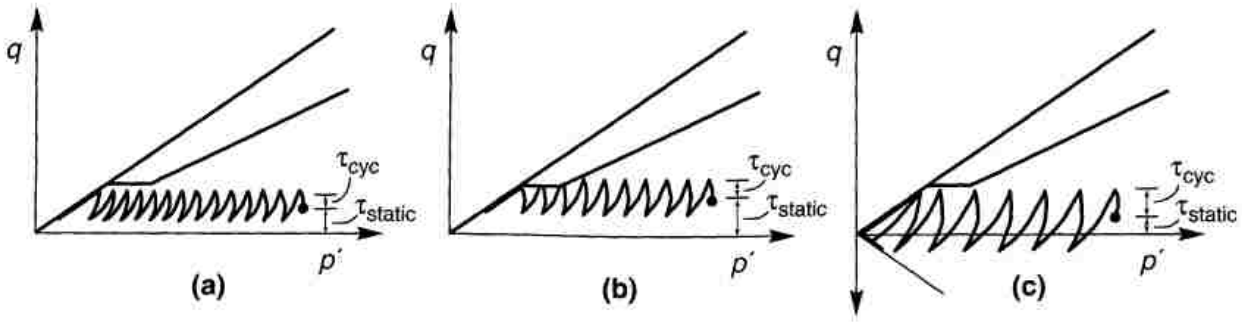

Figure 2.20. Stress paths for soils with different initial shear stress and cyclic shear stress utilized to show the difference between cyclic mobility and cyclic liquefaction (Kramer, 1996).

Cases (a) and (b) presented in Figure 2.20 represent cyclic mobility, whereas case (c) illustrates cyclic liquefaction. Case (a) shows a cyclically loaded soil that stays below the steady state strength. Upon reaching the drained failure envelope the soil in case (a) will dilate and contract along the same path without ever reaching an effective stress of zero. Because of this the soil did not undergo cyclic liquefaction, but it did experience cyclic mobility where permanent strains developed throughout each loading cycle. These permanent strains become much larger when the state of stress is near an effective stress of zero because the soil stiffness decreases dramatically (see Section 2.4.1.1.4.2**)** when approaching liquefaction initiation. Case (b) also does not reach an effective stress value of zero, however, differs from the soil in (a) because the state

of stress of the soil in (b) briefly exceeds the steady state strength during multiple cycles of loading. Because the soil in (b) briefly exceeds the steady state strength, large permanent strains may occur in these brief moments of exceedance. Therefore, the soil in case (b) will not only obtain cyclic strains as those discussed for the soil in (a), but also may experience large permanent strains during the moments the steady state strength is exceeded. The soil in case (c), does reach the state of initial liquefaction because the effective stress does reach a value of zero. In fact, no soil will undergo cyclic liquefaction unless stress reversals occur as shown in case (c) (Kramer, 1996). In order for stress reversals to occur, the cyclic shear stress must be larger than the initial static shear stress as presented in case (c) where the stress path crosses the axis. Therefore, permanent strains will accumulate throughout loading for the soil in case (c), similar to the soil in case (a), however, the soil in (c) will also undergo permanent strains due to liquefaction of the soil. Kramer (1996) also illustrated in Figure 2.20 that fewer cycles of loading were required for the soil in case (c) because soils undergoing stress reversals have larger increases in pore pressure based on the work of Dobry et al. (1982) whom inferred the latter when developing a simplified cyclic strain approach for liquefaction analysis.

2.4.2.2.1 Factors Affecting the Potential of Cyclic Liquefaction

Many factors affect the initiation of cyclic liquefaction including the load amplitude, soil density, the plasticity of the fines, initial shear stress, and initial effective stress. These factors are practically the same as described by Seed and Harder (1990) in regards to impacting the equivalent uniform cyclic stress ratio required to initiate liquefaction. In order to clearly show the effects of each of these factors, stress controlled cyclic simple shear tests are performed showing the resulting shear stress versus shear strain curves and the corresponding stress path of shear stress versus initial effective stress. The effects on liquefaction will be noted based on the number of

cycles to reach liquefaction and because part of the initiation of cyclic liquefaction is characterized by the earthquake loading, Equation 2.4 is used to represent this loading since the following tests are cyclic simple shear tests,

$$CSR = \frac{\tau_{cyc}}{\sigma'_{vo}} \tag{2.4}$$

where CSR is the cyclic stress ratio, τ_{cyc} is the horizontal cyclic shear stress, and σ'_{vo} initial vertical effective stress.

2.4.2.2.1.1 Load Amplitude

As one would expect, increasing the load amplitude (with all other factors the same) would decrease the number of cycles required to reach initial liquefaction because increasing the load amplitude causes an increase in pore pressure per cycle which in turn decreases the effective vertical stress per cycle. Figure 2.21 from Kramer (2009) shows the same soil subjected to cyclic shear stresses of 15 kPa and 20 kPa at a relative density of 60%. Therefore, the soil subjected to a cyclic shear stress of 15 kPa will have a lower CSR than the soil subjected to 20 kPa. The soil subjected to the higher cyclic shear stress amplitude of 20 kPa clearly requires less cycles to reach a vertical effective stress of zero (initiation of liquefaction) as the pore pressure is generated much more quickly than the same soil subjected to a cyclic shear stress of 15 kPa. The soil subjected to 20 kPa reached initial liquefaction in 7 cycles of loading whereas the same soil subjected to 15 kPa reach initial liquefaction in 23 cycles.

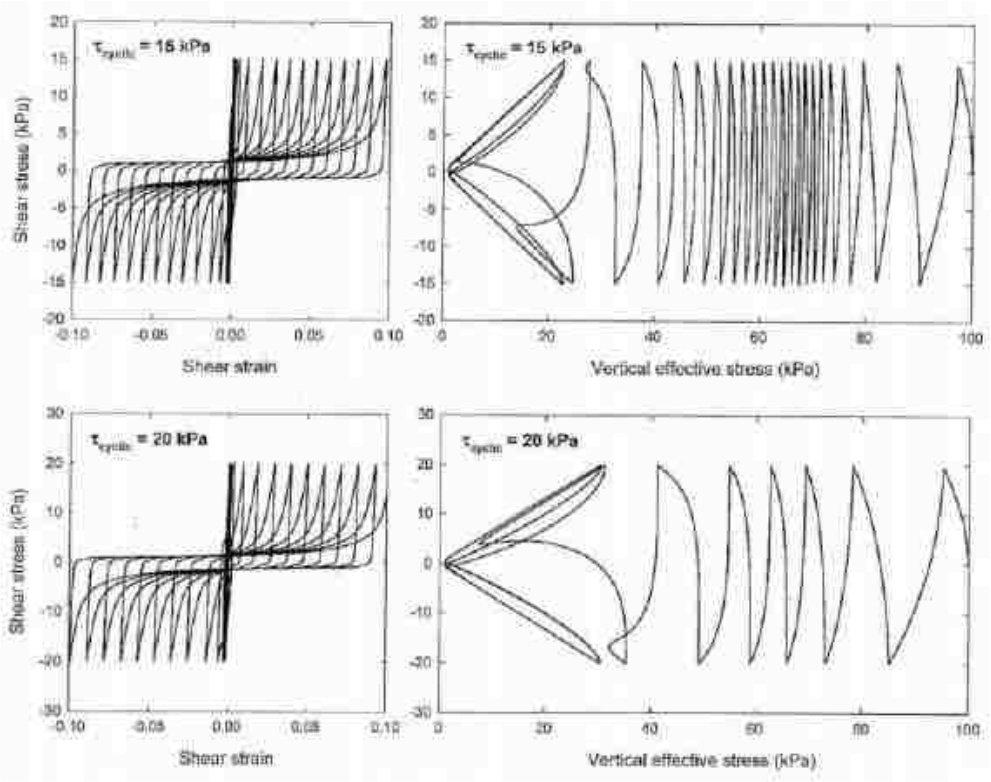

Figure 2.21. Two identical soils subjected to different cyclic shear stress amplitudes causing a different amount of cycles of loading to reach initial liquefaction (Kramer, 2009).

For earthquake engineering applications, it's also important to remember that although increasing load amplitude decreases the number of cycles to reach the initiation of liquefaction, a smaller load amplitude, but a longer duration of motion can also cause a soil to liquefy. For example, two identical soils termed soils A and B are subjected to the same weak amplitude ground motion, but soil A is exposed to this motion for 60 seconds, and soil B is exposed to this same motion for 75 seconds. Soil A does not liquefy, but soil B does reach initial liquefaction. Since the soils had identical properties, one can interpret that the additional duration of soil B allowed pore pressure generation to continue and thus keep reducing the effective stress allowing initial liquefaction to occur, whereas, soil A was not subjected to generate enough pore pressure to bring the soil to the initiation of liquefaction.

2.4.2.2.1.2 Soil Density

Two soils with the same properties except for differing density, but at the same vertical effective confining stress, will behave differently. The soil at the lower density would be more contractive and because more contractive soils generate pore pressure more quickly, the looser soil would decrease in effective stress quicker than the denser soil. Therefore, the loose, and more contractive soil, would require less cycles of loading to reach the initiation of liquefaction compared to the denser soil. Figure 2.22 from Kramer (2008) shows two soils at same vertical effective stress with the same properties except for one of the soils is at a relative density of 40% and the other 50%. The looser soil with the relative density of 40% clearly shows larger decreases in vertical effective stress due to the increased rate of pore pressure generation and therefore required 15 cycles of loading to reach the initiation of liquefaction, whereas, the denser soil at a relative density of 50% required 39 cycles of loading to reach the initiation of liquefaction.

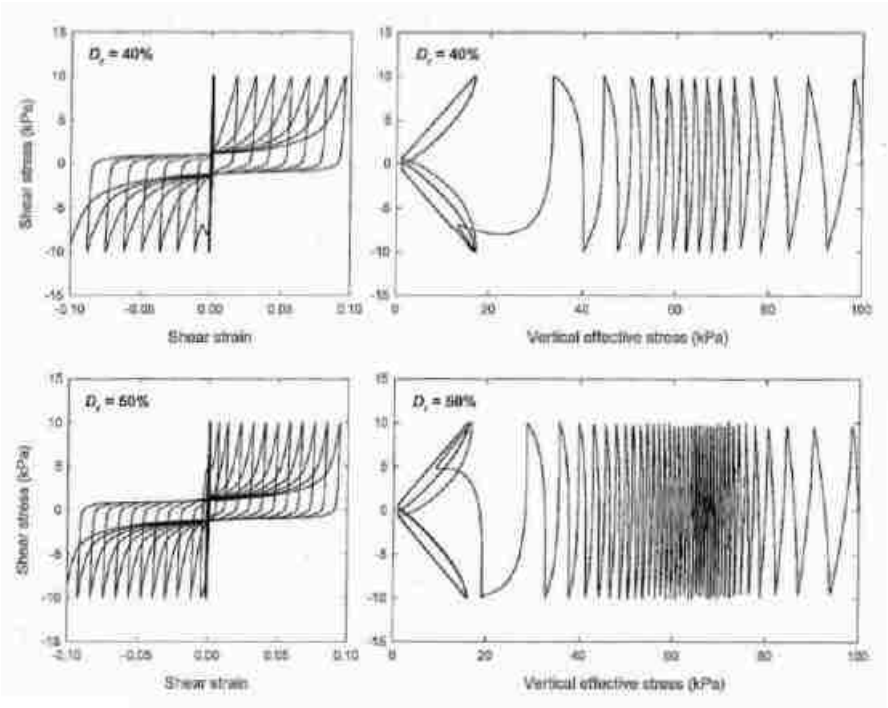

Figure 2.22. Number of cycles of loading required to reach the initiation of liquefaction for two soils at the same vertical effective stress with the same soil properties, except differing relative densities of 40% and 50% (Kramer 2008).

2.4.2.2.1.3 Fines Plasticity

The plasticity of the fines in a soil can play an important role in determining whether a soil will undergo liquefaction or not. It has already been established in Section 2.3 that a certain plasticity index prevents a soil from being able to liquefy because this soil is not able to generate enough pore pressure to bring the soil to a state of liquefaction. Boulanger and Idriss (2006) recommended that a soil with a plasticity index of greater than 7 is not susceptible to liquefaction. Figure 2.23 modified by Kramer (2008) and originally from Dahl et al. (2014) helps illustrate why soils with higher plasticity index do not liquefy. Figure 2.23 shows two soils, one with a plasticity index (PI) of 0 classified as a silty sand (SM), and the second with a PI of 26 and classified as a low-plasticity clay (CL) subjected to cyclic simple shear tests. It is important to note that although the name "low-plasticity clay" may be a bit confusing because of the word "low," it does represent the soil with the PI of 26 compared to the silty sand with the PI of 0.

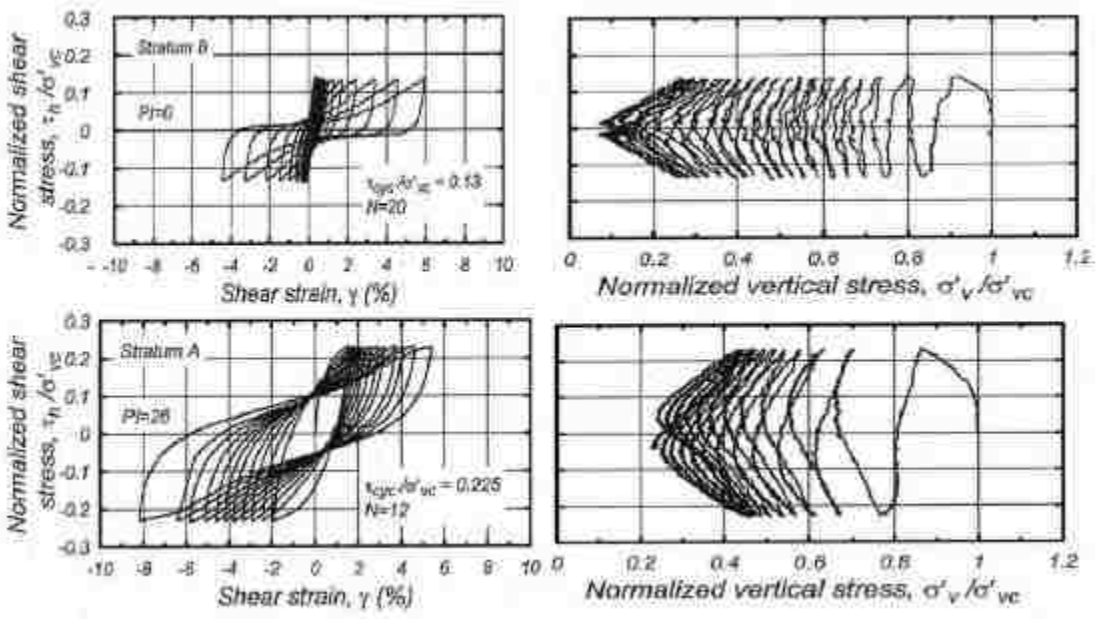

Figure 2.23. Cyclic softening of a silty sand (PI = 0) and low-plasticity clay (PI = 26) subjected to a cyclic simple shear tests (Kramer, 2008).

First, it should be noted neither the silty sand (PI = 0) or low-plasticity clay (PI = 26) reach a state of initial liquefaction (therefore these soils are exhibiting cyclic softening) as indicated by the normalized vertical effective stress not reaching a value of 0, however, there are stark differences between the two soils due to their different plasticity. It is clear that the silty sand (lowest normalized vertical stress approximately 0.08) becomes closer to a state of liquefaction than the low-plasticity clay (lowest normalized vertical stress approximately 0.23). This is because the silty sand is more contractive (generates more pore pressure) than the low-plasticity clay as indicated by the lower slope of the normalized shear stress to normalized vertical stress for the silty sand as it moves farther to the left each cycle of loading. It is noticeable from the normalized shear stress versus shear strain plots that the low-plasticity clay initially has a lower stiffness than the silty sand, however, by the end of loading the low-plasticity clay has a higher stiffness as the slope is greater (higher shear modulus) than the silty sand. The low-plasticity clay has more "stretched" stress strain loops than the silty-sand, therefore, the low-plasticity clay has a higher rate of energy dissipation. In summary, the low-plasticity clay (PI = 26) is not able to generate as much pore pressure as the silty sand (PI = 0), and therefore the low-plasticity clay is farther from a state of initial liquefaction and retains a higher stiffness than the silty sand.

2.4.2.2.1.4 Initial Static Shear Stress

As with the previous factors described thus far, the generation of pore pressure is key in the generation of initial liquefaction. An initial shear stress on a soil is generated from either sloping ground or from some sort of structure (e.g., a building) that induces additional shear stress on a soil element that would not be there if the soil was either on flat ground or if there was no structure was present. Because the stability of a soil element is lower when subjected to an initial shear stress, it would seem reasonable to believe that a higher initial shear stress would reduce the

number of cycles to liquefaction initiation. However, this has been found to not always be the case (Castro and Poulos, 1977). While performing a series of cyclic triaxial tests, Castro and Poulos (1977) noticed that higher shear stresses actually produced smaller "cyclic mobility stress" (cyclic stress ratio). Lower CSRs would then mean more cycles to cause liquefaction initiation. Seed and Harder (1990) found that increased initial static shear stress on the soil favorably increased the liquefaction resistance (more cycles of loading to induce liquefaction) and that only relatively loose soils decreased the liquefaction resistance (less cycles of loading to induce liquefaction). The latter has been attributed to soil particle reorientation when an initial static shear stress is present when a soil is subjected to cyclic shear stresses. Relatively loose soils are able to continue particle reorientation as they fill void space (reduce void ratio) and cause contraction which generates pore pressures. The presence of an initial static shear stress for dense soils, on the other hand, inhibits particle reorientation and therefore less pore pressure is able to be generated each cycle of loading. Figure 2.24 from Kramer (2008) shows two soils both with a relative density of 60%, however subjected to different initial static shear stresses of 5 kPa and 8kPa. The shear strain versus vertical effective stress plots show that the soil specimen subjected to a lower initial static shear stress "triggered" liquefaction after 15 cycles, whereas the soil specimen subjected to a higher initial static shear stressed took 16 cycles to trigger liquefaction with slightly less pore pressure generation each cycle.

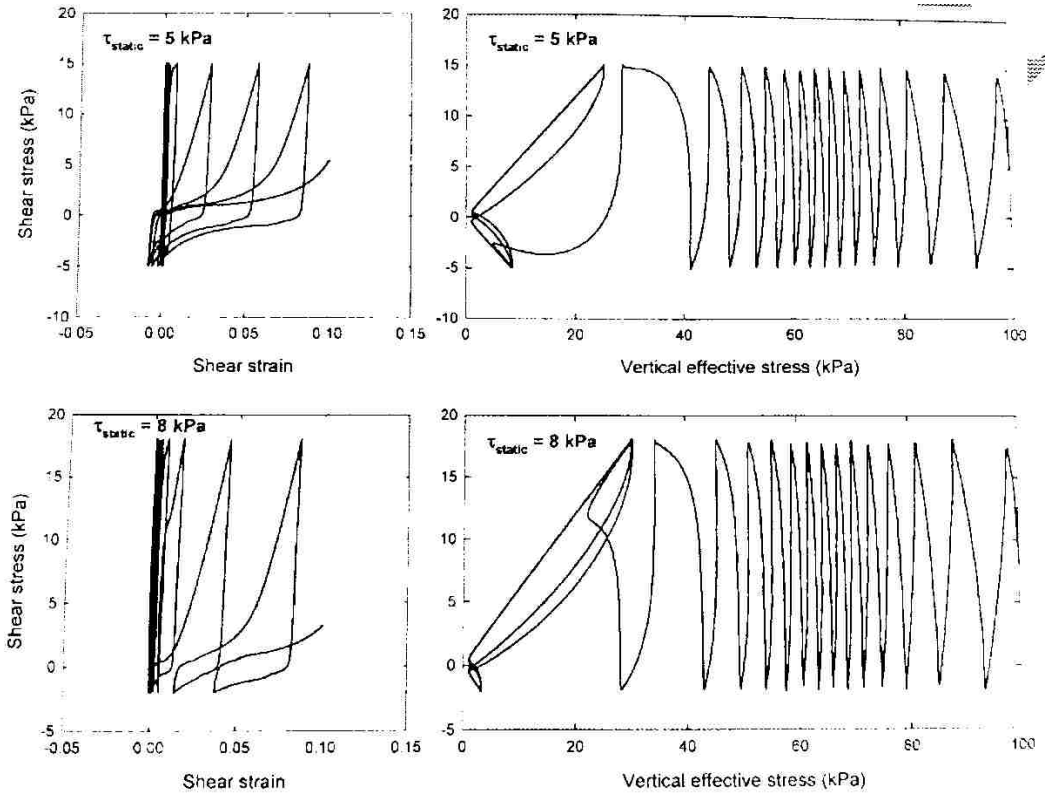

Figure 2.24. Two soils with loaded with identical cyclic stress ratios and the same relative density of 60%, but with differing initial static shear stresses of 5 kPa and 8 kPa applied (Kramer, 2008).

2.4.2.2.1.5 Initial Effective Stress

There are two key components to consider when evaluating the effects of initial effective stress on a soil. First, a soil that is subjected to a higher initial effective stress will be more contractive as can be observed from re-examining the state of a soil with respect to the critical state line shown in Figure 2.9. Second, increasing the initial effective stress naturally increases the density of soil, and the denser a soil is, the less contractive it becomes. As noted in Vaid et al. (1985) and Seed and Harder (1990), the impact of initial effective stress generally decreases the liquefaction resistance because increased initial effective stress causes increased pore pressure generation due to the first component (higher initial effective stress causes a soil to be more contractive). Therefore, the first component generally outweighs the second component in terms of cycles to reach the triggering of liquefaction. Kramer (2008) illustrated this behavior with Figure

2.25 comparing two soils subjected to the same cyclic stress ratios and relative density of 60%, however, differing initial vertical effectives stresses of 100 kPa and 200 kPa were applied. The soil subjected to the 200 kPa initial vertical effective stress reached initial liquefaction in 15 cycles due to the increase rate of pore pressure generation compared to the sample applied a 100 kPa initial effective vertical stress which reached initial liquefaction after 22 cycles of loading.

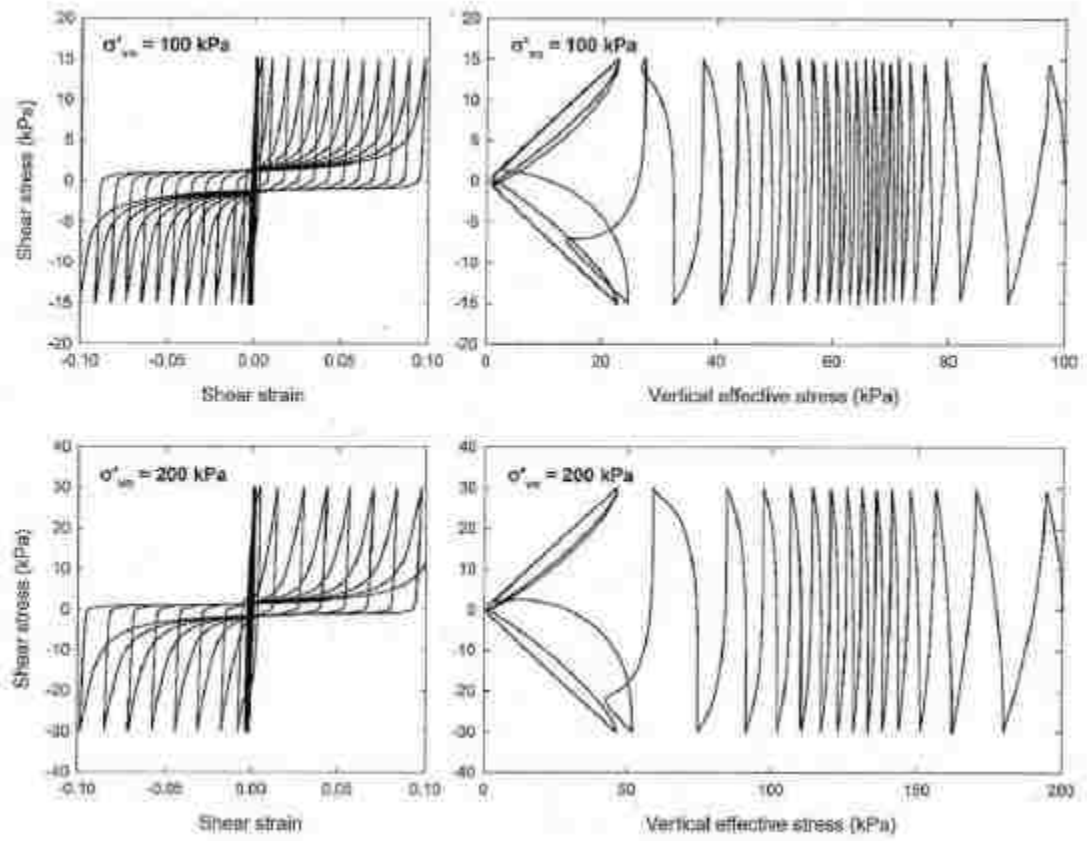

Figure 2.25. Stress path behavior of two soils applied differing initial vertical effective stresses of 100 kPa and 200 kPa that were subjected to the same cyclic stress ratios at a relative density of 60% (Kramer, 2008).

2.4.2.2.1.6 Other Factors

Several other factors can influence liquefaction triggering in a soil, however, to a lesser extent than the prior five factors. Seed et al. (1975) found that a soil subjected to prior shaking took more cycles of loading to reach liquefaction initiation with only negligible increase in relative density from the prior vibrations. Therefore, this prior shaking increased the soils liquefaction

resistance. A summary of many of the other factors can be found in Finn (1981) who highlighted the effects that the overconsolidation ratio (OCR) and the lateral earth pressure coefficient have on liquefaction initiation. It was first realized that increasing the OCR of a soil increased the liquefaction resistance of that soil. It was found that the increase in liquefaction resistance was partially attributed to the increase in the lateral earth pressure coefficient, however, the lateral earth pressure coefficient could not explain all of the increased liquefaction resistance. Therefore, both the OCR and the lateral earth pressure coefficient have been shown to increase a soils liquefaction resistance. Finn (1981) also provided a summary of the increased liquefaction resistance of a soil due to aging effects. Vaid et al. (1985) found that particle angularity also plays a role in liquefaction resistance. Generally, sand with more angular grains is more resistant to liquefaction compared to sand with rounded grains especially at low confining pressures. It should also be noted particle sorting (well graded or poorly graded) is also a factor in liquefaction resistance. Generally, sands that are poorly graded (well sorted) have similar grain sizes and therefore have more void space than a sand that's well graded (poorly sorted) because well graded sands consist of sand particles of varying sizes that can fill the void space between particles of larger size. Thus, well graded sands have lower void ratios and thus higher density than poorly graded sands which lead to well graded sands having a higher liquefaction resistance.

In order to summarize the effects of the primary and secondary factors on liquefaction resistance Table 2.2 was created showing whether the number of cycles to reach liquefaction increases or decreases based on an increase in the previously discussed primary and secondary factors.

Table 2.2. Increase or decrease of number of cycles to reach cyclic liquefaction initiation based on known factors to affect cyclic liquefaction.

Type	Factor Affecting the Potential of Cyclic Liquefaction	Increase in Factor Affecting Liquefaction Potential	Increase or Decrease in Number of Cycles to Reach Liquefaction Initiation
Primary	Load Amplitude	↑	↓
	Soil Density	↑	↑
	Fines Plasticity	↑	↑
	Initial Static Shear Stress	↑	Both*
	Initial Effective Stress	↑	↓
Secondary	Prior Shaking	↑	↑
	OCR and Lateral Earth Pressure Coefficient	↑	↑
	Age of Soil Deposit	↑	↑
	Particle Angularity	↑	↑
	Gradation	↑	↑

***For loose sand number of cycles decreases and for medium dense to dense sand number of cycles increases.**

2.4.2.2.2 Cyclic Stress Approach

A simple way to determine whether liquefaction will or will not occur is the factor of safety. The factor of safety against liquefaction can be split into two parts: earthquake loading and liquefaction resistance. Therefore, the factor of safety against liquefaction can be represented as

$$FS_L = \frac{R}{L} \tag{2.5}$$

where R is the liquefaction resistance and L is the earthquake loading. Several methods have been developed in order to best characterize liquefaction potential. Each method has its strengths and weaknesses. The most common method implemented today is the cyclic stress approach which characterizes earthquake loading and liquefaction resistance in terms of cyclic shear stresses and the amplitude and duration of these cyclic shear stresses is related to pore pressure generation (Kramer, 1996). For the cyclic stress approach, earthquake loading is represented by the cyclic stress ratio (CSR) previously shown in Equation 2.4, and the cyclic resistance ratio (CRR), both of which will be discussed in detail. With the latter being said, Equation 2.5 can be written as

$$FS_L = \frac{CRR}{CSR} \tag{2.6}$$

where CRR is the cyclic resistance ratio and CSR is the cyclic stress ratio. The cyclic stress approach needs several correction factors because earthquake magnitude, initial shear stress, and initial vertical effective stress vary based on location. A weakness to the cyclic stress approach is that in-situ factors such as previous shaking history, age of the soil deposit, and soil fabric cannot be replicated in reconstituted lab specimens therefore field exploration of the liquefaction resistance of a soil is required.

2.4.2.2.2.1 Earthquake Loading

The earthquake loading component is broken into two methods: site response analysis and the simplified procedure, each of which will be explained in detail. It is important to note that the cyclic stresses that are used in empirical liquefaction potential evaluation are not to be impacted by pore pressure generation. This is because the case histories in which the empirical procedures to evaluate liquefaction potential are derived are based on ground motion prediction equations (GMPEs) that assume no pore pressure generation, or from recorded ground motions at sites that did not liquefy.

2.4.2.2.2.1.1 Site Response Analysis

Site response analysis is a detailed assessment of how ground motions will change characteristics when propagating from rock to soil. Several factors influence the behavior of a ground motion when transitioning from rock to soil and this change in behavior can be either good, or bad for the structures this ground motion is subjected to depending on many variables such as the natural frequency of the structure and amplification or de-amplification of the ground motion from rock to soil. An overview of a site response analysis procedure is as follows:

1) Obtain or scale/modify an input ground motion on rock (acceleration time history) that is expected for the site of interest with similar magnitude, frequency content, and duration;

2) Utilize a computer program to apply a fourier transform and break the ground motion into a series of simple harmonic motions to develop the fourier amplitude spectrum (FAS) for rock which shows how the amplitude of the ground motion is distributed with frequency;
3) Apply a transfer function to account for how each frequency of the rock input motion is altered when propagating through a soil deposit;
4) The result of multiplying each FAS by the transfer function is the FAS on soil;
5) Utilize a computer program to perform an inverse fourier transform to combine the FAS on soil into the ground motion on soil (acceleration time history).

A transfer function is applied because soil acts as a "filter" which can amplify or de-amplify, change the frequency content, change the duration, or have only minor impact on the input rock ground motion (Kramer, 1996). A site response analysis therefore allows one to predict the ground motions on soil, and thus allows one to be able to design a structure to withstand the predicted level of shaking given the probability of that shaking occurring in some period of time.

There are three approaches to site response analysis: linear, equivalent linear, and non-linear. The linear approach assumes that the soil behaves linear and the dynamic soil properties (shear modulus and damping) remain constant throughout loading although the shear strain is changing. This means that a soils shear modulus, or stiffness of the soil, is assumed to remain at its initial value (the maximum) and damping is assumed to remain at its initial value (the minimum). It is known that the dynamic soil properties change with changing shear strain, therefore, to account for this the equivalent linear approach was developed. Because the equivalent linear analysis is still a linear analysis, constant shear modulus and damping are used, however, it assigns a constant shear modulus and damping based on the amount of strain in each soil layer. The level of strain is selected using an iterative approach because the dynamic soil properties and

shear strain depend on each other (Joyner and Chen, 1975). The strain selected is typically 65% of the peak shear strain (Kramer, 1996). The equivalent linear approach provides a more reasonable approximation of soil behavior than the linear approach, however, can underestimate and overestimate ground motions because the shear modulus and damping are constant and do not change with shear strain. Typically, equivalent linear analyses can provide results that are similar to nonlinear analyses when shear strains are small to moderate, however, when shear strains are large the equivalent linear approach can approximate soil behavior in an average sense, but the shear modulus may largely differ at certain shear strains (Kramer, 1996). Because soils behave linear only at small strains, the non-linear approach provides the most accurate representation of soil behavior. The non-linear approach can allow for the changing shear modulus and damping with changing shear strains. The non-linear approach integrates the wave equation for a visco-elastic medium in small time steps, therefore, allowing for capturing the changing material properties. Because the non-linear model captures these changes and is able to be modeled in terms of effective stresses, one can model permanent displacements and pore pressure generation. From a commercial point of view, one downside to the non-linear approach at this point in time is that it requires expertise that oftentimes there is not time to learn, or if experienced personnel are available, it simply takes too long to compute from an economic standpoint.

An important final note on site response analysis is to know when 1-D site response analyses can be applied. 1-D site response analyses should only be used when the propagating shear waves are vertical when reaching the ground surface. Instances where vertical propagating shear waves will not occur, and thus where 1-D site response analysis should not be used, are a dam in a narrow canyon, retaining structures, dams and embankments, and tunnels (Kramer, 1996).

Vertical propagating shear waves are also likely to not occur for complex soil conditions (non-horizontal soil boundaries) and inclined ground surface.

2.4.2.2.2.1.2 Simplified Procedure

Although site response analysis provides a more comprehensive evaluation of earthquake loading, the simplified procedure developed by Seed and Idriss (1971) provided an alternative to the computational extensive site response analysis. Seed and Idriss (1971) highlighted five factors that were known to influence the potential for liquefaction: soil type, relative density/void ratio, initial confining pressure, the intensity of ground shaking, and the duration of ground shaking. Therefore, from these five factors and Newton's Second Law of Motion, Seed and Idriss developed the original form of the simplified procedure. Starting from Newton's Second Law of Motion the force applied to an object is expressed as

$$F = ma \tag{2.7}$$

where m is the objects mass and a the objects acceleration. Noting the force can be represented as the maximum shear stress applied multiplied by the area, along with knowing the mass is simply the weight of the object divided by gravity, the latter expression can be written as

$$\tau_{max} A = \frac{W}{g} a_{max} \tag{2.8}$$

where τ_{max} is the maximum shear stress, A the area (thickness times width), W the weight, and g gravity. The weight of the soil can be represented in terms of the soil unit weight multiplied by the volume (depth multiplied by thickness and width), therefore cancelling out like terms gives

$$\tau_{max} = \frac{\gamma h}{g} a_{max} \tag{2.9}$$

where γ is the soil unit weight and h the depth to the soil element. Knowing that the soil does not behave as a rigid body and therefore the maximum shear stress decreases with depth, Seed and Idriss (1971) modified Equation 2.9 to account for the maximum shear stress decreasing with depth

$$\tau_{max} = \frac{\gamma h}{g} a_{max} r_d \tag{2.10}$$

where r_d is the stress reduction coefficient that can be estimated from Figure 2.26 originally developed by Seed and Idriss (1971).

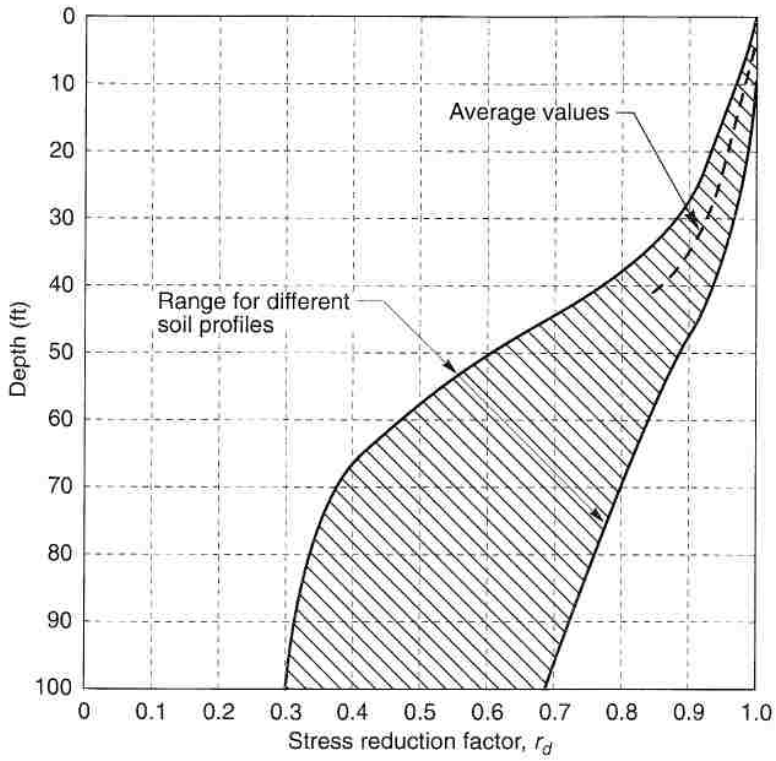

Figure 2.26. Stress reduction coefficient representing the cyclic shear stress variation with depth for flat or nearly flat ground (After Kramer, 1996).

Seed and Idriss also realized that an earthquakes transient acceleration time history could not be exactly replicated in the laboratory and that τ_{max}, the maximum shear stress, may or may not occur more than once during shaking. To account for the latter and develop an average equivalent uniform shear stress, a shear stress value of 65% of τ_{max} was taken, giving

$$\tau_{cyc} = 0.65 \frac{\gamma h}{g} a_{max} r_d \tag{2.11}$$

where τ_{cyc} is the average equivalent uniform shear stress. To take into account earthquakes of different magnitudes, Seed and Idriss proposed Table 2.3 which shows the number of significant stress cycles to apply for a given earthquake magnitude to implement with Equation 2.11 to calculate the stresses induced at variable depths for multiple magnitude earthquakes.

Table 2.3. Number of significant stress cycles, N_c, for multiple magnitude earthquakes.

Earthquake Magnitude	Number of Significant Stress Cycles, N_c
7	10
7-1/2	20
8	30

Since Seed and Idriss proposed the simplified procedure, changes have taken place. One of which was the introduction to the standardized cyclic stress ratio which is found when dividing both sides of Equation 2.11 by the initial vertical effective stress and also noting that the soil unit weight multiplied by the depth to the soil element is equal to the total initial vertical stress, therefore giving

$$CSR = 0.65 \frac{a_{max}}{g} \frac{\sigma_{vo}}{\sigma'_{vo}} r_d \tag{2.12}$$

where CSR is the standardized cyclic stress ratio, σ_{vo} is the total initial vertical stress, and σ'_{vo} is the initial vertical effective stress. As an alternative to Table 2.3, Seed et al. (1975) developed a Magnitude Scaling Factor (MSF) in order to better account for the duration of earthquakes of varying magnitude therefore giving rise to

$$CSR = 0.65 \frac{a_{max}}{g} \frac{\sigma_{vo}}{\sigma'_{vo}} \frac{r_d}{MSF} \tag{2.13}$$

where the larger a given earthquake magnitude, the smaller the value of MSF, and therefore the larger the CSR. More modern adjustments have been made as well including Idriss (1999), Cetin

et al. (2004), Idriss and Boulanger (2008), and Boulanger and Idriss (2014) developing/modifying the r_d and the MSF terms.

Idriss and Boulanger

From site response analyses it is known that r_d depends on characteristics of earthquake ground motion, the shear wave velocity profile of the site, and the non-linear shear modulus and damping (Idriss and Boulanger, 2008). From the work of Golesorkhi (1989), Idriss (1999) presented a new r_d based on hundreds of parametric site response analyses and concluded that r_d could adequately be used in liquefaction evaluation procedures based on the depth and the magnitude of an earthquake. Equation 2.14, 2.15, and 2.16 show Idriss and Boulangers r_d expression

$$r_d = \exp(\alpha(z) + \beta(z)M) \tag{2.14}$$

where $\alpha(z)$ and $\beta(z)$

$$\alpha(z) = -1.012 - 1.126 \sin(\frac{z}{11.73} + 5.133) \tag{2.15}$$

$$\beta(z) = 0.106 + 0.118 \sin(\frac{z}{11.28} + 5.142) \tag{2.16}$$

where M is the moment magnitude, z is the depth in meters, and the portion of the equations in the sin terms are in radians. Figure 2.27 shows how the updated stress reduction coefficient decreases differently with depth based on magnitude from Idriss and Boulanger (2008).

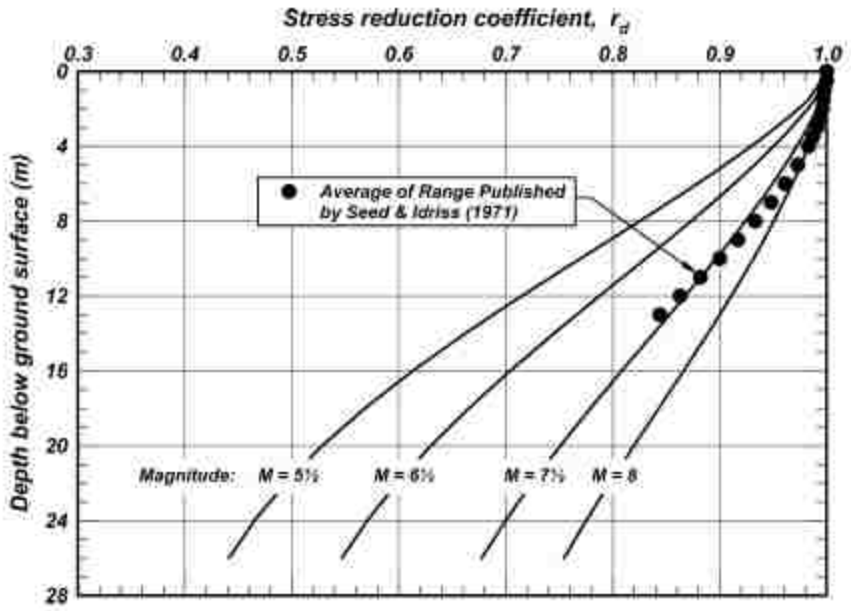

Figure 2.27. Revised stress reduction coefficient with varying magnitude and depth (After Idriss and Boulanger, 2008).

Idriss (1999) also presented an updated MSF to better account for equivalent uniform stress cycles for earthquakes other than moment magnitude 7.5. This is needed because earthquakes of differing magnitude produce different amounts of energy. Larger earthquakes will produce more equivalent uniform stress cycles and therefore decrease the value of MSF and increase the value of CSR. Idriss (1999) developed the Equation 2.17 to account different magnitude earthquakes causing more/less equivalent uniform stress cycles with respect to a moment magnitude 7.5

$$MSF = 6.9 \exp\left(-\frac{M_w}{4}\right) - 0.058 \leq 1.8 \qquad (2.17)$$

where M_w is the moment magnitude and the upper bound limiting value of 1.8 for MSF is used to account for smaller earthquakes with a single dominant stress pulse (Idriss and Boulanger, 2008).

Boulanger and Idriss (2014) further updated the MSF in which Kramer and Stewart (unpublished manuscript) modified the equations to be more easily understood in terms of the effects on loading (CSR) and resistance (CRR). The loading MSF will be presented here and the resistance MSF will be presented in Section 2.4.2.2.2.4. For the SPT penetration procedure

$$\mathrm{MSF}_L = 0.5803 + 2.7368\exp(\tfrac{-M}{4}) \leq 1.32 \quad (2.18)$$

and for the CPT penetration procedure

$$\mathrm{MSF}_L = 0.5803 + 2.7368\exp(\tfrac{-M}{4}) \quad (2.19)$$

where MSF_L is the loading magnitude scaling factor for calculating CSR. It should be noted the MSF developed by Boulanger and Idriss (2014) was not used for liquefaction analysis presented hereon in this thesis, but has been shown here to provide a thorough literature review. Equation 2.17 was used for the liquefaction analysis presented later in this thesis.

Cetin et al. (2004) also created their own r_d from 2,153 site response analyses. They found that r_d could be represented by depth, moment magnitude, peak ground acceleration, and site stiffness. Cetin et al. realized that below approximately 18 meters depth the r_d decreased rather linearly with depth. Because of this, Cetin et al. represented their r_d term for $d < 20\ m$ as

$$r_d = \frac{\left[1+\frac{-23.013-2.949a_{max}+0.999M_W+0.0525V^*_{s,12\ m}}{16.258+0.201exp^{0.341(-d+0.0785V^*_{s,12\ m}+7.586)}}\right]}{\left[1+\frac{-23.013-2.949a_{max}+0.999M_W+0.0525V^*_{s,12\ m}}{16.258+0.201exp^{0.341(0.0785V^*_{s,12\ m}+7.586)}}\right]} \pm \sigma_{\varepsilon_{r_d}} \quad (2.20)$$

and for $d \geq 20\ m$

$$r_d = \frac{\left[1+\frac{-23.013-2.949a_{max}+0.999M_W+0.0525V^*_{s,12\ m}}{16.258+0.201exp^{0.341(-20+0.0785V^*_{s,12\ m}+7.586)}}\right]}{\left[1+\frac{-23.013-2.949a_{max}+0.999M_W+0.0525V^*_{s,12\ m}}{16.258+0.201exp^{0.341(0.0785V^*_{s,12\ m}+7.586)}}\right]} - 0.0046(d-20) \pm \sigma_{\varepsilon_{r_d}} \quad (2.21)$$

where r_d is a function of depth d in meters, moment magnitude M_w, peak ground acceleration a_{max} in g's, site stiffness (shear wave velocity for the top 12 m) $V^*_{s,12\ m}$ in m/s, and $\sigma_{\varepsilon_{r_d}}$ for $d < 12\ m$ is given as

$$\sigma_{\varepsilon_{r_d}}(d) = d^{0.8500}0.0198 \quad (2.22)$$

and for $d \geq 12\ m$ as

$$\sigma_{\varepsilon_{r_d}}(d) = d^{0.8500}0.0198 \quad (2.23)$$

where $\sigma_{\varepsilon_{r_d}}$ is the standard deviation. It should be noted, Equations 2.20 and 2.21 are for "typical" stiffness conditions as stated by Cetin et al. (2004) who recommended that site response analyses be performed for sites with $V^*_{s,12\,m}$ less than 120 m/s or greater than approximately 250 m/s. As an alternative, Cetin et al. suggested limiting values could be used as 120 m/s and 250 m/s for considerably soft soils and considerably stiff soils respectively. Cetin et al. (2004) also developed a duration weighting factor (DWF), analogous to the magnitude to scaling factor (MSF) that was first developed by Seed et al. (1975). Kramer (2008) determined the duration weighting factor of Cetin et al. (2004) could be written as

$$DWF = \left(\frac{7.5}{M_w}\right)^{2.217} \tag{2.24}$$

where M_w is the moment magnitude.

Before going into liquefaction resistance, it is important to understand where each of the parameters in the simplified procedure come from and the processes that have been used to generate a_{max} values to implement into the simplified procedure. Up to this point, it has not been stated how a_{max} is obtained in order to perform the simplified procedure. In order to do so deterministic seismic hazard analysis (DSHA) and probabilistic seismic hazard analysis (PSHA) are explained in the following sections prior to liquefaction resistance.

2.4.2.2.2.2 Deterministic Seismic Hazard Analysis

In order to evaluate earthquake hazards, geotechnical earthquake engineers initially used deterministic seismic hazard analysis (DSHA) to obtain an expected level of ground shaking. DSHA uses a single magnitude and distance scenario to calculate this expected level of ground shaking. For DSHA it is common practice to select the largest magnitude earthquake at the shortest source to site distance in at attempt to consider a "worst-case" scenario seismic event. The DSHA procedure can be broken down into four steps (modified from Reiter, 1990):

1) Compile and analyze a list of all seismic sources that are relevant to capturing the most damaging ground motions at the site of interest. Largest magnitude earthquakes are usually selected, however, careful consideration should be taken for a smaller magnitude earthquake at a small site-to-source distance.
2) Classify the site-to-source distances from the latter seismic sources. It is important to note that site-to-source distance has been described in multiple ways (e.g., Joyner-Boore distance, epicentral distance, hypocentral distance) and the same distance measure selected in this step should also be implemented into the ground motion intensity calculation method used for step 3. Typically, the shortest site-to-source distance is used.
3) Evaluate and select the "controlling" earthquake which produces the strongest level of shaking at the site of interest typically computed with a ground motion prediction equation (GMPE). The strongest level of shaking may or may not correspond to the largest magnitude earthquake. Similarly, the strongest level of shaking may or may not correspond to the shortest site-to-source distance.
4) The selected controlling earthquake found to produce the largest ground shaking intensity allows for the hazard to be defined. Depending on several factors (e.g., the fundamental period of a structure) the ground shaking intensity can be defined in terms of an intensity measure such as peak ground acceleration (PGA), peak ground velocity (PGV), peak ground displacement (PGD), spectral acceleration (S_a), etc.

Kramer (1996) illustrated the latter four steps with Figure 2.28. It should be noted "Y" in step four of Figure 2.28 represents the ground motion intensity measure defined in step four of the written procedure shown above.

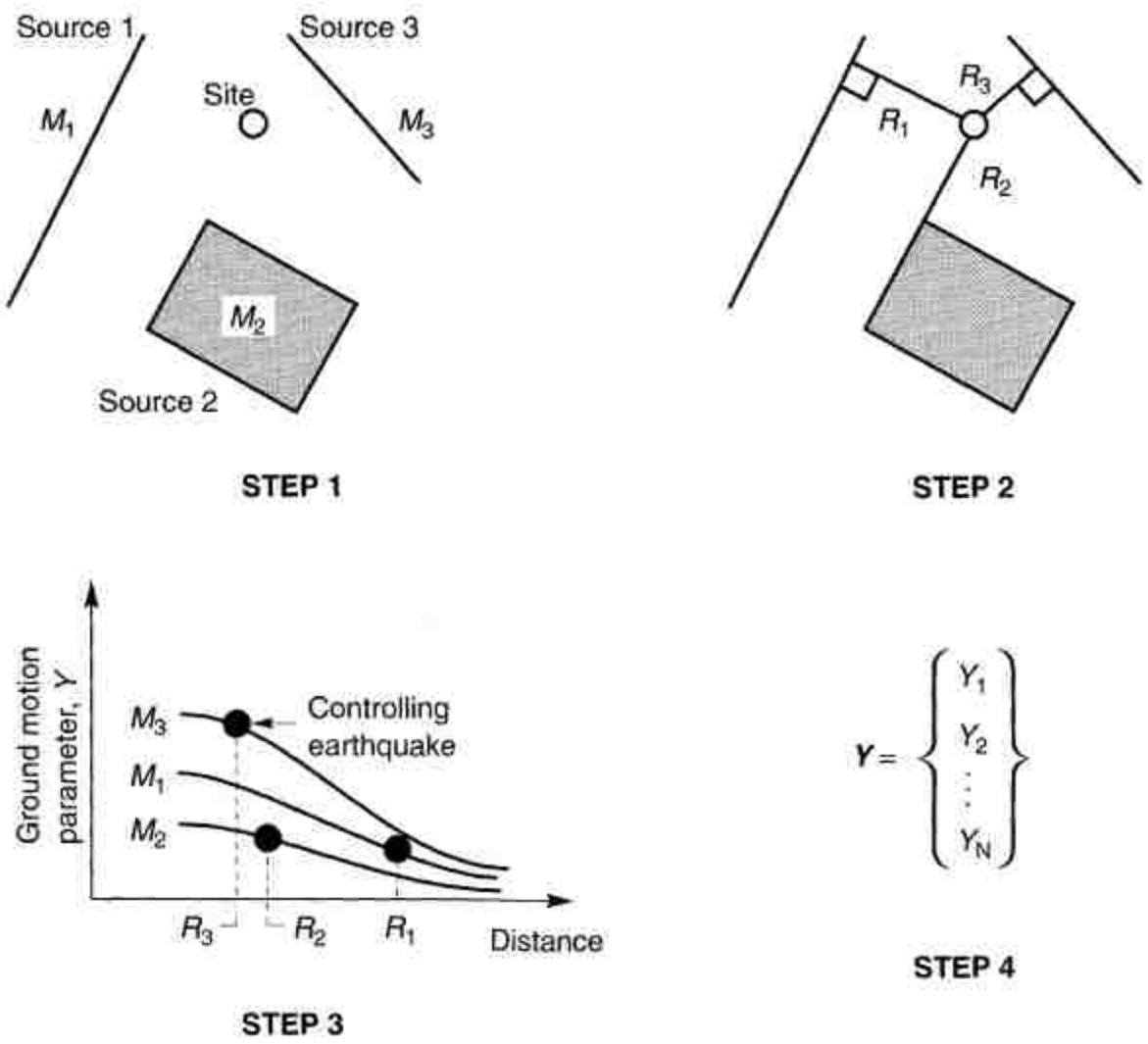

Figure 2.28. Four steps of DSHA: selection of characterizing seismic sources, identifying site-to-sources distances for those seismic sources, calculating the controlling earthquake, and characterizing the hazard given the calculated intensity measures (Kramer, 1996).

Although DSHA is relatively simple to use, it does not always produce the "worst-case" scenario earthquake, and even if it does, no probability of that earthquake occurring is associated with it. Baker (2008) provided an example of the "worst-case" scenario not actually being the "worst-case" scenario as illustrated in Figure 2.29 Baker used the Campbell and Bozorgnia 2008 GMPE model to obtain the median prediction response spectra shown in Figure 2.29 (b). Figure 2.29 (a) shows two faults capable of producing different magnitudes at differing site-to-source

distance. Fault A is capable of producing a magnitude 6.5 event at a distance of 10 km from the site and Fault B is capable of producing a magnitude 7.5 event at a distance of 20 km from the site. The spectral acceleration versus period plot shows that the spectral acceleration at the site is greater when generated from Fault A up until a period of 0.8 seconds and after 0.8 seconds the spectral acceleration at the site is greater when generated from Fault B. This situation shows that there is not a single "worst-case" scenario for the maximum spectral acceleration across all periods.

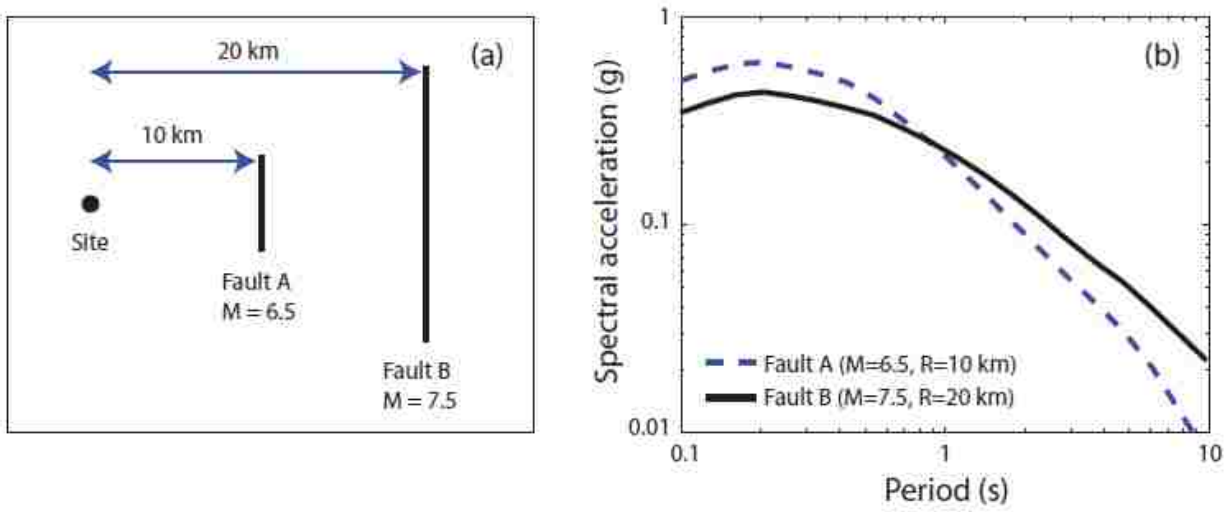

Figure 2.29. An example of multiple sources providing a "worst-case" scenario event. (a) Map view of two seismic sources and their respective site-to-source distance. (b) Median predicted response spectra from using the Campbell and Bozorgnia 2008 GMPE model (Baker, 2008).

Kramer and Stewart (unpublished manuscript) provide another excellent viewpoint of why the DSHA is not an ideal way to characterize the seismic hazard of a site. Does the analysis consider if multiple fault segments, or multiple nearby faults rupture? Clearly, if one considers multiple faults rupturing at once because of one fault causing the other to rupture, then one would expect to encounter a larger magnitude event and more significant ground motions. In the example of Baker (2008), the Campbell and Bozorgnia 2008 GMPE prediction shown considered the median response. In order to actually have a "worst-case" scenario you would want to consider the intensity of the ground motion at for example 2 standard deviations above the mean (95th

percentile). When taking into account factors such as multiple faults rupturing and taking the 95th or higher percentile of ground shaking, the design that would be required to adequately perform against this design event may be so expensive (while the probability of the event actually occurring is extremely low) that it is not reasonable to complete the project. Even if the probability of this "worst-case" scenario is not extremely low, the DSHA procedure does not actually given an actual probability of the ground motions that may occur at a site. The latter is because a DSHA fails to consider all possible ground motions due to not taking into account all magnitudes and site-to-source distances.

2.4.2.2.2.3 Probabilistic Seismic Hazard Analysis

In order to account for all sources and all the magnitudes and source-to-site distances from these sources (and therefore all possible ground motion combinations) probabilistic seismic hazard analysis (PSHA) is required to be used. PSHA was derived mainly from the works of Cornell (1968) who developed a method to take into account all seismic sources, the likelihood of these seismic sources rupturing, and source to site distance in order to obtain a hazard curve for the average return period of a ground motion parameter such as peak ground acceleration. In order to account for all possible ground motions and their relative likelihood, the PSHA procedure can be broken into five steps (modified from Baker, 2008):

1) Determine all seismic sources and their respective geometries (point, line, area, volume) that have the potential to cause and inadequate amount of damage.
2) Determine the probability distribution of magnitudes from each of the seismic sources from step one in order to generate a magnitude hazard curve.

3) Determine the probability distribution of site-to-source distance from each of the seismic sources from step one in order to generate a site-to-source distance hazard curve.

4) Determine the probability distribution of the desired ground motion intensity measure from steps one through three which include all seismic sources, all possible magnitudes, and all possible site-to-source distances. The ground motion intensity measure probability distribution is typically generated using GMPE's. Because all the ground motions are considered this means that all percentiles of ground motion are considered.

5) Use the total probability theorem to combine all of the earthquake magnitude, source-to-site distance, and ground motion intensity measure uncertainties to find the annual rate of exceedance (or return period) of the desired intensity measure.

Baker (2008) illustrated the latter five steps as shown in Figure 2.30. Each of these steps will be further described in order to make the PSHA procedure more transparent.

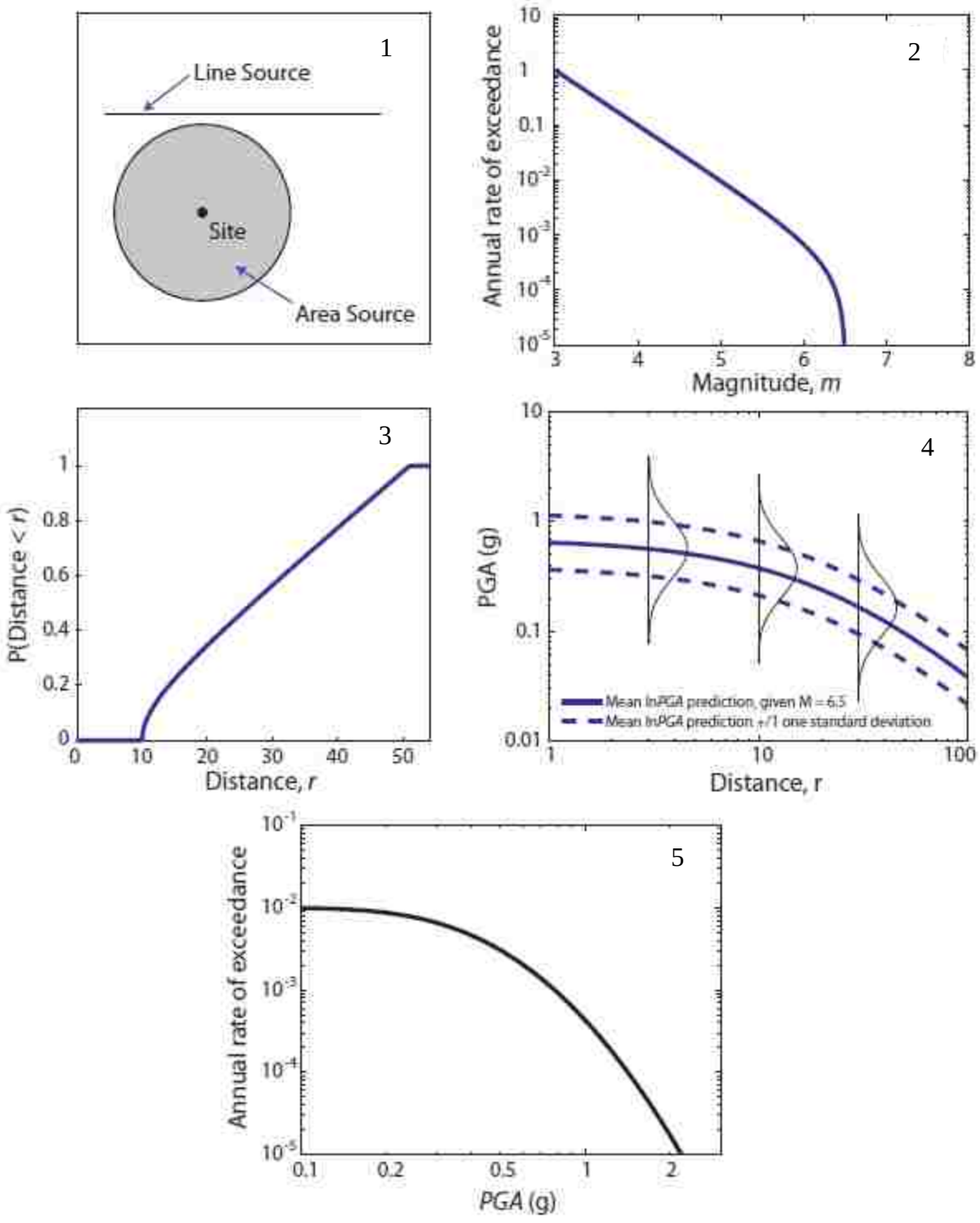

Figure 2.30. PSHA broken into five steps (Baker, 2008).

Determining All Earthquake Sources

All earthquake sources that are capable of producing ground motions that are potentially damaging should be characterized whether these seismic sources can be represented as point, line, areal, or volumetric features. Point features may be a volcano, a fault that ruptures along a small region that continually erupts at the same location, or a fault that is relatively close to the design site. A line feature is typically represented by a fault that is not known to rupture at a certain location and is located relatively close to a site. An areal feature may be used to represent seismic activity where the source location is unknown, but the general area of seismic activity is. A volumetric source feature may be used to represent seismic activity where not only the area of the seismic source is unknown, but also the depth extent of the feature is unknown as well. Therefore, because areal and volumetric seismic sources have more uncertainty, the energy (moment magnitude) generated by these events are less confined. An example of an areal source is the New Madrid Fault Zone which is located in the Central U.S. and not on a plate boundary. Because of the infrequency of earthquakes in the New Madrid Fault Zone, and although widespread liquefaction took place during the 1811-1812 sequence of earthquakes, instruments to locate the seismic source had yet to be invented. According to the USGS (2018) earthquakes similar to the 1811-1812 sequence have taken place approximately every 500 years over the last 1,200 year period.

Determining Earthquake Magnitude

The second step in the PSHA process is determining the distribution of earthquake magnitude. In order to determine the relative likelihood of a given earthquake occurring a probability density function (PDF) can be developed from the Gutenberg-Richter recurrence law. Gutenberg and Richter (1944) developed the Gutenberg-Richter recurrence law as

$$\log \lambda_m = a - bm \tag{2.25}$$

where λ_m is the occurrence rate of earthquakes with a magnitude greater than m, a is a statistical constant indicating the total earthquakes in a region, b is a statistical constant indicate the ratio of small and large magnitude earthquakes, and m is the magnitude. The following expressions for developing a probability distribution for earthquake magnitude are based on Kramer (1996). Equation 2.25 can be written in terms of an exponential function as

$$\lambda_m = 10^{a-bm} = \exp(\alpha - \beta m) \tag{2.26}$$

where a and b are written in terms of $\alpha = 2.303a$ and $\beta = 2.303b$ due to changing to the exponential function. Kramer (1996) normalized the expression of Equation 2.26 (the rate of earthquakes with a magnitude greater than m) by taking into account the rate of all earthquake magnitudes greater than a value of zero ($m > 0$) to give

$$P(M > m|m > 0) = \frac{\lambda_m}{\lambda_0} = \frac{\exp(\alpha - \beta m)}{\exp(\alpha)} = exp^{-\beta m} \tag{2.27}$$

where M is some earthquake with a magnitude greater than m and λ_0 is the recurrence rate for earthquakes with a magnitude greater than zero. Equation 2.27 therefore reads: the probability of some earthquake with magnitude M being greater than an earthquake with magnitude m given that m is greater than zero is equal to the exponential value of negative β multiplied by m. In order to reach the goal of a PDF of earthquake magnitude (the relative likelihood of a given earthquake magnitude occurring), the cumulative distribution function (CDF) must first be found. A CDF is the probability that some variable (e.g., earthquake magnitude) is a value less than or equal to some value. Because the CDF is less than or equal to some value, Equation 2.27 should be re-written as

$$P(M < m|m > 0) = F_M(m) = 1 - \frac{\lambda_m}{\lambda_0} = 1 - exp^{-\beta m} \tag{2.28}$$

where $F_M(m)$ is the CDF of some earthquake with magnitude M given $m > 0$. Therefore, an expression for the PDF of earthquake magnitude can now be found by taking the derivative of the CDF (Equation 2.28) giving

$$f_M(m) = \frac{d}{dm} = F_M(m) = \beta exp^{-\beta m} \tag{2.29}$$

where $f_M(m)$ is the PDF of some earthquake with magnitude M given $m > 0$.

Thus far, the expression for the PDF of earthquake magnitude has been for an earthquake of magnitude $m > 0$, however, for the purposes of earthquake engineering, it is often typical that a lower bound of magnitude be set because earthquakes with a moment magnitude less than approximately 4 to 5 are oftentimes not significant to engineering applications (although small magnitude earthquakes may be useful for seismologists). Not only is there usually a lower bound for earthquake magnitude, but the source geometries can dictate the maximum magnitude that can occur. This brings about what is known as the truncated exponential model where the CDF and PDF for earthquake magnitude can be written in terms of a lower and upper bound earthquake magnitude. Accounting for these bounds the Equation 2.28 CDF can be written as

$$P(M < m | M_0 < m < M_{max}) = F_M(m | M_0 < m < M_{max}) = \frac{1 - exp^{-\beta(m - M_0)}}{1 - exp^{-\beta(M_{max} - M_0)}} \tag{2.30}$$

where M_0 is the lower bound minimum earthquake magnitude considered for engineering applications and M_{max} is the upper bound earthquake magnitude dependent on the seismic source size. The portion of the exponent in the numerator "$m - M_0$" is the same form as Equation 2.28, however, the minimum magnitude is no longer taken as zero and the denominator still represents normalizing by the rate of all earthquakes considered which is now $M_0 < m < M_{max}$. Taking the derivative of the CDF with respect to m as before, the PDF can be found as

$$f_M(m | M_0 < m < M_{max}) = \frac{\beta exp^{-\beta(m - M_0)}}{1 - exp^{-\beta(M_{max} - M_0)}} \tag{2.31}$$

Figure 2.31 is an example of a magnitude probability distribution for a range of magnitudes of 5.0 to 7.7 with a bin size of 0.1. It should be noted that Figure 2.31 is a typical earthquake magnitude probability distribution for sources when not accounting for a characteristic earthquake or geologic data that may refine magnitude probabilities.

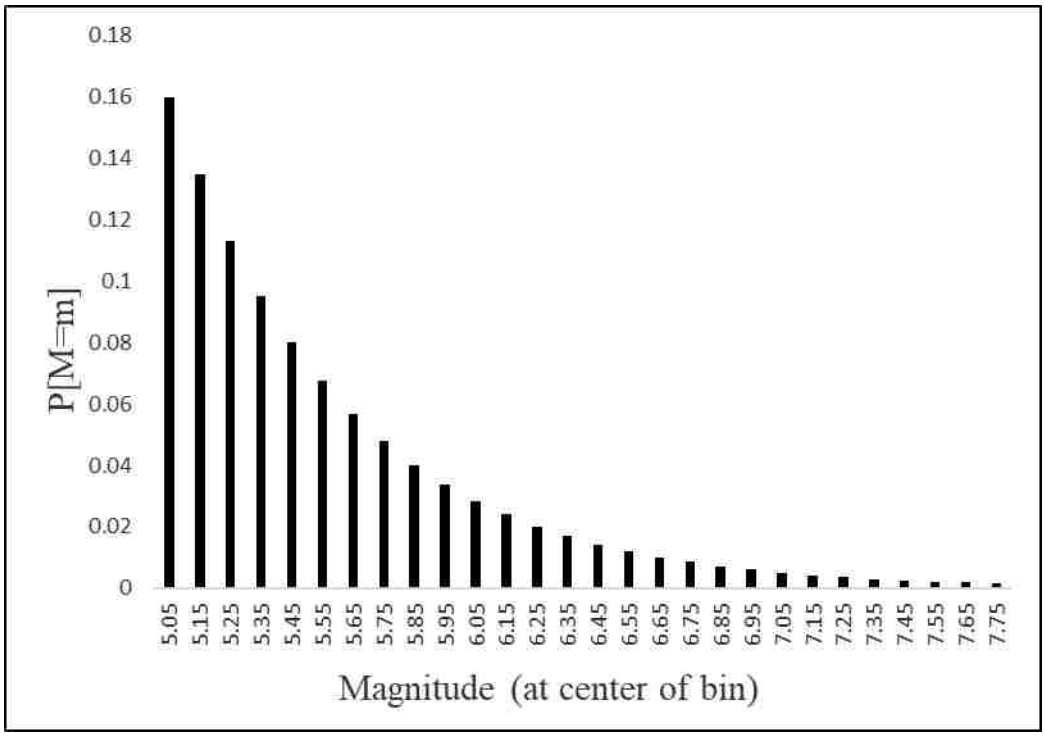

Figure 2.31. Example of an earthquake magnitude probability distribution.

Determining Source-to-Site Distance

The distance to the rupture of an earthquake source is typically considered to be uniformly distributed meaning that the likelihood of an earthquake occurring along a seismic source is the same at every point of that seismic source (Kramer, 1996). This may not always be the case, for example, the San Andreas fault which runs along most of California in the United States, has had more activity along some fault segments than others. This suggests that the fault segments with less recent activity will have a higher likelihood of stress release in the form of an earthquake (After Kramer, 1996). In order to understand how a uniform probability distribution for an

earthquake source can be developed, it is beneficial to start with a point source. For a point source there is only one source-to-site distance, for example, "r_{point}," therefore, the probability that the source-to-site distance is r_{point} is equal to 1, and all other distances have a probability of zero of occurring. For explaining the source-to-site distance of a line source (e.g., a fault) assuming the rupture location of the earthquake is equally likely anywhere along the fault, Baker (2008) considered a 100 km fault with a site located 10 km from the center of the fault as shown in Figure 2.32.

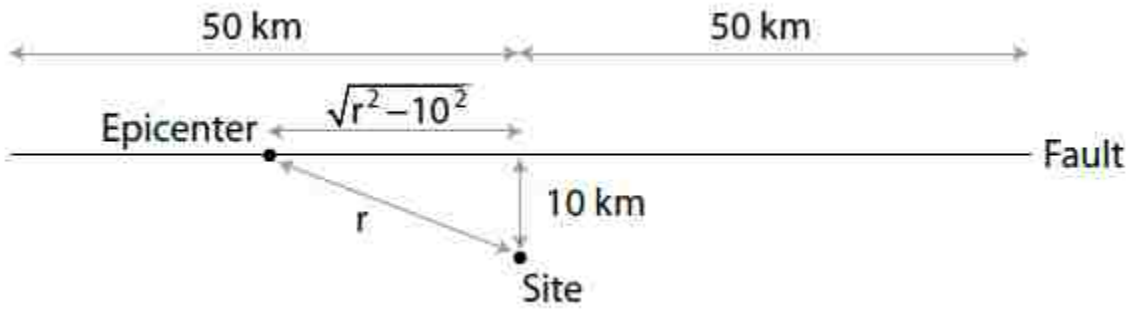

Figure 2.32. Example site and line source geometry for calculating the source-to-site distance probability distribution (Baker, 2008).

From the geometry of Figure 2.32 it is noticeable to see that the probability of a source-to-site distance less than 10 km and a source-to-site distance greater than 51 km is zero (when r greater than 51 km then the distance from the center of the 100 km long line source is greater than 50 km which is not possible). For the example shown in Figure 2.32, the arbitrary value for the distance to the seismic source is represented as r. To obtain the PDF, one must first find the CDF which is the probability that some source-to-site distance R is less than r in this case. Therefore, the probability that the source-to-site distance R is less than 10 km is zero and the probability that the source-to-site distance R is less than 51 is one (because the length from the site to the end of the 100 km long fault cannot be greater than 51). To determine the CDF at source-to-site distances between 10 km and 51 km the length of the line source less than r can be divided by the total

length of the fault (100 km), therefore, using the Pythagorean theorem to calculate the distance of the rupture location from the center of the fault the CDF can be represented as

$$F_R(r) = P(R \leq r) = \frac{2\sqrt{r^2-10^2}}{100} \tag{2.32}$$

where the "2" in the numerator comes from the $\sqrt{r^2 - 10^2}$ term being on both sides of the center of the fault. Considering the source-to-site distance r less than 10 km and r greater than or equal to 51 km, Equation 2.32 can be extended to

$$F_R(r) = P(R \leq r) = \begin{cases} 0 & , \ if\ r < 10\ km \\ = \frac{2\sqrt{r^2-10^2}}{100} & , \ if\ 10 \leq r < 51\ km \\ 1 & , \ if\ r \geq 51\ km \end{cases} \tag{2.33}$$

Taking the derivative of Equation 2.33 gives the PDF as

$$f_R(r) = \frac{d}{dr} F_R(r) = \begin{cases} 0 & , \ if\ r < 10\ km \\ = \frac{r}{50\sqrt{r^2-10^2}} & , \ if\ 10 \leq r < 51\ km \\ 0 & , \ if\ r \geq 51\ km \end{cases} \tag{2.34}$$

The resulting PDF and CDF from Baker (2008) are shown in Figure 2.33

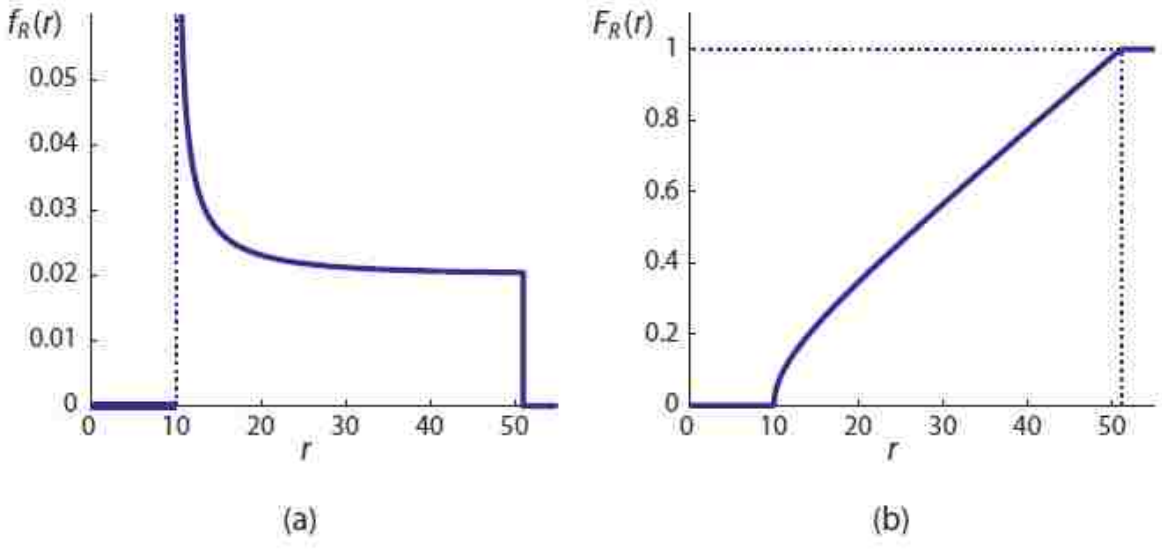

Figure 2.33. PDF and CDF for the example line source geometry in Figure 2.32 (Baker, 2008).

In the event that the source of seismic energy is unknown, an area or volumetric source may be more beneficial to use instead. For example, for a circular area source with earthquakes equally likely to occur anywhere, the probability that the epicenter of an earthquake will occur at a distance r from the site will be the ratio of the area of the circle with a radius r to the area source as a whole (Baker, 2008).

Determining Ground Motion Intensity Measure

Upon determining the magnitude and site to source distance probability distributions the probability of exceeding some intensity measure (IM) level can be computed. Intensity measures may be peak ground acceleration (PGA), peak ground velocity (PGV), peak ground displacement (PGD), spectral intensity measures, etc. To determine the probability of exceeding some IM level given an earthquake event E, the total probability theorem can be applied to give

$$P[IM > im|E] = \iint_{MR} P[IM > im|m,r] f_M(m) f_R(r) dmdr \quad (2.35)$$

where the $P[IM > im|m,r]$ is the attenuation relationship where the probability of an IM exceeding some intensity measure value of im given magnitude m and source to site distance r where IM is typically obtained from a ground motion prediction equation (GMPE), $f_M(m)$ is the PDF for magnitude, and $f_R(r)$ is the PDF of source to site distance. Equation 2.35 can be re-written instead in terms of some rate of exceedance of some minimum intensity measure by introducing the rate of occurrence of earthquake magnitudes greater than some minimum magnitude

$$\lambda[(IM > im)|E] = \lambda[(M > M_o)|E] \iint_{MR} P[IM > im|m,r] f_M(m) f_R(r) dmdr \quad (2.36)$$

where $\lambda[(IM > im)|E]$ is the rate of exceedance of some IM greater than im given an earthquake event E and $\lambda[(M > M_o)|E]$ is the rate of exceedance of a magnitude occurring greater than M_o given an earthquake event E. Because evaluating the integrals analytically is quite complex, the evaluation is typically done using numerical integration using small intervals (e.g. small intervals

of magnitude and source to site distance) (Kramer 1996). In order to take into account multiple earthquake sources (not just a single event E), Equation 2.36 can be written in summation form to account for all sources and for numerical integration purposes of the magnitude and site to source distance. Equation 2.36 can be written as

$$\lambda(IM > im) = \sum_{i=1}^{N_s} \sum_{j=1}^{N_M} \sum_{k=1}^{N_R} \lambda_i[M_i > M_o]\, P[IM > im|m_j, r_k] P[M_i = m_j] P[R_i = r_k] \quad (2.37)$$

where $P[M_i = m_j]$ and $P[R_i = r_k]$ are the probability that a magnitude m_j and distance r_k are produced from a source.

Therefore, Equation 2.37 now allocates for the uncertainties in occurrence, the magnitude, and the source to site distance for earthquakes in order to produce a probability that a certain IM will be exceeded. In order to account for all levels of shaking, Equation 2.37 can be implemented for additional IM to produce the rate of exceeding all intensity IM of interest. In doing so one can develop a curve such Figure 2.34 (after Kramer, 1996).

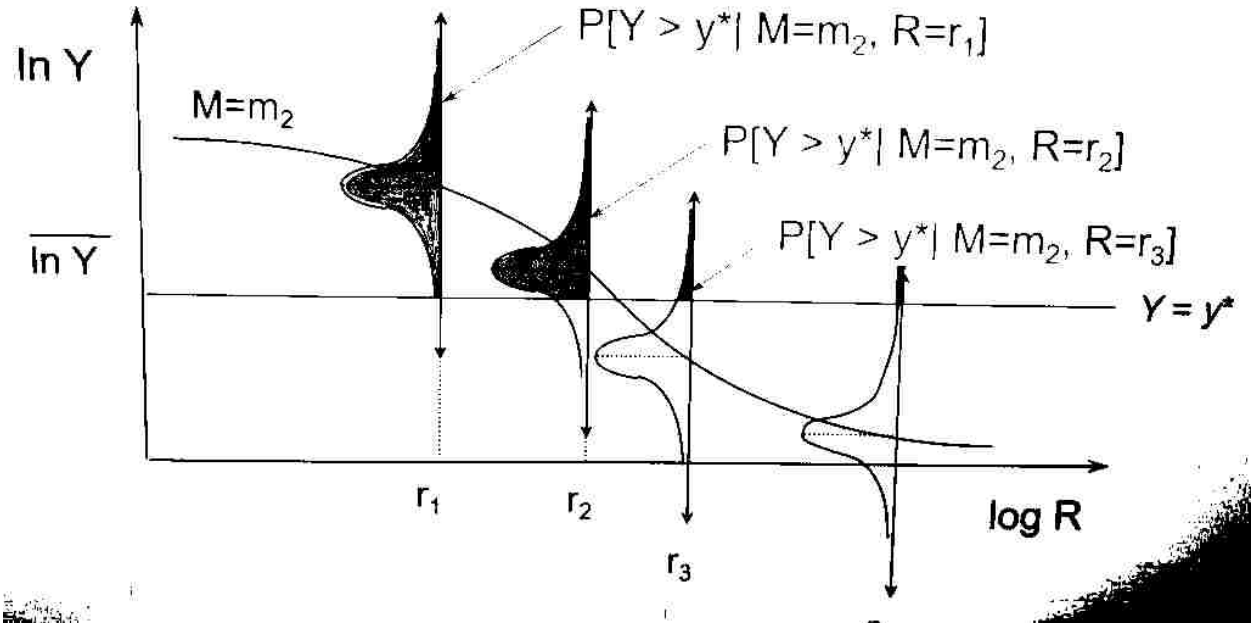

Figure 2.34. Log normal distributions of an IM "Y" for a magnitude and multiple source to site distances (after Kramer, 1996).

Each magnitude and source to site distance combination shown in Figure 2.34 gives the rate of exceeding an IM, λ (Y=y*). Equation 2.37 can be used to compute the rate of exceedance of y* for every magnitude and source to site distance combination in order to give the total rate of exceedance of a single IM y*. This process can be done for multiple y* values in order to develop a hazard curve similar to that shown in Figure 2.35. It should be noted the IM for Figure 2.35 is PGA (instead of being labeled as y*) and Tr is the return period of this PGA. The return period is the reciprocal of the rate of exceeding an IM and is given as

$$T_R(im) = \frac{1}{\lambda(IM>im)} \tag{2.38}$$

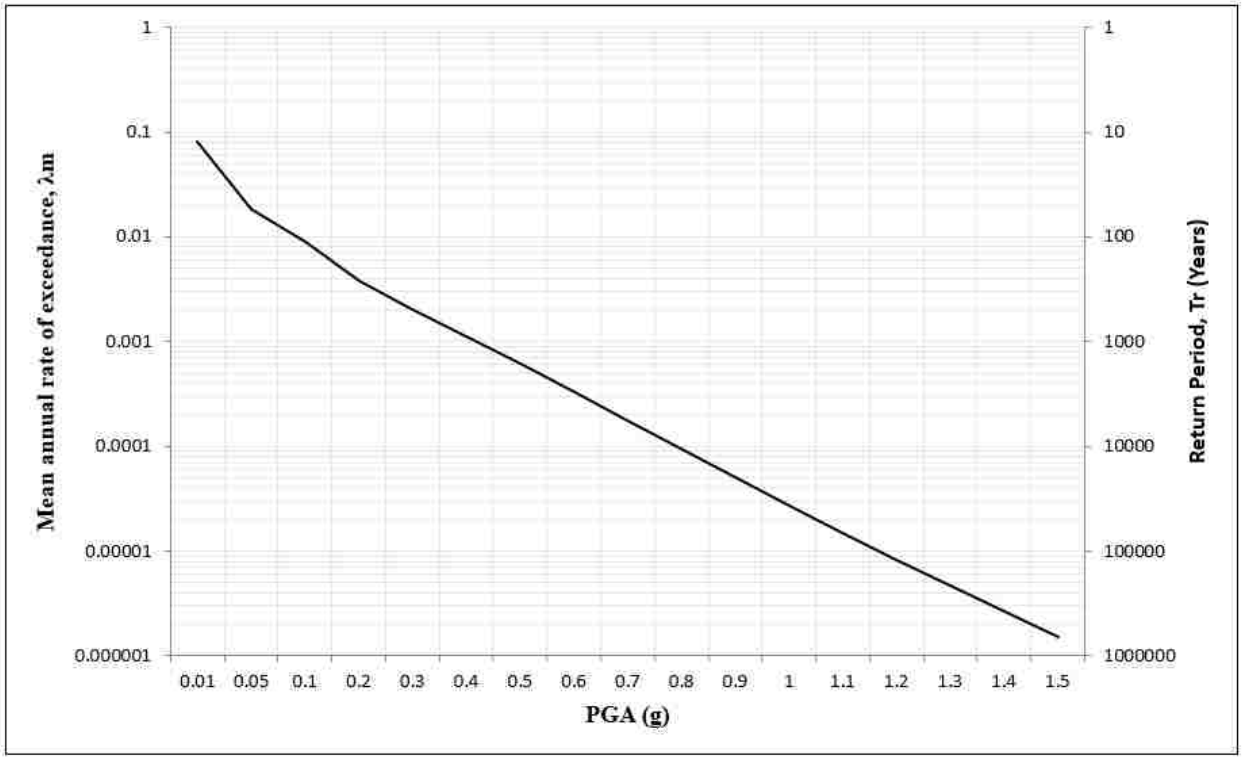

Figure 2.35. Hazard Curve showing the rate of exceedance and return period of PGA.

DSHA and PSHA were covered in order to describe how the value of a_{max} is calculated in order to perform the simplified procedure. The conventional liquefaction hazard evaluation

consists of obtaining an a_{max} from a hazard curve generated via a PSHA for a specific mean annual rate of exceedance and inputting this value into a procedure for calculating CSR such as Cetin et al. (2004) and Boulanger and Idriss (2012) procedures. Liquefaction loading has now been covered in detail, however, whether liquefaction will occur also depends on the resistance of a soil to liquefaction.

2.4.2.2.2.4 Liquefaction Resistance

The next step proved to be a tough test for researchers to overcome. In the 1960's and 1970's researchers believed that reconstituted sand soil specimens would replicate field conditions based on the assumption that the reconstituted sand specimens would have similar behavior as the field conditions if prepared to the same density (void ratio) and effective stress. The laboratory methods used to "deposit" the sand material were moist-tamped, dry-pluviated, and wet-pluviated. In the mid 1970's researchers recognized that the sampling process itself (which caused disturbance of the soil fabric) was one of the reasons for inconsistent results in liquefaction behavior because the soil fabric of the soil specimen in-situ was altered and reconstituted soil specimens (and the different methods of preparing the specimen) thus do not replicate the in-situ field conditions (Ladd, 1974). Ladd (1974) recommended to perform laboratory tests on undisturbed samples when possible, however, this is very difficult to achieve for sand. The moist-tamped, dry-pluviated, and wet-tamping depositional methods not only did not replicate field conditions, but these pseudo-depositional types could not achieve similar results themselves. Not long after the discovery of the effects of depositional environment on soil fabric, Youd and Hoose (1977) first recognized that the age of the soil plays a role in soil behavior as well, realizing that older soils typically have a greater resistance to liquefaction. Due to the soil fabric and aging effects researchers moved toward in-situ testing methods for determining liquefaction resistance.

Three methods for quantifying the liquefaction resistance of soil will be discussed: the SPT procedure, the CPT procedure, and the shear wave velocity procedure. The SPT and CPT procedures will be described by the Cetin et al. (2004) and Boulanger and Idriss (2012) procedures.

2.4.2.2.2.4.1 Liquefaction Resistance – Standard Penetration Test

The second component to calculating the factor of safety against liquefaction for the cyclic stress-based approach (refer back to Equation 2.6) is the cyclic resistance ratio (CRR). The CRR describes the liquefaction resistance of the soil. Penetration resistance procedures (such as the SPT) for determining the CRR require many correction factors including the effective overburden stress, energy, equipment, and fines content adjustments for the penetration resistance "N" values. Calculation of the CRR also often includes adjustments for earthquake magnitudes that are not 7.5, the effective confining stress, and initial shear stress. Because researchers calculate and employ different methods for calculating CRR, the methods described by Cetin et al. (2004) and Boulanger and Idriss (2012) will be described separately.

2.4.2.2.2.4.1.1 Cetin et al. – SPT

Cetin et al. (2004) originally developed an expression for calculating a value of the probability of liquefaction using a Bayesian updating analysis and extended it to develop a deterministic expression for the CRR given as

$$CRR_{Cetin} = \exp\left[\frac{\left((N_1)_{60}(1+0.004FC) - 29.53\ln(M_w) - 3.70\ln\left(\frac{\sigma'_v}{P_a}\right) + 0.05FC + 16.85 + 2.70\phi^{-1}(P_{L,Cetin})\right)}{2.70}\right] \quad (2.39)$$

where $(N_1)_{60}$ is the overburden, energy, and equipment corrected SPT penetration resistance, FC is the fines content (by dry weight) expressed in percent, M_w is the moment magnitude, σ'_v is the effective overburden stress, ϕ^{-1} is the inverse of the standard cumulative normal distribution with

a mean of zero and standard deviation of one, and $P_{L,Cetin}$ is the probability of liquefaction taken as 15 percent for deterministic analyses. Cetin et al. (2004) recommended the CRR expression shown in Equation 2.39 not be used at very high CSR values greater than 0.4 because there is limited field data at such high CSR values and soils that require these large CSR values to liquefy are typically very dense with $(N_1)_{60}$ values of at least 30 which only have a small amount of strain potential upon liquefaction. Use of Equation 2.39 requires knowing how the corrected SPT penetration resistance is obtained. Cetin et al. (2004) mainly followed the 1997 National Center of Earthquake Engineering Research (NCEER 1997) procedure for correcting SPT penetration resistance values, however, there are some differences as will be discussed. The Cetin et al. (2004) procedure for correcting SPT penetration resistance can be expressed in the form of Equation 2.40

$$(N_1)_{60,cs} = N_1 C_R C_S C_B C_E C_{Fines} \tag{2.40}$$

where $(N_1)_{60,cs}$ is the overburden, fines content, energy, equipment, and procedural effects corrected penetration resistance, N_1 is the overburden correction, C_R is the rod length correction, C_S is the liner correction, C_B is the borehole diameter correction, C_E is the hammer energy correction, and C_{Fines} is the fines content correction. The overburden correction is represented as

$$N_1 = N \times C_N \tag{2.41}$$

where N is the field measured uncorrected SPT resistance value and C_N is a factor correcting for the effective overburden stress given as

$$C_N = \left(\frac{1}{\sigma'_v}\right)^{0.5} \leq 1.6 \tag{2.42}$$

where σ'_v is the effective overburden stress at the depth of N. Cetin et al. (2004) differed from the NCEER (1997) procedure by adding the limiting value of 1.6 for the overburden correction instead of a value of 2.0. The rod length correction also differed from the NCEER (1997) procedure in

that the non-linear curve in Figure 2.36 was used instead of correction values assigned based on increments of rod length (e.g., 3 to 4 m C_R = 0.75, 4 to 6 m C_R = 0.85, etc.).

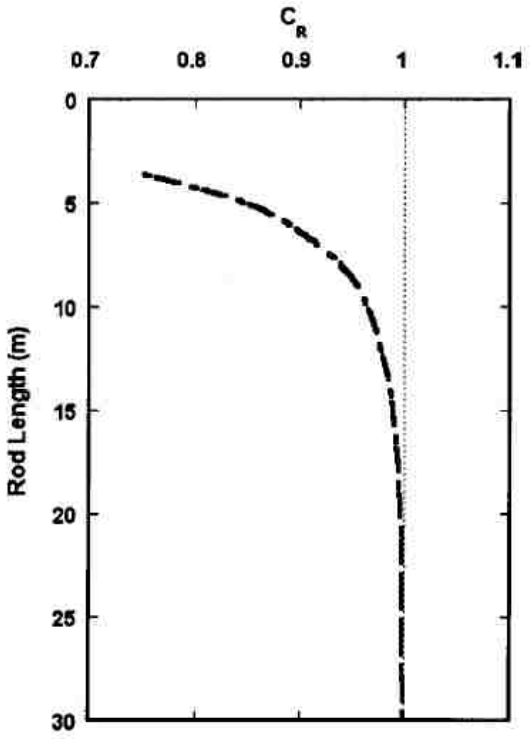

Figure 2.36. Non-linear relationship of the rod length correction factor (Cetin et al. 2004).

The liner correction given by Cetin et al. (2004) is given as

$$C_S = 1 + \frac{(N_1)_{60}}{100} \; where \; 1.10 \leq C_S \leq 1.30 \qquad (2.43)$$

where $(N_1)_{60}$ is the overburden, energy, and equipment corrected SPT penetration resistance value that can be found from Equation 2.40 by excluding the fines content correction factor. The borehole diameter correction factor is shown in Table 2.1 which is the same as the NCEER (1997) guidelines.

Table 2.4. Borehole diameter correction factor (NCEER 1997).

Borehole Diameter (mm)	C_B
65 to 115	1.00
150	1.05
200	1.15

The hammer energy correction factor for the Cetin et al. (2004) procedure slightly differs from the NCEER (1997) procedure and is generally given as shown in Table 2.5.

Table 2.5. Hammer type energy correction factor (after Cetin et al. 2004).

Hammer Type	C_E
Donut Hammer	0.5 to 1.0
Safety Hammer	0.7 to 1.2
Automatic -Trip Hammer (Safety or Donut Type)	0.8 to 1.4

Cetin et al. (2004) gave an approximation for their fines content correction factor as

$$C_{Fines} = (1 + 0.004FC) + 0.05\left(\frac{FC}{(N_1)_{60}}\right) where\ 5\% \leq FC \leq 35\% \qquad (2.44)$$

where FC is the fines content in percent. Fines contents below 5 percent are assumed to have a correction factor value of 1.0. It is important to recognize that the CRR expressed in Equation 2.39 incorporates this fines content correction in the equation itself, therefore, Equation 2.39 is also limited to fines content values from 5 to 35 percent.

The deterministic CRR of Cetin et al. (2004) procedure assumes a probability of liquefaction, $P_{L,Cetin}$, of 15 percent in Equation 2.39. Cetin et al. (2004) originally developed Equation 2.39 to account for the CRR probabilistically accounting for the variability of the probability of liquefaction given as

$$P_{L,Cetin} = \phi\left[-\frac{\left((N_1)_{60}(1+0.004FC)-13.32\ln(CSR)-29.53\ln(M_w)-3.70\ln\left(\frac{\sigma'_v}{P_a}\right)+0.05FC+16.85\right)}{2.70}\right] \qquad (2.45)$$

where $P_{L,Cetin}$ is the probability of liquefaction given as a decimal, ϕ is the standard cumulative normal distribution, and CSR is the cyclic stress ratio without accounting for magnitude duration effects (termed DWF by Cetin et al. 2004) given by Equation 2.12. The reason CSR in Equation 2.45 does not take into account the magnitude duration effects is because Equation 2.45 itself accounts for this. Therefore, in order calculate the CRR probabilistically, the value of $P_{L,Cetin}$

determined from Equation 2.45 should be implemented into the CRR expression given in Equation 2.39.

2.4.2.2.2.4.1.2 Idriss and Boulanger – SPT

The original derivation of the SPT correlation for CRR of Idriss and Boulanger (2004, 2008) can be written as

$$CRR_{M,\sigma'_{vo},\tau_{static}} = \exp\left[\left(\frac{(N_1)_{60,cs}}{14.1}\right) + \left(\frac{(N_1)_{60,cs}}{126}\right)^2 - \left(\frac{(N_1)_{60,cs}}{23.6}\right)^3 + \left(\frac{(N_1)_{60,cs}}{25.4}\right)^4 - 2.8\right] \times K_\sigma \times MSF \times K_\alpha \quad (2.46)$$

where $CRR_{M,\sigma'_{vo},\tau_{static}}$ is the CRR corrected for overburden, magnitude, and shear stress, $(N_1)_{60,cs}$ is the overburden, fines content, energy, and equipment corrected SPT penetration resistance, K_σ is the overburden correction factor, MSF is the magnitude scaling factor, and K_α is the static shear stress correction factor. Use of Equation 2.46 requires knowing how the corrected SPT penetration resistance is obtained. Similar to Cetin et al. (2004), Idriss and Boulanger (2008) mainly followed the 1997 National Center of Earthquake Engineering Research (NCEER 1997) procedure for correcting SPT penetration resistance values, however, there are differences between these three procedures as will be discussed. The Idriss and Boulanger (2004) procedure for correcting SPT penetration resistance can be expressed in the form of Equation 2.40

$$(N_1)_{60} = N_{field} C_R C_S C_B C_E C_N \quad (2.47)$$

where $(N_1)_{60}$ is the overburden, energy, equipment, and procedural effects corrected penetration resistance, N_{field} is measured SPT penetration resistance in the field, C_R is the rod length correction, C_S is the liner correction, C_B is the borehole diameter correction, C_E is the hammer energy correction, and C_N is the overburden correction factor. The rod length correction used by Idriss and Boulanger (2008) is the same as from the NCEER (1997) procedure and is shown in Table 2.6.

Table 2.6. Rod length correction factor (after Idriss and Boulanger 2008).

Rod Length (m)	C_R
< 3	0.75
3-4	0.80
4-6	0.85
6-10	0.95
10-30	1.00

The liner correction given by Idriss and Boulanger 2008 is taken to be a value of 1.0 for split spoon samplers that do not have room for liners and for those with room for liners the values depend on the $(N_1)_{60}$ values as shown in Table 2.7.

Table 2.7. Liner correction factor based on $(N_1)_{60}$ for standard split spoon samplers with room for liners (after Idriss and Boulanger 2008).

$(N_1)_{60}$	C_S
$(N_1)_{60} \leq 10$	1.1
$10 \leq (N_1)_{60} \leq 30$	$1+\frac{(N_1)_{60}}{100}$
$(N_1)_{60} \geq 30$	1.3

The borehole diameter correction factor is shown in Table 2.8 which is the same as the NCEER (1997) guidelines.

Table 2.8. Borehole diameter correction factor (NCEER 1997).

Borehole Diameter (mm)	C_B
65 to 115	1.00
150	1.05
200	1.15

The hammer energy correction factor for Idriss and Boulanger (2008) is the same as the NCEER (1997) procedure and is given in Table 2.9

Table 2.9. Hammer type energy correction factor (after Cetin et al. 2004).

Hammer Type	C_E
Donut Hammer	0.5 to 1.0
Safety Hammer	0.7 to 1.2
Automatic Trip Hammer	0.8 to 1.3

Idriss and Boulanger (2008) express the overburden correction factor as

$$C_N = \left(\frac{1}{\sigma'_v}\right)^{0.784-0.0768\sqrt{(N_1)_{60,cs}}} \leq 1.7 \quad (2.48)$$

where σ'_v is the effective overburden stress at the depth of $(N_1)_{60,cs}$ and $(N_1)_{60,cs}$ is the overburden, fines content, energy, equipment, and procedural effects corrected SPT penetration resistance. In order to solve Equation 2.48, $N_{1,60}$ from Equation 2.47 must be corrected for fines content to obtain $N_{1,60cs}$. This expression can be given as

$$(N_1)_{60,cs} = (N_1)_{60} + \Delta(N_1)_{60} \quad (2.49)$$

where $\Delta(N_1)_{60}$ is the change in the corrected SPT penetration resistance due to the fines content of the soil which can be expressed as

$$\Delta(N_1)_{60} = \exp\left(1.63 + \frac{9.7}{FC+0.01} - \left(\frac{15.7}{FC+0.01}\right)^2\right) \quad (2.50)$$

where FC is the fines content of the soil. As can be seen from Equations 2.47 through 2.50, iteration is required to solve for $N_{1,60cs}$.

As shown in Equation 2.46 the CRR can be extended to account for differing values of effective overburden stress, earthquake magnitude of than a moment magnitude of 7.5, and initial shear stress. After Idriss and Boulanger (2008), effective overburden stress correction factor, K_σ, can be computed as

$$K_\sigma = 1 - C_\sigma \ln\left(\frac{\sigma'_v}{P_a}\right) \leq 1.1 \quad (2.51)$$

where the coefficient C_σ can be expressed as

$$C_\sigma = \frac{1}{18.9-2.55\sqrt{(N_1)_{60,cs}}} \leq 0.3 \quad (2.52)$$

In order to account for earthquakes of moment magnitude other than 7.5, Idriss and Boulanger (2008) expressed the magnitude scaling factor as

$$MSF = 6.9\exp\left(\frac{-M_w}{4}\right) - 0.058 \leq 1.8 \quad (2.53)$$

Finally, the correction factor for static shear stress, K_α, that is used to account for the static shear stress imposed by conditions such as sloping ground or from a nearby or overlying foundation, can be expressed (after Idriss and Boulanger 2008) as

$$K_\alpha = a + bexp(\frac{-\xi_R}{c}) \tag{2.54}$$

where ξ_R is the relative state parameter index and a, b, and c are coefficients expressed as

$$a = 1267 + 636\alpha^2 - 634\exp(\alpha) - 631\exp(-\alpha) \tag{2.55}$$

$$b = \exp(-1.11 + 12.3\alpha^2 + 1.31\ln(\alpha + 0.0001)) \tag{2.56}$$

$$c = 0.138 + 0.126\alpha + 2.52\alpha^3 \tag{2.57}$$

where α is the initial static shear stress ratio given as

$$\alpha = \frac{\tau_s}{\sigma'_v} \tag{2.58}$$

where τ_s is the shear stress and σ'_v is the effective overburden stress. The relative state parameter index, ξ_R, is based on the penetration resistance as

$$\xi_R = \frac{1}{Q - \ln(\frac{100(1+2K_O)\sigma'_v)}{3P_a}} - \sqrt{\frac{(N_1)_{60}}{46}} \tag{2.59}$$

where the initial shear stress ratio and relative state parameter index should be constrained to $\alpha \leq 0.35$ and $-0.6 \leq \xi_R \leq 0.1$ respectively, K_o is the coefficient of lateral earth pressure at rest with typical values of 0.45 to 0.5 for a simple shear device normally consolidated in one dimension, and Q is an empirical constant.

Boulanger and Idriss (2014) updated their MSF equation for liquefaction resistance from Idriss and Boulanger (2008) to

$$MSF = 1 + (MSF_{max} - 1)(8.64\exp\left(\frac{-M}{4}\right) - 1.325) \tag{2.60}$$

where MSF_{max} can be written as

$$MSF_{max} = 1.09 + \left(\frac{(N_1)_{60,cs}}{31.5}\right)^2 \leq 2.2 \quad (2.61)$$

Based on Equations 2.60 and 2.61 Kramer and Stewart (unpublished manuscript) re-wrote Equation 2.46 to be in terms of K_M instead of MSF as

$$CRR_{M,\sigma'_{vo},\tau_{static}} = \exp\left[\left(\frac{(N_1)_{60,cs}}{14.1}\right) + \left(\frac{(N_1)_{60,cs}}{126}\right)^2 - \left(\frac{(N_1)_{60,cs}}{23.6}\right)^3 + \left(\frac{(N_1)_{60,cs}}{25.4}\right)^4 - 2.8\right] \times K_\sigma \times K_M \times K_\alpha \quad (2.62)$$

where K_M is the correction factor for magnitude expressed as

$$K_M = \frac{1+(MSF_{max}-1)\left(8.64\exp\left(\frac{-M}{4}\right)-1.325\right)}{0.5803-2.7368\exp\left(-M/4\right)} \quad (2.63)$$

It should be noted the new MSF developed by Boulanger and Idriss (2014) and the CRR expression shown in Equation 2.62 was not used for liquefaction analysis presented hereon in this thesis, but has been shown here to provide a thorough literature review. The CRR used in deterministic liquefaction analyses is shown in Equation 2.46.

In order to develop a fully probabilistic liquefaction triggering procedure for SPT resistance, Boulanger and Idriss (2012) incorporated the performance-based method developed by Kramer and Mayfield (2007). The Boulanger and Idriss (2012) probabilistic liquefaction resistance in terms of CRR can be written as

$$CRR_{M,\sigma'_{vo},\tau_{static}} = \exp\left[\left(\frac{(N_1)_{60,cs}}{14.1}\right) + \left(\frac{(N_1)_{60,cs}}{126}\right)^2 - \left(\frac{(N_1)_{60,cs}}{23.6}\right)^3 + \left(\frac{(N_1)_{60,cs}}{25.4}\right)^4 - 2.67 + \varepsilon_{\ln(R)}\right] K_\sigma \times K_M \times K_\alpha \quad (2.64)$$

where $\varepsilon_{\ln(R)}$ is the error term for the CRR which is normally distributed with a mean of 0.0 and a recommended standard deviation, $\sigma_{\ln(R)}$, of 0.13 by Boulanger and Idriss (2012). Equation 2.64 can be re-written as

$$CRR_{M,\sigma'_{vo},\tau_{static}} = \exp\left[\left(\frac{(N_1)_{60,cs}}{14.1}\right) + \left(\frac{(N_1)_{60,cs}}{126}\right)^2 - \left(\frac{(N_1)_{60,cs}}{23.6}\right)^3 + \left(\frac{(N_1)_{60,cs}}{25.4}\right)^4 - 2.67 + \sigma_{\ln(R)} \times \phi^{-1}(P_L)\right] K_\sigma \times K_M \times K_\alpha \quad (2.65)$$

where $\sigma_{\ln(R)}$ is the standard deviation, ϕ^{-1} is the inverse of the standard cumulative normal distribution, and P_L is the probability of liquefaction which Boulanger and Idriss (2012) expressed as

$$P_L((N_1)_{60,cs}, CSR_{M=7.5,\,\sigma'_{vo}=1\ atm}) = \phi\left[\frac{-\left(\frac{(N_1)_{60,cs}}{14.1}\right)+\left(\frac{(N_1)_{60,cs}}{126}\right)^2-\left(\frac{(N_1)_{60,cs}}{23.6}\right)^3+\left(\frac{(N_1)_{60,cs}}{25.4}\right)^4-2.67-\ln(CSR_{M=7.5,\,\sigma'_{vo}=1\ atm})}{\sigma_{\ln(R)}}\right] \quad (2.66)$$

where $CSR_{M=7.5,\,\sigma'_{vo}=1\ atm}$ is the cyclic stress ratio adjusted to a reference moment magnitude of 7.5 and effective overburden stress of 1 atm. Equation 2.64, which represents the probabilistic triggering relationship for the CRR, is equal to the deterministic expression for the CRR proposed by Idriss and Boulanger (2004, 2008) when $\varepsilon_{\ln(R)} = -0.13$. Therefore, the deterministic expression is one standard deviation below the expected triggering curve. This gives a probability of liquefaction of approximately 16 percent that can be input into Equation 2.65 to determine the CRR deterministically (Boulanger and Idriss 2012).

It should be noted that the Kramer and Mayfield (2007) performance-based framework will be discussed in depth in Chapter 3 (Probabilistic Liquefaction Hazard Analysis) and has been introduced here to provide context as to how Boulanger and Idriss (2012) developed their probabilistic SPT liquefaction triggering procedure.

2.4.2.2.2.4.2 Liquefaction Resistance – Cone Penetration Test

Cone penetration tests (CPTs) involve mechanically pushing a steel cone into the ground while an electronic measuring system records the tip resistance and sleeve friction of the soil. In this manner the in-situ resistance of the soil can be determined. Oftentimes, the steel cone will also

be equipped with a pore pressure transducer to measure the pore pressure of the soil while the cone is pushed. The following CPT liquefaction triggering procedure is by Boulanger and Idriss (2014).

The CPT correlation for CRR of Boulanger and Idriss (2014) can be written as

$$CRR_{M,\sigma'_{vo},\tau_{static}} = \exp\left[\left(\frac{q_{c1Ncs}}{113}\right) + \left(\frac{q_{c1Ncs}}{1000}\right)^2 - \left(\frac{q_{c1Ncs}}{140}\right)^3 + \left(\frac{q_{c1Ncs}}{137}\right)^4 - 2.8\right] K_\sigma \times MSF \times K_\alpha \quad (2.67)$$

where $CRR_{M,\sigma'_{vo},\tau_{static}}$ is the CRR corrected for overburden, magnitude, and shear stress, q_{c1Ncs} is the overburden and fines content corrected cone tip resistance, K_σ is the overburden correction factor, MSF is the magnitude scaling factor, and K_α is the static shear stress correction factor. Use of Equation 2.67 requires knowing how the corrected CPT penetration resistance is obtained. The measured cone tip resistance can be corrected for unequal end area effects via the expression

$$q_t = q_c + (1 - A_r)u_2 \quad (2.68)$$

where q_t is the unequal end area effects corrected cone tip resistance, q_c is the measured cone tip resistance, A_r is the area ratio for the tip of the cone which has typical values between 0.65 and 0.85, and u_2 is the pore pressure that is measured behind the tip of the cone. For sands, q_t and q_c have been found to be approximately equal whether the unequal end area correction is completed (Boulanger and Idriss 2014). Therefore, because the context of this thesis has to do with liquefaction (which typically occurs in sands) the cone tip resistance will be presented in terms of q_c.

In order to correct the cone tip resistance for overburden stress, the cone tip resistance can be presented as

$$q_{c1N} = C_N q_{cN} = C_N \frac{q_c}{P_a} \quad (2.69)$$

where q_{c1N} is the overburden corrected cone tip resistance, P_a is the atmospheric pressure, and C_N is the overburden correction factor which from Idriss and Boulanger (2008) can be expressed as

$$C_N = \left(\frac{P_a}{\sigma'_v}\right)^{1.338-0.249\sqrt{q_{c1Ncs}}} \leq 1.7 \tag{2.70}$$

where σ'_v is the effective overburden stress at the depth of q_{c1Ncs} and q_{c1Ncs} is the overburden and fines content corrected CPT resistance. In order to solve Equation 2.70, q_{c1N} from Equation 2.69 must be corrected for fines content to obtain q_{c1Ncs}. This expression can be given as

$$q_{c1Ncs} = q_{c1N} + \Delta q_{c1N} \tag{2.71}$$

where Δq_{c1N} is the change in the corrected CPT resistance due to the fines content of the soil which Boulanger and Idriss (2014) expressed as

$$\Delta q_{c1N} = \left(11.9 + \frac{q_{c1N}}{14.6}\right) \exp\left(1.63 - \frac{9.7}{FC+2} - \left(\frac{15.7}{FC+2}\right)^2\right) \tag{2.72}$$

where FC is the fines content of the soil. As can be seen from Equations 2.69 through 2.72, iteration is required to solve for q_{c1Ncs}.

As shown in Equation 2.46 the CRR can be extended to account for differing values of effective overburden stress, earthquake magnitude of than a moment magnitude of 7.5, and initial shear stress. After Idriss and Boulanger (2008), effective overburden stress correction factor, K_σ, can be computed as

$$K_\sigma = 1 - C_\sigma \ln\left(\frac{\sigma'_v}{P_a}\right) \leq 1.1 \tag{2.73}$$

where the coefficient C_σ can be expressed as

$$C_\sigma = \frac{1}{37.3 - 8.27(q_{c1Ncs})^{0.264}} \leq 0.3 \tag{2.74}$$

In order to account for earthquakes of moment magnitude other than 7.5, Idriss and Boulanger (2008) expressed the magnitude scaling factor as

$$MSF = 6.9 \exp\left(\frac{-M_w}{4}\right) - 0.058 \leq 1.8 \tag{2.75}$$

Finally, the correction factor for static shear stress, K_α, that is used to account for the static shear stress imposed by conditions such as sloping ground or from a nearby or overlying foundation, can be expressed (after Idriss and Boulanger 2008) as

$$K_\alpha = a + bexp(\frac{-\xi_R}{c}) \tag{2.76}$$

where ξ_R is the relative state parameter index and a, b, and c are coefficients expressed previously in Equations 2.55, 2.56, 2.57, and 2.58. The relative state parameter index, ξ_R, is based on the penetration resistance as

$$\xi_R = \frac{1}{Q - \ln(\frac{100(1+2K_O)\sigma'_v)}{3P_a}} - (0.478(q_{c1N})^{0.264} - 1.063) \tag{2.77}$$

where q_{c1N} is constrained to values ≥ 21 and the initial shear stress ratio and relative state parameter index should be constrained to $\alpha \leq 0.35$ and $-0.6 \leq \xi_R \leq 0.1$ respectively, K_o is the coefficient of lateral earth pressure at rest with typical values of 0.45 to 0.5 for a simple shear device normally consolidated in one dimension, and Q is an empirical constant.

Boulanger and Idriss (2014) updated their MSF equation for liquefaction resistance from Idriss and Boulanger (2008) to

$$MSF = 1 + (MSF_{max} - 1)(8.64 \exp\left(\frac{-M}{4}\right) - 1.325) \tag{2.78}$$

where MSF_{max} can be written as

$$MSF_{max} = 1.09 + (\frac{q_{c1Ncs}}{180})^3 \leq 2.2 \tag{2.79}$$

Based on Equations 2.78 and 2.79 Kramer and Stewart (unpublished manuscript) re-wrote Equation 2.67 to be in terms of K_M instead of MSF as

$$CRR_{M,\sigma'_{vo},\tau_{static}} = \exp\left[\left(\frac{q_{c1Ncs}}{113}\right) + (\frac{q_{c1Ncs}}{1000})^2 - \left(\frac{q_{c1Ncs}}{140}\right)^3 + \left(\frac{q_{c1Ncs}}{137}\right)^4 - 2.8\right] K_\sigma \times K_M \times K_\alpha \tag{2.80}$$

where K_M is the correction factor for magnitude expressed as

$$K_M = \frac{1+(MSF_{max}-1)(8.64\exp(\frac{-M}{4})-1.325)}{0.5803-2.7368\exp(^{-M}/_{4})} \quad (2.81)$$

Equation 2.80 represents the CPT deterministic expression for calculating the cyclic resistance ratio corrected for overburden, magnitude, and shear stress.

In order to develop a fully probabilistic liquefaction triggering procedure for CPT resistance, Boulanger and Idriss (2014) incorporated the performance based method developed by Kramer and Mayfield (2007). The Boulanger and Idriss (2012) probabilistic liquefaction resistance in terms of CRR can be written as

$$CRR_{M,\sigma'_{vo},\tau_{static}} = \exp\left[\left(\frac{q_{c1Ncs}}{113}\right) + (\frac{q_{c1Ncs}}{1000})^2 - \left(\frac{q_{c1Ncs}}{140}\right)^3 + \left(\frac{q_{c1Ncs}}{137}\right)^4 - 2.60 + \varepsilon_{\ln(R)}\right] K_\sigma \times K_M \times K_\alpha \quad (2.82)$$

where $\varepsilon_{\ln(R)}$ is the error term for the CRR which is normally distributed with a mean of 0.0 and a recommended standard deviation, $\sigma_{\ln(R)}$, of 0.20 by Boulanger and Idriss (2012). Equation 2.82 can be re-written as

$$CRR_{M,\sigma'_{vo},\tau_{static}} = \exp\left[\left(\frac{q_{c1Ncs}}{113}\right) + (\frac{q_{c1Ncs}}{1000})^2 - \left(\frac{q_{c1Ncs}}{140}\right)^3 + \left(\frac{q_{c1Ncs}}{137}\right)^4 - 2.60 + \sigma_{\ln(R)} \cdot \phi^{-1}(P_L)\right] K_\sigma \times K_M \times K_\alpha \quad (2.83)$$

where $\sigma_{\ln(R)}$ is the standard deviation, ϕ^{-1} is the inverse of the standard cumulative normal distribution, and P_L is the probability of liquefaction which Boulanger and Idriss (2012) expressed as

$$P_L(q_{c1Ncs}, CSR_{M=7.5,\,\sigma'_{vo}=1\,atm}) = \phi\left[\frac{-\left(\frac{q_{c1Ncs}}{113}\right)+\left(\frac{q_{c1Ncs}}{1000}\right)^2-\left(\frac{q_{c1Ncs}}{140}\right)^3+\left(\frac{q_{c1Ncs}}{137}\right)^4-2.60-\ln(CSR_{M=7.5,\,\sigma'_{vo}=1\,atm})}{\sigma_{\ln(R)}}\right] \quad (2.84)$$

where $CSR_{M=7.5,\,\sigma'_{vo}=1\,atm}$ is the cyclic stress ratio adjusted to a reference moment magnitude of 7.5 and effective overburden stress of 1 atm. Equation 2.82, which represents the probabilistic triggering relationship for the CRR, is equal to the deterministic expression for the CRR proposed

by Idriss and Boulanger (2004, 2008) when $\varepsilon_{\ln(R)} = -0.20$. Therefore, the deterministic expression is one standard deviation below the expected triggering curve. This gives a probability of liquefaction of approximately 16 percent that can be input into Equation 2.83 to determine the CRR deterministically (Boulanger and Idriss 2014).

It should be noted that the Kramer and Mayfield (2007) performance-based framework will be discussed in depth in Chapter 3 (Probabilistic Liquefaction Hazard Analysis) and has been introduced here to provide context as to how Boulanger and Idriss (2014) developed their probabilistic CPT liquefaction triggering procedure. It should also be noted that other probabilistic CPT based liquefaction triggering procedures have been introduced (such as Moss et al. 2006), however, have not been discussed due to the prominence of the Boulanger and Idriss (2014) procedure.

Up to this point the uncertainty in the prediction of response of a system has only been briefly introduced for the purpose of explaining probabilistic liquefaction triggering relationships. Chapter 3 discusses combining a probabilistic response model with a probabilistic seismic hazard analysis which forms what is now known as Probabilistic Liquefaction Hazard Analysis.

2.4.2.2.2.4.3 Liquefaction Resistance – Shear Wave Velocity

Evaluating liquefaction resistance does not need to be performed using a costly penetration based procedure such as the SPT and CPT. Instead, a cheaper non-invasive alternative for evaluating liquefaction potential can be performed using a shear wave velocity liquefaction potential method. Shear wave velocity can be measured via several different methods such as spectral analysis of surface waves (SASW), multichannel analysis of surface waves (MASW), and seismic cross-hole to name a few. Andrus and Stokoe (2000) developed one of the first shear wave velocity based liquefaction potential procedures incorporating the simplified method originally

developed by Seed and Idriss (1971) and previously discussed in Section 2.4.2.2.2.1.2, however, using correlations with shear wave velocity instead of SPT resistance.

Andrus and Stokoe (2003) updated the Andrus and Stokoe (2000) procedure and highlighted several advantages of using a shear wave velocity based liquefaction method:

1) Shear wave velocity measurements can be performed in soils (e.g., gravel) that are difficult or even impossible for penetration based methods such as the SPT and CPT to be performed.
2) Shear wave velocity is directly related to the shear modulus, and the shear modulus is directly related to a materials shear strain, and shear strain is directly related to the generation of pore pressure, which is a critical factor in assessing the potential of liquefaction.
3) Because shear wave velocity is directly related to the shear modulus, G_{max}, it can be important for characterizing earthquake loading via a site response analysis because it allows for the measurement of the anchor point on modulus degradation curves that are used in equivalent-linear site response analyses.
4) Shear wave velocity methods may be used where invasive penetration based procedures are not allowed. For example, a paleoliquefaction site of interest may be located on a wildlife refuge where invasive testing may not be allowed to evaluate the liquefaction resistance due to the noise and vibrations disturbing wildlife, whereas, a method such as an active MASW or passive MASW (analogous to the Microtremor Array Measurement, or MAM method) may be used to obtain shear wave velocity measurements.

Andrus and Stokoe (2003) also noted a couple of disadvantages of the shear wave velocity approach to evaluating liquefaction potential:

1) Shear wave velocity measurements are made at small strains and liquefaction occurs at relatively large strains.
2) Because shear wave velocity testing does not obtain a sample of the soil it can be difficult to discertain between liquefiable and non-liquefiable soils even though both soils may have the same shear wave velocity.

Based on these disadvantages, a preferred usage of the shear wave velocity based procedure would be when it's used in conjunction with a SPT, CPT, dynamic cone penetration test, vibrocore, or hand auger in order to identify the type of soil and/or soil characteristics to determine whether the soil is susceptible or not susceptible to liquefaction.

There are multiple shear wave velocity procedures for assessing liquefaction potential, however, the shear wave velocity procedures of Andrus and Stokoe (2003) and Kayen et al. (2013) for evaluating liquefaction potential provide a good basis for comprehending shear wave velocity methods and provide an understanding one of the first procedures and a relatively new procedure for assessing liquefaction potential based on shear wave velocity.

Andrus and Stokoe

The shear wave velocity procedure presented by Andrus and Stokoe (2003) evaluates the earthquake loading via the CSR based on the simplified method (Seed and Idriss 1971) previously expressed in Equation 2.12. Andrus and Stokoe (2003) recommended that the stress reduction coefficient, r_d, be determined from the average curve shown in Figure 2.26 originally developed by Seed and Idriss (1971).

Andrus and Stokoe (2003) developed the following expression for the CRR

$$CRR = MSF\left[0.022\left(\frac{K_c V_{S1}}{100}\right)^2 + 2.8\left(\frac{1}{V^*_{S1} - K_c V_{S1}} - \frac{1}{V^*_{S1}}\right)\right] \quad (2.85)$$

where MSF is the magnitude scaling factor, V_{S1} is the overburden corrected shear wave velocity, V^*_{S1} is the upper constraint on V_{S1} for the occurrence of cyclic liquefaction, and K_c is a correction factor to handle high V_{S1} values due to cementation and aging effects. They also noted that the CRR expression given in Equation 2.85 is for cases where severe liquefaction behavior has occurred such as where sand boils and ground cracks are present. Andrus and Stokoe (2003) recommended using the magnitude scaling factor initially recommended by the 1996 NCEER Workshop as

$$MSF = \left(\frac{M_w}{7.5}\right)^n \tag{2.86}$$

where M_w is the moment magnitude and n is an exponent with a recommended value by Andrus and Stokoe (2003) of -2.56. As with the penetration based procedures, the shear wave velocity procedure is corrected for the overburden pressure. The expression used by Andrus and Stokoe to correct the shear wave velocity to a standard vertical effective stress of 1 atm is

$$V_{S1} = V_s \left(\frac{P_a}{\sigma'_{vo}}\right)^{0.25} \tag{2.87}$$

where V_s is the shear wave velocity, P_a is the atmospheric pressure in kPa, and σ'_{vo} is the initial effective overburden stress in kPa. Based on case history data, along with penetration tests correlated with shear wave velocity, Andrus and Stokoe (2003) estimated V^*_{S1} values for sandy soils based on the fines content. For sands with a fines content less than or equal to 5 percent a value of 215 m/s is used for V^*_{S1}, for sands and silts with a fines content greater than or equal to 35 percent a value of 200 m/s is used for V^*_{S1}, and if the fines content is between 5 percent and 35 percent then the following expression is used

$$V^*_{S1} = 215 - 0.5(FC - 5)\frac{m}{s} \tag{2.88}$$

where FC is the fines content of the soil. Andrus and Stokoe (2003) also recommended that the latter values of V^*_{S1} developed for sandy soils could also be used for gravelly soils.

Because the case history database generally consisted of soils that were uncemented and less than 10,000 years old, Andrus and Stokoe (2003) developed the cementation and aging correction factor, K_c, to extend to soils conditions other than those from which the case history database consists of. Andrus and Stokoe (2003) recommended that a K_c value of 1 be used for soils that are uncemented and less than 10,000 years old (Holocene age soils), for soils weakly cemented and older than 10,000 years old (Pleistocene age soils) Andrus and Stokoe suggested K_c be determined from correlations with the SPT and CPT penetration test data as shown in Figures 2.37-2.38 below. For soils without penetration data and no cementation and aging information, Andrus and Stokoe recommended assuming a K_c value of 0.6.

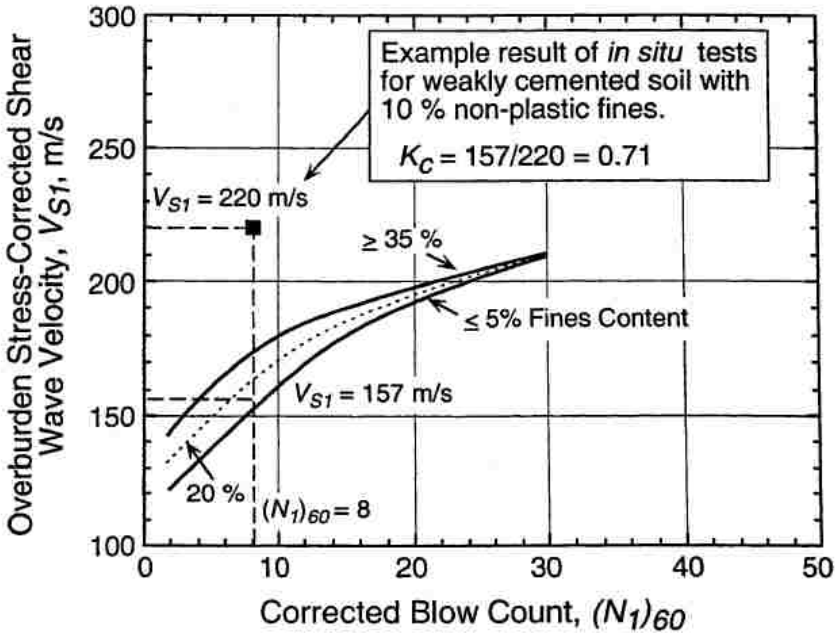

Figure 2.37. Method for evaluating K_c for soils that are weakly cemented and based on V_{S1}, $(N_1)_{60}$, and FC (Andrus and Stokoe 2003).

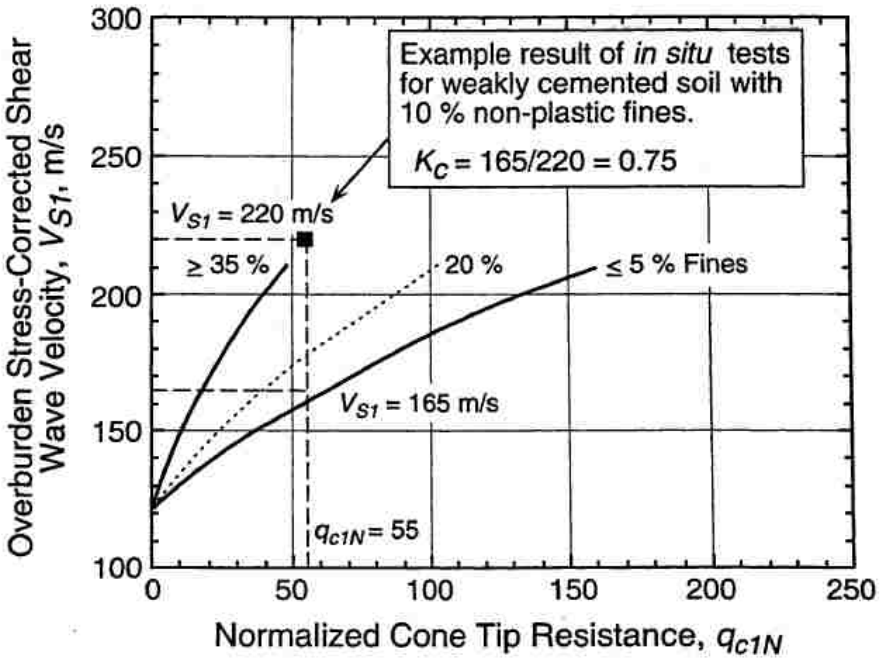

Figure 2.38. Method for evaluating K_c for soils that are weakly cemented and based on V_{S1}, q_{c1N}, and FC (Andrus and Stokoe 2003).

The Andrus and Stokoe (2003) deterministic shear wave velocity procedure then evaluated the potential for liquefaction based on Equation 2.6 where if the factor of safety is less than or equal to 1 liquefaction would occur, and when the factor of safety is greater than 1 liquefaction does not occur. In order to calculate the probability of liquefaction Andrus and Stokoe used the expression

$$P_L = \frac{1}{1+\left(\frac{FS_L}{0.73}\right)^{3.4}} \tag{2.89}$$

where P_L is the probability of liquefaction and FS_L is the factor of safety against liquefaction. Andrus and Stokoe realized that this approach did not take into account the uncertainties in CSR and CRR, however, believed these uncertainties to be relatively small. Using this approach, a deterministic factor of safety against liquefaction value of 1 corresponds to a 26 percent chance of the occurrence of liquefaction.

Kayen et al.

The shear wave velocity procedure of Kayen et al. (2013) is based on 422 liquefaction case histories, many of which correspond to case histories where penetration testing had been previously performed, however, shear wave velocity measurements had not been made until the Kayen et al. (2013) study. The shear wave velocity procedure of Kayen et al. (2013) is based on the simplified method introduced by Seed and Idriss (1971), however, incorporated the stress reduction coefficient based on Cetin et al. (2004) shown in Equation 2.20 with the standard deviation term in Equation 2.20 given by Equations 2.22 or 2.23 depending on whether the depth is less than or greater than 12 meters respectively. Kayen et al. (2003) did not use Equation 2.21 (calculation of r_d for depths greater than 20 meters) because the global case history dataset mainly consists of depths less than 20 meters.

Similar to Cetin et al. (2004), Kayen et al. (2013) developed an expression for calculating a value of the probability of liquefaction using a Bayesian updating analysis and extended it to develop a deterministic expression for the CRR given as

$$CRR_{Kayen} = \exp\left[\frac{\left((0.0073V_{s1})^{2.8011} - 2.6168\ln(M_w) - 0.0099\ln(\sigma'_v) + 0.0028FC - 0.4809\phi^{-1}(P_{L,Kayen})\right)}{1.946}\right] \quad (2.90)$$

where V_{s1} is the shear wave velocity corrected for overburden pressure as given in Equation 2.87, M_w is the moment magnitude, σ'_v is the effective overburden stress, FC is the fines content (by dry weight) expressed in percent, ϕ^{-1} is the inverse of the standard cumulative normal distribution, and $P_{L,Kayen}$ is the probability of liquefaction taken as 15 percent for deterministic analyses.

In the Kayen et al. (2013) study, the authors adjusted the CSR by normalizing it by the effective stress and accounting for durations of earthquake shaking other than an M_w of 7.5. The expression for this is

$$CSR^* = CSR_{M_w=7.5,\,\sigma'_v=1\ atm} = \frac{CSR}{DWF \cdot K_\sigma} \tag{2.91}$$

where $CSR_{M_w=7.5,\,\sigma'_v=1\ atm}$ is the cyclic stress ratio corrected to an equivalent M_w of 7.5 and overburden stress of 1 atm, DWF is the duration weighting factor, and K_σ is the overburden correction factor. The K_σ relationship from Kayen et al. (2013) is

$$K_\sigma = {\sigma'_v}^{-0.0099/1.946} = {\sigma'_v}^{-0.00509} \tag{2.92}$$

Due to limitations of the 422 liquefaction sites (e.g., all liquefaction sites having a vertical effective stress less than 180 kPa) K_σ should not be evaluated for vertical effective stress greater than 200 kPa (Kayen et al. 2013).

Kayen et al. (2013) expressed the DWF from Equation 2.91 as

$$DWF = 15{M_w}^{-1.342} \tag{2.93}$$

and this expression for DWF is valid for moment magnitudes between 5.5 to 9.0 based on this being the range of earthquake magnitudes in the dataset. Kayen et al. (2013) also noted the shear wave velocity measurements are relatively insensitive to fines content and exclaimed that the uncertainty in fines content is relatively small when compared the uncertainty in the estimation of CSR^* and V_{s1}. The Kayen et al. (2013) paper does not provide a specific adjustment for fines content, however, does provide an example of how little variability there is between a CSR versus V_{s1} curve for fines contents of 0 percent and 35 percent for a probability of liquefaction of 50 percent given a moment magnitude 7.5 earthquake and initial effective stress of 100 kPa as shown below in Figure 2.39.

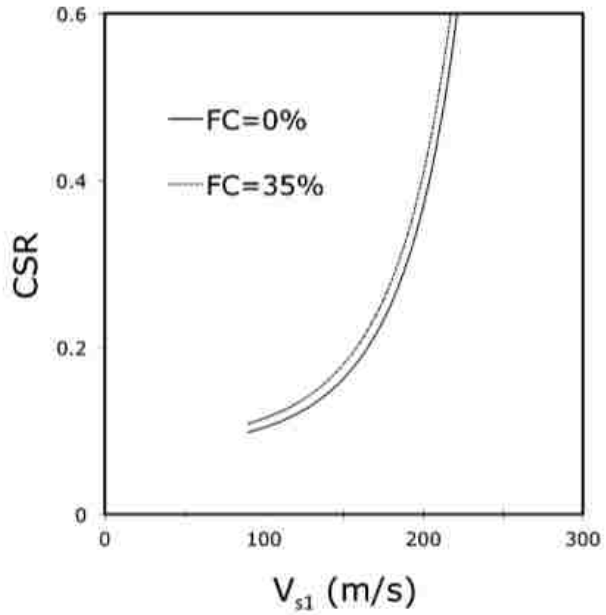

Figure 2.39. Influence of a fines content adjustment for fines content values of 0 percent and 35 percent for a probability of liquefaction of 50 percent, moment magnitude 7.5 event, and initial vertical effective stress of 100 kPa (Kayen et al. 2013).

The deterministic CRR of Kayen et al. (2013) procedure assumes a probability of liquefaction, $P_{L,Kayen}$, of 15 percent in Equation 2.90. Kayen et al. (2013) originally developed Equation 2.90 to account for the CRR probabilistically accounting for the variability of the probability of liquefaction given as

$$P_{L,Kayen} = \phi\left[-\frac{\left((0.0073V_{S1})^{2.8011} - 1.946\ln(CSR) - 2.6168\ln(M_w) - 0.0099\ln(\sigma'_v) + 0.0028FC\right)}{0.4809}\right] \quad (2.94)$$

where $P_{L,Kayen}$ is the probability of liquefaction given as a decimal, ϕ is the standard cumulative normal distribution, and CSR is the cyclic stress ratio without accounting for magnitude duration effects (termed DWF by Kayen et al. 2013) given by Equation 2.93. The reason CSR in Equation 2.94 does not take into account the magnitude duration effects is because Equation 2.94 itself accounts for this. Therefore, in order calculate the CRR probabilistically, the value of $P_{L,Kayen}$ determined from Equation 2.94 should be implemented into the CRR expression given in Equation 2.90.

2.5 LIQUEFACTION EFFECTS

The consequences of liquefaction can range from minor cracks in buildings to the collapse of bridges. Liquefaction can range across large areas of naturally deposited loose sand to localized zones where loose sand fill has been placed. Flow liquefaction oftentimes causes catastrophic effects such as the static liquefaction flow failure of Fort Peck Dam described in Section 2.4.1.1.2. The effects of cyclic liquefaction, while not usually as severe as flow liquefaction, can also cause tremendous damage as shown previously in Figure 2.2 showing liquefaction induced lateral spreading during the 2010 Haiti earthquake. Flow failures, floatation of light buried structures, bearing capacity failures, and retain wall failures are oftentimes the results of flow liquefaction. The most common effects of cyclic liquefaction include alteration of ground motions, sand boils, settlement, and lateral spreading (Kramer 1996). These liquefaction effects will be described in this section except for lateral spreading which will be thoroughly discussed in Chapter 5.

2.5.1 **Alteration of Ground Motions**

Soils that undergo cyclic liquefaction are subject to continuous cycles of loading that cause the pore pressure in a liquefaction susceptible soil to increase which reduces the effective stress and therefore reduces the shear strength and stiffness of the soil. This is important because a soil at the beginning of earthquake shaking may amplify or de-amplify ground motions from underlying bedrock depending on the amplitude and frequency content of the motion and the natural period of the soil which is based on the soil stiffness. Therefore, as the shaking continues the stiffness of the soil decreases which causes the natural period of the soil to change as well. Ground motions will therefore respond differently at the end of shaking than at the beginning of shaking. This can cause problems if not accounted for in design, for example, consider a twenty story building with a fundamental period of 2 seconds resting on top of a liquefiable soil that

initially has a natural period of 0.1 seconds. Initially, the building may not be impacted much because the oscillation of the building doesn't match the period of the ground motion, however, as the shaking continues, and the soil softens, the fundamental period of the soil may progressively or abruptly change to 2 seconds upon liquefaction. If this were to occur the ground motions would bring about a maximum response on the building due to resonance where the frequency of the ground motion matches the frequency of the building.

A soil liquefying at depth can also cause a variety of other potential design problems. Consider a liquefiable soil between two non-liquefiable soils for a level ground surface. Upon the occurrence of liquefaction the liquefiable soil could disconnect from the non-liquefiable soils and this could cause tension cracks in the overlying soil to form due to ground oscillations and separate the overlying soil into blocks as shown in Figure 2.40. Clearly a structure resting on top of a soil where this occurs would be introduced to forces and moments that it was not subjected to prior to liquefaction. A liquefiable soil decoupling from an overlying non-liquefiable soil can also cause major problems for pile foundations. Piles extending through the non-liquefiable and liquefiable layers may be introduced to large bending moments upon liquefaction (Kramer 1996). This is because the non-liquefiable soil below the liquefiable layer exhibits little deformation, whereas, the liquefiable soil may undergo displacement due to the loss in shear strength caused by liquefaction. Large lateral forces causing bending moments may form causing the pile to fail. Kramer (1996) illustrated the possible effects of liquefaction on a pile foundation as shown in Figure 2.41

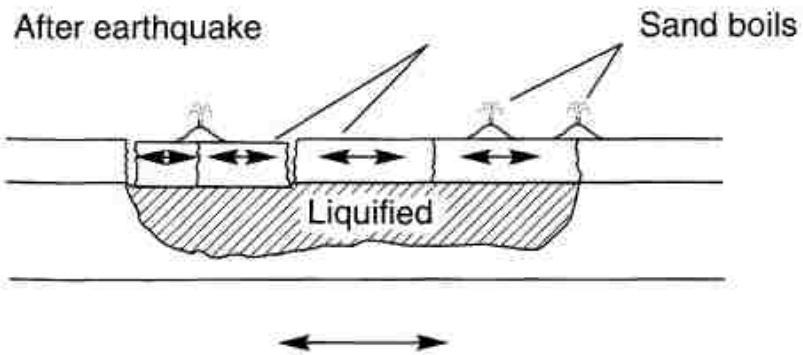

Figure 2.40. The effects of liquefaction decoupling a liquefiable layer from an overlying non-liquefiable layer due to ground oscillation on a level ground surface (Kramer 1996).

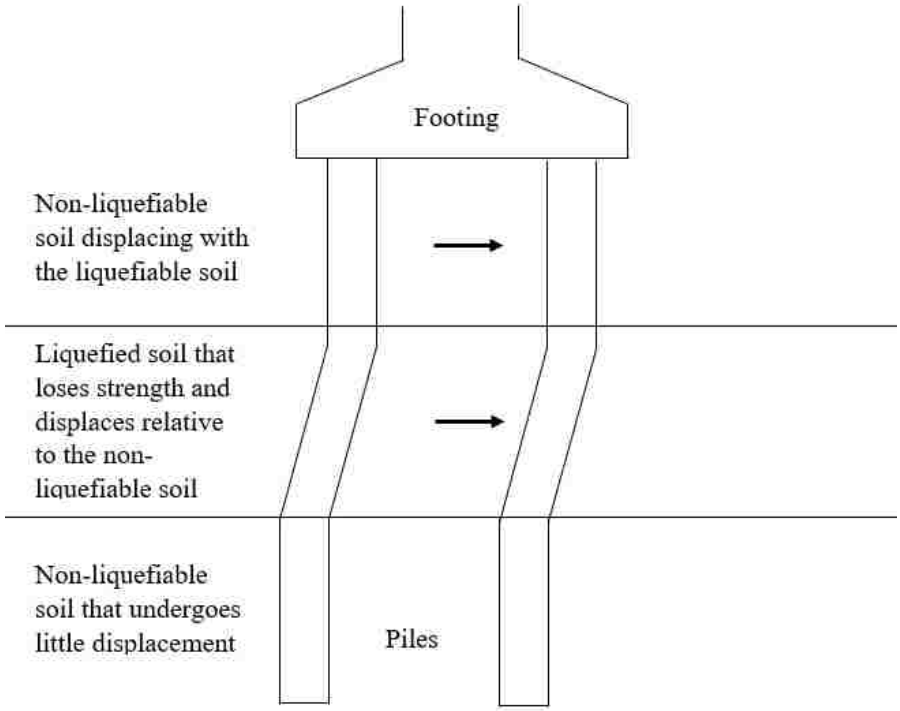

Figure 2.41. The effects of liquefaction on a pile foundation where a liquefiable layer displaces relative to an underlying non-liquefiable layer. The non-liquefiable layer above the liquefied layer moves with it causing large bending moments which may cause failure of the pile.

2.5.2 **Sand Boils**

Sand boils are a mixture of water and sand ejected from below the ground surface due to the build up of pore pressure caused by the tendency of a soil to contract during earthquake shaking. As water escapes toward the ground surface following the path of least resistance, it brings with it sand particles of the liquefied soil and potentially particles of any overlying soil as

well. Oftentimes, sand boils (and the ejecta they leave on the ground surface) are used as evidence to claim that liquefaction occurred at a site due to an earthquake. However, sand boils are not only evidence for liquefaction, they can potentially have severe consequences as well. A sand boil developing in a localized area underneath a building can cause large settlements of the soil to that area of the building. These settlements would cause less resistive force to support the building and add stress in parts of the building affected that may not be designed to handle these stresses.

Although sand boils are used as evidence for liquefaction, the lack of them does not indicate that liquefaction has not occurred. Liquefaction that occurs at deeper depths, in small thickness soil layers, or a liquefied soil that does not experience continued duration of ground motions may not reach the ground surface. Evidence for cases like these are dikes and sills that form in overlying non-liquefiable soils from sand boils that did not reach the surface and left behind the remnants of the particles the water brought along with it that never reached the ground surface. Liquefaction evidence from dikes and sills are much more difficult to obtain because they are below the ground surface and either require erosional processes (such as a river) or man-made processes (such as excavation for a structure) to take place in order for them to be discovered. Oftentimes, these dikes and sills are discovered from prehistoric earthquakes and are indicators for paleoliquefaction. Areas of the world that have a relatively short time period of a documented earthquake records (such as the Western United States) may benefit largely from paleoliquefaction studies which may provide a better indication of the recurrence rate of earthquakes in these areas allowing for better earthquake design codes.

2.5.3 **Flow Failures**

Flow failures are the consequence of flow liquefaction and are the most severe form of liquefaction due to the large movements of soil involved. Flow failures occurs when the shear

strength of the soil drops below the static shear stresses present in the soil due to the reduction of shear strength from loading (seismic or non-seismic). When the shear strength is less than the static shear stress this means that the resistance of the soil is less than the initial static load. The National Research Council (1985) described four different types of flow failure that will be discussed below.

2.5.3.1 Flow Failure Mechanisms

NRC Mechanism A

Flow failure NRC Mechanism A is flow liquefaction which was previously discussed in Section 2.4.2.1. A brief review of flow liquefaction is that it occurs when the initial shear stress imposed on a soil exceeds the steady state shear strength of the soil. The steady state shear strength is the strength of the soil at which constant shearing resistance is obtained meaning a soil will strain at the same rate for a given applied stress. The generation of pore pressure from undrained loading (either monotonic or cyclic) decreases the strength of the soil to this steady state shear strength. Assuming the soil is initially stable, a soil exhibiting flow liquefaction will initially have a shear strength greater than the initial shear stress imposed on the soil, however, due to either monotonic or cyclic loading the strength of the soil will be decreased below the initial static stress on the soil at which point flow liquefaction will occur. Soil that is initially at a state where the imposed initial shear stress is slightly below the initial strength of the soil would only require a small undrained disturbance to occur in order to drop the shear strength of the soil below the initial shear stress on the soil (Kramer and Seed 1988).

NRC Mechanism B

Flow failure NRC Mechanism B occurs when a liquefiable soil is capped by a non-permeable layer that does not allow the pore pressure, caused by the densification of sand grains during shaking, to escape. The liquefiable soil layer as a whole may initially be at the same state

having the same void ratio, however, when shaking takes place causing the densification of soil particles the action of gravity may drive the soil to a state in which the lower portion of the liquefiable layer is denser (at a lower void ratio) than the upper portion of the liquefiable layer. Castro (1975) observed this phenomenon, which was later termed void redistribution by Fiegel and Kutter (1992), in cyclic triaxial tests when studying the conservatism in regards to liquefaction occurrence for medium dense and dense sands in cyclic triaxial tests. Because the upper portion of the soil layer is at a looser state than it originally was, the steady state strength of the soil will decrease. If the steady state strength of the soil in this upper portion of the soil is lower than the initial shear stress applied to the soil a flow failure may occur. Because the steady state strength of the upper portion of the soil is lower than the initial shear stress, a further undrained disturbance of the soil is capable of achieving a soil state in which the shear strength of the soil is less than the initial static shear stress at which point a flow failure will occur. It is important to remember that just because a soils steady state strength is lower than the initial static shear stress imposed on the soil, does not mean flow failure will occur. A flow failure will only occur if there is a disturbance that causes the soils shear strength to drop below the imposed initial static shear stress. A steady state strength below the initial static shear stress simply implies that a soil is capable of having a flow failure.

Void redistribution is the phenomenon that causes NRC flow failure mechanism B. When a saturated soil between two impermeable layers begins to reconsolidate after reaching zero effective stress (initial liquefaction) the particles of the liquefied layer will start to settle out and become denser at the base and looser at the top due to the effects of gravity (see Figure 2.42). It also should be noted that the pore pressure generated during liquefaction applies a force to the above impermeable layer as the water tries to escape causing the soil skeleton of this impermeable

layer to rebound, which in turn reduces the effective confining pressure allowing for the liquefiable soil to reach a looser state during the reconsolidation process (Kramer and Stewart, unpublished manuscript). Because the soil at the top of the liquefied layer is at a looser state than the base of the liquefied layer after liquefaction, the steady state strength of the top of the soil layer will be reduced. Therefore, if the steady state strength of the upper portion of the liquefied layer is below the initial shear stress on the soil, then a flow failure is capable of occurring.

Void redistribution may also cause thin water interlayers at the boundary between the liquefied layer and the above impermeable layer (Fiegel and Kutter, 1992). If the water interlayer is large in extent (continuous) along this boundary (e.g., the sand/clay boundary in Figure 2.42), a flow failure may occur because the water has zero shear strength. Therefore, if this water interlayer takes the place of enough of the soil that was resisting a slide from occurring along this boundary a flow failure would occur.

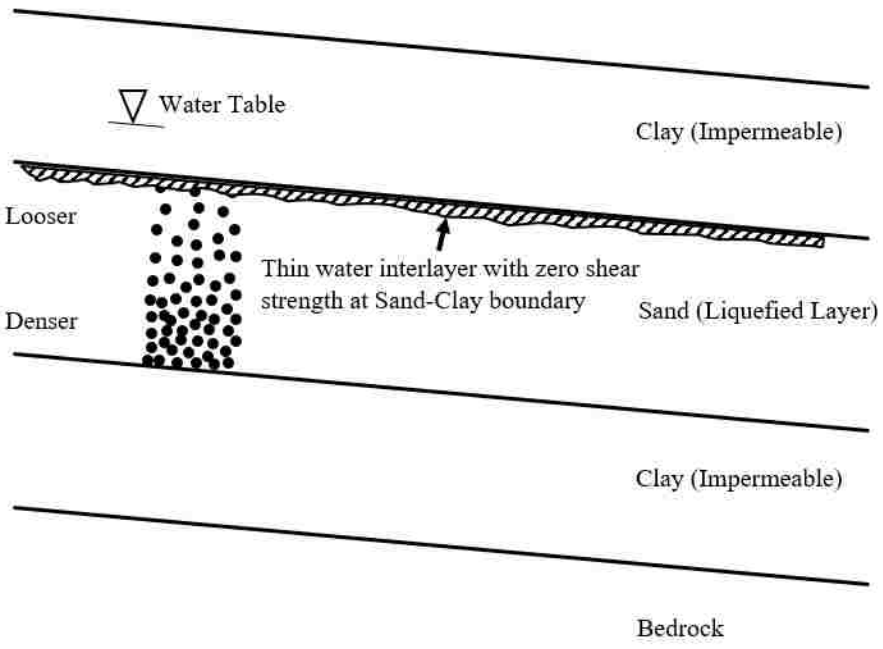

Figure 2.42. Illustration of the effects of void redistribution causing the soil particles of a liquefied soil to rearrange into a loose state above a dense state between two impermeable boundaries with a water interlayer between the upper sand-clay boundary.

NRC Mechanism C

When pore pressures generated in a layer at depth due to shaking are not impeded by an overlying impermeable layer, the pressurized water will intrude the overlying soil causes cracks and pathways into the soil. These cracks would reduce the shear strength of the soil above the layer where the pore pressures were generated. Therefore, not only will the upper portion of the high pore pressure soil be loosened and undergo a reduction in shear strength, but the overlying soil along the boundary will also be reduced as well causing a further reduction of the total shear strength along the boundary between the soils (National Research Council, 1985). Therefore, if the total shear strength along this boundary is reduced to a value lower than the initial shear stress, a flow failure will occur. This process is the same as that for how sand boils are generated which leave dikes and sills of sand in soils that a sand boil passed through on its journey from the source sand layer that liquefied to the ground surface. Conceptually, this can be thought of being a natural hydraulic fracturing process as the pore pressure escapes from the its origin to the ground surface. It is also worth noting that flow failure via NRC Mechanism C does not need to occur during earthquake shaking because the effective stress, and therefore the steady state strength, in the overlying soil is not actually reduced until the water penetrates into the overlying soil (Kramer, 1996). Flow failure NRC Mechanism C is similar to NRC Mechanism B, however, the pore pressures generated do not need to be prevented by an overlying impermeable soil layer. Because flow failure NRC Mechanism C causes changes in shear strength in not only the layer where high pore pressures develop, but also the surrounding soil (see Figure 2.43) this is a global loosening failure, contrary to flow failure NRC Mechanism B which causes the reduction of shear strength in only the layer where high pore pressures develop.

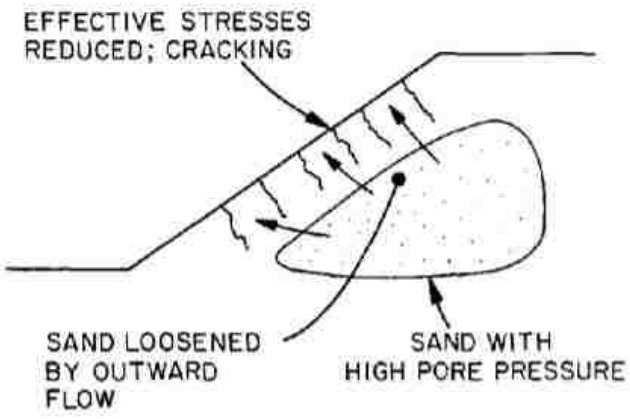

Figure 2.43. Illustration of flow failure NRC Mechanism C showing the zone of high pore pressure causing loosening of the sand at the upper portion of the sand layer along with reducing the shear strength of the overlying soil (National Research Council, 1985).

NRC Mechanism D

Flow failure NRC Mechanism D occurs when a liquefiable soil (e.g., sand and coarse silts) is in contact with a stiff body (such as steel or concrete structures) and pore pressure build up due to shaking reduces the shear strength of the soil below what is required for equilibrium (National Resource Council, 1985). Contacts between soil layers are almost always continuous, gradual, and are not smooth (e.g., the transition from a silt to a sand due to the progradation of a coast), whereas, the contact between a soil and a steel pile would be well-defined. Consider the development of a high pore pressure zone along the side of a friction pile that causes the reduction in shear strength of the soil along the soil and pile interface. If the strength of the soil at the interface is reduced enough, and this extent of loss of strength along the pile interface long enough, the pile can undergo a plunging failure where a large amount of settlement can occur instantaneously. The effects of high pore pressure reducing the shear strength along the interface of friction piles and causing plunging failure has been studied by De Alba (1983).

2.5.3.2 Residual Strength of Liquefied Soil

Because flow failures cause severe consequences when they occur, estimating the shear strength of liquefied soil is of critical importance in geotechnical engineering. Up to this point it has only been discussed that when the shear strength of a soil is reduced below the initial shear stress imposed on the soil then a flow failure will occur, however, methods for calculating the shear strength of liquefied soil up to this point have not been discussed.

Estimating the shear strength of soil at which flow failures occur is typically done by using residual strengths that have been back-calculated from flow slide case histories. This is done because the conditions for steady state concepts hardly ever exist for actual flow slides because during flow failures drainage can occur (causing changes in effective stress) and strain rates are variable throughout flow failures (Kramer and Wang, 2014). Steady state concepts also require laboratory testing of soil specimens which are very sensitive to small changes in density which oftentimes occur from disturbance during the sampling of soil specimens.

Currently, there is a limited number of case histories for flow failures due to their relatively uncommon occurrence along with uncertainty and the lack of key parameters in these case histories which occur for many reasons such as the locations of occurrence often are in unpopulated areas (Kramer and Wang, 2014). Because of the uncertainties in parameters involved for the back calculation of residuals strengths and the subjective assumptions involved in developing procedures for calculating residual strength, it is wise to weight the results of the different procedures based upon application to the site of interest. The three primary methods for estimating the shear strength of liquefied soil based on flow slide case histories are the direct approach, the normalized strength approach, and a mixed approach that incorporates parts of the direct and normalized strength approaches.

2.5.3.2.1 Direct Approach

The direct approach relates the residual strength of the soil directly to the corrected SPT resistance and the first correlation was developed by Seed (1987) as a tentative relationship and is shown in Figure 2.44. The SPT values shown in Figure 2.44 were corrected for energy, overburden, and fines content. The expression for the fines content was given as

$$(N_1)_{60,cs} = (N_1)_{60} + \Delta(N_1) \tag{2.95}$$

where $(N_1)_{60}$ is the overburden and energy corrected SPT resistance and $\Delta(N_1)$ was the fines correction given by Table 2.10.

Table 2.10. Correction of SPT resistance for fines content (Seed, 1987).

Fines content (%)	$\Delta(N_1)$
10	1
25	2
50	4
75	5

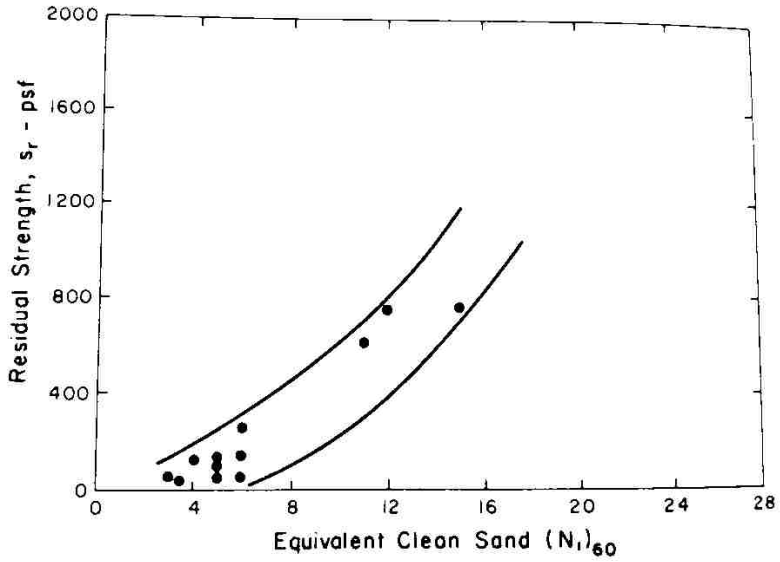

Figure 2.44. Tentative estimation of residual strength from clean sand corrected SPT resistance values (Seed, 1987).

The correlation by Seed (1987) was revised by Seed and Harder (1990) who reexamined several of the case history flow slides and added additional data. The revised residual strength correlation by Seed and Harder (1990) is shown in Figure 2.45. The SPT values shown in Figure 2.45 were

corrected for energy, overburden, and fines content. The expression for the fines content can be expressed as given in Equation 2.95 where the fines correction ΔN_1 was slightly adjusted and given by Table 2.11.

Table 2.11. Correction of SPT resistance for fines content (Seed, 1987).

Fines content (%)	ΔN_1
0	0
10	1
25	2
50	4
75	5

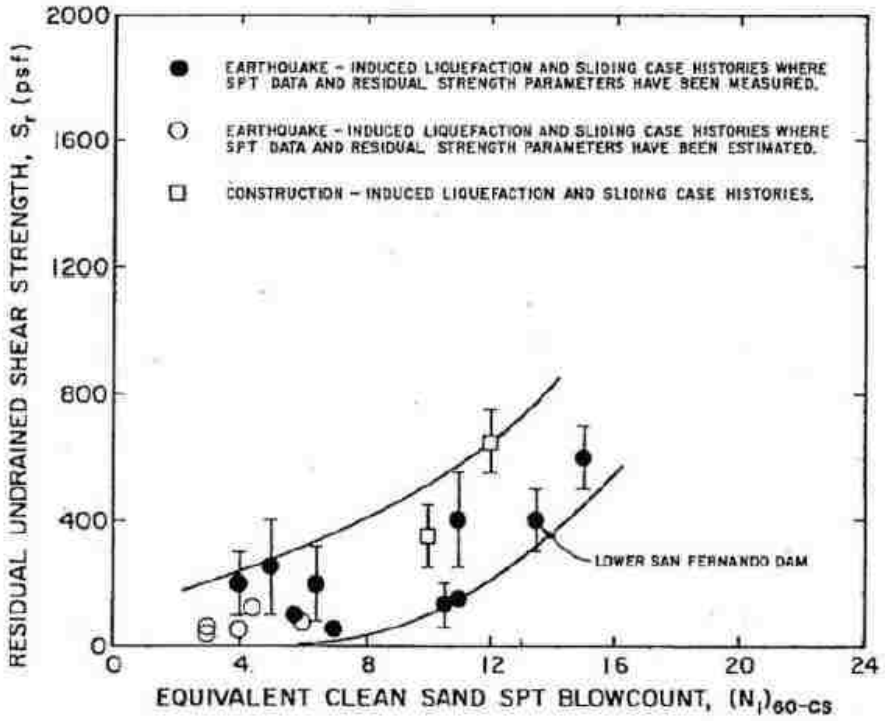

Figure 2.45. Estimation of residual strength from clean sand corrected SPT resistance values (Seed and Harder, 1990).

As shown in Figure 2.45 the relationship between the corrected SPT resistance and residual strength has a large amount of uncertainty as given by the large spread of the data. One main attribute to this spread is likely from the mixing soils that occurred during the flow failure.

Therefore, the SPT resistance values used in the correlation may not correspond to the soil that was the main factor in causing the flow failure.

Idriss (1999) reexamined the flow slide case histories and developed an exponential relationship using the median measured SPT resistance as shown in Figure 2.46 and given by

$$S_r = 0.0236exp\left(0.16(N_1)_{60,cs}\right) \tag{2.96}$$

where the residual strength, S_r, is in atm.

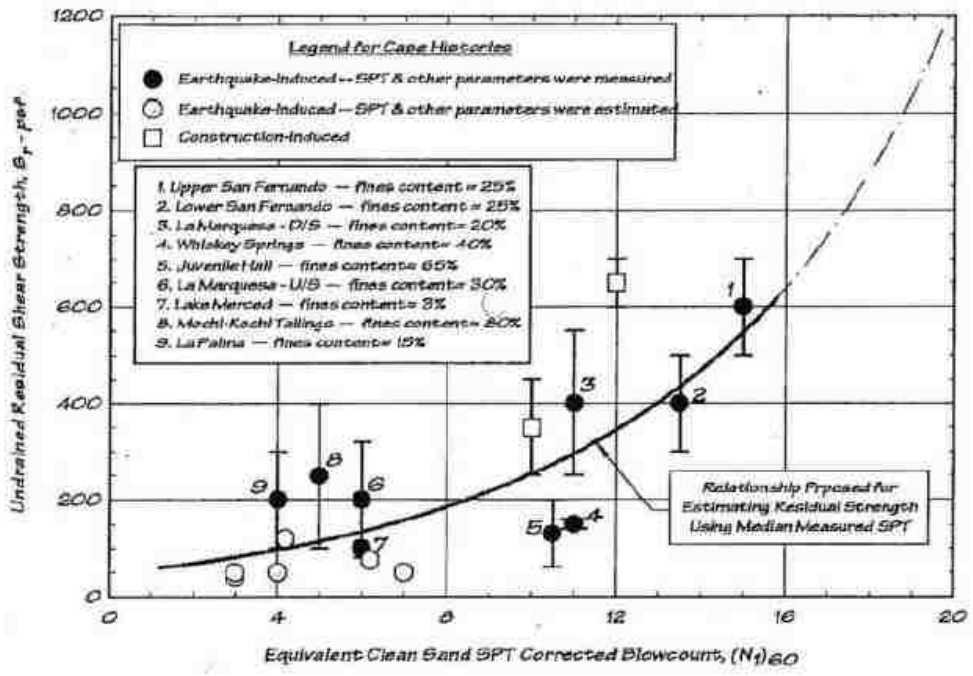

Figure 2.46. Estimation of residual strength from clean sand corrected SPT resistance values (Seed and Harder, 1990).

2.5.3.2.2 Normalized Strength Approach

The normalized strength approach stems from the basis of how the consolidation curve compares to the steady state line. If the consolidation curve and steady state line were parallel for a soil, then the ratio of steady state strength to consolidation stress would be constant for that soil. If this were true for sandy soils, the steady state strength could be obtained from performing consolidation tests on the soil, however, this is known to not be the case. This has not stopped

researchers from developing relationships for the normalized strength ratio. Stark and Mesri (1990) developed a correlation of normalized strength ratio based upon normalized SPT penetration resistance because the strength ratio of liquefied soil and values of SPT penetration resistance are both dependent upon the density of the soil and its effective confining stress. The correlation to the normalized penetration resistance was based upon back calculated and laboratory measured residual strengths from the flow failure case histories and was given as

$$\frac{S_r}{\sigma'_{vo}} = 0.0055(N_1)_{60,cs} \tag{2.97}$$

where $(N_1)_{60,cs}$ is the overburden, energy, and fines content correct SPT penetration resistance. Olson and Stark (2002) updated the case history database used by Stark and Mesri (1990) to a total of 33 case histories and developed their own linear normalized strength ratio expression dependent upon normalized SPT resistance and cone penetration tip resistance as

$$\frac{S_r}{\sigma'_{vo}} = 0.03 + 0.0075(N_1)_{60} \pm 0.03 \quad where \quad (N_1)_{60} \leq 12 \tag{2.98}$$

$$\frac{S_r}{\sigma'_{vo}} = 0.03 + 0.0143 q_{c1} \pm 0.03 \quad where \quad q_{c1} \leq 6.5\ MPa \tag{2.99}$$

where the normalized penetration resistances were not corrected for fines content and the ± 0.03 term represents the range of the linear relationship although Olson and Stark (2002) specify the standard deviation to be 0.025. Figure 2.47-2.48 show the linear relationship between the residual strength ratio and the corrected SPT and CPT resistances respectively.

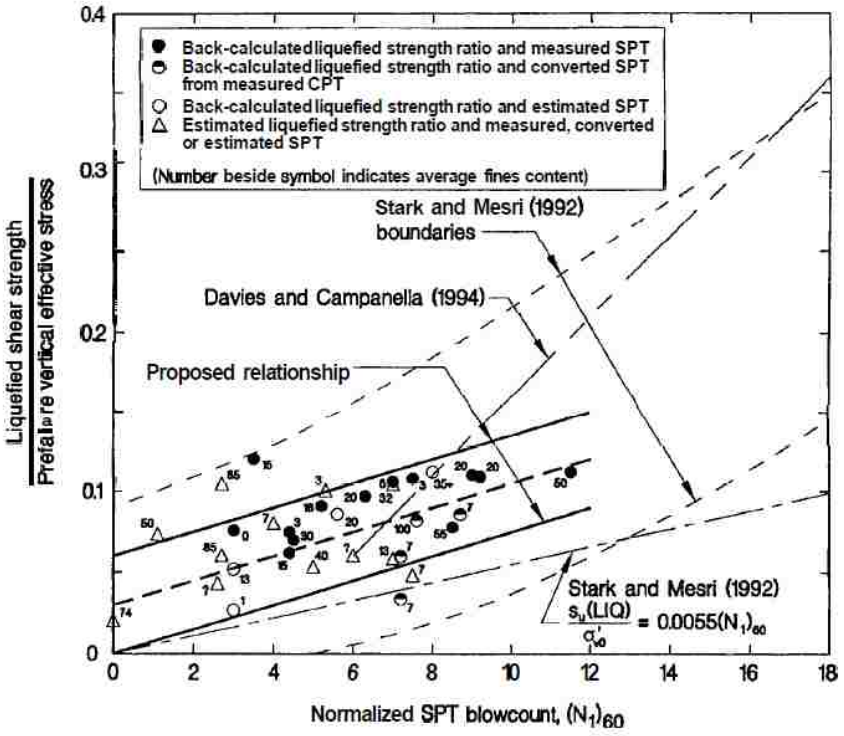

Figure 2.47. Linear relationship of the residual strength ratio and normalized SPT resistance for liquefied soil (Olson and Stark, 2002).

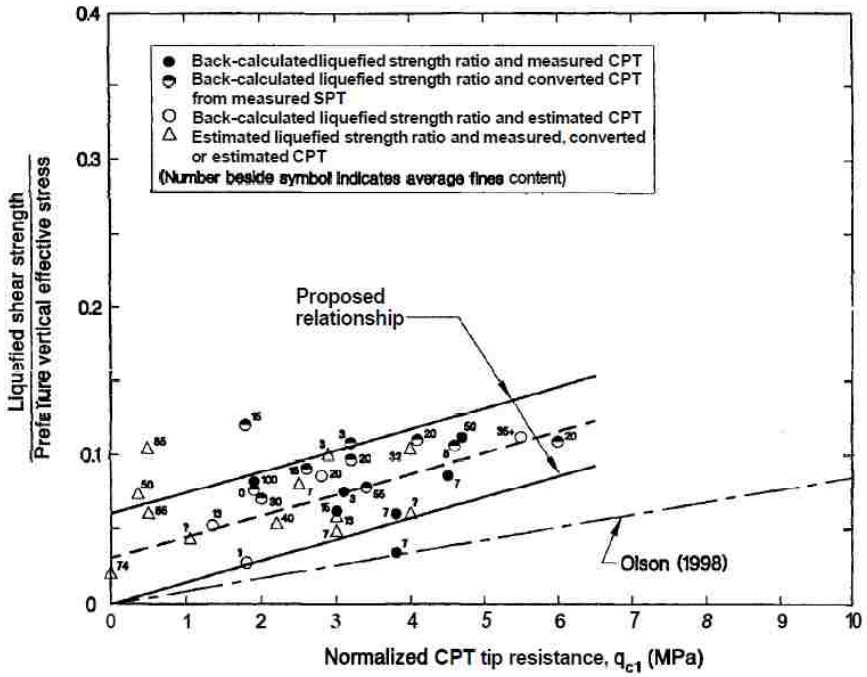

Figure 2.48. Linear relationship of the residual strength ratio and normalized CPT tip resistance for liquefied soil (Olson and Stark, 1992).

Idriss and Boulanger (2007) reduced the size of the case history database from 33 as investigated by Olson and Stark (2002) to 18 case histories. Idriss and Boulanger broke the 33 case histories from Olson and Stark (2002) into three main groups where group 1 consisted of 7 case histories with adequate SPT/CPT and geometric details, group 2 consisted of 11 case histories with either adequate SPT/CPT or geometric details, and group 3 consisted of the 17 case histories eliminated from consideration due to inadequate details in regards to SPT/CPT resistances and the geometry. Kramer and Stewart (unpublished manuscript) expressed the normalized residual strength expressions of Idriss and Boulanger (2007) for correct SPT resistance and void redistribution effects as

$$\frac{S_r}{\sigma'_{vo}} = exp\left(\frac{(N_1)_{60,cs-S_r}}{16} + \left(\frac{(N_1)_{60,cs-S_r}-16}{21.2}\right)^3 - 3.0\right) \times \left(1 + \beta exp\left(\frac{(N_1)_{60,cs-S_r}}{2.4} - 6.6\right)\right) \leq tan\phi' \quad (2.100)$$

where β is 0 when void redistribution effects are significant and β is 1 when void redistribution is insignificant and $(N_1)_{60,cs-S_r}$ is expressed as

$$(N_1)_{60,cs-S_r} = (N_1)_{60,cs} + \Delta(N_1)_{60,cs-S_r} \quad (2.101)$$

where $\Delta(N_1)_{60,cs-S_r}$ is a fines content correction to determine the SPT resistance for residual strength given in Table 2.12. Idriss and Boulanger (2007) also developed an expression for corrected CPT resistance from a conversion from SPT resistance that can be expressed as

$$\frac{S_r}{\sigma'_{vo}} = exp\left(\frac{q_{c1Ncs-S_r}}{24.5} - \left(\frac{q_{c1Ncs-S_r}}{61.7}\right)^2 + \left(\frac{q_{c1Ncs-S_r}}{106}\right)^3 - 4.42\right) \times \left(1 + \beta exp\left(\frac{q_{c1Ncs-S_r}}{11.1} - 9.82\right)\right) \leq tan\phi' \quad (2.102)$$

where $q_{c1Ncs-S_r}$ is expressed as

$$q_{c1Ncs-S_r} = q_{c1Ncs} + \Delta q_{c1N-S_r} \quad (2.103)$$

where Δq_{c1N-S_r} is a fines content correction to determine the CPT resistance for residual strength given in Table 2.12.The relationships normalized residual strength relationships to corrected SPT and CPT resistance proposed by Idriss and Boulanger (2007) are graphically shown in Figure 2.49-2.50 respectively.

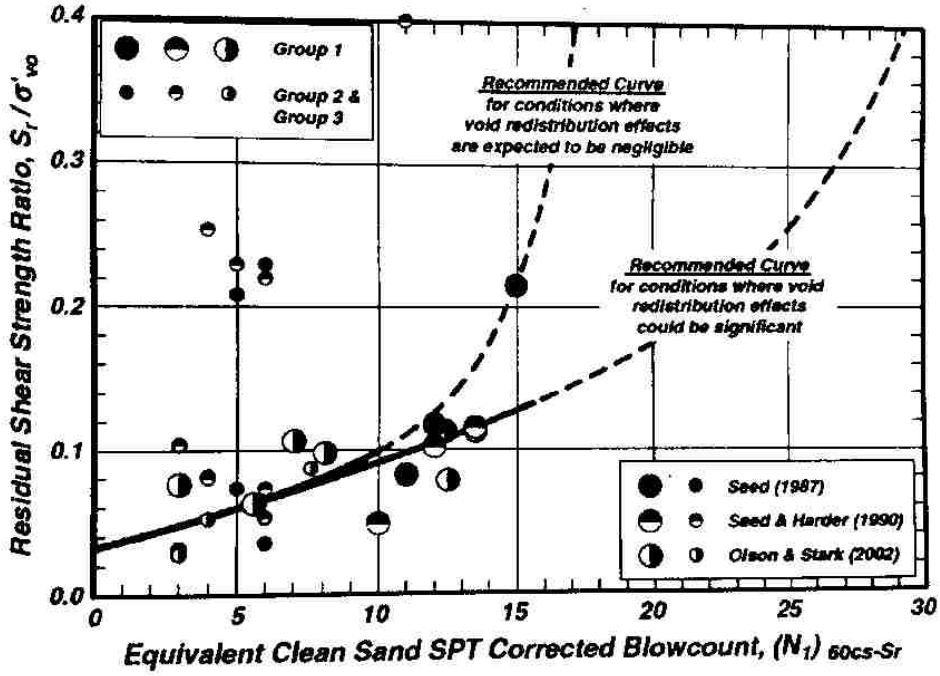

Figure 2.49. Residual shear strength versus median SPT resistance relationship for significant and insignificant void redistribution effects (Idriss and Boulanger, 2007).

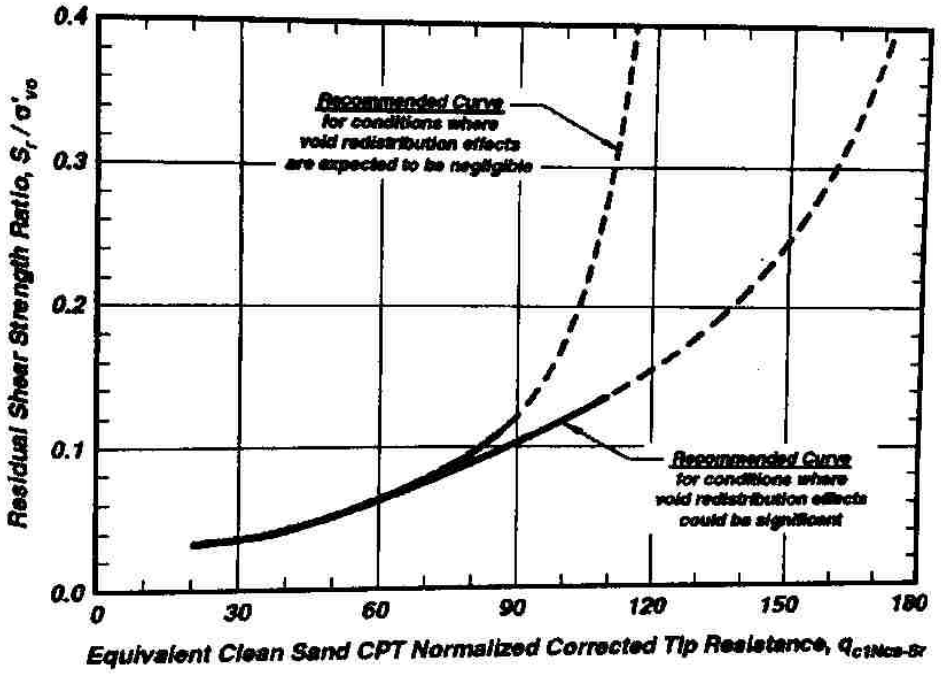

Figure 2.50. Residual shear strength versus median CPT resistance relationship for significant and insignificant void redistribution effects (after Kramer and Stewart, unpublished manuscript).

Table 2.12. Correction of SPT and CPT resistance for fines content (Idriss and Boulanger (2007).

Fines content (%)	$\Delta(N_1)_{60,cs-S_r}$	Δq_{c1N-S_r}
10	1	10
25	2	25
50	4	45
75	5	55

Based on Figure 2.49-2.50 the void redistribution effects have little influence up until the clean sand correct SPT and CPT resistances are at values of 8 and 75 respectively. Upon exceeding the latter values it is very important to distinguish if void redistribution effects should be accounted for or not because there is a large spread between the curves based on whether β is 0 or 1. In current practice it is typical to consider the void redistribution effects to be significant as it is more conservative in the liquefaction analysis for flow failures which can cause devastating effects.

2.5.3.2.3 Mixed Approach

In order to account for the deviation of the steady state line from parallel with the consolidation curve as effective stress increases (see Figure 2.51), Kramer and Wang (2014) developed a non-linear relationship for determining the residual strength based upon both corrected SPT resistance and initial vertical effective stress expressed as

$$lnS_r = -8.444 + 0.109(N_1)_{60} + 5.379(\sigma'_{vo})^{0.1} \tag{2.104}$$

where the standard deviation in the relation is given as

$$\sigma_{lnS_r} = \sqrt{\sigma^2{}_m + 0.00073N^2\left(COV^2{}_N\right) + 4.935S^{0.2}\left(COV^2{}_S\right)} \tag{2.105}$$

where N is the mean value of the overburden and energy corrected SPT resistance $(N_1)_{60}$, S is the mean value of the vertical effective stress σ'_{vo}, and COV is the coefficient of variation. Kramer and Wang (2014) developed their relationship after re-analyzing several of the case histories from the database used by Olson and Stark (2002). In doing so they assigned a weighting factor based on the quality of the case histories and differentiated between conditions where lateral spreading

would occur instead of flow sliding. The Kramer and Wang (2014) relationship for relation for estimating the residual strength is shown in Figure 2.52 for median residual strengths.

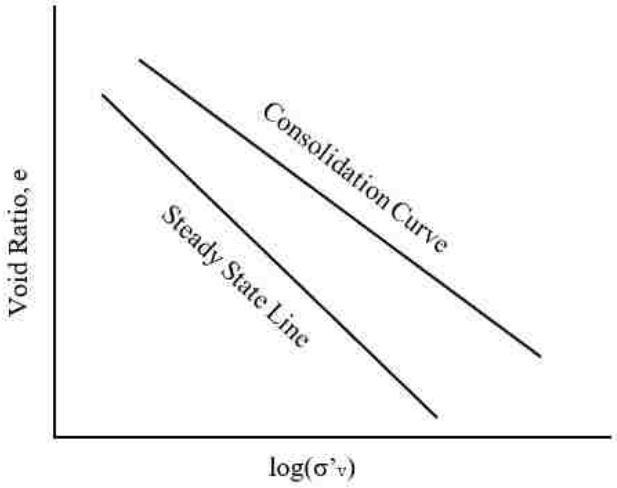

Figure 2.51. Example illustration of how the steady state line deviates from parallel with the consolidation curve at high vertical effective stresses.

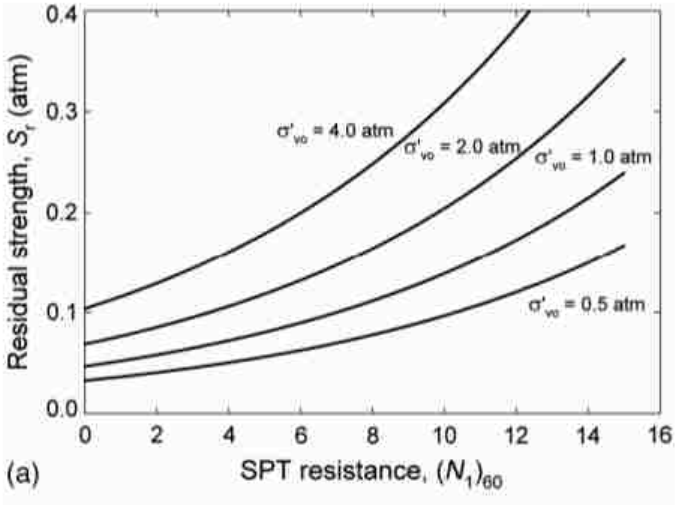

Figure 2.52. Estimation of median residual strength values based on corrected SPT resistance and vertical effective stress (Kramer and Wang, 2014).

2.5.4 **Settlement**

Settlement occurs from liquefaction due to the tendency of a soil to densify when shaken. Initially upon liquefaction, soils lose their strength and an immediate punching or rotational bearing capacity failure may occur due to the structure settling with respect to the soil around it. Settlement from liquefaction may also occur after earthquake shaking has ended. Because sands

are undrained when liquefaction occurs, there is no volume change until the pore pressure escapes and the water filling the voids of the soil is expelled. Therefore, if the pore pressure cannot escape right away (as would be the case for a liquefied sand trapped between two very low permeability clay layers) the sand may not settle until minutes, hours, or even days after shaking has ended.

The effects of settlement are dependent on where the settlement occurs. Three types of settlement will be discussed including free-field settlement, foundation settlement, and settlement due to ejecta. The two most common procedures for estimating settlement induced by liquefaction will be discussed as well. It should be noted that non-seismic related settlement calculations typically exhibit 25-50% errors, therefore, settlements due to seismic loading are likely to have less accuracy (Tokimatsu and Seed, 1987).

2.5.4.1 Free-Field Settlement

The simplest case of settlement is that which occurs on level ground and away from any structures. The amount of settlement that occurs is dependent on the volumetric strain incurred during and after earthquake shaking. When level ground conditions exist, it is typical to consider compression in a single dimension and therefore consider the volumetric strain to be approximately equal to the vertical strain. It is only logical to incur that the amount of settlement also depends on the thickness of the liquefiable layer. Therefore, conceptually it is not hard to see that any settlement model will include both the amount of vertical strain and thickness of the liquefiable layer. Therefore, similar to static settlement calculations, the amount of settlement can be found by breaking up the thickness of the soil profile into small sublayers (oftentimes no larger than 1m thick) and integrating the vertical strain over the thickness of each of the sublayers. The latter can be written as the sum of the vertical strain of each sublayer multiplied by each sublayers thickness

$$\Delta H = \sum_{i=1}^{n} (\varepsilon_v)_i \Delta z_i \qquad (2.106)$$

where i represents the i^{th} sublayer, n is the total number of sublayers, ε_v is the vertical strain in the i^{th} sublayer, and Δz is the thickness of the i^{th} sublayer. The latter relationship for settlement is relatively simple to comprehend, however, understanding the factors that influence the amount of vertical strain must be considered as well. One such factor is the void ratio (density) of the soil. As discussed in Section 2.4.2.2.2.4 (Liquefaction Resistance) laboratory procedures are not able to replicate field conditions adequately so in-situ tests for measuring density via penetration resistance (SPT and CPT) have often been used. With that being said, laboratory tests did help Tokimatsu and Seed (1987) find that the volumetric strain from liquefaction is related to relative density and peak shear strain. Tokimatsu and Seed (1987) then extended these findings and related the relative density to SPT resistance and the peak shear strain to the CSR as shown in Figure 2.53 in order to obtain the volumetric strain. Therefore, with the latter process of determining the volumetric strain along with knowing the liquefiable layer thicknesss, Tokimatsu and Seed (1987) could then calculate settlements based on Equation 2.106.

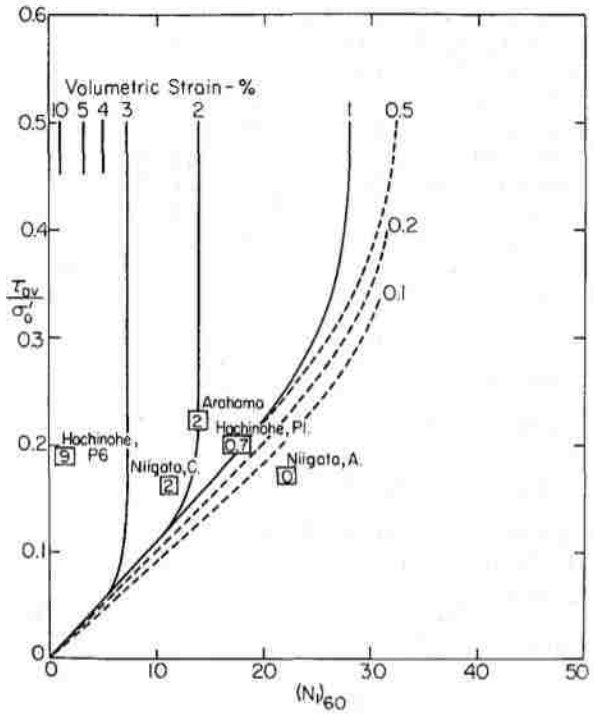

Figure 2.53. Evaluation of volumetric strain from CSR and corrected SPT resistance (Tokimatsu and Seed, 1987).

Ishihara and Yoshimine (1992) were able to relate post-liquefaction volumetric strain to the density of a sand and factor of safety against liquefaction using a simple shear apparatus. Ishihara and Yoshimine (1992) broke their procedure into three steps:

1) Evaluate the factor of safety against liquefaction at the center of each sublayer (see Sections 2.4.2.2.2.1.2 and 2.4.2.2.2.4 on obtaining values of CSR and CRR to calculate the factor of safety against liquefaction using Equation 2.6).
2) Obtain the in-situ relative density via correlations from in-situ penetration resistance tests (SPT or CPT) performed on sand and then use Figure 2.54 to obtain the post-liquefaction volumetric strain for each sublayer.
3) Upon determining the volumetric strains for each sublayer, apply Equation 2.106 in order to calculate the total earthquake induced settlement.

Ishihara and Yoshimine noted that their procedure is only applicable for deposits consisting mainly of sand.

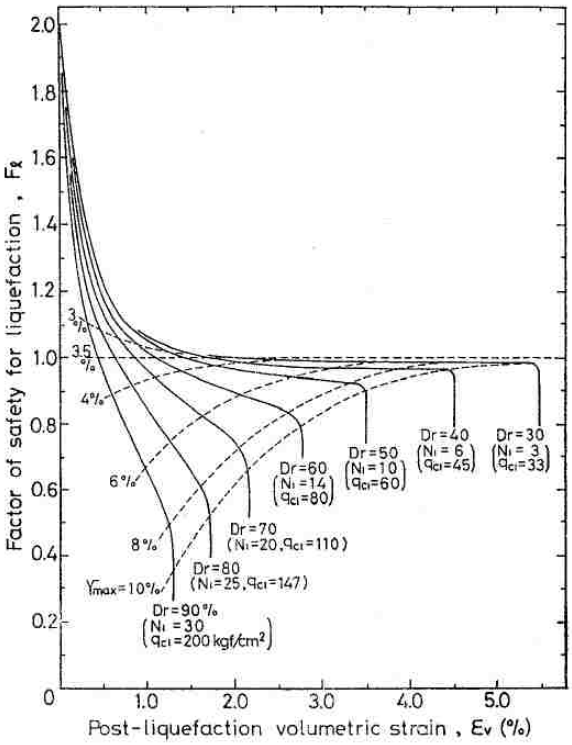

Figure 2.54. Evaluation of volumetric strain from the factor of safety against liquefaction and relative density based on corrected SPT or CPT resistance (Ishihara and Yoshimine, 1992).

2.5.4.2 Foundation Settlement

Foundation settlement can occur when a shallow foundation rests upon, or is above, a soil layer that liquefies during an earthquake. The settlement of ground in the vicinity of a foundation is oftentimes found to be more than that of free-field settlement. This is because as a structure shakes due to an earthquake it will impose additional shear stresses on the soil, especially at the corners of buildings (Kramer and Stewart, unpublished manuscript). Therefore, the CSR beneath a building, especially at the corners, will be greater than the CSR for a free-field situation for a liquefiable deposit with the same properties.

Currently, there are no simple empirical relations to estimate the complex phenomena of settlement of structures overlying liquefiable soil deposits. There does, however, appear to be a

relation between building width and thickness of a liquefied soil to the quantity of settlement observed. Liu and Dobry (1997) normalized the building width and average foundation settlement by the thickness of the liquefied layer for the 1964 Niigata earthquake and the 1990 Luzon Philippine earthquakes to create Figure 2.55 to show how the amount of foundation settlement increases when the liquefied layer thickness increases and the building width decreases.

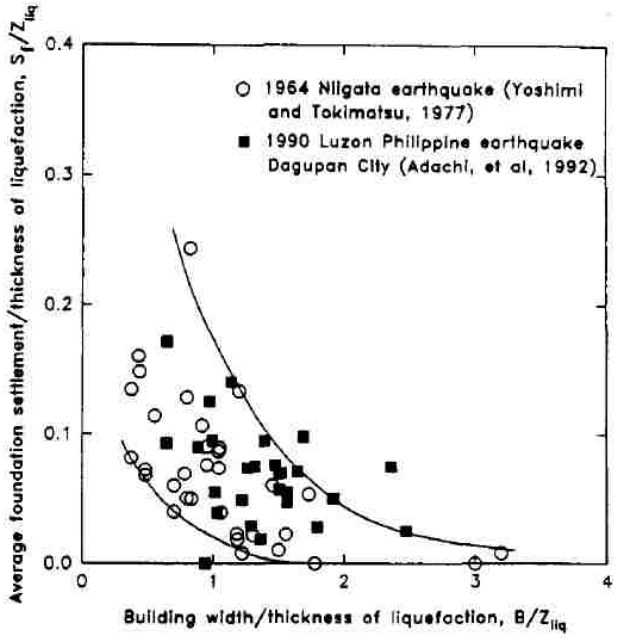

Figure 2.55. Relation between normalized average foundation settlement and building width by the liquefied layer thickness (Liu and Dobry, 1997).

Kramer and Stewart (unpublished manuscript) show a simple, but effective illustration of pockets of liquefiable sand that can cause differential settlement problems to buildings. Differential settlement may occur from shallow small pockets of liquefied soil beneath isolated areas of a building, or large pockets of liquefiable soil at greater depths.

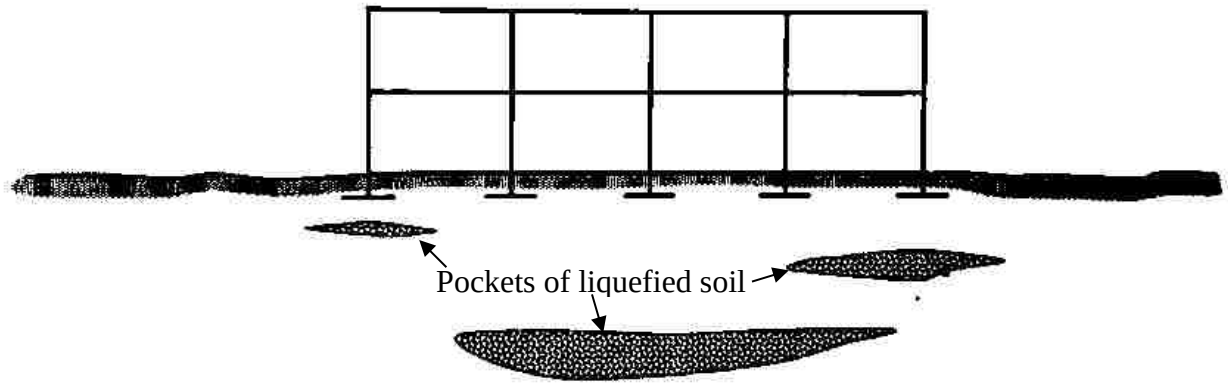

Figure 2.56. Possible differential settlement from small isolated pockets of liquefied soil at shallow depths and large pockets of liquefied soil at larger depths (Kramer and Stewart, unpublished manuscript).

2.5.4.3 Settlement Due to Ejecta

Large settlements have been observed due to sand ejecta that is spewed when the excess pore pressure from liquefaction escapes to the ground surface carrying with it soil particles from the liquefied layer and likely particles from any other layer it passed through in route to the ground surface. The latter phenomenon is often called a sand boil. Sand boils can occur in the free-field or near/beneath structures. As discussed in the previous section, the shear stresses imposed beneath the corners of buildings causes generation of more pore pressure in the liquefiable layer than in the free-field. For this reason, it is not uncommon for buildings to have large differential settlements due to a sand boil forming beneath the corner of a building. For example, during the Canterbury Earthquake Sequence that occurred in the vicinity of Christchurch, New Zealand between September 2010 and December 2011 sand ejecta from liquefaction caused numerous differential settlements for residential buildings in the suburbs of Christchurch, New Zealand causing substantial damage to the building foundations (Cubrinovski, 2013).

Many of the factors that influence the severity of liquefaction also influence the amount of settlement due to sand ejecta (e.g., density, effective stress, and fines content), however, an

important factor to consider must also be the depth of the liquefiable layer and the geotechnical properties of any overlying layers that may inhibit the flow of water that carries the ejecta particles.

2.6 CONCLUSION

Liquefaction is a significant result to earthquake shaking causing pore pressure to build up in saturated loose sand/coarse silts which reduces the strength and the stiffness of the soil which can cause severe consequences to natural and man-made structures. There are two types of liquefaction, flow liquefaction and cyclic liquefaction. Flow liquefaction occurs when the shear strength of soil is reduced (due to pore pressure generation) to a level below the initial static shear stress acting on the soil from a slope and/or a foundation. Cyclic liquefaction occurs when the initial static shear stress is less than the shear strength of the soil, i.e., during earthquake shaking, the cyclic nature of the ground motion causes deformations to develop incrementally and cause lateral spreading when the combination of the initial static stresses and the cyclic stress exceed the shear strength of the soil for a brief period of time.

The first step in any liquefaction analysis is evaluating the susceptibility of the soil. Many soils are not considered liquefiable for several reasons including they are too dense, contain too many plastic fines, and/or have too little water to generate pore pressures. It's important to remember that just because a soil is susceptible to liquefaction, does not necessarily mean that it will liquefy given that an earthquake occurs.

The simplified procedure developed by Seed and Idriss (1971) is the most common procedure for the evaluation of earthquake loading and still provides the basis for simplified approaches today. Liquefaction resistance is characterized by in-situ testing (typically SPT, CPT, or shear wave velocity) due to the effects of the disturbance of the soil fabric during sampling, transportation, and lab testing. Several liquefaction initiation procedures have been developed with

the two most common procedure today being those of Cetin et al. (2004) and Boulanger and Idriss (2012) for both deterministic and probabilistic liquefaction analysis.

The effects of liquefaction include alteration of ground motion, sand boils, flow failures, lateral spreading, and settlement – all of which can have severe consequences. There are procedures for evaluating the effects of liquefaction, however, many are empirical and are typically based on a database lacking the size and consistency needed to not have large uncertainty in them. Numerical procedures for evaluating the effects of liquefaction show promise, and will be discussed later in this thesis.

Chapter 3. **PROBABILISTIC LIQUEFACTION HAZARD ANALYSIS**

3.1 INTRODUCTION

In professional practice it is common to use PSHA (Section 2.4.2.2.2.3) to define ground motion hazards, however, it is not currently common to account for the liquefaction potential probabilistically. Originally termed performance-based liquefaction analysis, a probabilistic liquefaction hazard analysis (PLHA) takes the seismic loading and the liquefaction resistance into account probabilistically. PLHA uses probabilistic CRR curves and accounts for ground motion contributions from all hazard levels and all earthquake magnitudes that contribute to each ground motion hazard level (Kramer and Mayfield, 2007). This chapter will: (a) discuss a framework to quantify liquefaction hazards, (b) discuss the current tools available for PLHA analysis, (c) discuss relatively new methods of mapped parameters, (d) introduce a new liquefaction-targeted intensity measure that can be mapped, and (e) discuss the current role of PLHA in design.

3.2 CONVOLUTION OF HAZARD AND RESPONSES

Kramer and Mayfield (2007) presented a methodology for the convolution of hazard and response through integrating a probabilistic liquefaction resistance procedure with a PSHA. Kramer and Mayfield's methodology allows design to be based on a certain return period of liquefaction (or some effect of liquefaction, e.g., lateral spreading) that accounts for all levels of ground shaking, whereas, conventional procedures determine the probability of liquefaction or factor of safety against liquefaction for only a single level of shaking. Because earthquake sources can be highly variable (i.e., weak ground motions occur relatively frequently and strong ground

motions relatively rarely) designs based on a single ground motion do not define the true hazard for a site.

This methodology to design for the return period of liquefaction allows for a complete probabilistic evaluation of liquefaction and can be incorporated into the Pacific Earthquake Engineering Research (PEER) center framework to determine the effects of liquefaction which allows decision makers to design for decision variables such as repair costs. The PEER probabilistic framework (Deierlein et al., 2003) can be given as

$$\lambda_{dv} = \sum_{k=1}^{N_{DM}} \sum_{j=1}^{N_{EDP}} \sum_{i=1}^{N_{IM}} P[DV > dv|DM = dm_k] P\left[DM = dm_j \middle| EDP = edp_j\right] P[EDP = edp_k|IM = im_i] \Delta\lambda_{IM_i} \quad (3.1)$$

where the effects of an intensity measure (IM) such as PGA can be evaluated by an engineering demand parameter (EDP) such as the factor of safety against liquefaction. The actual effects of the EDP are termed damage measures (DM) which are effects such as lateral spreading displacement and settlement. The actual risk can be communicated to decisionmakers in the form of a decision variable (DV) such as repair cost or downtime, and $\Delta\lambda_{IM_i}$ is the incremental mean annual rate of exceedance of an IM which is given by Equation 2.37. From this, one could create a hazard curve of some decision variable versus return period.

3.3 TOOLS FOR PLHA

The difficulty in attracting the professional community to use PLHA in evaluation for site design is the time involved in learning the theoretical background of a PLHA and the computational effort required to carry out an analysis. Researchers have recognized this gap and have attempted to bridge it by developing tools that make carrying out a PLHA relatively easy for the practicing engineer with the goal of requiring less, or no additional work, than what's needed for a conventional liquefaction hazard analysis.

3.3.1 WSliq

WSliq was developed by researchers at the University of Washington for the purpose of allowing Washington State Department of Transportation (WSDOT) engineers to evaluate liquefaction hazards more accurately, consistently, and reliably, while also requiring less time than conventional procedures used in engineering practice for liquefaction evaluation. The WSliq interface is organized in a series of tabs that follow how a typical liquefaction hazard evaluation would be performed – there are tabs for the soil profile, susceptibility to liquefaction, initiation of liquefaction, and the effects of liquefaction. An additional tab presents the results of the liquefaction analysis.

Susceptibility Tab

Liquefaction susceptibility in WSliq can be determined either by the Boulanger and Idriss (2006) procedure, the Bray and Sancio (2006) procedure, or some combination of the two procedures by applying a weighting factor. The Boulanger and Idriss (2006) and Bray and Sancio (2006) procedures were discussed in Section 2.3.

Liquefaction Initiation Tab

The liquefaction initiation tab allows for computation of liquefaction initiation based upon the three most commonly used procedures at the time WSliq was created, which were the NCEER (Youd et al. 2001), Idriss and Boulanger (2004), and Cetin et al. (2004) procedures. WSliq allows for the use of one, two, or all three procedures for liquefaction triggering analyses along with an equally weighted average of the results of all three procedures termed the "WSDOT Recommended" liquefaction model.

WSliq also allows for a single scenario and multiple scenario analyses, and performance-based analysis of liquefaction initiation. All three procedures can be used for the single scenario and multiple scenario analysis, whereas, only the Cetin et al. (2004) procedure can be used for the

performance-based analysis. The multiple scenario analysis accounts for all magnitudes and source to site distances whereas the single scenario analysis only accounts for a single magnitude (typically chosen as the mean or modal magnitude from a PGA deaggregation). The performance-based analysis integrates the results of a PSHA with a probabilistic response analysis. Therefore, the performance-based analysis accounts for all peak acceleration values produced by all magnitudes and source-to-site distances at all return periods. The probabilistic liquefaction model of Cetin et al. (2004) is used to account for uncertainty in triggering, and is implemented into the PEER probabilistic framework (Deierlein et al., 2003).

Liquefaction Effects Tab

WSliq allows for the evaluation of liquefaction effects including: lateral spreading, settlement, response spectrum, and residual strength computations. Each of the liquefaction effects have several different models associated with them allowing the user the option to use a preferred model, or a logic tree method that computes a weighted average of the results of the individual models. Each of the four liquefaction effects computed in WSliq can be analyzed using single scenario, multiple scenario, and performance-based analyses.

Limitations

WSliq is an excellent program for evaluating liquefaction susceptibility, initiation, and effects with a user-friendly interface and a concise explanatory manual. However, it was developed in 2006, and does not reflect the significant advances that have been made in both the development of triggering and effects models (e.g., the Boulanger and Idriss probabilistic models for SPT [2012] and CPT [2015]) and the updating of USGS seismic hazard maps over the last decade or so.

3.3.2 PB LiquefY

Similar to WSliq, PB LiquefY was developed to make carrying out a PLHA relatively easy for the practicing engineer with the goal of requiring less, or no additional work than what's needed for a conventional liquefaction hazard analysis. PB LiquefY is a Microsoft Excel-based program with Visual Basic macros that can perform both deterministic and probabilistic liquefaction analysis. PB LiquefY allows for the evaluation of liquefaction susceptibility, initiation, and effects for multiple SPT-based procedures.

The PB LiquefY Excel Spreadsheet has several tabs. One presents a flow chart explaining how to perform a liquefaction analysis in PB LiquefY. The others consist of a soil profile tab, a loading information tab, a liquefaction analysis options tab, several deterministic and probabilistic output factor of safety against liquefaction and required SPT resistance to prevent liquefaction tabs, and several liquefaction effects tabs. Only the main tabs, which include the "Soil_Profile_Info" tab, the "Loading_Info" tab, and the "Liquefaction_Analysis_Options" tab, will be discussed in this section of the thesis.

Soil Profile

The "Soil_Profile_Info" tab allows for input of a soil profile for the site of interest. The soil profile input in PB LiquefY requires uncorrected SPT resistance values and information required to correct the SPT resistance for energy and overburden effects (e.g., borehole diameter, hammer efficiency, etc.). Once the soil profile information has been input, the susceptibility of the soil, along with the total and effectives stresses at the center of each soil layer, is computed. PB LiquefY's default susceptibility criteria are based on Bray and Sancio (2006), however, the program does allow you to manually specify whether a soil is susceptible or not.

Loading USGS Seismic Hazard Deaggregation Data

The "Loading_Info" tab allows the user to specify the type of soil amplification factor and the magnitude bin size for deaggregation purposes, and to download the seismic hazard data. The seismic hazard data is collected through using the National Seismic Hazard Mapping Project (NSHMP) tool "nshmp-haz" which was developed by the USGS earthquake hazards program. The "nshmp-haz" tool can be downloaded to one's local Root C:\ drive. The user then selects the deaggregation type, inputs the file path to the nshmp-haz folder (e.g., C:\nshmp-haz), and specifies the latitude and longitude of the site of interest. Downloading the data may take 5-15 minutes, however, this depends on the site location specified and the machine used to run the "nshmp-haz" java script.

Liquefaction Analysis

The "Liquefaction_Analysis_Options" tab allows the user to specify whether to compute a deterministic analysis, a performance-based analysis, or both. The deterministic option allows for the input of a mean magnitude, modal magnitude, or a user defined maximum acceleration and magnitude. If mean or modal magnitude is selected the user must specify the return period of interest to obtain a consistent maximum acceleration value based on the downloaded USGS seismic hazard data. Although PB LiquefY calls this a deterministic approach, it is a pseudo-probabilistic approach if a mean or modal magnitude is selected from the PSHA output. Therefore, the method will be termed conventional instead of deterministic throughout the remainder of this thesis. For performance-based analysis, the user must specify the "# of runs" or the number of increments of the hazard curve that are analyzed. The higher the specified value input of "# of runs," the more precise the performance-based computation will be, however, it will also take longer to run. The creators of PB LiquefY specify that a value of 250 is acceptable for most cases.

PB LiquefY also allows the user to specify multiple analysis types, which include Boulanger and Idriss (2012), Juang et al. (2012), and Cetin et al. (2004) for the conventional and performance-based computations.

Limitations

One of PB LiquefY's most useful qualities is that it provides easy access to the USGS deaggregation data through the "nshmp-haz" tool. However, as with many programs, PB LiquefY was found to have some limitations. PB LiquefY had difficulty characterizing the seismic hazard at moderate to long return periods for sites in moderate to low areas of seismicity. For example, specifying a return period of 475 years for Philadelphia, Pennsylvania caused the program to produce output factors of safety against liquefaction values based on a return periods of 2000-7000 years. The program did, however, work well in areas of higher seismicity such as the west coast of the United States. Perhaps the biggest limitation results from the program having been created on a Microsoft Excel platform with Visual Basic macros. The latter combination at times led to unexpected Visual Basic errors or caused the program to stop altogether. Although these limitations were found to exist, PB LiquefY provides an excellent service for comparing liquefaction triggering models for areas of moderate to high seismicity. PB LiquefY will be discussed further in Chapter 4 in regards to the latter.

3.3.3 Mapped Parameters

Mapped parameters are those for which a practicing engineer could simply enter the latitude and longitude coordinates of their site of interest, extract the mapped parameter related to liquefaction potential that has been developed by researchers using a PLHA, and input this mapped parameter into the practicing engineer's conventional liquefaction analysis method to generate a result that they would obtain if they were to carry out a full PLHA themselves. The latter enables

practicing engineers to realize the benefits of a full PLHA without having to do the voluminous calculations required for PLHA – this is the goal of mapped liquefaction parameters.

3.3.3.1 Required Blowcount, N_{req}

Mayfield et al. (2010) used the penetration resistance required to prevent initiation of liquefaction, N_{req}, for a specific 6-meter-deep reference element within a reference soil profile as the scalar parameter. Mayfield et al. (2010) showed that maps of N_{req}, such as those shown in Figure 3.1, provided a good estimate of the results of a full PLHA with two simple adjustment factors. The two adjustment factors account for different site conditions and depths other than 6 meters that were characteristic of the reference soil profile, to obtain the factor of safety against liquefaction and required penetration resistance to resist liquefaction. The Mayfield et al. (2010) procedure was limited to the use of the Cetin et al. (2004) procedure which was the only appropriate probabilistic liquefaction triggering procedure available at the time. The more recent Boulanger and Idriss (2012) liquefaction initiation model was included in PB LiquefY.

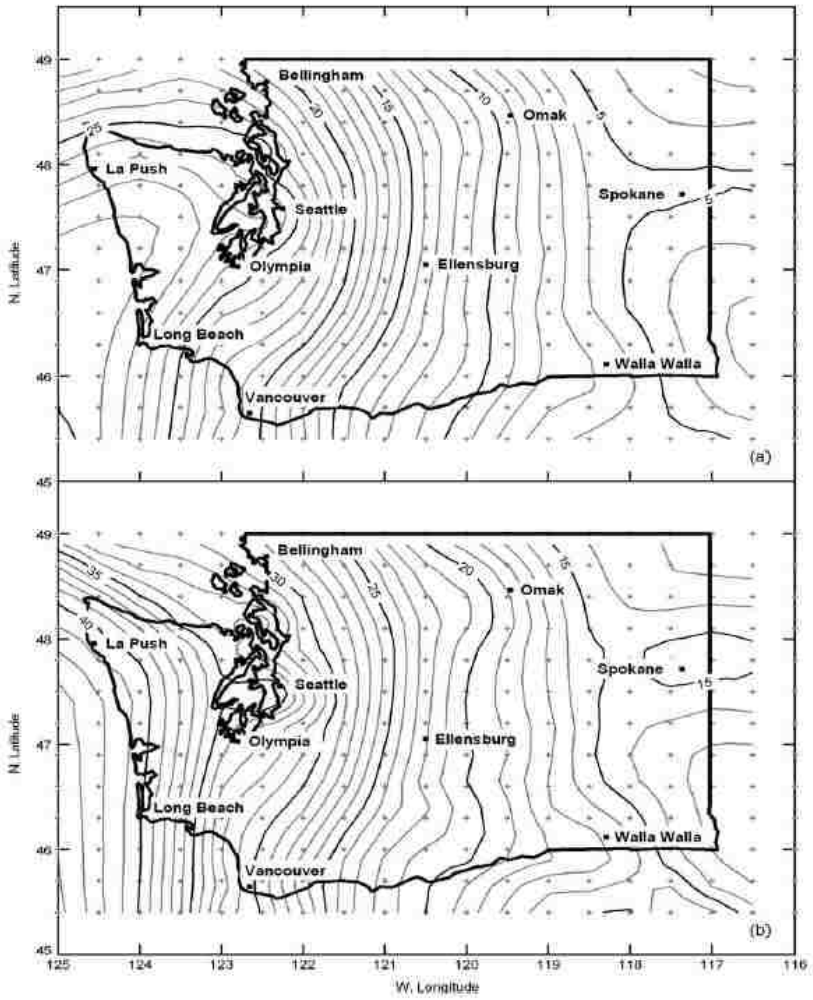

Figure 3.1. Mapped contours of N_{req} for Washington State for return periods of (a) 475 years; (b) 2475 years (Mayfield et al., 2010).

3.3.3.2 *CSR*

To add another tool to the practicing engineer, Ulmer and Franke (2016) created a new simplified performance-based procedure for CSR instead of N_{req} using the Boulanger and Idriss (2012) liquefaction initiation model for return periods of 475 years, 1,033 years, and 2,475 years. The goal of Ulmer and Franke (2016) was to develop an alternative mapped liquefaction parameter using the Boulanger and Idriss (2012) liquefaction triggering curves to complement the Mayfield et al. (2010) mapped parameter procedure which used the Cetin et al. (2004) liquefaction triggering curves. Ulmer and Franke (2016) found that their modified performance-based procedure could

reasonably estimate hazard-targeted liquefaction triggering metrics such as the factor of safety against liquefaction, and probability of liquefaction, at return periods of 475 years, 1,033 years, and 2,475 years. Since CSR is based on multiple factors, however, five adjustment factors were required.

3.3.3.3 Liquefaction-Targeted, Magnitude-Corrected PGA

The goal of a mapped liquefaction parameter that can be used by the practicing engineer to obtain the results of a full PLHA would be aided by the use of a parameter that eliminated the need for a reference element and for any adjustment factors required. Starting with the simplified procedure, Equation 2.13 can be rewritten as

$$CSR = 0.65\left[\frac{PGA/g}{MSF}\right]\frac{\sigma_{vo}}{\sigma'_{vo}}r_d \tag{3.2}$$

which can be replaced by

$$CSR = 0.65PGA_M\frac{\sigma_{vo}}{\sigma'_{vo}}r_d \tag{3.3}$$

where

$$PGA_M = \frac{PGA/g}{MSF} \tag{3.4}$$

Therefore, this combination of PGA and MSF produces the parameter, PGA_M, that represents the ground surface motion and its contribution to liquefaction loading. With the use of PGA_M, values of σ_{vo}, σ'_{vo}, and r_d can be used directly in the liquefaction potential calculations instead of through adjustment factors.

To implement PGA_M into a conventional liquefaction analysis, FS_L will be used as a limit state variable. Performing a full PLHA with FS_L as the limit state variable, a FS_L hazard curve can be obtained (Figure 3.2a). Performing multiple conventional analyses, a relation between PGA_M and FS_L (Figure 3.2b) can be established. This allows for a PGA_M from a conventional method to

be related to a FS_L from a PLHA at a specific return period. For example, Point A in Figure 3.2 represents a 475-year return period that intersects the FS_L hazard curve at Point B, which has a single FS_L associated with it. Continuing along the dotted line the conventional hazard curve is intersected at Point C which has the same FS_L, however, obtained from the conventional method. Following the dashed line to Point D on the PGA_M axis, a PGA_M value of 0.24 g is obtained. This PGA_M value represents the PGA_M associated a 475-year return period of liquefaction itself. Conventional PGA_M values associated with different return periods of liquefaction can be computed. If these PGA_M values were then mapped, and accessible to the practicing engineer, implementation of this mapped PGA_M value into the practicing engineers conventional method would output a FS_L that represents the FS_L that would be un-exceeded at the specified return period. Validation of this approach, however, requires investigation of the sensitivity of PGA_M to site conditions and liquefaction triggering models.

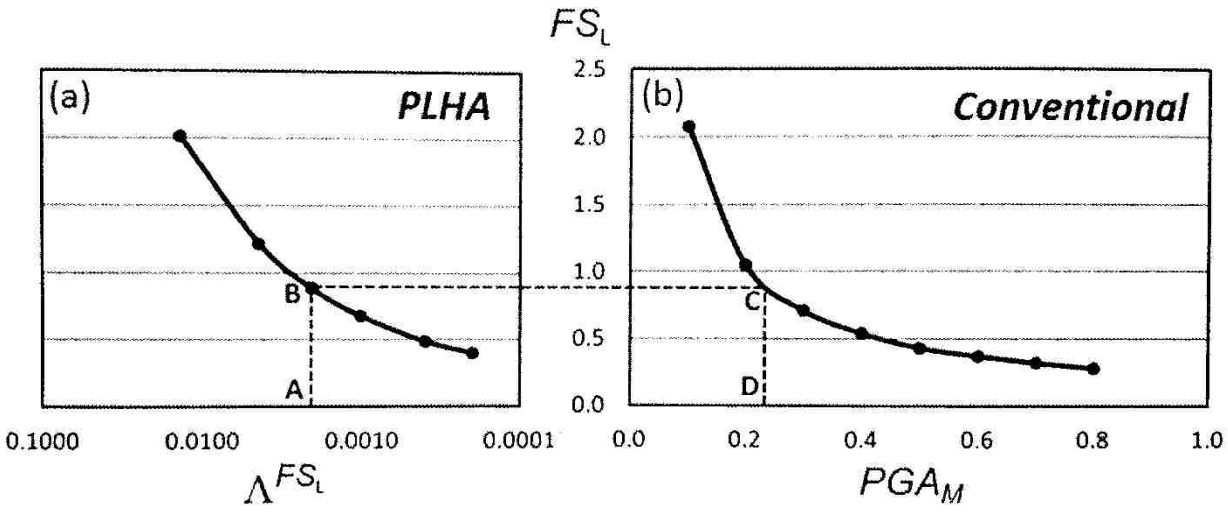

Figure 3.2. Illustration illuminating the procedure of how a conventional PGA_M value can be associated with a return period of a full PLHA.

3.3.4 Role of PLHA in Design

Kramer and Mayfield (2007) demonstrated that conventional methods of liquefaction analysis provide a non-uniform likelihood of liquefaction initiation and effects in different

geographic regions. For example, Kramer and Mayfield (2007) showed that soil deposits with the same factor of safety against liquefaction produced by conventional methods would be twice as likely to liquefy in San Jose, CA as one in Memphis, TN. Franke and Kramer (2014) showed that conventional lateral spreading hazard procedures produce severely inconsistent lateral spreading hazards in different geographic areas, and therefore different seismic environments. Their results indicate the consistent application of conventional lateral spreading procedures can lead to highly inconsistent safety standards across different locations in the US. This leads to US residents in one seismic area being at a higher safety risk than residents in another seismic area, or vice-versa. It can also be interpreted as requiring residents in one seismic environment to incur greater expenses for earthquake damage mitigation than residents of other seismic environments. The latter inconsistencies stem from the incomplete characterization of the seismic hazard. Conventional liquefaction hazard methods use the results of a PSHA to define earthquake loading in terms of a PGA at a single design return period. One magnitude (mean or modal) is typically taken from the many magnitudes that contribute to the PGA value. This, however, does not represent the true seismic hazard of a site because liquefaction can be triggered by weak motions that occur more often, or strong motions that occur less often. Therefore, to solve the problem of inconsistent seismic hazards across different locations, one must consider all levels of shaking, along with the magnitudes that contribute to each level of shaking, for each site. PLHA does the latter, and therefore, produces more consistent and uniform safety across different seismic environments – this is the role of PLHA in design.

3.4 CONCLUSION

PLHA allows for a fully probabilistic evaluation of liquefaction initiation/effects by accounting for not only seismic loading probabilistically, but also the liquefaction resistance

probabilistically. Currently, PLHA is not often performed for typical engineering projects by practicing professionals due to the voluminous calculations that are involved and the limited time that is often available on engineering projects. In order to address this issue, researchers have developed programs such as WSliq and PB LiquefY in order to help practicing professionals implement PLHA into their designs. Although these tools are available, most practicing engineers continue to use conventional methods for liquefaction analysis. To solve this problem, researchers have now been working towards developing a mapped liquefaction parameter that could be extracted by a practicing engineer and implemented into their typical conventional liquefaction analyses in order to receive the benefits of a full PLHA without having to do the voluminous calculations. Current mapped parameter procedures have two limitations: (a) they require adjustment factors needed to account for varying site conditions and (b) the sensitivity to the liquefaction triggering model used is unknown. The liquefaction targeted ground motion parameter, PGA_M, aims to address these limitations.

Chapter 4. SENSITIVITY OF PGA_M TO SITE CONDITIONS AND LIQUEFACTION TRIGGERING MODELS

4.1 INTRODUCTION

Improving the prediction of liquefaction triggering has already been undertaken for many years, however, in ways that can be burdensome, involved, and heavily time dependent for the practicing engineer. In order to help the practicing geotechnical engineering community, and in turn the people/community they work with, new methods for prediction of liquefaction triggering need to be easy for practicing engineers to implement. The liquefaction targeted intensity measure, PGA_M, provides an opportunity for practicing engineers to use the same, or less effort, than the conventional liquefaction triggering methods they are used to while allowing the user to obtain the liquefaction triggering results that would be obtained had they ran a full PLHA. This would be achieved by users being able to enter the latitude and longitude of their site location, along with a Vs_{30} value, to obtain a mapped PGA_M value at the return period of interest. The user would then be able to use this value of PGA_M to compute FS_L using current conventional procedures and obtain the same FS_L value that would be produced by a full PLHA. This chapter describes the use of PB LiquefY to validate a PGA_M-based procedure for PLHA. It will include discussion of the procedural setup to obtain conventional and probabilistic liquefaction triggering results in PB LiquefY, the calculation of PGA_M from the PB LiquefY results, a comparison of the two common liquefaction triggering procedures, and an evaluation of the sensitivity of site conditions (e.g., density and depth) on PGA_M for each triggering procedure.

4.2 PROCEDURAL SETUP

The Excel-based software program, PB LiquefY, was used to perform both conventional and probabilistic liquefaction triggering analysis. The general format of PB LiquefY was discussed in Section 3.3.2. Additional information about the methods used for this research are explained in this chapter.

4.2.1 **Soil Profiles**

The "Soil_Profile_Info" tab of PB LiquefY allows for input of soil profile data for the site of interest. The soil profile input includes uncorrected SPT resistance values and data that allows the SPT resistance to be corrected for energy (e.g., borehole diameter, hammer efficiency, etc.) and overburden effects, and fines content. The profiles used for this research consisted of a 16-meter depth clean sand layer split into 18 sublayers with the water table located one meter below the ground surface. Because the soil is a clean sand, the corrected SPT resistance will be defined as $(N_1)_{60}$ in this chapter. The soil profiles were defined by the uncorrected SPT resistances required to produce $(N_1)_{60}$ values of 5, 10, 15, 20 and 25 blows using both the Cetin et al. (2004) and Boulanger and Idriss (2012) procedures. A total of 10 soil profiles were needed for the five desired $(N_1)_{60}$ values because the calculation of the corrected SPT resistance is slightly different between the Cetin et al. (2004) and Boulanger and Idriss (2012) procedures. The unit weight for the clean sand input into PB LiquefY was found using Equations 4.1-4.4 with typical clean sand values for a minimum and maximum void ratio of 0.4 and 1.0 respectively. The relative density, D_r, can be estimated (Meyerhof, 1957) as

$$D_r = \sqrt{\frac{(N_1)_{60}}{46}} \tag{4.1}$$

and then input into

$$e = D_r \times (e_{max} - e_{min}) + e_{max} \quad (4.2)$$

where e_{max} is the maximum void ratio, e_{min} is the minimum void ratio, and e is the current void ratio. With the latter, the dry unit weight, γ_d, (for soils above the water table) and the saturated unit weight, γ_{sat}, (for soils below the water table) can be calculated using Equation 4.3 and 4.4 assuming a specific gravity, G_s, of 2.65 for the sand and a unit weight of water, γ_w, of 9.81 kN/m^3.

$$\gamma_d = \frac{G_s \times \gamma_w}{1+e} \quad (4.3)$$

$$\gamma_{sat} = \frac{(G_s+e) \times \gamma_w}{1+e} \quad (4.4)$$

The shear wave velocity was obtained from correlation to SPT resistance using the Brandenberg et al. (2010) procedure

$$\ln V_s = \beta_0 + \beta_1 \times \ln N_{60} + \beta_2 \times \ln \sigma'_{vo} \quad (4.5)$$

where V_s is the shear wave velocity, N_{60} is the energy-corrected SPT resistance given by Equations 4.6 and 4.7, σ'_{vo} is the vertical effective stress at the depth of the SPT measurement, and β_0, β_1, and β_2 are coefficients shown in Table 4.1. The value of N_{60} was computed as

$$N_{60} = \frac{(N_1)_{60}}{C_N} \quad (4.6)$$

where C_N is the overburden correction given by

$$C_N = \sqrt{\frac{P_a}{\sigma'_{vo}}} \quad (4.7)$$

where P_a is the atmospheric pressure assumed to be 101.325 kPa. Upon entering the soil profile information, the corrected SPT resistance for each sublayer and the total and effective stresses at the midpoint of each sublayer were computed by the program.

Table 4.1. Coefficients for shear wave velocity estimation (Brandenberg et al., 2010).

Soil Type	β_0	β_1	β_2
Sand	4.045	0.096	0.236
Silt	3.783	0.178	0.231
Clay	3.996	0.230	0.164

4.2.2 Loading Information

The "Loading_Info" tab allows the user to specify the type of soil amplification factor, the magnitude bin size for deaggregation purposes, and download the seismic hazard data (See Section 3.3.2). The soil amplification factor used to compute the peak ground acceleration at the ground surface was computed from the Stewart et al. (2003) expression given as

$$F_a = \frac{PGA_{surface}}{PGA_{rock}} = exp(a + b \ln PGA_{rock}) \quad (4.8)$$

where F_a is the soil amplification factor, $PGA_{surface}$ is the peak ground acceleration at the surface of a soil site, PGA_{rock} is the peak rock outcrop acceleration (obtained from the nshmp-haz tool), and a and b are statistical regression coefficients. The default a and b values used in PB LiquefY, and for this research, are a = -0.15 and b = -0.13, which are values corresponding to Quaternary age alluvium (see Stewart et al. 2003). Rearranging Equation 4.8, $PGA_{surface}$ is calculated as

$$PGA_{surface} = F_a \times PGA_{rock} \quad (4.9)$$

The magnitude bin size for each site observed in this research was set to a value of 0.1 to adequately assess the contributions of each magnitude for the particular site latitude and longitude entered into the nshmp-haz tool (see Section 3.3.2). The seismic hazard data was downloaded using the nshmp-haz tool selecting the USGS 2014 Interactive Deaggregation option and then entering the longitude and latitude of the site of interest.

4.2.3 Liquefaction Analysis Options

The "Liquefaction_Analysis_Options" tab allows the user to specify whether to compute a conventional analysis, a performance-based analysis (PLHA), or both, for a user-selected liquefaction triggering model. To find the PGA_M values that correspond to a PLHA factor of safety against liquefaction, and in turn the return period of liquefaction, both conventional and PLHA were performed for this research. Both the Cetin et al. (2004) and the Boulanger and Idriss (2012) liquefaction triggering procedures were selected for the conventional and probabilistic analyses. The conventional analyses used a mean magnitude and the overburden correction factor limit of 1.1 was used for the Boulanger and Idriss procedure. A probability of liquefaction of 15% was used for the Cetin et al. (2004) deterministic procedure. For the PLHA, the overburden correction factor limit of 1.1 was used for the Boulanger and Idriss procedure. PLHA requires the user to specify the "# of runs" or the number of increments of the hazard curve that are analyzed. The creators of PB LiquefY specify that a value of 250 is acceptable for most cases. For this research the "# of runs" was selected to be 500 in order to adequately characterize site locations which have a steep sloping hazard curve. The option to run the conventional and PLHA was then selected.

4.2.4 Calculation of a liquefaction-targeted intensity measure, PGA_M

After setting up the soil profile, the loading information, and selecting the desired liquefaction analysis options, PB LiquefY was used to compute a full PLHA at the site of interest and conventional analyses with ground motion parameters corresponding to seven return periods. For each return period of the conventional analyses, PGA_M and FS_L were calculated. The PLHA allowed calculation of a FS_L hazard curve, so that PLHA-based FS_L could be plotted as a function of return period (or mean annual rate of non-exceedance). Therefore, the conventional PGA_M value that corresponds to a PLHA FS_L at a certain return period can be determined using the process

shown graphically in Section 3.3.3.3. The determination of this PGA_M that corresponds to a certain PLHA FS_L at a particular return period can be automated from the PB LiquefY result through linear interpolation (in log-log space) using Equation 4.10 and Equation 4.11.

$$\log PGA^*_M = \log PGA_{M_1} + \left(\frac{\log FS^*_L - \log FS_{L_1}}{\log FS_{L_2} - \log FS_{L_1}}\right) \times \left(\log PGA_{M_2} - \log PGA_{M_1}\right) \quad (4.10)$$

$$PGA^*_M = 10^{\log PGA^*_M} \quad (4.11)$$

where PGA^*_M is the magnitude corrected peak ground acceleration at a desired PLHA return period, FS^*_L is the PLHA factor of safety at a desired return period, and PGA_{M_1}, PGA_{M_2}, FS_{L_1}, and FS_{L_2} are the magnitude corrected peak ground acceleration and factor of safety against liquefaction that correspond to the closest return periods on the conventional FS_L vs PGA_M curve to where the FS^*_L intersects (see Figure 4.1a). Linear interpolation in log-log space can be used because the FS_L and PGA_M data plots nearly linear in log-log space (see Figure 4.1b). To make the latter clear, the following example is shown illustrating the graphical and linear interpolated PGA^*_M methods.

For example, a site located in Seattle, WA with a $(N_1)_{60}$ value of 15 at a depth of 4 meters was analyzed. The data shown in Table 4.2 and Figure 4.1 were obtained from PB LiquefY in order to find the conventional PGA^*_M value that corresponds to a PLHA FS_L at a return period of 1,039 years.

Table 4.2. Conventional and PLHA data for a site located in Seattle, WA.

Return Period	Mean annual rate of non-exceedance	Conventional FS_L	Conventional $\log(FS_L)$	Conventional PGA_M	Conventional $\log(PGA_M)$	PLHA - FS^*_L	PLHA - $\log(FS^*_L)$	$\log(PGA^*_M)$	PGA^*_M
475 [1]	0.00211	0.610	-0.215	0.269	-0.569	0.632	-0.199	-0.585	0.260
1039 [2]	0.00096	0.440	-0.357	0.373	-0.428	0.442	-0.355	-0.430	0.372
2475	0.00040	0.325	-0.489	0.505	-0.296	0.322	-0.492	-0.293	0.510
4975	0.00020	0.264	-0.578	0.621	-0.207	0.259	-0.587	-0.198	0.633
9950	0.00010	0.217	-0.663	0.755	-0.122	0.215	-0.668	-0.118	0.762

[1] Return period for FS_{L_1} and PGA_{M_1}
[2] Return period for FS_{L_2} and PGA_{M_2}

Using the values in Table 4.2, Equations 4.10 and 4.11 were used in order to find the $PGA^*{}_M$ value that corresponded to a FS_L at a return period of 1,039 years from a full PLHA.

$$\log PGA^*{}_M = -0.569 + \left(\frac{-0.355-(-0.215)}{-0.357-(-0.215)}\right) \times (-0.428-(-0.569)) \quad (4.12)$$

$$\log PGA^*{}_M = -0.430 \quad (4.13)$$

$$PGA^*{}_M = 10^{-0.430} \quad (4.14)$$

$$PGA^*{}_M = 0.372 \quad (4.15)$$

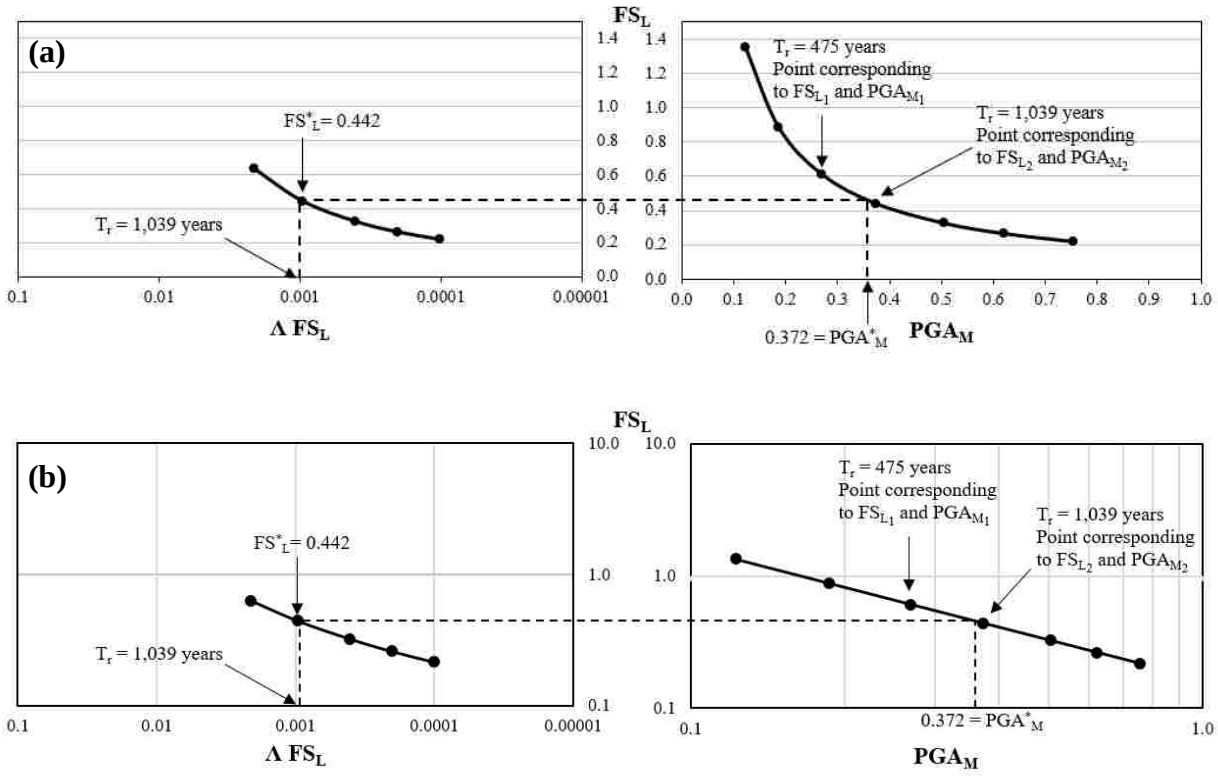

Figure 4.1. Graphical Illustration of determining the conventional magnitude corrected peak ground acceleration, $PGA^*{}_M$, for an event with a return period of 1,039 years from a full PLHA for a site in Seattle, WA in (a) linear space (b) log-log space.

The figures in the results section that follows were generated using the automated way described. For simplicity, the conventional magnitude corrected peak ground acceleration, $PGA^*{}_M$, that

corresponds to a particular return period from a PLHA will be termed PGA_M for the remainder of this thesis.

4.2.5 Correction Factor for Site Conditions

Ideally, a mapped PGA_M value would be applicable to all conditions – all components of CSR and CRR. That means it would apply to all depths, all $(N_1)_{60}$ values, all water table locations, all σ_{vo}/σ'_{vo} ratios, etc. In order for that to happen, the FS_L values in the conventional and PLHA analyses have to be influenced identically by those parameters. Graphically, that means Site Conditions A and B in Figure 4.2 would have to intersect the PGA_M axis at the same location.

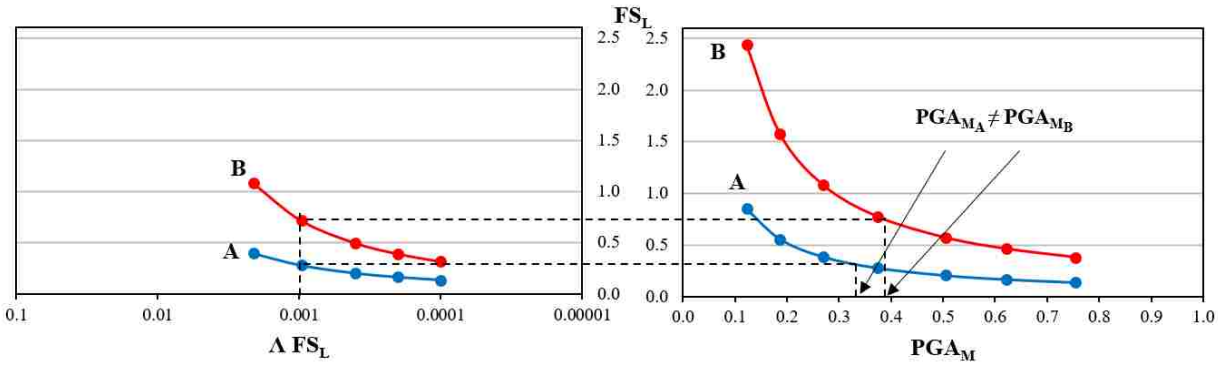

Figure 4.2. Graphical Illustration comparing Site Condition A to Site Condition B showing an example of when a correction factor is needed.

Site Condition A represents an $(N_1)_{60}$ = 5 at a depth of 2 meters BGS, and Site Condition B represents an $(N_1)_{60}$ = 25 at a depth of 15 meters BGS. If the conventional PGA_M values, based on a particular return period of liquefaction, are not the same (as illustrated in Figure 4.2), a separate map for Conditions A and B (which is not very practical) would be required. Instead of a separate map, a correction factor that allows a value of PGA_M for Condition B to be computed from a mapped value of PGA_M for Condition A can be used.

4.3 RESULTS

Two of the most generally accepted liquefaction triggering procedures are compared for a moderate seismicity location (Charleston, SC) and a very high seismicity location (Eureka, CA). The trends of the PGA_M values obtained when implementing the Cetin et al. (2004) and Boulanger and Idriss (2012) procedures are discussed with respect to the insensitivity to depth, SPT resistance, and water table location. Because of the large difference in seismicity between sites, the PGA_M axis on the plots have a different range of values in order to see trends in the data. Following the discussion on the procedural trends, the Cetin et al. (2004) and Boulanger and Idriss (2012) results are compared, while several site locations were analyzed, this chapter focuses on two site locations, one of moderate seismicity, and another representing the highest seismicity site analyzed. The highest seismicity site was chosen because if PGA_M is insensitive to site conditions at this site, then it would be insensitive at all sites. The reader is referred to Appendix A to see the results for all 27 locations observed in this research. For the remainder of this thesis, the Cetin et al. (2004) procedure will be termed "CEA2004" and the Boulanger and Idriss (2012) procedure will be termed "IB2012."

4.3.1 Influence of SPT resistance on PGA_M

To gain an understanding of how the CEA procedure performs in different seismic environments, a very high seismicity location (Eureka, CA) and a moderate seismicity location (Charleston, SC) were used to observe the influence of SPT resistance on PGA_M.

Cetin et al. (2004)

The liquefaction-targeted intensity measure, PGA_M, is influenced by SPT resistance (a proxy for the soils density) for both moderate and very high seismicity sites for the CEA2004 procedure. Figures 4.3-4.4 show PGA_M vs $(N_1)_{60}$ plots at six depths for three return periods at

Charleston, SC and Eureka, CA. If the PGA_M value was perfectly insensitive to SPT resistance, which would be a desirable result, these curves would be perfectly flat. The slopes of the curves show that there is sensitivity of PGA_M to blow counts – particularly at longer return periods and in higher seismicity locations like Eureka, CA.

A linear regression equation was developed for each sublayer/return period for each of the sites. Therefore, the slope of the lines indicates the sensitivity of PGA_M to SPT resistance. The linear regression equations developed for each site are shown in Appendix B and were used to develop normalized sensitivity plot shown in Figures 4.5-4.6. Each figure has 6 different lines corresponding to each depth of interest. If the SPT resistance did not influence the PGA_M the plots would appear as six horizontal lines with normalized PGA_M values of 1.0. The moderate seismicity site of Charleston, SC only shows minor variation of the normalized PGA_M at the different return periods. The high seismicity site of Eureka, CA, however, shows significant influence of SPT resistance on PGA_M at longer return periods. Therefore, a correction factor to account for the influence of SPT resistance in high seismicity areas may be required.

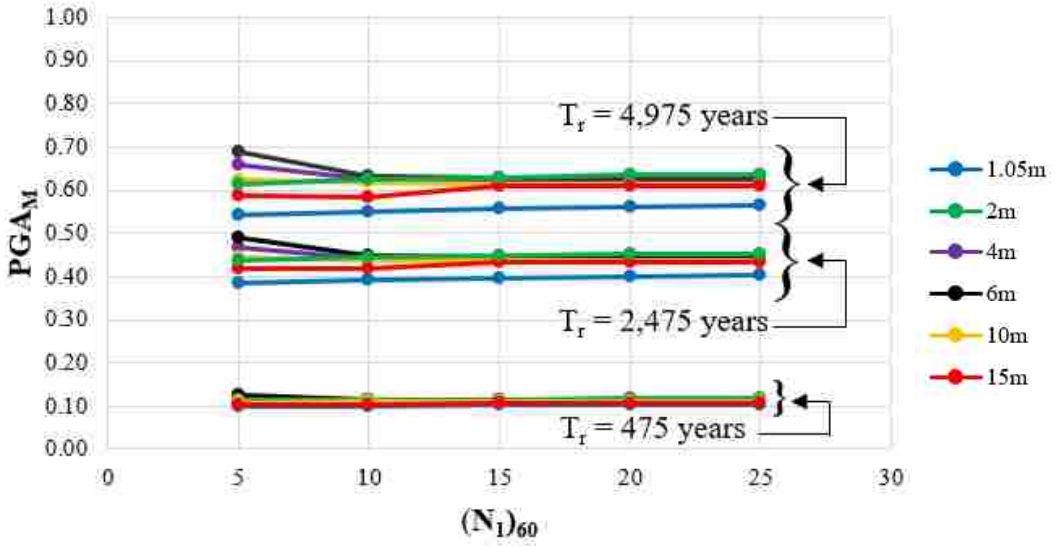

Figure 4.3. Charleston, SC – Magnitude corrected peak ground acceleration dependent upon SPT resistance, $(N_1)_{60}$, for the CEA2004 procedure.

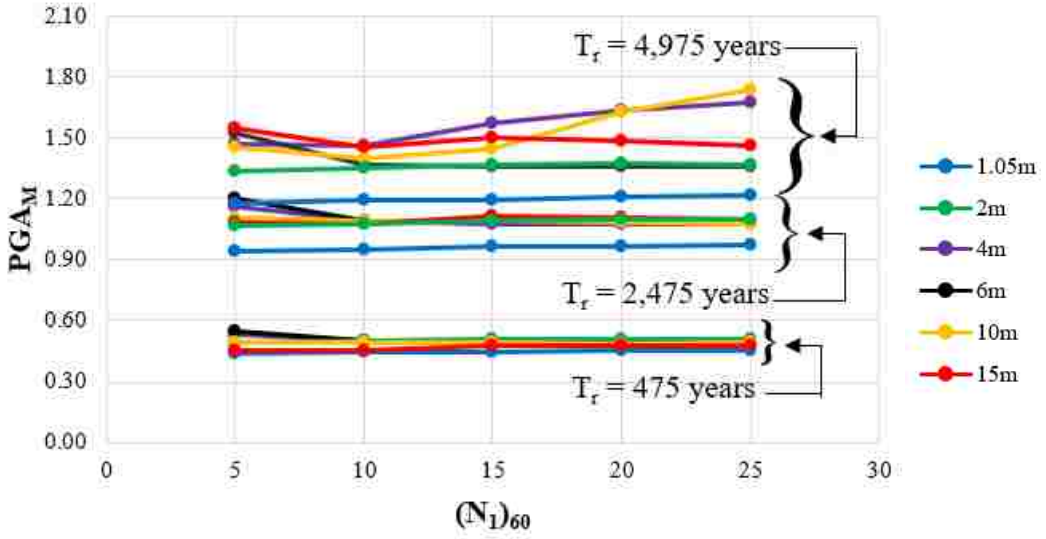

Figure 4.4. Eureka, CA – Magnitude corrected peak ground acceleration dependent upon SPT resistance, $(N_1)_{60}$, for the CEA2004 procedure.

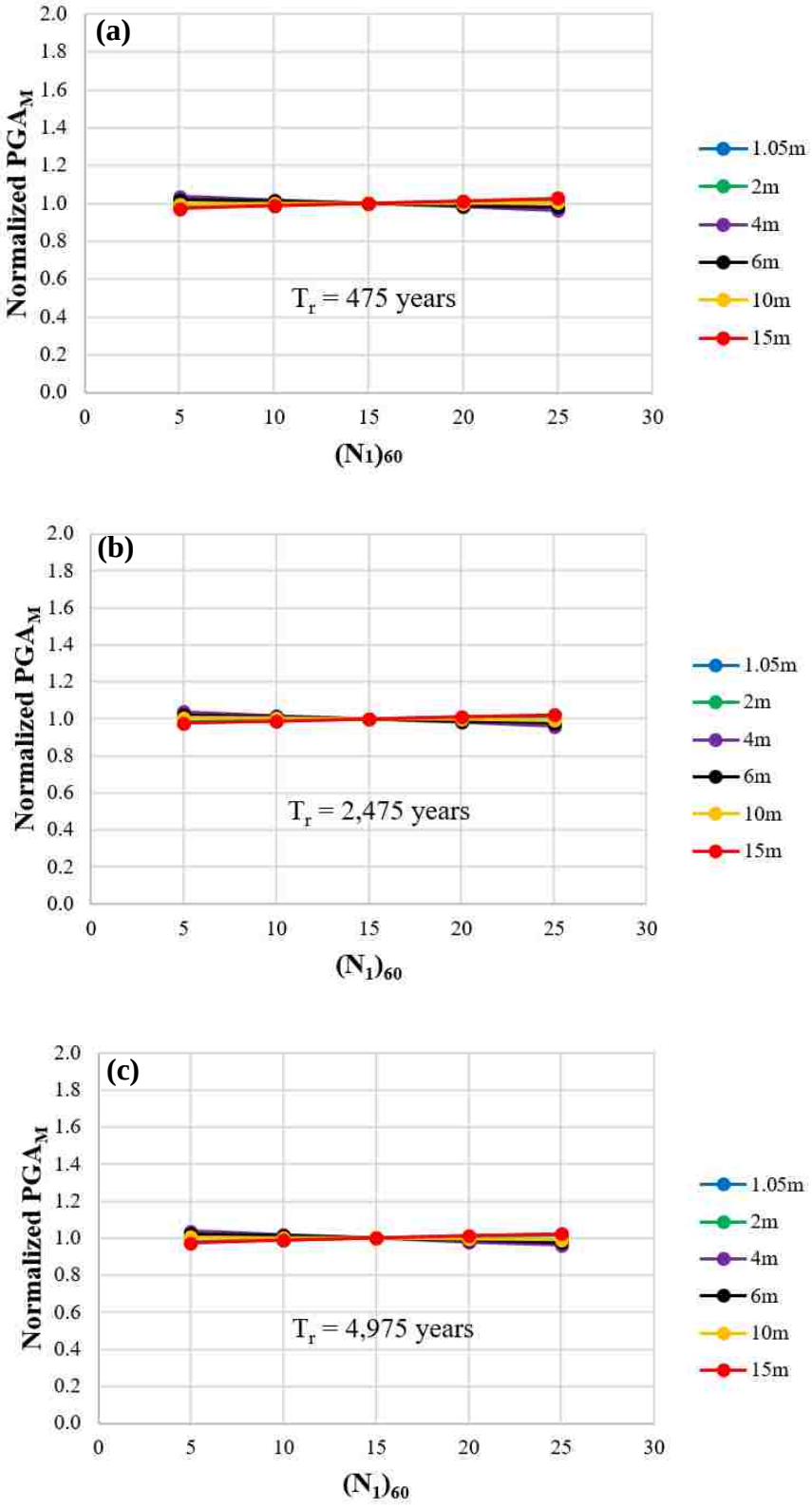

Figure 4.5. Charleston, SC – Normalized PGA_M dependent upon SPT resistance, $(N_1)_{60}$, for the CEA2004 procedure at return periods of (a) 475 years, (b) 2,475 years, and (c) 4,975 years.

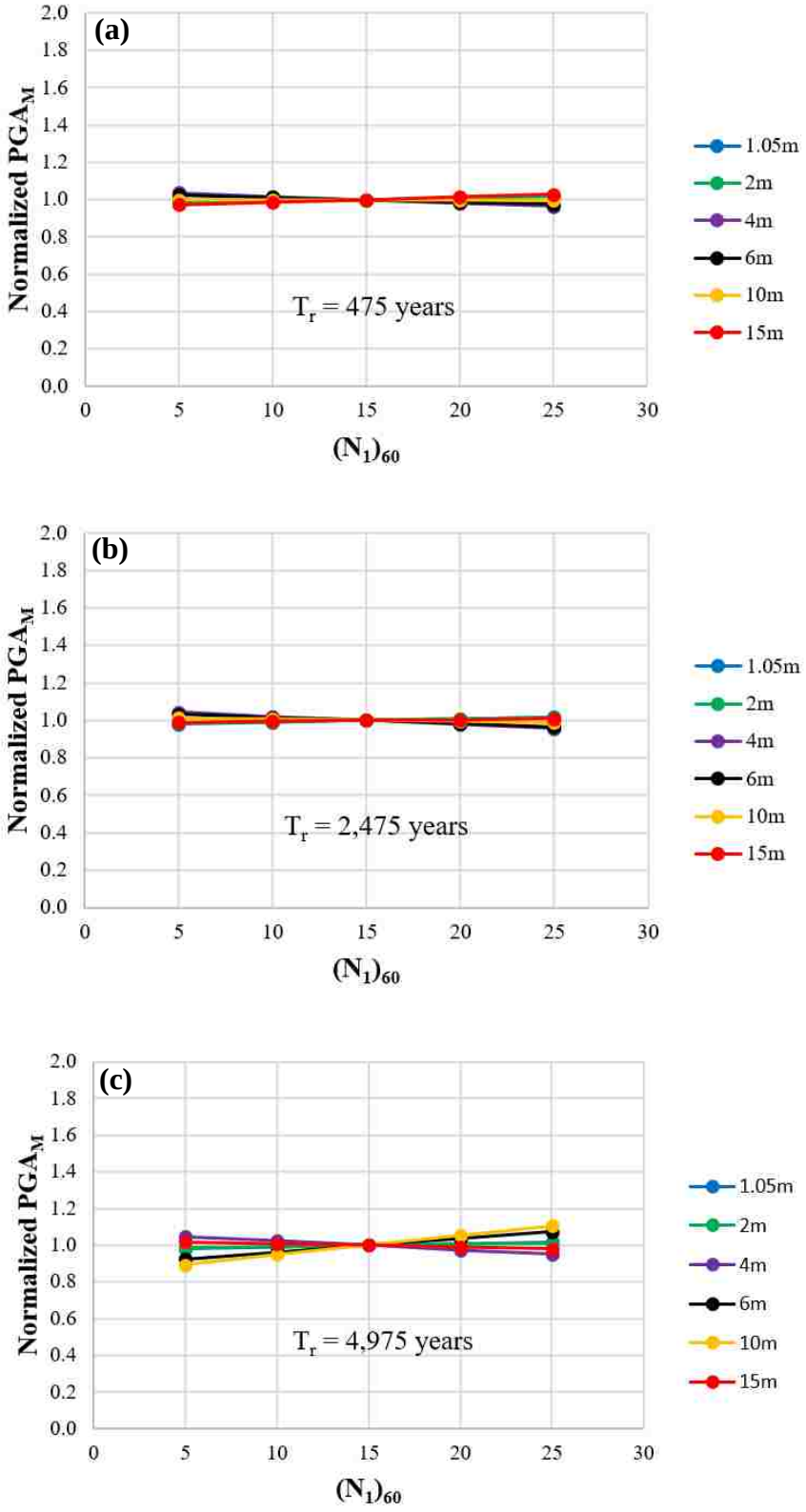

Figure 4.6. Eureka, CA – Normalized PGA_M dependent upon SPT resistance, $(N_1)_{60}$, for the CEA2004 procedure at return periods of (a) 475 years, (b) 2,475 years, and (c) 4,975 years.

Boulanger and Idriss (2012)

The same type of analysis was performed using the liquefaction triggering procedure of IB2012. The liquefaction-targeted intensity measure, PGA_M, was found to be negligibly influenced by SPT resistance for both moderate and very high seismicity sites with this procedure. Figures 4.7-4.8 show PGA_M vs $(N_1)_{60}$ plots at six depths for three return periods at Charleston, SC and Eureka, CA. The IB2012 procedure performed well as indicated by the curves in Figures 4.7-4.8 being flat. Therefore, this suggests PGA_M is insensitive to $(N_1)_{60}$ for this procedure.

A linear regression equation was developed for each sublayer/return period for each of the sites (see Appendix B). Following the same method as before, Figures 4.9-4.10 were developed for the IB2012 procedure. Because the normalized PGA_M plots show a flat line with no variation with respect to $(N_1)_{60}$ at all return periods and for both site locations, SPT resistance has little to no influence on PGA_M values for the IB2012 procedure in areas of moderate to high seismicity. This same trend persists for 25 other site locations as shown in the Appendix A. Therefore, an $(N_1)_{60}$ correction factor is not needed for PGA_M when using the IB2012 procedure,

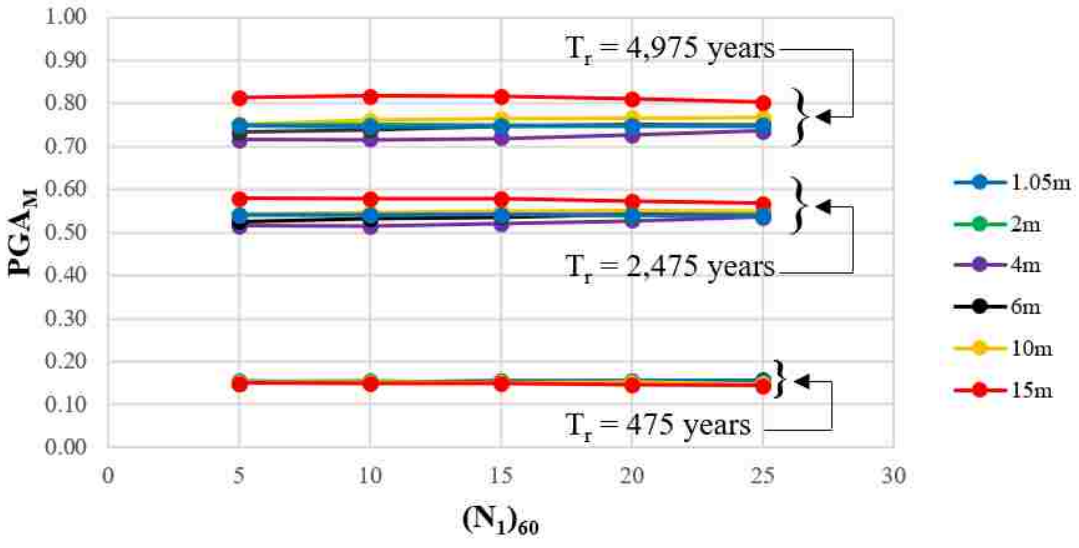

Figure 4.7. Charleston, SC – Magnitude corrected peak ground acceleration dependent upon SPT resistance, $(N_1)_{60}$, for the IB2012 procedure.

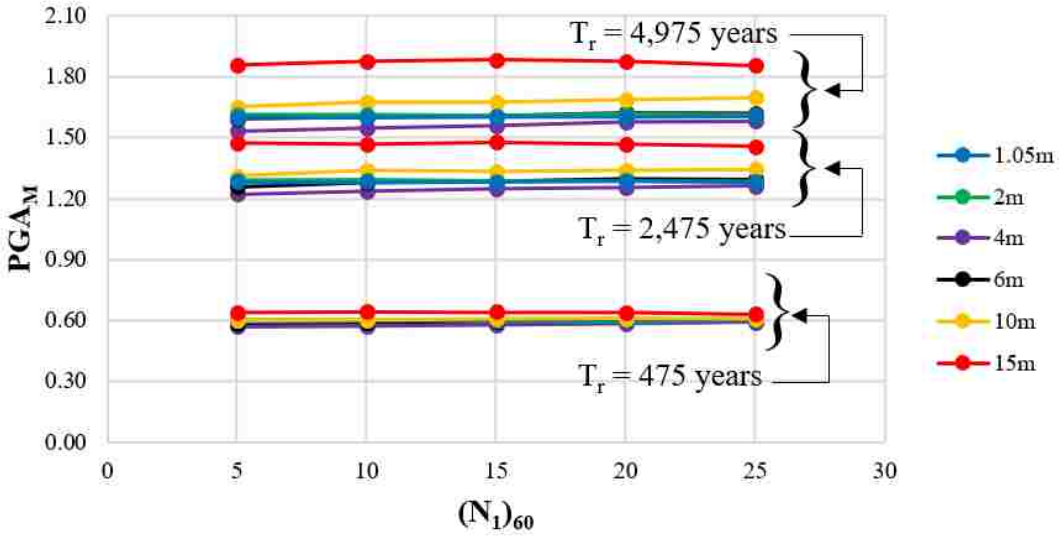

Figure 4.8. Eureka, CA – Magnitude corrected peak ground acceleration dependent upon SPT resistance, $(N_1)_{60}$, for the IB2012 procedure.

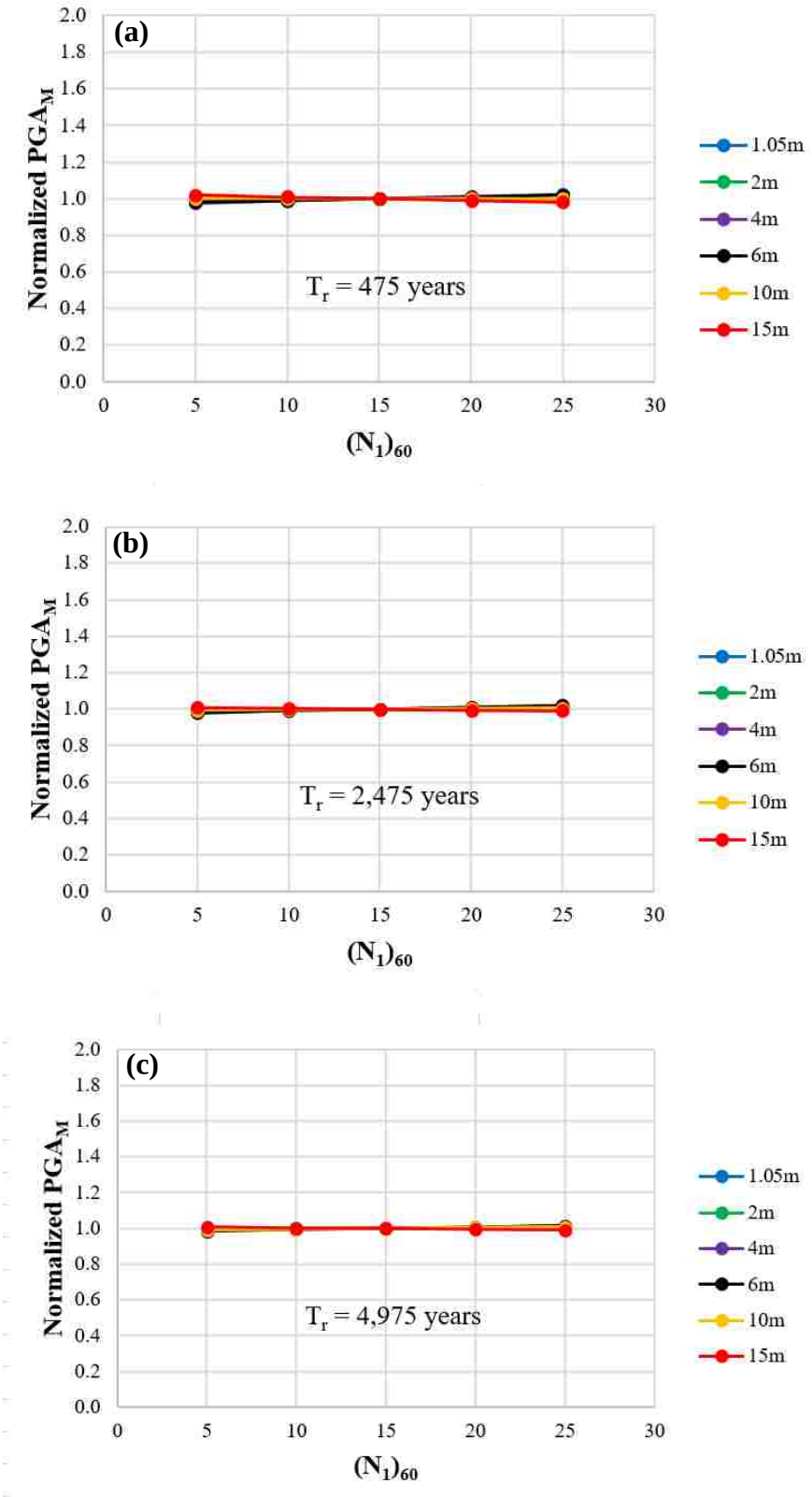

Figure 4.9. Charleston, SC – Normalized PGA_M dependent upon SPT resistance, $(N_1)_{60}$, for the IB2012 procedure at return periods of (a) 475 years, (b) 2,475 years, and (c) 4,975 years.

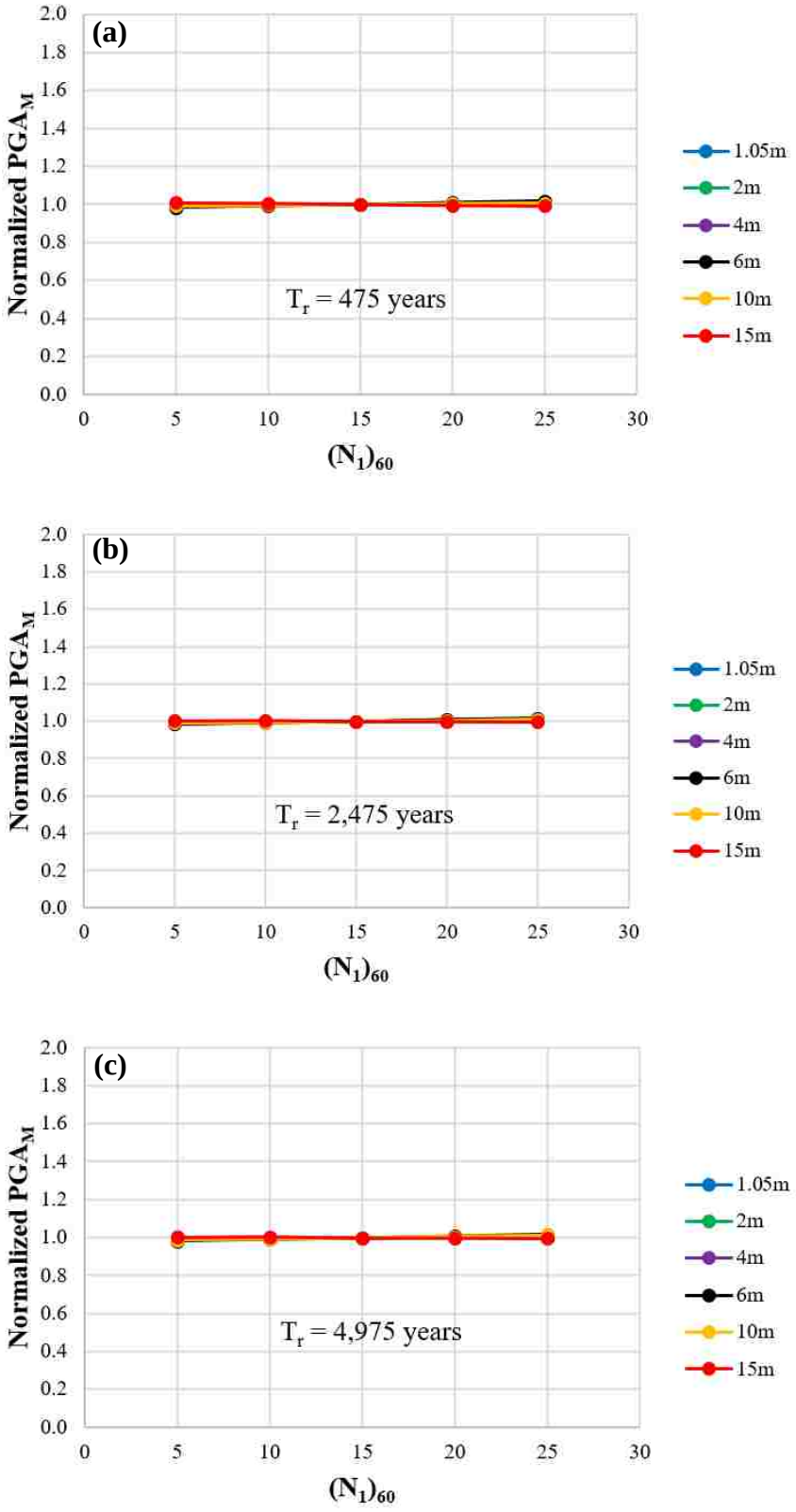

Figure 4.10. Eureka, CA – Normalized PGA_M dependent upon SPT resistance, $(N_1)_{60}$, for the IB2012 procedure at return periods of (a) 475 years, (b) 2,475 years, and (c) 4,975 years.

4.3.2 Influence of depth on PGA_M

Cetin et al. (2004)

Figure 4.11 shows the PGA_M dependent upon the depth BGS for a site in Charleston, SC. If PGA_M was insensitive to depth, the curves shown would be flat. This plot shows from a depth of one meter to approximately four meters BGS there is a rather steep positive slope present. After four meters the PGA_M has a negative slope with increasing depth down to 16 meters. A site in Eureka, CA (see Figure 4.12) has similar behavior to the site in Charleston, SC for a return period of 475 and 2,475 years, however, there is considerable difference in behavior between the sites at a return period of 4,975 years. The difference stems from the significant variation of PGA_M with depth for Eureka, CA at this return period. Therefore, the PGA_M obtained by the CEA2004 procedure appears to be influenced by the seismicity of the site locations in addition to the depth BGS. Thus, the CEA2004 procedure requires a depth correction factor and a correction factor dependent on return period.

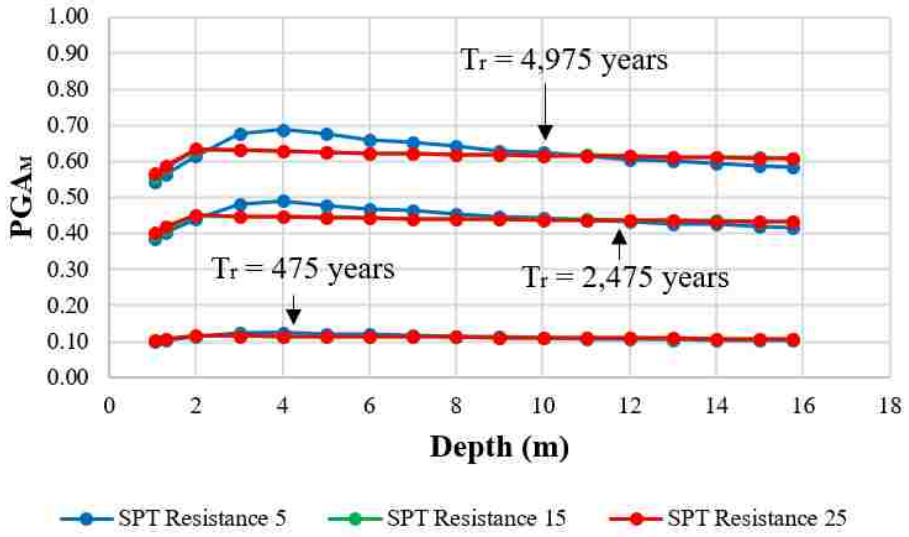

Figure 4.11. Charleston, SC – Magnitude corrected peak ground acceleration dependent upon depth for the CEA2004 procedure.

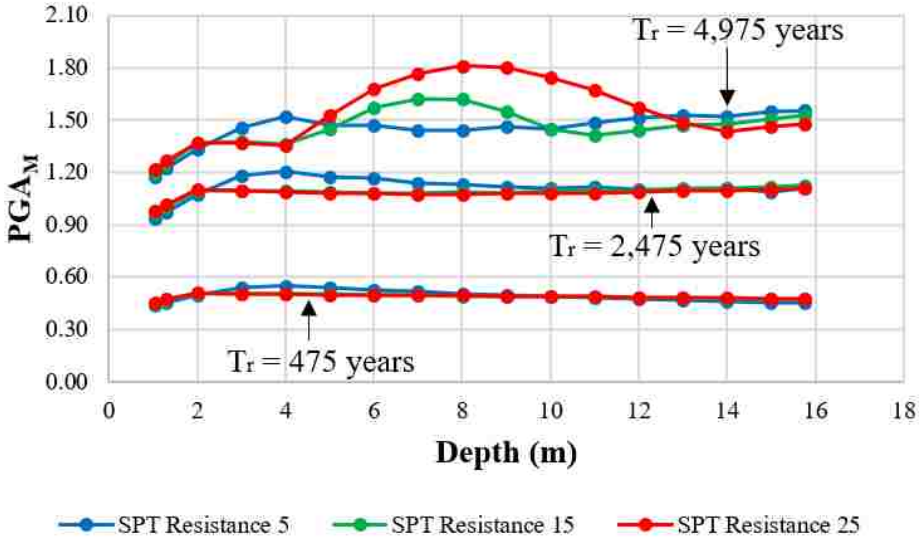

Figure 4.12. Eureka, CA – Magnitude corrected peak ground acceleration dependent upon depth for the CEA2004 procedure.

Boulanger and Idriss (2012)

Figures 4.13-4.14 (Charleston, SC and Eureka, CA, respectively) show that the curves are not flat and have a positive slope at deeper depths at longer return periods. The trend of a positive slope at deeper depths persisted for all 27 locations observed and appears to be steeper with

increasing seismicity. At shallow depths (ranging from 1-5 meters) the curves are flat for all return periods at both sites. Although behavior at longer return periods will need a correction factor, it appears to be sufficiently consistent that a relatively simple depth correction factor could be developed.

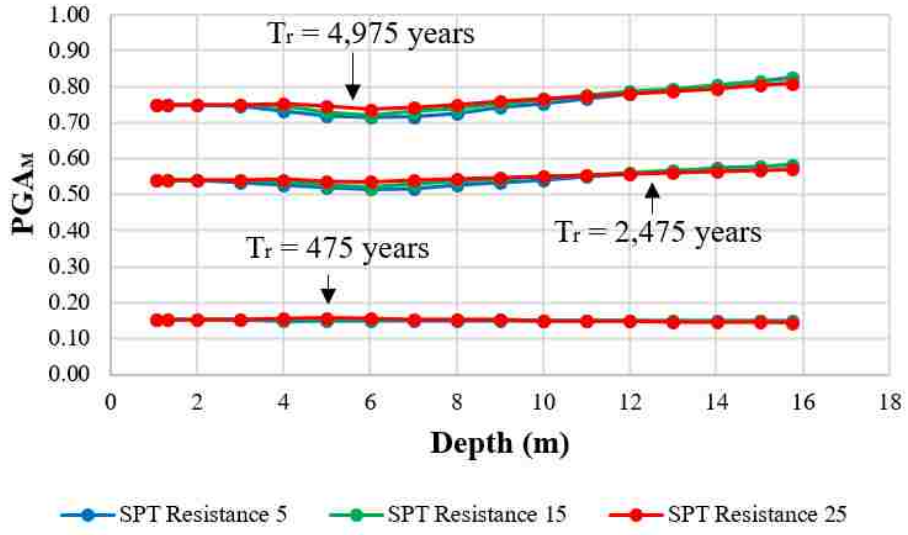

Figure 4.13. Charleston, SC – Magnitude corrected peak ground acceleration dependent upon depth for the IB2012 procedure.

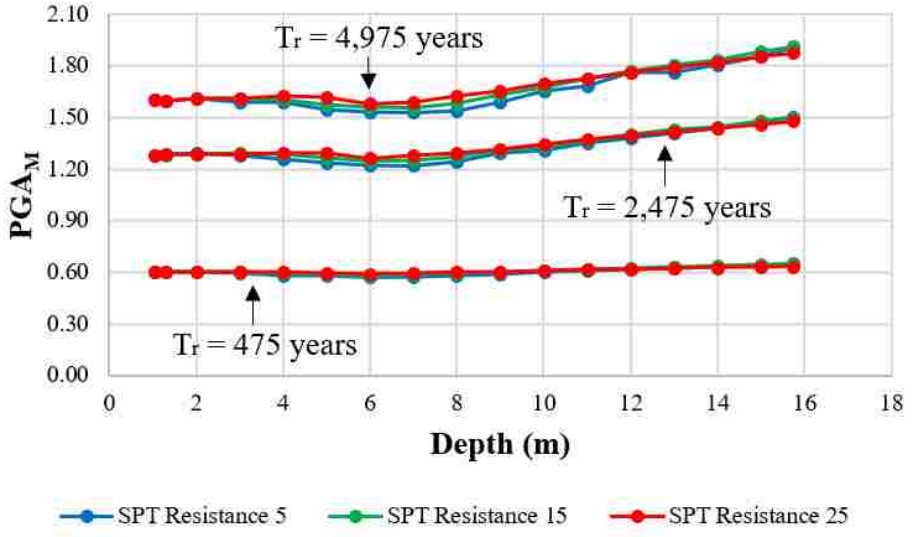

Figure 4.14. Eureka, CA – Magnitude corrected peak ground acceleration dependent upon depth for the IB2012 procedure.

4.3.3 Influence of water table depth on PGA_M

The water table was analyzed at six different depths ranging from 0-4.5 meters for a soil profile with an $(N_1)_{60}$ = 15 in order to see how the ratio of total stress to effective stress, which influences CSR, ultimately affects PGA_M values. In order to change the water table depth, each soil profile was updated to maintain the desired $(N_1)_{60}$ value in light of different total and effective vertical stress and shear wave velocity values.

Analyses were performed two sites, one of moderate seismicity (Charleston, SC), and another of high seismicity (Eureka, CA). Figures 4.15-4.18 illustrate the sensitivity of PGA_M to water table depth at both locations. Examination of these figures shows that water table depth has little impact on PGA_M for all return periods for the CEA2004 procedure for Charleston, SC and for shorter return periods (475, 1,039, and 2,475 years) for Eureka, CA. The CEA2004 procedure is strongly influenced by water table depth at return periods of 4975 and 9950 years. The IB2012 procedure shows little impact from changing the water table depth except at longer return periods where it appears to have a minor influence on PGA_M.

The CEA2004 and the IB2012 procedures appear to give PGA_M values that are negligibly influenced by water table depth except at longer return periods. Based on these results, the CEA2004 procedure may be better suited for higher return periods in moderate seismic environments like Charleston, SC, while the IB2012 procedure may be more suitable at high return periods in high seismicity environments like Eureka, CA where the CEA2004 procedure doesn't perform well.

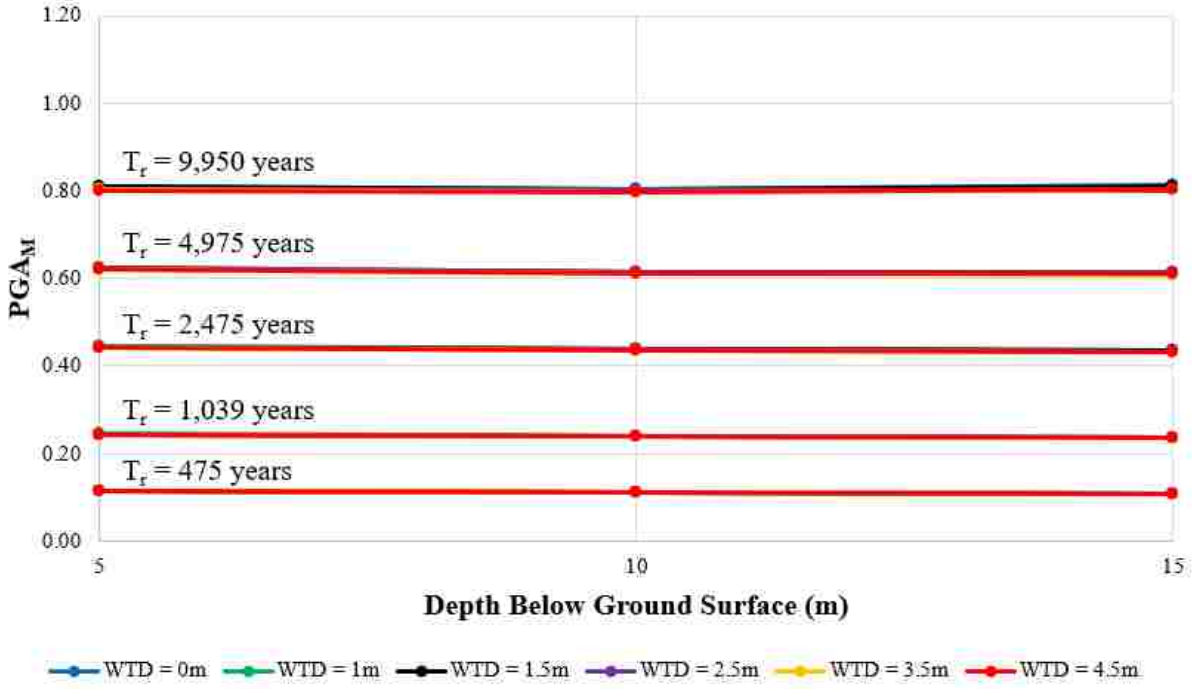

Figure 4.15. Charleston, SC – PGA_M dependent upon water table depth (WTD) in meters (m) for the CEA2004 procedure.

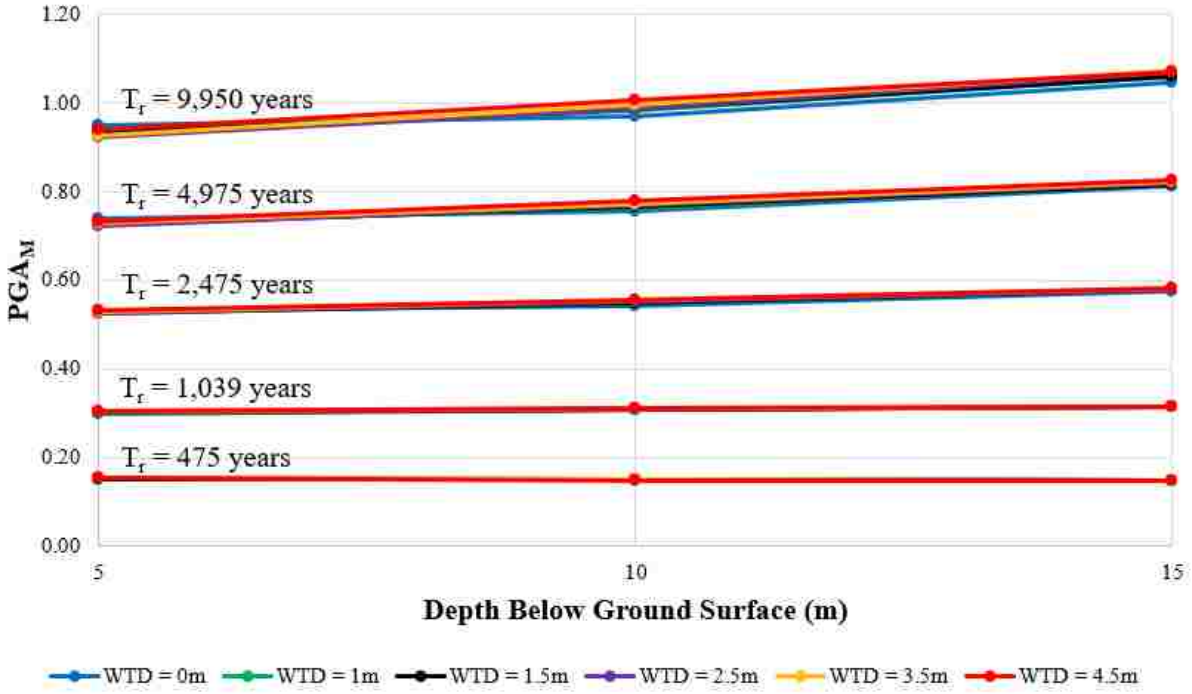

Figure 4.16. Charleston, SC – PGA_M dependent upon water table depth (WTD) in meters (m) for the IB2012 procedure.

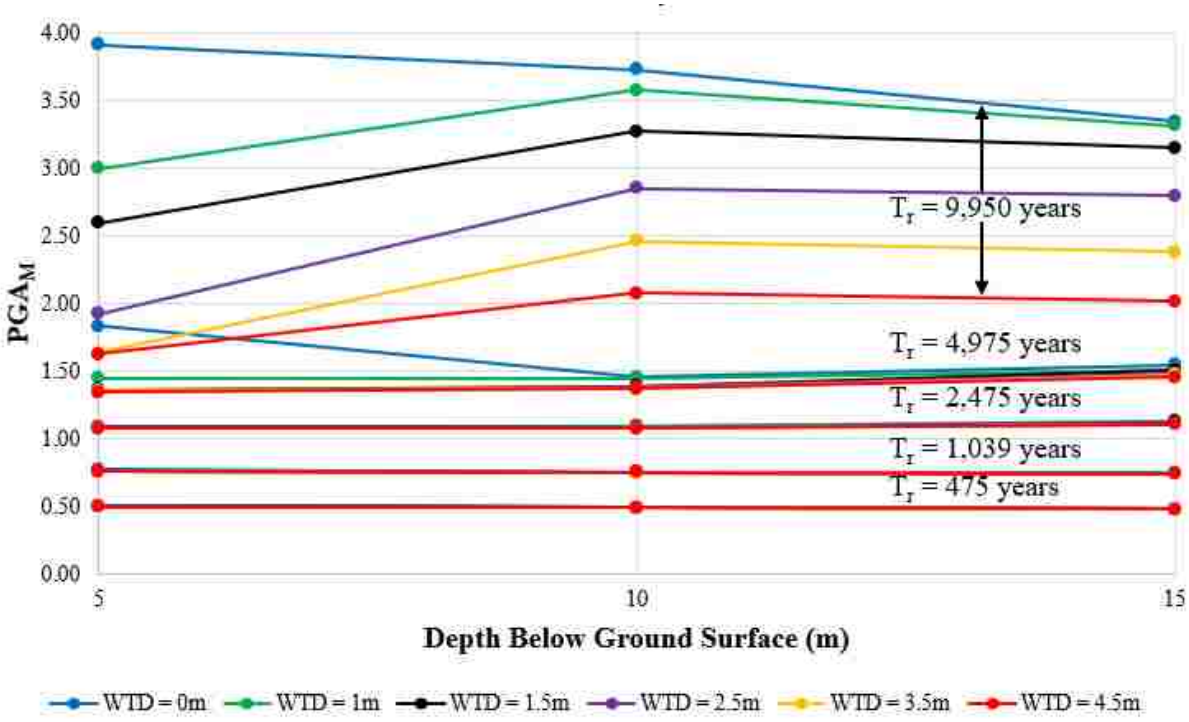

Figure 4.17. Eureka, CA – PGA_M dependent upon water table depth (WTD) in meters (m) for the CEA2004 procedure.

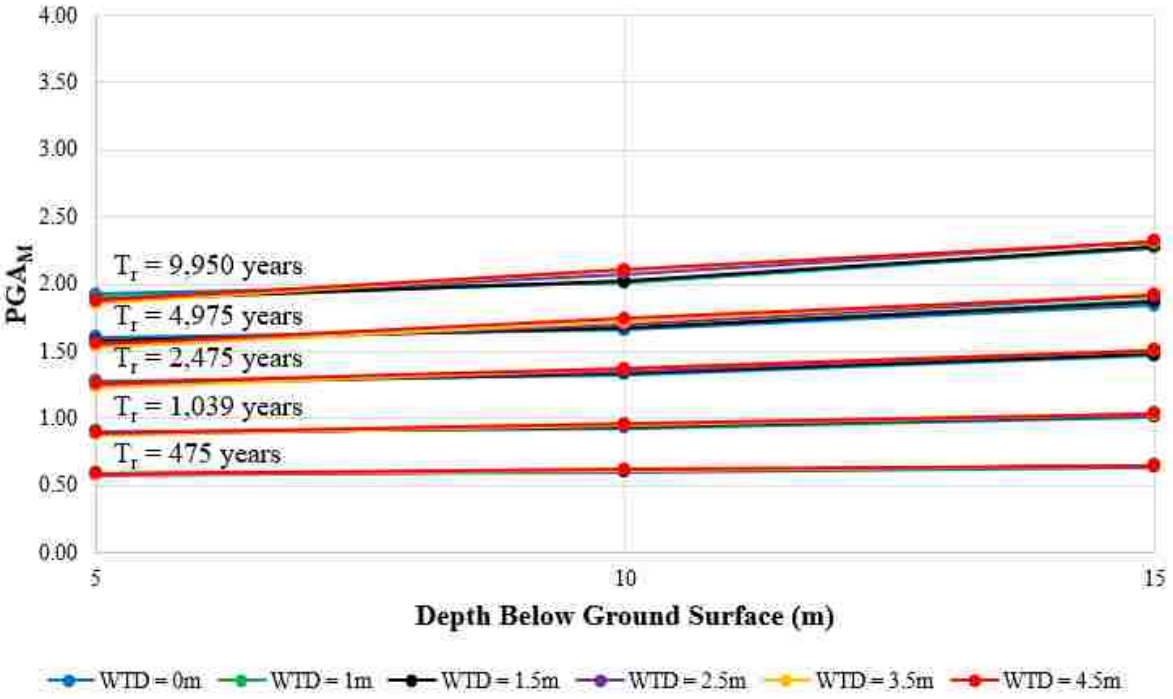

Figure 4.18. Eureka, CA – PGA_M dependent upon water table depth (WTD) in meters (m) for the IB2012 procedure.

4.3.4 Comparison of Liquefaction Triggering Procedures on PGA_M

The results of the CEA2004 liquefaction triggering procedure indicate that correction factors for both depth and $(N_1)_{60}$ would be needed to use the mapped PGA_M parameter at most return periods. Furthermore, the correction factor would depend on seismicity of the site. Locations of high seismicity show stronger variation of PGA_M with both depth and $(N_1)_{60}$ at all return periods investigated. Moderate seismicity sites such as Charleston, SC appear to have a rather constant PGA_M with varying depth and $(N_1)_{60}$ for a return period of 475 years, however, PGA_M is still sensitive to both depth and $(N_1)_{60}$ at longer return periods of 2475 and 4975 years.

The IB2012 procedure performed better overall than the CEA2004 procedure with negligible influence of $(N_1)_{60}$ on PGA_M with only a simple depth correction factor needed. These general trends of variation of depth and $(N_1)_{60}$ on the PGA_M values obtained using the CEA2004 and IB2012 procedures persisted throughout all site locations analyzed as can be viewed in Appendix A.

The CEA2004 and IB2012 procedures have showed negligible sensitivity to water table depth except at longer return periods in high seismicity environments. The IB2012 procedure had only minor variation of PGA_M with water table depth at a return period of 9,950 years, whereas, the CEA2004 procedure was strongly influenced by water table depth at return periods of 4,975 and 9,950 years in a high seismicity environment.

4.4 DIFFICULTIES WITH PB LiquefY

PB LiquefY is an excellent program for evaluating liquefaction potential via conventional and PLHA methods for areas of moderate to high seismicity, however, there are limitations that can be detrimental to the user. The two main limitations of PB LiquefY that will be discussed include:

(1) The inability of the program to evaluate liquefaction potential in areas of lower seismicity at return periods commonly desired by the practicing engineer.

(2) Errors occurring due to the program being created on a Microsoft Excel platform with Visual Basic macros.

Liquefaction Potential in Areas of Low Seismicity

PB LiquefY evaluates liquefaction potential at a return period other than the one specified for sites with lower seismic activity. For example, Figure 4.19 shows a Microsoft Excel warning that occurred when a 475-year return period was specified "RPuserspec" and was automatically replaced by the program to a different return period "RPused" for the IB2012 procedure at several depths, and for an $(N_1)_{60}$ = 5. Sublayer 4, which corresponds to a depth of 2 meters BGS, for instance, is evaluated for liquefaction potential at a return of 1,573 years instead of the 475-year return period specified. Two important ramifications of this are:

(a) Liquefaction potential is calculated at a return period other than specified,

(b) Only the first "10-20 exceptions" are shown which are for the IB2012 procedure so it is unknown if the CEA2004 procedure (which was performed at the same time) is having its return period changed, and if so, what return period it is being changed to.

Because this occurs for all sites of lower seismicity, this impacts major cities like New York City, NY, along with a vast majority of the Central and Eastern U.S.

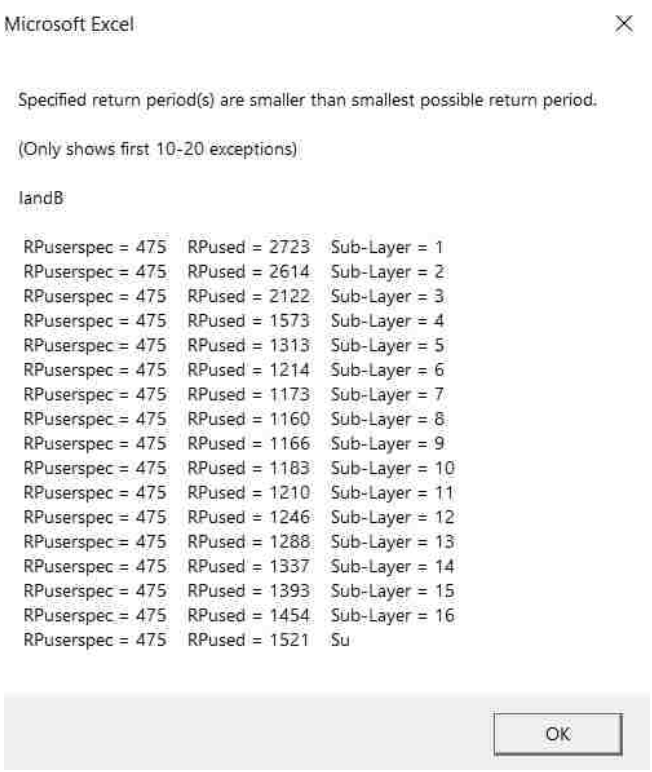

Figure 4.19. Microsoft Excel error that occurred for New York City, NY when specifying a return period of 475 years for a soil with an SPT resistance of five.

Microsoft Excel Platform with Visual Basic Macros

In general, the use of Visual Basic Macros in Microsoft Excel made the program slow when transitioning between tabs in the Microsoft Excel Worksheet, caused PB LiquefY to quit for no apparent reason at times, and led to several Microsoft Visual Basic "Run-time error." Although PB LiquefY has the capability of performing PLHA analyses at multiple site locations at once, these problems made it nearly impossible to do so for sites in different seismic areas, therefore, only a single site could be feasibly performed causing a significant amount of manual labor.

Several Microsoft Visual Basic run time errors, which cause the code to stop during the execution of a command, were encountered during the use of PB LiquefY. Two of the more common errors were "Run-time error 13" and "Run-time error 6." Run-time error 13 is termed a "mismatch" error and occurred when attempting to view the PLHA results for longer return periods for some sites. For example, run-time error 13 occurred for a site location in Reno, NV when

attempting to view PLHA results for a return period of 4,975 years or greater. Because of this, PLHA results for a return period of 4,975 years or greater were not possible for this site. Run-time error 6 is termed "Overflow" and occurs when the program tries to store too much data in temporary folders. Run-time error 6 occurred for multiple situations, one of the common situations was during the middle of a PLHA computation (which typically takes 5-20 minutes to complete), and another when trying to view PLHA results for return periods less than 475 years. In general, most site locations that did not have problems performing the PLHA calculation, were still unable to have PLHA results extracted for return periods less than 475 years.

In addition to the difficulties with low seismicity areas and Microsoft Visual Basic run-time errors, the way in which PB LiquefY analyzes the hazard curve causes unnecessary computation time. For PLHA analyses, PB LiquefY requires the input of "# of runs," or the number of increments of the hazard curve that are analyzed. These increments are equally spaced for the entire hazard curve, therefore, the increment size is the same for steeper and gently sloping portions of the curve. This causes unnecessary additional computation time during analyses because if a high "# of runs" is needed for the steep portion of a hazard curve, the same incremental spacing is used for the more gently sloping portion of the curve where it may be unneeded.

4.5 CONCLUSIONS

PLHA requires voluminous calculations leading many practicing engineers to continue to use less accurate and less consistent methods for evaluating liquefaction potential. The goal of a liquefaction-targeted intensity measure, PGA_M, is to enable the practicing engineer to input a mapped PGA_M value into their conventional liquefaction hazard analysis procedure and receive the liquefaction triggering results that would be obtained had they performed a full PLHA. This chapter has described the process of obtaining this conventional PGA_M value that corresponds to

an event with a return period of a full PLHA and has discussed how the PGA_M values obtained by two common liquefaction triggering procedures are influenced by various site conditions. It has been shown that both procedures would require a correction factor for depth, however, only the CEA2004 procedure appears to require a correction factor for $(N_1)_{60}$. The IB2012 procedure also appears to give consistent results between moderate and high seismicity sites with respect to the effects of variations in depth, $(N_1)_{60}$, and water table depth on PGA_M. Excluding long return periods in a high seismic environment, the CEA2004 procedure does, however, appear to be slightly less sensitive to the water table depth than the IB2012 procedure.

Chapter 5. **LATERAL SPREADING**

5.1 INTRODUCTION

Lateral spreading refers to the incremental displacements that can occur due to cyclic liquefaction within gentle slopes or flat ground near steeper slopes such as river banks. Lateral spreading often occurs near water bodies such as rivers, lakes, or oceans where the water table is high and soils have been deposited in a loose state as soil particles settle through water. Because fresh water is a necessity of life, and salt water often provides for transportation of goods, humans have always constructed dwelling and engaged in commerce near water bodies where lateral spreading hazards may occur. Lateral spreading is one of the most common, and most severe, effects of liquefaction. The lateral displacements resulting from lateral spreading is the most common cause of damage to bridges from liquefaction (Youd, 1993). Lateral spreading has also been known to cause failure of underground utilities that traverse areas where displacements occur, and can cause failure of deep foundations due to bending failure (see Figure 2.41).

One of the most iconic remnants of a lateral spread are tension cracks that are observed at the ground surface as the underlying soil deforms. Figure 5.1 shows a schematic of lateral spreading deformations that occur beneath a non-liquefiable crust. The non-liquefiable crust is split into several blocks after failing in tension as the liquefiable soil moves downslope. Where tension cracks form, ejecta from sand boils may be spewed to the surface causing settlement to accompany the lateral deformation. Figure 5.2 shows the damage to a quay wall from liquefaction-induced lateral spreading during the 1995 Kobe, Japan earthquake having similar characteristics to the schematic shown in Figure 5.1.

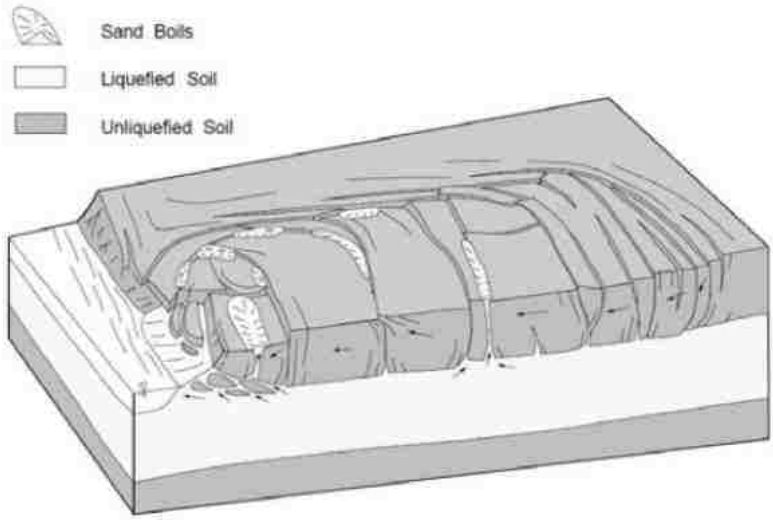

Figure 5.1. Schematic of lateral spreading displacements adjacent to a water body (Rauch, 1997).

Figure 5.2. Liquefaction-induced lateral spreading from the 1995 Kobe, Japan earthquake causing severe damage to a quay wall (UW).

This chapter will briefly review current common lateral spreading case history databases and a future next generation liquefaction (NGL) case history database. An overview of the most

common procedures used to predict lateral spreading displacement used today will be presented and their crude interpretation of the static stress state highlighted. The bulk of this chapter will focus on characterizing the static stress state of lateral spread slope geometries through the use of numerical tools. A function that predicts the static stress ratio within a wide range of lateral spreading slope geometries will be introduced and future research for the development of a uniform model to predict lateral spreading displacement discussed.

5.2 CASE HISTORIES

Lateral spreading case histories are locations where lateral spreading has been documented following an earthquake event. Documentation includes collection of data about the displacement due to lateral spreading, the site characteristics where the displacements occurred (e.g., the slope of the ground or the density of the soil), and the ground motion characteristics that caused the displacements. Case history data has been used to develop empirical and semi-empirical models, and to validate numerical models for prediction of future lateral spreading displacments. The prediction of lateral spreading from case history data is influenced by many things, a few of these are: (a) the quality of case histories, (b) the size of the case history database and its applicability to a range of different lateral spreading conditions, and (c) interpretation/estimation of soil properties either made by the original author, or interpretation of that authors work by another. Two of the most common lateral spreading case history databases are Youd et al. (2002) and Olson and Johnson (2008) databases, which will be discussed briefly.

5.2.1 **Youd et al. (2002) Lateral Spreading Database**

The Youd et al. (2002) database consists of 484 observed lateral spreading displacements from ten earthquake events ranging from the 1906 San Francisco, California earthquake to the 1995 Kobe, Japan earthquake. The Youd et al. (2002) database is an extension of the initial lateral

spreading database of Bartlett and Youd (1992). Youd et al. (2002) made three modifications to the initial database: (1) a correction was made to displacements calculated from the 1983 Nihonkai-Chubu, Japan earthquake, (2) eight displacement vectors were removed where boundary effects impeded displacement, and (3) additional case histories from the 1983 Borah Peak, Idaho, 1989 Loma Prieta, California, and 1995 Kobe, Japan earthquakes were added. Because of the size of the Youd et al. (2002) database, and the range of lateral spreading conditions it encompasses, it is currently the most commonly used lateral spreading case history database, however, it does not cover the entire range of conditions that may occur in the field.

5.2.2 **Olson and Johnson (2008)**

The Olson and Johnson (2008) lateral spreading database consists of 39 lateral spread case histories from a total of 12 earthquakes. The earliest of these was the 1971 San Fernando, California earthquake and the latest the 2003 San Simeon, California earthquake. Olson and Johnson (2008) did not include the 1906 San Francisco, CA, 1964 Alaska, 1964 Niigata, Japan, 1983 Nihonkai-Chubu, Japan, or 1995 Kobe, Japan earthquakes, which were included in the Youd et al. (2002) database. They did, however, include lateral spreads from the 1987 Edgecumbe, New Zealand, 1990 Luzon, Phillippines, 1990 Manjil, Iran, 1994 Northridge, California, 1999 Chi-Chi, Taiwan, 1999 Kocaeli, Turkey, and 2003 San Simeon, California earthquakes. Because of the exclusion of higher moment magnitude case histories (1964 Alaska and 1906 San Francisco, California earthquakes) their database had a relatively small range of moment magnitudes of 6.5 to 7.6 which consisted of peak ground accelerations of 0.16 to 0.84g and caused displacements of about 15 centimeters to 6 meters. For an in-depth, qualitative assessment of the Olson and Johnson (2008) database the reader is referred to Makdisi (2016).

5.2.3 Future NGL Database

Based on the recommendation of the National Research Council liquefaction committee, the development of an open-source liquefaction case history database is currently underway. The Next Generation Liquefaction (NGL) open-source database is a relational database that allows users to query and use advanced tools to relate information more easily than current databases, which are typically in the form of spreadsheets. The NGL database has the benefit of having case history data from different events in a consistent format that can be accessed by anyone. The NGL database includes lateral spread data from the numerous earthquakes (e.g., the Canterbury Earthquake Sequence from 2010-2016) that have occurred over the last 16 years and are not included in the Youd et al. (2002) or Olson and Johnson (2008) databases. The NGL database will be updated as data from future earthquakes becomes available.

5.3 LATERAL SPREADING PROCEDURES TODAY

Due to the severe effects of lateral spreading, several procedures to predict lateral spreading displacements have been developed. These procedures have based on (a) lateral spreading case histories (empirical), (b) case histories and laboratory data characterizing cyclic strain amplitude (semi-empirical), and (c) numerical methods. Because of their ease of use, empirical and semi-empirical procedures are the most commonly used approaches in practice today.

5.3.1 Empirical Procedures

Empirical procedures for lateral spreading are based upon collections of case histories of past lateral spreading events. The better the documentation of the case history and the better quality the data, better will be the empirical model developed from it. Bartlett and Youd (1992) collected an expansive database for lateral spreads that occurred in the western United States and Japan, and developed multilinear regression equations to estimate lateral spread displacements. Bartlett and

Youd (1992) found that two general types of failures occurred while developing their model and thus allowed for two geometry conditions – a free-face case and a ground-slope case. The geometries of the two cases are shown in Figure 5.3. It should be noted that, despite the implications of Figure 5.3, users of the Bartlett and Youd (1992) method were forced to determine whether the site should be modeled as a free-face or ground slope site. This leads to difficulties for sites where both H and S are greater than zero.

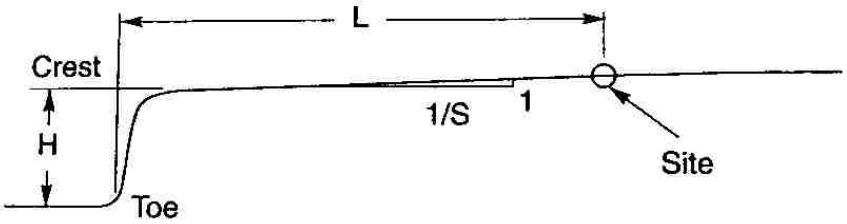

L = Distance from toe of free face to site
H = Height of free face (crest elev. - toe elev.)
W = Free-face ratio = (H/L) (100), in percent
S = Slope of natural ground toward channel in percent

Figure 5.3. Definitions of the free-face, W, and ground slope, S for Equation 5.1 (Kramer, 2008).

Youd et al. (2002) updated and made several corrections to the Bartlett and Youd (1992) case history database and developed new multilinear regression equations for the free-face and ground-slope cases. The cases can be combined into a single equation of the form

$$\log D_H = b_0 + b_1 M_w + b_2 log \log R^* + b_3 R + b_4 \log W + b_5 \log S + b_6 \log T_{15} + b_7 \log(100 - F_{15}) + b_8 \log(D50_{15} + 0.1\,mm) \quad (5.1)$$

where D_H is the estimated lateral spread displacement in meters, M_w is the moment magnitude, and R is the nearest horizontal distance to the energy source. The free-face ratio, W, is given as the ratio of the height of the site above the free face to the horizontal distance from the base of the free face in percent, and S is the inclination of the ground slope in percent (see Figure 5.3). The cumulative thickness of liquefiable soil, T_{15}, in meters, is soil that is saturated and has corrected

SPT resistance, $(N_1)_{60}$, less than or equal to 15 blows, F_{15} is the average fines content for the soil included in T_{15} in percent, and $D50_{15}$ is the mean grain size for the soil included in T_{15} in millimeters. The b values are regression coefficients shown in Table 5.1 and R^* is a modified source distance value given by

$$R^* = R + R_o \tag{5.2}$$

where R_o is a factor for distance that is dependent on moment magnitude given by

$$R_o = 10^{(0.89M_w - 5.64)} \tag{5.3}$$

Youd et al. (2002) developed Equation 5.1 from a large number of case histories, however, the case history data did not cover the entire range of conditions that may occur in the field. Hence, the predictive relationships based on that data only apply to restricted conditions. Therefore, Youd et al. recommended that Equation 5.1 be used only within the variable ranges shown in Table 5.2.

Table 5.1. Youd et al. (2002) regression coefficients for Equation 5.1.

Geometry	b_0	b_1	b_2	b_3	b_4	b_5	b_6	b_7	b_8
Ground-slope	-16.213	1.532	-1.406	-0.012	0	0.338	0.540	3.413	-0.795
Free-face	-16.713	1.532	-1.406	-0.012	0.592	0	0.540	3.413	-0.795

Table 5.2. Youd et al. (2002) variables, variable description, and recommended variable range for Equation 5.1.

Variable	Description of Variable	Range Recommended for Variable
M_w	Moment magnitude	$6 < M_w < 8$
R^*	Modified source to site distance value (in kilometers)	--
R	Nearest horizontal distance to the energy source from the site (in kilometers)	--
W	Free face ratio (in percent)	$1 < W < 20$ (in percent)
S	Ground slope (in percent)	$0.1 < S < 6$ (in percent)
T_{15}	Cumulative thickness of liquefiable soil where corrected SPT resistance is ≤ 15 (in meters)	$1 < T_{15} < 15$ (in meters)
F_{15}	Average fines content for the soil included in T_{15} (in percent)	See Figure 5.4
$D50_{15}$	Mean grain size for the soil included in T_{15} (in millimeters)	See Figure 5.4

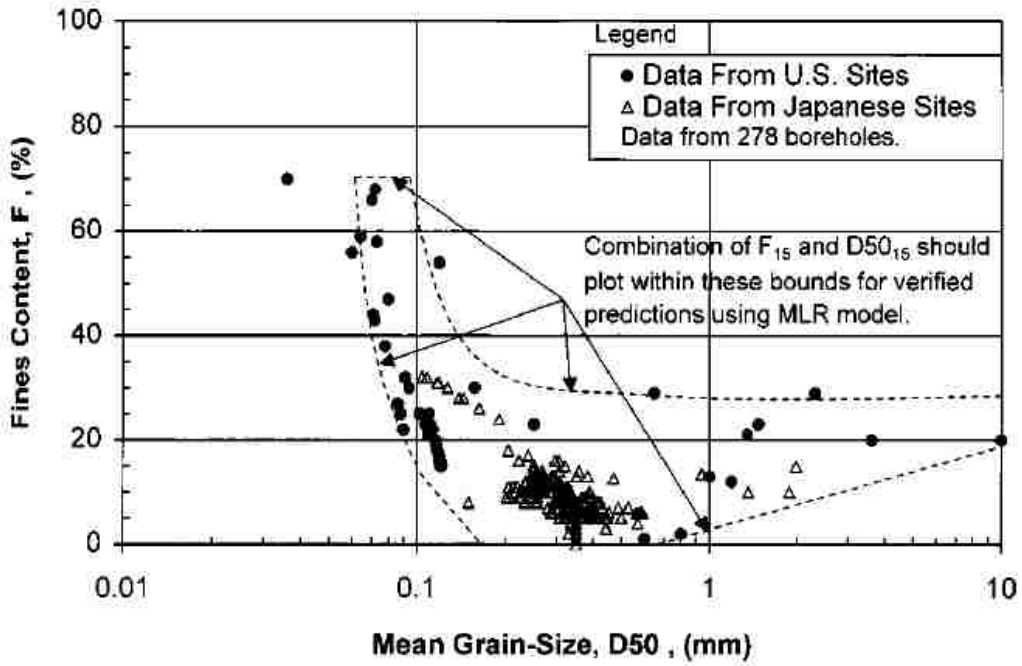

Figure 5.4. Plot of fines content and mean grain-size where the values of F_{15} and $D50_{15}$ for a soil must plot within the specified bounds to make Equation 5.1 eligible to be used (Youd et al., 2002).

The Youd et al. (2002) procedure requires determination of whether the site conditions are ground-slope or free-face conditions in order to calculate the lateral spread displacement. For ground-slope conditions the regression coefficient, b_4, is zero cancelling out the free-face ratio term, W, in Equation 5.1, and for free-face ratio conditions the regression coefficient, b_5, is zero taking care of the ground-slope term, S (see Table 5.1). For sites with a distant free face, Youd et al. (2002) recommended that ground-slope conditions be used when the free-face ratio is less than 1% and that free-face conditions be used when the free-face ratio is greater than 5%. For sites that have a free-face ratio $1\% \leq W \leq 5\%$ both the ground slope and free-face conditions can be used, however, Youd et al. (2002) recommend selecting the condition that provides the larger predicted displacement and using that for design. Youd et al. (2002) did not recommend summing the displacements from both ground-slope and free-face conditions for the latter case because the results would be overly conservative. Youd et al. (2002) indicate that 90% of the displacement

predicted by their model fall within a factor of two of the observed displacement when staying within the recommended variable ranges shown in Table 5.2. Franke and Kramer (2014) found the actual total model uncertainty of Youd et al. (2002) to have a logarithmic standard deviation of $\sigma_{\log D_H}$ = 0.197, which corresponds to $\sigma_{\ln D_H}$ = 0.464.

The Youd et al. (2002) procedure has been one of the most common procedures used to evaluate lateral displacements in practice. Their procedure makes the inherent assumption that any soil with an $(N_1)_{60}$ value of less than 15 blows is capable of contributing to lateral spreads, whereas, an $(N_1)_{60}$ value greater than 15 is not capable of lateral spreads. This can create a problem for soils that are subjected to strong shaking (i.e., high amplitudes and long duration motion). For example, a soil that has an $(N_1)_{60}$ of 16 and is subjected to strong shaking (e.g., $M_w = 7.9$ and $R = 10$ kilometers), will not undergo lateral spread displacement according to the Youd et al. (2002) model. This model also does not differentiate in lateral spread displacement for $(N_1)_{60}$ values that are less than or equal to 15. Therefore, an $(N_1)_{60}$ value of 5 will give the same lateral spread displacement value as an $(N_1)_{60}$ value of 14 when considering the same magnitude earthquake, source-to-site distance, slope geometry, soil profile thickness, fines content, and mean grain size. The latter assumptions are inconsistent with laboratory data and the mechanical properties of soil.

Gillins and Bartlett (2014) modified the Youd et al. (2002) empirical expression for lateral spread displacements by removing the fines content and mean grain size variables and replacing them with a descriptive soil index, *SI*, variable (Table 5.3). This approach was taken because several of the case histories lacked fines content and mean grain size values, but did have useful soil descriptions. The modified expression for calculating the lateral spread displacements by Gillins and Bartlett (2014) can be expressed as

$$\text{Log}\, D_H = b_0 + b_1 M_w + b_2 log \log R^* + b_3 R + b_4 \log W + b_5 \log S + b_6 \log T_{15} + a_1 x_1 + a_2 x_2 + a_3 x_3 + a_4 x_4 + a_5 x_5 \quad (5.4)$$

where x_i is the ratio of the soil description type thickness in T_{15} to the cumulative thickness of T_{15}, and b_0-b_6 are regression coefficients shown in Table 5.4. The a values are coefficients that either reduce or increase the lateral spread displacement value based on their susceptibility to liquefaction (e.g., *SI* 3 which consists mainly of sand adds to the value of $\log D_H$, whereas, *SI* 1 which consists of mainly silty gravel with sand reduces the value of $\log D_H$) and are shown in Table 5.5. The remaining variables are as described previously for the Youd et al. (2002) model.

Table 5.3.* SI *group soil descriptions from the Youd et al. (2002) database.

SI	Typical Soil Description	General USCS Symbol
1	Silty gravel with sand, silty gravel, fine gravel	GM
2	Very coarse sand, sand and gravel, gravelly sand, Coarse sand, sand with some gravel	GM-SP, SP
3	Sand, medium to fine sand, sand with some silt	SP-SM
4	Fine sand, sand with silt, Very fine sand, silty sand, dirty sand, silty/clayey sand	SM, SM-ML
5	Sandy silt, silt with sand	ML

Table 5.4. Gillins and Bartlett (2014) regression coefficients for Equation 5.4.

Geometry	b_0	b_1	b_2	b_3	b_4	b_5	b_6
Ground-slope	-8.208	1.318	-1.073	-0.016	0	0.337	0.592
Free-face	-8.208	1.318	-1.073	-0.016	0.445	0	0.592

Table 5.5. Gillins and Bartlett (2014) soil coefficients for Equation 5.4.

Soil Coefficients	a_1	a_2	a_3	a_4	a_5
Values	-0.683	-0.2	0.252	-0.04	-0.535

The Youd et al. (2002) model, and the modification by Gillins and Bartlett (2014), are limited to certain slope conditions, but many slopes in nature do not neatly fit within the requirements of their procedure. According to the National Center for Biotechnology Information (NCBI), 90% of the world's population lives within 10 kilometers of a surface freshwater body and over half the world's population lives within 3 kilometers (NCBI, 2011). The latter is surface water and does not include oceans in which approximately 2.4 billion people live within 100

kilometers (The Ocean Conference, 2017). Liquefaction-induced lateral spreading can occur from soil saturated with fresh water or salt water, therefore, improvement upon the factor of 2 between the predicted and observed lateral displacements would have tremendous impacts on society. As one can imagine, the geometry of slopes composed of soil rarely match that shown in Figure 5.3 and likely more closely align with something similar to Figure 5.5 where the ground slopes, S_1 and S_2, are different whether caused by nature, or by anthropogenic interaction with the land.

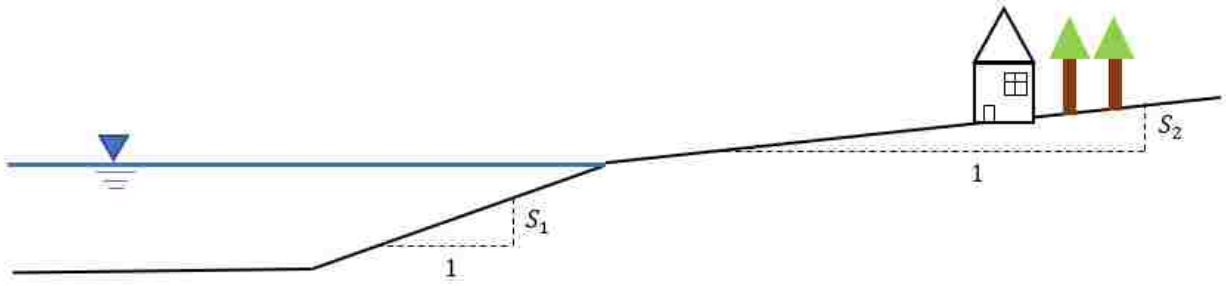

Figure 5.5. Example slope geometry in nature where ground slopes, S_1 and S_2, are different.

Using the Youd et al. (2002) lateral spreading model for a slope geometry such as that depicted in Figure 5.5 can lead to many problems. For a ground slope interpretation, what is the slope variable, S? For a free-face interpretation, what is the slope height, H? Different engineers will likely answer those questions differently, leading to uncertainty and inconsistency in predicted displacements.

5.3.2 Semi-Empirical Procedures

Empirical procedures benefit from the fact that they are based on actual observed data, however, there is often insufficient case history data to develop empirical procedures that are applicable to a sufficiently broad range of situations. For this reason, semi-empirical procedures were developed to estimate lateral spread displacements that can extend the range of lateral spreading displacement predictions. Semi-empirical procedures use both observations (case histories of lateral spreading) and laboratory test data to estimate the maximum cyclic shear strains

of liquefiable soils. The commonly used Zhang et al. (2004) semi-empirical procedure will be discussed.

The Zhang et al. (2004) procedure used a modified version of the maximum cyclic shear strain, γ_{max}, and factor of safety against liquefaction relationship for different relative densities developed by Ishihara and Yoshimine (1992) for a clean sand. Under the assumption that soils at any density should reach a limiting shear strain, the Seed (1979) approach was taken to modify the Ishihara and Yoshimine (1992) relationship by limiting the maximum shear strain as shown in Figure 5.6.

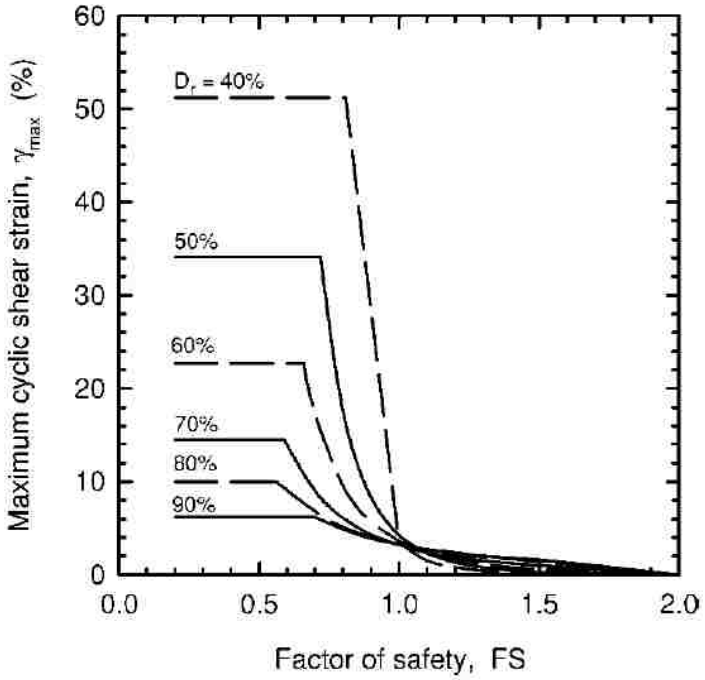

Figure 5.6. Modified maximum cyclic shear strain versus factor of safety relationship (Zhang et al., 2004).

Figure 5.6 shows that both the factor of safety against liquefaction and relative density are required to calculate γ_{max}. Zhang et al. (2004) at the time recommended evaluation of the factor of safety against liquefaction using the Youd et al. (2001) procedure for SPT or CPT liquefaction resistance methods. To estimate relative density, Zhang et al. (2004) used a modified version of

the Meyerhof (1957) empirical relationship for SPT resistance and the empirical relationship of Tatsuoka et al. (1990) for CPT resistance as shown in Equations 5.5 and 5.6 respectively.

$$D_r = 14\sqrt{(N_1)_{60,cs}} \qquad where\ (N_1)_{60,cs} \leq 42 \tag{5.5}$$

$$D_r = -85 + 76\log\left(q_{c1N,cs}\right) \quad where\ q_{c1N,cs} \leq 200 \tag{5.6}$$

Zhang et al. (2004) used the value of γ_{max} from Figure 5.6. to calculate a lateral displacement index (LDI) by integrating γ_{max} over the depth of the liquefiable zone of soil,

$$LDI = \int_0^{Z_{max}} \gamma_{max} dz \tag{5.7}$$

where Z_{max} is defined as the maximum depth below all of the potentially liquefiable layers with a factor of safety against liquefaction less than 2.0.

LDI does not directly characterize the geometric characteristics of a site. Site geometry is an important factor in lateral spreading since sloping ground induces static shear stresses in the soil. Because of this, Zhang et al. (2004) calibrated their model against empirical case history data using the ground slope and free-face geometric parameters of Youd et al. (2002) described previously in Figure 5.3. This resulted in the following equations that could be used to estimate lateral spread displacements,

$$D_H = (S + 0.2)LDI \quad for\ 0.2\% < S < 3.5\% \tag{5.8}$$

$$D_H = (6W^{-0.8})LDI \qquad for\ 4 < W < 40 \tag{5.9}$$

Zhang et al. (2004) recommended their procedure be restricted to cases of moment magnitudes between 6.4 and 9.2, peak ground surface accelerations from 0.19 g to 0.6g, free face heights less than 18 meters, and $q_{c1N,cs} \geq 50$. According to Zhang et al. (2004), the calculated lateral displacements of their approach gave values between 50 and 200% of the measured values from the case histories their model is based on. Zhang et al. (2004) stated that LDI should be interpreted

as an index of potential lateral displacements (e.g., high, low, or medium displacement) for a given resistance and loading.

Although semi-empirical approaches like Zhang et al. (2004) incorporate laboratory testing to make up for the lack of case histories, they still have large differences between calculated and measured error. The Zhang et al. (2004) procedure also doesn't characterize the initial static stress state any better than the Youd et al. (2002) procedure. Therefore, applying the Zhang et al. (2004) procedure to slopes with varying ground slopes (such as Figure 5.5) leads to the same challenging questions as the Youd et al. (2002) model – how do the ground slopes interact with each other? A more thorough characterization of the initial static stress state would provide key insight into how to handle geometries such as Figure 5.5.

5.3.3 **Numerical Analysis**

Numerical analyses provide an alternative to empirical and semi-empirical procedures for modeling lateral spreading. Numerical analysis of lateral spreading solves partial differential equations (e.g., the wave equation and diffusion equation) in order to model the mechanical and hydraulic response of the model. In order to model soil behavior, the numerical model needs to have constitutive models that are able to relate stresses to strains and also model the increase in pore pressure due to cyclic loading before and up to the point of liquefaction initiation. These constitutive models need to be calibrated via laboratory testing at the element level to ensure they are working properly. Numerical models also need to be validated against physical models (such as centrifuge tests) and/or lateral spreading case histories to prove they can provide reasonable predictions of lateral displacements.

While such models have increasingly become available, they tend to be time-consuming to use both from input parameter development and computational standpoints. Their responses can

also be sensitive to details of soil profiles that are difficult to characterize accurately. As a result, they have not been well validated against case history data, and have not seen widespread adoption in engineering practice.

5.4 CHARACTERIZATION OF STATIC STRESS STATE – A UNIFIED APPROACH

It has been postulated (S. Kramer, personal communication, 2018) that up to three mechanisms drive lateral spreading:

1) Softening of the liquefied material that causes shearing distortion of the soil under the static shear stresses that act upon it;
2) Cumulative cyclic deformations during earthquake shaking that are driven by cyclic shear stresses superimposed on the existing static shear stresses;
3) Post-shaking deformations associated with void redistribution phenomena and driven by static shear stresses.

Each of these potential deformation mechanisms is influenced by static shear stresses yet both empirical and semi-empirical procedures for prediction of lateral spreading displacements currently characterize static shear stresses in a crude and incomplete manner. The work described in the remainder of this chapter was directed toward developing an improved procedure for characterizing the initial static shear stresses over a continuous range of site conditions commonly encountered at lateral spreading sites.

Given the importance of the static shear stresses to the lateral spreading problem and the simple, binary procedures by which they are represented in current empirical and semi-empirical procedures for prediction of lateral spreading displacement, an effort was made to identify a function that could describe the static stress distribution in a continuous, but reasonably simple

manner. This approach was considered to involve two parts: (1) description of the driving stresses (shear and normal) in a general slope with, a geometry representative of those involved in lateral spreading failures, and (2) a procedure for using these stresses to characterize the resulting forces acting on the soil bounded by the ground surface and a failure surface.

The first of these parts, i.e. development of a unified stress function, is the subject of the remainder of this chapter. The description of the process of developing that function is organized about the following steps taken to accomplish it:

1) Definition of a generic slope geometry for slopes susceptible to lateral spreading (Section 5.4.1);
2) Definition of a transformed slope geometry system that would facilitate comparison of different slope geometries and lead to a simpler stress function (Section 5.4.2);
3) Establishment of a range of slope geometries representative of those involved in lateral spreading case histories (Section 5.4.3);
4) Development of a numerical model for computation of stresses (Section 5.4.4);
5) Analysis of the results of the numerical analyses (Section 5.4.5);
6) Development of a procedure to map computed stresses from the numerical model to a regular, standard grid in the transformed geometry space (Section 5.4.6); and
7) Development of stress functions by optimization analysis (Section 5.4.7).

5.4.1 **Generic Slope Geometry**

The two binary geometries used in common empirical and semi-empirical procedures for estimation of lateral spreading analyses were described in Section 5.3.1. In reality, however, slopes can be more complicated than either of those geometries. Figure 5.7 illustrates possible slope

geometries that could range from a ground slope geometry (Figure 5.7a) to a free-face geometry (Figure 5.7e), but could include intermediate geometries with different, non-zero slope angles.

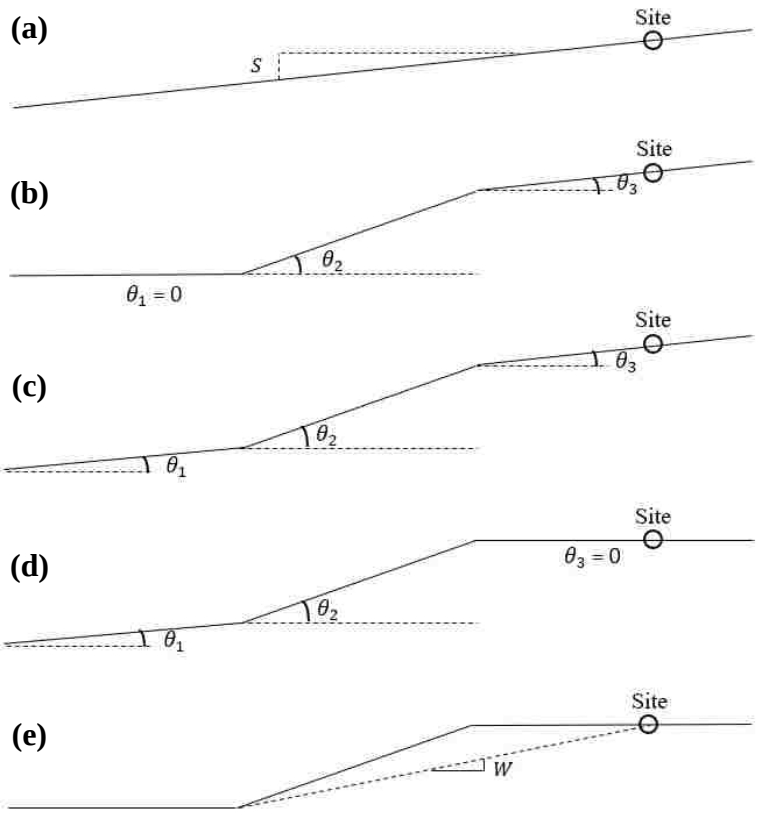

Figure 5.7. Slope geometries ranging from (a) ground slope to (e) free-face cases.

A more general geometry that would more accurately represent the range of slope geometries encountered at liquefiable sites, could consist of three linear segments with variable inclinations (Figure 5.8). By specifying the three slope angles and the height of the intermediate segment, a general geometry can be defined by four parameters – θ_1, θ_2, θ_3, and H. For slopes with different heights and/or central slope angles, the length shown in Figure 5.8 can change.

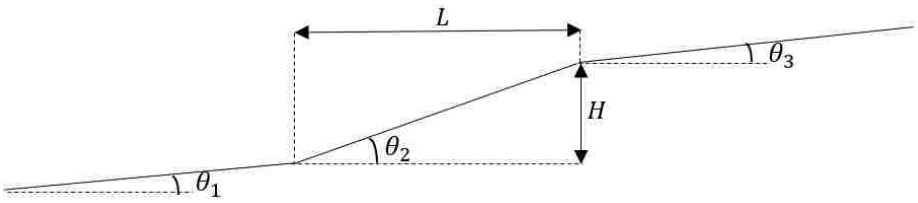

Figure 5.8. Generic slope geometry model depicting parameters that vary for each profile.

5.4.2 Transformed Coordinate System

To develop a unified approach to characterizing the static stress state for different forms of the three-segment slope geometry, transformation to a dimensionless coordinate system was required so different geometries could be related to each other. PLAXIS takes compressive stresses and forces as negative, while tensile stresses and forces as positive, as shown in Figure 5.9. The coordinate transformation chosen for this research took x to be positive to the right and y to be positive downwards. The PLAXIS x and y coordinates were then transformed into a dimensionless coordinate system composed of delta (δ) and eta (η) coordinates by normalizing both x and y by the slope height, H. Therefore, points at the same depth below the ground surface would have the same value of η, as illustrated in Figure 5.10. The ground surface position is designated by y_o, and is different for the three slope segments, as shown in Figure 5.11. As a result, the expressions for δ and η must be developed individually for the materials directly beneath each slope segment. These expressions are presented in Figures 5.11-5.14.

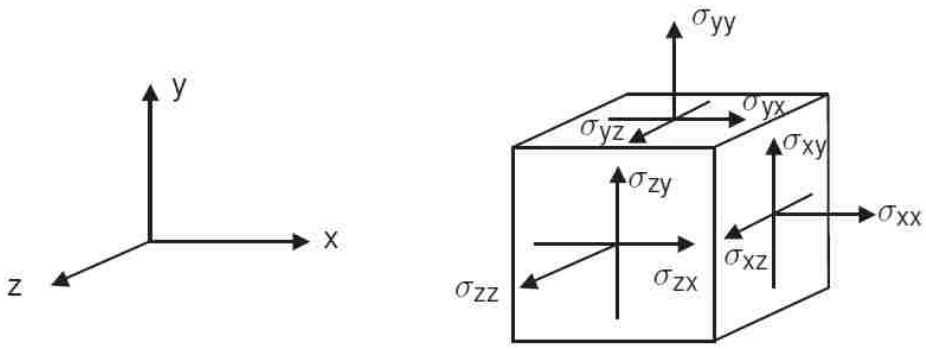

Figure 5.9. PLAXIS sign convention.

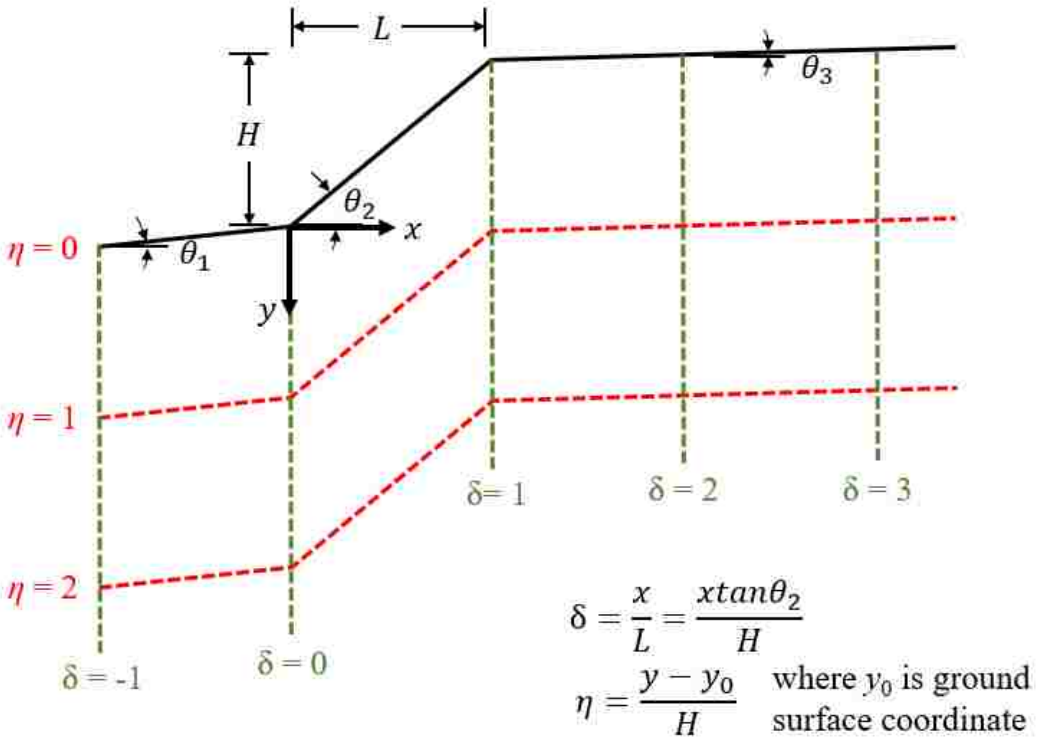

Figure 5.10. Illustration depicting the grid of the dimensionless coordinate system of $\delta = x/L$ versus $\eta = (y - y_0)/H$.

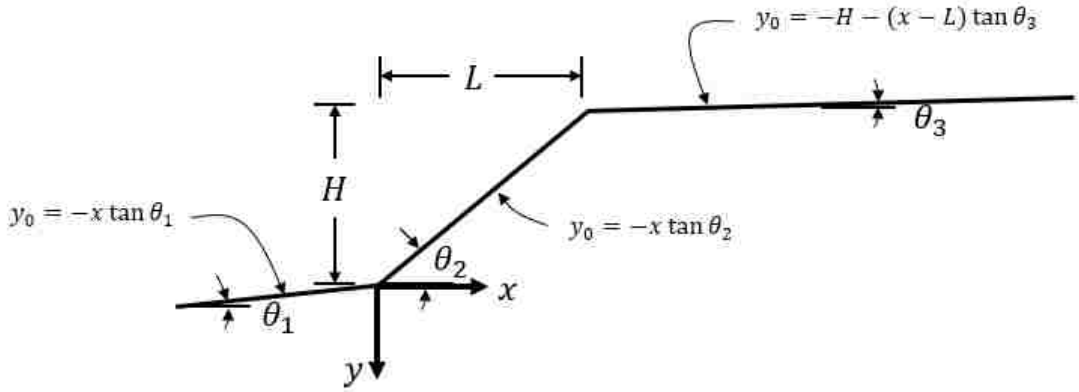

Figure 5.11. Calculation of vertical ground surface coordinate, y_0, relative to the toe of the slope.

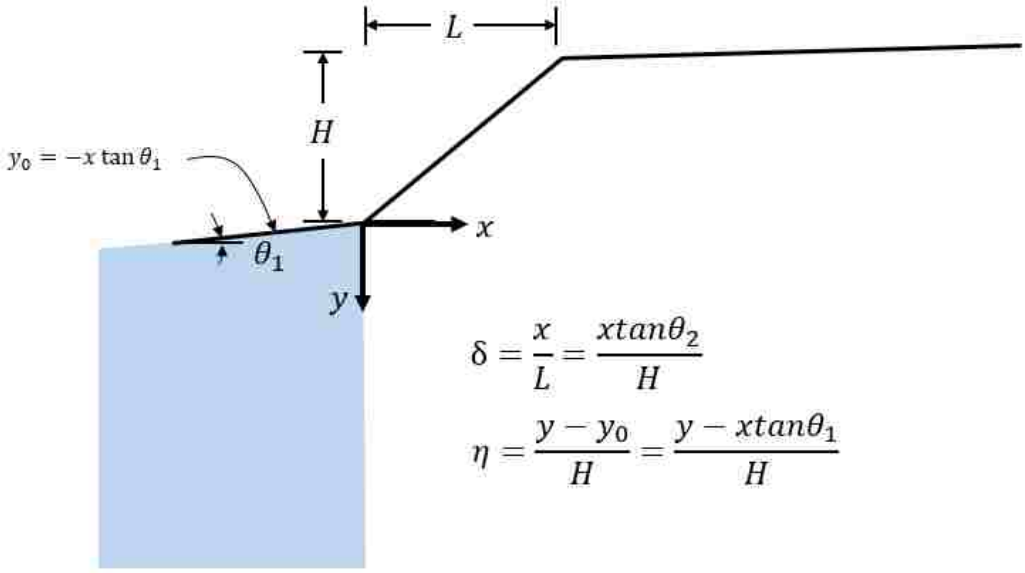

Figure 5.12. Calculation of δ and η for x < 0 (shaded region).

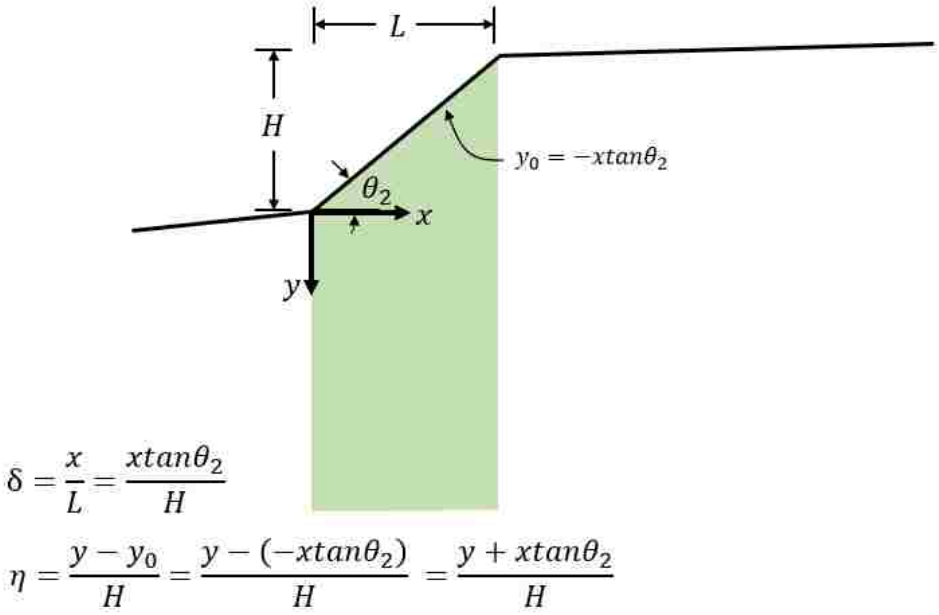

Figure 5.13. Calculation of δ and η for 0 < x < L (shaded region).

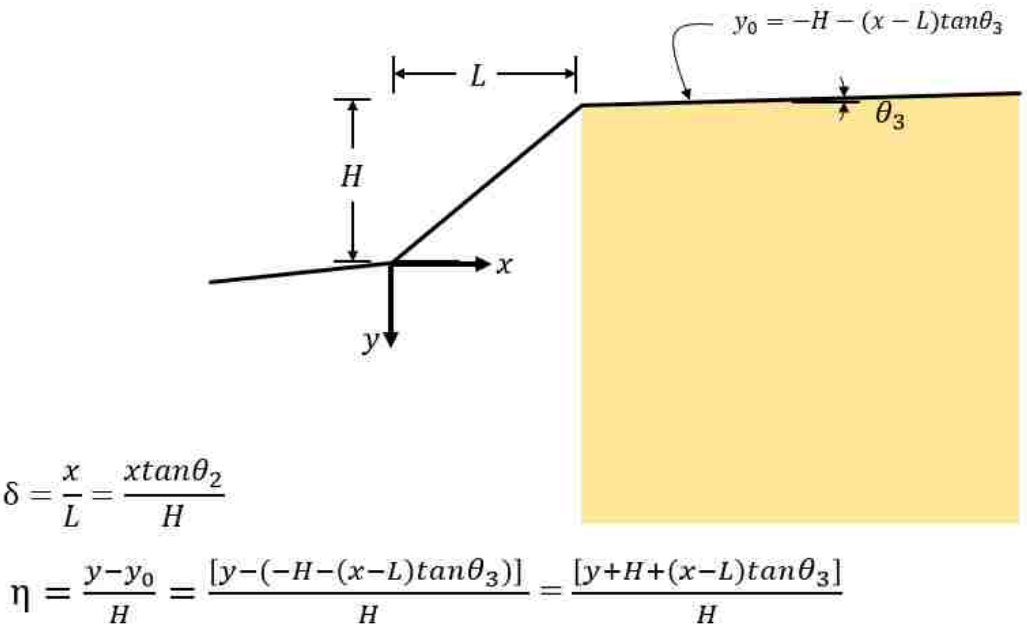

$$\delta = \frac{x}{L} = \frac{xtan\theta_2}{H}$$

$$\eta = \frac{y-y_0}{H} = \frac{[y-(-H-(x-L)tan\theta_3)]}{H} = \frac{[y+H+(x-L)tan\theta_3]}{H}$$

Figure 5.14. Calculation of δ and η for < x ≥ L (shaded region).

5.4.3 Investigated Slope Geometries

In order to cover the range of slope geometries that can lead to lateral spreading hazards, a suite of 102 different geometries (Table 5.6) was developed and used in the subsequently described numerical analyses. For simplicity and conciseness, the geometries in the remainder of this thesis will be described in the short hand form H-θ_1-θ_2-θ_3. For example, a slope with H = 5 meters, θ_1 = 0 degrees, θ_2 = 15 degrees, and θ_3 = 3 degrees will be described as 5-0-15-3.

Table 5.6. Slope geometries analyzed to develop data for a stress function.

Case	Model_ID	Height (m)	θ_1 (deg)	θ_2 (deg)	θ_3 (deg)	Case	Model_ID	Height (m)	θ_1 (deg)	θ_2 (deg)	θ_3 (deg)
Infinite Slope	INF_S_1	1	0.5	0.5	0.5	Case 3	2-0-15-1	2	0	15	1
Infinite Slope	INF_S_2	1	1	1	1	Case 3	2-0-15-3	2	0	15	3
Infinite Slope	INF_S_3	1	1.5	1.5	1.5	Case 3	2-0-15-5	2	0	15	5
Infinite Slope	INF_S_4	1	2	2	2	Case 3	2-0-20-1	2	0	20	1
Infinite Slope	INF_S_5	1	3	3	3	Case 3	2-0-20-3	2	0	20	3
Infinite Slope	INF_S_6	1	4	4	4	Case 3	2-0-20-5	2	0	20	5
Infinite Slope	INF_S_7	1	5	5	5	Case 3	2-0-25-1	2	0	25	1
Case 2	1-0-5-0	1	0	5	0	Case 3	2-0-25-3	2	0	25	3
Case 2	2-0-5-0	2	0	5	0	Case 3	2-0-25-5	2	0	25	5
Case 2	3-0-5-0	3	0	5	0	Case 3	3-0-5-1	3	0	5	1
Case 2	4-0-5-0	4	0	5	0	Case 3	3-0-5-3	3	0	5	3
Case 2	5-0-5-0	5	0	5	0	Case 3	3-0-10-1	3	0	10	1
Case 2	1-0-10-0	1	0	10	0	Case 3	3-0-10-3	3	0	10	3
Case 2	2-0-10-0	2	0	10	0	Case 3	3-0-10-5	3	0	10	5
Case 2	3-0-10-0	3	0	10	0	Case 3	3-0-15-1	3	0	15	1
Case 2	4-0-10-0	4	0	10	0	Case 3	3-0-15-3	3	0	15	3
Case 2	5-0-10-0	5	0	10	0	Case 3	3-0-15-5	3	0	15	5
Case 2	1-0-15-0	1	0	15	0	Case 3	3-0-20-1	3	0	20	1
Case 2	2-0-15-0	2	0	15	0	Case 3	3-0-20-3	3	0	20	3
Case 2	3-0-15-0	3	0	15	0	Case 3	3-0-20-5	3	0	20	5
Case 2	4-0-15-0	4	0	15	0	Case 3	3-0-25-1	3	0	25	1
Case 2	5-0-15-0	5	0	15	0	Case 3	3-0-25-3	3	0	25	3
Case 2	1-0-20-0	1	0	20	0	Case 3	3-0-25-5	3	0	25	5
Case 2	2-0-20-0	2	0	20	0	Case 3	4-0-5-1	4	0	5	1
Case 2	3-0-20-0	3	0	20	0	Case 3	4-0-5-3	4	0	5	3
Case 2	4-0-20-0	4	0	20	0	Case 3	4-0-10-1	4	0	10	1
Case 2	5-0-20-0	5	0	20	0	Case 3	4-0-10-3	4	0	10	3
Case 2	1-0-25-0	1	0	25	0	Case 3	4-0-10-5	4	0	10	5
Case 2	2-0-25-0	2	0	25	0	Case 3	4-0-15-1	4	0	15	1
Case 2	3-0-25-0	3	0	25	0	Case 3	4-0-15-3	4	0	15	3
Case 2	4-0-25-0	4	0	25	0	Case 3	4-0-15-5	4	0	15	5
Case 2	5-0-25-0	5	0	25	0	Case 3	4-0-20-1	4	0	20	1
Case 3	1-0-5-1	1	0	5	1	Case 3	4-0-20-3	4	0	20	3
Case 3	1-0-5-3	1	0	5	3	Case 3	4-0-20-5	4	0	20	5
Case 3	1-0-10-1	1	0	10	1	Case 3	4-0-25-1	4	0	25	1
Case 3	1-0-10-3	1	0	10	3	Case 3	4-0-25-3	4	0	25	3
Case 3	1-0-10-5	1	0	10	5	Case 3	4-0-25-5	4	0	25	5
Case 3	1-0-15-1	1	0	15	1	Case 3	5-0-5-1	5	0	5	1
Case 3	1-0-15-3	1	0	15	3	Case 3	5-0-5-3	5	0	5	3
Case 3	1-0-15-5	1	0	15	5	Case 3	5-0-10-1	5	0	10	1
Case 3	1-0-20-1	1	0	20	1	Case 3	5-0-10-3	5	0	10	3
Case 3	1-0-20-3	1	0	20	3	Case 3	5-0-10-5	5	0	10	5
Case 3	1-0-20-5	1	0	20	5	Case 3	5-0-15-1	5	0	15	1
Case 3	1-0-25-1	1	0	25	1	Case 3	5-0-15-3	5	0	15	3
Case 3	1-0-25-3	1	0	25	3	Case 3	5-0-15-5	5	0	15	5
Case 3	1-0-25-5	1	0	25	5	Case 3	5-0-20-1	5	0	20	1
Case 3	2-0-5-1	2	0	5	1	Case 3	5-0-20-3	5	0	20	3
Case 3	2-0-5-3	2	0	5	3	Case 3	5-0-20-5	5	0	20	5
Case 3	2-0-10-1	2	0	10	1	Case 3	5-0-25-1	5	0	25	1
Case 3	2-0-10-3	2	0	10	3	Case 3	5-0-25-3	5	0	25	3
Case 3	2-0-10-5	2	0	10	5	Case 3	5-0-25-5	5	0	25	5

5.4.4 Numerical Model

To analyze the stresses within slopes with different geometries, the finite element program PLAXIS was used. In finite element analysis, a region of interest is broken up into a finite number of elements where calculations are performed – these elements make up the mesh of the model. PLAXIS allows the user to select from 6-noded or 15-noded triangular elements. For this research 15-noded triangular elements were used due to increased accuracy of results (PLAXIS, 2019a). Each 15-noded triangular element has 12 stress points within the element where stresses are calculated. Figure 5.15 shows the locations of the nodes and stress points for a 15-noded triangular element.

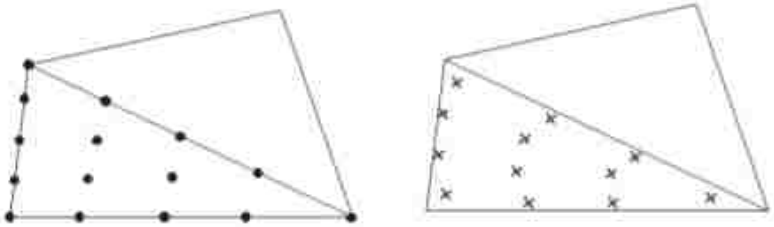

Figure 5.15. Illustration of location of PLAXIS node and stress point locations within a 15-noded triangular element (PLAXIS, 2019a).

For this research, the introductory version of PLAXIS was used because it had the capability to analyze the static stresses within lateral spreading slope geometries and was freely available. The general constraints of the PLAXIS introductory version are:

(1) Limited to one material dataset and therefore soil type;

(2) Limited to a certain number of structural elements;

(3) Limited to the choice of three simple material models;

(4) Limited to five calculations phases;

(5) Unable to print/copy using the PLAXIS software.

Limitations (1), (3), and (4) did not impact the research as only one soil type is used, a simple material model is all that's needed to characterize the static stress, and only gravity loading is needed to characterize the static stress within a slope. Constraints (2) and (5) provided the following minor limitations:

(a) Structures in PLAXIS can be used for the development of the model geometry, boundary conditions, and additional mesh zones. Because the model geometry and boundary conditions are essential to any model, the creation of zones of different mesh size within the model was limited to three. However, three mesh zones still allowed for a very fine mesh at shallow depths of lateral spreading interest and a progressively coarser mesh farther away.

(b) The inability to print/copy data/results from PLAXIS caused the graphics used in this thesis to have the words "Introductory version" imprinted on them.

5.4.4.1 Material Model

Two material models were used in the PLAXIS introductory version – the linear elastic and Mohr-Coulomb models.

Linear Elastic Model

The linear elastic model is the simplest constitutive model and is governed by Hooke's law of linear and isotropic elasticity. The linear elastic model is characterized by two elastic parameters, Young's modulus, E, and Poisson's ratio, ν. Materials modeled via the linear elastic model use a constant average E value. Figure 5.16 shows how stresses are related to strains for the linear elastic model.

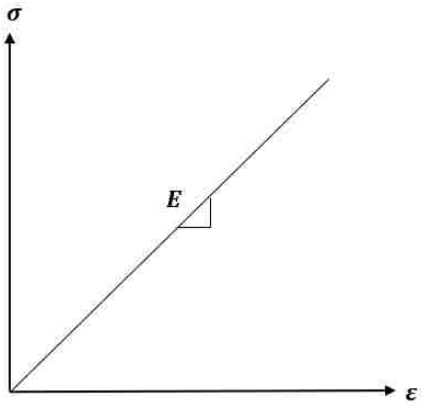

Figure 5.16. Linear elastic definition of how stresses are related to strains.

The linear elastic model was initially used in this research because it is simple, has a long history of use for modeling stress distributions in geotechnical engineering, and was hypothesized to be able to handle the shear stresses produced by gravity loading for the relatively flat slope geometries typically associated with lateral spreading case histories. However, the complex behavior of the computed shear stresses for even simple slope geometries in terms of a static stress ratio, led to the use of the Mohr-Coulomb model.

Mohr-Coulomb Model

The Mohr-Coulomb material model is a simple constitutive model that behaves as a linear elastic material until the shear strength is mobilized, after which it behaves as a perfectly plastic material. The initial linear elastic behavior is governed by Hooke's Law (Figure 5.16) and the perfectly plastic behavior is governed by the Mohr-Coulomb failure criterion shown in Equation 5.10. The Mohr-Coulomb model is therefore termed an elastic-perfectly plastic material model and is governed by five parameters Young's modulus, E, Poisson's ratio, ν, cohesion, c, friction angle, φ, and dilatancy angle, ψ. Materials modeled via the Mohr-Coulomb model use a constant average E value. Figure 5.17 shows how stresses are related to strains for the elastic-perfectly plastic model.

$$\tau = c + \sigma \tan \varphi \tag{5.10}$$

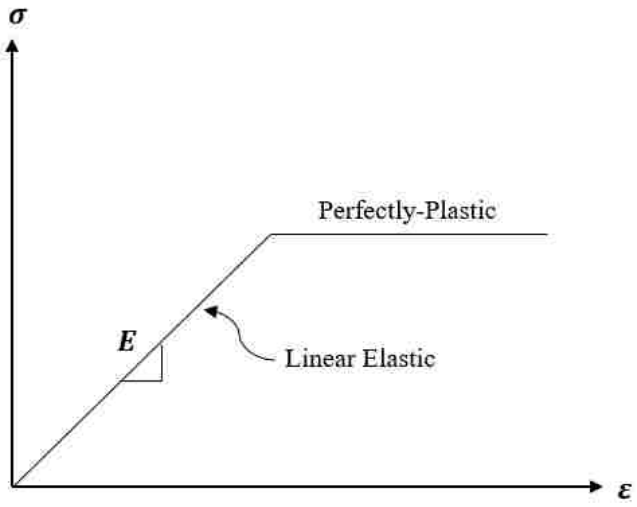

Figure 5.17. Mohr-Coulomb linear elastic perfectly-plastic stress-strain behavior.

The Mohr-Coulomb model is used in this research because it is a simple model that is easy to implement, it has relatively quick computation times compared to more advanced material models, and it is capable of developing a simple stress function in terms of the static stress ratio.

5.4.4.1.1 Soil Parameters

Table 5.7 shows the soil parameters of the sand material used in the linear elastic PLAXIS analyses. A shear wave velocity of 500 m/s, corresponding to that of a very dense soil, was initially used to prevent overly excessive deformations in the sand material during gravity loading. However, during the early stages of research the PLAXIS models included a water table and a saturated unit weight of 20 kN/m^3 was used to calculate the stiffness parameters. Because the goal was to model the static shear stress, the water table was removed for simplicity and an unsaturated unit weight of 17 kN/m^3 was used. Using the unsaturated unit weight required the shear wave velocity to be changed to 542 m/s to give the same stiffness parameters as were used when the water table was present. Therefore, the stiffness parameters were the same, however, the unit

weight used differed between the analysis of boundary condition effects and the bulk of analyses to follow.

Table 5.7. Model parameters, general soil properties, and stiffness parameters for the sand material used in PLAXIS linear elastic analyses.

Material Name	Sand
Material Model	Linear Elastic
Drainage Type	Drained
γ_{unsat} (kPa)	17
γ_{sat} (kPa)	20
V_s (m/s)	542
Elastic Modulus, E (kPa)	1.325×10^6
Poisson Ratio, ν	0.30
Shear Modulus, G (kPa)	5.097×10^5

5.4.4.2 Mesh

Three different mesh zones with varying resolution were used to allow for a very fine mesh to be used in the vicinity of the slope and a coarser mesh farther away from the slope. This was done to achieve accurate results in the region of interest, but also limit the total number of elements, which affects PLAXIS file sizes and calculation times. The geometry and dimensions of the different mesh zones are shown in Figures 5.18-5.20 where H and L are as defined in Figure 5.8.

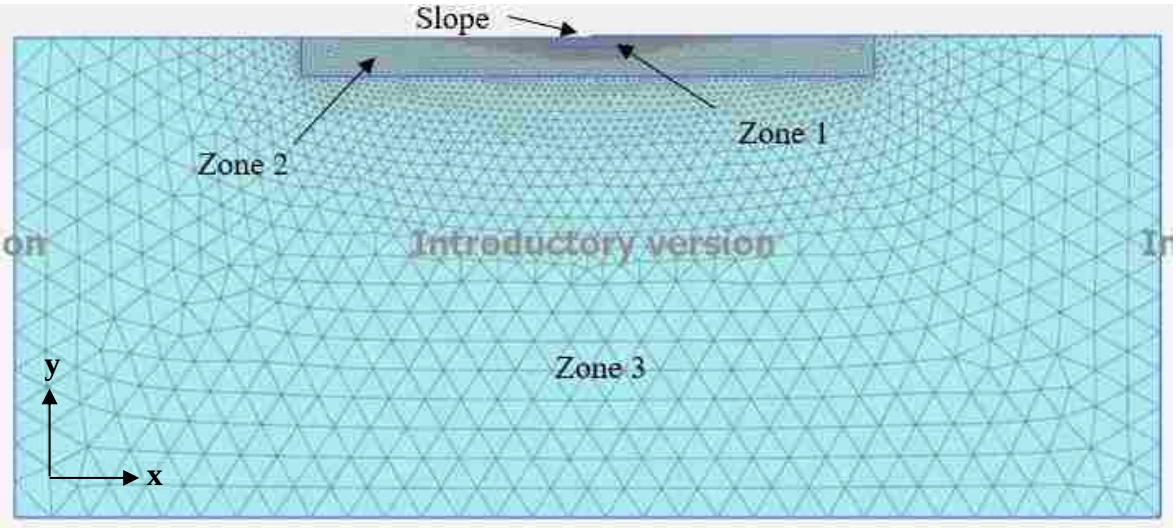

Figure 5.18. Mesh used in PLAXIS analysis of 5-0-25-0.

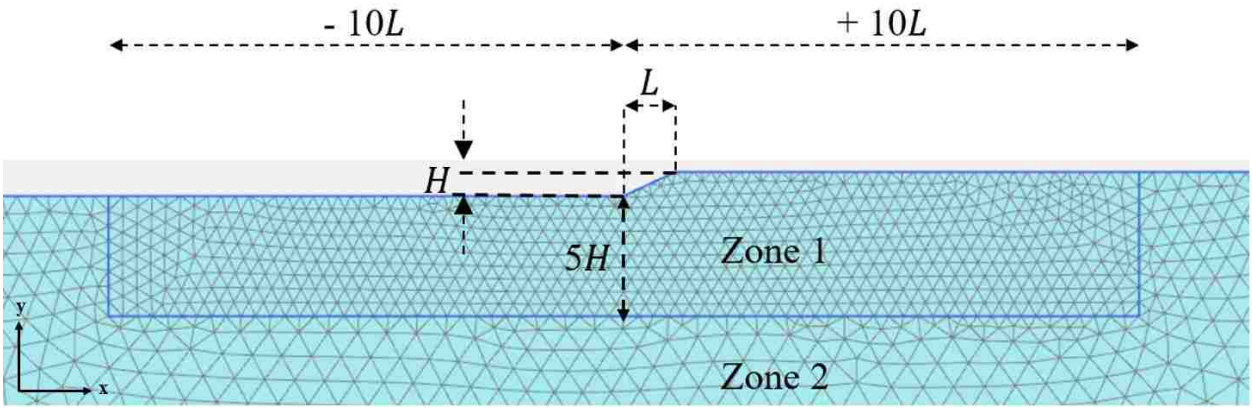

Figure 5.19. Geometry of mesh Zone 1 for PLAXIS model 5-0-25-0.

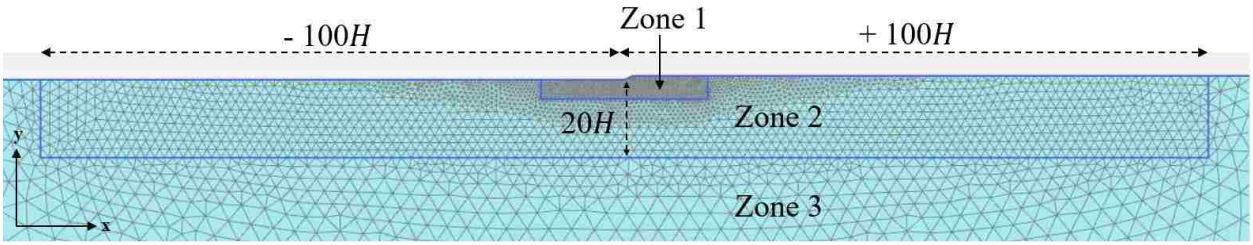

Figure 5.20. Geometry of mesh Zone 2 for PLAXIS model 5-0-25-0.

The desired mesh size in Zone 1 would have stress points spaced laterally at L/10 and vertically at H/5. For the 5-0-25-0 model, L is 10.7 meters. Therefore, the desired stress points would be spaced at about 1 meter both laterally and vertically in Zone 1 for 5-0-25-0. Zones 2 and 3 would having progressively larger spacing between stress points.

The size of elements in a mesh is controlled by three components in PLAXIS: the size of the overall model created by the user, a factor for the relative element size, and the local refinement settings. Based on the overall dimensions for the created PLAXIS model (x_{min}, x_{max}, y_{min}, y_{max}) and the relative element size factor, r_e, the PLAXIS mesh generator creates an average element size, I_{avg}, given as

$$I_{avg} = 0.06 \times r_e \sqrt{(x_{max} - x_{min})^2 + (y_{max} - y_{min})^2} \qquad (5.11)$$

The relative element size factor, and the mesh type it corresponds to, is shown in Table 5.8. Table 5.8 also shows the approximate number of elements for each mesh size specified where the actual number of elements depends on the geometry shape and local refinement settings (PLAXIS, 2019a).

Table 5.8. Mesh type corresponding to r_e and the approximate number of elements associated with it for default local refinement settings (PLAXIS, 2019a).

Mesh	r_e	# of elements
Very coarse	2.00	30-70
Coarse	1.33	50-200
Medium	1.00	90-350
Fine	0.67	250-700
Very fine	0.50	500-1250

For each of the three zones shown in Figures 5.18-5.20, a "Very fine" mesh was specified in PLAXIS, however, whether the mesh is specified as "Very fine" or "Very coarse" in PLAXIS only initially controls the number of elements for the default local refinement settings. Local refinement was accomplished using the PLAXIS coarseness factor.

For this research, the mesh for Zones 1-3 are as follows:

- Zone 1: very fine mesh with a coarseness factor of 0.03125 (the smallest coarseness factor possible);
- Zone 2: very fine mesh with a coarseness factor of 0.1250;
- Zone 3: very fine mesh with default coarseness factor of 1.0.

The latter mesh/coarseness factor specifications produced the mesh shown in Figure 5.18 for the 5-0-25-0 model. The important part of the mesh can be examined in more detail by zooming into the region of Zones 1 and 2. Figure 5.21a shows the relative element sizes of all three zones and Figure 5.21b shows the locations of stress points within the elements within a portion of Zone 1.

Figure 5.21b shows that the diamond shaped stress points are less than 1 meter apart, thereby meeting the desired lateral and vertical spacings within Zone 1.

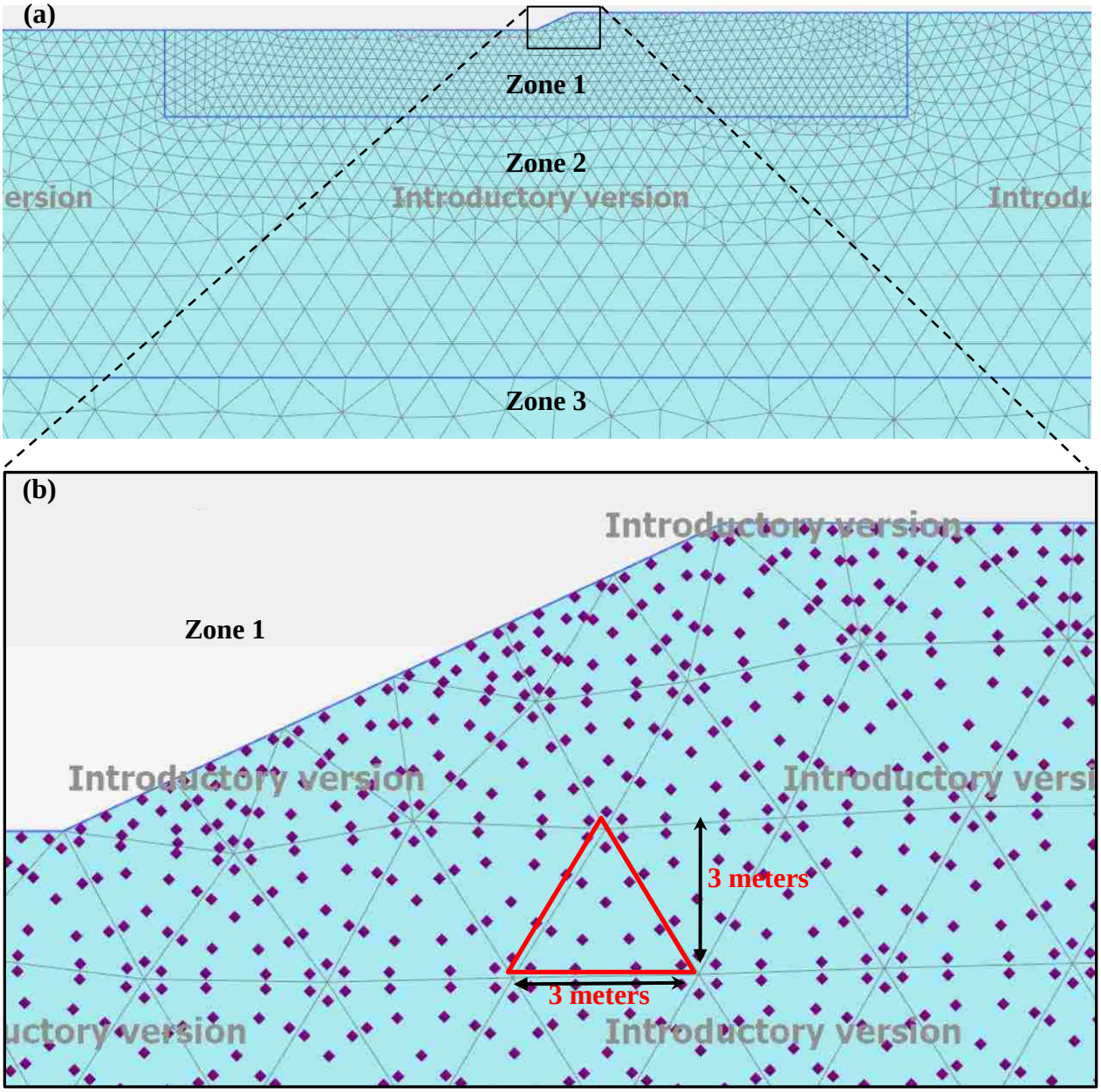

Figure 5.21. Mesh used in PLAXIS analysis of 5-0-25-0 (a) zoomed into Zones 1 and 2; (b) further zoomed into the slope in Zone 1 with the stress points shown.

5.4.4.3 Boundary Conditions

A linear elastic constitutive model was used in order to identify the model dimensions required to ensure that the boundary conditions (BC) would not significantly impact the stresses

in the region of interest of the model. For lateral spreading, the desired distance of negligible influence of the stress within the slope was conservatively set at the boundaries of Zone 2 (Figure 5.20). Therefore, if the BC effects do not impact the shear stress results within Zone 2, the shear stress results obtained from PLAXIS were considered to represent stress conditions unaffected by the boundary conditions. The desired BCs for the model are shown in Figure 5.22 where the base and sides of the model are constrained against vertical and horizontal displacement, respectively, and the ground surface is free in both the x and y directions. In order to test the sensitivity of the stresses within a model, a 5-0-25-0 model was used as it represented the steepest slope of the geometries associated with lateral spreading (Table 5.6). A θ_3 = 0 model was chosen for the purpose of evaluating the horizontal extent because it produces sharper "kinks" in the ground surface profile, which result in locally increased shear stresses. The horizontal extents can be interpreted to have negligible influence when at a lateral distance at which the horizontal shear stresses within the model return to very nearly zero.

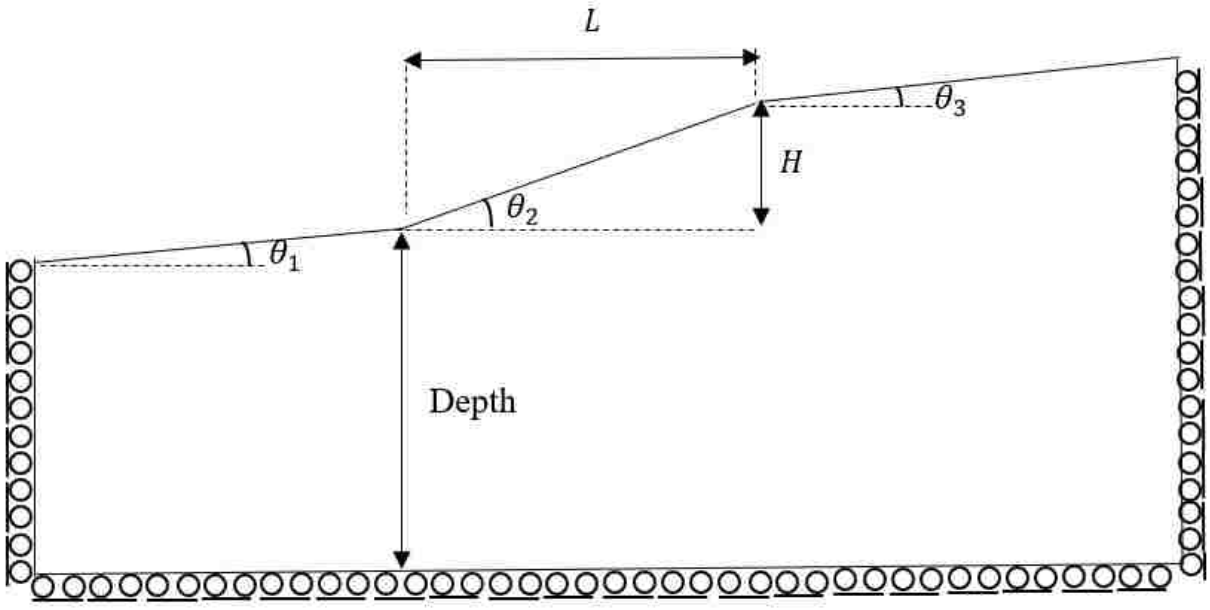

Figure 5.22. Generic slope geometry with rollers on the base and sides of the model.

The BCs were evaluated by comparing the computed shear stress with respect to depth and lateral distance from the toe for various combinations of "fixed" and "free" BCs. An illustration of each of these BCs is shown in Figure 5.23. The desired BC was compared to two control BCs which will further be denoted as:

- Desired BC: base: x = free, y = fixed, vertical: x = fixed, y = free (Figure 5.23a)
- Control BC 1: base: x = fixed, y = fixed, vertical: x = fixed, y = free (Figure 5.23b)
- Control BC 2: base: x = free, y = fixed, vertical: x = fixed, y = fixed (Figure 5.23c)

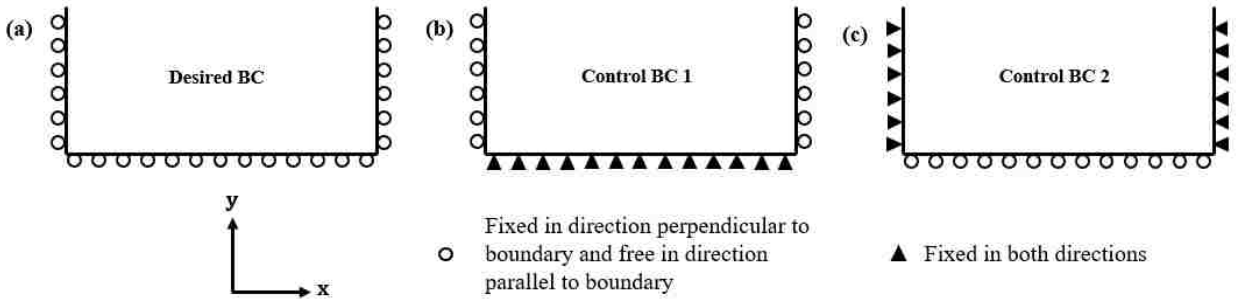

Figure 5.23. Illustration of boundary conditions (a) Desired BC, (b) Control BC 1, and (c) Control BC 2.

By comparing the Desired BC with the control BCs, the vertical and lateral extents of the PLAXIS model could be determined in terms of the number of multiples of H the model boundaries needed to be placed at in order to meet the previously described requirement of negligible effects within Zone 2. After many iterations of experimenting with different vertical and lateral model extents, an overall model depth of $250H$ and width of $\pm 300H$ were found to meet the conservative criteria.

5.4.4.3.1 Validating Vertical Extent of Models

In order to validate that the depth of the models was large enough to ensure that the BCs do not impact the shear stresses, the shear stress with depth was compared between the Desired BC and Control BC 1 at eight vertical cross-sections (Table 5.9) within the 5-0-25-0 model. The cross-sections ranged from 200 meters to the left and right of the toe of the slope and extended

from the ground surface to the base of the mesh at a depth of 1250 meters. Figure 5.24 shows the shear stress with respect to depth for both BCs. From Figure 5.24, it appears that the shear stress is negligibly impacted by the BCs down to a depth of about 100 meters for all cross-section locations. Table 5.9 supports the latter showing that the maximum shear stress difference between the BCs is 0.27 kPa and 0.04 kPa within 100 meters and 15 meters depth from the toe of the slope, respectively. The lateral spreading depth of interest was conservatively taken to be 20H vertically, therefore, for geometry 5-0-25-0 the 5-meter high slope meets this condition.

Table 5.9. Vertical cross-section locations for validating model depth and the maximum shear stress difference between fixed and free BC. The toe of the slope is at x = 0, y = 0.

Cross-Section	A		A'		Max Shear Stress Difference Between Fixed and Free (kPa)	
	x (m)	y (m)	x (m)	y (m)	From 0 to 100 m below toe	From 0 to 15 m below toe
1	-200	0	-200	-1250	0.27	0.03
2	-100	0	-100	-1250	0.26	0.03
3	-40	0	-40	-1250	0.26	0.03
4	0	0	0	-1250	0.26	0.04
5	10.72	5	10.72	-1250	0.26	0.03
6	50	5	50	-1250	0.25	0.04
7	100	5	100	-1250	0.26	0.04
8	200	5	200	-1250	0.27	0.04

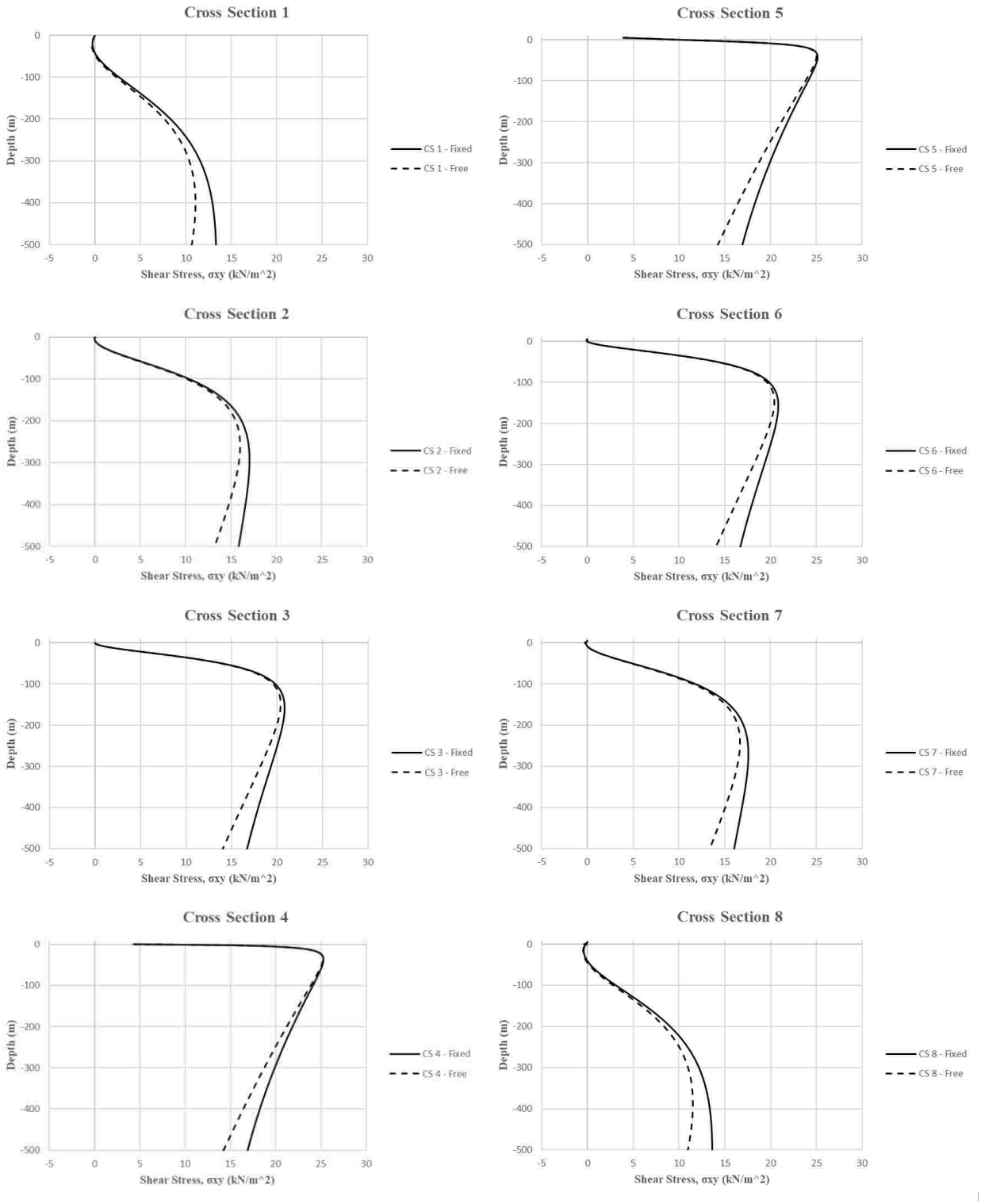

Figure 5.24. Shear stress versus depth plots for validating vertical extent of models via eight cross-sections where the solid lines labeled "Fixed" are Control BC 1 and the dotted lines labeled "Free" are the Desired BC.

5.4.4.3.2 Validating Lateral Extent of Models

To confirm that the lateral extent of the models was large enough to ensure that the BCs did not impact the shear stresses, the normalized shear stresses (shear stress divided by the unit weight multiplied by the slope height) for the Desired BC and Control BC 2 were compared for seven different horizontal cross-sections (Table 5.10) within the 5-0-25-0 model. The comparison of the normalized shear stress between the Desired BC and Control BC 2 is shown in Figure 5.25. To make clear the shear stress difference between the Desired BC and Control BC 2, plots of the difference of the normalized shear stress between these conditions were also created as shown in Figure 5.26. These plots show that there is negligible difference between shear stress for the Desired BC and Control BC 2 up to almost 1000 meters laterally from the toe of the slope for all cross-section locations. The lateral spreading depth of interest was taken to be 100H laterally, therefore, for geometry 5-0-25-0 the 5-meter high slope meets this condition.

Table 5.10. Horizontal cross-section locations for validating model lateral extents from the toe of the slope.

Cross-Section	A		A'	
	x (m)	y (m)	x (m)	y (m)
1	5.36	2.5	1500	2.5
2	-1500	-1	1500	-1
3	-1500	-10	1500	-10
4	-1500	-25	1500	25
5	-1500	-50	1500	50
6	-1500	-100	1500	100
7	-1500	-400	1500	-400

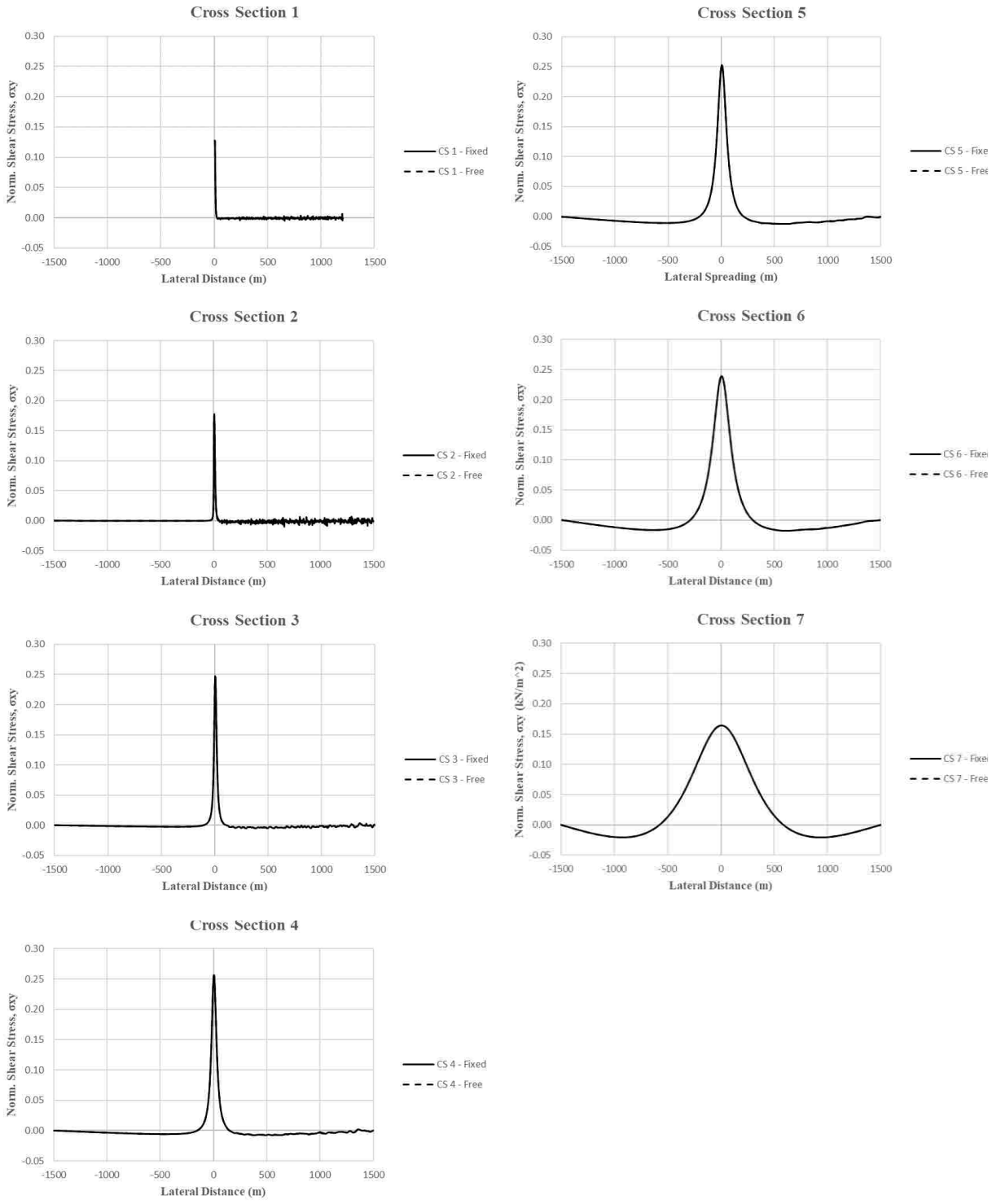

Figure 5.25. Normalized shear stress with respect to lateral distance from the toe of the slope for validating lateral extent of models via seven cross-sections where the solid lines labeled “Fixed” are Control BC 2 and the dotted lines labeled “Free” are the Desired BC.

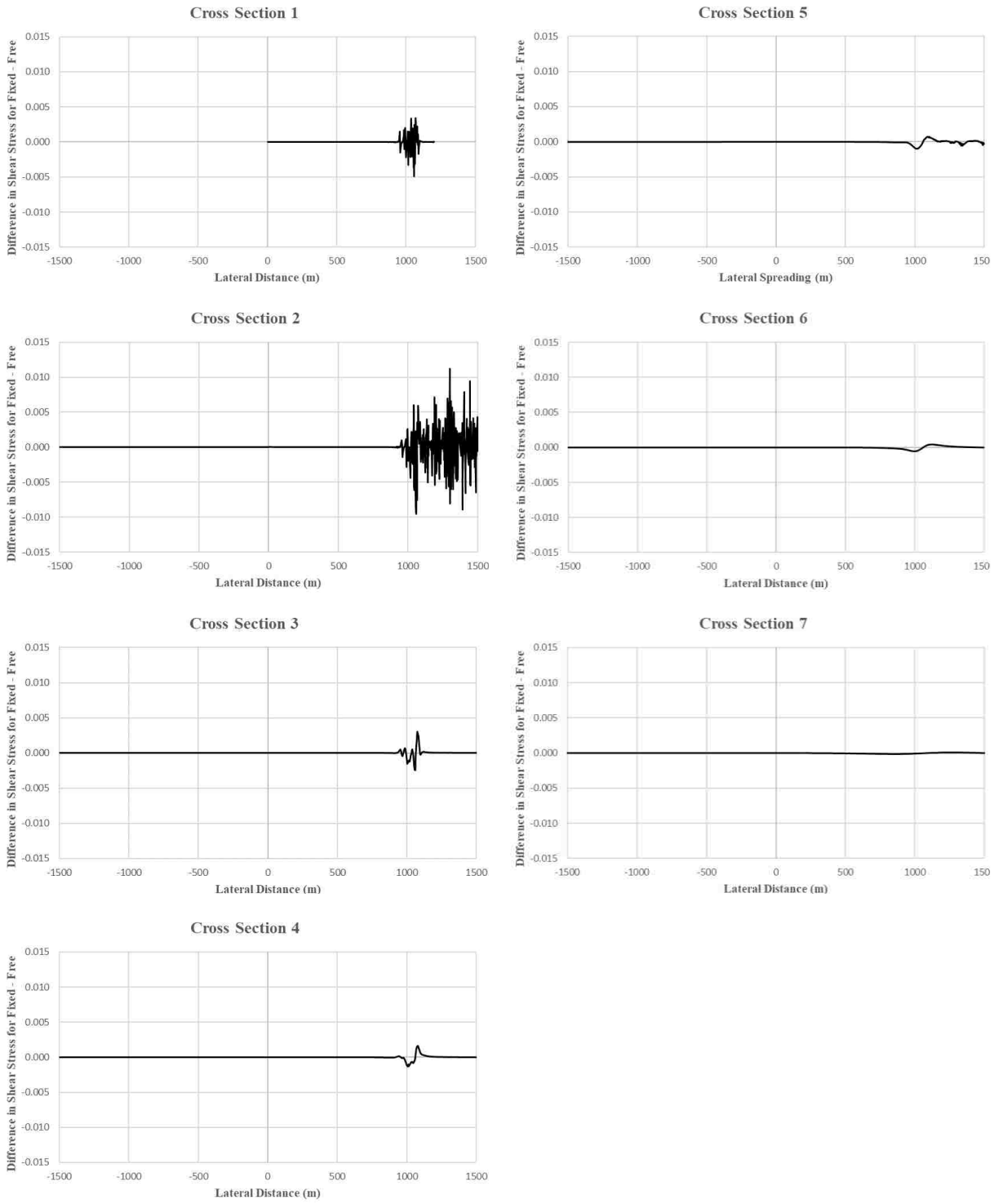

Figure 5.26. The difference in normalized shear stress with respect to lateral distance from the toe of the slope for validating lateral extent of models via seven cross-sections where the solid lines labeled “Fixed” are Control BC 2 and the dotted lines labeled “Free” are the Desired BC.

5.4.4.3.3 Discussion

Shear stress with depth was compared between the Desired BC and Control BC 1 at eight different vertical cross-sections within the model. Shear stress with lateral distance from the toe of the slope was compared between the Desired BC and Control BC 2 at seven different horizontal cross-sections within the model. The results show that model extents of depth = 250H and lateral extent = +/- 300H from the toe of the slope will give reasonable shear stresses within the depth and lateral extents of interest (20H vertically and +/- 100H laterally from the toe) for lateral spreading.

Validation of the model extents was done when the model had a water table that corresponded to the height of the toe of the slope. After completion of these analyses on BC effects, it was decided to remove the water table altogether for simplicity because a water table is not required to determine the static stresses within a slope. While the water table was incorporated during the analysis of BC effects, the saturated unit weight was 20 kN/m^3 and the unsaturated unit weight 17 kN/m^3. The normalized shear stress was found using the saturated unit weight because most of the model was below the water table. It was decided not necessary to re-validate the boundary conditions of the model after removing the water table from the profile.

5.4.5 Results of Numerical Analyses

Two material models – linear elastic and elastic-perfectly plastic (Mohr-Coulomb) were investigated in the process of developing a unified stress function that would be applicable to a wide array of slope geometries. The material model used to calculate the stresses for the large number of lateral spreading slope geometries (see Table 5.6) needed to be simple to limit the computation time and file size, while also producing reasonable results. The linear elastic model was initially selected because it is the simplest material model and is governed by only two

parameters, one of which being a constant average stiffness. Because the stiffness is not stress-dependent for the linear elastic model, the computational time is much faster than a material model that has a stress-dependent stiffness. However, because complex shear stress behavior was observed to occur from gravity loading, it was decided to use the static stress ratio for the development of a unified stress function. The linear elastic model had a fundamental problem with accurately modeling the static stress ratio at shallow depths, therefore, it was decided to use the non-linear Mohr-Coulomb material model. The Mohr-Coulomb model is based on five parameters, however, has a constant average stiffness while also being able to provide reasonable static stress ratio values for the determination of a unified stress function. The calculation settings used for PLAXIS numerical analyses are shown in Table 5.11.

Table 5.11. Calculation settings used in PLAXIS for the linear elastic analyses.

Phase	Initial Phase
Calculation Type	Gravity Loading
Loading Type	Staged Construction
Total Multiplier for Material Weight	1
Time Interval (days)	0
Ignore Suction	Yes
Max Cores to Use	256
Max Number of Steps Stored	100
Use Default Iteration Parameters	Yes
Max Steps	250
Tolerated Error	0.01
Max Unloading Steps	5
Max Load Fraction Per Step	0.5
Over-relaxation Factor	1.2
Max Number of Iterations	60
Desired Minimum Number of Iterations	6
Desired Maximum Number of Iterations	15
Arc-length Control Type	On
Use Line Search	No
Use Gradual Error Reduction	No

5.4.5.1 Results – Linear-Elastic Constitutive Model

Linear elastic analyses were performed using the soil parameters shown in Table 5.7 and the PLAXIS calculation settings shown in Table 5.11. Figure 5.27 shows the shear stress distribution for the entire 5-0-5-0 model. As the depth below the slope increases the larger the lateral extent effected by the stresses imposed by the slope – similar to a stress bulb below a footing, i.e., as the depth increases below the footing the wider the stress bulb becomes and thus the larger area effected. Figure 5.27 also shows that the horizontal shear stresses diminish as moving laterally away from the central slope segment. This shear stress behavior appears to be reasonable.

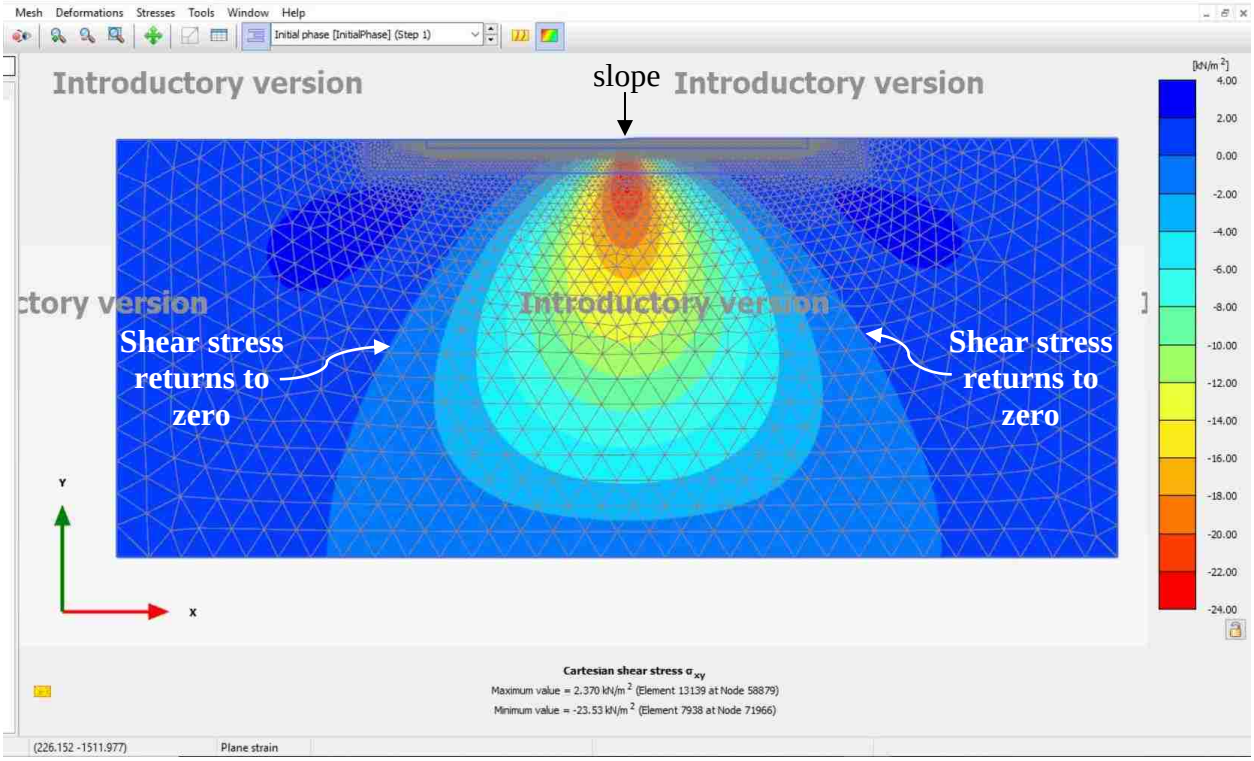

Figure 5.27. Shear stress distribution for geometry 5-0-5-0.

Recognizing that the goal was to develop a simple stress function, limiting the number of variables in the function was important. To remove the effect of slope height, the shear stress was normalized by the product of the unit weight of the soil and the height of the slope, H, thereby

reducing the number of geometries by a factor of five. For example, geometry 5-0-5-3 would have the same normalized shear stress as geometry 1-0-5-3.

Figure 5.28 depicts the variation of normalized shear stress near the central slope in the relatively simple 5-0-5-0 geometry. The shear stress distribution shows significant asymmetry beneath the central slope segment (i.e., $0 \leq \delta \leq 1$). These sharp and rapid variations in shear stress were recognized as being potentially difficult to model with simple stress functions. It was determined, however, that normalizing the shear stress by the vertical stress (instead of normalizing by γH) would produce a static stress ratio, SSR, that was better behaved and still removed the effect of slope height along with providing a useful measure of initial shear stress for the purpose of lateral spreading displacement estimation.

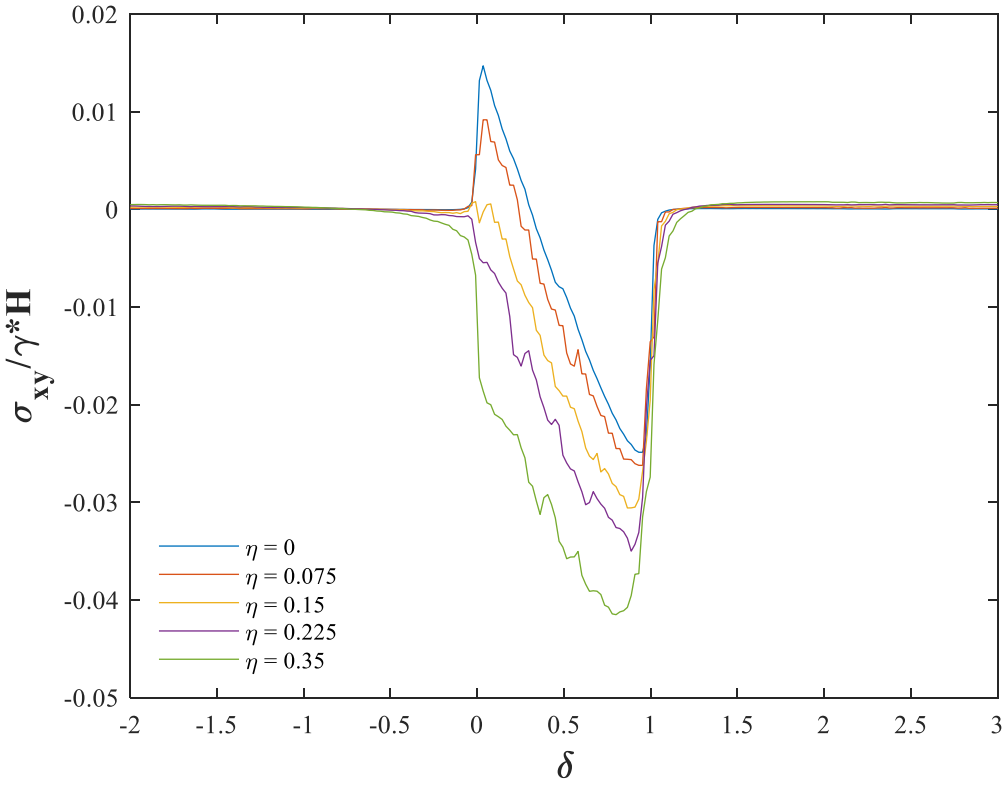

Figure 5.28. Normalized shear stress versus δ for various η values.

A Fundamental Problem With an Elasticity-based Approach

The static stress ratio can be defined as

$$SSR = \frac{\sigma_{xy}}{\sigma_{yy}} \tag{5.12}$$

For an infinite slope of inclination, β, the value of SSR can be represented as

$$SSR = \tan\beta \tag{5.13}$$

Therefore, if a slope is composed of three linear ground surface segments as shown in Figure 5.29, elements of soil close to the ground surface (elements that are so shallow that the slopes of the other segments have no effect) should each have SSR values corresponding to their respective infinite slope values. In other words, the values of SSR at the ground surface can be represented as

$$SSR = \begin{cases} \tan\theta_1 & for\ \delta < 0, \eta = 0 \\ \tan\theta_2 & for\ 0 < \delta < 1, \eta = 0 \\ \tan\theta_3 & for\ \delta > 1, \eta = 0 \end{cases} \tag{5.14}$$

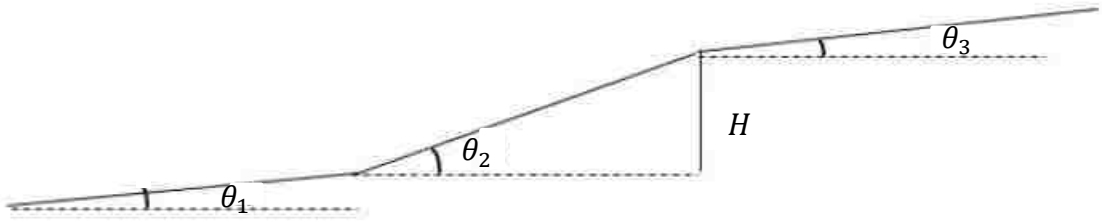

Figure 5.29. Slope geometry composed of three linear ground surface segments controlled by angles θ_1, θ_2, and θ_3.

Examining Figure 5.29, it is clear that the SSR values will have a transition in the vicinity of $\delta = 0$ and $\delta = 1$, and will also vary with η as the stresses spread out with depth.

The SSR given in Equation 5.12 illustrates a fundamental problem with an elasticity-based analysis approach. As the surface of a slope is approached, the vertical stress is observed to decrease faster than the shear stress, thus causing SSR to be extremely large at shallow depths. It's

known that for cohesionless soils, SSR cannot be greater than tangent of the infinite slope angle, which it can be at shallow depths in steep profiles as SSR continues to increase as approaching the ground surface. Because of this, the Mohr-Coulomb model was used in subsequent PLAXIS analyses.

5.4.5.2 Results – Mohr-Coulomb Constitutive Model

The analysis for 5-0-5-3 was performed using the Mohr-Coulomb model under drained conditions. All soil parameters were the same as for the linear elastic case, but zero cohesion, and an effective stress friction angle, φ', of 33 degrees were used to model the shear strength. For quartz sand, the dilatancy angle was taken as $\varphi' - 30$, or 3 degrees. As in the linear elastic analyses, default iteration parameters were used.

Figure 5.30 presents shear stress contours of geometry 5-0-5-3, for a portion of the lateral spreading region of interest, near the toe of the slope. These contours show an unusual shear stress pattern near the ground surface where values alternate from a small negative shear stress to a small positive shear stress. This pattern of shear stress corresponds to a region of the slope where plastic points were computed, which indicates that the Mohr-Coulomb failure envelope was reached.

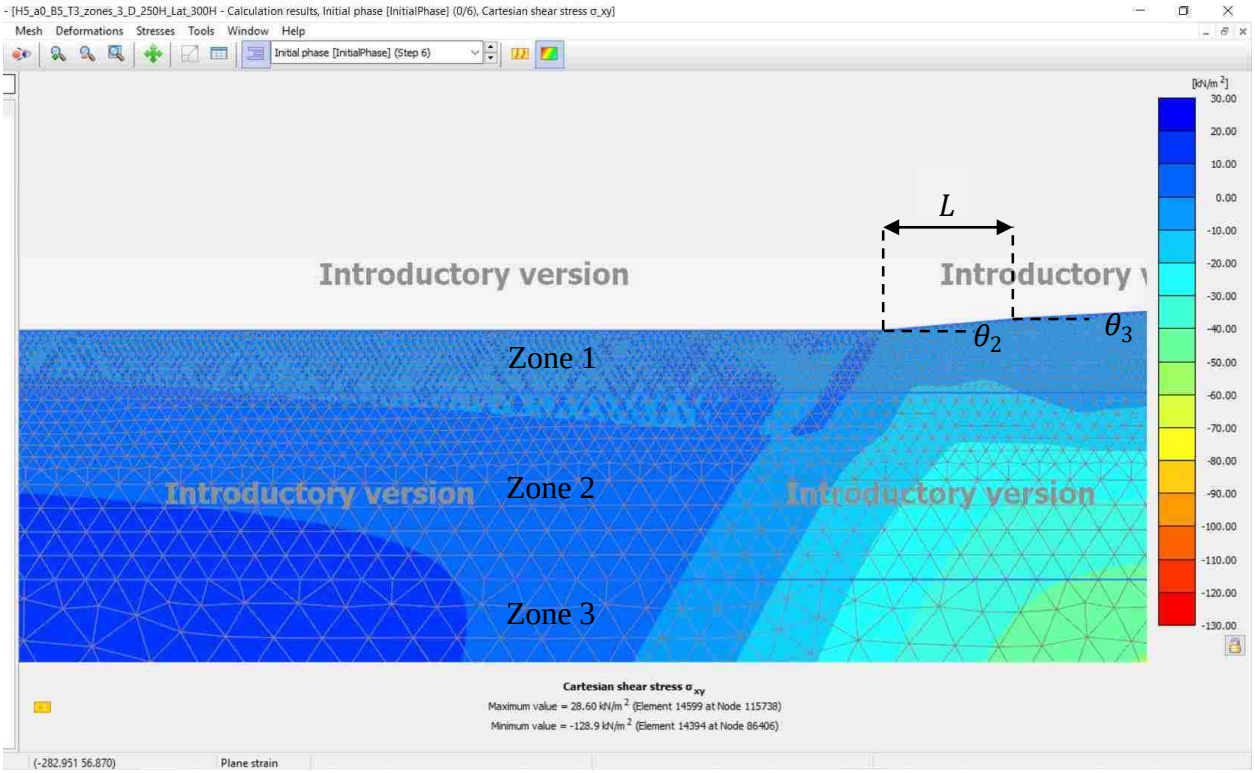

Figure 5.30. Shear stress for the 5-0-5-3 model in the lateral spreading region of interest.

When such results are encountered, the PLAXIS material model manual advises that the cohesion be increased from zero to a small non-zero value (c > 0.2 kPa) to avoid complications associated with the very low strengths of cohesionless sands (PLAXIS, 2019b) at shallow depths. The cohesion value of the sand was increased to values ranging from 0.3 to 25 kPa and the model analyzed for each cohesion value. The increased cohesion, however, did not prevent plastic points from occurring and shear stress results were similar to those obtained with no cohesion. In fact, a cohesion value of 185 kPa was needed to fully prevent plastic points from occurring for model 5-0-5-3; the fact that such a high cohesion value (nearly two atmospheres) was needed to prevent yielding in a very gentle slope indicates that the shallow stresses computed by PLAXIS are not reliable.

A strong effort was made to inhibit the plastic points from occurring. These efforts include, but were not limited to, decreasing the error tolerance, changing the default iteration settings, increasing mesh size, incorporating a plastic nil-step, including tension cut-off, excluding tension cut-off, changing the dilation angle from three degrees to zero degrees, and using six-noded triangular elements instead of 15-noded triangular elements.

5.4.5.2.1 Level Ground Models

Because plastic points had developed in the sloping ground models, a level-ground case was performed to determine whether plastic points would persist for a model without shear stresses. A level ground model with the same overall dimensions as the 5-0-5-3 model was developed. A Mohr-Coulomb model was implemented with the same material parameters (c = 0 kPa), calculation settings, and iteration settings. Level-ground analyses showed that the shear stress was zero and that no plastic points developed. The level-ground stresses from PLAXIS were found to agree with those calculated from basic elasticity theory (Table 5.12).

$$K_o = \frac{\nu}{1-\nu} \tag{5.15}$$

$$\sigma_{yy} = Depth \times \gamma \tag{5.16}$$

$$\sigma_{xx} = \sigma_{zz} = \sigma_{yy} \times K_o \tag{5.17}$$

Although Table 5.12 shows this for a single element (5128) near the ground surface, the stresses also agree at larger depths. Based on the results of level ground case, it was determined to track the response of the stresses in PLAXIS by analyzing infinite slopes of incrementally greater inclination.

Table 5.12. Shallow-depth stresses from PLAXIS compared to calculated stresses using depth and Equations 5.15-5.17 for a level-ground case for Element 5128.

			Plaxis Output			Equations 5.19-5.21			Percent Error		
Stress point	x (m)	y (m)	σ_{xx} (kPa)	σ_{yy} (kPa)	σ_{xy} (kPa)	σ_{xx} (kPa)	σ_{yy} (kPa)	σ_{xy} (kPa)	σ_{xx}	σ_{yy}	σ_{xy}
61525	-59.149	-0.146	-1.063	-2.480	0.000	-1.063	-2.480	0.000	0%	0%	0%
61526	-57.924	-2.020	-14.719	-34.344	0.000	-14.719	-34.344	0.000	0%	0%	0%
61527	-56.678	-0.146	-1.063	-2.480	0.000	-1.063	-2.480	0.000	0%	0%	0%
61528	-58.300	-0.576	-4.199	-9.798	0.000	-4.199	-9.798	0.000	0%	0%	0%
61529	-57.919	-1.159	-8.446	-19.708	0.000	-8.446	-19.708	0.000	0%	0%	0%
61530	-57.531	-0.576	-4.199	-9.798	0.000	-4.199	-9.798	0.000	0%	0%	0%
61531	-58.806	-0.718	-5.228	-12.198	0.000	-5.228	-12.198	0.000	0%	0%	0%
61532	-58.313	-1.472	-10.721	-25.016	0.000	-10.721	-25.016	0.000	0%	0%	0%
61533	-57.529	-1.472	-10.721	-25.016	0.000	-10.721	-25.016	0.000	0%	0%	0%
61534	-57.028	-0.718	-5.228	-12.198	0.000	-5.228	-12.198	0.000	0%	0%	0%
61535	-57.416	-0.123	-0.895	-2.089	0.000	-0.895	-2.089	0.000	0%	0%	0%
61536	-58.410	-0.123	-0.895	-2.089	0.000	-0.895	-2.089	0.000	0%	0%	0%

5.4.5.2.2 Infinite Slope Models

Figure 5.31 shows the geometry of the infinite slope models in PLAXIS, albeit at an exaggerated slope angle. Infinite slope angles of 0.5, 1, 2, and 3 degrees were analyzed and the resulting stresses checked with a vertical cross-section at δ = 0. The Mohr-Coulomb constitutive model was used with a cohesion of 5 kPa, and a Poisson's ratio of 0.49 to reduce locked-in stresses (i.e. due to the difference between σ_{xx} and σ_{yy}). Other material and stiffness parameters, along with the calculation and iteration settings, were the same as previous analyses. It was expected that non-zero shear stresses would start to develop, but the vertical stresses would be similar to those for the level-ground case. For brevity, only the results of the 0.5- and 3-degree infinite slope models will be presented, although the results were similar between all of the infinite slope analyses.

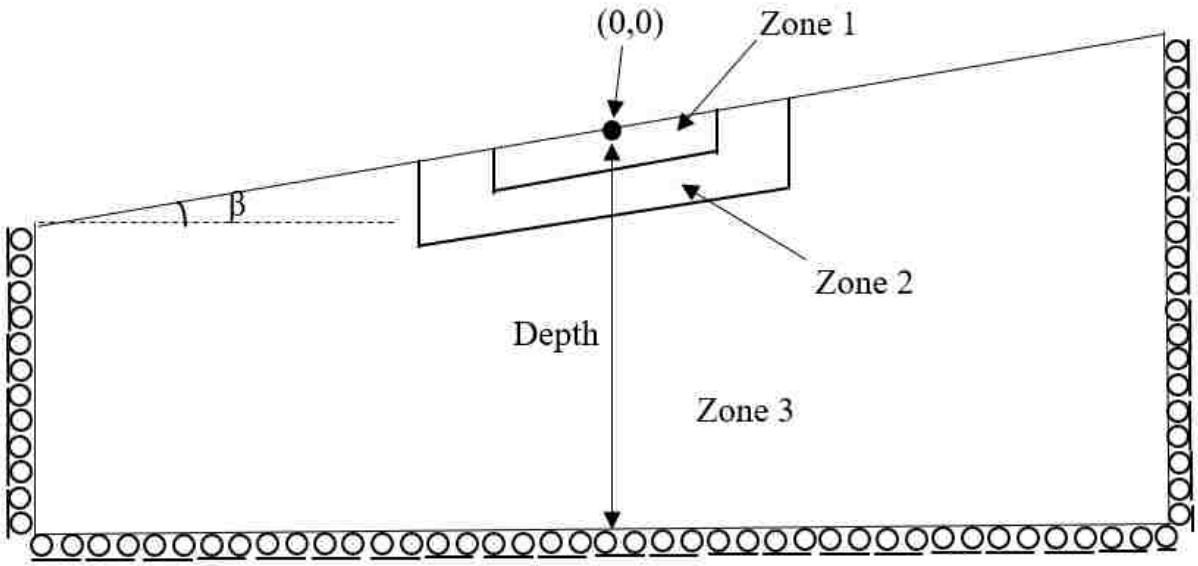

Figure 5.31. General form of infinite slope geometry modeled in PLAXIS.

Analyses of the 0.5- and 3-degree infinite slope models produced plastic points near the ground surface and the non-uniform shear stress distribution previously observed in the analysis of profile 5-0-5-3. For example, Figure 5.32 shows the non-uniform shear stress distribution for the three-degree infinite slope case. To determine if the shear stresses in this region of interest output by PLAXIS were correct, the vertical stress, shear stress, and SSR from the PLAXIS results are compared to the vertical stress, shear stress, and SSR calculated using the equilibrium equations for the exact solution of an infinite slope given by Cruikshank (2002).

$$\sigma_{yy} = \gamma * Y * cos(\beta) \tag{5.18}$$

$$\sigma_{xy} = \gamma * Y * sin(\beta) \tag{5.19}$$

$$SSR = \frac{\sigma_{xy}}{\sigma_{yy}} = tan(\beta) \tag{5.20}$$

Figures 5.33-5.35 compare the PLAXIS stress values with those obtained by the infinite slope equilibrium equations (ISEE) for 0.5- and 3-degree infinite slope models along vertical cross sections at δ = 0.

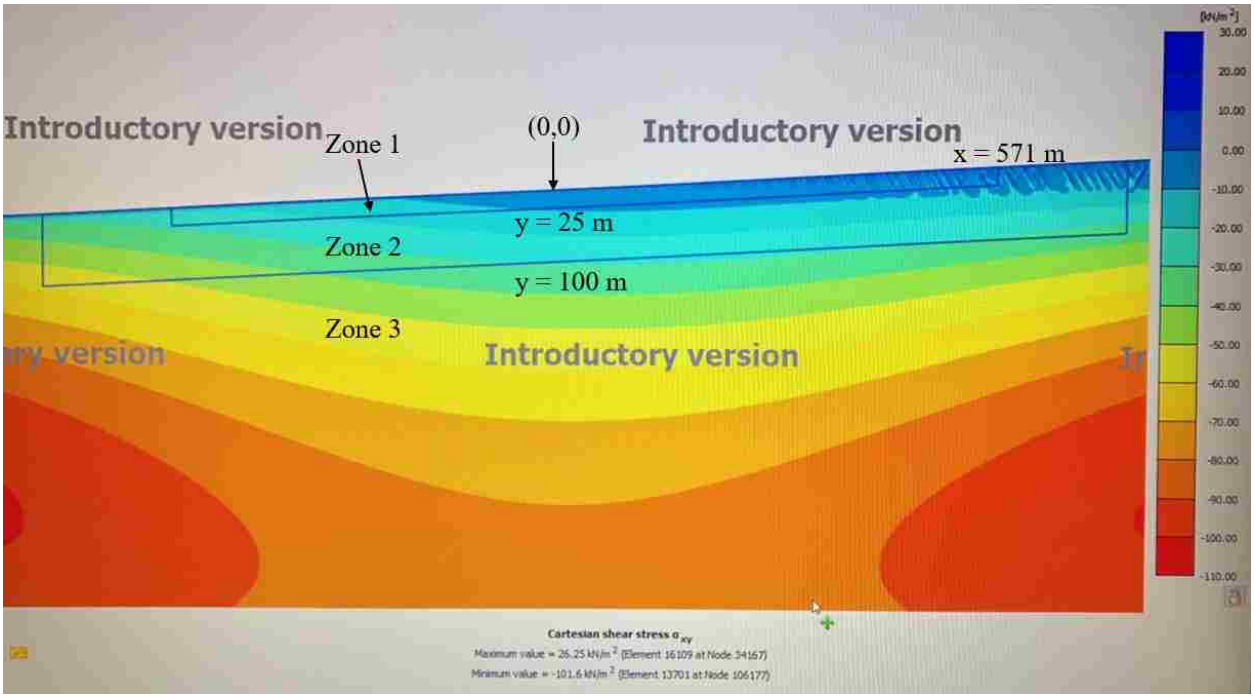

Figure 5.32. Shear stress distribution for a three-degree infinite slope.

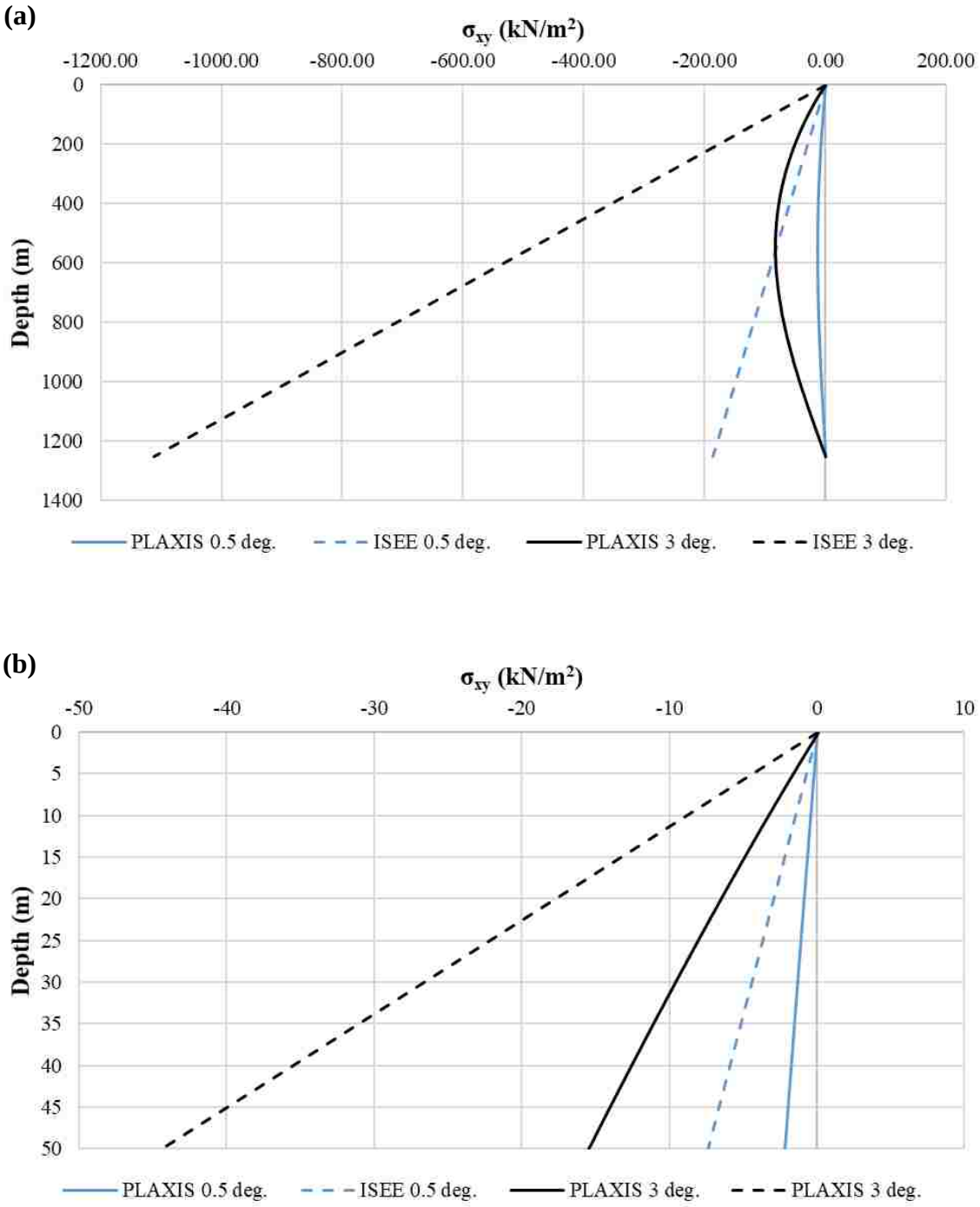

Figure 5.33. Comparing PLAXIS and ISEE shear stress versus depth at $\delta = 0$ for infinite slope angles of 0.5- and 3-degrees where (a) shows the entire model and (b) shows the shear stress near the ground surface.

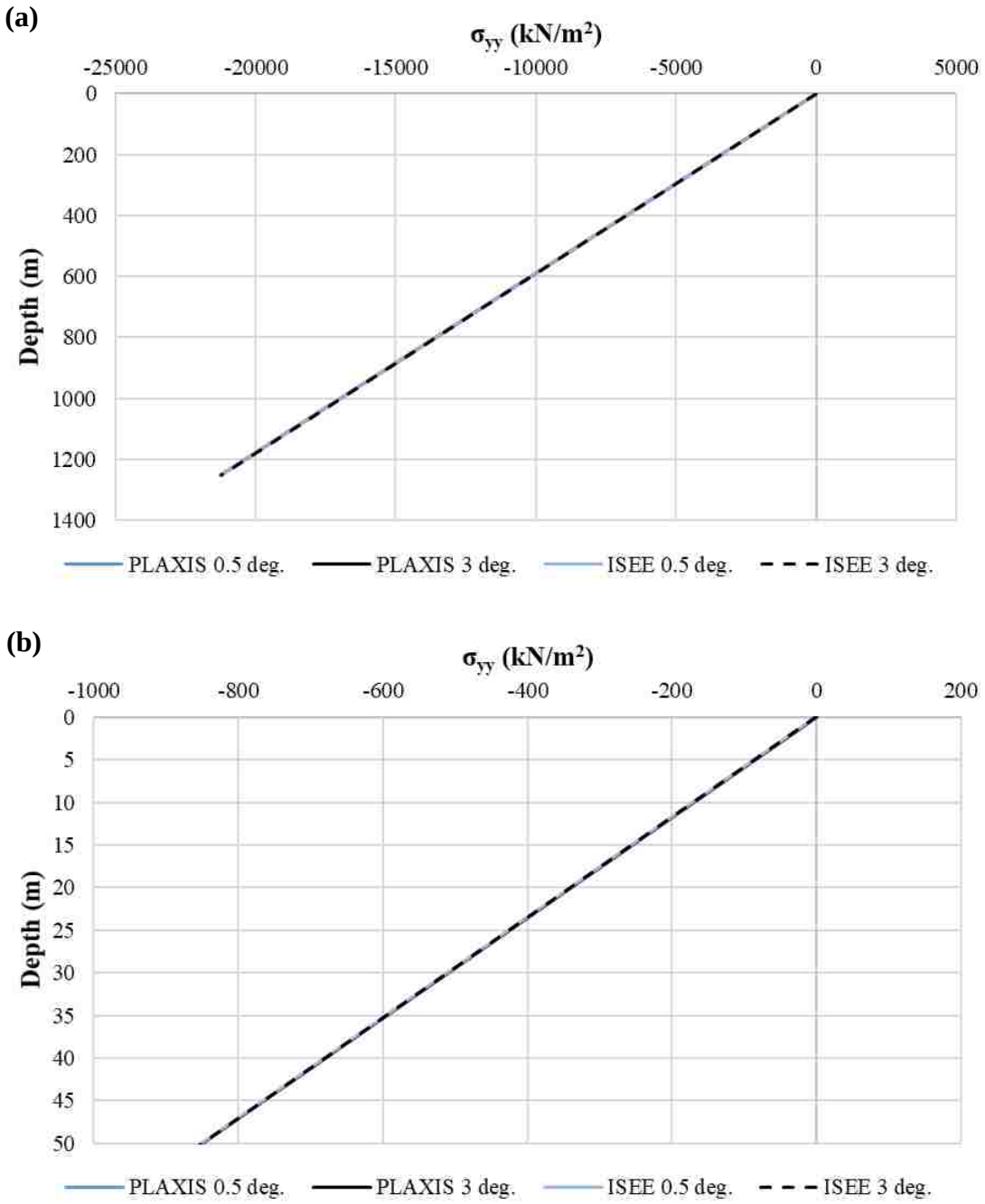

Figure 5.34. Comparing PLAXIS and ISEE vertical stress versus depth at δ = 0 for infinite slope angles of 0.5- and 3-degrees where (a) shows the entire model and (b) shows the vertical stress near the ground surface.

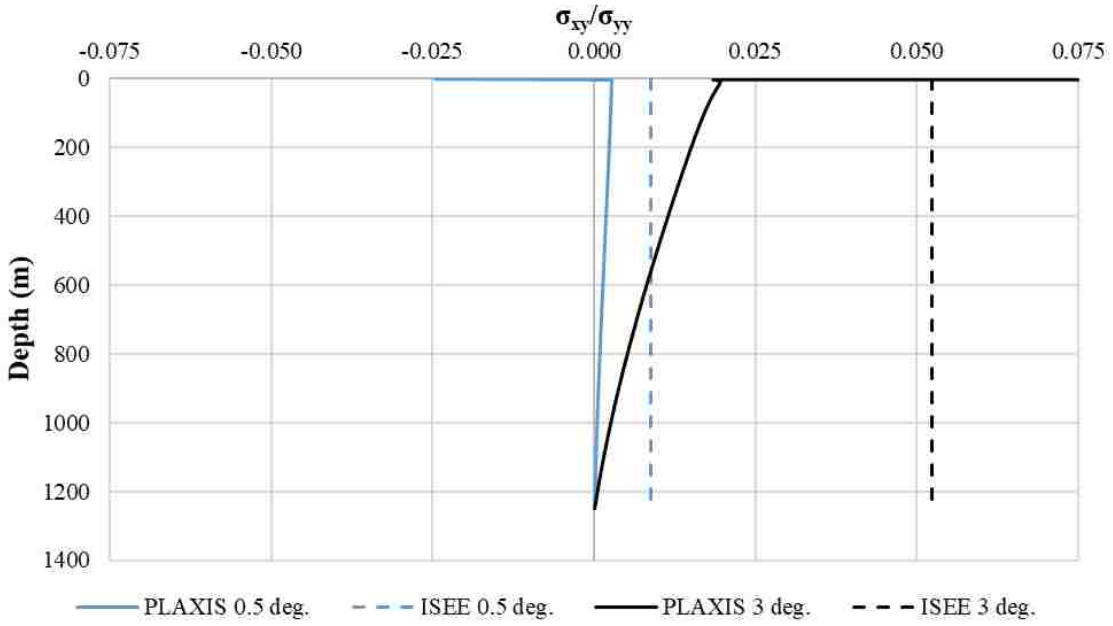

Figure 5.35. Comparing PLAXIS and ISEE SSR versus depth at δ = 0 for infinite slope angles of 0.5- and 3-degrees. The 3-degree PLAXIS results exclude a very high negative SSR value of 17 near the ground surface.

Figures 5.33-5.35 show significant differences in the stresses calculated via PLAXIS and those calculated from the ISEE. Figure 5.33 shows that the difference in shear stress begins immediately at shallow depths. Figure 5.34, however, shows that the vertical stresses calculated by PLAXIS and the ISEE agree for the entire depth of the cross-section at δ = 0. Figure 5.35, therefore, confirms that the stress ratios calculated by PLAXIS and the ISEE do not agree. At the ground surface (η = 0) PLAXIS computes σ_{yy} = 0.00514 kPa and σ_{xy} = 0.0873 kPa, which result in a stress ratio of approximately 17, which is excluded from Figure 5.35b.

Because of these results, further comparisons between the PLAXIS results and the ISEE were performed at the element level. Four soil elements were chosen from the three-degree infinite slope model as shown in Figure 5.36. Figure 5.37 shows typical locations of stress points within an element.

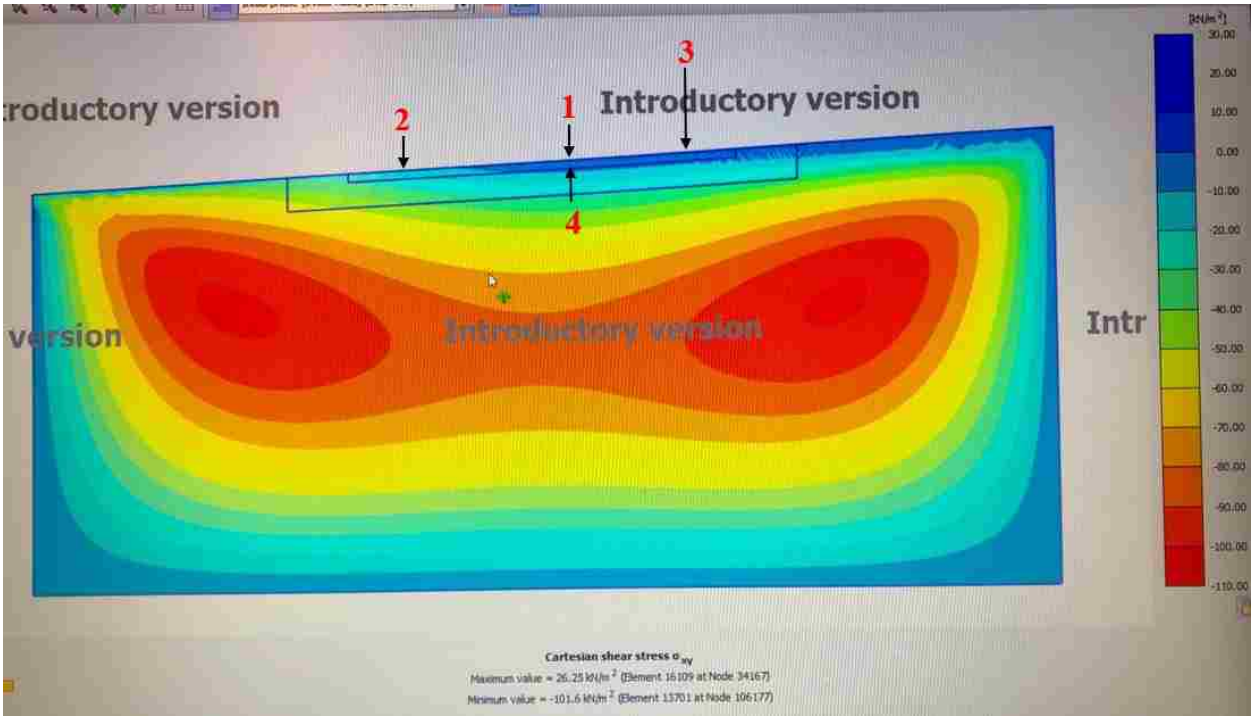

Figure 5.36. Shear stress distribution for the three-degree infinite slope model with four soil element general locations noted.

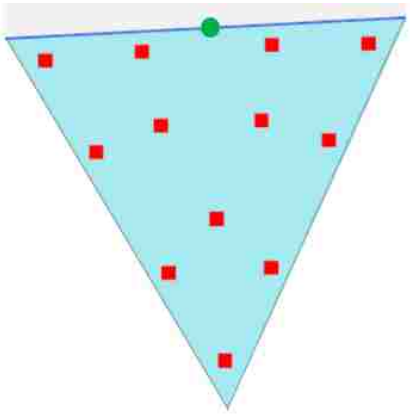

Figure 5.37. Example locations of stress points (squares) within an element.

The ISEE results were calculated using Equations 5.18-5.20 where the "Y" value in these equations is termed y_{BGS}, the vertical distance a stress point is below the ground surface. Because the model is sloping, y_{BGS} is calculated from the y-coordinate of each stress point output from PLAXIS, y, and the y-coordinate of the ground surface, y_{GS}, as follows:

$$y_{BGS} = \begin{cases} y_{GS} - y & for\ x > 0\ and\ y > 0 \\ y_{GS} + y & for\ x > 0\ and\ y < 0 \\ y - y_{GS} & for\ x < 0 \end{cases} \quad (5.21)$$

where careful attention to the coordinate system is needed to determine whether the value of y_{GS} and y are positive or negative. For clarity, the calculation of y_{BGS} is shown for an exaggerated slope angle in Figure 5.38

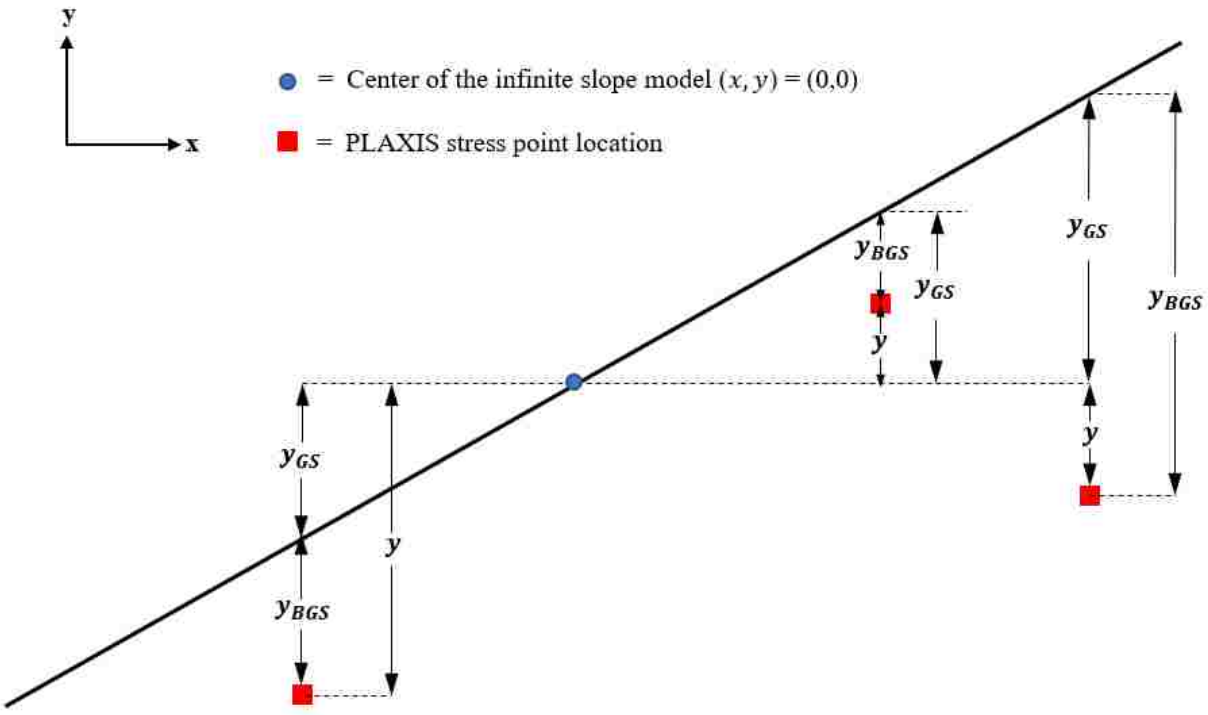

Figure 5.38. Illustration defining the variables y, y_{GS}, and y_{BGS} at different locations beneath an infinite slope.

To compare the PLAXIS and ISEE results percent error is used which is given as

$$\%\ error = \frac{|Plaxis_{value} - ISEE_{value}|}{|ISEE_{value}|} \times 100 \quad (5.22)$$

Soil Element 1

Soil Element 1 is located at the center of the model with coordinates (x, y) = (0,0). The center of the model at the ground surface should be the least influenced region of the model from boundary conditions and is one of the two chosen soil elements (out of the four) that did not have any plastic

stress points (i.e., all points remained elastic). Table 5.13 shows the PLAXIS and ISEE results for Soil Element 1. Examining the percent error in Table 5.13, one can see the σ_{yy} values are very similar between the PLAXIS and ISEE results, however, the σ_{xy} and SSR values are significantly different with error values ranging from about 65% to 137%. Figure 5.39 shows the shear stress contours for Soil Element 1. Detailed analysis of Soil Elements 2-4 is included in Appendix C and is excluded here for brevity, however, the results of all four elements will be discussed.

Table 5.13. Comparison of PLAXIS and ISEE stresses for Soil Element 1 of the three-degree infinite slope.

Location Information					**PLAXIS Output**			**ISEE**			**Percent Error**		
Stress point	x (m)	y (m)	y_{GS} (m)	y_{BGS} (m)	σ_{yy} (kPa)	σ_{xy} (kPa)	SSR	σ_{yy} (kPa)	σ_{xy} (kPa)	SSR	σ_{yy}	σ_{xy}	SSR
3805	0.141	-2.420	0.007	-2.427	-41.244	-0.750	0.018	-41.207	-2.160	0.052	0.088%	65.275%	65.306%
3806	1.189	-0.113	0.062	-0.175	-2.972	0.058	-0.019	-2.975	-0.156	0.052	0.120%	137.014%	137.058%
3807	-1.169	-0.237	-0.061	-0.175	-2.975	-0.005	0.002	-2.975	-0.156	0.052	0.012%	97.094%	97.094%
3808	0.081	-1.389	0.004	-1.393	-23.664	-0.394	0.017	-23.646	-1.239	0.052	0.075%	68.208%	68.232%
3809	0.407	-0.671	0.021	-0.692	-11.761	-0.143	0.012	-11.756	-0.616	0.052	0.048%	76.809%	76.820%
3810	-0.326	-0.710	-0.017	-0.692	-11.762	-0.162	0.014	-11.756	-0.616	0.052	0.055%	73.780%	73.795%
3811	0.477	-1.743	0.025	-1.768	-30.040	-0.514	0.017	-30.016	-1.573	0.052	0.080%	67.294%	67.320%
3812	0.898	-0.815	0.047	-0.862	-14.643	-0.190	0.013	-14.635	-0.767	0.052	0.053%	75.283%	75.297%
3813	0.483	-0.122	0.025	-0.148	-2.503	0.049	-0.019	-2.506	-0.131	0.052	0.121%	137.144%	137.189%
3814	-0.466	-0.172	-0.024	-0.148	-2.504	0.024	-0.009	-2.506	-0.131	0.052	0.069%	118.035%	118.047%
3815	-0.798	-0.904	-0.042	-0.862	-14.645	-0.232	0.016	-14.635	-0.767	0.052	0.067%	69.723%	69.744%
3816	-0.271	-1.782	-0.014	-1.768	-30.040	-0.532	0.018	-30.016	-1.573	0.052	0.082%	66.174%	66.201%

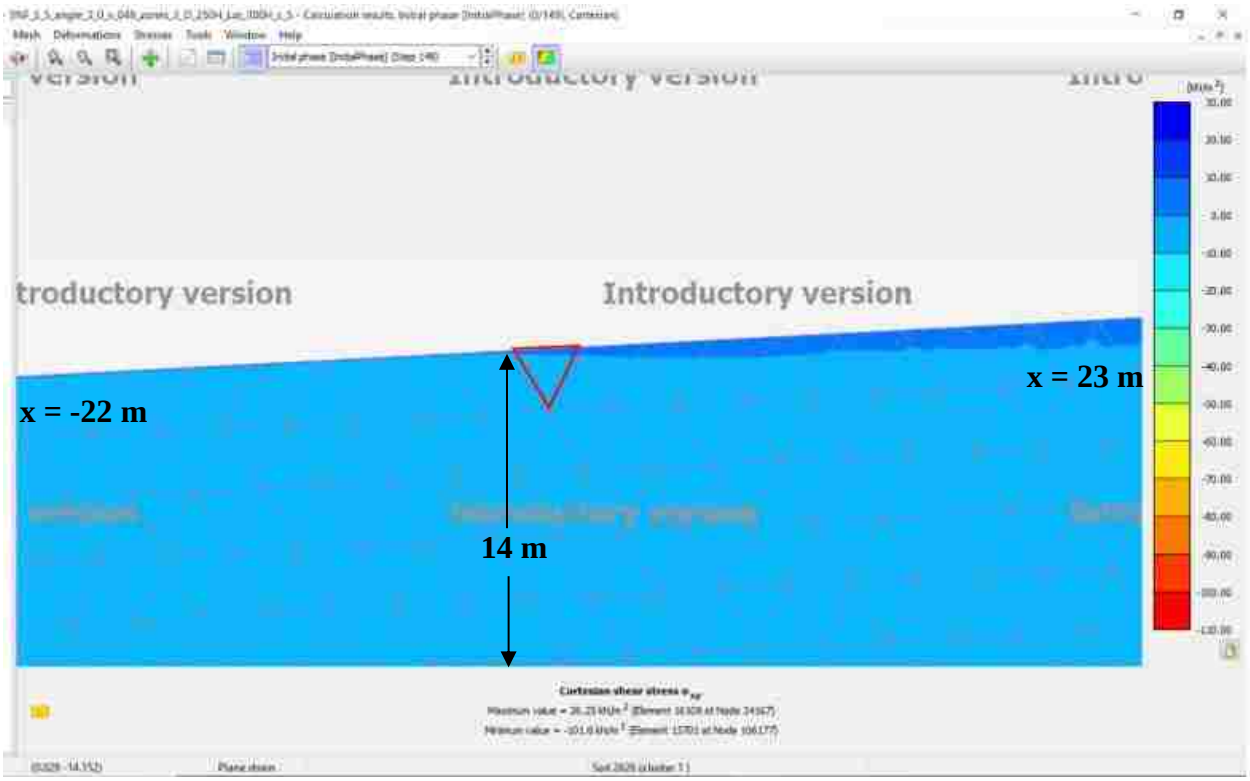

Figure 5.39. Shear stress distribution for the three-degree infinite slope model in the region of Soil Element 1.

Discussion

The difference in PLAXIS and the ISEE infinite slope stress results appear to indicate the stresses calculated in PLAXIS for the infinite slope model are being impacted by the boundary conditions although the models extend 1500 meters in each lateral direction and are 1250 meters in depth from the toe. Analysis of the infinite slope Soil Elements 1-4 shows that areas where plastic points occur (Soil Elements 2 and 3) had larger percent error values for shear stress and SSR than where the behavior was elastic (Soil Elements 1 and 4), although, even where elastic, percent error for shear stress and SSR were at least 60%. The PLAXIS vertical stress values near the center of the model (Soil Elements 1 and 4) were negligibly influenced from the boundary conditions based on the percent error values typically being 0.1% between PLAXIS and ISEE values. Soil Elements 1 and 4 were at the ground surface and a depth of approximately 22 meters,

respectively, indicating vertical stress is negligibly influenced at typical lateral spreading depths at the center of the infinite slope model. The vertical stress for Soil Elements 2 and 3 were influenced by the boundary conditions with percent error values between the PLAXIS and ISEE results ranging from approximately 1-6% for Soil Element 2, and 6-57% for Soil Element 3.

A similar set of analyses were performed by Mr. Long Chen in OpenSees for a three-degree infinite slope model with the same geometry, boundary conditions, material parameters, and stiffness parameters. The OpenSees stress results were similar to the PLAXIS stress results. Therefore, OpenSees results also did not match the stress values obtained by the ISEE equations when modeled that same way as discussed in PLAXIS because of the boundary conditions. However, when simulating a 3-degree infinite slope model in OpenSees by using a level-ground model with gravity applied at an angle of three degrees from the vertical and the boundary conditions shown in Figure 5.40, results matching the ISEE were able to be obtained. Therefore, this suggests that the boundary conditions are the problem with the PLAXIS analyses. The introductory version of PLAXIS does not allow for changing the inclination of gravity from the vertical, therefore, a "simulated" 3-degree infinite slope model was not able to be performed.

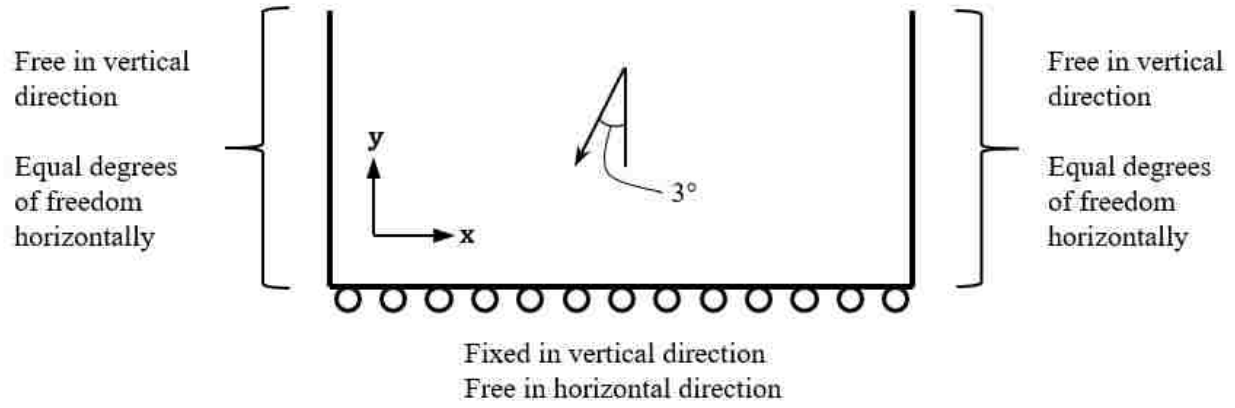

Figure 5.40. Simulated 3-degree infinite slope model used in OpenSees with gravity applied three degrees from vertical.

5.4.5.2.3 SSR Behavior at Shallow Depths

It was previously discussed that a high cohesion value (nearly two atmospheres) was needed to prevent yielding in geometry 5-0-5-3. The fact that yielding occurred pervasively in gentle slopes for which shear stresses should have been well below strengths indicates that the shallow stresses computed by PLAXIS are not reliable. To obtain a better idea of how stresses at shallow depths are behaving, SSR was plotted with respect to δ for η values ranging from 0 to 3 for geometries 5-0-5-3, 5-0-5-0, and 5-0-25-0. Based on the δ-η coordinate system (see Section 5.4.2) η values ranging from 0 to 3 correspond to depths of zero to 15 meters for geometries with an H = 5 meters. Figure 5.41(a) shows unstable complex variations of SSR from $0 < \eta < 0.51$ and Figure 5.41(b) shows reasonable, smooth behavioral trends of SSR when $\eta > 0.51$ for geometry 5-0-5-3. Figure 5.42(a) shows unstable rapid variations of SSR from $0 < \eta < 0.51$ and Figure 5.42(b) shows reasonable, smooth behavioral trends of SSR when $\eta > 0.51$ for geometry 5-0-5-0. The results of 5-0-25-0 were similar to that of 5-0-5-0 as illustrated in Figure 5.43.

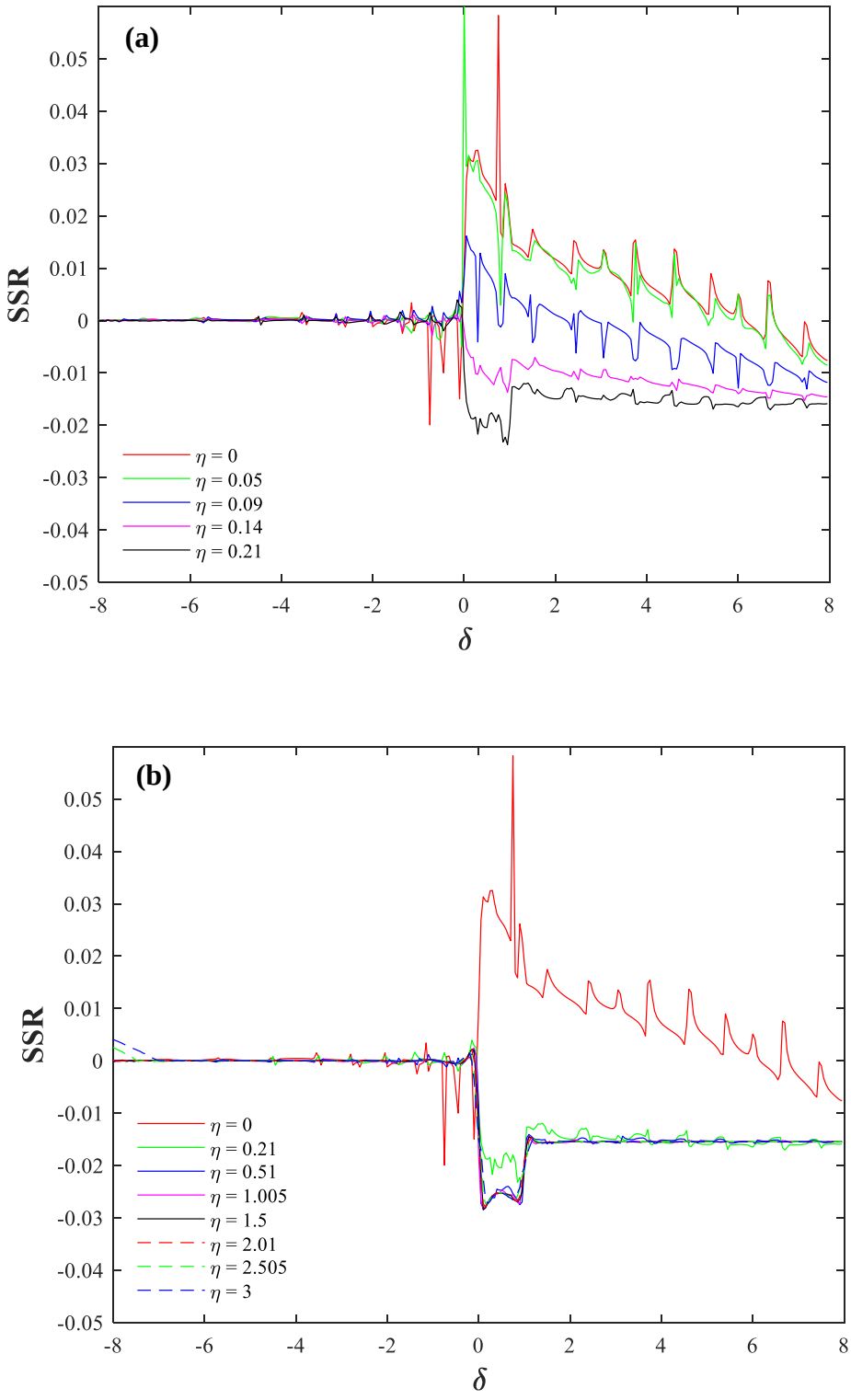

Figure 5.41. Geometry 5-0-5-3 unstable SSR behavior at shallow depths where (a) is equivalent to depths from 0-1 meter and (b) is equivalent to depths of 0-15 meters.

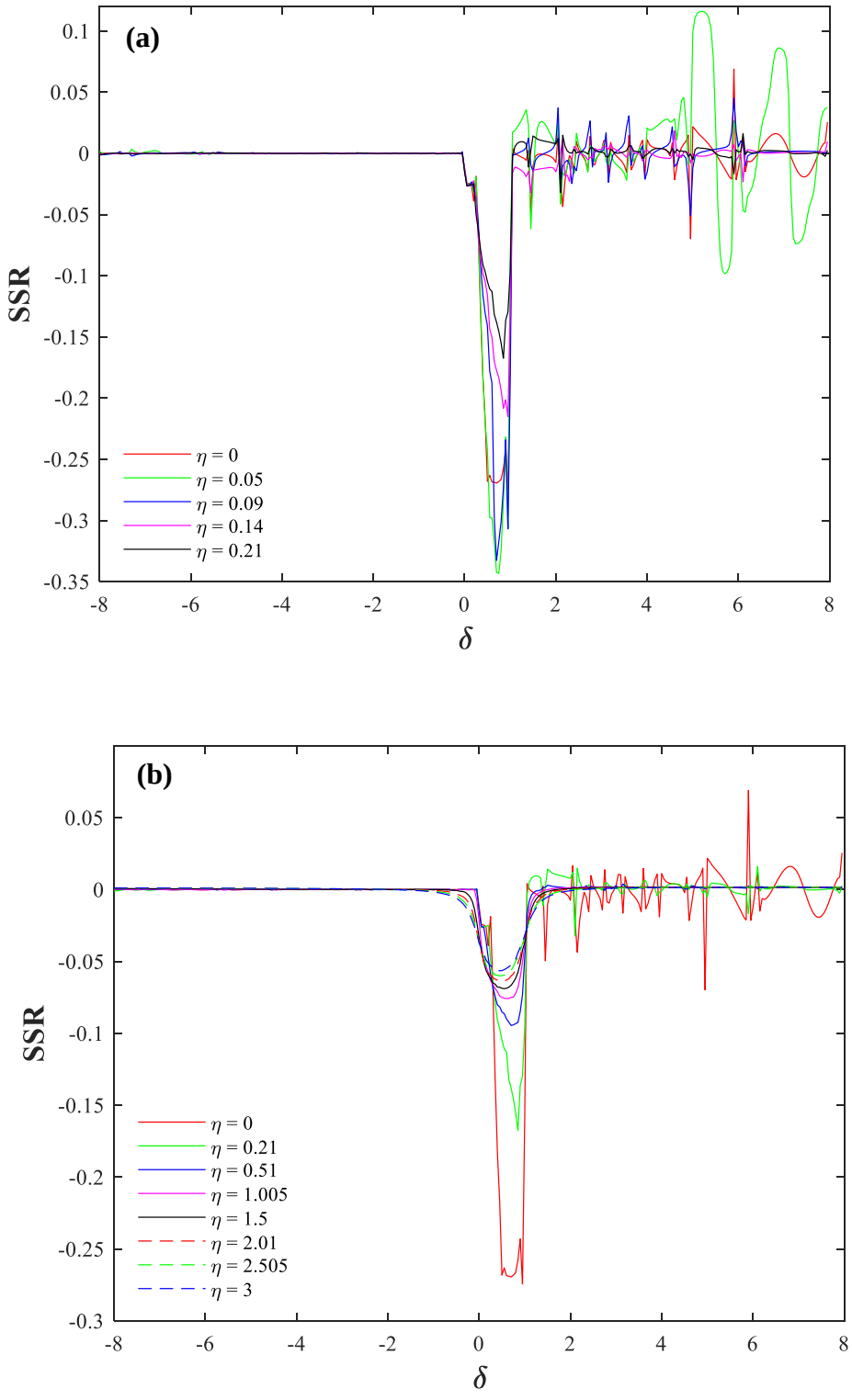

Figure 5.42. Geometry 5-0-5-0 unstable SSR behavior at shallow depths where (a) is equivalent to depths from 0-1 meter and (b) is equivalent to depths of 0-15 meters.

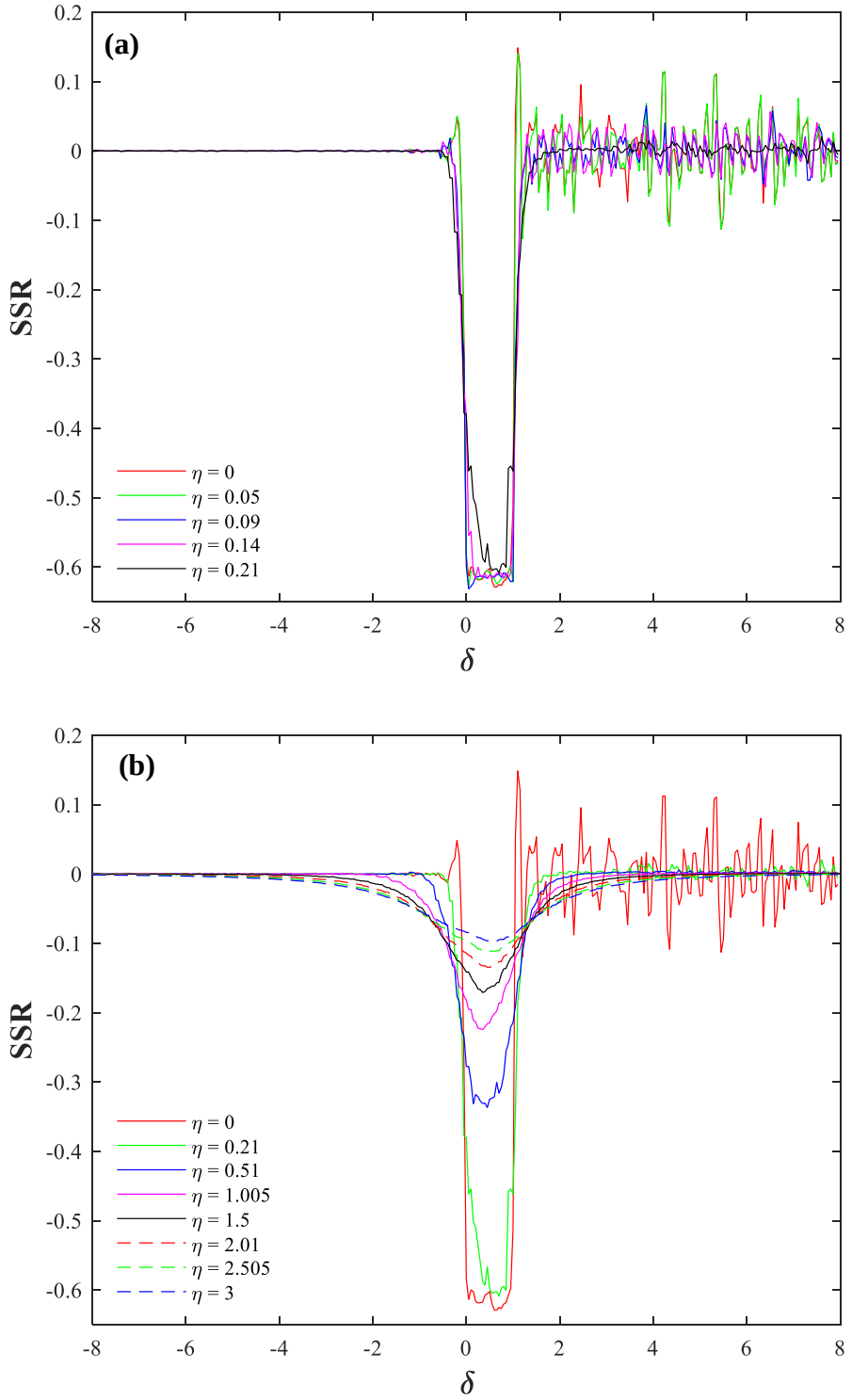

Figure 5.43. Geometry 5-0-25-0 unstable SSR behavior at shallow depths where (a) is equivalent to depths from 0-1 meter and (b) is equivalent to depths of 0-15 meters.

Discussion

Based on Figures 5.41-5.43 the SSR values for $\eta < 0.51$ are variable, and the behavior is complex. The SSR behavior between $\eta = 0.51$ to $\eta = 3$ is simple, and shows reasonable trends, even if the actual values don't agree well with the theoretical solutions. Because $\eta = 0.51$ to $\eta = 3$ represent an important lateral spreading area of interest, developing a function that could predict the static stresses within lateral spreading slopes via the SSR became an achievable task.

5.4.5.2.4 Results of Parametric Analyses

The preceding analyses have shown that there were some significant practical difficulties with the PLAXIS results. These included: (a) apparent unstable behavior at shallow depths, as illustrated in Figures 5.41-5.43, (b) an inability to produce shear stresses that agree with theoretical solutions based on simple limit equilibrium concepts, and (c) apparent effects of boundary conditions despite the very large domain being modeled.

After extensive and time-consuming attempts to understand and correct the deficiencies in the PLAXIS results, the decision was made to shift the focus of the work to developing procedures for fitting a stress function to the reasonable portion of the PLAXIS results, i.e., the stress at $\eta > 0.51$ which, although likely inaccurate, vary in a manner likely to be similar to that anticipated for more accurate analyses. These procedures would then be applied to more accurate finite element analyses performed by a subsequent researcher.

The following pages present typical SSR behavior produced by PLAXIS. These results illustrate the effects of slope height, H, central slope angle, θ_2, and upper slope angle, θ_3, on the vertical and horizontal variation of SSR. The term peak amplitude (Figure 5.44) will be frequently used when describing these results.

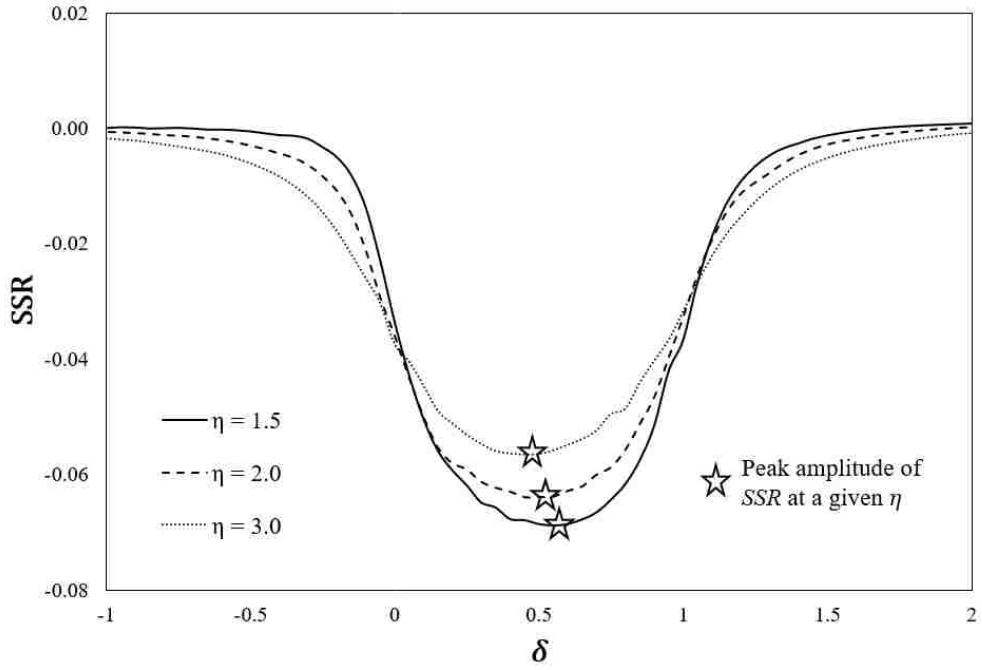

Figure 5.44. Illustration of the term peak amplitude.

Effects of Slope Height on SSR

The SSR represents the shear stress normalized by the vertical stress. One should expect the variation of SSR vertically and horizontally to be the same for slope geometries that have the same θ_1, θ_2, and θ_3, but differing H values if the behavior of the stresses are linear elastic. To illustrate the effects of H on the SSR, geometries 1-0-5-0, 5-0-5-0, 1-0-25-0, and 5-0-25-0 are given in Figure 5.45. These figures indicate:

(1) There is no effect of H on the SSR since the material is behaving linear elastically,

(2) The peak amplitude of SSR is largest at smaller values of η,

(3) SSR widens laterally with increasing η,

(4) SSR increases vertically with increasing θ_2.

Because there is no effect of H on the SSR only the H = 5 meters geometries will be shown in the remainder of this thesis.

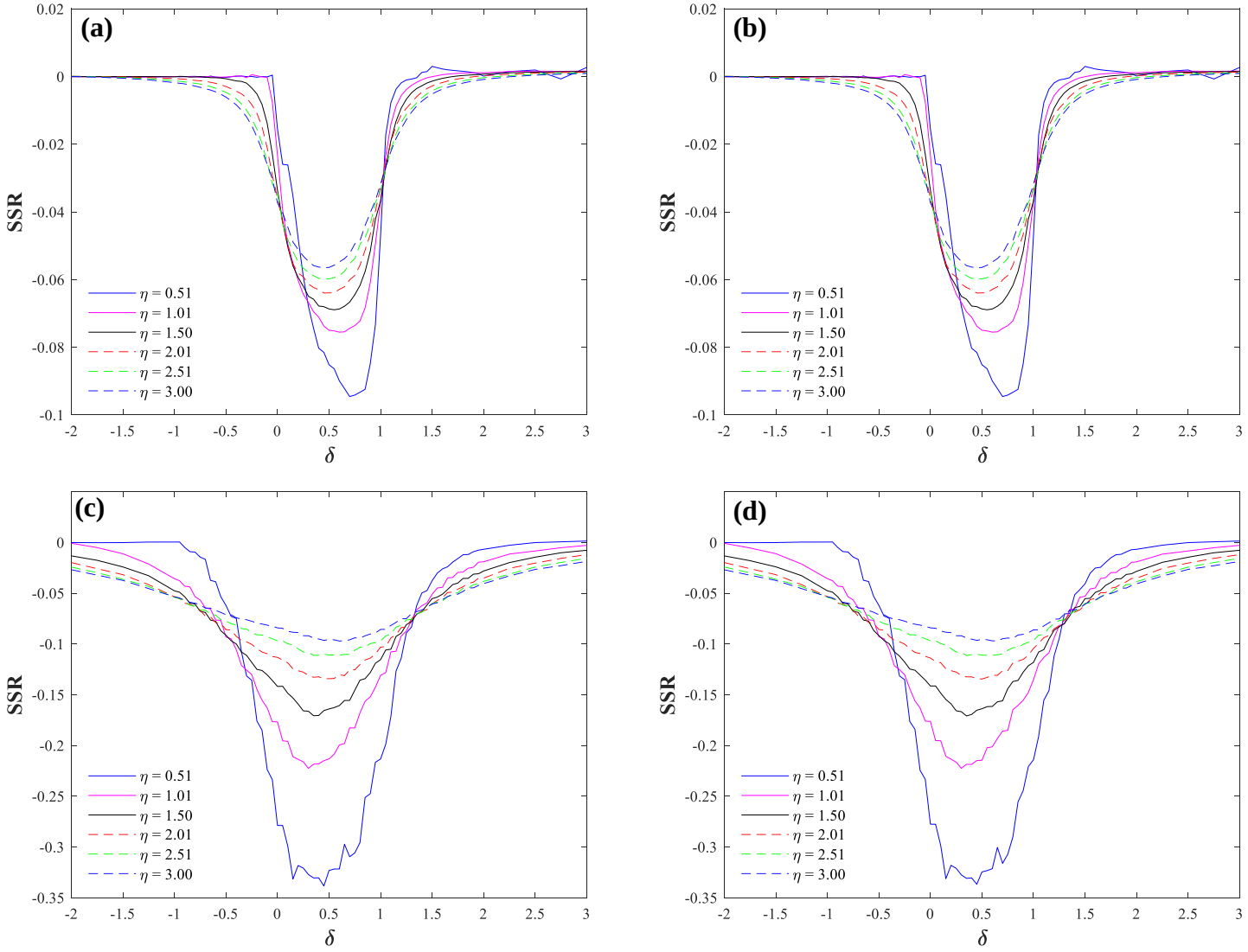

Figure 5.45. Geometries (a) 1-0-5-0, (b) 5-0-5-0, (c) 1-0-25-0, and (d) 5-0-25-0 illustrating that changing the slope height for a given θ_1, θ_2, and θ_3 does not change the SSR.

Effects of central slope angle, θ_2, on SSR

To visualize the effects of θ_2 on the SSR, geometries with different θ_2 values, but identical θ_1 and θ_3 values, were compared. Figure 5.46 shows the 5-0-X-0 (where X = 5, 10, 15, 20, and 25) geometries at η = 0.51 and η = 2.01 to cover a range of depths. These plots indicate:

(1) SSR increases with increasing θ_2,

(2) SSR widens laterally with increasing η,

(3) The peak amplitude of SSR is largest at smaller values of η,

Further interpretation of Figure 5.46 indicates that θ_2 may vary as a power function with respect to SSR based on the distance between successive θ_2 values.

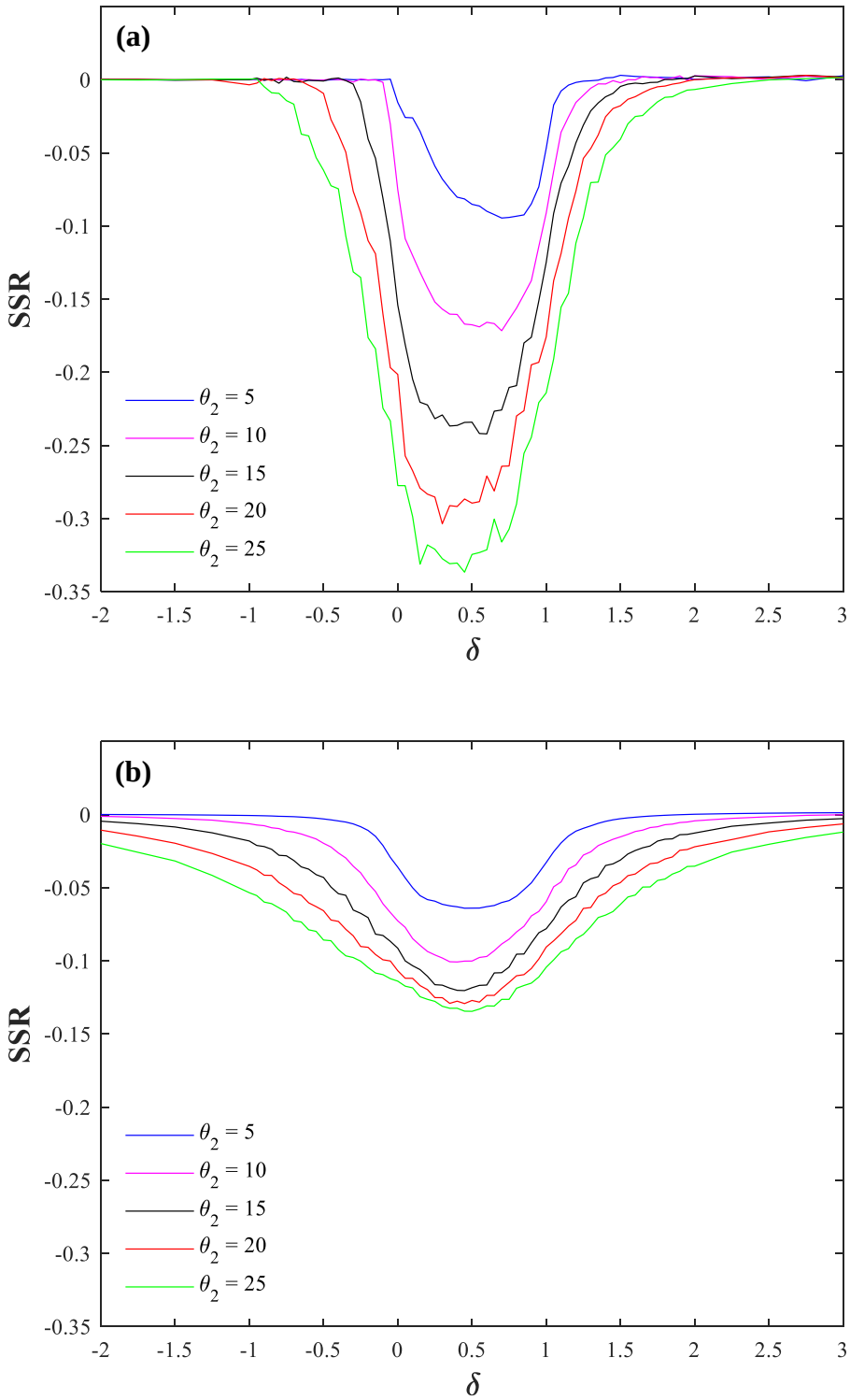

Figure 5.46. Geometry 5-0-X-0 illustrating the effects of changing θ_2 on the SSR for a given θ_1 and θ_3 for (a) η = 0.51 and (b) η = 2.01.

Effects of upper slope angle, θ_3, on SSR

To determine the effect of θ_3 on the SSR, geometries with varying θ_3 values, but identical θ_1 and θ_2 values, were compared. Figure 5.47 shows the 5-0-15-Y (where Y = 0, 1, 3, and 5) geometries at η = 0.51 and η = 2.01 to cover a range of depths. These plots indicate:

(1) The amplitude of SSR appears to drop quickly as soon as $\theta_3 > 0$ between $0 < \delta < 1$

(2) SSR is nearly constant in the lower and central slope regions for $\theta_3 > 0$,

(3) SSR increases in a linear fashion with increasing θ_3 in the upper region of the slope,

(4) The addition of a $\theta_3 > 0$ value causes the SSR to decrease beneath the central slope region,

(5) SSR widens laterally with increasing η.

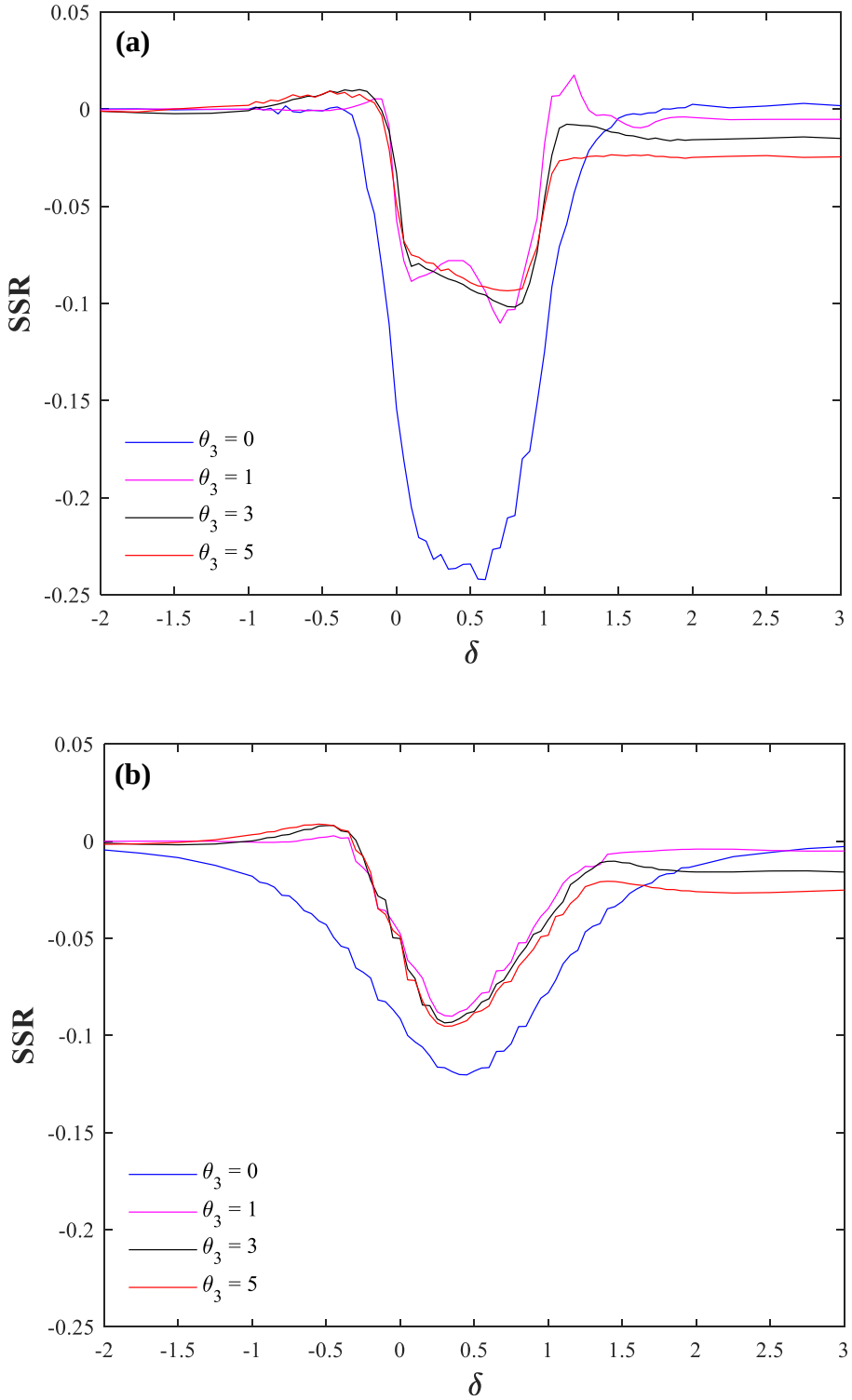

Figure 5.47. Geometry 5-0-15-Y illustrating the effects of changing θ_3 on the SSR for a given θ_1 and θ_2 for (a) η = 0.51 and (b) η = 2.01.

5.4.6 Mapping Stresses to Regular Grid

There are aspects of the PLAXIS response that could not be captured (infinite slope cases and shear stress at shallow depths), however, the model is considered to have captured the most important trends in the stresses within deeper parts of a slope. The results of the analyses were therefore processed in a manner that would expedite development of a predictive relationship for SSR. Because PLAXIS uses triangular elements that can be oriented irregularly for different slope geometries, it was considered advisable to improve consistency of the computed stresses across different geometries by mapping the computed stresses for each geometry to a consistent and regular grid in δ-η space. Figure 5.48 illustrates the grid, which is refined in the area of greatest interest.

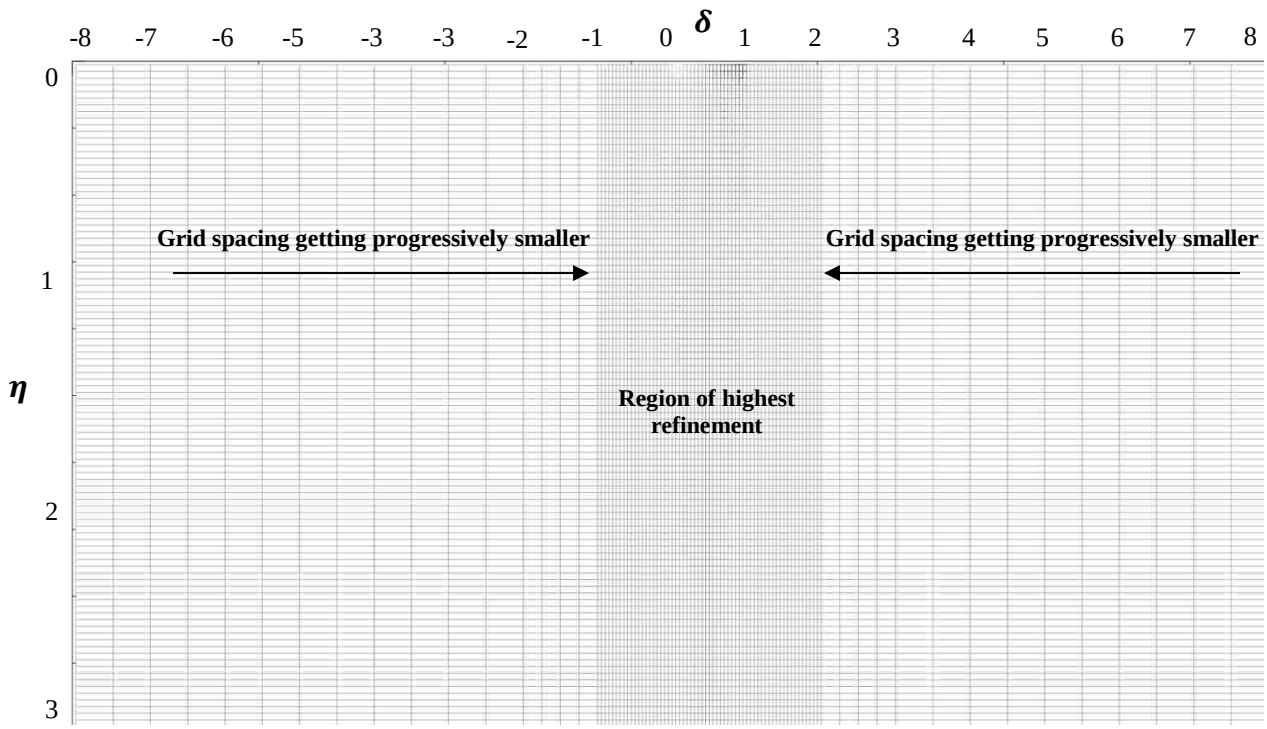

Figure 5.48. Grid used for mapping stresses with higher refinement in the area of greatest interest (area under/near the central slope segment).

Because the values of δ and η at PLAXIS stress points did not coincide with regular grid points, stress values at the grid points had to be interpolated. The mapping procedure was based

on inverse distance weighting (IDW), which assigns weighting factors inversely proportional to their distances from PLAXIS stress points. Therefore, the stress at each grid point had contributions from all PLAXIS stress points. However, only the PLAXIS stress points close to each grid point have a significant impact on the target stress value, σ_{target}, so PLAXIS stress points beyond a radius of two meters were not used in the interpolation process. Equation 5.23 shows the IDW factors used to calculate the σ_{target} values

$$\sigma_{target} = \frac{\sum_{i=1}^{n}\left(\frac{\sigma_i}{D_i^p}\right)}{\sum_{i=1}^{n}\left(\frac{1}{D_i^p}\right)} \tag{5.23}$$

where σ_i is the stress ratio at a PLAXIS stress point, D_i is the distance from σ_i, and p is a power that dictates the rate of decay of the weighting factor with distance. A higher value of p will cause a higher rate of decay with distance.

In order to accomplish these tasks, the PLAXIS stress data including x and y coordinate locations of stress points, vertical stress, horizontal stress, shear stress, and geometry identification number were extracted to Microsoft Excel and Matlab Code "*load data"* (see Appendix D) executed to create a .mat file. The .mat file was then read into Code *"Coordinate Transformation"* (Appendix D) to transform the PLAXIS x-y coordinates into the δ-η dimensionless coordinate system. Code *"Mapping Stresses to Regular Grid"* (Appendix D) was then executed to map the stresses from the irregularly distributed PLAXIS stress points to the uniform grid and then refine this grid to provide higher resolution of stresses in areas where they changed more quickly.

5.4.7 Development of Stress Function

The results of the non-linear analyses presented in Figures 5.45-5.47 indicated a generally regular variation of SSR within and beneath the simple slopes considered in this research. Examination of the results of the PLAXIS analyses showed that the distributions of SSR exhibited the following characteristics:

(1) SSR values were constant beneath the outer portions of the left and right slope segments. The values were zero when those slopes were level and increased with increasing slope angle when they were not.

(2) SSR values increased with increasing central slope angle when it was steeper than the left or right slopes.

(3) SSR values decreased with increasing depth beneath the central slope segment.

(4) The distribution of SSR at a particular depth became wider with increasing depth.

(5) The distribution of SSR at a particular depth was able to be relatively symmetric or asymmetric.

(6) SSR was nearly constant beneath the left and central slope segments for $\theta_3 > 0$.

(7) SSR values increased in a linear fashion with increasing θ_3 beneath the right slope segment.

(8) SSR values beneath the central slope decreased with increasing θ_3.

These characteristics required identification of a stress function that had the capability of representing this type of behavior. After consideration of a number of possible functions, a two-part function was established. One part took the form of a sigmoidal function that could transition smoothly from one constant value to another; this function, henceforth termed the filter function, was used to model the generally constant SSR values beneath the left and right slopes. The second

part took the form of a four-parameter beta distribution function, which gives the ability to control its amplitude, width, and symmetry.

The four-parameter beta distribution consists of two shape parameters, α and β, and the minimum and maximum bound parameters, δ_{min} and δ_{max}, which represent the lateral extent of the distribution. The beta distribution is undefined beyond its bounding values. The general form of the four-parameter beta distribution can be expressed as

$$B_D = \left[(\delta - \delta_{min})^{(\alpha-1)}(\delta_{max} - \delta)^{(\beta-1)}\right] \tag{5.24}$$

In order to validate the four-parameter beta distribution function used to represent the SSR, the predicted values it outputs will be compared to the PLAXIS SSR data. From this point on, the four-parameter beta distribution will be termed B_D.

The B_D consists of four shape-related parameters and its amplitude. Understanding how the parameters of the B_D interact with each other is key in developing a stress function that can match the PLAXIS SSR data. Figure 5.49 shows the predicted B_D compared to the PLAXIS SSR for geometry 5-0-10-0 and illustrates how each parameter influences the shape of the predicted SSR function. The shape of the predicted SSR function changes from Figure 5.49(a) to Figure 5.49(f) by changing one parameter at a time (the other parameters stay constant) while the PLAXIS SSR data does not change. Key observations from Figure 5.49 include:

(1) Decreasing δ_{min} shifts the predicted function to the left and widens the distribution (Figure 5.49b).

(2) Increasing δ_{max} shifts the predicted function to the right and widens the distribution (Figure 5.49c).

(3) When the ratio β/α > 1, the predicted function shifts to the left (Figure 5.49e).

(4) When the ratio β/α < 1, the predicted function shifts to the right (Figure 5.49f).

(5) When $\alpha \neq \beta$ the predicted function becomes asymmetric (Figures 5.49(e) and 5.49(f)).

(6) The δ value where the predicted SSR returns to nearly zero is affected by α and β as well as δ_{min} and δ_{max}.

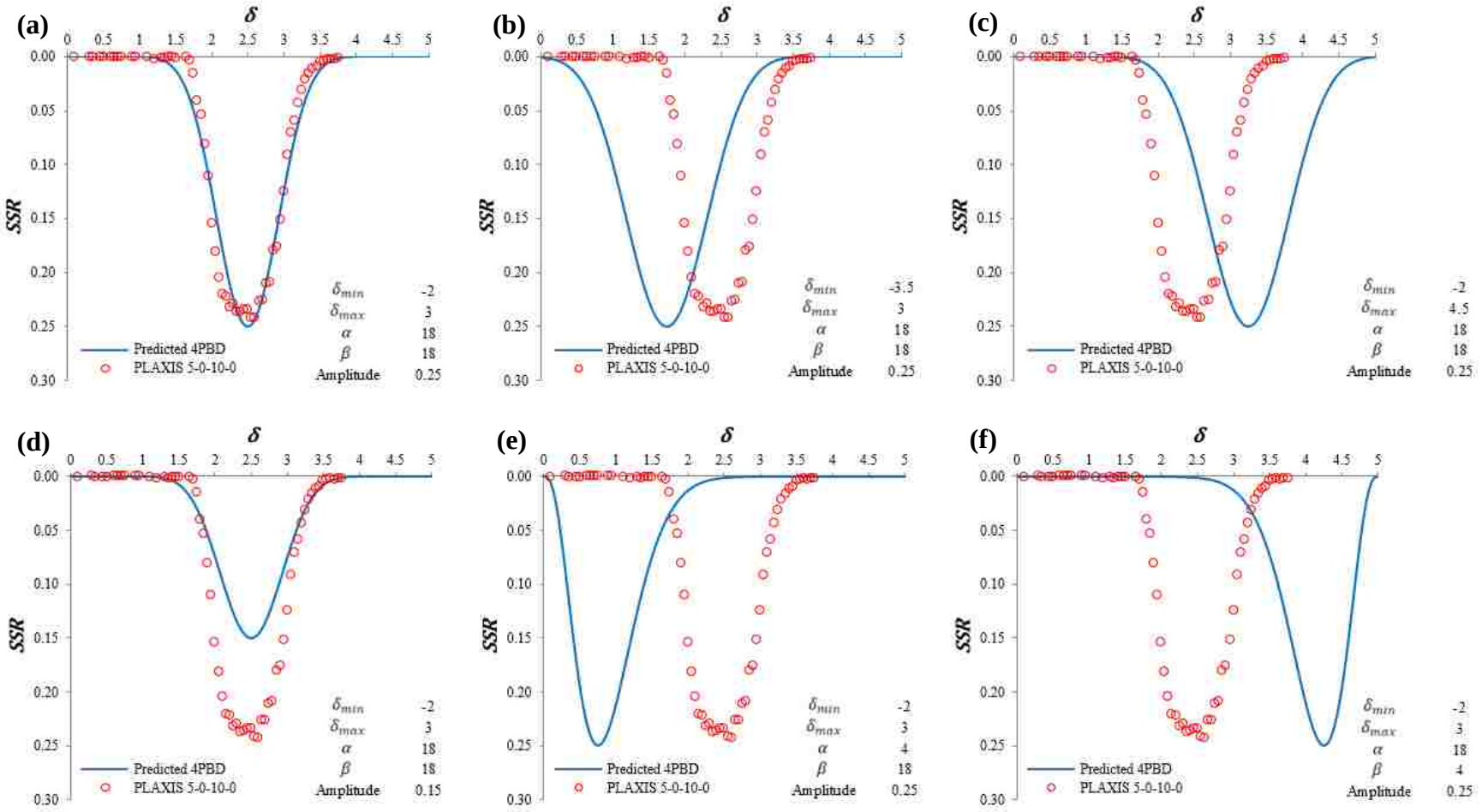

Figure 5.49. Influence of B_D parameters on the shape of the predicted SSR function: (a) control figure, (b) effect of reduced δ_{min}, (c) effect of increased δ_{max}, (d) effect of reduced amplitude, (e) effect of reduced α, and (f) effect of reduced β.

The filter function (FF) is represented by four parameters, c_1-c_4, that define two plateaus and the transition between them. The c_1 parameter defines the center of the transition zone, c_2 controls the steepness of the transition, c_3 defines the left plateau, and c_4 defines the right plateau.

$$FF = c_3 + \frac{(c_4 - c_3)}{\left(1+\left(\frac{c_1}{\delta}\right)^{c_2}\right)} \tag{5.25}$$

The left plateau depends on the left slope segment value of θ_1, which is taken to be zero for all geometries considered in this research, therefore, c_3 is always 0. The right plateau depends on the right slope segment value of θ_3. c_1 parameter needs to ensure that the center of the FF is near the center of the B_D, and c_2 needs to make the FF smoothly transition from the left to right plateau generally within the central slope segment.

5.4.8 Calibration of Stress Function

The variation of SSR on a plane of constant η beneath the central slope segment (e.g., Figures 5.45-5.47) takes the general form of a probability density function (PDF) of δ. If interpreted in that manner, the position and breadth of the δ distribution can be characterized by its mean and standard deviation. If the SSR curves are considered to be approximated by a beta distribution function, the moments of the distribution will be related to the parameters, α, β, δ_{min}, and δ_{max} from Equation 5.24. Specifically,

$$\mu_\delta = \delta_{min} + \frac{\alpha-1}{\alpha+\beta-2}(\delta_{max} - \delta_{min}) \tag{5.26}$$

$${\sigma_\delta}^2 = \frac{\alpha\beta}{(\alpha+\beta)^2(\alpha+\beta+1)}(\delta_{max} - \delta_{min})^2 \tag{5.27}$$

These equations can be used to solve for α and β, i.e.,

$$\alpha = \frac{\left(\frac{\mu_\delta - \delta_{min}}{\delta_{max} - \delta_{min}}\right)^2 \times \left(1 - \frac{\mu_\delta - \delta_{min}}{\delta_{max} - \delta_{min}}\right)}{\frac{{\sigma_\delta}^2}{(\delta_{max} - \delta_{min})^2}} - \frac{\mu_\delta - \delta_{min}}{\delta_{max} - \delta_{min}} \tag{5.28}$$

$$\beta = \frac{\left(\frac{\mu_\delta - \delta_{min}}{\delta_{max} - \delta_{min}}\right) \times \left(1 - \frac{\mu_\delta - \delta_{min}}{\delta_{max} - \delta_{min}}\right)}{\frac{{\sigma_\delta}^2}{\left(\delta_{max} - \delta_{min}\right)^2}} - \alpha \qquad (5.29)$$

Equations 5.28 and 5.29 give shape parameters that are consistent with the moments and the bounds of the PLAXIS SSR distribution.

The mean δ-value typically occurs beneath the central slope segment i.e., with a δ values between 0 and 1. The distribution of δ, however, can be quite broad. For example, the mean stress ratio may be at δ = 0.5 with a standard deviation of 0.35 which would give a coefficient of variation of 70%. High coefficients of variation were found to cause problems when the B_D was used to fit an array of lateral spreading geometries and depths. To correct this, the δ scale was shifted upward by a constant (a value of 2 was found to be sufficient) for all δ values. The shift would increase the mean, but not affect the standard deviation; the coefficient of variation for the previous case would drop from 70% to 14%, which is in a reasonable range for a B_D to be used. For this reason, all of the δ values (i.e., δ values at grid locations) were shifted by 2.0 for all geometries. The shift in δ by a value of 2.0 will be termed δ_{Global}. For example, the central slope segment, prior to a shift of δ_{Global}, ranges from $0 < \delta < 1$. After the shift of δ_{Global} the central slope segment now ranges from $2 < \delta < 3$.

5.4.8.1 Statistical Moments of a PDF

A PDF can be defined in terms of its statistical moments – a specific quantitative measure of the shape of the function. The first three statistical moments are the mean, variance, and skewness. The first moment, the mean, describes the central location of the data and can be expressed as

$$Mean = \mu_\delta = \sum_{all\ j} \left[\delta_j \times PDF_{SSR}(\delta_j)\right] \qquad (5.30)$$

where SSR is the static stress ratio of the PLAXIS data, μ_δ is the central location (mean) of δ, δ_j is the δ increment, and PDF_{SSR} is the PDF of the SSR. The shifted δ value range that the mean is evaluated over is wide enough to encompass when the SSR returns to a constant value beneath the lower and upper slope segments for the desired η range of 0.5 to 3.0.

The second moment, i.e., the variance, represents the spread of the data and can be expressed as

$$Variance = {\sigma_\delta}^2 = \sum_{all\ j} \left[\left(\delta_j - \mu_\delta\right)^2 \times PDF_{SSR}(\delta_j) \right] \tag{5.31}$$

where ${\sigma_\delta}^2$ is the variance of δ. The third statistical moment, the skewness, measures the asymmetry of the PDF about its peak and can be expressed as

$$Skewness = \sum_{all\ j} \left[\left(\delta_j - \mu_\delta\right)^3 \times PDF_{SSR}(\delta_j) \right] \tag{5.32}$$

The statistical moments of a PDF can be used to obtain α and β (without having to solve nonlinear equations) of the B_D if δ_{min} and δ_{max} of the PDF are known. The α and β shape parameters are calculated from the μ_δ, ${\sigma_\delta}^2$, δ_{min}, and δ_{max} using Equations 5.28 and 5.29, respectively. Therefore, because the SSR at each η value takes the general form of a PDF, and the PDF can be used to determine α and β from its statistical moments if δ_{min} and δ_{max} are known at every η, then the predicted B_D can be calculated at each η if δ_{min} and δ_{max} are known at every η. This procedure helps define the values of α and β as functions of η for each case, and can be used as good initial parameter estimates for optimization analyses.

5.4.8.2 Estimating δ_{min} and δ_{max}

To calculate δ_{min} and δ_{max}, the PDF of SSR is integrated to produce an analog to a cumulative distribution function (CDF) at each η. The δ_{min} and δ_{max} are estimated at each η as the δ values that correspond to CDF values of 0.01 and 0.99. Figure 5.50 shows the estimated

values of δ_{min} and δ_{max} at CDF values of 0.01 and 0.99, respectively, for geometry 5-0-10-0 at η = 1.5. PDF and CDF plots like those shown in Figure 5.50 were calculated at all η values in the range of interest (0.51 < η < 3.0). Plotting these estimated δ_{min} and δ_{max} values with respect to η for geometry 5-0-10-0 is shown in Figure 5.51.

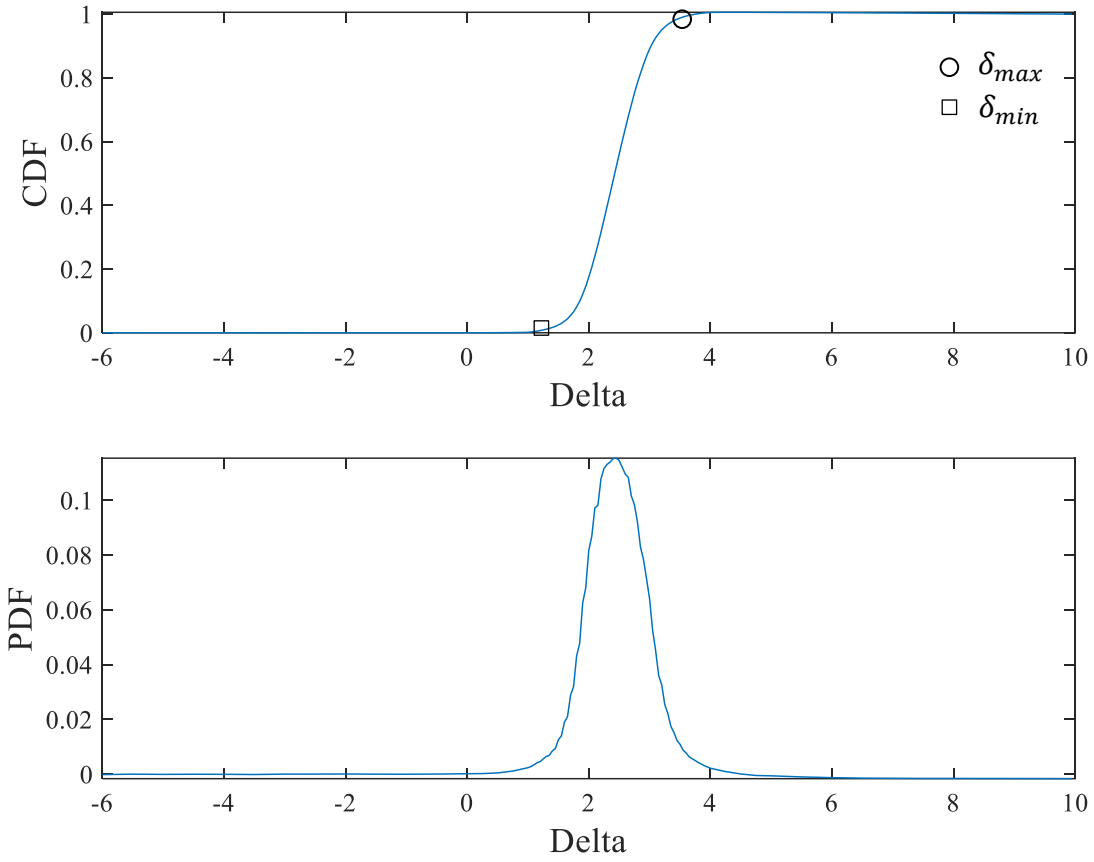

Figure 5.50. CDF and PDF of the PLAXIS stress ratio distribution at η = 1.5 for geometry 5-0-10-0.

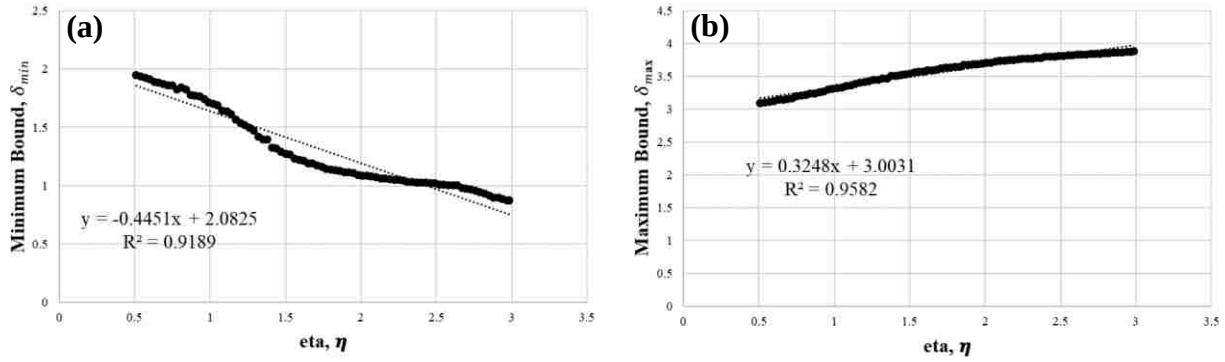

Figure 5.51. B_D parameters (a) δ_{min} and (b) δ_{max} as a linear function of η for geometry 5-0-10-0.

5.4.8.3 Calculation of the Predicted SSR With Respect to η for a Single Geometry

The α and β shape parameters are calculated from the aforementioned μ_δ, ${\sigma^2}_\delta$, δ_{min}, and δ_{max} using Equations 5.28 and 5.29, respectively. The B_D is calculated by inputting these α and β values, along with the δ_{min} and δ_{max} found from the CDF, using Equation 5.24. The predicted B_D can be compared to the PLAXIS data to see how well the predicted function matches it. This requires the PLAXIS SSR data to be normalized by the peak amplitude at each η value to be comparable to the predicted function given by Equation 5.24. Figure 5.52 shows the comparison between the predicted B_D and the PLAXIS SSR data at η values of 1, 1.5, and 2 for geometry 5-0-10-0. The poor fit of the predicted function shown in Figure 5.52 is due to the B_D calculating complex values from δ = 3.35 to δ = 3.7. The complex values occur when the α and/or β parameters have a value less than one.

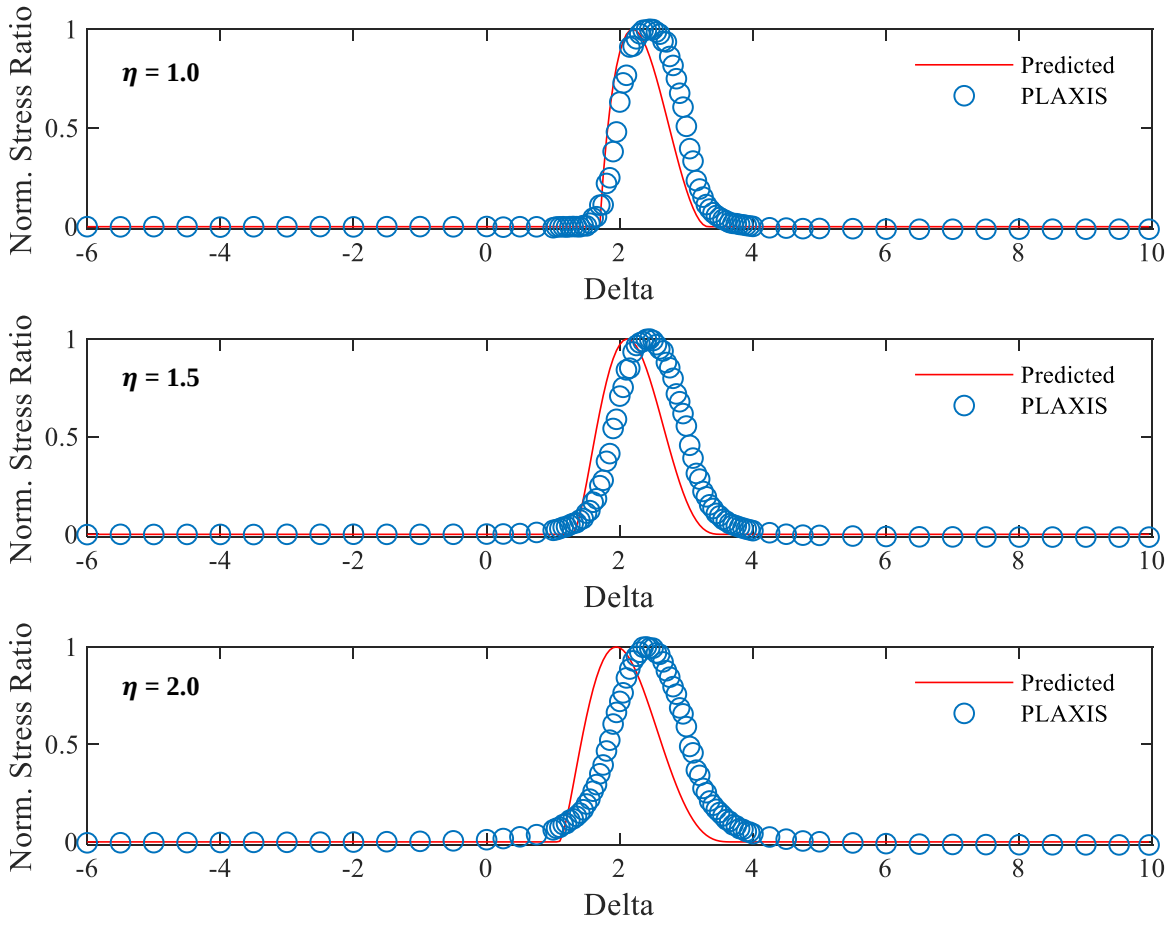

Figure 5.52. Comparison between the predicted B_D and the PLAXIS SSR data at η values of 1.0, 1.5, and 2.0 for geometry 5-0-10-0.

It was determined that additional shifts of the minimum and maximum δ values could be applied to the CDF estimated δ_{min} and δ_{max} values to push the bounds outward to obtain a better match between the predicted SSR and the PLAXIS SSR. The additional shifts, $\delta_{\min\_shift}$ and $\delta_{\max\_shift}$, were added to δ_{min} and δ_{max} causing the α and β shape parameters to change in order to obtain the better fit. Figure 5.53 shows the benefit of the modification for the 5-0-10-0 geometry.

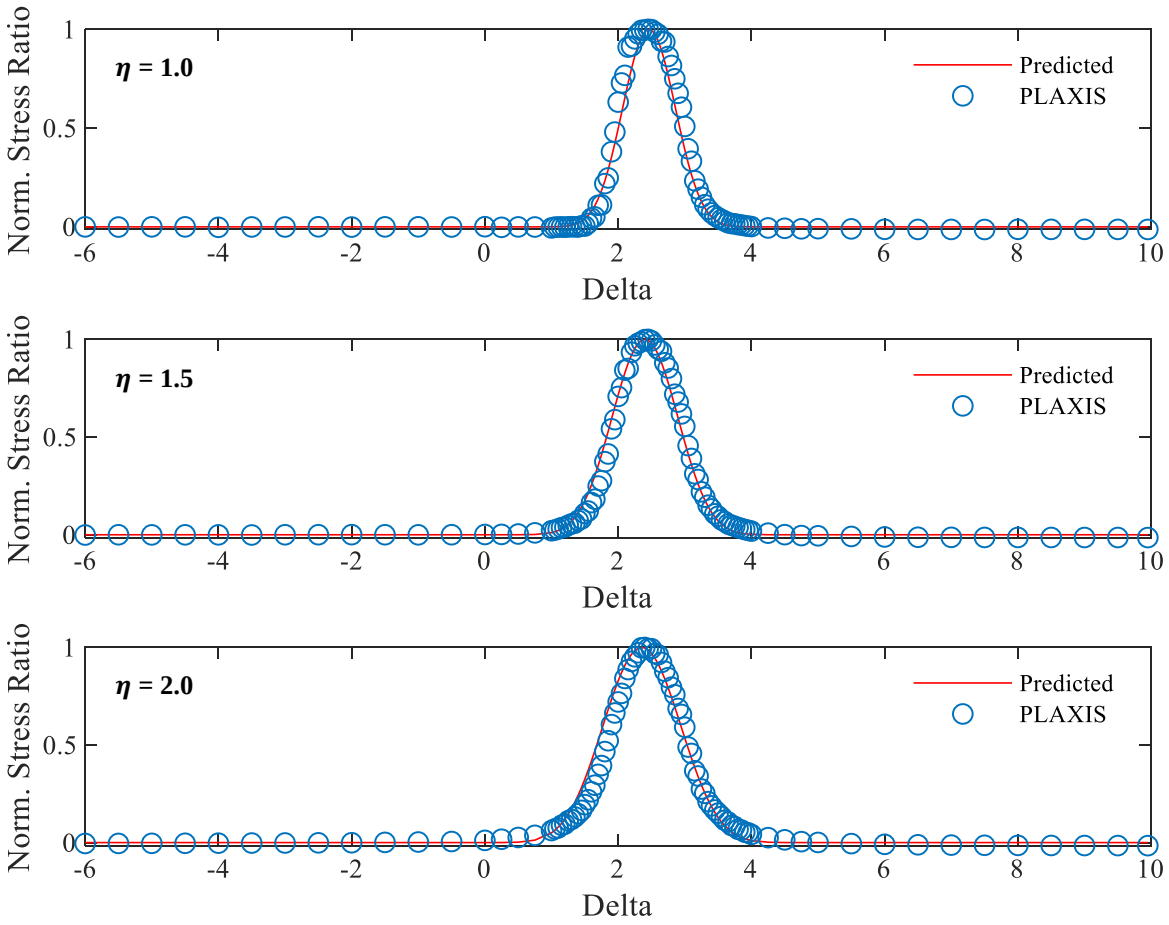

Figure 5.53. Comparison between the predicted B_D and the PLAXIS SSR data at η values of 1.0, 1.5, and 2.0 for geometry 5-0-10-0 with δ_{min_shift} and δ_{max_shift} included.

It should be noted there are several more PLAXIS SSR points plotted in Figure 5.53 than the δ range of -6 to 10 in Equations 5.30-5.32 appear to indicate. This is because: (a) the stress points in mesh zone 1 are spaced approximately one meter apart which corresponds to about 28 stress points (for geometry 5-0-10-0) for every one δ moved laterally and (b) these stress points are interpolated to a regular grid and then mapped to a grid of variable size that is refined in the region of the central slope segment, $1 < \delta < 4$. Figure 5.48 in Section 5.4.6 shows the grid of variable size prior to δ_{Global} shift.

The values for $\delta_{\min\_shift}$ and $\delta_{\max\_shift}$ were found by trial and error for each of the five 5-0-X-0 geometries. The best match, and therefore the best combination of δ_{min}, δ_{max}, α, and β

parameters, was evaluated by a number of factors including plotting and visually inspecting the difference between the PLAXIS SSR and the predicted SSR, and by calculating the coefficient of determination, sum of squared errors, normalized error, and absolute error. It was found that $\delta_{\min\_shift}$ and $\delta_{\max\_shift}$ generally provided a better fit to PLAXIS SSR data as constant values for geometries with lower θ_2 values and a better fit to PLAXIS SSR data as values varying with η for geometries with higher θ_2 values. A more in-depth look at the process of obtaining α and β from the moments of the stress ratio distribution can be referenced in Code *"Moments"*.

5.4.8.4 Calculation of α and β at All η Values for a Single Geometry

After matching the predicted B_D to the PLAXIS data, the α and β values calculated at every depth were plotted in order to develop simple expressions for α and β as functions of η. For example, Figure 5.54 shows α and β approximated as exponential functions of η for geometry 5-0-10-0. The decreasing values of both α and β with increasing η reflect the broadening and flattening of the SSR distribution with increasing depth below the ground surface.

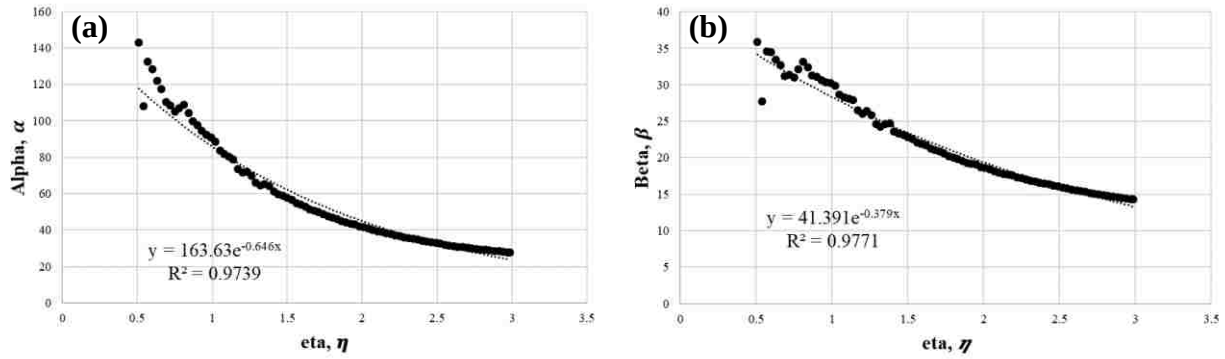

Figure 5.54. Shape parameters (a) α and (b) β as an exponential function of η for geometry 5-0-10-0.

5.4.8.5 Calculation of Peak Amplitude at all η Values for a Single Geometry

The peak amplitude of the predicted B_D is the maximum absolute value of the PLAXIS SSR distribution at each η value. Figure 5.55 shows peak amplitude modeled as a power function of η for geometry 5-0-10-0.

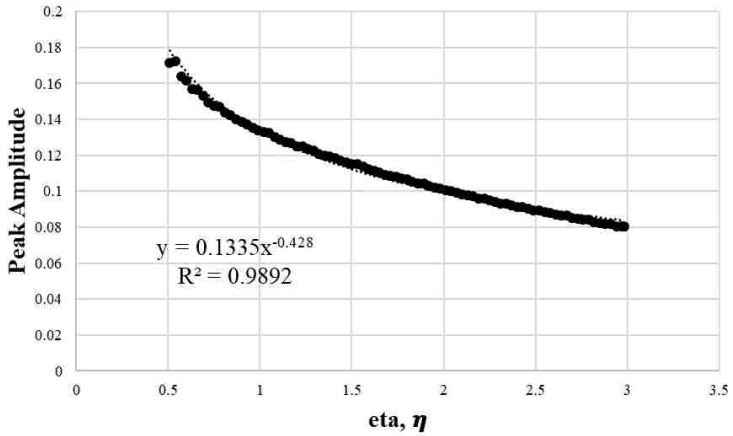

Figure 5.55. Peak amplitude of B_D as a power function with respect to η for geometry 5-0-10-0.

5.4.8.6 Optimization of Minimum and Maximum Bounds

Using the expressions shown in Figures 5.51, 5.54, and 5.55, the B_D prediction function was calculated and compared to the PLAXIS SSR data for geometry 5-0-10-0 as shown in Figure 5.56. Figure 5.56 shows the fit obtained when using the estimated δ_{min} and δ_{max} from Figure 5.51. Because the alpha and beta were found from additional shifts of the minimum and maximum δ values, it makes sense why the match in Figure 5.56 is unsatisfactory.

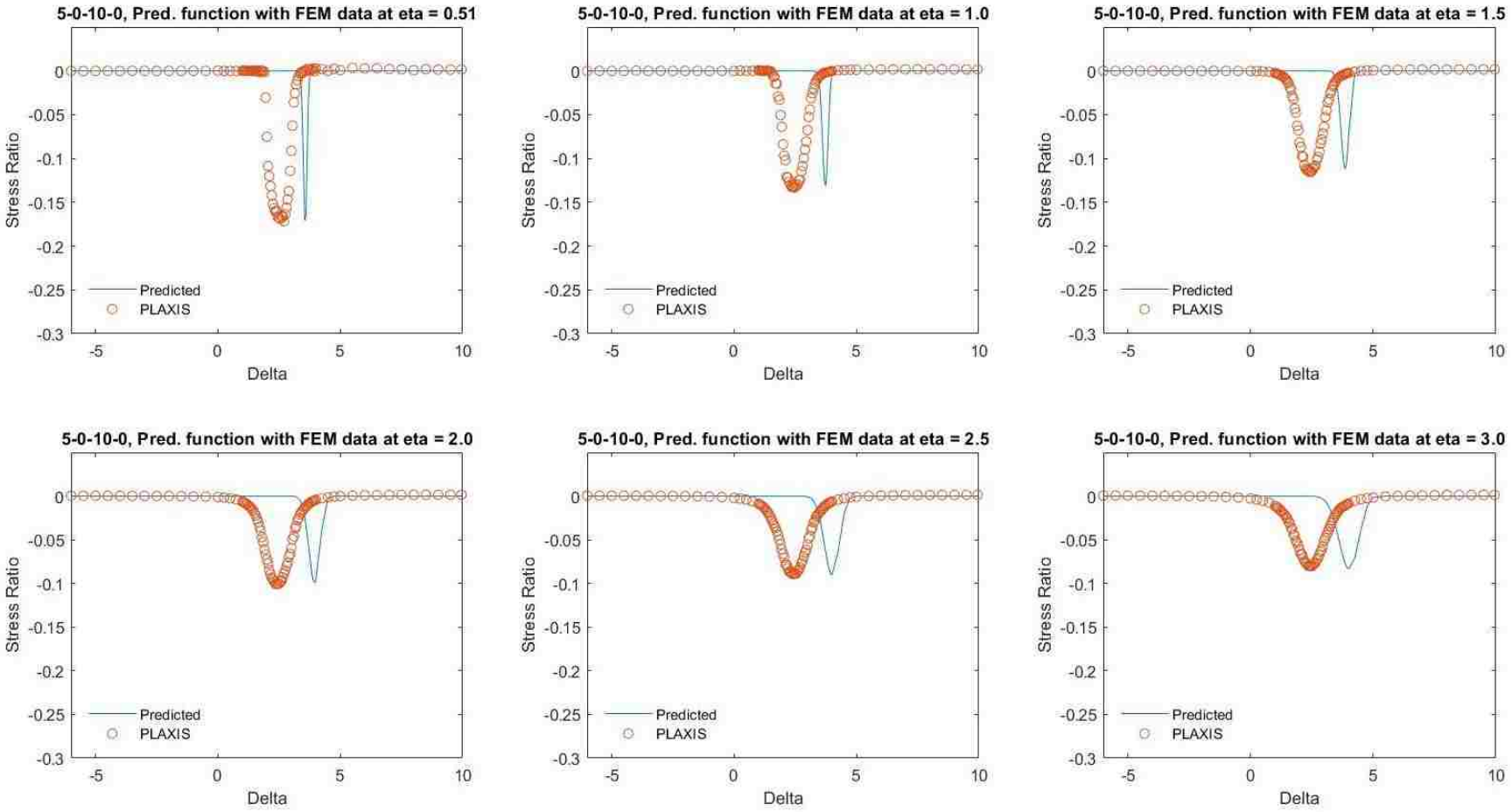

Figure 5.56. Predicted stress ratio function based on estimated minimum and maximum bounds compared to PLAXIS stress ratio for geometry 5-0-10-0.

To correct the estimated values of δ_{min} and δ_{max}, and to obtain a better predicted SSR fit to the PLAXIS data, the coefficients for δ_{min} and δ_{max} in Figure 5.51 were optimized using Codes *"Optimization Function"* and *"Optimizing Coefficients"*, and then plotted using *"Optimization Plotting"* (Appendix D). Optimization was performed using the Matlab command, fminsearch, which finds the minimum value of an error function. For this research, the error function described the difference between the SSR predicted from the B_D and the PLAXIS SSR data. In this initial phase, expressions for the α and β shape parameters and the amplitude of the predicted B_D were locked and only the δ_{min} and δ_{max} bound values were optimized. Two formulations of the error function guiding fminsearch were investigated: the sum of squared errors (SSE) and normalized error as shown in the Equations 5.33 and 5.34.

$$SSE = \sum_{\eta=0.5}^{\eta=3} \sum_{\delta=-6}^{\delta=10} \left[SSR(\eta,\delta)_{predicted} - SSR(\eta,\delta)_{PLAXIS}\right]^2 \quad (5.33)$$

$$Normalized\ Error = \sum_{\eta=0.5}^{\eta=3} \sum_{\delta=-6}^{\delta=10} \left[\frac{SSR(\eta,\delta)_{predicted} - SSR(\eta,\delta)_{PLAXIS}}{SSR(\eta,\delta)_{PLAXIS}}\right]^2 \quad (5.34)$$

The ranges of $0.5 < \eta < 3$ and $-6 < \delta < 10$ in these error functions are based on the vicinity of the slope that would typically be most important for lateral spreading.

For optimization of a single geometry, the normalized error was found to provide a better match between the predicted SSR and the PLAXIS data. Optimization of δ_{min} and δ_{max} for geometry 5-0-10-0 was performed and Figure 5.57 was obtained.

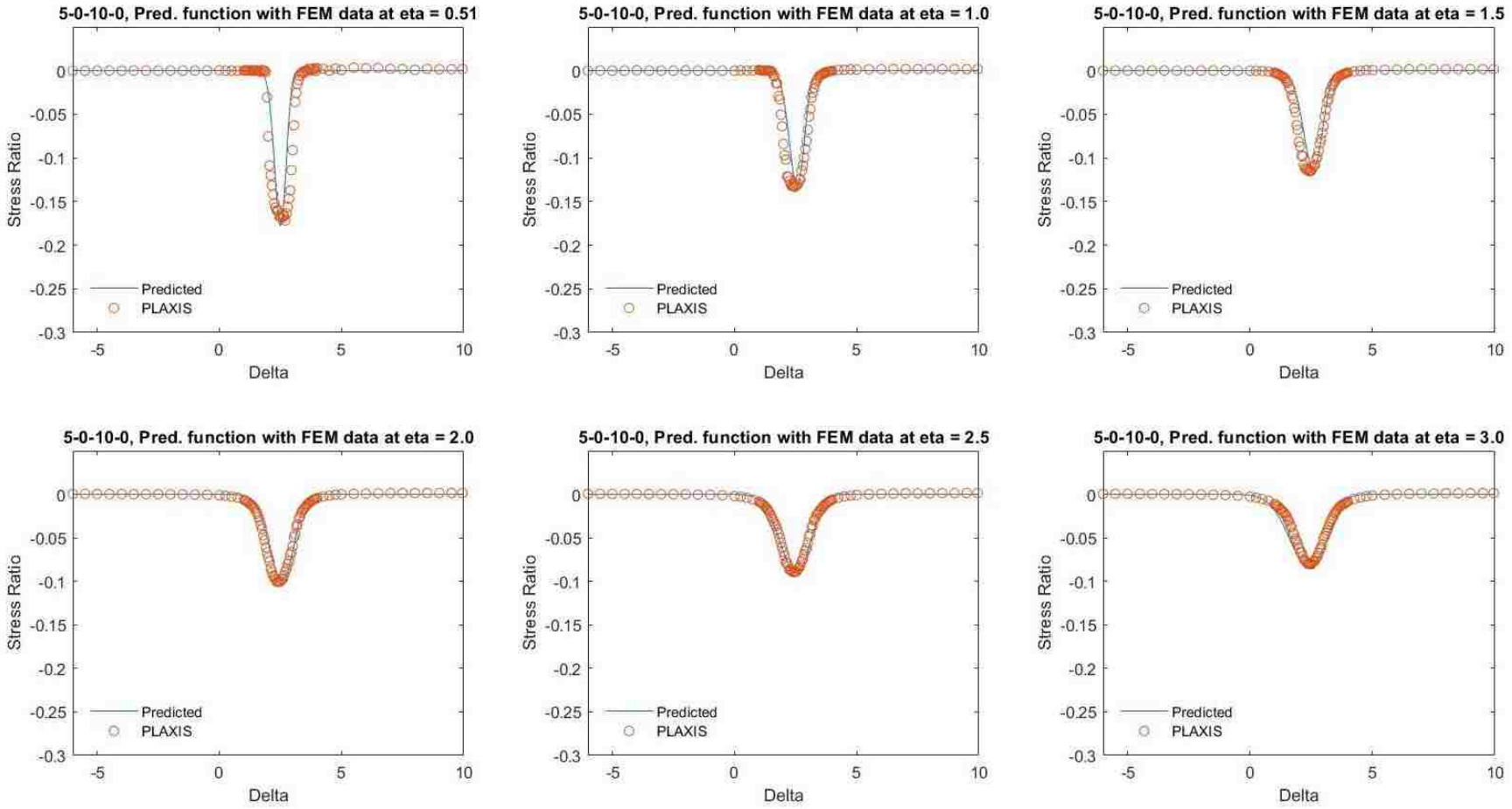

Figure 5.57. Predicted stress ratio function based on optimized minimum and maximum bounds compared to PLAXIS stress ratio for geometry 5-0-10-0.

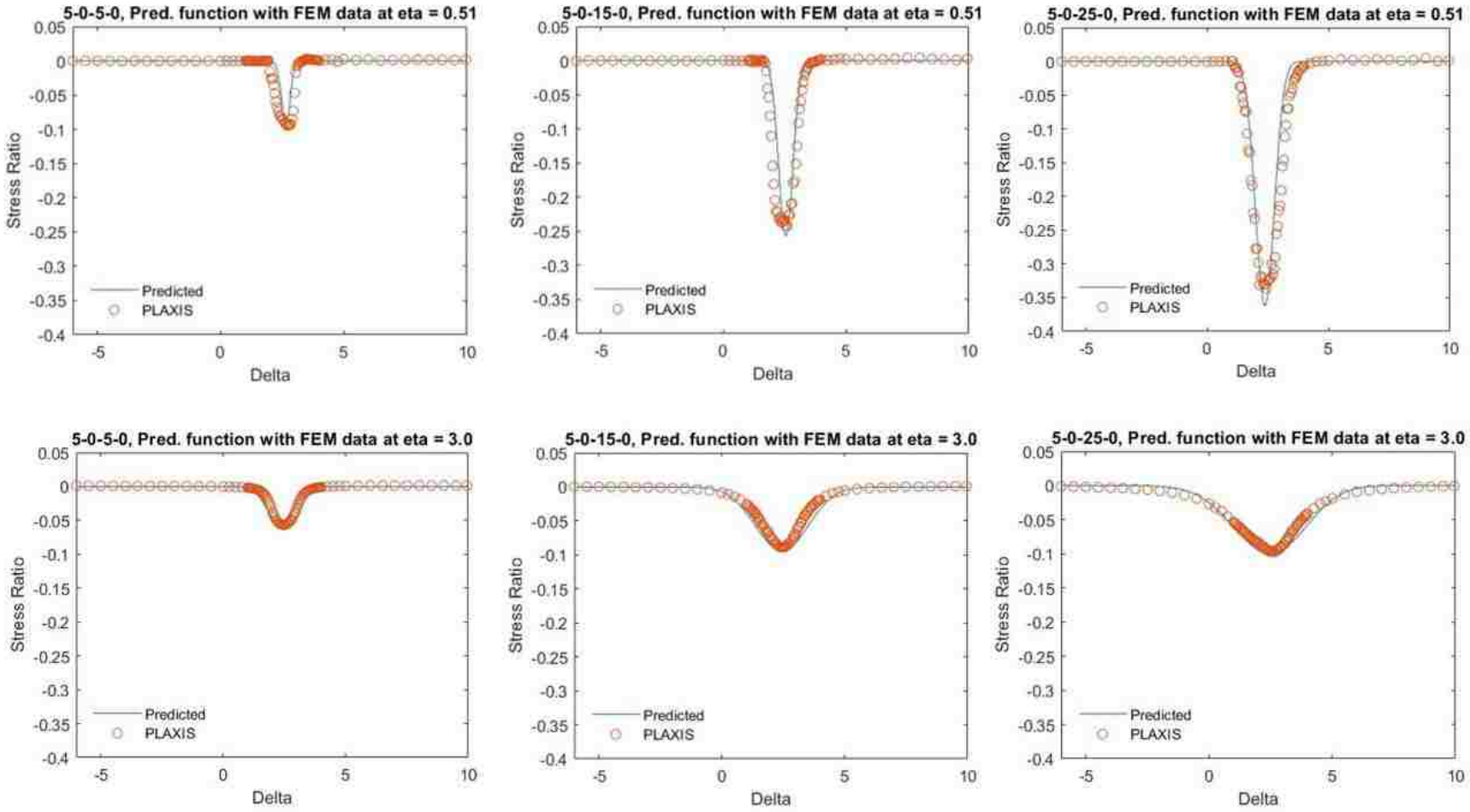

Figure 5.58. Predicted stress ratio function based on optimized minimum and maximum bounds compared to PLAXIS stress ratio for geometry 5-0-5-0, 5-0-15-0, and 5-0-25-0 at η = 0.51 and η = 3.0.

Following the same process described for geometry 5-0-10-0 for determining δ_{min}, δ_{max}, α, β, and peak amplitude, plots similar to Figures 5.51, 5.54, and 5.55 can be made for the remaining 5-0-X-0 geometries (where X represents the θ_2 values of 5, 10, 15, 20, and 25). The same optimization routine as was done for 5-0-10-0 was then performed for all the 5-0-X-0 geometries individually. For brevity, the predicted/PLAXIS matches are shown in Figure 5.58 for geometries 5-0-5-0, 5-0-15-0, and 5-0-25-0 at η = 0.51 and η = 3 to show the match is good at a wide range of θ_2 values and depths. The coefficients used to obtain these matches for the 5-0-X-0 geometries are shown in Figures 5.59-5.63 with the exception of the optimized δ_{min} and δ_{max} which are shown in Table 5.14. Figures 5.62-5.63 show the coefficients of the initial δ_{min} and δ_{max} prior to optimization.

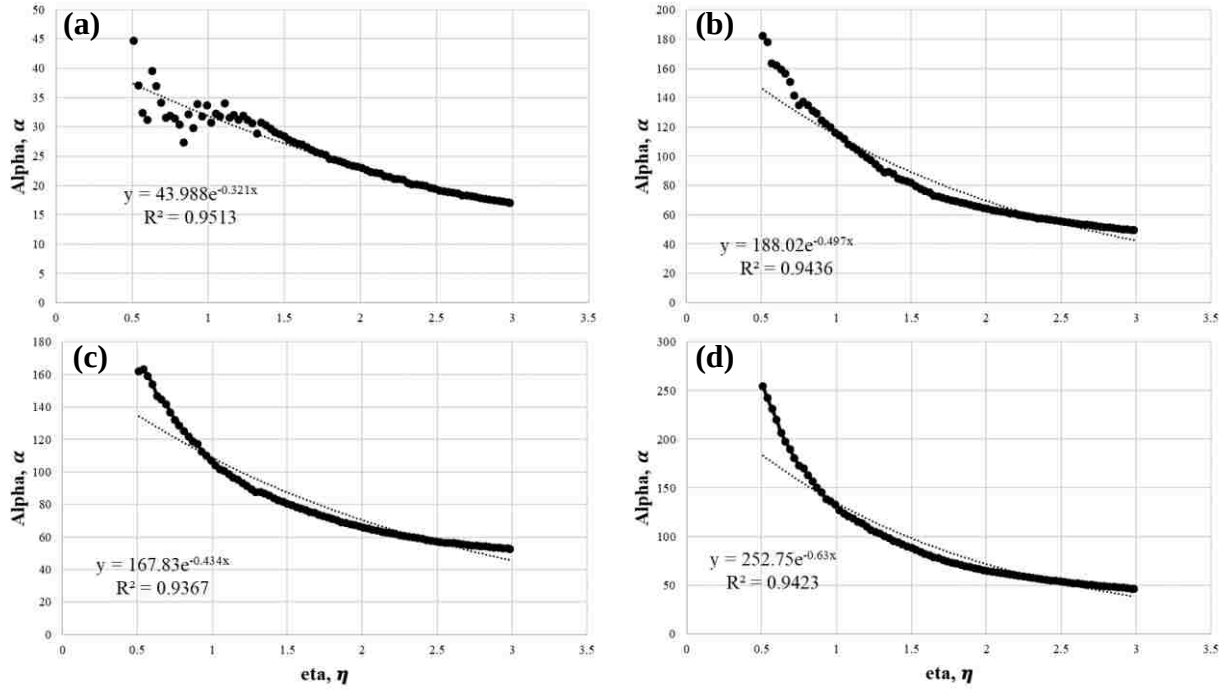

Figure 5.59. Shape parameter α as an exponential function of η for geometry (a) 5-0-5-0, (b) 5-0-15-0, (c) 5-0-20-0, and (d) 5-0-25-0.

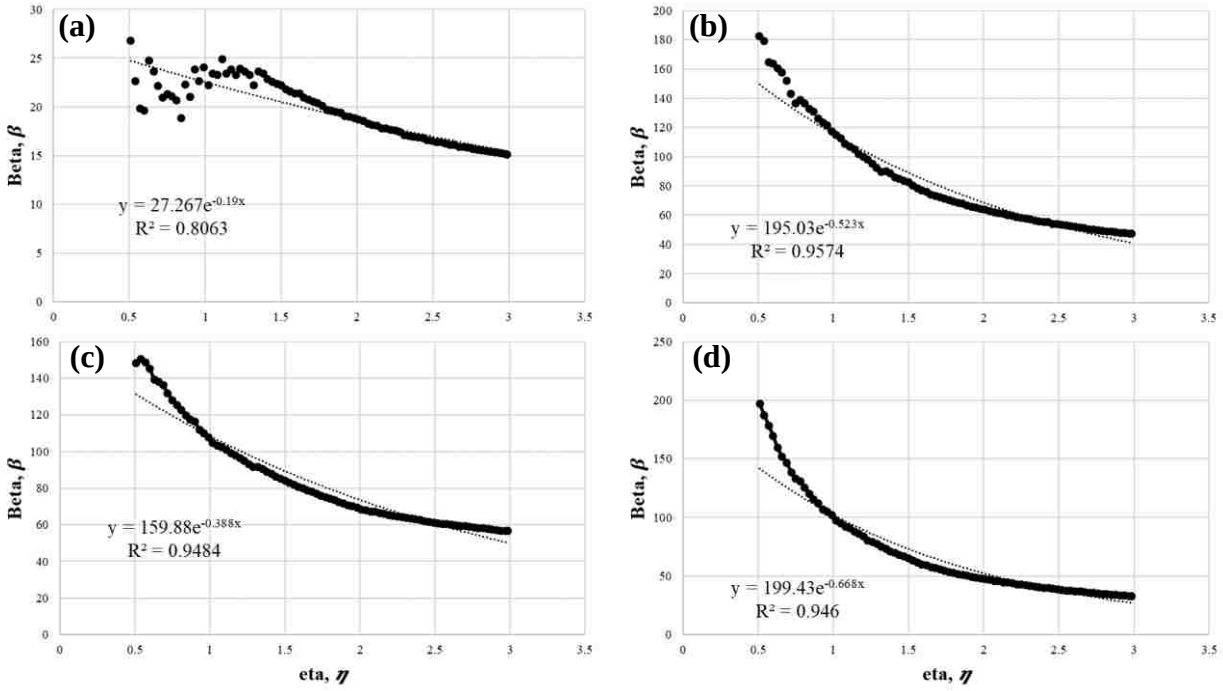

Figure 5.60. Shape parameter β as an exponential function of η for geometry (a) 5-0-5-0, (b) 5-0-15-0, (c) 5-0-20-0, and (d) 5-0-25-0.

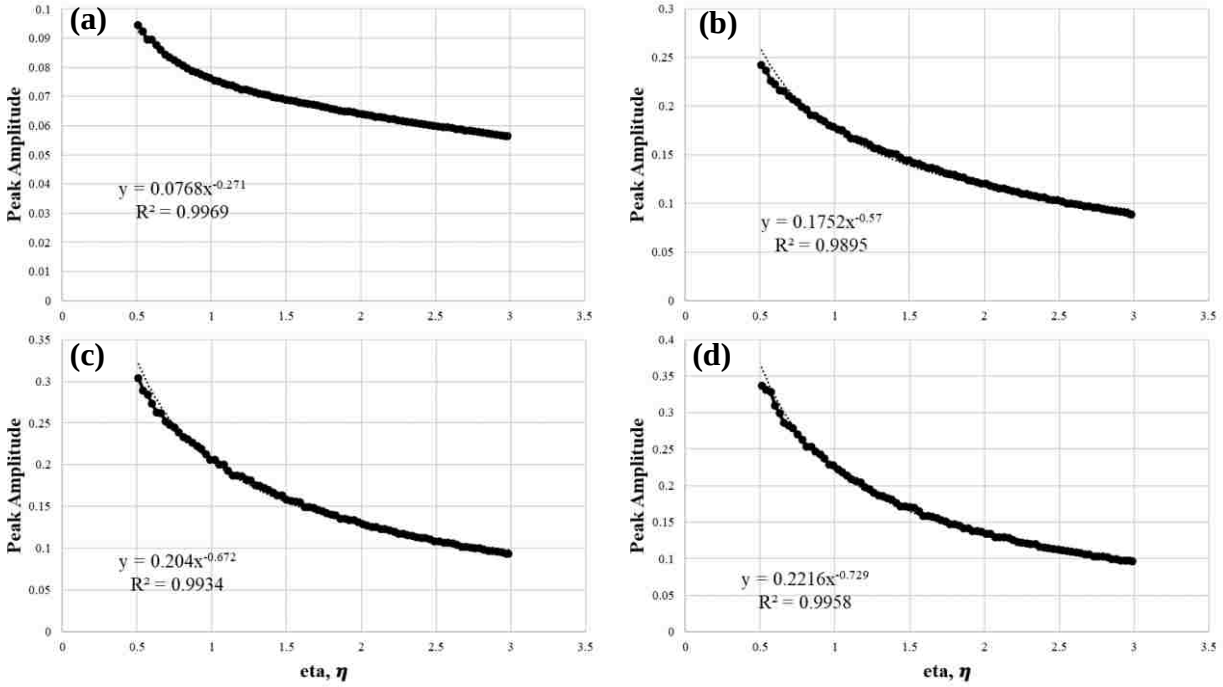

Figure 5.61. Peak amplitude as a power function of η for geometry (a) 5-0-5-0, (b) 5-0-15-0, (c) 5-0-20-0, and (d) 5-0-25-0.

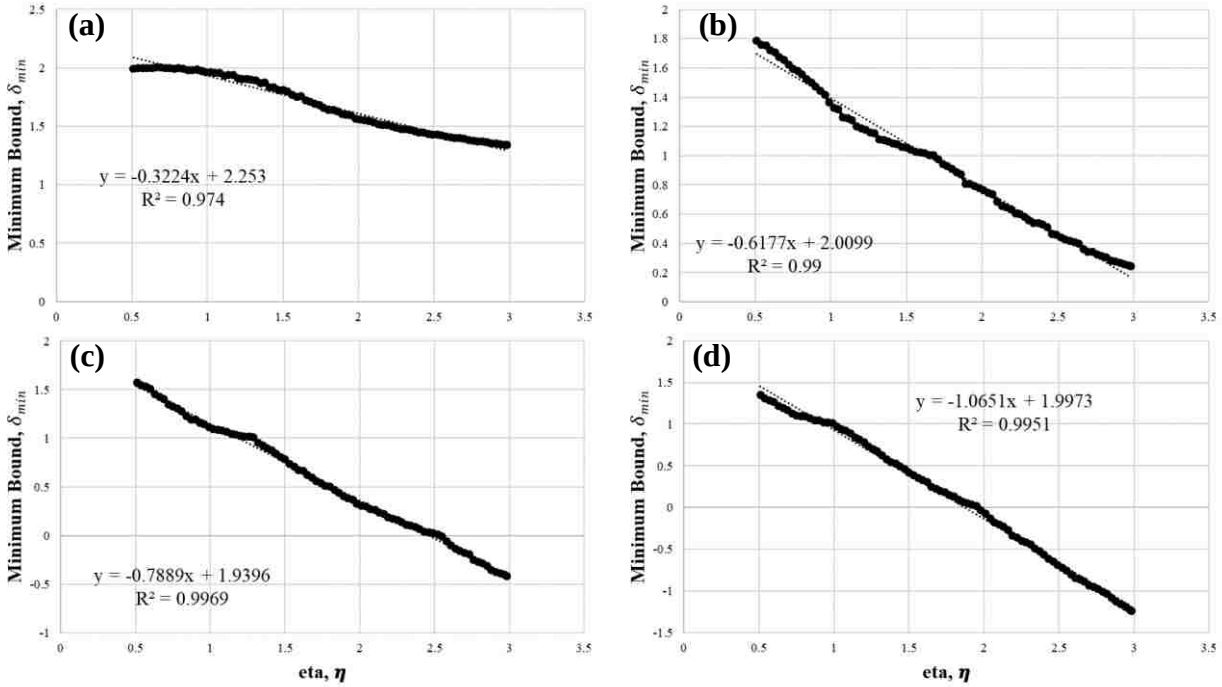

Figure 5.62. δ_{min} as a linear function of η for geometry (a) 5-0-5-0, (b) 5-0-15-0, (c) 5-0-20-0, and (d) 5-0-25-0.

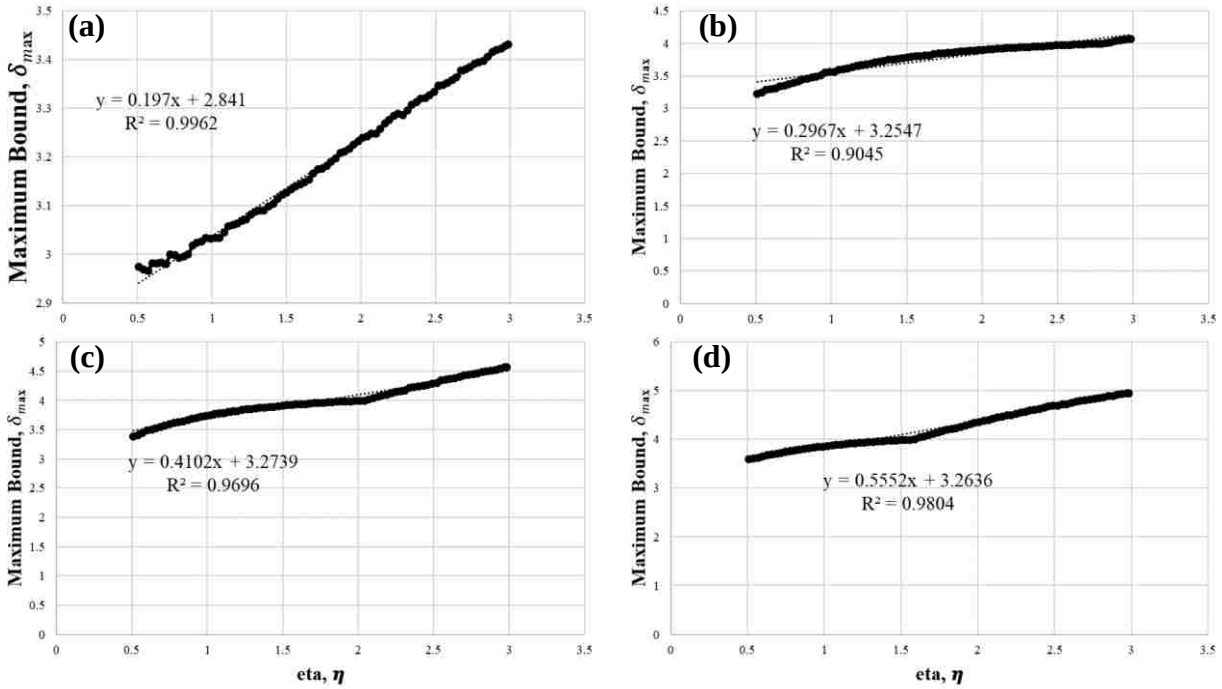

Figure 5.63. δ_{max} as a linear function of η for geometry (a) 5-0-5-0, (b) 5-0-15-0, (c) 5-0-20-0, and (d) 5-0-25-0.

Table 5.14. Optimized δ_{min} and δ_{max} for each individual 5-0-X-0 geometry.

Geometry	θ_2	δ_{min} intercept	δ_{min} coefficient	δ_{max} intercept	δ_{max} coefficient
5-0-5-0	5	1.3000	-0.6809	3.4845	0.5469
5-0-10-0	10	-2.8000	-0.3500	3.7001	0.7021
5-0-15-0	15	-1.3000	-2.1000	6.6557	1.8000
5-0-20-0	20	-1.9000	-2.9000	6.6304	3.2723
5-0-25-0	25	-4.4000	-2.4000	7.7893	1.5000

5.4.8.7 *SSR* Prediction Function for all θ_2 Geometries

The matches between the Predicted/PLAXIS SSR were shown for each individual 5-0-X-0 geometry, however, these all use different coefficients based on that single geometry. This section discusses obtaining a single SSR prediction function, based on both η and θ_2, that can be used for any 5-0-X-0 geometry. Therefore, a single set of coefficients is used to match the predicted/PLAXIS SSR data instead of using coefficients for each particular geometry. This requires the development of a function that depends on η and θ_2 for each of the B_D parameters and its peak amplitude. For example, the variation of α with η for a given θ_2 value was observed to be reasonably modeled by an exponential function, of the form

$$\alpha = \alpha_1 * \exp(-\alpha_2 * \eta) \tag{5.35}$$

however, as shown in Figure 5.59, the coefficients, α_1 and α_2, of the exponential functions that provided the best fit to each θ_2 value were different. Those coefficients varied with θ_2 as shown in Figure 5.64.

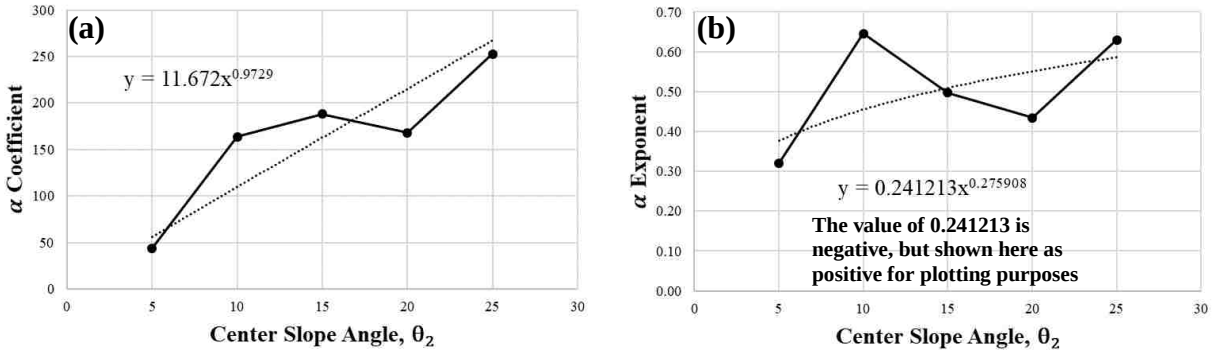

Figure 5.64. The α parameter (a) coefficient and (b) exponent coefficient (from α with respect to η) for the 5-0-X-0 geometries behavior as a power function with respect to θ_2.

While the variation was observed to be irregular, the basic trends in the data can be expressed in terms of power law functions. The best fits to the coefficients were given by

$$\alpha_1 = 11.672{\theta_2}^{0.9729} \tag{5.36}$$

$$\alpha_2 = -0.2412{\theta_2}^{0.2759} \tag{5.37}$$

Therefore, the final expression for α was given by

$$\alpha = \left(11.672{\theta_2}^{0.9729}\right) * \exp\left(\left[-0.2412{\theta_2}^{0.2759}\right] * \eta\right) \tag{5.38}$$

Power (θ_2) Power (θ_2)

Exponential (η)

Following the same logic, the behavior of the other B_D parameters that depend on η and θ_2 are developed and shown in Figures 5.65-5.68.

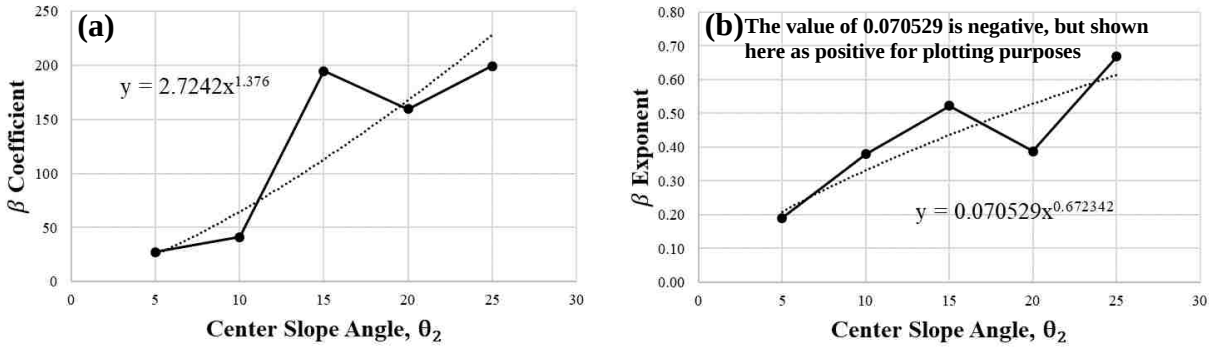

Figure 5.65. The β parameter (a) coefficient and (b) exponent coefficient (from β with respect to η) for the 5-0-X-0 geometries behavior as a power function with respect to θ_2.

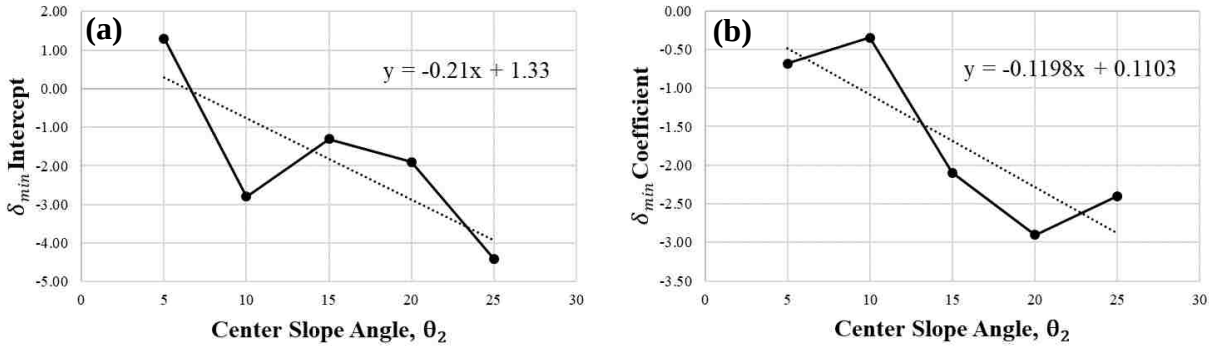

Figure 5.66. The δ_{min} parameter (a) intercept and (b) coefficient (from δ_{min} with respect to η) for the 5-0-X-0 geometries behavior as a power function with respect to θ_2.

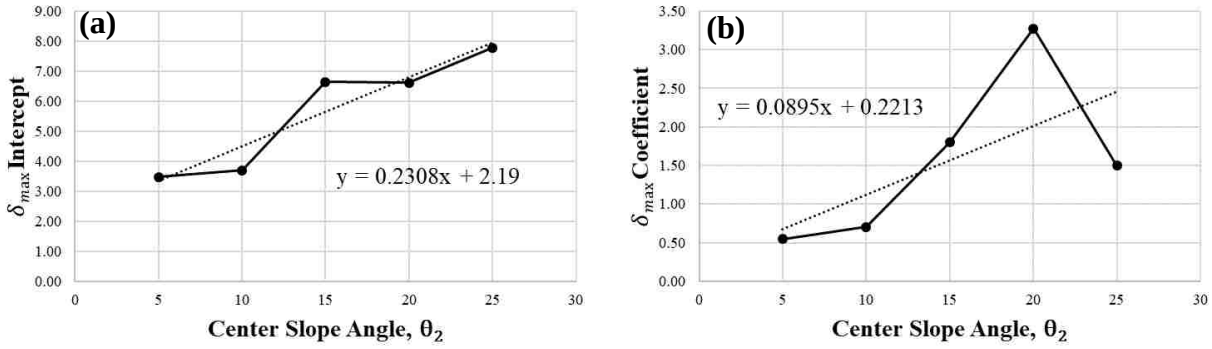

Figure 5.67. The δ_{max} parameter (a) intercept and (b) coefficient (from δ_{max} with respect to η) for the 5-0-X-0 geometries behavior as a power function with respect to θ_2.

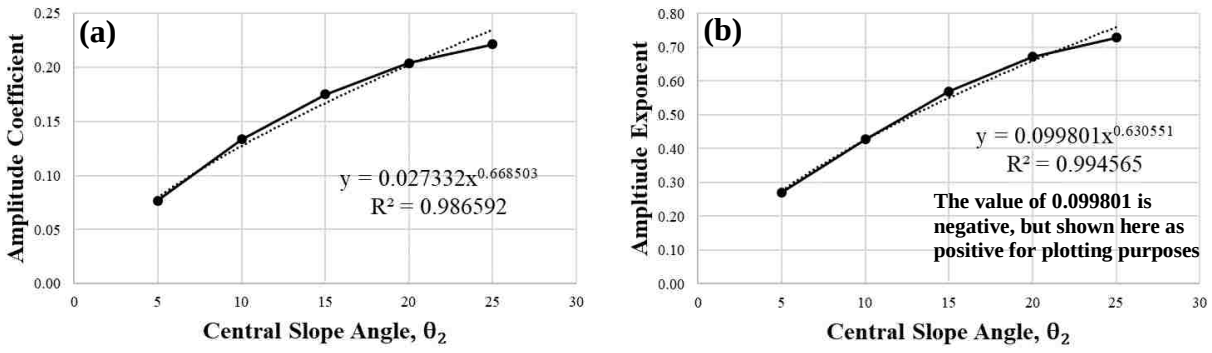

Figure 5.68. The peak amplitude parameter (a) coefficient and (b) exponent coefficient (from peak amplitude with respect to η) for the 5-0-X-0 geometries behavior as a power function with respect to θ_2.

Figure 5.65 shows how the coefficients of β, that were found with respect to η in Figure 5.54, vary with θ_2 as a power function and is given as

$$\beta = \left(2.7242{\theta_2}^{1.376}\right) * \exp\left(\left[-0.07053{\theta_2}^{0.6723}\right] * \eta\right) \quad (5.39)$$

Figure 5.66 shows how the coefficients of δ_{min}, that were found with respect to η in Figure 5.51, vary with θ_2 as a linear function and is given as

$$\delta_{min} = (1.33 - 0.21\theta_2) + (0.1103 - 0.1198\theta_2) * \eta \quad (5.40)$$

Figure 5.67 shows how the coefficients of δ_{max}, that were found with respect to η in Figure 5.51, vary with θ_2 as a linear function.

$$\delta_{max} = (2.19 + 0.2308\theta_2) + (0.2213 + 0.0895\theta_2) * \eta \quad (5.41)$$

Figure 5.68 shows how the coefficients of peak amplitude, A_{peak}, that were found with respect to η in Figure 5.55, vary with θ_2 as a power function.

$$A_{peak} = \left(0.027332{\theta_2}^{0.668503}\right) * \eta^{\left(-0.099801{\theta_2}^{0.630551}\right)} \quad (5.42)$$

Therefore, Equations 5.38-5.42 are used to calculate the predicted SSR as functions of η and θ_2 to match the PLAXIS data for all of the 5-0-*X*-0 geometries. Entering these coefficients into Code *"Optimization Plotting"* and then running the code gives the predicted/PLAXIS SSR fits shown in Figure 5.69. To compare the predicted and PLAXIS SSR fits at a range of geometries and depths, Figure 5.69 shows the predicted/PLAXIS SSR for geometries 5-0-5-0, 5-0-15-0, and 5-0-25-0 at η values of 0.51 and 3.0.

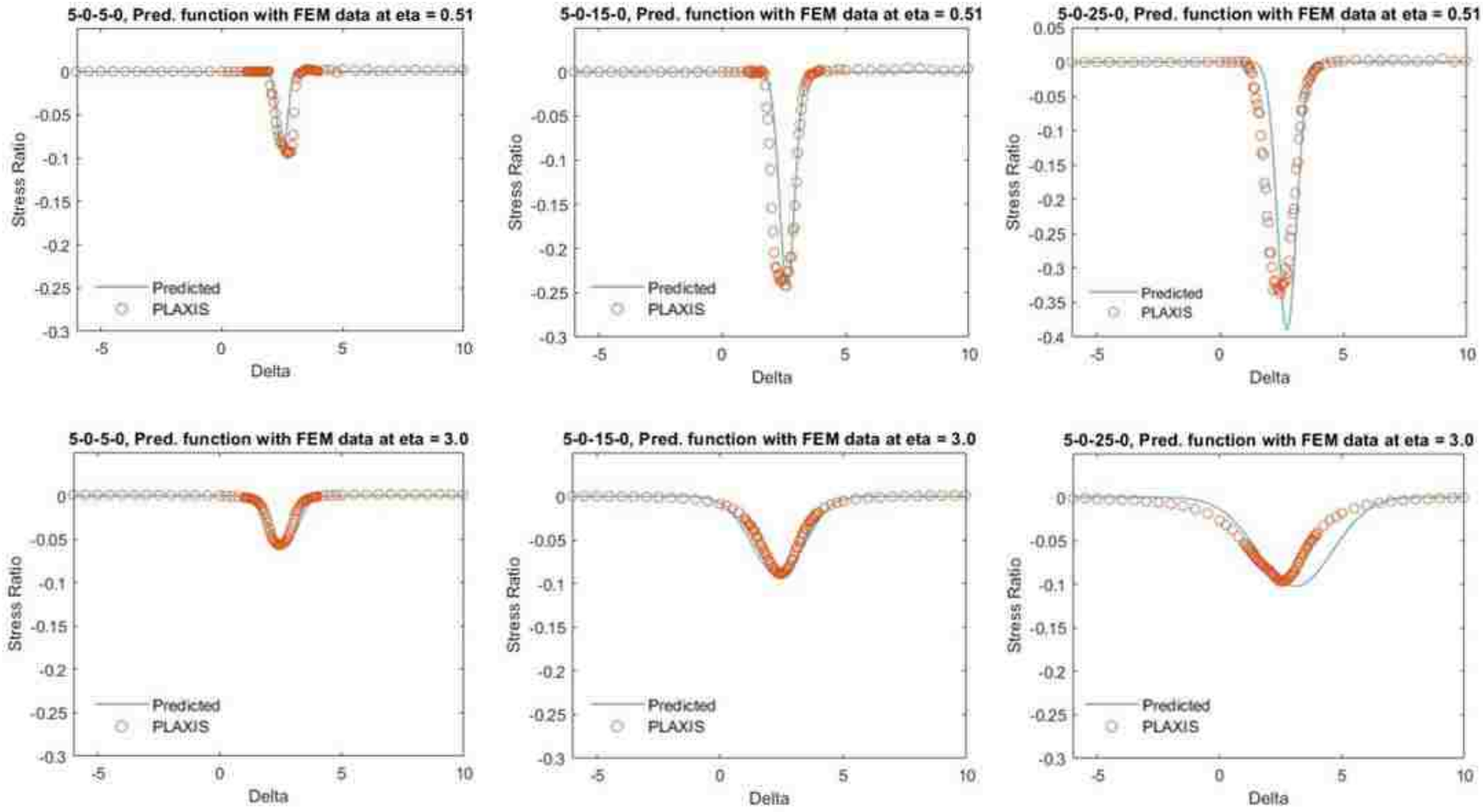

Figure 5.69. Predicted stress ratio function using initial coefficients compared to PLAXIS stress ratio for the 5-0-X-0 geometries.

The match between the predicted/PLAXIS SSR using the initial coefficients appears good except at larger depths and steep slopes (i.e., at η = 3.0 for geometry 5-0-25-0) where the predicted function is shifted to the right. To correct this, and to obtain a better predicted SSR fit to the PLAXIS data, the coefficients for δ_{min} and δ_{max} shown in Figures 5.66-5.67 were optimized using Codes *"Optimization Function"* and *"Optimizing Coefficients"*, and then plotted using Code *"Optimization Plotting"* (Appendix D). Optimization was performed with SSE and normalized error (Equations 5.33 and 5.34) to guide the Matlab command, fminsearch, in the same manner as was done for each individually geometry. However, when incorporating more than a single geometry both of these error functions favor limiting a certain geometry.

The SSE function in Equations 5.33 is influenced more by larger SSR values, and consequently produced better fits to shallower depths (lower η) and steeper slopes (higher θ_2) at the expense of other conditions. To illustrate this point, the predicted/PLAXIS results obtained by optimization of the 5-0-X-0 geometries with the SSE error function are shown in Figure 5.70. A clear trend is shown – the match obtained between the predicted/PLAXIS SSR improves as θ_2 increases, while η decreases. Therefore, the best match between the predicted/PLAXIS SSR for the η values shown is at an η = 0.51 for geometry 5-0-25-0, while the worst match is at η = 3.0 for geometry 5-0-5-0 in Figure 5.70.

The normalized error was then used to reduce that effect. However, using normalized error instead of SSE to guide the optimization also led to unsatisfactory results. The largest total normalized error occurred when the PLAXIS SSR distribution extended over a wide range of δ values. A wide SSR distribution occurs with increasing depth and steepness of the central slope segment, therefore, the best match between predicted/PLAXIS SSR occurs at η = 3.0 for geometry 5-0-25-0, while the worst match is at η = 0.51 for geometry 5-0-5-0 as shown in Figure 5.71.

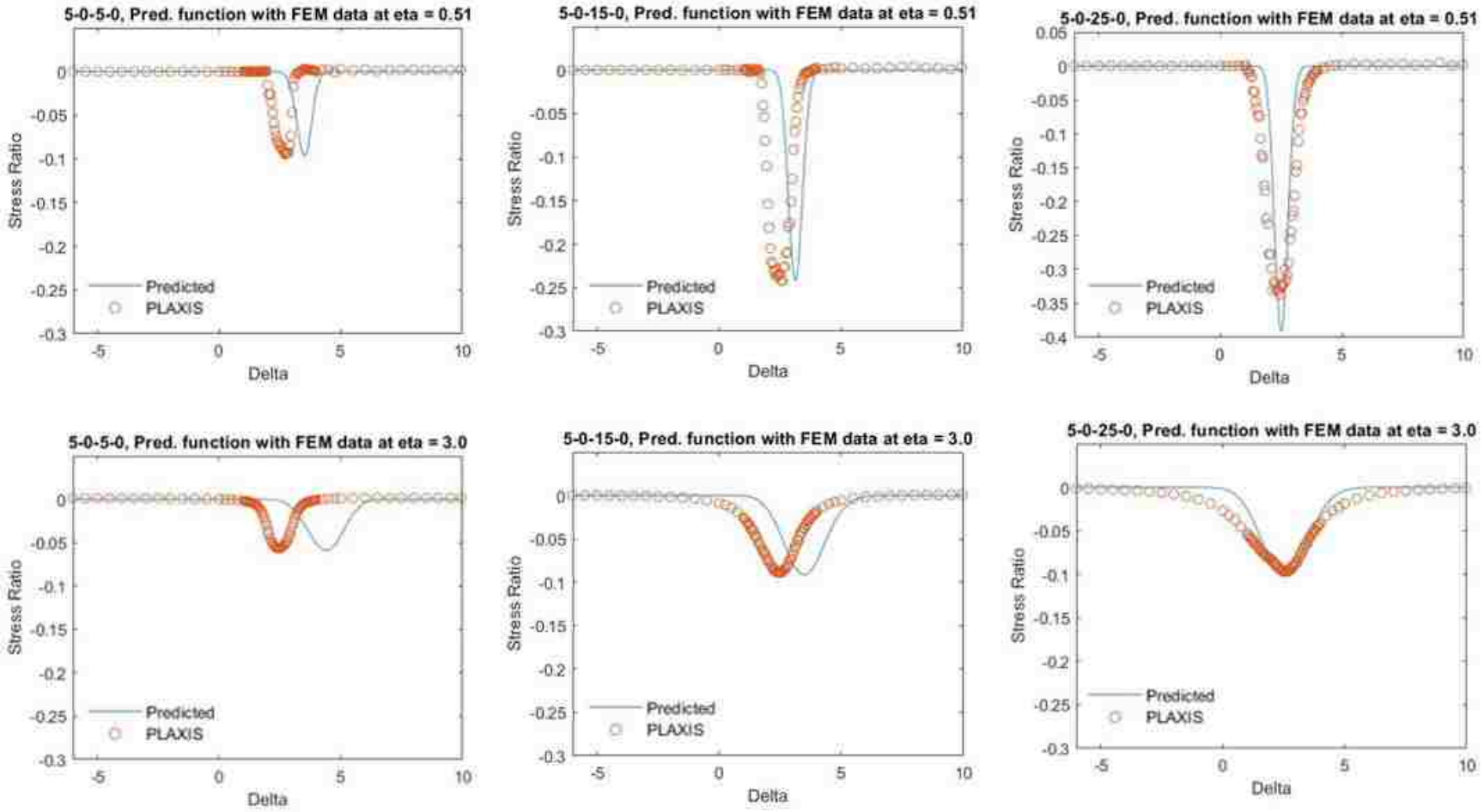

Figure 5.70. Predicted stress ratio function optimized via SSE compared to PLAXIS stress ratio for the 5-0- X-0 geometries.

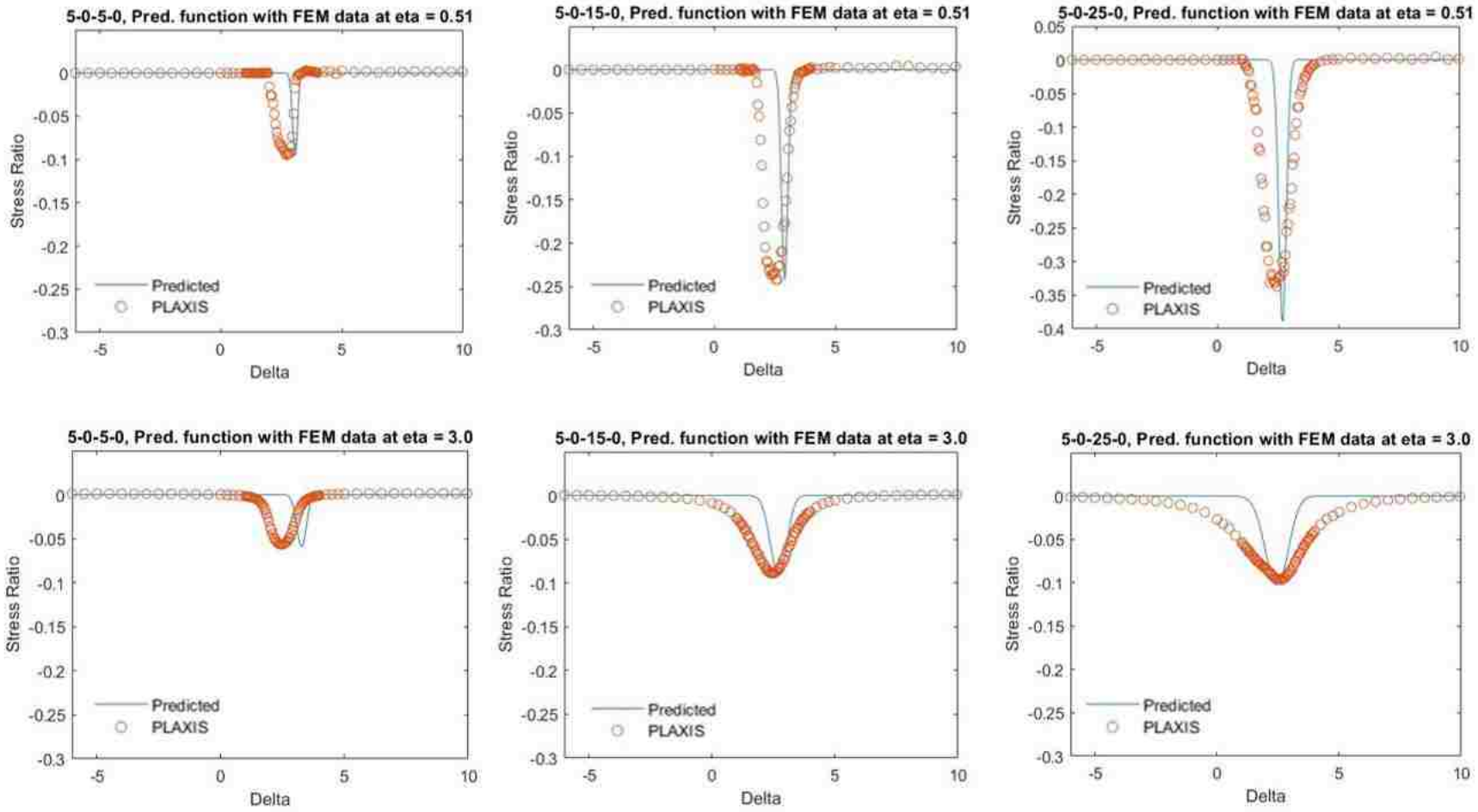

Figure 5.71. Predicted stress ratio function optimized via normalized error compared to PLAXIS stress ratio for the 5-0-X-0 geometries.

Closer examination of the PLAXIS data revealed that δ_{max} behavior was sufficiently simple and consistent that it could be adequately characterized by a more manual process. The predicted/PLAXIS SSR fits found using the initial values show that the predicted function veers away from the PLAXIS SSR data at large depths and for steep slopes (see Figure 5.69). Therefore, δ_{max} needs to be reduced at high η and θ_2 values. A manual adjustment was made, resulting in Equations 5.43 being used for calculating δ_{max} for the 5-0-X-0 geometries. A separate small manual adjustment was also made to one of the β coefficients to improve the predicted/PLAXIS SSR fit. Equation 5.44 gives the equation for calculating the final expression for β for the 5-0-X-0 geometries. The simple manual adjustments to δ_{max} and β gives the predicted function a good fit to the PLAXIS SSR for the 5-0-X-0 geometries as shown in Figure 5.72. The reader is referred to Appendix E for additional predicted/PLAXIS SSR fits for the 5-0-X-0 geometries.

$$\delta_{max} = (2.19 + 0.2308 * \theta_2) + (0.2213 + 0.077 * \theta_2) * \eta \quad (5.43)$$

$$\beta = \left(2.6{\theta_2}^{1.376}\right) * \exp\left(\left[-0.07053{\theta_2}^{0.6723}\right] * \eta\right) \quad (5.44)$$

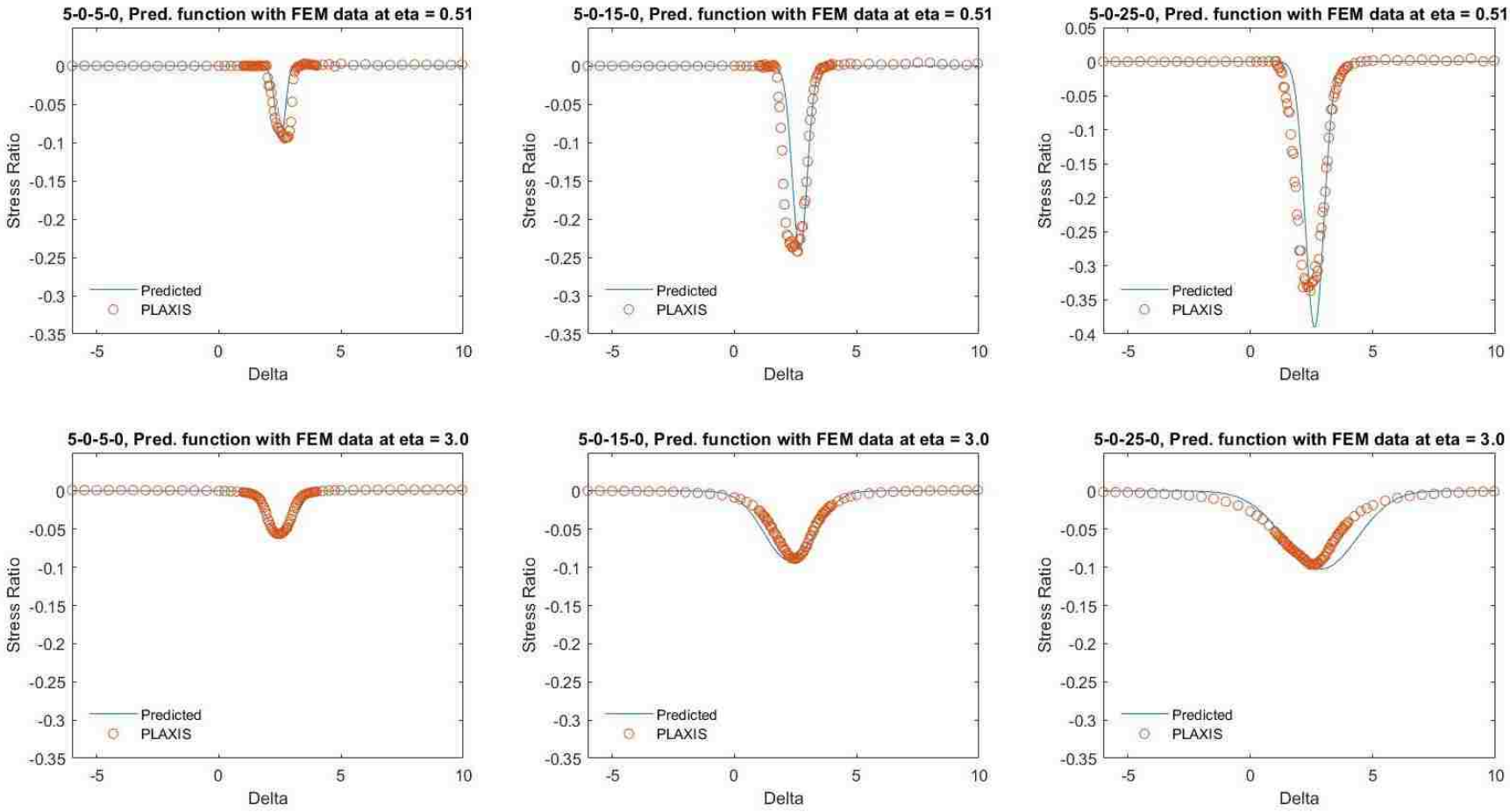

Figure 5.72. Predicted stress ratio function optimized manually compared to PLAXIS stress ratio for the 5-0-X-0 geometries.

Discussion

Incorporating the δ_{min} and δ_{max} from the CDF, α and β parameters found from the moments of the PLAXIS SSR PDF, manually optimizing one of the δ_{max} coefficients, and using the peak amplitudes from the PLAXIS SSR data, led to the B_D predicted SSR and PLAXIS SSR fit shown in Figure 5.72. Simple visual inspection of Figure 5.72 shows the predicted B_D matches the PLAXIS SSR well. The "best fit" between the predicted/PLAXIS SSR is first determined by visual inspection to analyze the how reasonable the fit is, then minor adjustments are made based on calculated SSE and normalized error values. Geometry 5-0-25-0 does have a small amount of variability between the predicted and PLAXIS SSR at large depths, however, generally performs well for all depths and 5-0-X-0 geometries.

5.4.8.8 Accounting for a Steeper Upper Slope Angle, θ_3

Thus far, the geometries incorporated into the predicted SSR function had a flat upper slope which caused the stress ratio to return to zero at the maximum extent. Figure 5.73 shows an example of this behavior.

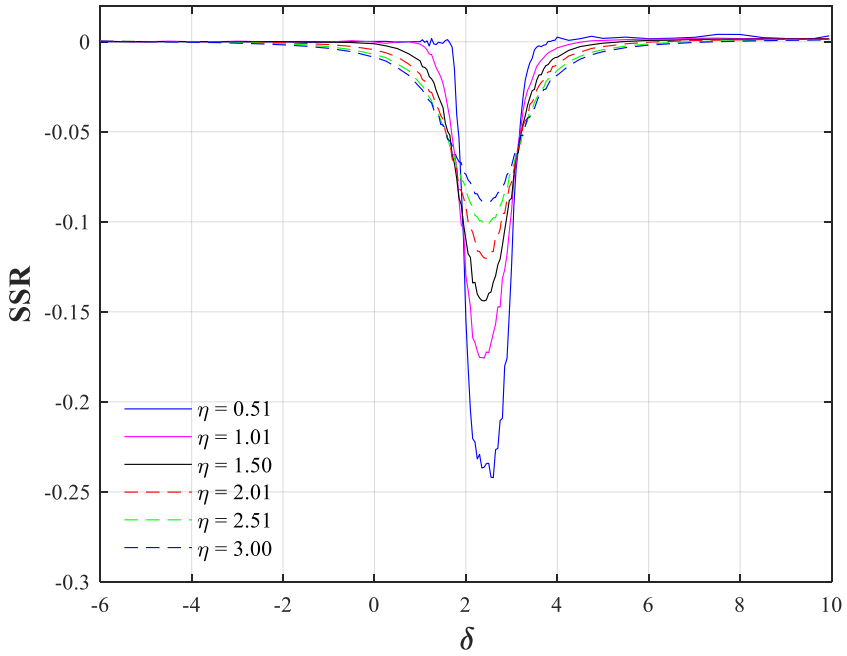

Figure 5.73. PLAXIS stress ratio values for geometry 5-0-15-0.

For cases with $\theta_3 > 0$, the minimum extent will still have a stress ratio value of zero since $\theta_1 = 0$, however, the maximum extent will have a constant non-zero stress ratio as is shown for the 5-0-15-3 geometry in Figure 5.74.

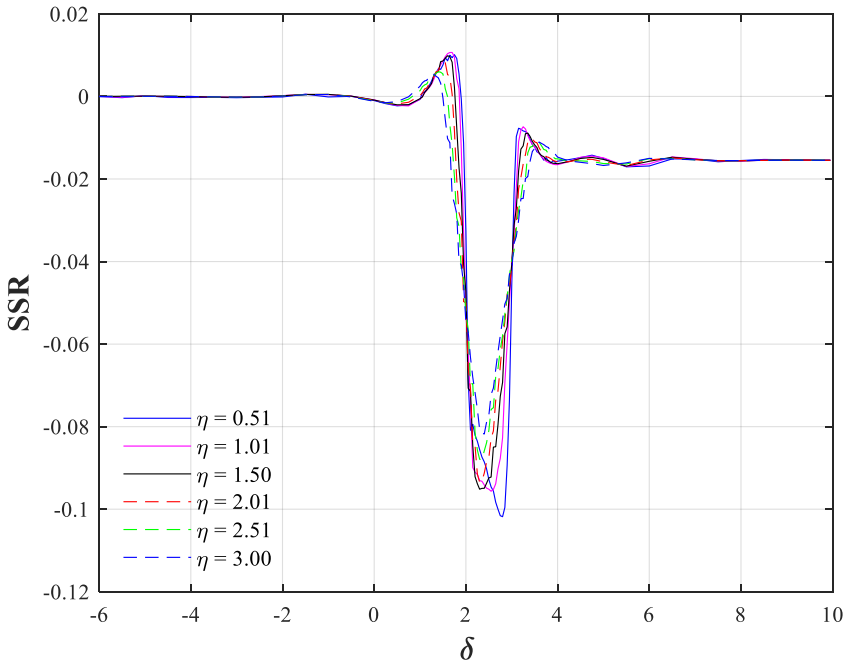

Figure 5.74. PLAXIS stress ratio values for geometry 5-0-15-3.

Therefore, the previously described FF must be added to the B_D function to allow the predicted stress ratio to transition from a value of zero at δ values well to the left of the slope, to a constant non-zero value for δ values well to the right of the slope. For the 5-0-15-3 geometry, the predicted stress ratio should vary from zero for the left plateau to a constant value of approximately -0.016 computed by PLAXIS for the right plateau.

Geometries with $\theta_3 > 0$ degrees will therefore require identification of eight parameters to predict the SSR – four from the B_D, the amplitude of the B_D, and the three FF parameters (since $c_3 = 0$). To incorporate the addition of $\theta_3 > 0$ geometries, the predicted fit from geometry 5-0-15-0 was plotted with the PLAXIS SSR data for 5-0-15-1, 5-0-15-3, and 5-0-15-5 to determine how the predicted functions parameters would need to be adjusted for different θ_3 values (see Figures 5.75-5.77).

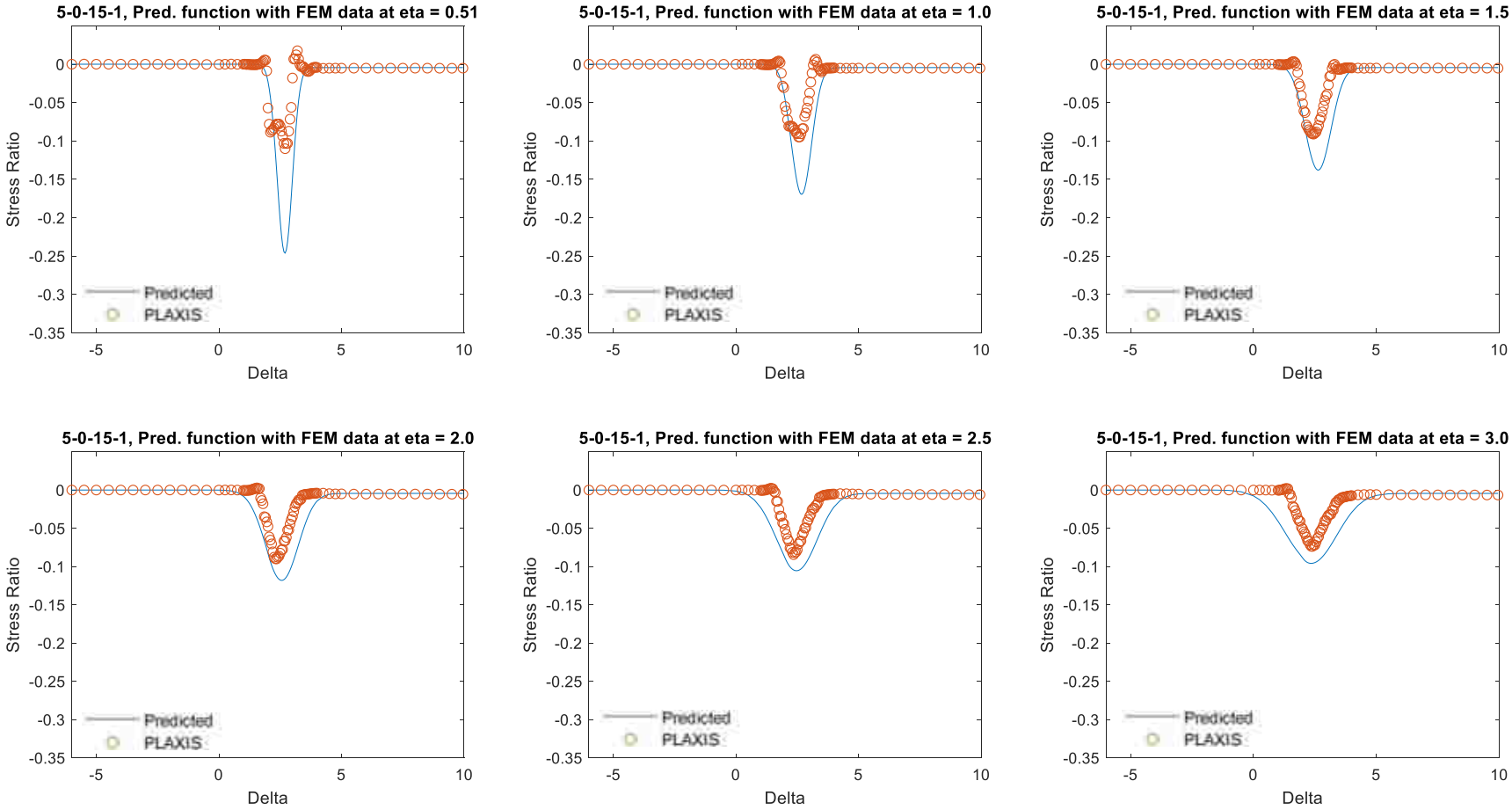

Figure 5.75. Predicted function for geometry 5-0-15-0 compared to the PLAXIS stress ratio data for geometry 5-0-15-1.

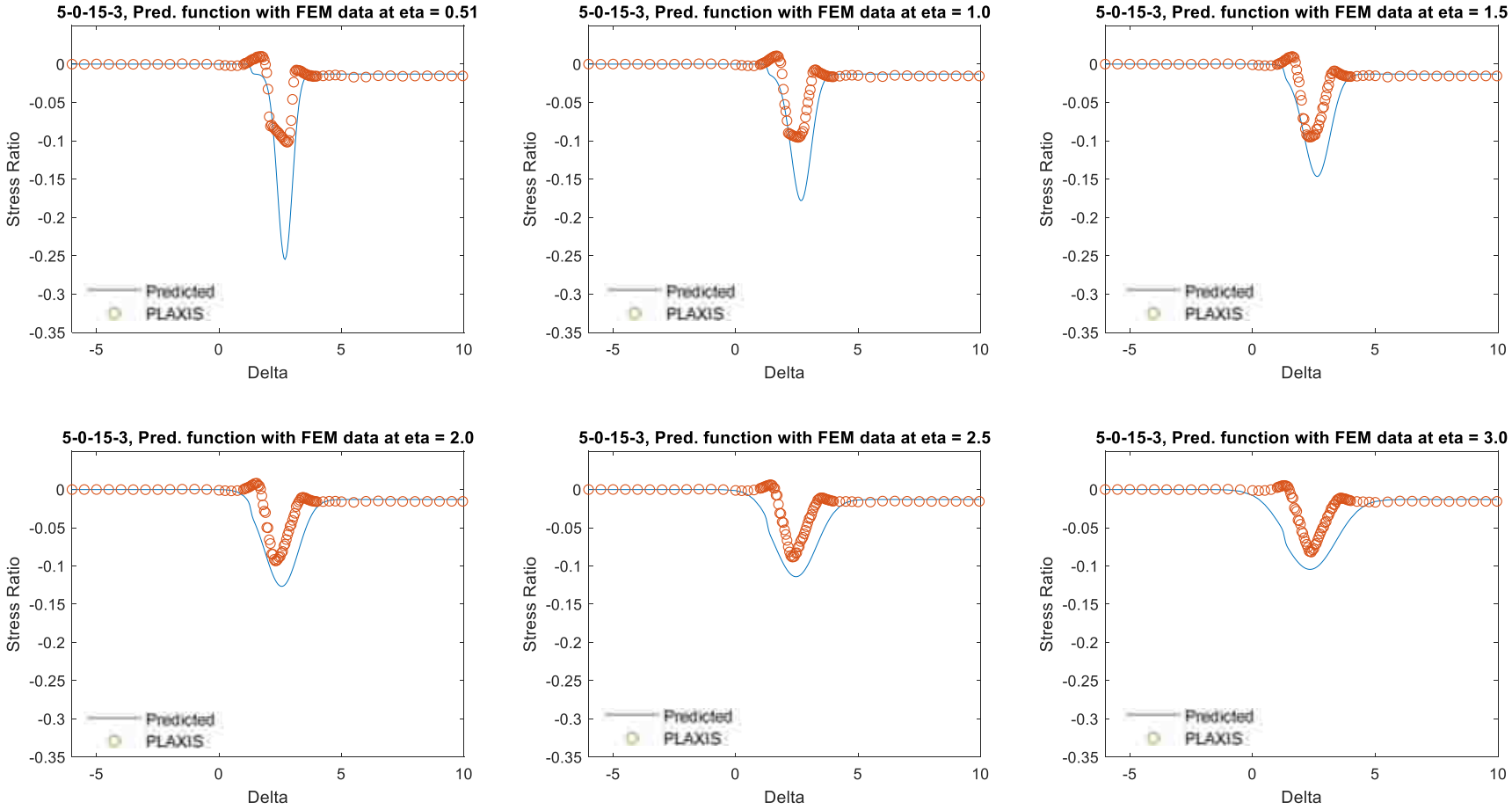

Figure 5.76. Predicted function for geometry 5-0-15-0 compared to the PLAXIS stress ratio data for geometry 5-0-15-3.

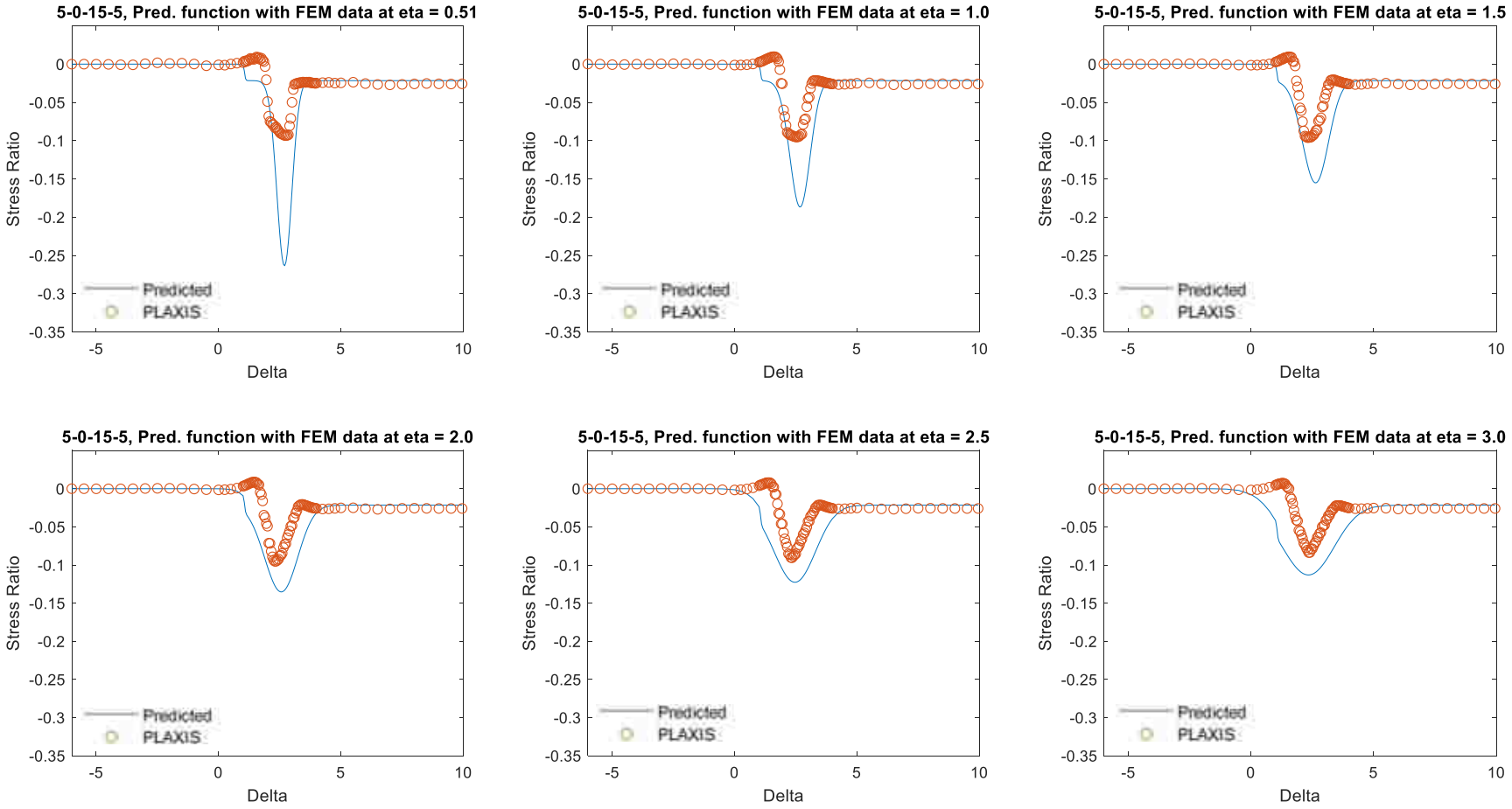

Figure 5.77. Predicted function for geometry 5-0-15-0 compared to the PLAXIS stress ratio data for geometry 5-0-15-5.

Figure 5.75 indicates, even for an upper slope of only 1°, the amplitude of the PLAXIS SSR decreases significantly from the level-ground case. The decrease in amplitude is small at large depths (η = 3) and greater at shallower depths (η = 0.51). The separation of δ_{min} and δ_{max} also needs to be reduced (increase $\delta_{min}$and decrease δ_{max},) when going from a θ_3 = 0 geometry to a θ_3 > 0 geometry. However, the decrease in separation of δ_{min} and δ_{max} is smallest at shallow depths and greatest at larger depths.

The predicted/PLAXIS SSR trends in Figures 5.76-5.77 (the θ_3 = 3 and θ_3 = 5 cases) are the same as discussed for Figure 5.75 except the right plateau increases to a larger SSR as the incline of the upper slope segment increases. To illustrate this effect, the PLAXIS SSR data for the 5-0-15-1, 5-0-15-3, and 5-0-15-5 geometries are shown in Figure 5.78. Figure 5.78 shows the PLAXIS SSR behavior for these geometries is generally constant beneath the left and central slope segments and the only difference in SSR between them is the SSR beneath the right plateau. In fact, the difference in SSR beneath the right slope segment for these geometries appears to be evenly spaced – indicating the SSR increase with increasing θ_3 values behaves in a linear fashion.

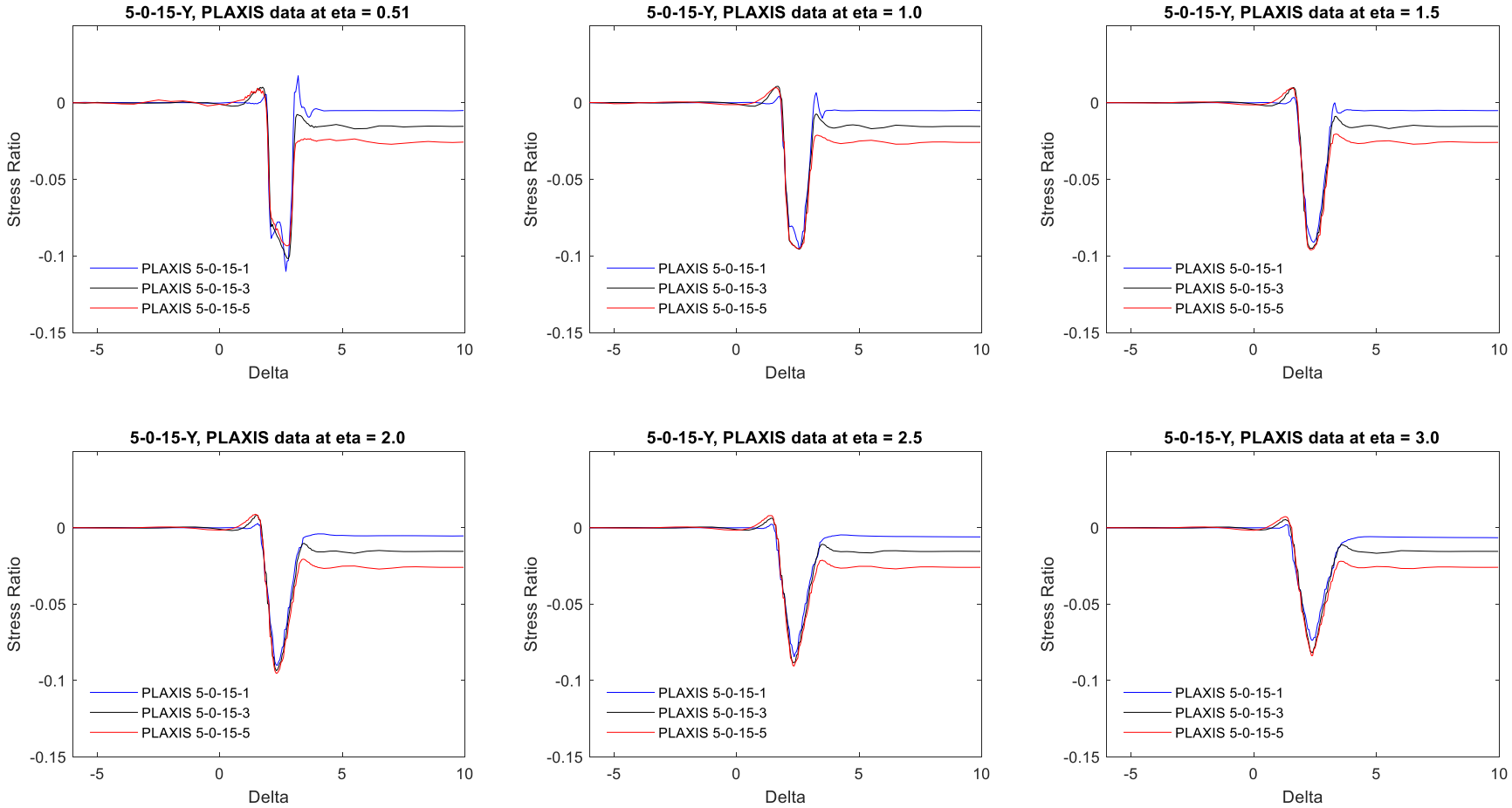

Figure 5.78. PLAXIS stress ratio data for geometries 5-0-15-1, 5-0-15-3, and 5-0-15-5.

Amplitude Adjustments

Figures 5.75-5.77, show that the computed peak stress ratio for 5-0-15-0 was greater than that computed for the θ_3 = 1, 3, and 5 degrees models. The predicted SSR amplitude for the θ_3 = 0 case, therefore, needs to decrease when $\theta_3 > 0$. The computed amplitude reduction for the $\theta_3 > 0$ models appears to be the same whether θ_3 = 1, 3, and 5 degrees (see Figure 5.78). This amplitude decreases with increasing depth. The latter observations of the peak amplitude dropping quickly between $\theta_3 = 0$ to $\theta_3 = 1°$, and the constant peak amplitude once $\theta_3 > 0$, agree with the parametric analyses discussed in Section 5.4.5.2.4 and shown in Figure 5.47.

To obtain a reduction function, one can subtract the peak predicted amplitude from the peak PLAXIS amplitude at each η as shown in Table 5.15. The difference in peak amplitude between the predicted/PLAXIS SSR data was fit with a power function as shown in Figure 5.79. This adjustment is notable for the fact that it does not depend on θ_3 because the peak amplitude computed by PLAXIS does not vary with θ_3 for $\theta_3 > 0$. This unexpected, and currently unexplained, result complicates the modeling process because it implies a nearly binary condition for $\theta_3 = 0$ and $\theta_3 > 0$.

Table 5.15. Calculation of the peak amplitude difference between the predicted and PLAXIS SSR.

η	Predicted Amplitude	PLAXIS Amplitude	Amplitude Difference
0.5	-0.2635	-0.0920	0.1715
1	-0.1865	-0.0940	0.0925
1.5	-0.1552	-0.0950	0.0602
2	-0.1349	-0.0950	0.0399
2.5	-0.1224	-0.0900	0.0324
3	-0.1130	-0.0830	0.0300

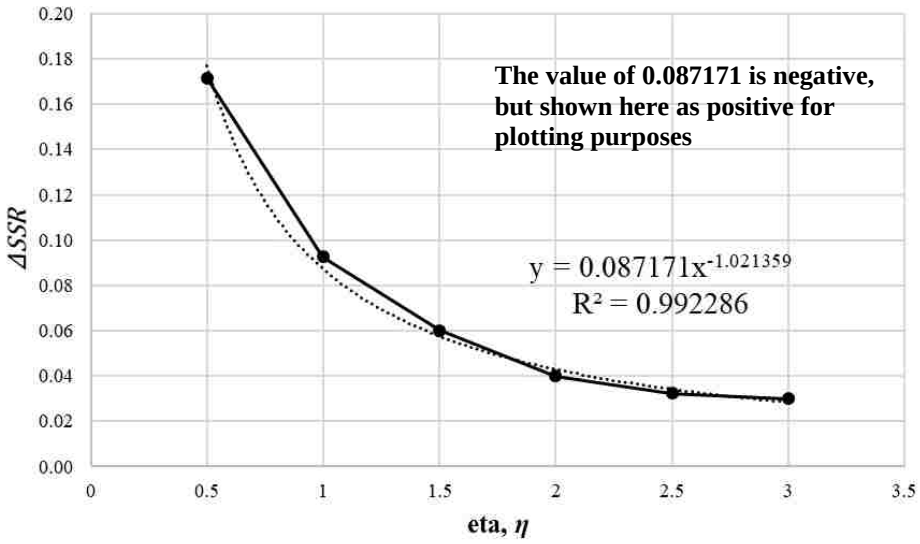

Figure 5.79. Predicted function peak amplitude decrease to fit $\theta_3 > 0$ geometries.

Therefore, the peak amplitude adjustment expression shown in Figure 5.79 can be added to the predicted function base θ_2 expressions (expression for the 5-0-X-0 geometries) for peak amplitude. Adding this peak amplitude adjustment (which is a negative value) gives a relatively good fit for amplitude for the 5-0-15-1, 5-0-15-3, and 5-0-15-5 geometries. To account for the observed θ_3 sensitivity, a pseudo-Kronecker delta function was developed. The Kronecker delta function gives a value of 1 if a condition ($\theta_3 > 0$) is met and 0 if it is not ($\theta_3 = 0$) met.

$$\delta_K = \begin{cases} 0 & if\ \theta_3 = 0 \\ 1 & if\ \theta_3 > 0 \end{cases} \tag{5.45}$$

where δ_K is the Kronecker delta. The pseudo-Kronecker delta developed replicates the Kronecker delta, however, does not require a conditional statement. The pseudo-Kronecker delta was developed by carefully creating data that ranges from 0 to 1 for a θ_3 ranging from 0 to 5 and fitting a power function to the data. The absolute difference between the power function fit, and the data it is fit to, was calculated. This absolute difference was plotted and a linear function was fit to it with the intercept set to a value of 0.05. The power function was subtracted by the linear function

and this difference was plotted to give the pseudo-Kronecker delta function as shown in Figure 5.80 and shown in Equation 5.46.

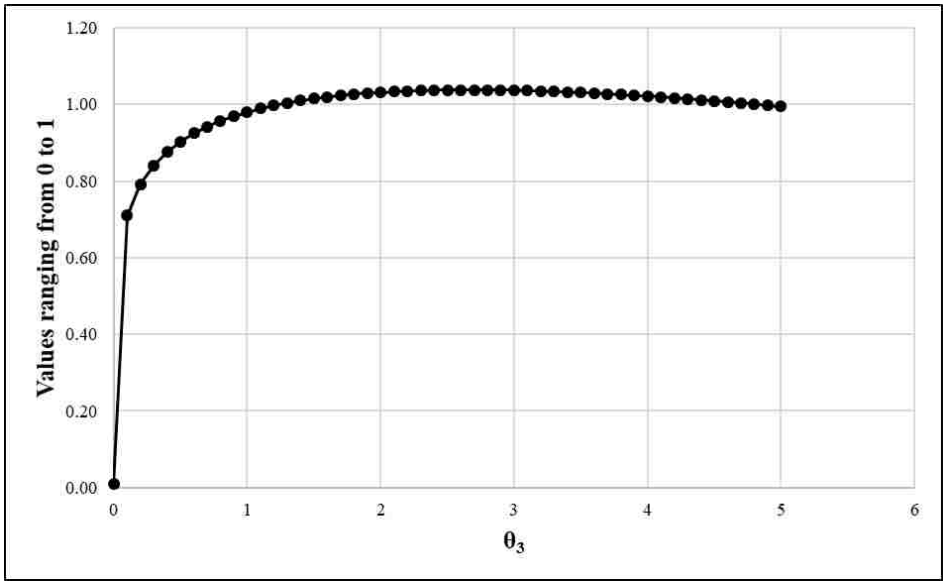

Figure 5.80. Pseudo Kronecker delta function developed.

$$\delta_K = \left(1.1065{\theta_3}^{0.15847}\right) - (0.0767\theta_3 + 0.05) \tag{5.46}$$

The pseudo-Kronecker delta function in Figure 5.80 goes from a value of 0.01 at θ_3 = 0.00000001 to a value of approximately 1 from θ_3 = 1 to 5. Even a value of θ_3 = 0.5 degrees still returns 0.9. Therefore, the pseudo-Kronecker delta is sufficient in making the amplitude reduction 0, when θ_3 = 0, and whatever it calculates to be when $\theta_3 > 0$. Thus, multiplying the amplitude reduction shown in Figure 5.79 by the pseudo-Kronecker delta function given by Equation 5.46, allows the amplitude adjustment with respect to η to be applied for the 5-0-15-Y (where Y = 1, 3, and 5) cases without impacting the 5-0-15-0 case as shown in Figures 5.81-5.84. Therefore, the peak amplitude is given as

$$A_{peak} = \left[\left(0.027332{\theta_2}^{0.668503}\right) * \eta^{\left(-0.099801{\theta_2}^{0.630551}\right)}\right] + \left[\left(1.1065{\theta_3}^{0.15847}\right) - (0.0767\theta_3 + 0.05)\right] * \left(-0.087171\eta^{-1.021359}\right) \tag{5.47}$$

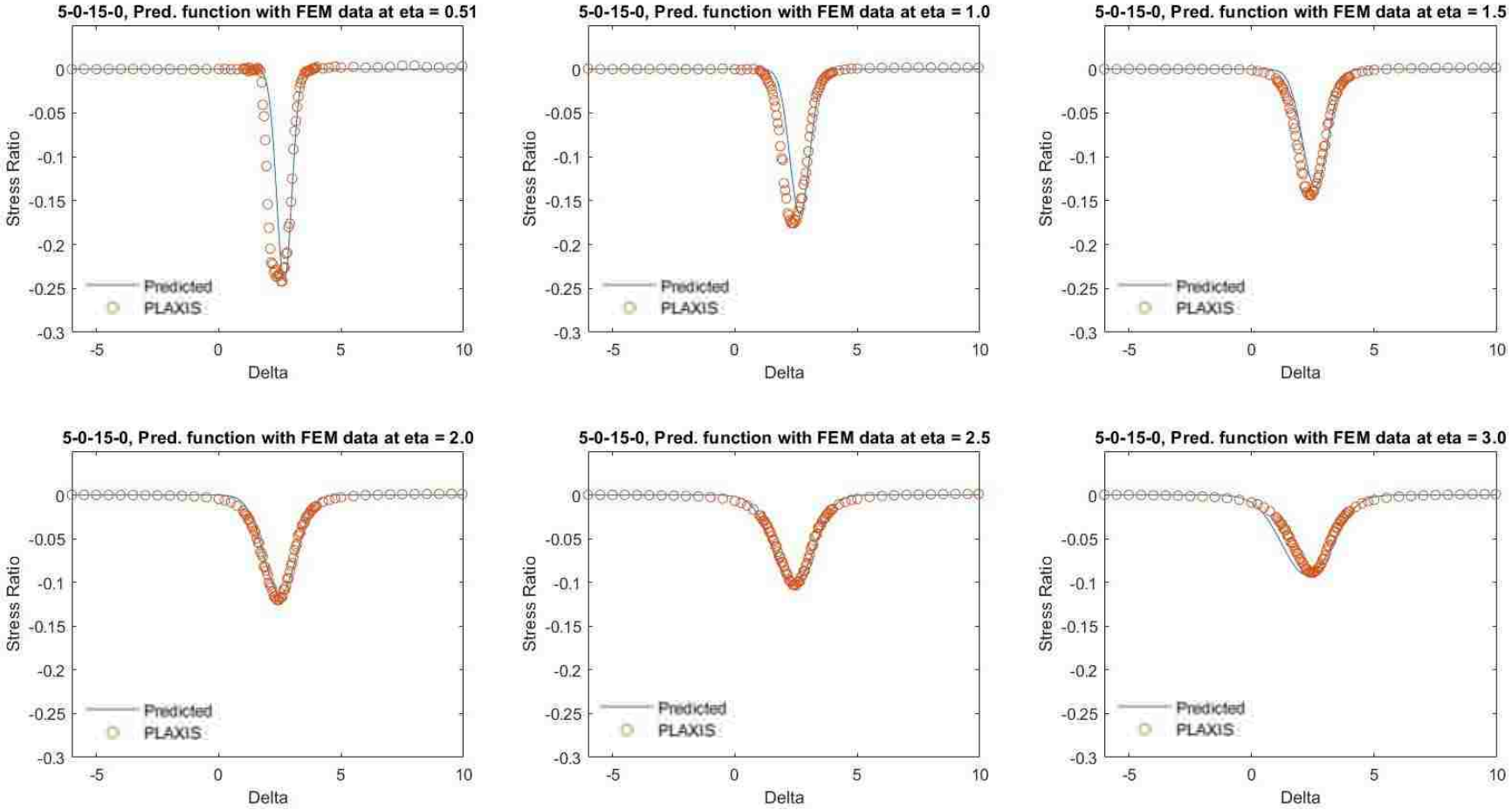

Figure 5.81. Predicted function for geometry 5-0-15-0 with amplitude reduction adjustment compared to the PLAXIS stress ratio data for geometry 5-0-15-0.

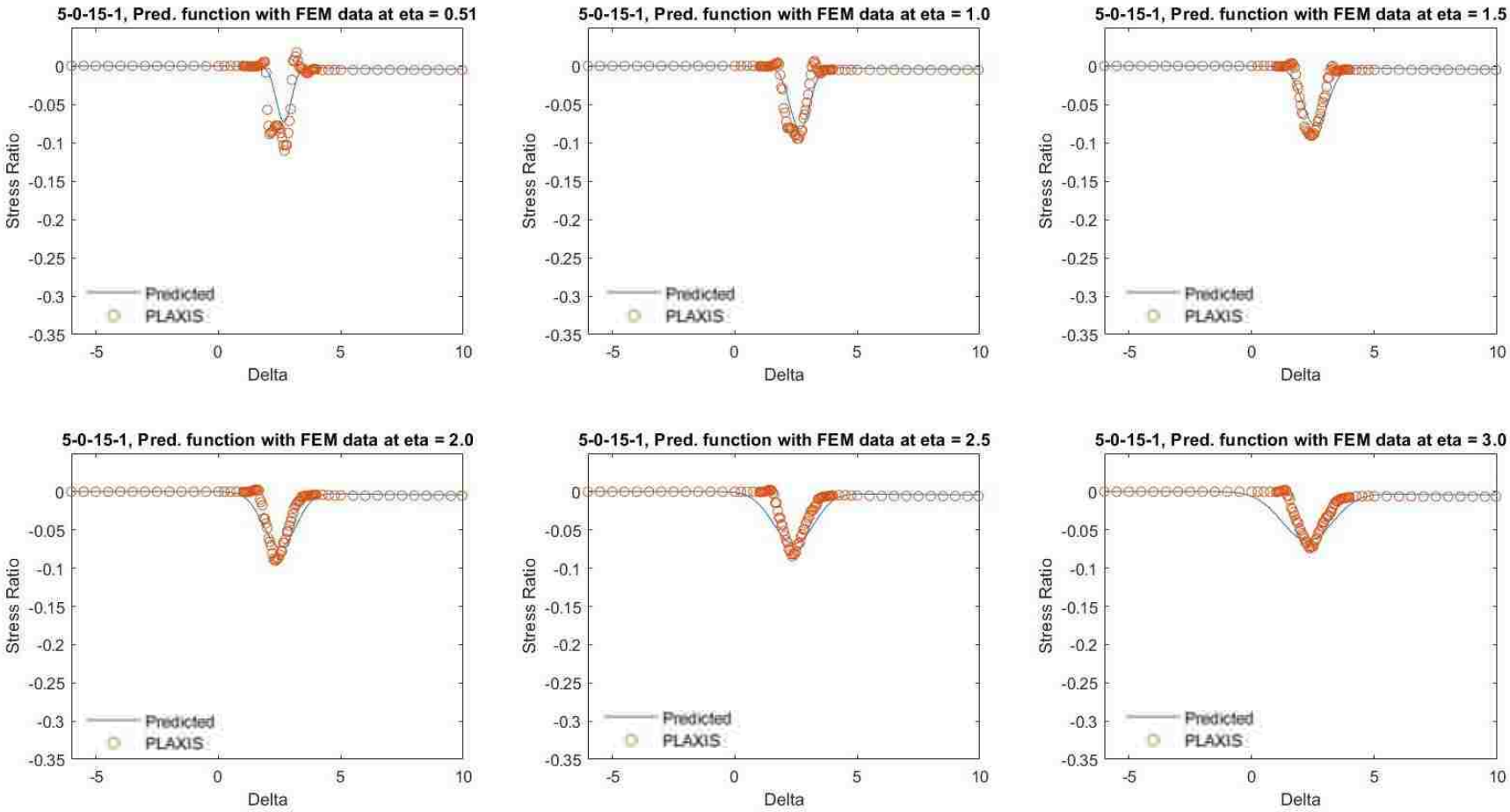

Figure 5.82. Predicted function for geometry 5-0-15-1 with amplitude reduction adjustment compared to the PLAXIS stress ratio data for geometry 5-0-15-1.

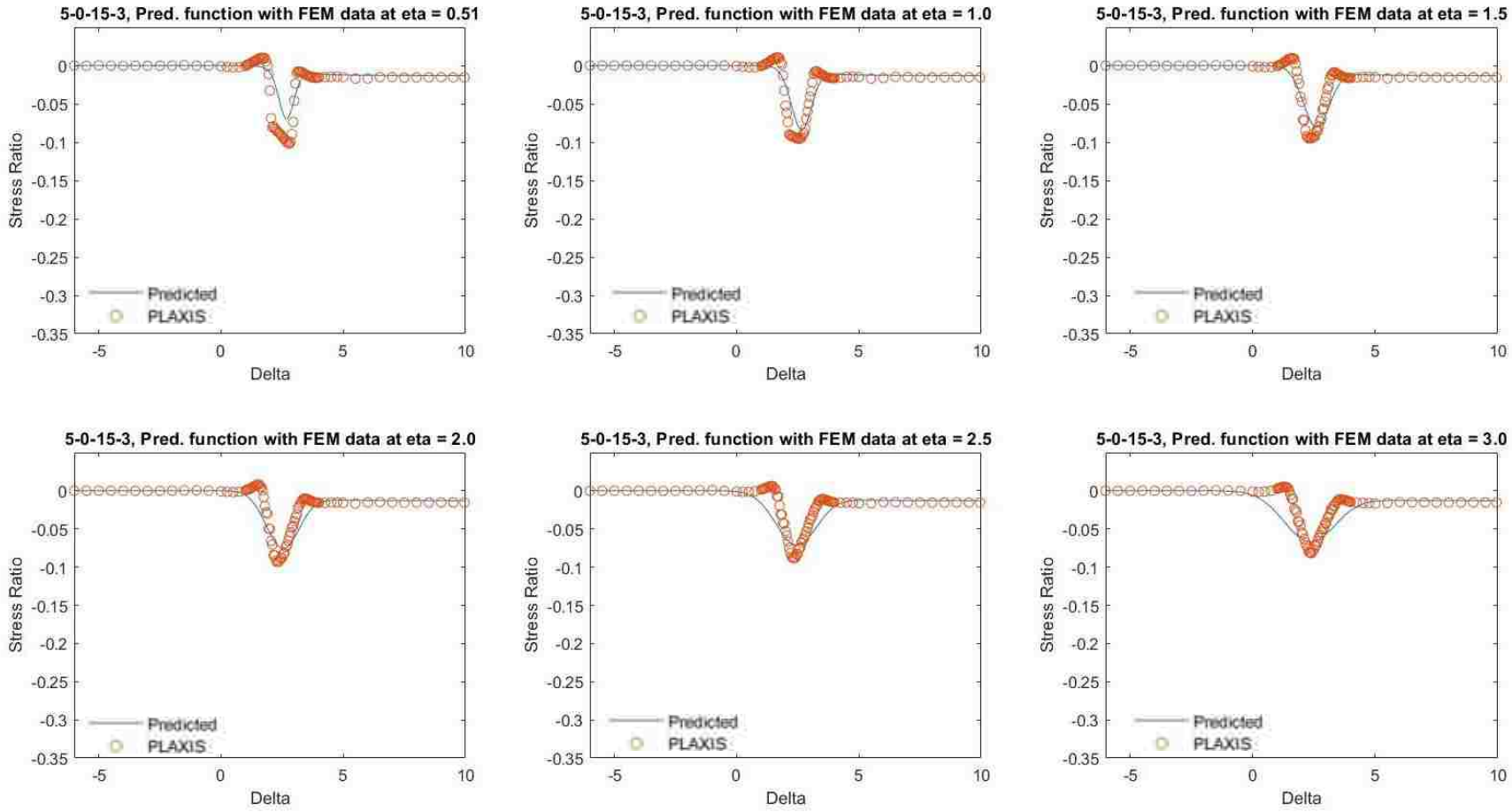

Figure 5.83. Predicted function for geometry 5-0-15-3 with amplitude reduction adjustment compared to the PLAXIS stress ratio data for geometry 5-0-15-3.

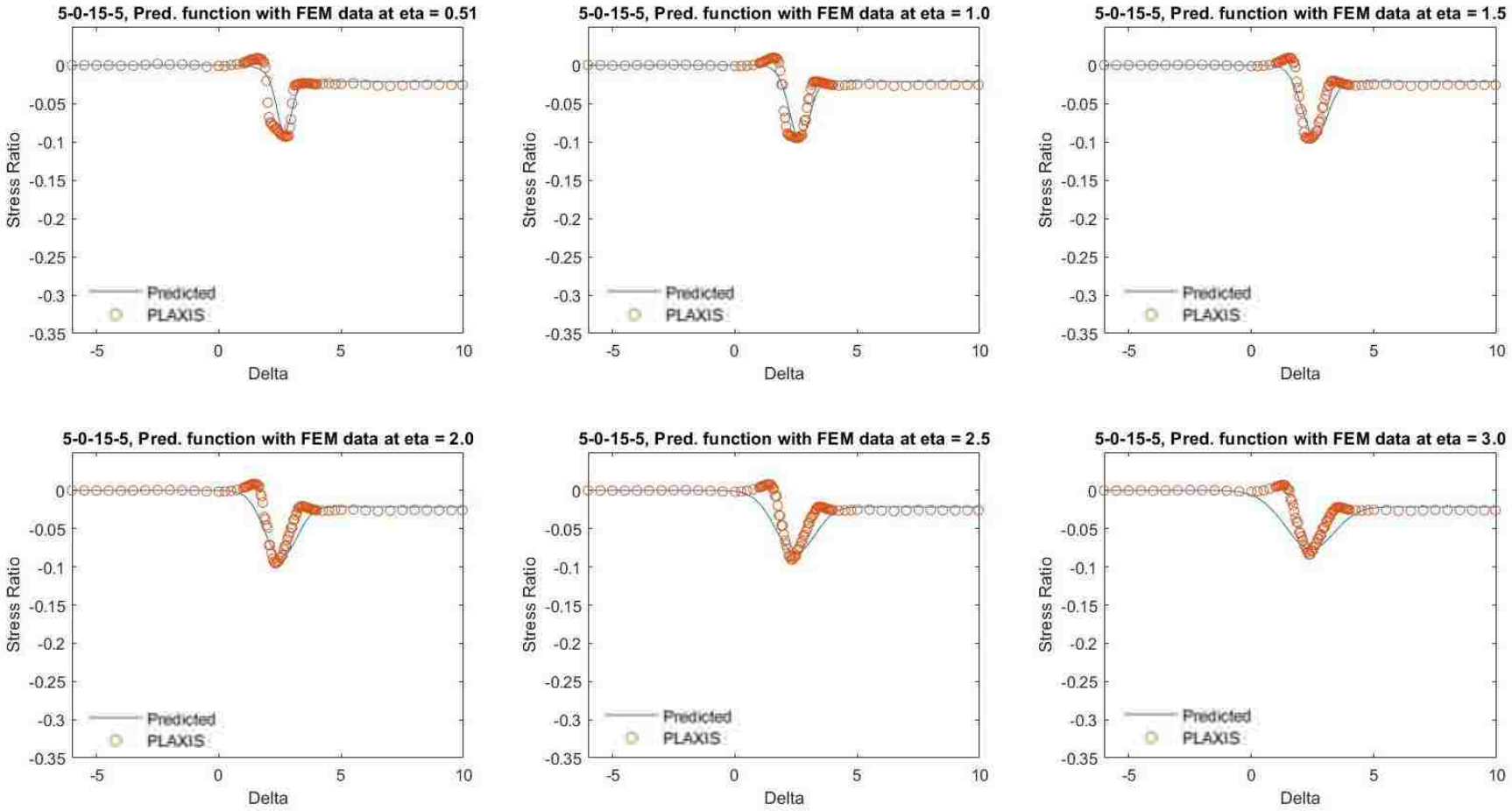

Figure 5.84. Predicted function for geometry 5-0-15-5 with amplitude reduction adjustment compared to the PLAXIS stress ratio data for geometry 5-0-15-5.

At this point, the amplitude of the predicted SSR matches the PLAXIS SSR data for the 5-0-X-0 geometries and the 5-0-15-Y geometries (where Y represents the θ_3 values of 1, 2, and 3 degrees), however, the SSR behavior will be different when including the 5-0-5-Y, 5-0-10-Y, 5-0-20-Y, and 5-0-25-Y geometries. Using the same method as was done for the 5-0-15-Y geometries, the behavior of the PLAXIS data for the 5-0-5-Y, 5-0-10-Y, 5-0-20-Y, and 5-0-25-Y geometries were carefully analyzed and trial and error was used to incorporate all 19 of the 5-0-X-Y geometries (see Table 5.6). Including all of these geometries into the predicted SSR function required adjustments to the amplitude, the minimum and maximum bounds, and the FF parameters. The α and β shape parameters were assumed to be influenced by θ_3, e.g., α and β values will not change between 5-0-10-0, 5-0-10-1, 5-0-10-3, and 5-0-10-5.

The amplitude has been corrected by decreasing it for changes in η, however, when adding the 5-0-5-Y, 5-0-10-Y, 5-0-20-Y, and 5-0-25-Y geometries an amplitude adjustment accounting for the change in θ_2 for $\theta_3 > 0$ geometries needed to be incorporated. Based on the PLAXIS SSR data from the new geometries added, the amplitude increase needed to be the greatest at $\theta_2 = 5$ degrees and smallest at $\theta_2 = 25$ degrees. The amplitude also needed to be increased more at $\eta = 0.5$ than at $\eta = 3$. Therefore, through trial and error and diligently examining the stress ratio plots for each geometry at each η value, the adjustments that needed to occur dependent upon θ_2 for $\theta_3 > 0$ geometries produced the amplitude adjustment shown in Figure 5.85. The amplitude expression shown in Figure 5.85 needs to be multiplied by $0.24/\eta^2$ (see Equation 5.48) to account for the larger increase in amplitude needed at $\eta = 0.5$ and a smaller increase in amplitude at $\eta = 3$.

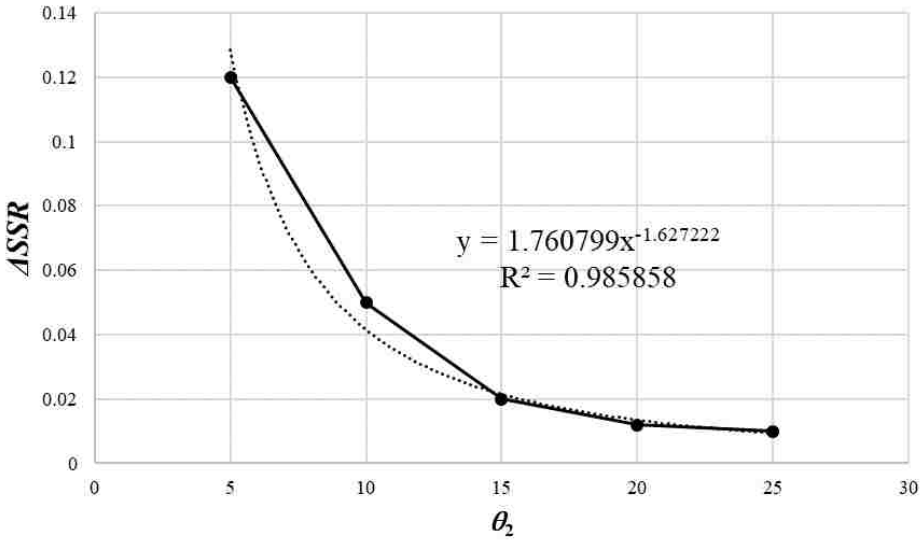

Figure 5.85. Amplitude increase as a function of θ_2.

$$Amplitude\ Increase\ Adjustment = 1.7608{\theta_2}^{-1.6272} \times \left(\frac{0.24}{\eta^2}\right) \qquad (5.48)$$

It's important to note that no amplitude adjustment is needed for the base 5-0-*X*-0 geometries, therefore, the amplitude increase adjustment shown in Equation 5.48 can be multiplied by the pseudo-Kronecker delta function (Equation 5.46) in order for this adjustment to only apply when $\theta_3 > 0$. Therefore, the peak amplitude has been corrected for all geometries with $5 \leq \theta_2 \leq 25$ degrees and $0 \leq \theta_3 \leq 5$ degrees for a slope height of 5 meters and a $\theta_1 = 0$. The final peak amplitude expression is given as

$$A_{peak} = \left[\left(0.027332{\theta_2}^{0.668503}\right) * \eta^{\left(-0.099801{\theta_2}^{0.630551}\right)}\right] + \left[\left(1.1065{\theta_3}^{0.15847}\right) - (0.0767\theta_3 + 0.05)\right] * \left[(-0.087171\eta^{-1.021359}) + \left(1.7608{\theta_2}^{-1.6272}\right) \times \left(\frac{0.24}{\eta^2}\right)\right] \qquad (5.49)$$

Minimum and Maximum Bound Adjustments

As the depth below the slope increases, the lateral extent affected by the stresses imposed by the slope increases. Therefore, it is reasonable that as η increases, the range between δ_{min} and

δ_{max} must increase. Examination of the PLAXIS SSR data shows the latter – the separation between the δ_{min} and δ_{max} for geometries with $\theta_3 > 0$ needed to increase from $\eta = 0.51$ to $\eta = 3$. For example, Figure 5.86 depicts the need for an increase between the δ_{min} and δ_{max} from $\eta = 0.51$ to $\eta = 3$ for geometry 5-0-15-3.

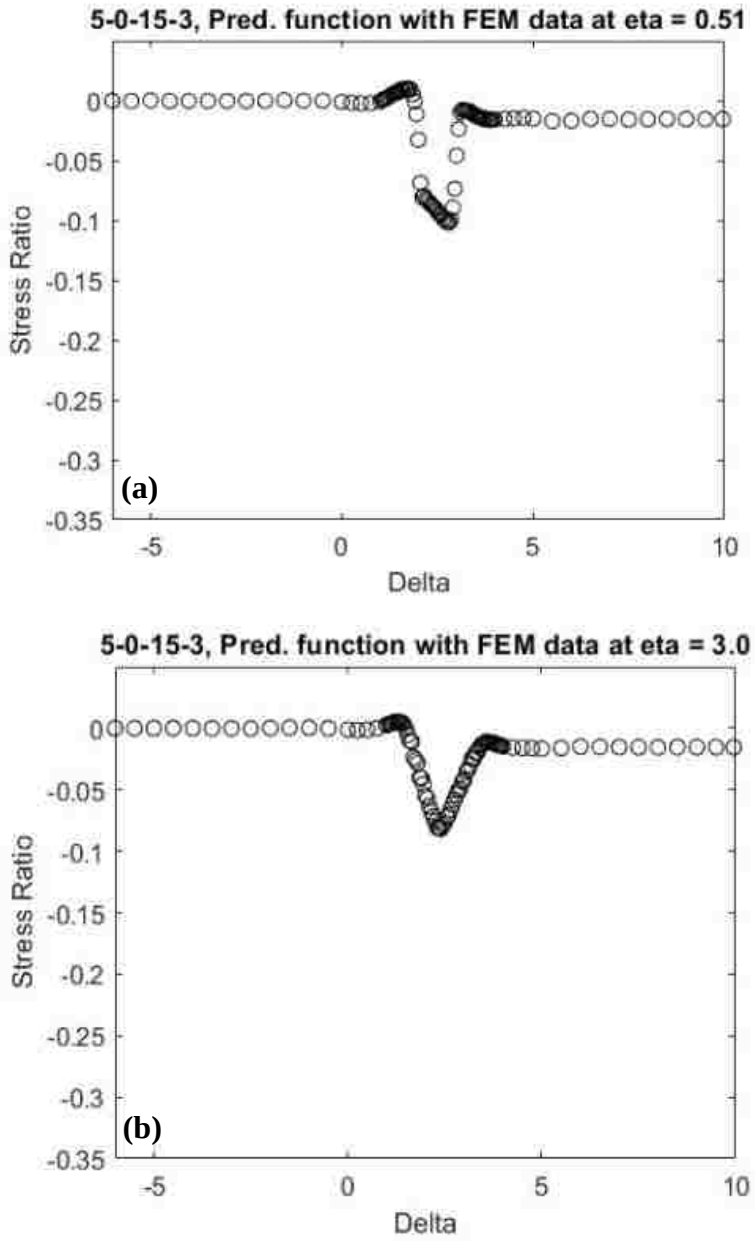

Figure 5.86. PLAXIS stress ratio data plotted for geometry 5-0-15-3 at $\eta = 0.51$ and $\eta = 3$ shown in (a) and (b) respectively.

Analyzing PLAXIS SSR results similar to Figure 5.86, a power function dependent on η for the δ_{min} and δ_{max} was created in order to increase the separation of the predicted function for the θ_3 > 0 cases (Figure 5.87). This adjustment is only needed for the θ_3 > 0 geometries, therefore, it should be multiplied by the pseudo Kronecker delta function (Equation 5.46) to not change the base 5-0-X-0 geometries.

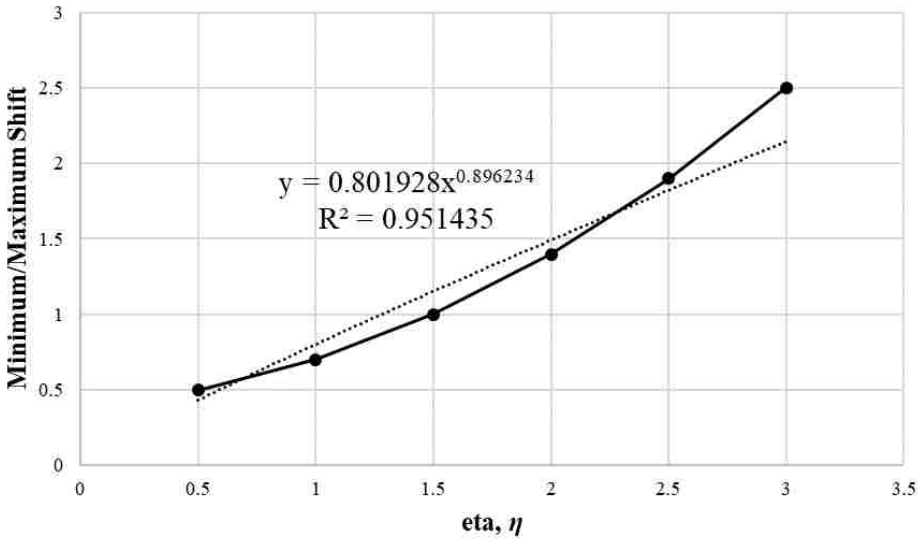

Figure 5.87. Minimum/Maximum Bound power function dependent on η adjustment.

The final expressions for δ_{min} and δ_{max} are given as

$$\delta_{min} = (1.33 - 0.21\theta_2) + (0.1103 - 0.1198\theta_2) * \eta + \left[\left(1.1065{\theta_3}^{0.15847}\right) - (0.0767\theta_3 + 0.05)\right] * 0.8019\eta^{0.8962} \quad (5.50)$$

$$\delta_{max} = (2.19 + 0.2308 * \theta_2) + (0.2213 + 0.077 * \theta_2) * \eta + \left[\left(1.1065{\theta_3}^{0.15847}\right) - (0.0767\theta_3 + 0.05)\right] * 0.8019\eta^{0.8962} \quad (5.51)$$

Filter Function Parameters

The FF parameters were discussed in 5.4.7, however, only the value of the left plateau, c_3, was provided. Because θ_1 = 0 for all of the geometries in this research c_3 = 0. The value of the SSR where the right plateau, c_4, occurs is dependent on the value of θ_3. Referring back to Figures

5.47-5.48, and careful examination of the PLAXIS SSR data for the other $\theta_3 > 0$ geometries, c_4 was established to vary as a linear function dependent on θ_3 as shown in Figure 5.88. This linear function dependent on θ_3 does not have an intercept, therefore, when $\theta_3 = 0$ the $c_4 = 0$ as it should.

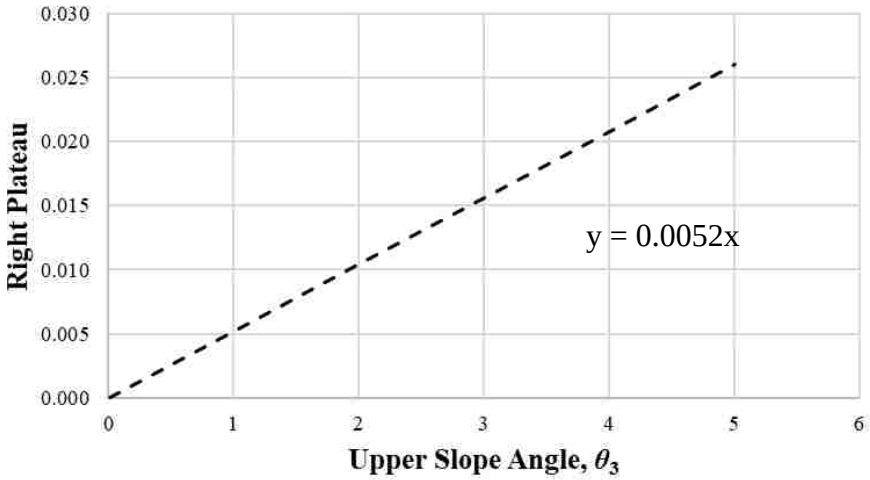

Figure 5.88. Right plateau behavior as a linear function dependent on θ_3.

Therefore, the final expression for the right plateau is given as

$$c_4 = 0.0052 * \theta_3 \tag{5.52}$$

The center of the FF, c_1, was taken to be a constant value of two in order for it to occur near the δ value at center of the predicted function since the B_D was shifted to the right by δ_{Global} = 2 to lower the coefficient of variation as described in Section 5.4.8. The steepness of the FF, c_2, was taken to be a constant value of four to have a smooth transition of the predicted function from the left plateau to the right plateau within the central slope segment.

The FF does change the amplitude slightly in order to drop from the left plateau to the right plateau, however, this slight amplitude change was accounted for in the amplitude adjustments already described, i.e., the FF described here was completed prior to making both of the amplitude adjustments. The latter constant values for the FF center and FF steepness do not impact the θ_3 =

0 case, because, the left and right plateau are zero at θ_3 = 0, which forces the FF to be zero (see Equation 5.25).

Therefore, starting with the base θ_2 expressions and then applying the peak amplitude, δ_{min}, δ_{max}, and c_4 adjustments, along with the constant values for the c_3, c_1, and c_2, 19 predicted functions were fit to the PLAXIS SSR data for the 5-0-X-Y geometries. Figures 5.89-5.107 show the results of the 19 predicted functions matching the PLAXIS SSR data for each of the corresponding geometries. Following these figures, the predicted function equations, and the coefficients of the nine parameters that make up the predicted function (the B_D, the amplitude of the B_D, and the FF), are given. Although only shown for the 19 5-0-X-Y geometries, the predicted function at this point could be applied geometries with $H > 0$, $\theta_1 = 0$, $5 \leq \theta_2 \leq 25$ degrees, $0 \leq \theta_3 \leq 5$ degrees.

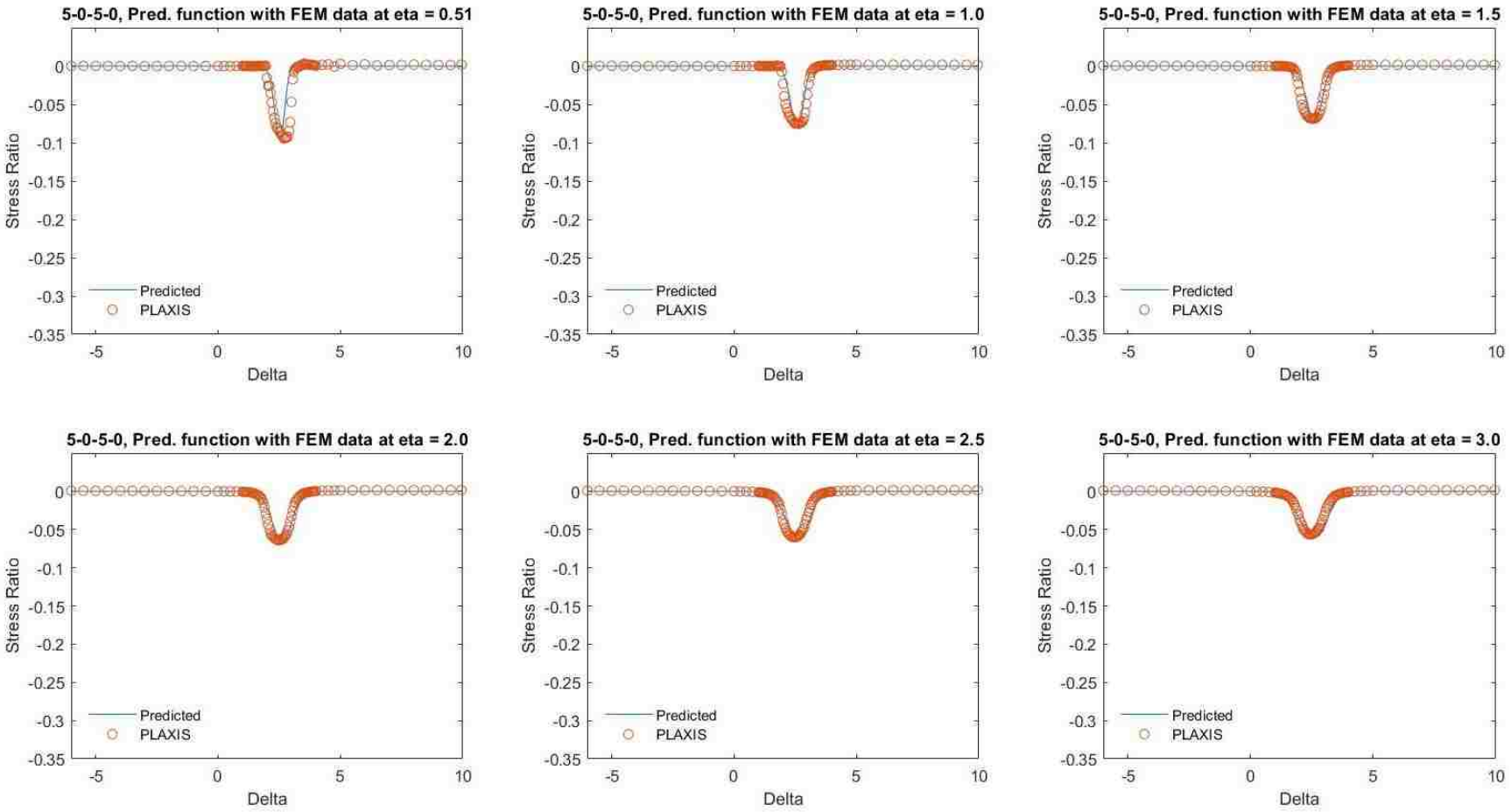

Figure 5.89. Predicted stress ratio function compared to PLAXIS stress ratio for geometry 5-0-5-0.

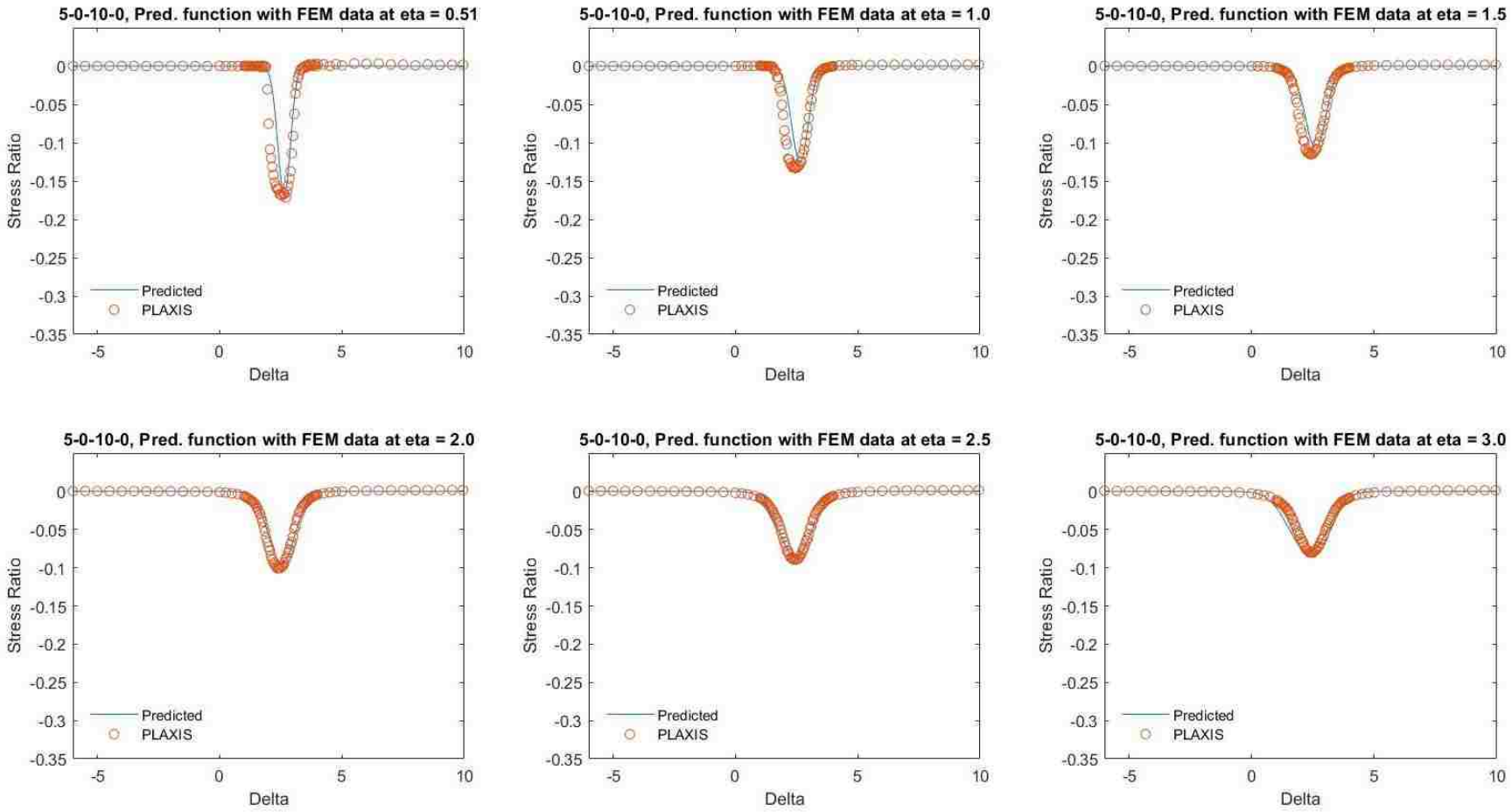

Figure 5.90. Predicted stress ratio function compared to PLAXIS stress ratio for geometry 5-0-10-0.

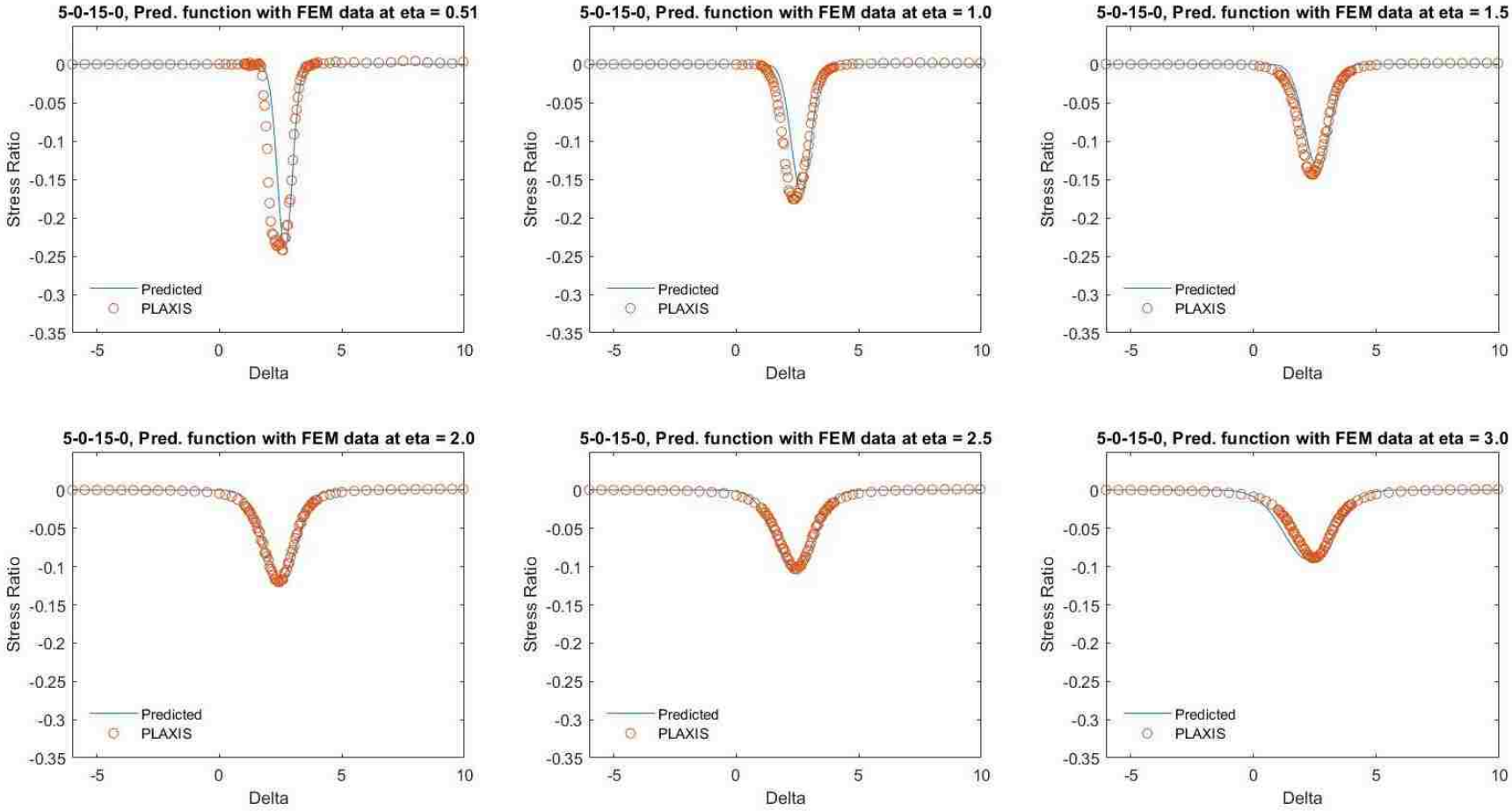

Figure 5.91. Predicted stress ratio function compared to PLAXIS stress ratio for geometry 5-0-15-0.

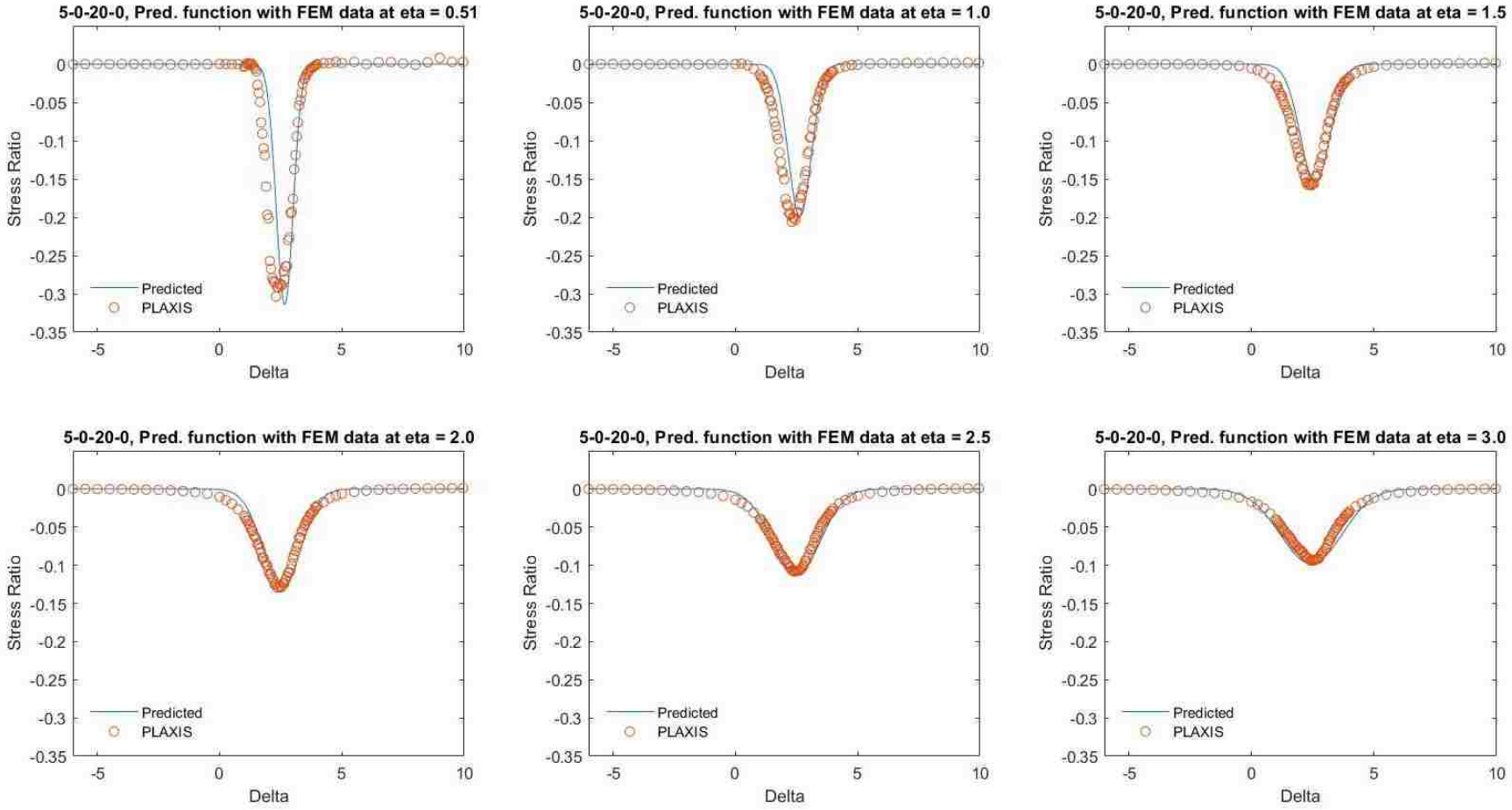

Figure 5.92. Predicted stress ratio function compared to PLAXIS stress ratio for geometry 5-0-20-0.

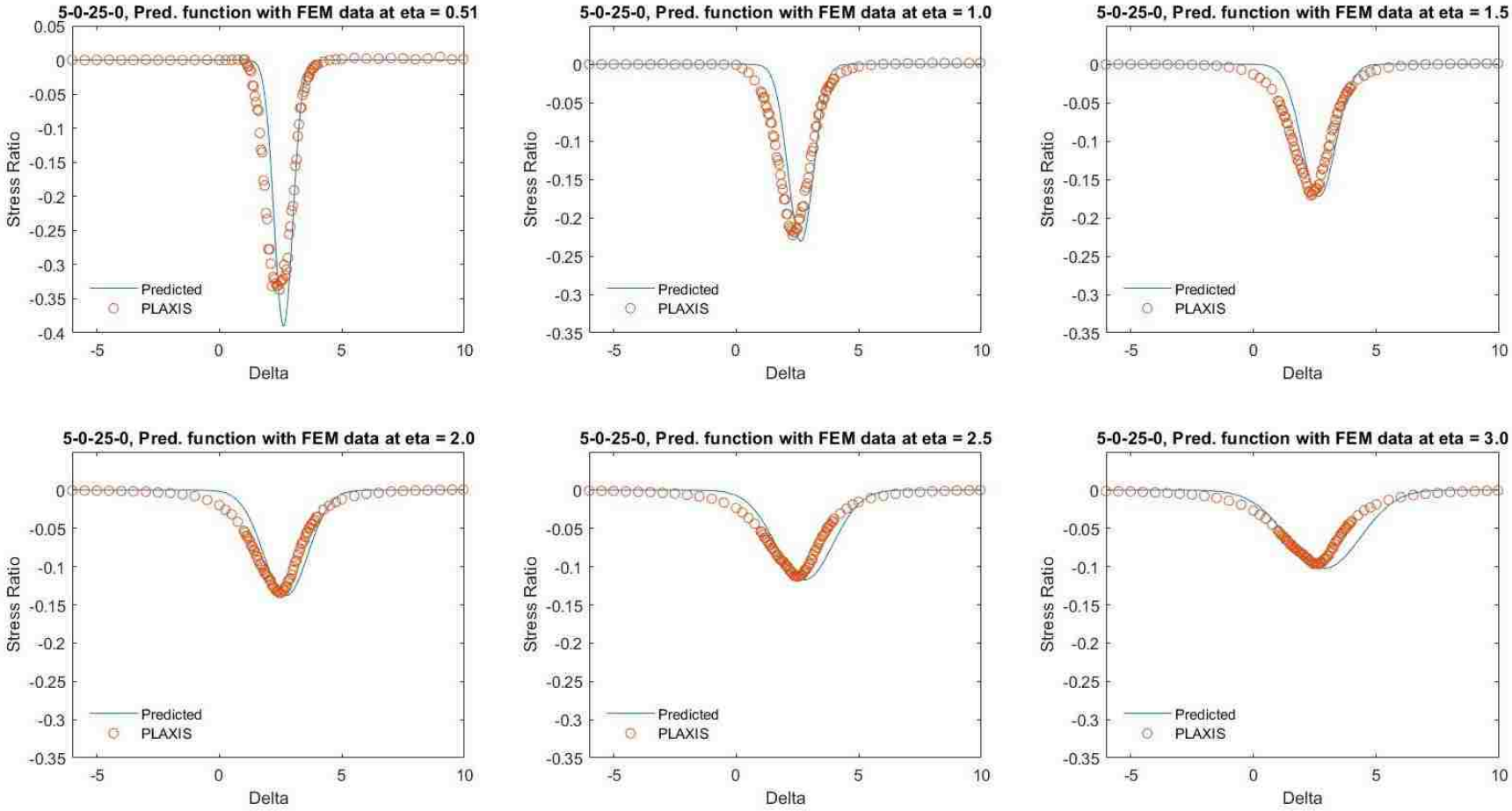

Figure 5.93. Predicted stress ratio function compared to PLAXIS stress ratio for geometry 5-0-25-0.

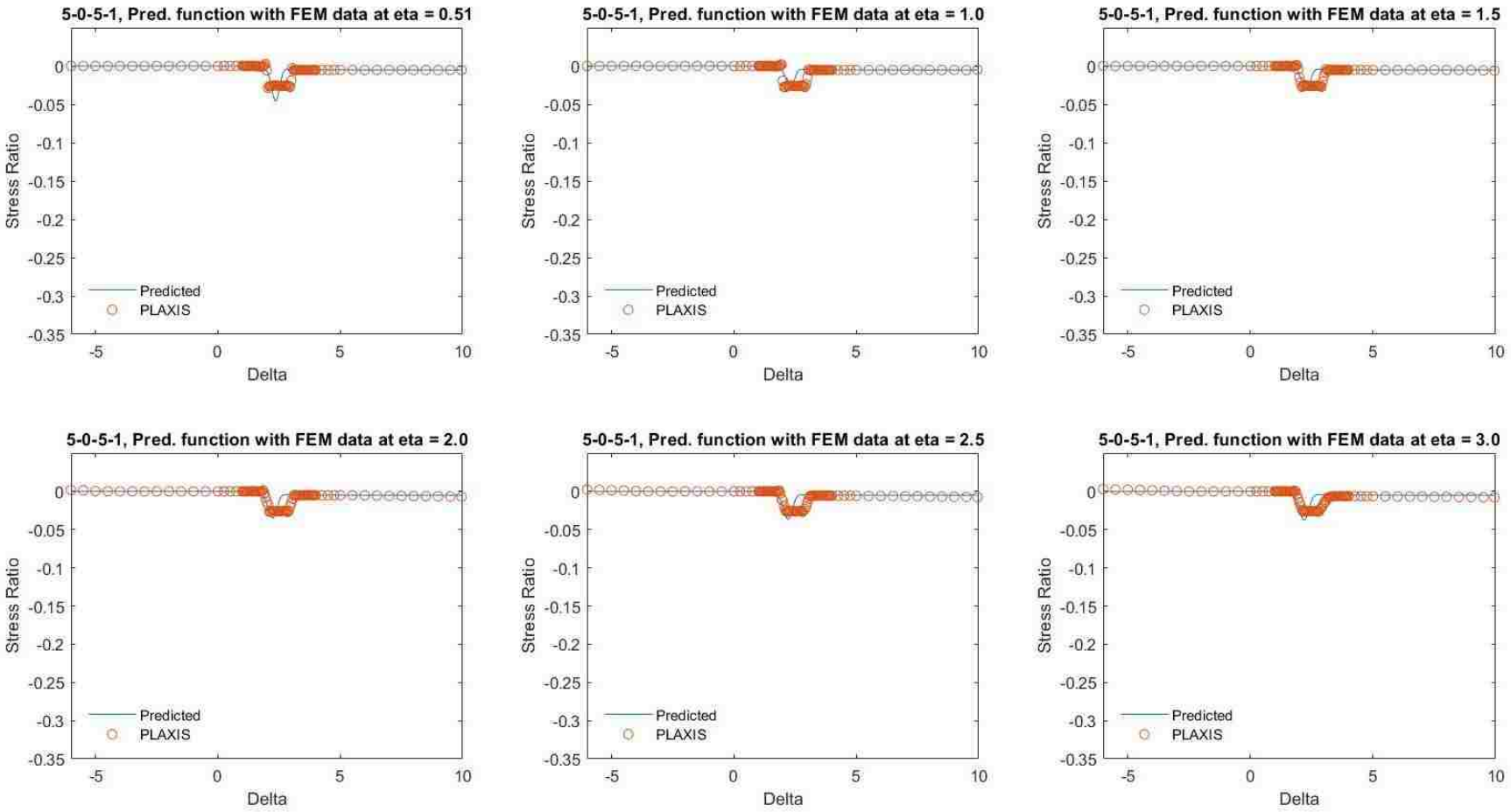

Figure 5.94. Predicted stress ratio function compared to PLAXIS stress ratio for geometry 5-0-5-1.

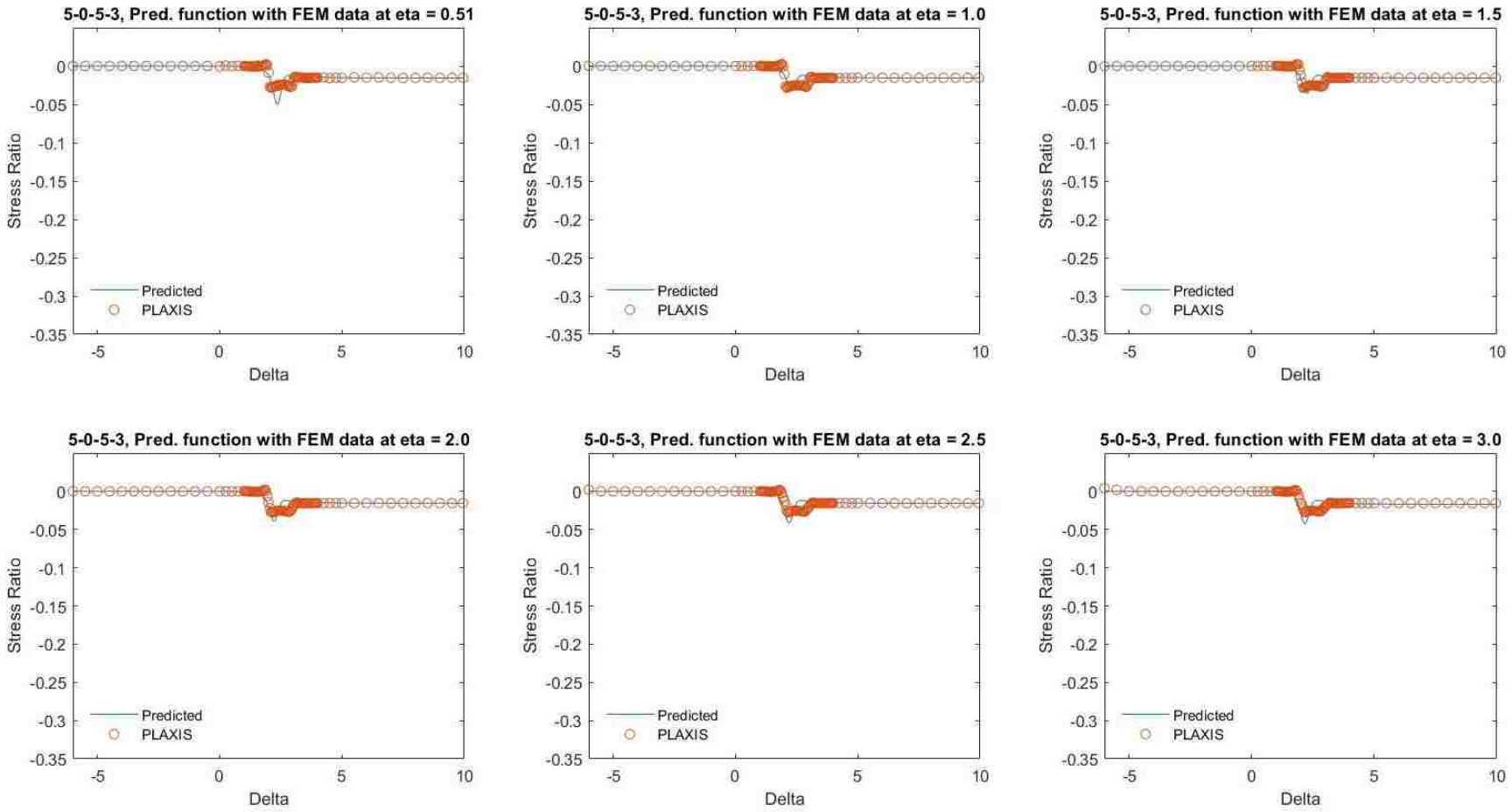

Figure 5.95. Predicted stress ratio function compared to PLAXIS stress ratio for geometry 5-0-5-3.

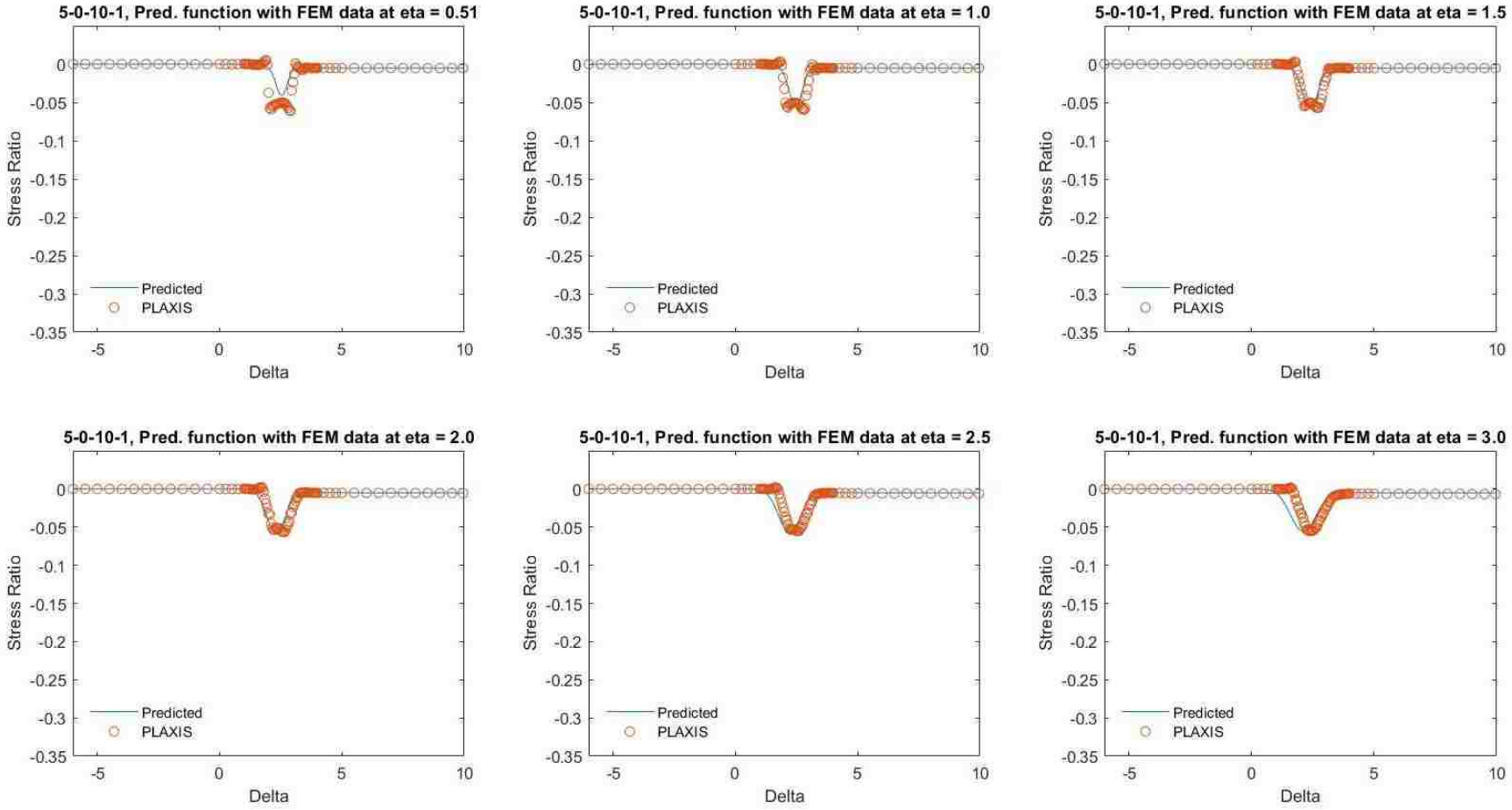

Figure 5.96. Predicted stress ratio function compared to PLAXIS stress ratio for geometry 5-0-10-1.

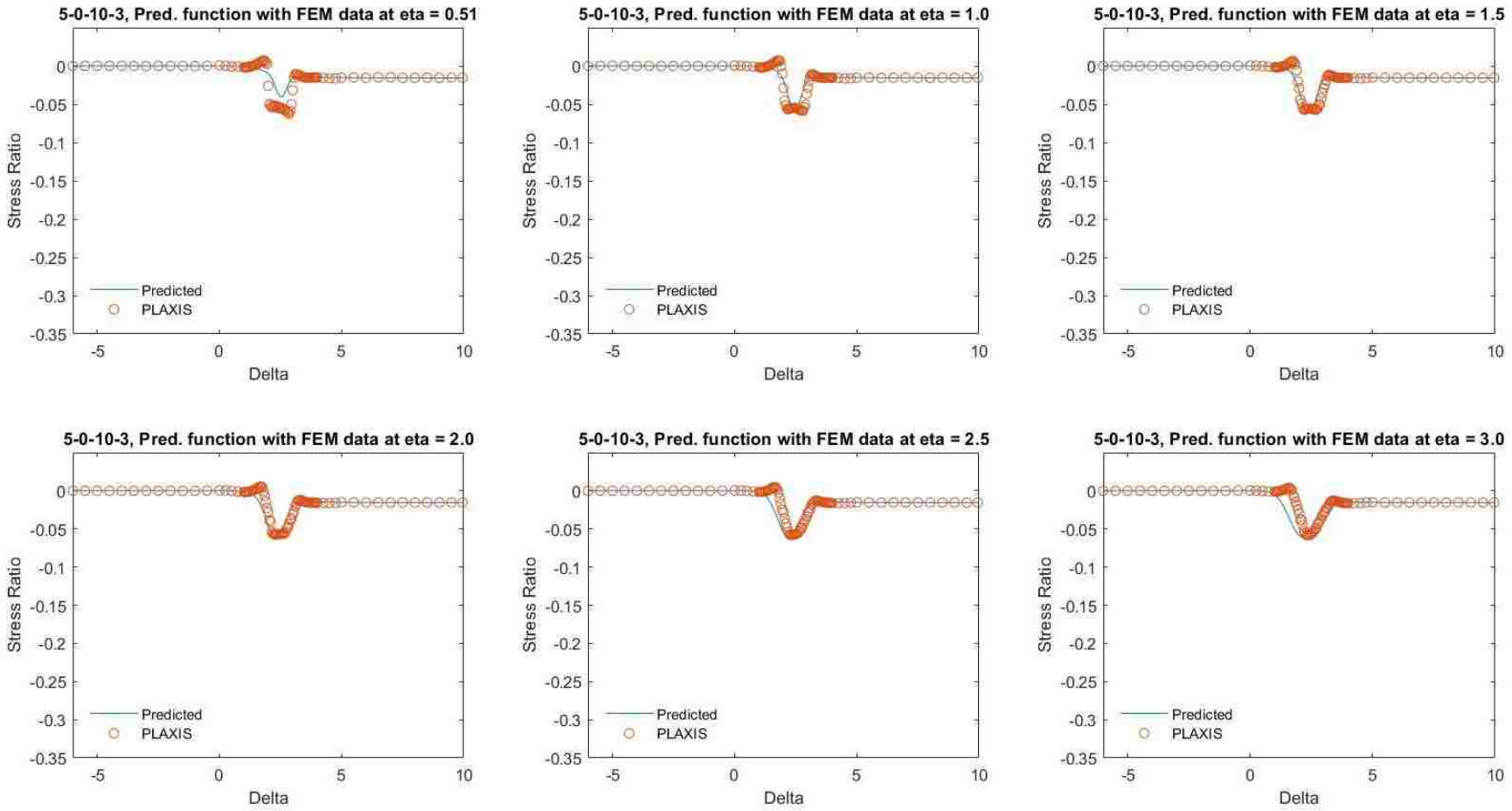

Figure 5.97. Predicted stress ratio function compared to PLAXIS stress ratio for geometry 5-0-10-3.

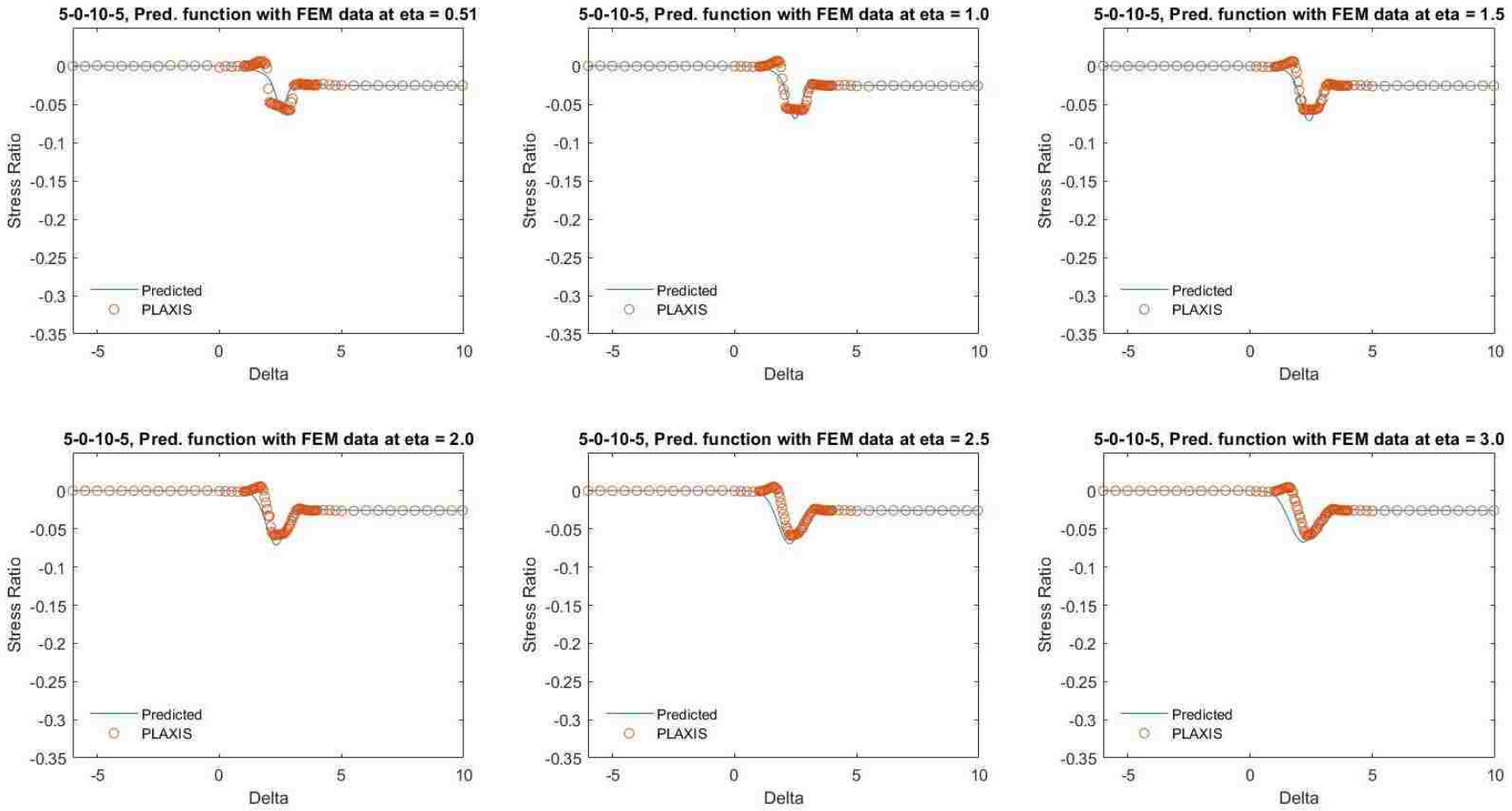

Figure 5.98. Predicted stress ratio function compared to PLAXIS stress ratio for geometry 5-0-10-5.

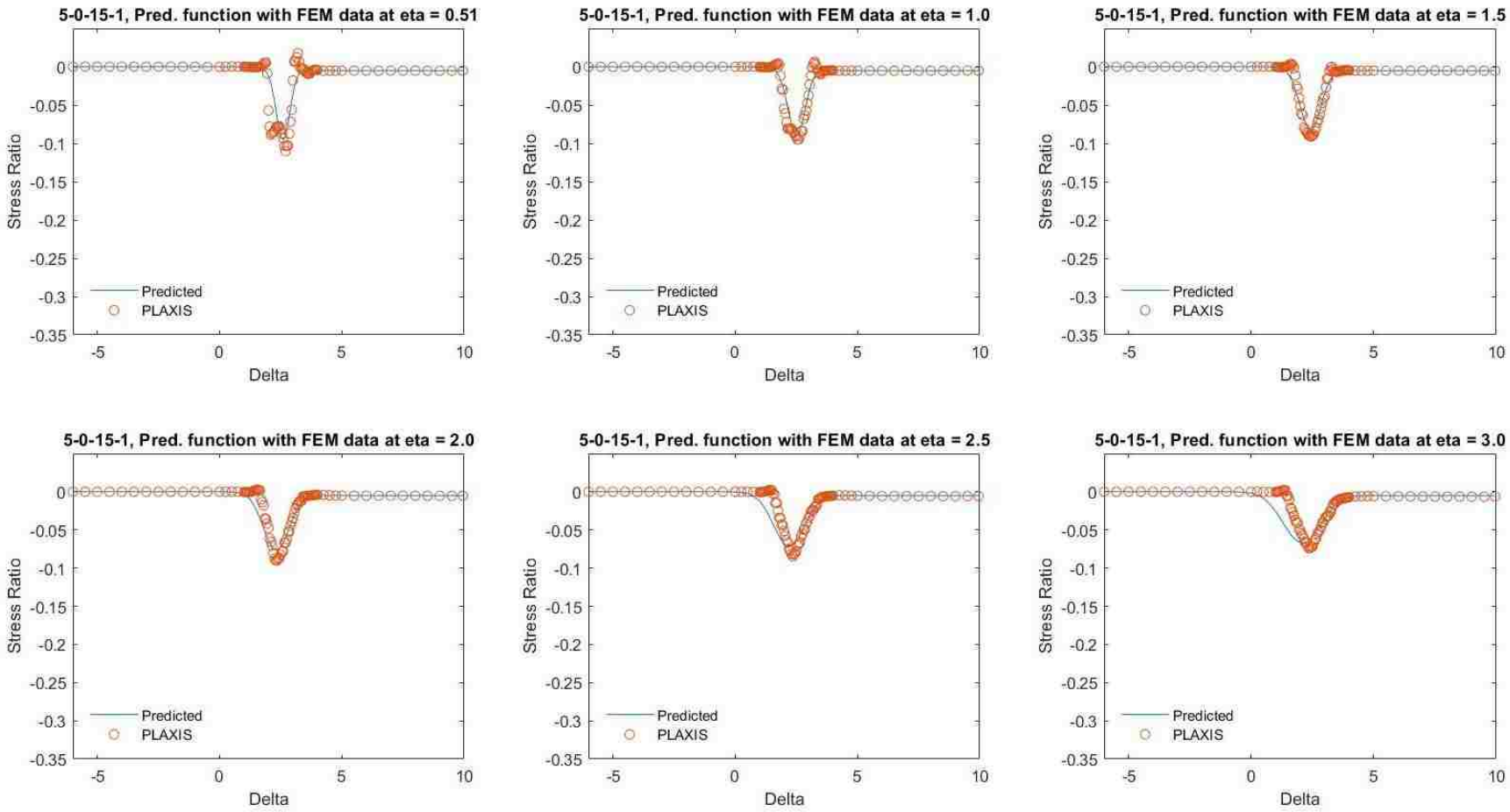

Figure 5.99. Predicted stress ratio function compared to PLAXIS stress ratio for geometry 5-0-15-1.

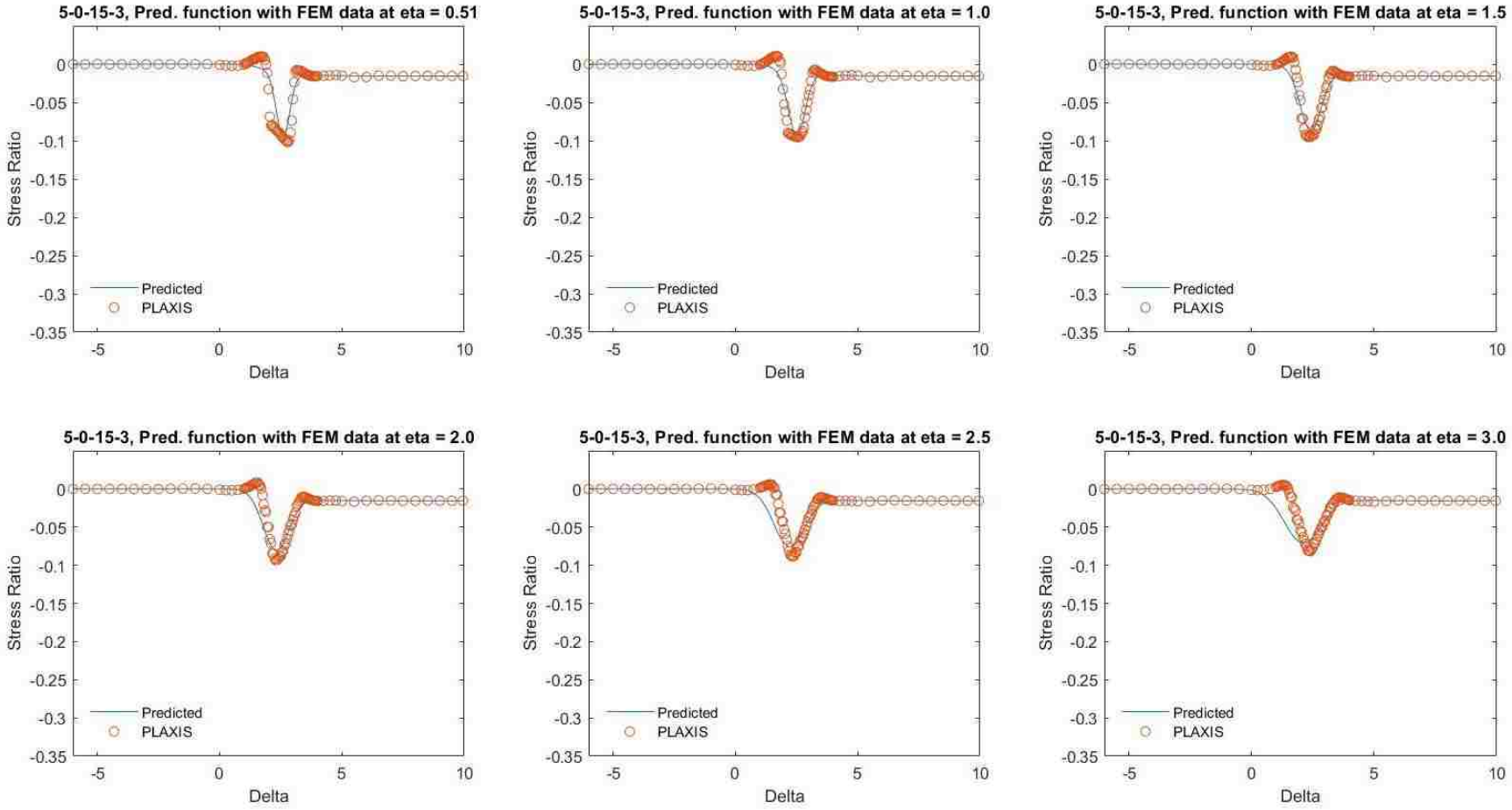

Figure 5.100. Predicted stress ratio function compared to PLAXIS stress ratio for geometry 5-0-15-3.

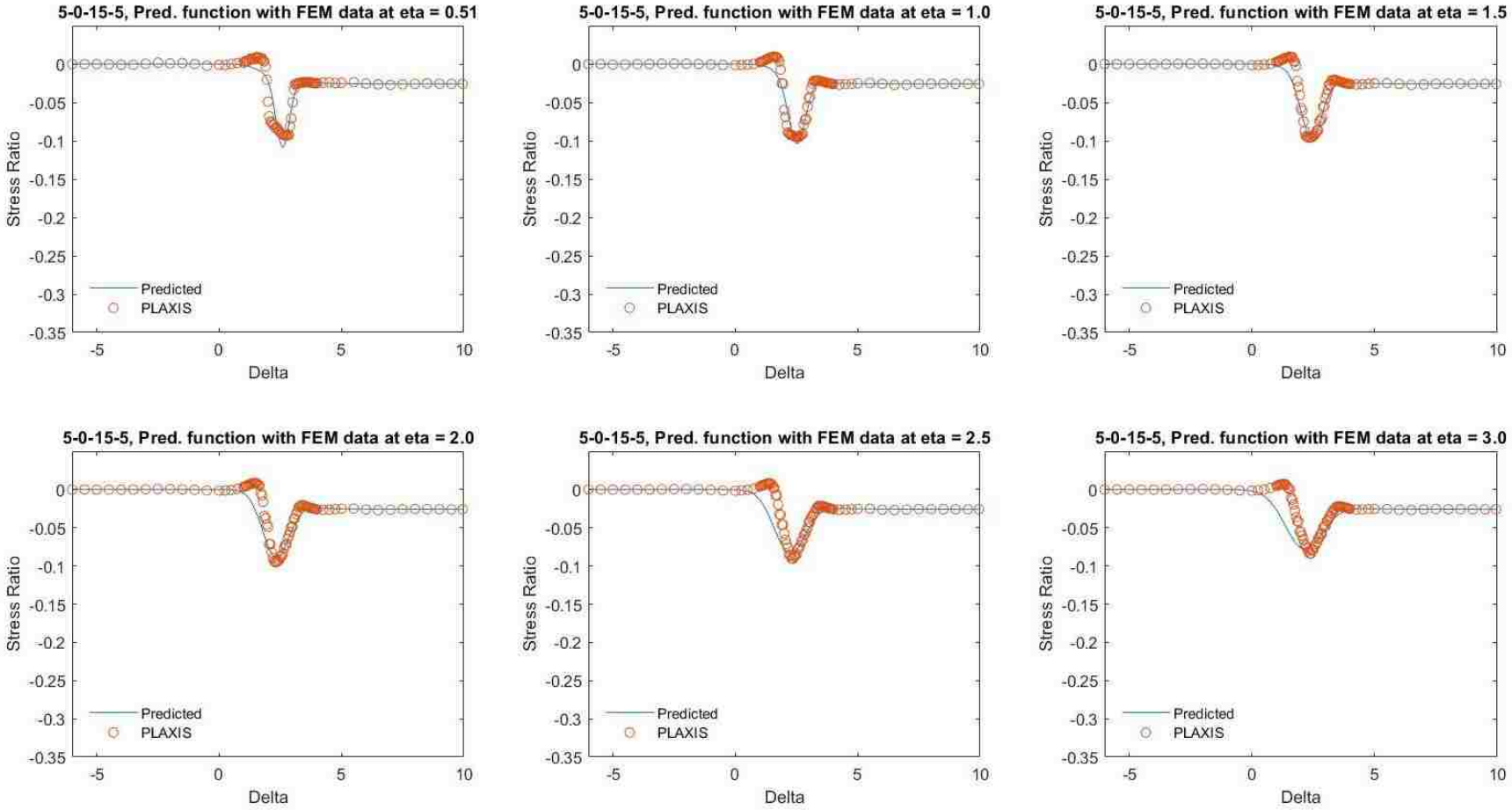

Figure 5.101. Predicted stress ratio function compared to PLAXIS stress ratio for geometry 5-0-15-5.

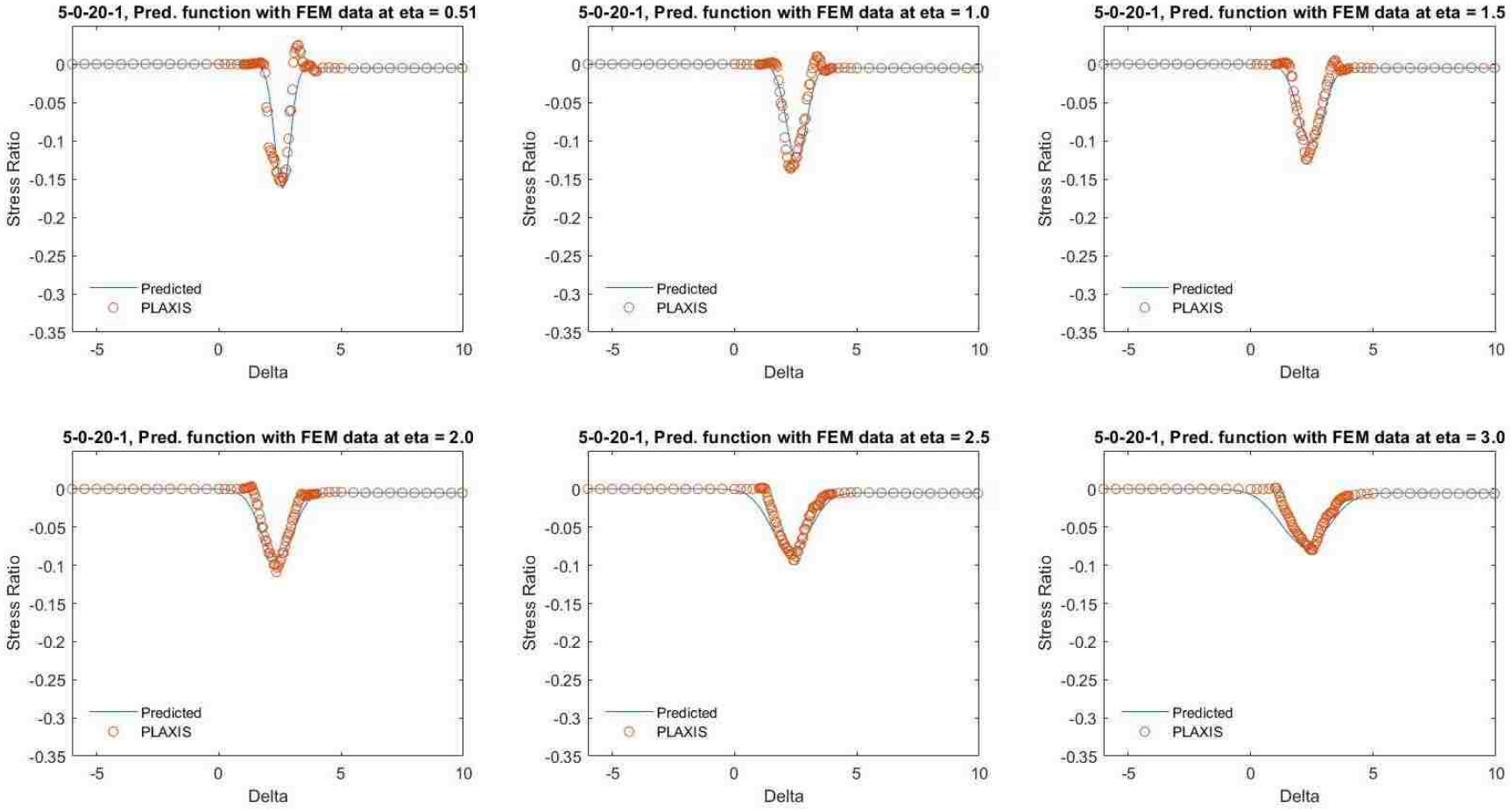

Figure 5.102. Predicted stress ratio function compared to PLAXIS stress ratio for geometry 5-0-20-1.

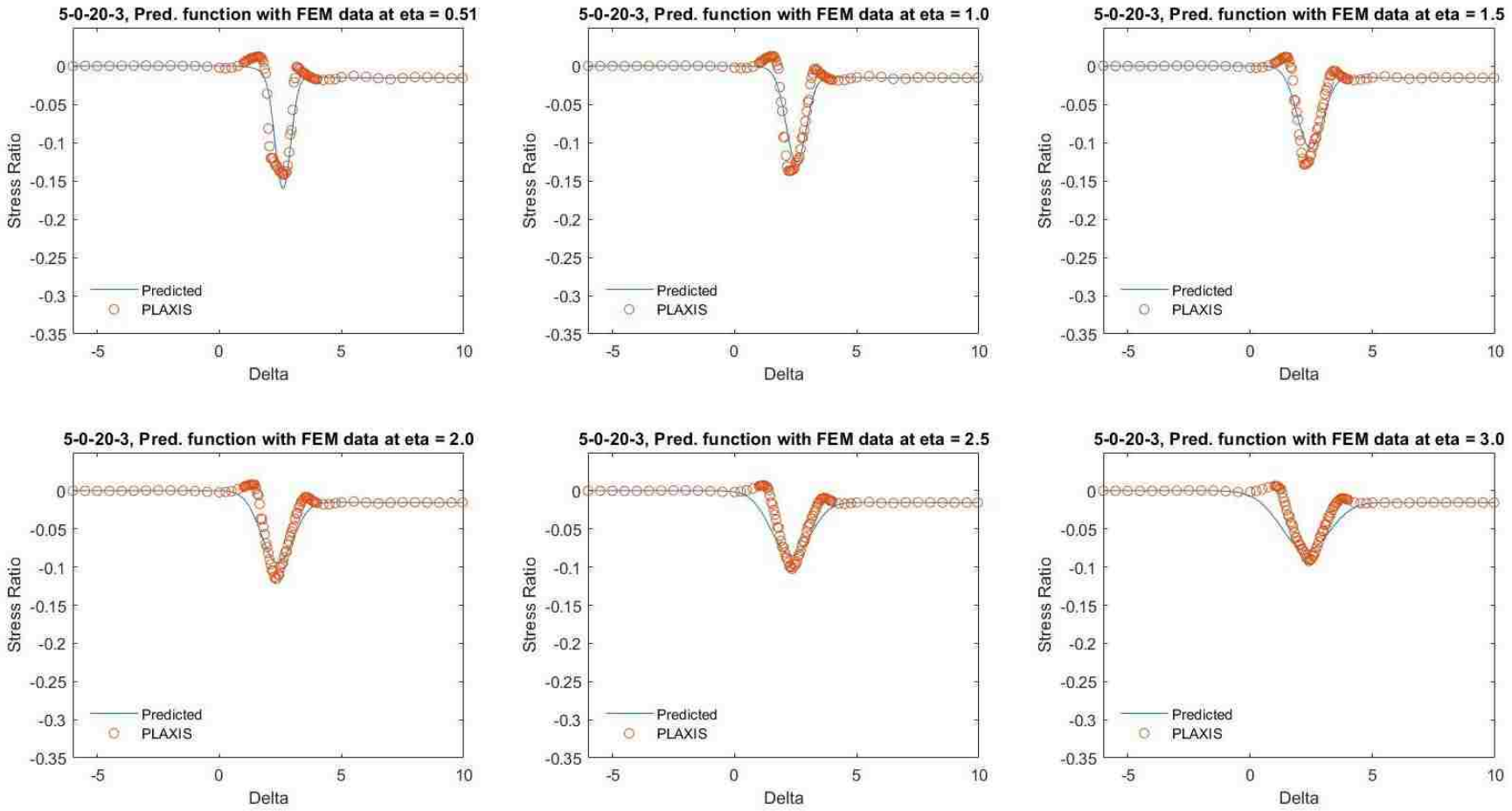

Figure 5.103. Predicted stress ratio function compared to PLAXIS stress ratio for geometry 5-0-20-3.

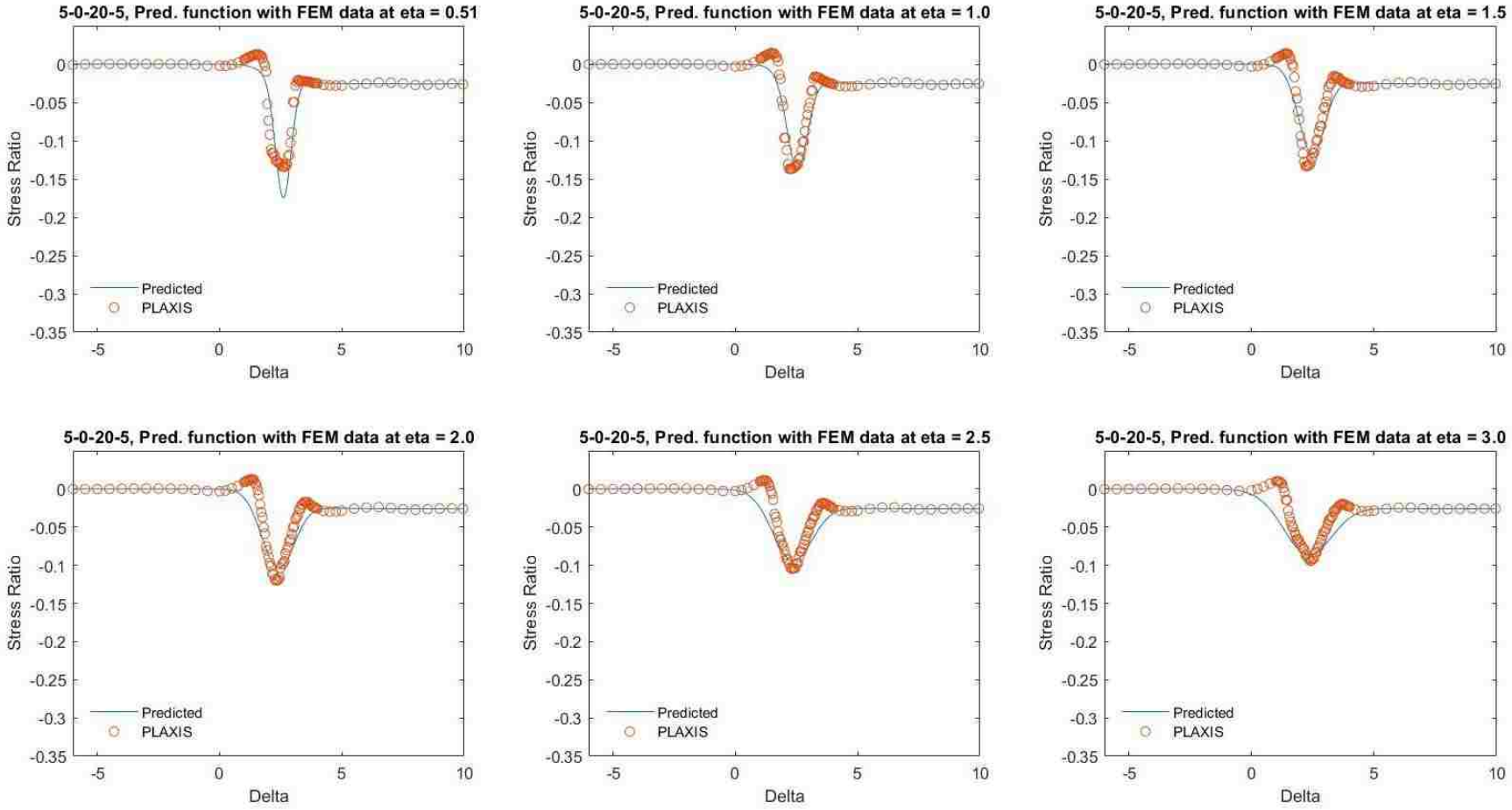

Figure 5.104. Predicted stress ratio function compared to PLAXIS stress ratio for geometry 5-0-20-5.

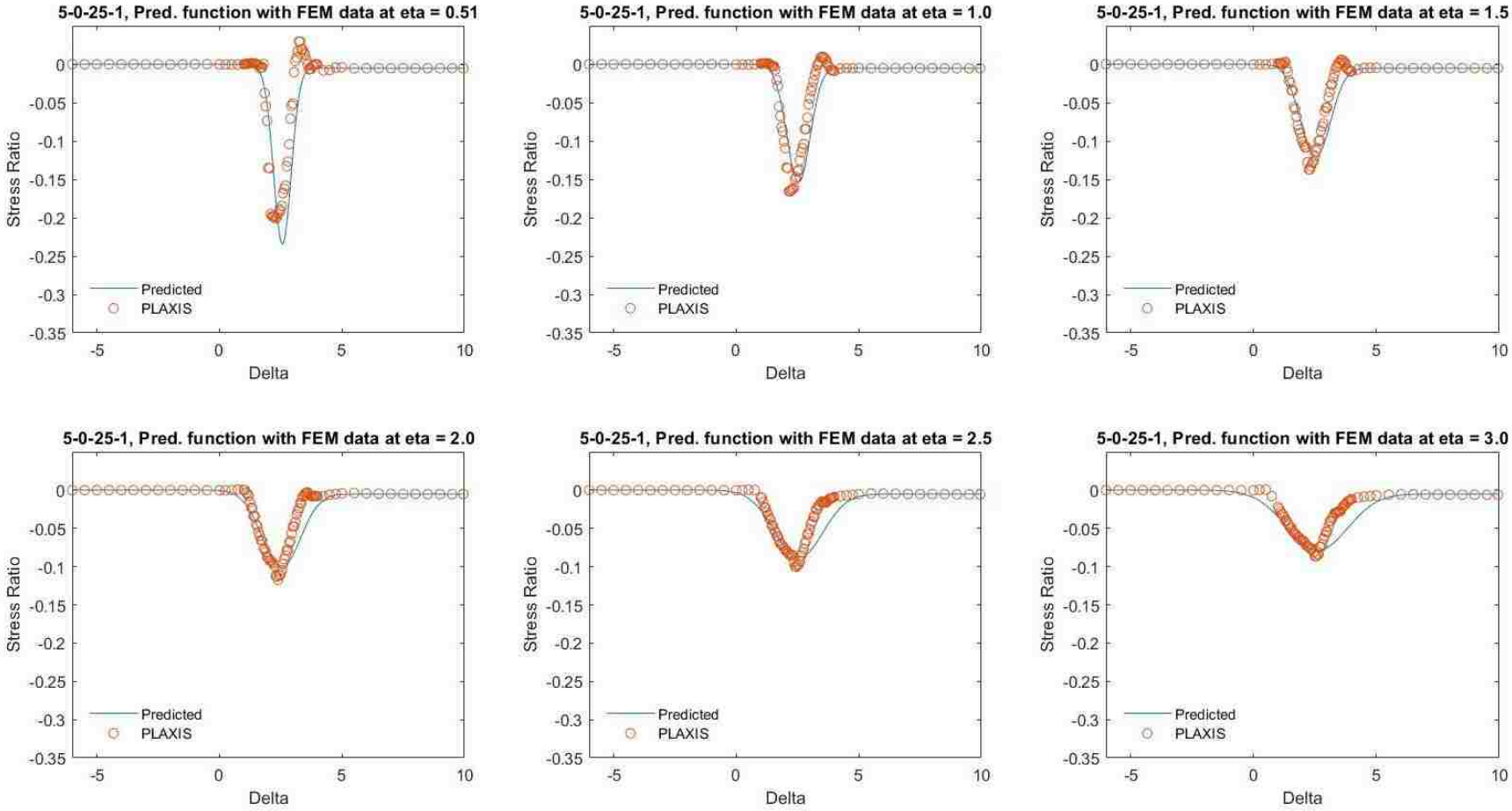

Figure 5.105. Predicted stress ratio function compared to PLAXIS stress ratio for geometry 5-0-25-1.

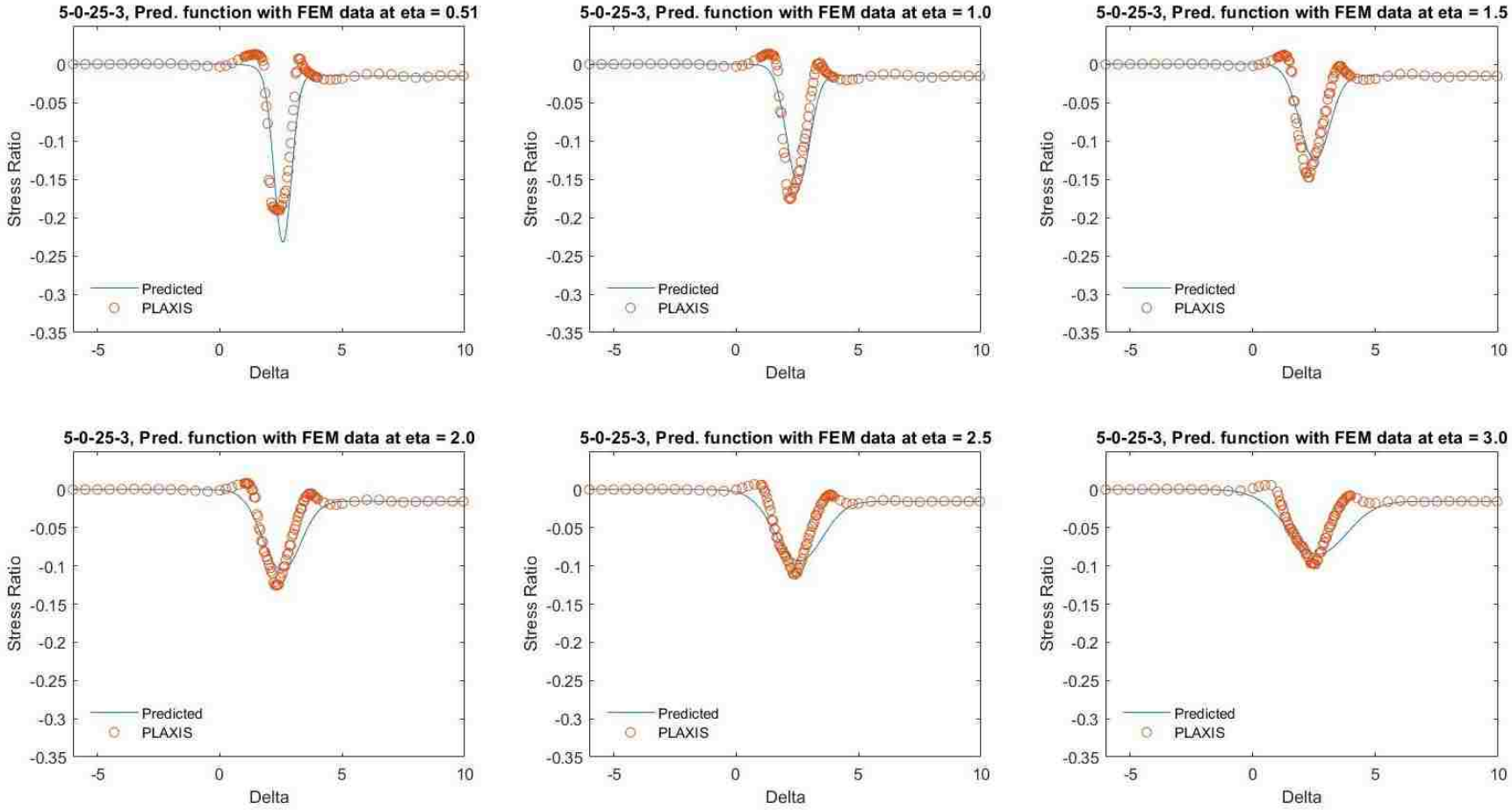

Figure 5.106. Predicted stress ratio function compared to PLAXIS stress ratio for geometry 5-0-25-3.

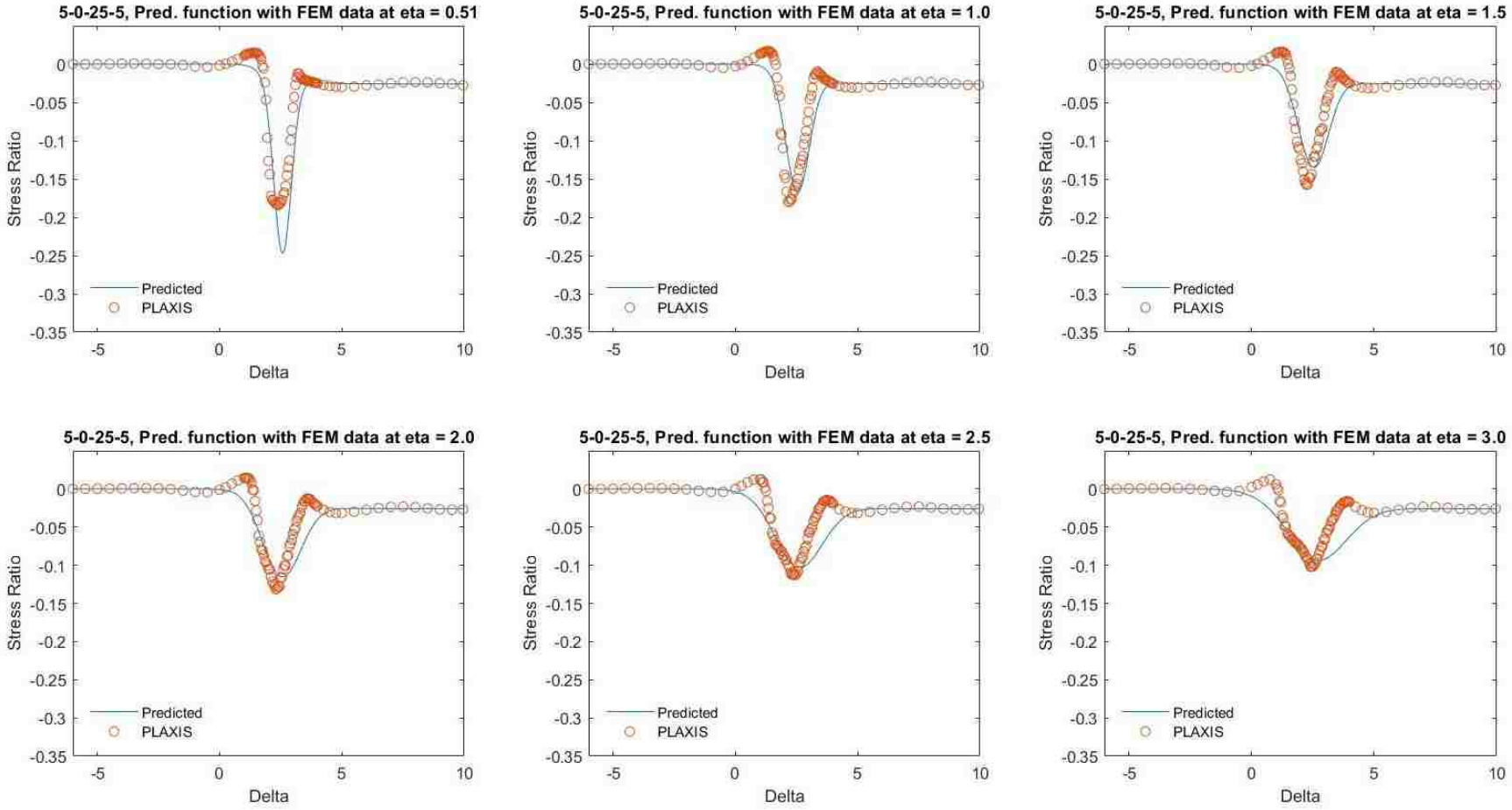

Figure 5.107. Predicted stress ratio function compared to PLAXIS stress ratio for geometry 5-0-25-5.

Calculation of the Predicted Function

Up to this point the full predicted function equation developed in order to match the PLAXIS stress ratio data has yet to be shown except for references to the codes in Appendix D. It has been explained that the predicted function is represented by a B_D for geometries with $\theta_3 = 0$ while geometries with $\theta_3 > 0$ also needed the addition of a FF to have the predicted function smoothly transition from a stress ratio of zero at the left plateau to a nonzero stress ratio at the right plateau. The predicted SSR function can be written as

$$SSR = -(A_{peak} * B_{D,norm} + FF) \tag{5.53}$$

where the negative is needed to match the PLAXIS coordinate system and $B_{D,norm}$ is the normalized four-parameter beta distribution which consists of the shape parameters α and β along with the δ_{min} and δ_{max} bounds, and FF is the filter function which consists of the left and right plateau, FF center, and FF steepness parameters. To find $B_{D,norm}$, the B_D must first be calculated. The B_D values outside of the δ_{min} and δ_{max} are set to the values of the left and right plateau respectively.

$$B_D = \begin{cases} 0 & \delta < \delta_{min} \\ [(\delta - \delta_{min})^{(\alpha-1)} * (\delta_{max} - \delta)^{(\beta-1)}] & \delta_{min} \le \delta \le \delta_{max} \\ c_4 & \delta > \delta_{max} \end{cases} \tag{5.54}$$

The B_D written as Equation 5.54 made it difficult to match the amplitude and the α and β shape parameters because changing the values of α and β also changed the amplitude of the B_D. in addition to the peak amplitude variable. To prevent the latter, the B_D was normalized by its peak value which occurs at the modal value of the distribution. The peak value of the B_D was calculated for each η value and then used to calculate $B_{D,norm}$ by dividing Equation 5.54 by the peak value.

Therefore, the peak value of the $B_{D,norm}$ at each η is 1.0 regardless of the bounds or exponents. This peak value for the B_D can be calculated as

$$B_{D,peak} = \left[\frac{\alpha-1}{\alpha+\beta-2} * (\delta_{max} - \delta_{min})\right]^{(\alpha-1)} * \left[\delta_{max} - \delta_{min} - \frac{\alpha-1}{\alpha+\beta-2} * (\delta_{max} - \delta_{min})\right]^{(\beta-1)} \quad (5.55)$$

and thus $B_{D,norm}$ can be calculated as

$$B_{D,norm} = \frac{B_D}{B_{D,peak}} \quad (5.56)$$

The FF in Equation 5.53 was shown in Equation 5.25. Therefore, with all of the parameters explained, and their values given, Equation 5.53 is used to calculate the predicted SSR.

The predicted SSR function requires a total of 36 coefficients to match the PLAXIS SSR data. Four of the 36 coefficients are for the pseudo-Kronecker Delta function created and given in Equation 5.46. The nine parameters that describe the B_D, the amplitude of the B_D, and the FF, have 32 coefficients between them. The description of each parameter, along with the values of their coefficients, are shown in Table 5.16 and the equations of each parameter are reshown in Equations 5.57 to 5.65.

Table 5.16. FF and 4BDP parameters, descriptions of those parameters, and the values of each of the coefficients.

Parameter	Coefficient Number	Value	Individual Description*	Description
FF Center (c_1)	x_1	2	N/A	N/A
FF Steepness (c_2)	x_2	4	N/A	N/A
Left Plateau (c_3)	x_3	0	N/A	N/A
Right Plateau (c_4)	x_4	0.0052	N/A	N/A
Minimum Bound (δ_{min})	x_5	1.33	Min Bound int - int	The minimum bound varies linearly w/r/t η as found from code 4 for each 5-0-x-0 case. The intercept and coefficient of this linear function varies linearly w/r/t θ_2
	x_6	-0.21	Min Bound int - coeff	
	x_7	0.1103	Min Bound coeff - int	
	x_8	-0.1198	Min Bound coeff - coeff	
	x_9	0.8019	Min shift coeff	Minimum shift w/r/t η for geometries with $\theta_3 > 0$ values - Power Law
	x_{10}	0.8962	Min shift exp	
Maximum Bound (δ_{max})	x_{11}	2.19	Max Bound int - int	The maximum bound varies linearly w/r/t eta as found from code 4 for each 5-0-x-0 case. The intercept and coefficient of this linear function varies linearly w/r/t θ_2
	x_{12}	0.2308	Max Bound int - coeff	
	x_{13}	0.2213	Max Bound coeff - int	
	x_{14}	0.077	Max Bound coeff - coeff	
	x_{15}	-0.8019	Max shift coeff	Maximum shift w/r/t η for geometries with $\theta_3 > 0$ values - Power Law
	x_{16}	0.8962	Max shift exp	
Alpha (α)	x_{17}	11.672	Alpha coeff - coeff	The alpha parameter varies exponentially w/r/t η as found from the code 4 for each 5-0-x-0 case. The alpha parameter coefficient and exponent of this exponential fit varies via Power Law w/r/t θ_2
	x_{18}	0.9729	Alpha coeff - exp	
	x_{19}	-0.24121	Alpha exp - coeff	
	x_{20}	0.27591	Alpha exp - exp	
Beta (β)	x_{21}	2.6	Beta coeff - coeff	The beta parameter varies exponentially w/r/t η as found from the code 4 for each 5-0-x-0 case. The beta parameter coefficient and exponent of this exponential fit varies via Power Law w/r/t θ_2
	x_{22}	1.376	Beta coeff - exp	
	x_{23}	-0.070529	Beta exp - coeff	
	x_{24}	0.67234	Beta exp - exp	
Amplitude (A_{peak})	x_{25}	0.0273316	Amplitude coeff - coeff	The Amplitude varies via Power law relationship w/r/t η as found from code 4 for each 5-0-x-0 case. The coefficient and exponent of this Power law varies via Power law w/r/t θ_2
	x_{26}	0.6685027	Amplitude coeff - exp	
	x_{27}	-0.099801	Amplitude exp - coeff	
	x_{28}	0.63055066	Amplitude exp - exp	
	x_{29}	-0.087171	Amplitude reduction coeff	Amplitude reduction w/r/t η for geometries with $\theta_3 > 0$ values - Power Law
	x_{30}	-1.021359	Amplitude reduction exp	
	x_{31}	1.760799	Amplitude increase coeff	Amplitude increase to fit all $\theta_3 > 0$ geometries (Power Law w/r/t θ_2) as well as vary w/r/t η via (0.24/η^2)
	x_{32}	-1.627222	Amplitude increase exp	
Pseudo-Kronecker Delta**	x_{33}	1.10653	Kronecker Delta coeff	Power Law w/r/t θ_3 used to develop the pseudo-Kronecker Delta function
	x_{34}	0.15847	Kronecker Delta exp	
	x_{35}	0.0767	Kronecker Delta int	Linear function subtracted from the Power Law to get the pseudo-Kronecker Delta function
	x_{36}	0.05	Kronecker Delta coeff	

***Min Bound int - int means: The first int stands for the minimum bound intercept for the linearly varying expression w/r/t η. The second "int" is because this linear intercept varies via a linear function w/r/t θ_2. Other Parameter "coeff" - "coeff" can be interpreted in a similar manner - see "Description" for details.**

****This is not a filter function or beta function parameter, but rather a constant that returns a value of 0 if $\theta_3 = 0$ and a value of approximately 1 if $\theta_3 > 0$.**

$$c_1 = x_1 \tag{5.57}$$

$$c_2 = x_2 \tag{5.58}$$

$$c_3 = x_3 \tag{5.59}$$

$$c_4 = x_4 * \theta_3 \tag{5.60}$$

$$\delta_{min} = (x_5 + x_6\theta_2) + (x_7 + x_8\theta_2) * \eta + [x_{33}{\theta_3}^{x_{34}} - (x_{35}\theta_3 + x_{36})] * x_9\eta^{x_{10}} \tag{5.61}$$

$$\delta_{max} = (x_{11} + x_{12}\theta_2) + (x_{13} + x_{14}\theta_2) * \eta + [x_{33}{\theta_3}^{x_{34}} - (x_{35}\theta_3 + x_{36})] * x_{15}\eta^{x_{16}} \tag{5.62}$$

$$\alpha = (x_{17}{\theta_2}^{x_{18}}) * \exp([x_{19}{\theta_2}^{x_{20}}] * \eta) \tag{5.63}$$

$$\beta = (x_{21}{\theta_2}^{x_{22}}) * \exp([x_{23}{\theta_2}^{x_{24}}] * \eta) \tag{5.64}$$

$$A_{peak} = \left[(x_{25}{\theta_2}^{x_{26}}) * \eta^{(x_{27}{\theta_2}^{x_{28}})}\right] + [x_{33}{\theta_3}^{x_{34}} - (x_{35}\theta_3 + x_{36})] * \left[(x_{29}\eta^{x_{30}}) + (x_{31}{\theta_2}^{x_{32}}) * \left(\frac{0.24}{\eta^2}\right)\right] \tag{5.65}$$

5.4.9 **Discussion**

Although stymied by time restrictions to justify the use of the static stress ratio for infinite slope geometries in this thesis, it is believed the static stress ratio has the capability to do so based on the theoretical solutions that have been developed (Cruikshank 2002). The inclusion of infinite slope models in the static stress state framework proposed in this thesis can be done in future work. A possible solution to model an infinite slope in PLAXIS or other software (without tilting the angle of gravity) would be to consider a slope geometry similar to that shown in Figure 5.108 where θ_1 is zero, θ_2 represents the infinite slope, θ_3 is a non-zero value less than θ_2, and the slope governed by θ_4 is zero and extends a large distance to minimize the effects of boundary conditions in the θ_2 and θ_3 regions. Such analyses, however, were beyond the scope of this study.

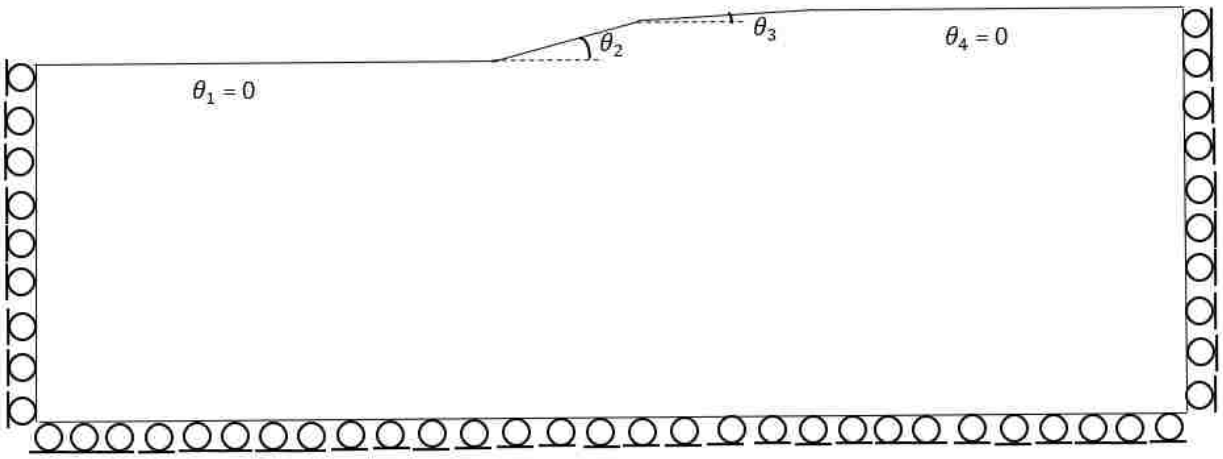

Figure 5.108. Proposed infinite slope geometry to limit the impacts of boundary conditions on the infinite slope with angle θ_2.

5.5 CONCLUSION

Lateral spreading involves the incremental displacements that can occur due to cyclic liquefaction within gentle slopes or flat ground near steeper slopes such as river banks. Although the initial static shear stress is a key component to lateral spreading, the most common lateral spreading procedures used in practice today characterize the static stresses crudely leading to a large uncertainty in displacement predictions. This chapter introduced a function that predicts the static stress ratio within a wide range of lateral spreading slope geometries based on numerical tools allowing for the determination of the initial static shear stress by simply multiplying the predicted static stress ratio by the vertical stress anywhere within a slope. The predictive static stress ratio function presented was shown for a finite number of geometries, however, it can be applied to any geometry with $H > 0$ meters, $5 \leq \theta_2 \leq 25$ degrees, $0 \leq \theta_3 \leq 5$ degrees, and $\theta_1 = 0$. The determination of the initial static stress is important because there are believed to be three mechanisms that drive lateral spreading:

1) Softening of the liquefied material that causes shearing distortion of the soil under the static shear stresses that act upon it;
2) Cumulative cyclic deformations during earthquake shaking that are driven by cyclic shear stresses superimposed on the existing static shear stresses;
3) Component of post-shaking deformations associated with void redistribution phenomena and driven by static shear stresses;

all of which are influenced by the initial static shear stress. Therefore, any lateral spreading model should completely characterize the initial static shear stress to better predict lateral spread displacement.

It has been shown that the PLAXIS and theoretical SSR values are inconsistent, stemming from the differences between the shear stress output by PLAXIS and the values calculated from the infinite slope equilibrium equations. Based on previous analyses in OpenSees, these inconsistencies are due to the boundary conditions of the PLAXIS models, even though the extents of the model used are quite large. Although this inconsistency exists, a framework has been developed for predicting SSR that can be used, after recalibration using more accurate data, by future researchers.

Chapter 6. **SUMMARY AND CONCLUSIONS**

6.1 INTRODUCTION

Soil liquefaction is a complex phenomenon that can cause tremendous damage to natural and man-made structures. Improvement upon the current state of knowledge of liquefaction and its effects is key to designing for, and mitigating, the damage it causes. The two focal points of this thesis were:

1) Introduction of a new liquefaction-targeted ground motion parameter, PGA_M, and discussion of the influences of various site conditions on its values for two common liquefaction triggering procedures.
2) Development of a unified framework for characterizing the static stress state for a continuous range of slope geometries (from free-face to ground slope) using numerical analyses.

6.2 PGA_M

The goal of a liquefaction-targeted intensity measure, PGA_M, is to enable the practicing engineer to input a mapped PGA_M value into their conventional liquefaction hazard analysis procedure and receive the liquefaction triggering results that would be obtained had they performed a full PLHA. The process of obtaining the conventional PGA_M value that corresponds to an event with the return period from a full PLHA has been demonstrated, and the effects of various site conditions on the value of PGA_M for two common liquefaction triggering procedures have been evaluated. The Boulanger and Idriss (2012) liquefaction triggering procedure was found to perform better, in terms of being less sensitive to various site conditions, than the Cetin et al. (2004) liquefaction triggering procedure. The key observations made were:

(a) Both procedures require a depth correction factor, however, the depth correction for the Boulanger and Idriss (2012) appeared to be sufficiently consistent between site locations that a relatively simple depth correction factor could be developed, whereas, the Cetin et al. (2004) procedure would require something more complex.

(b) The sensitivity of the Cetin et al. (2004) to SPT resistance also suggested a correction factor for SPT resistance would be needed, whereas, the Boulanger and Idriss (2012) procedure was insensitive to SPT resistance.

(c) The Cetin et al. (2004) was found to be slightly better suited for varying water table depth at higher return periods in moderate seismic environments like Charleston, SC, while the Boulanger and Idriss (2012) procedure more suitable at high return periods in high seismicity environments like Eureka, CA.

(d) PB LiquefY is a good tool for evaluating PLHA in high seismicity environments, however, the inability of the program to evaluate liquefaction potential at return periods specified in areas of lower seismicity, and the numerous Microsoft Excel/Visual Basic errors that occurred when running the program, make it an arduous program to use.

6.3 CHARACTERIZATION OF A STATIC STRESS STATE

Static shear stresses are believed to play a crucial role in the mechanisms that drive lateral spreading. Therefore, the second focal point of this thesis was to develop a function that could predict the initial static shear stress within a wide array of lateral spreading slope geometries at depths of lateral spreading interest. The initial static shear stress function developed could then be used by future researchers to more accurately predict lateral spreading displacements than current procedures. Numerical analyses were used to develop a function that predicts the static stress ratio within a wide range of lateral spreading slope geometries. During development of this function, it

was found that the PLAXIS and theoretical static stress ratio values were inconsistent, due to the differences between shear stresses computed by PLAXIS and the values calculated from the infinite slope equilibrium equations. The PLAXIS static stress ratio values for $\eta < 0.51$ were also found to be variable and have complex behavior. However, the static stress ratio behavior between $\eta = 0.51$ to 3 was simple, and showed reasonable trends (i.e., it smoothly transitioned between geometries in a manner consistent with basic elasticity theory). Because $\eta = 0.51$ to 3 represents important lateral spreading depths of interest, development of a function that could predict the static stress ratio within lateral spreading slopes for those depths was investigated. Therefore, a framework was presented that allows for the calculation of a static stress ratio dependent on 36 coefficients and applicable to any geometry with $H > 0$ meters, $5 \leq \theta_2 \leq 25$ degrees, $0 \leq \theta_3 \leq 5$ degrees, and $\theta_1 = 0$. The key observations made were:

(a) A coordinate transformation can be used to relate a wide array of lateral spreading geometries to one another.

(b) Irregularly spaced PLAXIS stress points can be mapped to a consistent and regular grid using an inverse distance weighting interpolation.

(c) A two-part function consisting of a four-parameter beta distribution and a sigmoidal (filter) function can be used to accurately model the static stress ratio for a wide array of slope geometries.

(d) Some aspects of the computed PLAXIS response could not be captured including (i) apparent unstable behavior at shallow depths, (ii) an inability to produce shear stresses that agreed with theoretical solutions based on simple limit equilibrium concepts, and (iii) apparent effects of boundary conditions despite the very large domain being modeled.

Although these aspects existed, the model is considered to have captured the most important trends in the stresses within deeper parts of a slope.

6.4 FINAL REMARKS AND POTENTIAL FUTURE WORK

Both the focal points of this thesis can be built upon by future researchers for the continued improvement of the current state of knowledge of liquefaction. The process of obtaining the conventional PGA_M value that corresponds to an event with a return period of a full probabilistic liquefaction hazard analysis has been shown for 27 site locations of moderate to very high seismicity. These 27 locations, therefore, only correspond to certain regions of at least moderate seismicity in the United States and do not include locations of low seismicity (e.g., New York City, NY and Philadelphia, PA). The reason is that PB LiquefY was not able to evaluate liquefaction potential at specified return periods in areas of lower seismicity. Therefore, future research could evaluate of the sensitivity of PGA_M to various site conditions in areas of low seismicity.

In this thesis, PGA_M was evaluated for a triggering limit state and its sensitivity to various site conditions analyzed. Following the same type of framework, PGA_M can be evaluated for different effects-based limit states by performing conventional and probabilistic liquefaction hazard analysis effects analyses. Sensitivity analysis of PGA_M to various site conditions could then be evaluated for different effects-based limit states.

Finally, the framework for characterizing the static stress state proposed in this thesis can be extended for the purpose of predicting lateral spreading displacement. The initial static shear stress plays a key role in the mechanisms that drive lateral spreading which are believed to include:

1) Softening of the liquefied material that causes shearing distortion of the soil under the static shear stresses that act upon it;

2) Cumulative cyclic deformations during earthquake shaking that are driven by cyclic shear stresses superimposed on the existing static shear stresses;
3) Component of post-shaking deformations associated with void redistribution phenomena and driven by static shear stresses;

Therefore, any lateral spreading procedure needs characterize the initial static shear stress in order to accurately predict lateral spreading displacement.

BIBLIOGRAPHY

Andrus, R. D., Stokoe, K. H. I., Chung, R. M., & Juang, C. H. (2003). Guidelines for evaluating liquefaction resistance using shear wave velocity measurement and simplified procedures. In *NIST GCR 03-854*. National Institute of Standards and Technology, Gaithersburg, MD.

Andrus, R. D., & Stokoe, K. H. (2000). Liquefaction resistance of soils from shear-wave velocity. *Journal of Geotechnical and Geoenvironmental Engineering*, *126*(11), 1015–1025.

Baker, J. W. (2013). Introduction to probabilistic seismic hazard analysis. *White Paper Version 2.0*, 79.

Bartlett, S. F., & Youd, T. L. (1992). *Empirical analysis of horizontal ground displacement generated by liquefaction-induced lateral spreads*. *National Center for Earthquake Engineering Research*.

Been, K., & Jefferies, M. G. (1985). A state parameter for sands. *Geotechnique*, *35*(2), 99–112.

Bolton, M. D. (1986). The strength and dilatancy of sands. *Geotechnique*, *36*(1), 65–78. Retrieved from http://fate.upc.edu/index.php

Boulanger, R. W., & Idriss, I. M. (2004). *Evaluating the Potential for Liquefaction or Cyclic Failure of Silts and Clays*. *Report No. UCD/CGM-04/01 Center for Geotechnical Modeling*.

Boulanger, R. W. (2003). Relating Kα to relative state parameter index. *Journal of Geotechnical and Geoenvironmental Engineering*, *129*(8), 770–773. https://doi.org/10.1061/(asce)1090-0241(2003)129:8(770)

Boulanger, R. W., & Idriss, I. M. (2012). Probabilistic standard penetration test–based liquefaction–triggering procedure. *Journal of Geotechnical and Geoenvironmental Engineering*, *138*(10), 1185–1195.

Boulanger, R. W., & Idriss, I. M. (2006). Liquefaction Susceptibility Criteria for Silts and Clays. *Journal of Geotechnical and Geoenvironmental Engineering*, *132*(11), 1413–1426. https://doi.org/10.1061/(ASCE)1090-0241(2006)132:11(1413)

Boulanger, R. W., & Idriss, I. M. (2015). CPT-Based Liquefaction Triggering Procedure. *Journal of Geotechnical and Geoenvironmental Engineering*, *142*(2), 04015065.

Boulanger, R. W., & Idriss, I. M. (2014). CPT and SPT based liquefaction triggering procedures. In *Report No. UCD/CGM-14/01*. Center for Geotechnical Modeling, University of California, Davis, CA.

Brandenberg, S. J., Bellana, N., & Shantz, T. (2010). Shear wave velocity as function of standard penetration test resistance and vertical effective stress at California bridge sites. *Soil Dynamics and Earthquake Engineering*, *30*(10), 1026–1035.

Bray, J. D., & Sancio, R. B. (2006). Assessment of the liquefaction susceptibility of fine-grained soils. *Journal of Geotechnical and Geoenvironmental Engineering*, *132*(9), 1165–1177. https://doi.org/10.1061/(ASCE)1090-0241(2006)132:9(1165)

Campbell, K. W., & Bozorgnia, Y. (2008). NGA ground motion model for the geometric mean horizontal component of PGA, PGV, PGD and 5% damped linear elastic response spectra for periods ranging from 0.01 to 10 s. *Earthquake Spectra*, *24*(1), 139–171.

Casagrande, A. (1936). Characteristics of cohesionless soils affecting the stability of slopes and earth fills. *Journal of the Boston Society of Civil Engineers*, 257–276.

Castro, G. (1969). Liquefaction of sands. *Harvard Soil Mechanics Series*, *81*(January 1969), 112. https://doi.org/-

Castro, G. (1975). Liquefaction and cyclic mobility of saturated sands. *Journal of the Geotechnical Engineering Division*, *101*(GT6), 551–569.

Castro, G., & Poulos, S. (1977). Factors affecting liquefaction and cyclic mobility. *Journal of the Geotechnical Engineering Division*, *106*(GT6), 501–506.

Cetin, K. O., Seed, R. B., Der Kiureghian, A., Tokimatsu, K., Harder, L. F., Kayen, R. E., & Moss, R. E. S. (2004). Standard penetration test-based probabilistic and deterministic assessment of seismic soil liquefaction potential. *Journal of Geotechnical and Geoenvironmental Engineering*, *130*(12), 1314–1340.

Cornell, C. A. (1968). Engineering seismic risk analysis. *Bulletin of the Seismological Society of America*, *58*(5), 1583–1606.

Cruikshank, K. M., & Johnson, A. M. (2002). *Theory of Slope Stability*. Retrieved from http://web.pdx.edu/~i1kc/programming/slopes/LandslideNotes.pdf

Cubrinovski, M. (2013). Liquefaction-Induced Damage in The2010-2011 Christchurch (New Zealand) Earthquakes. In *International Conference on Case Histories in Geotechnical Engineering. 1*. Retrieved from http://scholarsmine.mst.edu/icchge/7icchge/session12/1

Dahl, K. R., DeJong, J. T., Boulanger, R. W., Pyke, R., & Wahl, D. (2014). Characterization of an alluvial silt and clay deposit for monotonic, cyclic, and post-cyclic behavior. *Canadian Geotechnical Journal*, *51*(4), 432–440.

De Alba, P. A. (1983). Pile settlement in liquefying sand deposit. *Journal of Geotechnical Engineering*, *109*(9), 1165–1180.

Deierlein, G. G., Krawinkler, H., & Cornell, C. A. (2003). A framework for performance-based earthquake engineering. In *Pacific Conference on Earthquake Engineering* (Vol. 273, pp. 1–8).

DesRoches, R., Comerio, M., Eberhard, M., Mooney, W., & Rix, G. J. (2011). Overview of the 2010 Haiti earthquake. *Earthquake Spectra*, *27*(SUPPL. 1). https://doi.org/10.1193/1.3630129

Dobry, R., Ladd, R. S., Yokel, F. Y., Chung, R. M., & Powell, D. (1982). Prediction of pore water pressure buildup and liquefaction of sands during earthquakes by the cyclic strain method. *NBS Building Science Series*, *138*, 138–168.

Fiegel, G. L., & Kutter, B. L. (1992). *The mechanism of liquefaction in layered soils*. *Report CR92.009*. Naval Civil Engineering Laboratory, Port Hueneme, 34 pp.

Franke, K. W., & Kramer, S. L. (2013). Procedure for the Empirical Evaluation of Lateral Spread Displacement Hazard Curves. *Journal of Geotechnical and Geoenvironmental Engineering*, *140*(1), 110–120.

Gillins, D. T., & Bartlett, S. F. (2013). Multilinear Regression Equations for Predicting Lateral Spread Displacement from Soil Type and Cone Penetration Test Data. *Journal of Geotechnical and Geoenvironmental Engineering*, *140*(4), 04013047.

Golesorkhi, R. (1989). *Factors influencing the computational determination of earthquake-induced shear stresses in sandy soils*. Ph.D. Thesis, University of California, Berkeley.

Green, R. A., Olson, S. M., Cox, B. R., Rix, G. J., Rathje, E., Bachhuber, J., … Martin, N. (2011). Geotechnical aspects of failures at port-au-prince seaport during the 12 january 2010 Haiti earthquake. *Earthquake Spectra*, *27*(SUPPL. 1), 43–65. https://doi.org/10.1193/1.3636440

Idriss, I. M., & Boulanger, R. W. (2004). Semi-empirical procedures for evaluating liquefaction potential during earthquakes. *11th International Conference on Soil Dynamics and Earthquake Engineering and 3rd International Conference on Earthquake Geotechnical Engineering*, 32–56.

Idriss, I. M. (1999). An update to the Seed-Idriss simplified procedure for evaluating liquefaction potential. In *Proceedings, TRB Workshop on New Approaches to Liquefaction*. Federal Highway Administration, Washington, DC.

Idriss, I. M., & Boulanger, R. W. (2007). SPT- and CPT-based relationships for the residual shear strength of liquefied soils. In *Earthquake Geotechnical Engineering, 4th International Conference on Earthquake Geotechnical Engineering* (pp. 1–22). The Netherlands.

Idriss, I. M., & Boulanger, R. W. (2008). *Soil Liquefaction During Earthquakes*. Oakland, CA: Earthquake Engineering Research Institute.

Ishihara, K. (1993). Liquefaction and flow failure during earthquakes. *Géotechnique*, *43*(3), 351–415. https://doi.org/10.1680/geot.1993.43.3.351

Ishihara, K., Tatsuoka, F., & Yasuda, S. (1975). Undrained deformation and liquefaction of sand under cyclic stresses. *Soils and Foundations*, *15*(1), 29–44. https://doi.org/10.3208/sandf1972.15.29

Ishihara, K., & Yoshimine, M. (1992). Evaluation of Settlements in Sand Deposits Following Liquefaction During Earthquakes. *Japanese Society of Soil Mechanics and Foundation Engineering*, *32*(1), 173–188.

Joyner, W. B., & Chen, A. T. F. (1975). Calculation of nonlinear ground response in earthquakes. *Bulletin of the Seismological Society of America*, *65*(5), 1315–1336.

Kayen, R., Moss, R. E. S., Thompson, E. M., Seed, R. B., Cetin, K. O., Kiureghian, A. Der, … Tokimatsu, K. (2013). Shear-Wave Velocity–Based Probabilistic and Deterministic Assessment of Seismic Soil Liquefaction Potential. *Journal of Geotechnical and Geoenvironmental Engineering*, *139*(3), 407–419.

Konrad, J.-M. (1988). Interpretation of flat plate dilatomoeter tests in sands in terms of the state parameter. *Geotechnique*, *38*(2), 263–277.

Kramer, S. (1996). *Geotechnical Earthquake Engineering* (1st ed.). Upper Saddle River, NJ: Prentice Hall.

Kramer, S. L. (2008). *Evaluation of Liquefaction Lazards in Washington State*. Washington St. Transportation Center, Final Report.

Kramer, S. L., & Mayfield, R. T. (2007). Return period of soil liquefaction. *Journal of Geotechnical and Geoenvironmental Engineering*, *133*(7), 802–813.

Kramer, S. L., & Seed, H. B. (1988). Initiation of soil liquefaction under static loading conditions. *Journal of Geotechnical Engineering*, *114*(4), 412–430.

Kramer, S. L., & Wang, C. (2015). Empirical model for estimation of the residual strength of liquefied soil. *Journal of Geotechnical and Geoenvironmental Engineering*, *141*(9), 1–15.

Ladd, R. S. (1974). Specimen preparation and liquefaction of sands. *Journal of the Geotechnical Engineering Division*, *100*(GT10), 1180–1184.

Liu, L., & Dobry, R. (1997). Seismic Response of Shallow Foundation On Liquefiable Sand. *Journal of Geotechnical and Geoenvironmental Engineering*, *123*(6), 557–567.

Makdisi, A. J. (2016). *The Applicability of Sliding Block Analyses for the Prediction of Lateral Spreading Displacements*. University of Washington (Master's thesis). Retrieved from

https://digital.lib.washington.edu/researchworks/bitstream/1773/35555/1/Makdisi_washington_0250O_15535.pdf

Mayfield, R. T., Kramer, S. L., and Huang, Y. M. (2010). Simplified approximation procedure for performance-based evaluation of liquefaction potential. *J. Geotech. Geoenviron. Eng.*, 10.1061/(ASCE)GT.1943-5606.0000191, 140–150.

Meyerhof, G. G. (1957). Discussion on research on determining the density of sands. *Proc., 4th Int. Conf. of Soil Mechanics and Foundation Engineering*, London, Vol. 3,

Moss, R. E., Seed, R. B., Kayen, R. E., Stewart, J. P., Der Kiureghian, A., & Cetin, K. O. (2006). CPT-based probabilistic and deterministic assessment of in situ seismic soil liquefaction potential. *Journal of Geotechnical and Geoenvironmental Engineering*, *132*(8), 1032–1051.

National Research Council. (1985). Liquefaction of soils during earthquakes. National Academy Press, Washington, D.C., 240 pp.

Olson, S. M., & Johnson, C. I. (2008). Analyzing Liquefaction-Induced Lateral Spreads Using Strength Ratios. *Journal of Geotechnical and Geoenvironmental Engineering*, *134*(8), 1035–1049.

Olson, S. M., & Stark, T. D. (2002). Liquefied strength ratio from liquefaction flow failure case histories. *Canadian Geotechnical Journal*, *39*, 629–647.

PLAXIS. (2019). PLAXIS Material Models Manual 2019. Retrieved from https://www.plaxis.com/support/manuals/plaxis-2d-manuals/

PLAXIS. (2019). PLAXIS 2D Reference Manual 2019. Retrieved from https://www.plaxis.com/support/manuals/plaxis-2d-manuals/

Poulos, S. J. (1981). The steady state of deformation. *Journal of the Geotechnical Engineering Division, ASCE*, *107*(GT5), 553–562.

Rauch, A. F., & Martin, J. R. I. (2001). Predicting the Maximum and Distribution of Displacements on Liquefaction-Induced Lateral Spreads. In *International Conferences on Recent Advances in Geotechnical Earthquake Engineering and Soil Dynamics. 13.* Retrieved from http://scholarsmine.mst.edu/icrageesd/04icrageesd/session04/13

Reiter, L. (1990). *Earthquake hazard analysis*. New York, NY: Columbia University Press.

Reynolds, O. (1885). On the dilatancy of media composed of rigid partiles in contact. With experimental illustrations. *The London, Edinburgh, and Dublin Philosophical Magazine and Journal of Science*, *20*(127), 469–481. https://doi.org/DOI: 10.1080/14786448508627791

Salgado, R. (2008). *The Engineering of Foundations*. New York, NY: McGraw-Hill.

Seed, H. B., & Wilson, S. D. (1967). The Turnagain Heights landslide in Anchorage, Alaska. *Soil Mechanics and Bituminous Materials Research Laboratory*.

Seed, H. B. (1979). Soil liquefaction and cyclic mobility evaluation for level ground during earthquakes. *J. Geotech. Eng. Div., Am. Soc. Civ. Eng*., 105(2), 201–255.

Seed, H. B. (1987). Design problems in soil liquefaction. *Journal of Geotechnical Engineering*, *113*(8), 827–845.

Seed, H. B., & Idriss, I. M. (1971). Simplified procedure for evaluating soil liquefaction potential. *Journal of the Soil Mechanics and Foundations Division*, *97*(9), 1249–1273.

Seed, H. B., Idriss, I. M., Makdisi, F., & Banerjee, N. (1975). Representation of irregular stress time histories by equivalent uniform stress series in liquefaction analyses. *Earthquake Engineering Research Center*, EERC 75-29.

Seed, H. B., & Lee, K. L. (1966). Liquefaction of saturated sands during cyclic loading. *Journal of the Soil Mechanics and Foundations Division*, *92*(SM6), 105–134.

Seed, H. B., & Lee, K. L. (1967). Undrained strength characteristics of cohesionless soils. *Journal of Soil Mechanics and Foundation Division, ASCE*, *93*(SM6), 117–141.

Seed, R. B., & Harder, L. F. (1990). SPT-Based Analysis of Cyclic Pore Pressure Generation and Undrained Residual Strength. In *Proceedings, H. Bolton Seed Memorial Symposium* (pp. 351–376). University of California, Berkeley, CA.

Stark, T. D., & Mesri, G. (1992). Undrained shear strength of liquefied sands for stability analysis. *Journal of Geotechnical Engineering*, *118*(11), 1727–1747.

Stewart, J. P., Liu, A. H., Choi, Y., & Baturay, M. B. (2003). Amplification Factors for Spectral Acceleration in Active Regions. *Bulletin of the Seismological Soceity of America*, *93*(1), 332–352.

Tatsuoka, F., Zhou, S., Sato, T., and Shibuya, S. (1990). Method of evaluating liquefaction potential and its application. *Rep. on Seismic hazards in the soil deposits in urban areas*, Ministry of Education of Japan, 75–109 (in Japanese).

Tokimatsu, K., & Seed, H. B. (1987). Evaluation of Settlements in Sands Due to Earthquake Shaking. *Journal of Geotechnical and Geoenvironmental Engineering*, *113*(8), 861–878.

Ulmer, K., & Franke, K. W. (2016). Modified Performance-Based Liquefaction Triggering Procedure Using Liquefaction Loading Parameter Maps. *Journal of Geotechnical And*, *142*(3), 04015089.

USGS. (2019). Science of the New Madrid Seismic Zone. Retrieved from https://earthquake.usgs.gov/learn/topics/nmsz/1811-1812.php

Youd, L. (1993). Liquefaction-Induced Damage to Bridges. *Transportation Research Record, 1411*.

Youd, T. L., Hansen, C. M., & Bartlett, S. F. (2002). Revised Multilinear Regression Equations for Prediction of Lateral Spread Displacement. *Journal of Geotechnical and Geoenvironmental Engineering, 128*(12), 1007–1017.

Youd, T. L., & Hoose, S. N. (1977). Liquefaction susceptibility and geologic setting. In *Proceedings, 6th World Conference on Earthquake Engineering* (pp. 2189–2194). New Delhi.

Youd, T. L., Idriss, I. M., Andrus, R. D., Arango, I., Castro, G., Christian, J. T., … Stokoe, K. H. (2001). Liquefaction resistance of soils: summary report from the 1996 NCEER and 1998 NCEER/NSF Workshops on Evaluation of Liquefaction Resistance of Soils. *Journal of Geotechnical and Geoenvironmental Engineering*, *127*(10), 817–833.

Youd, T. L., Idriss, I. M., Andrus, R. D., Arango, I., Castro, G., Christian, J. T., … Stokoe, II, K. H. (1997). Evaluation of liquefaction resistance of soils. In *Proceedings, NCEER Workshop, Technical Report NCEER-97-0022* (p. 314). Salt Lake City, UT: NCEER.

Zhang, G., Robertson, P. K., & Brachman, R. W. I. (2004). Estimating Liquefaction-Induced Lateral Displacements Using the Standard Penetration Test or Cone Penetration Test. *Journal of Geotechnical and Geoenvironmental Engineering*, *130*(8), 861–871.

APPENDIX A

INFLUENCE OF $(N_1)_{60}$ AND DEPTH ON THE MAGNITUDE CORRECTED PEAK GROUND ACCELERATION

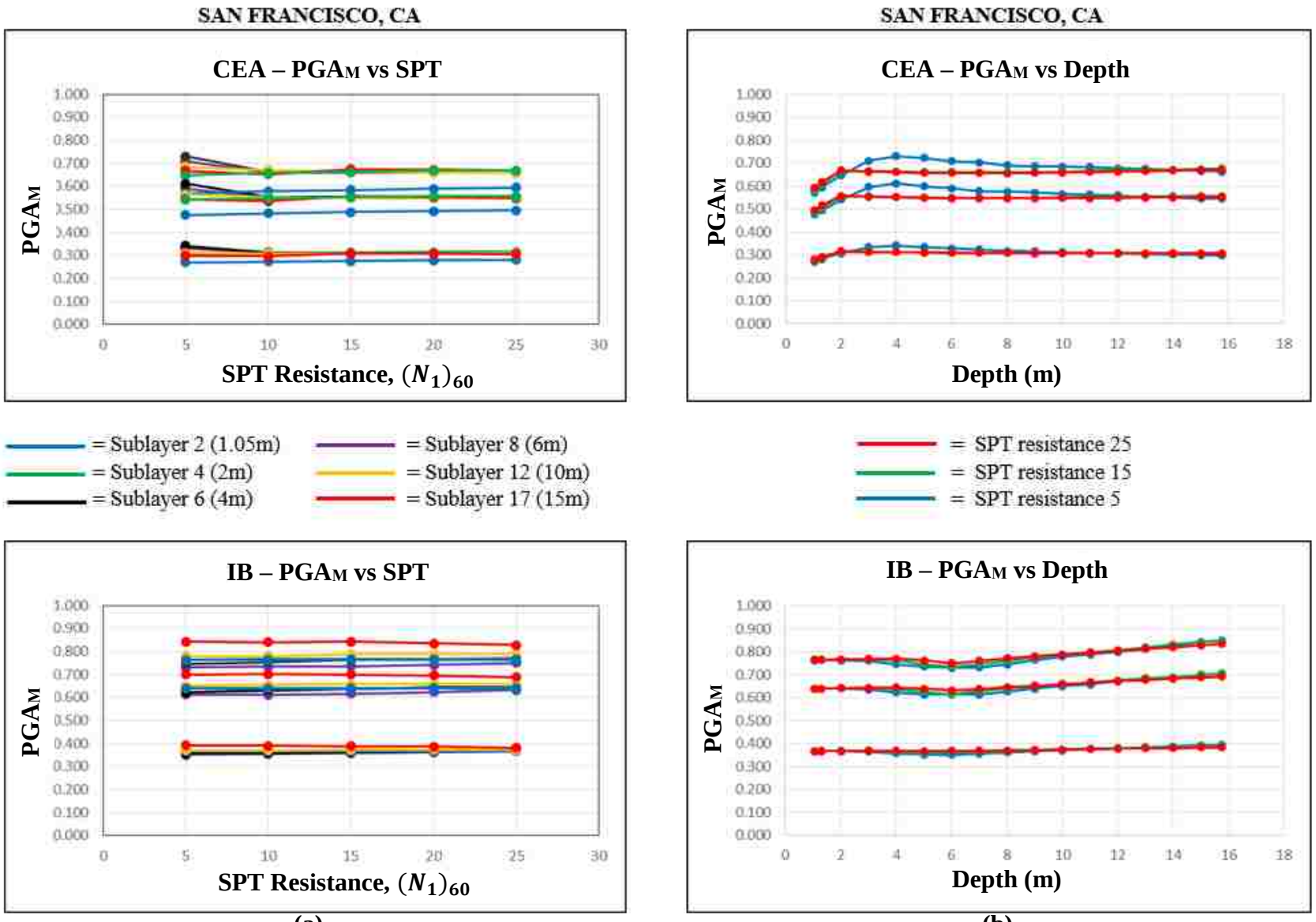

(a) **(b)**

Figure A.1. Plots showing the influence of (a) $(N1)_{60}$ on PGA_M and (b) Depth BGS on PGA_M – San Francisco, CA.

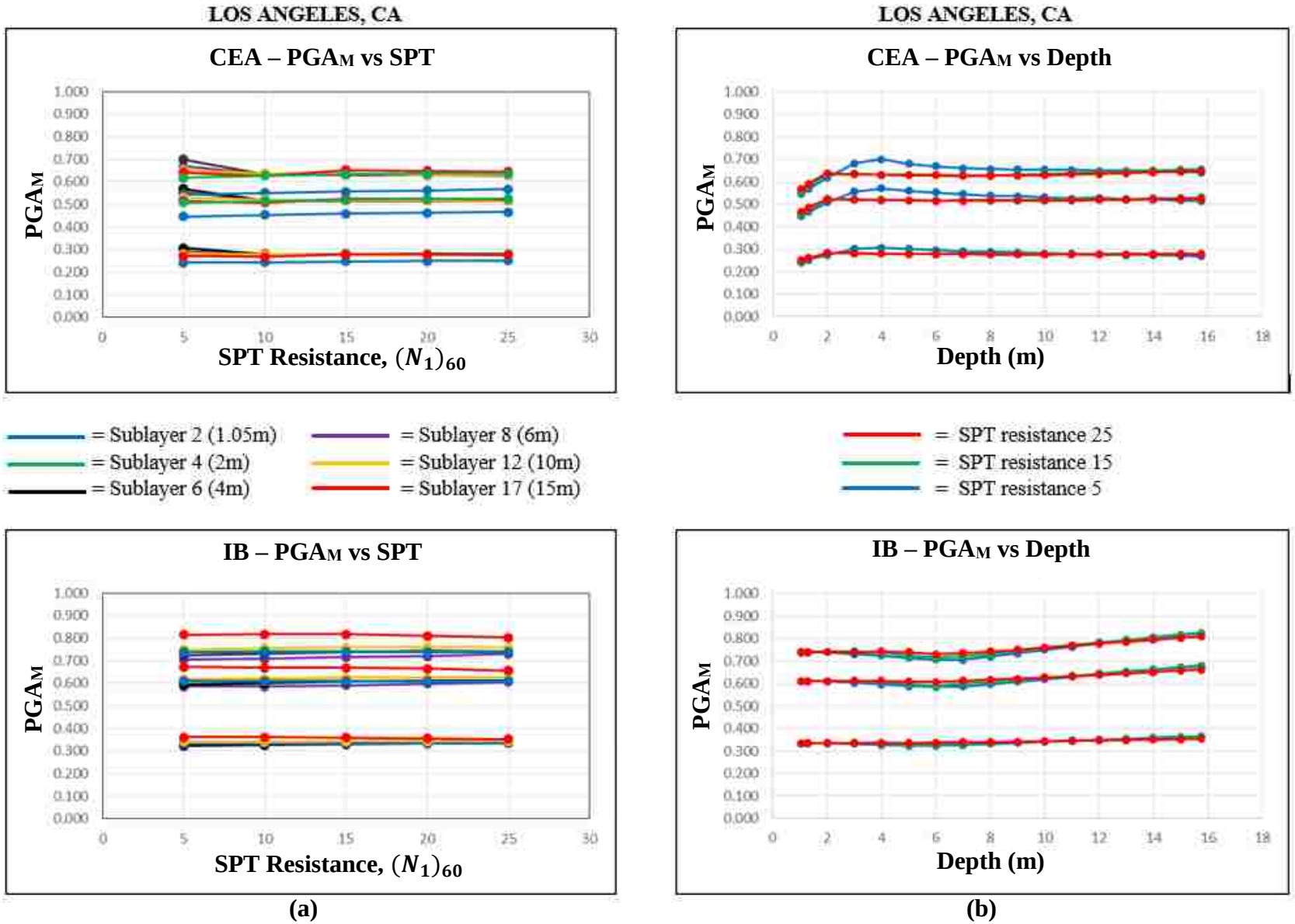

Figure A.1. Plots showing the influence of (a) $(N_1)_{60}$ on PGA_M and (b) Depth BGS on PGA_M – Los Angeles, CA.

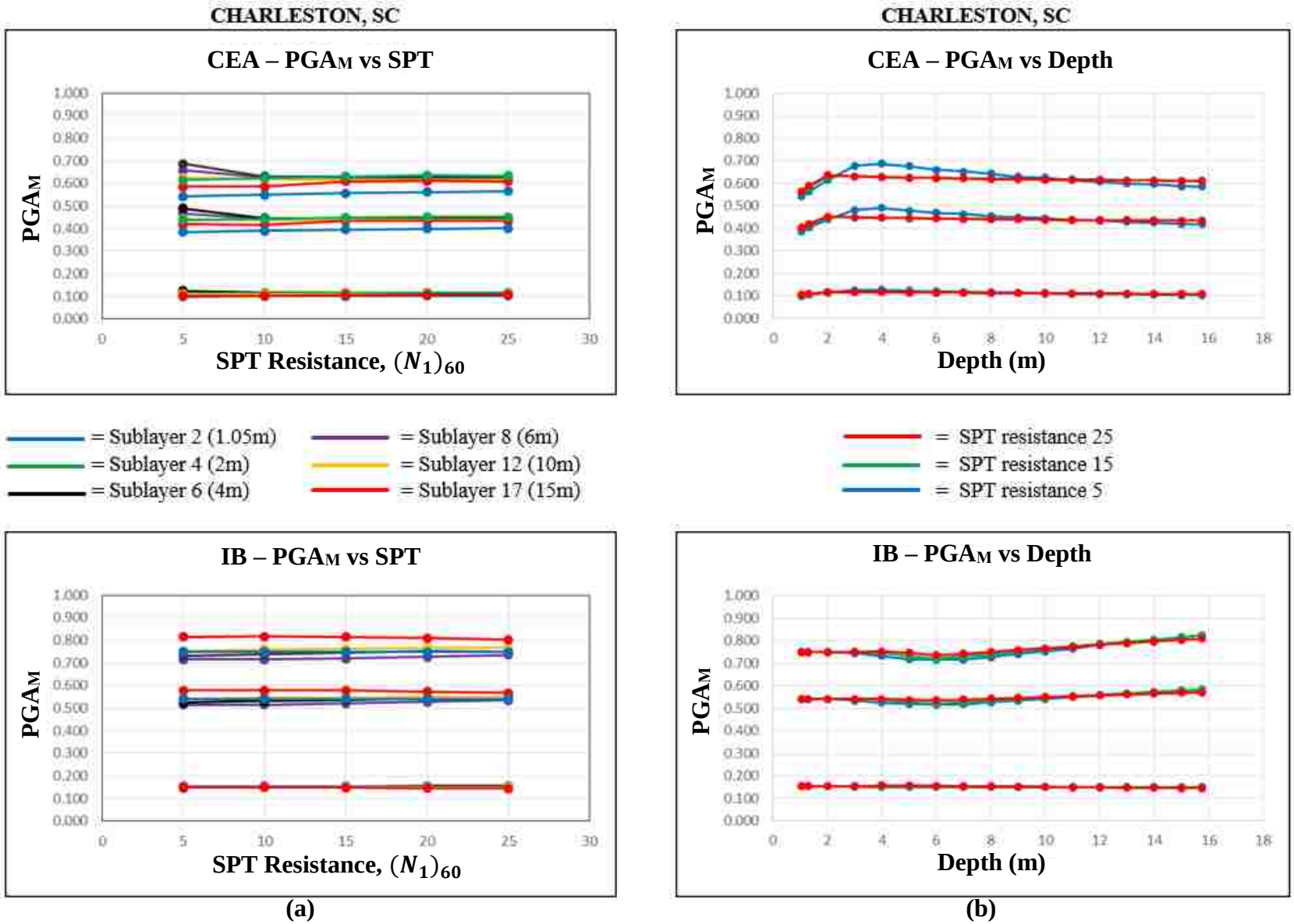

Figure A.2. Plots showing the influence of (a) $(N_1)_{60}$ on PGA_M and (b) Depth BGS on PGA_M – Charleston, SC.

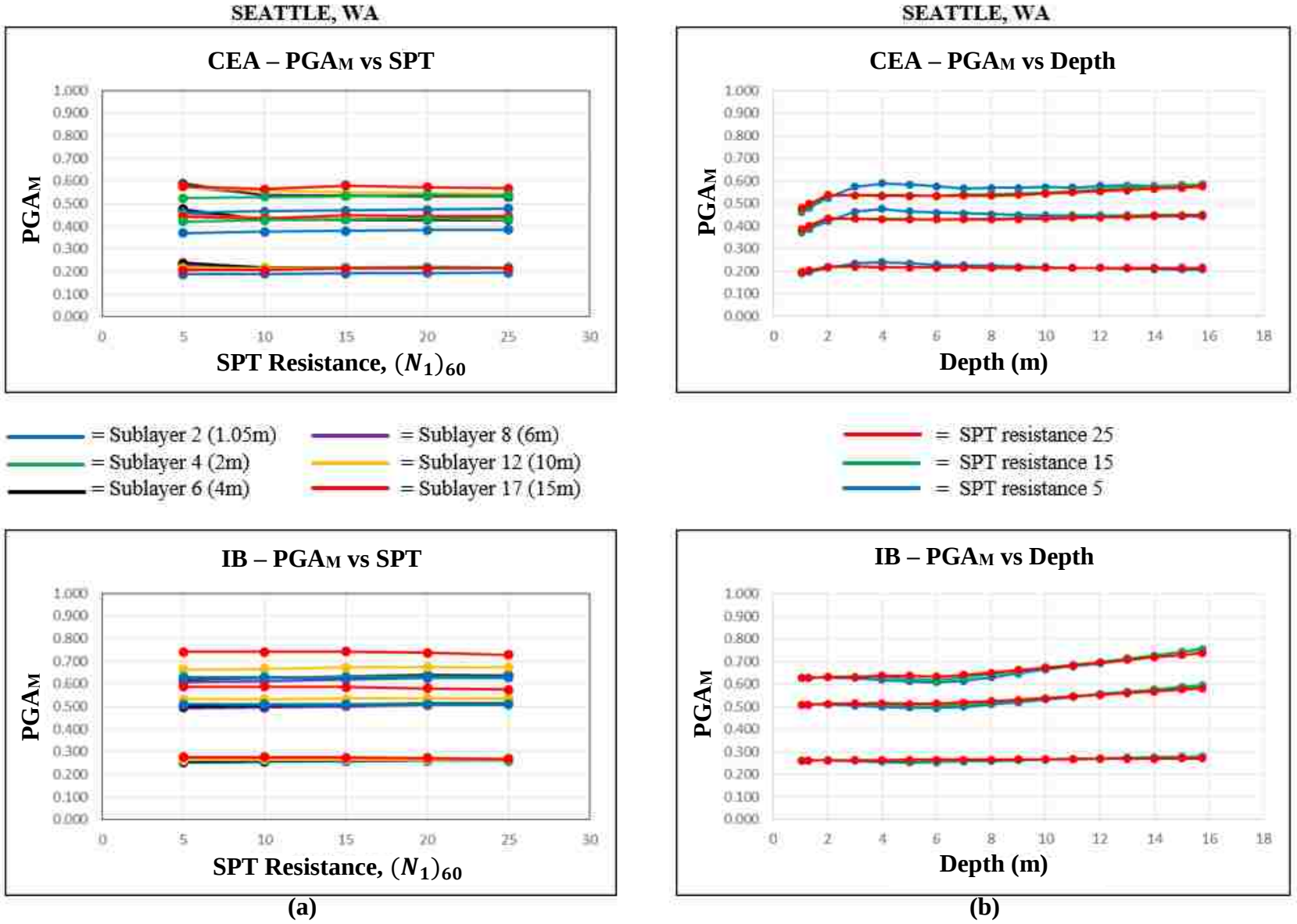

Figure A.3. Plots showing the influence of (a) $(N_1)_{60}$ on PGA_M and (b) Depth BGS on PGA_M – Seattle, WA.

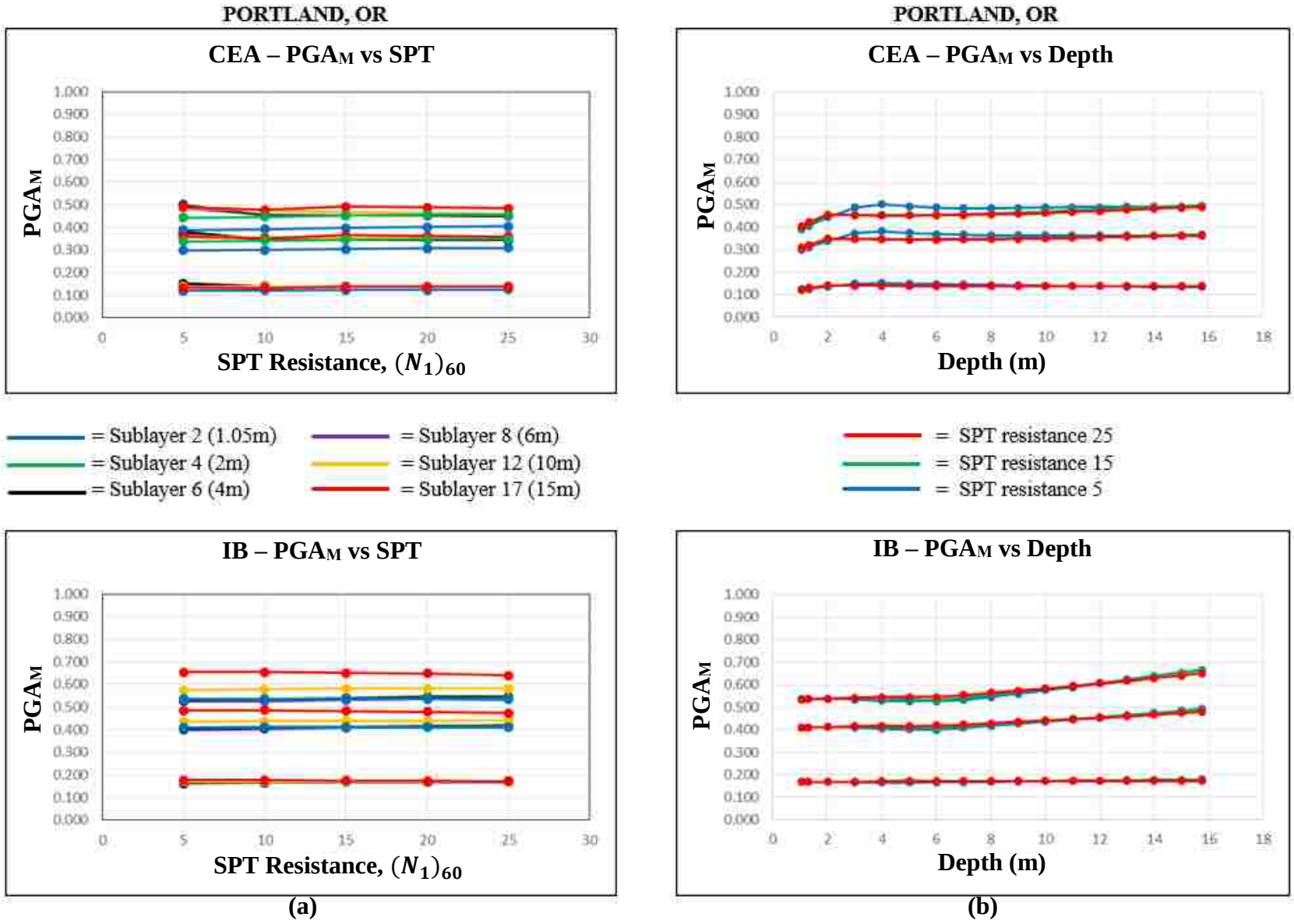

Figure A.4. Plots showing the influence of (a) $(N_1)_{60}$ on PGA$_M$ and (b) Depth BGS on PGA$_M$ – Portland, OR.

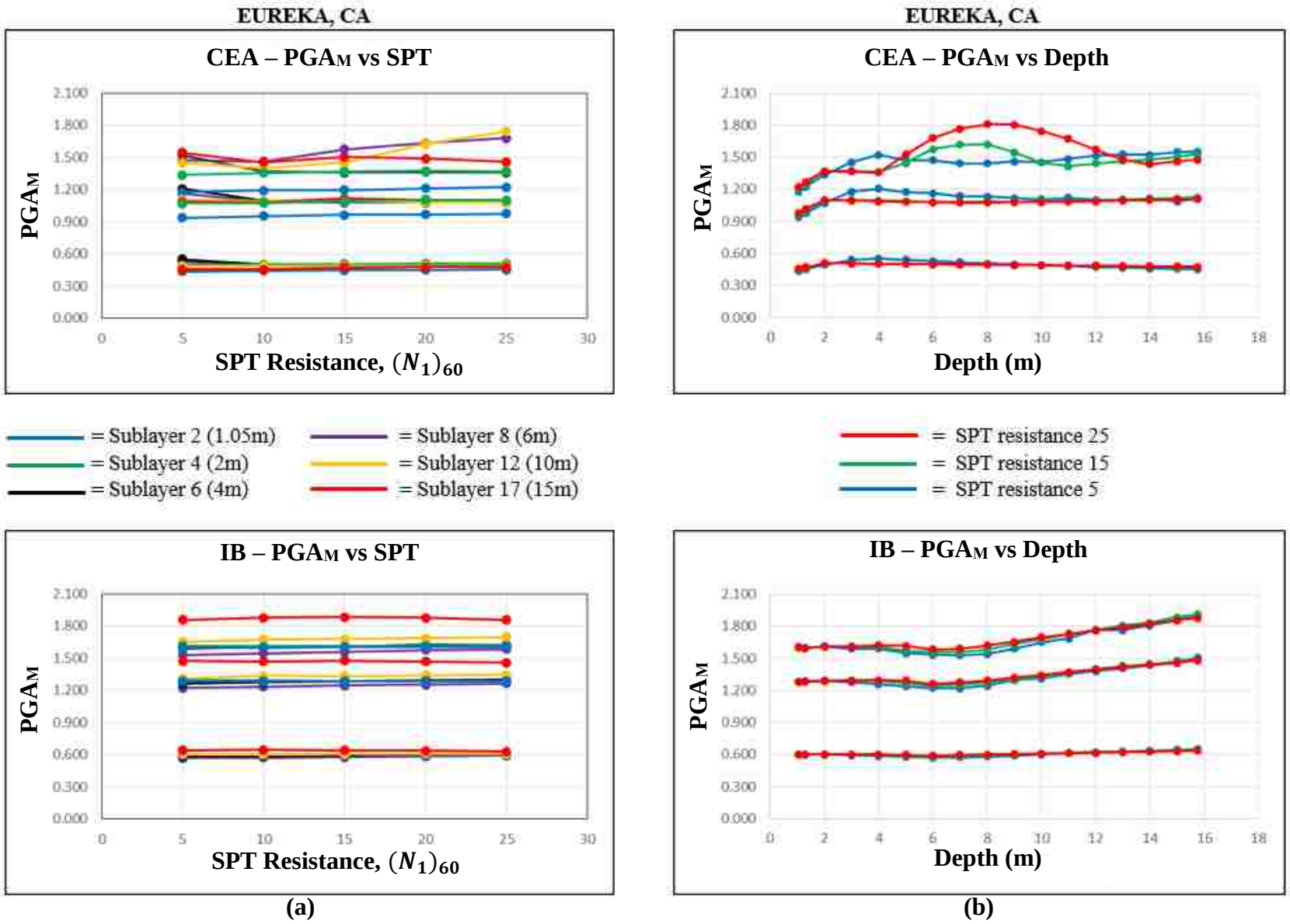

Figure A.5. Plots showing the influence of (a) $(N_1)_{60}$ on PGA_M and (b) Depth BGS on PGA_M – Eureka, CA.

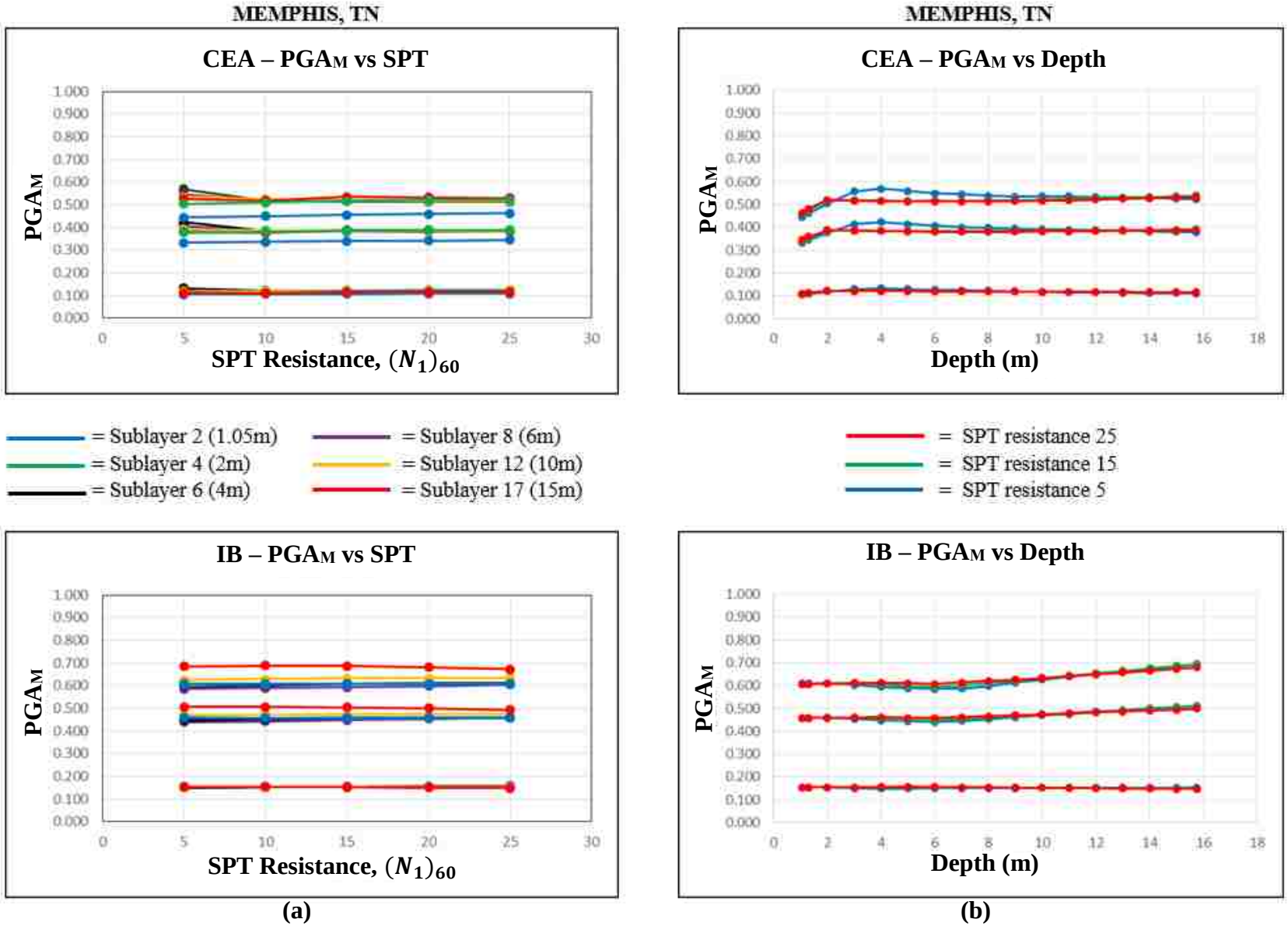

Figure A.6. Plots showing the influence of (a) $(N_1)_{60}$ on PGA_M and (b) Depth BGS on PGA_M – Memphis, TN.

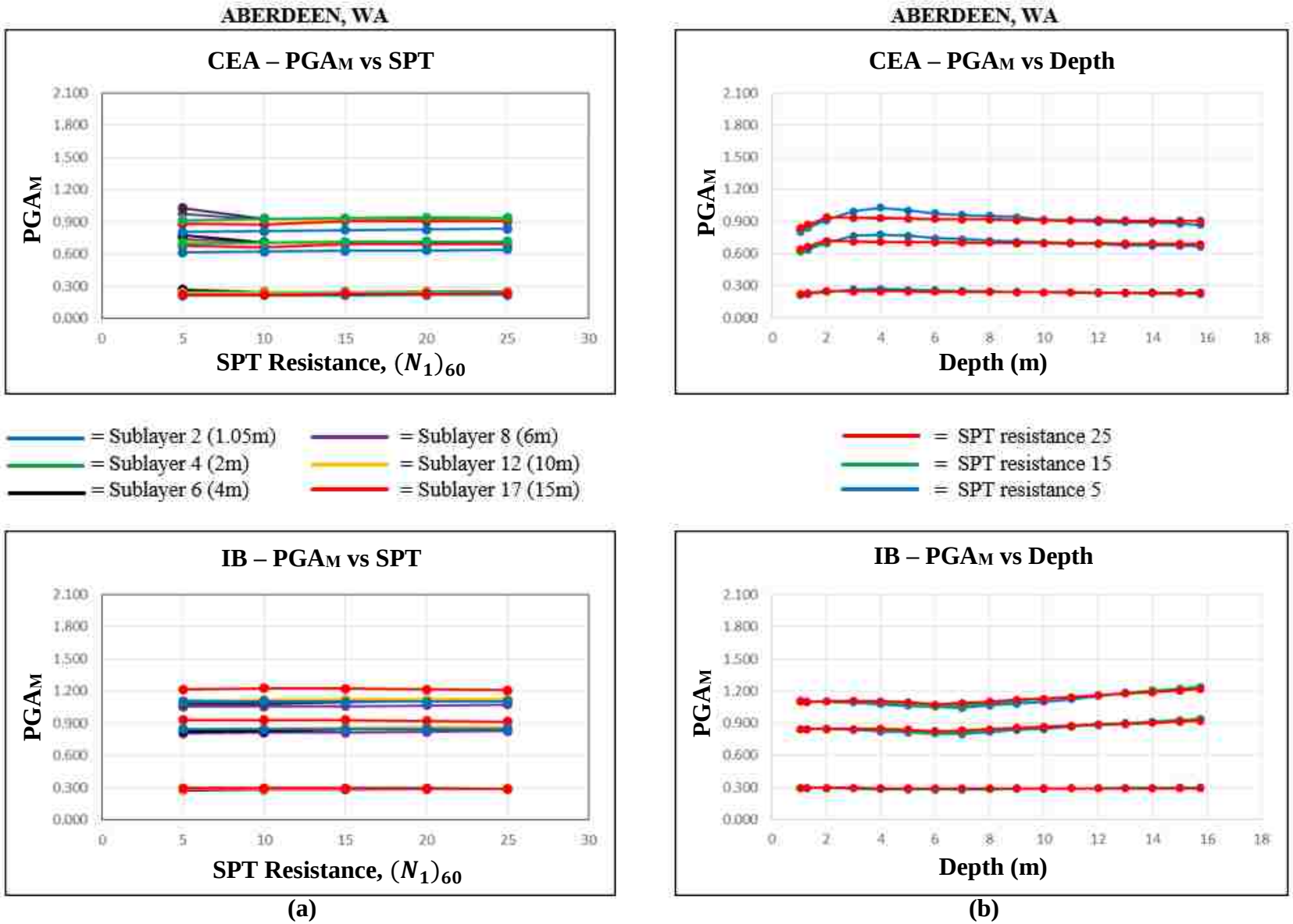

Figure A.7. Plots showing the influence of (a) $(N_1)_{60}$ on PGA_M and (b) Depth BGS on PGA_M – Aberdeen, WA.

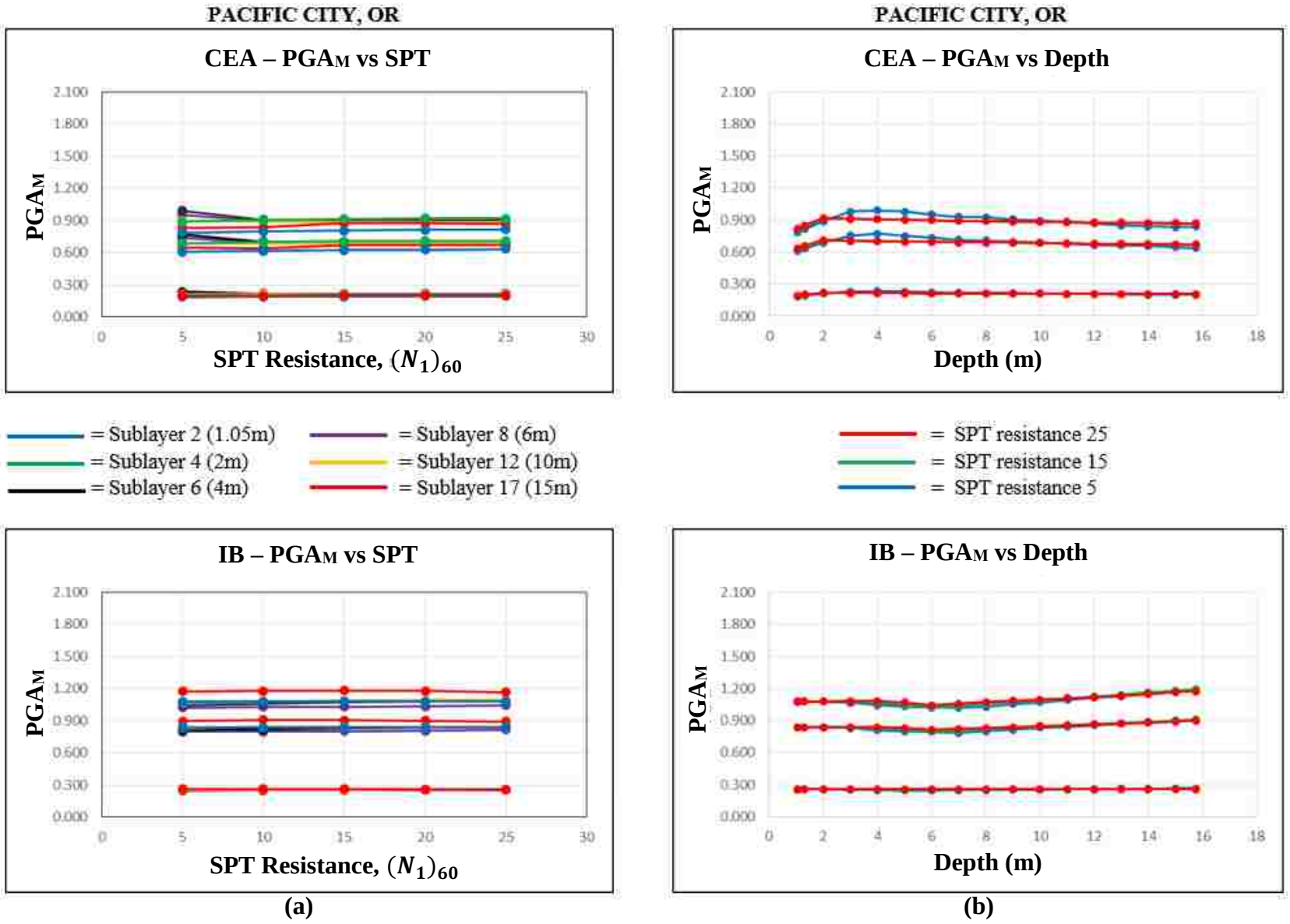

Figure A.8. Plots showing the influence of (a) $(N_1)_{60}$ on PGA_M and (b) Depth BGS on PGA_M – Pacific City, OR.

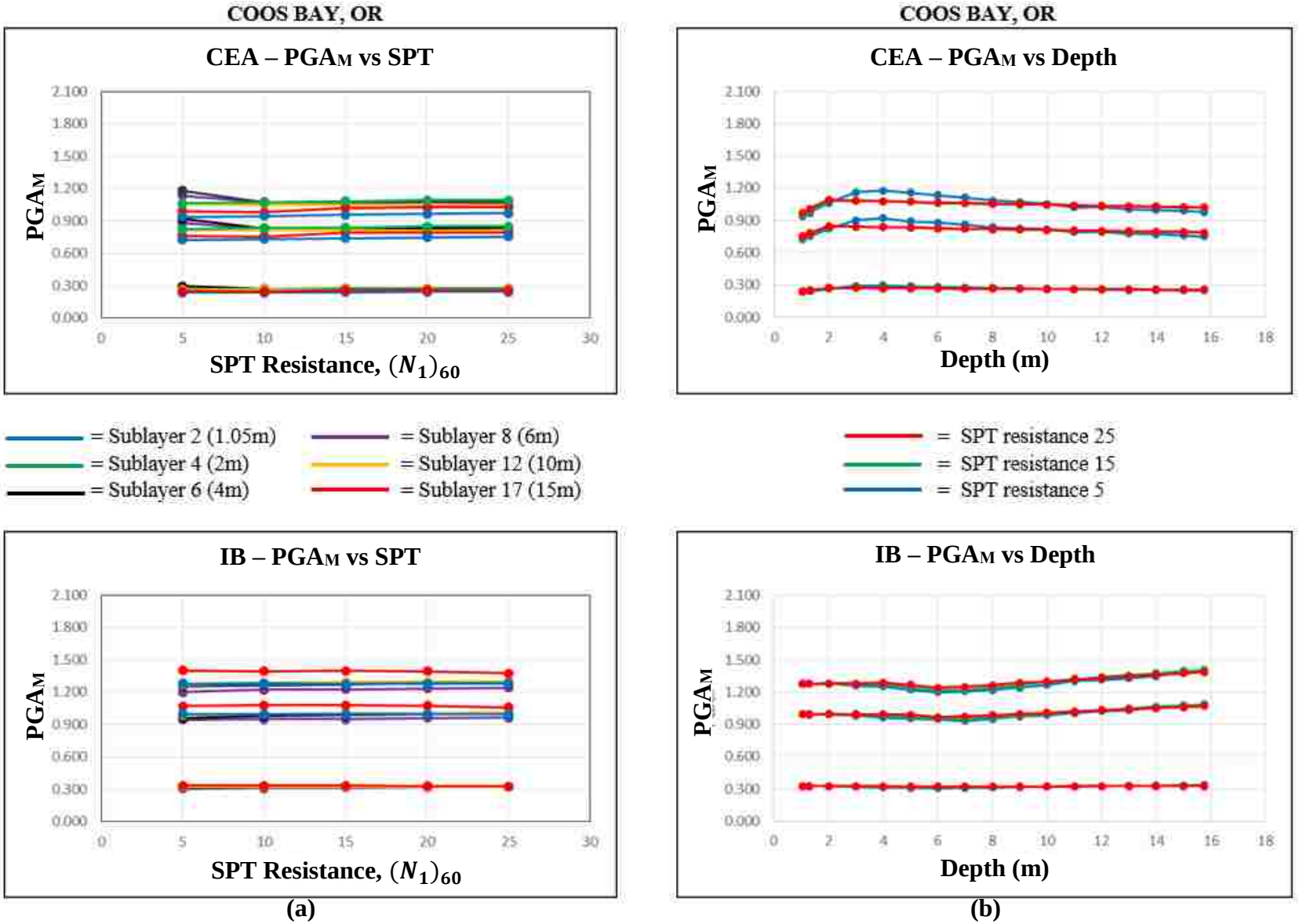

Figure A.9. Plots showing the influence of (a) $(N_1)_{60}$ on PGA_M and (b) Depth BGS on PGA_M – Coos Bay, OR.

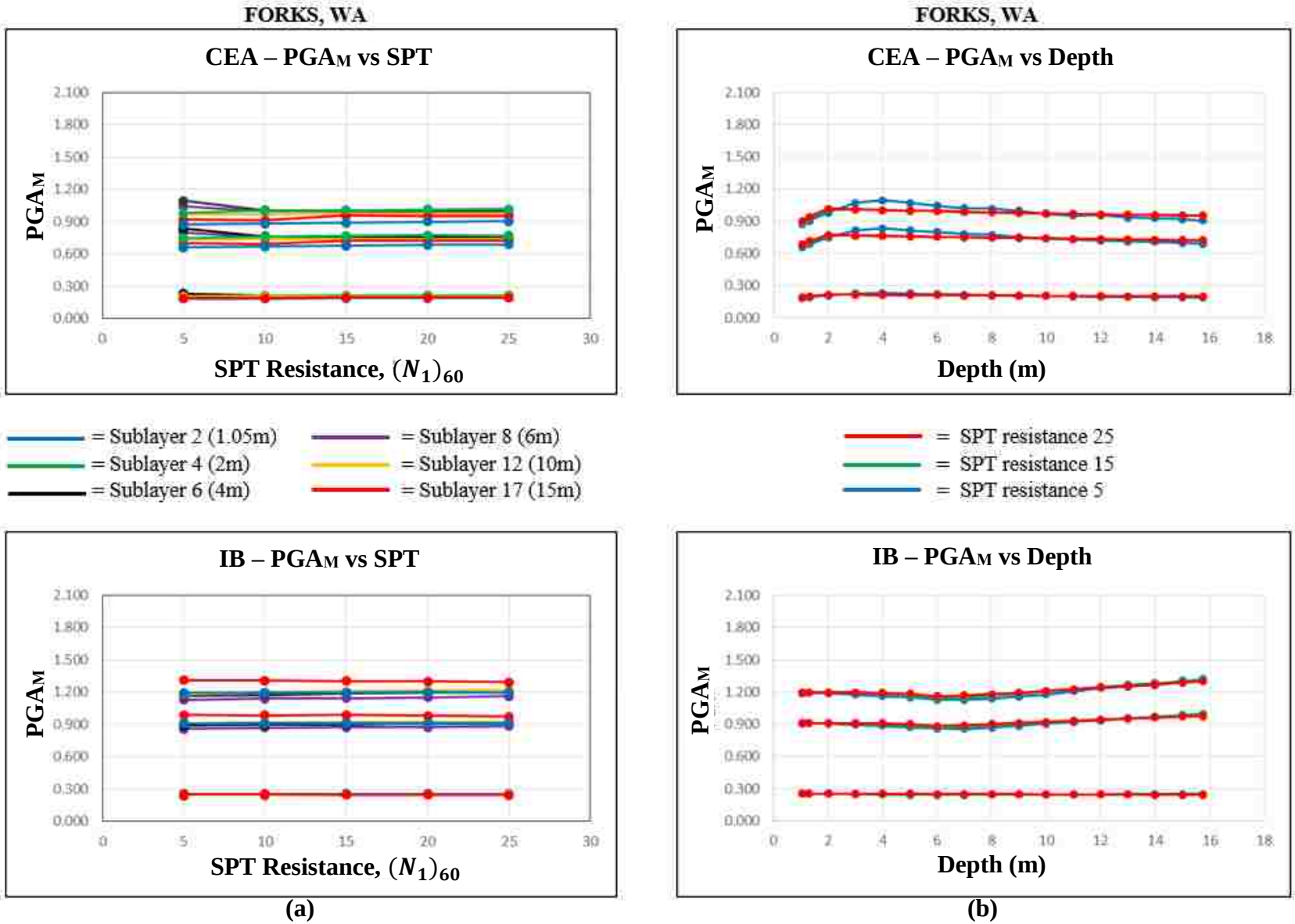

Figure A.10. Plots showing the influence of (a) $(N_1)_{60}$ on PGA_M and (b) Depth BGS on PGA_M – Forks, WA.

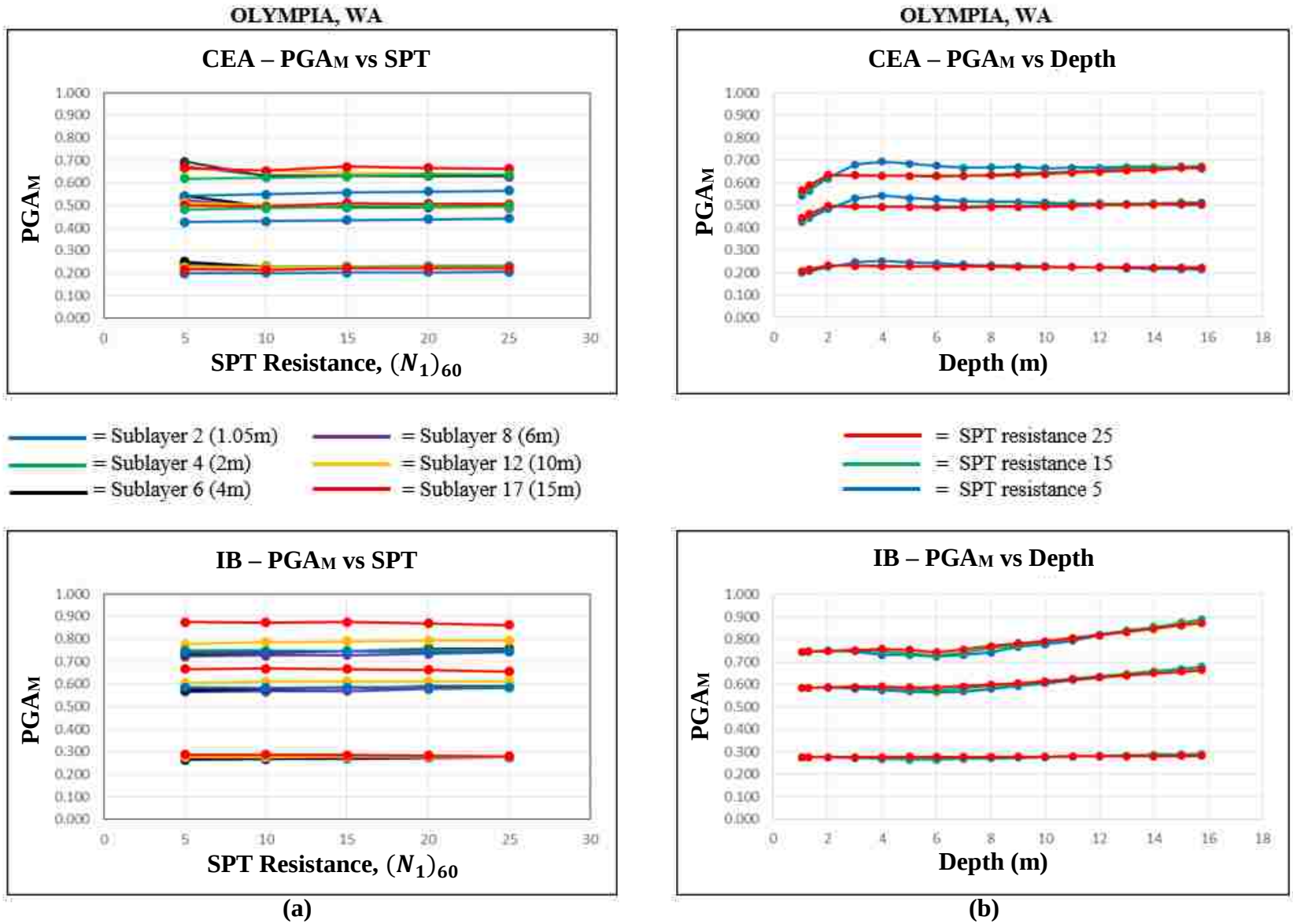

Figure A.11. Plots showing the influence of (a) $(N_1)_{60}$ on PGA_M and (b) Depth BGS on PGA_M – Olympia, WA.

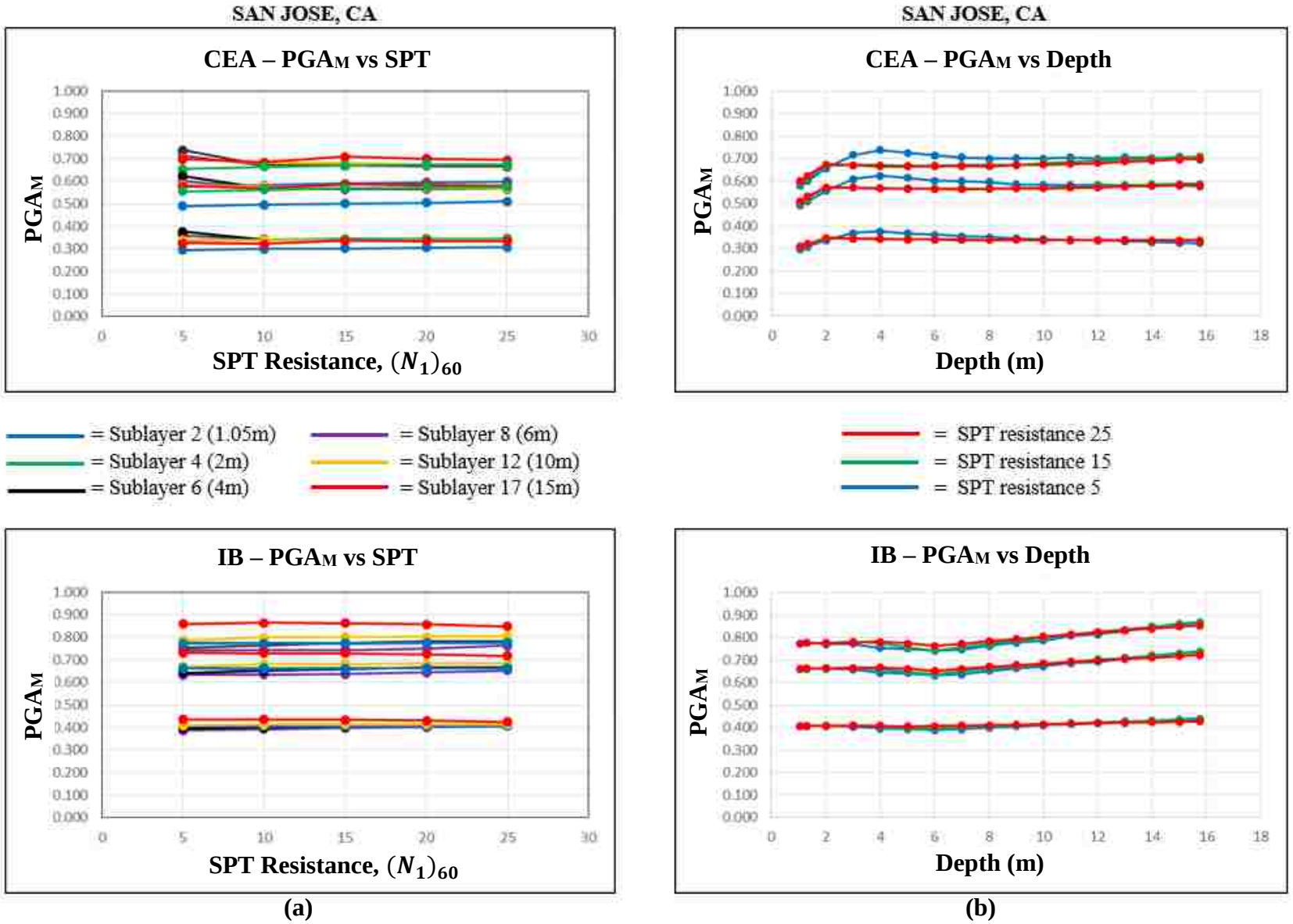

Figure A.12. Plots showing the influence of (a) $(N_1)_{60}$ on PGA_M and (b) Depth BGS on PGA_M – San Jose, CA.

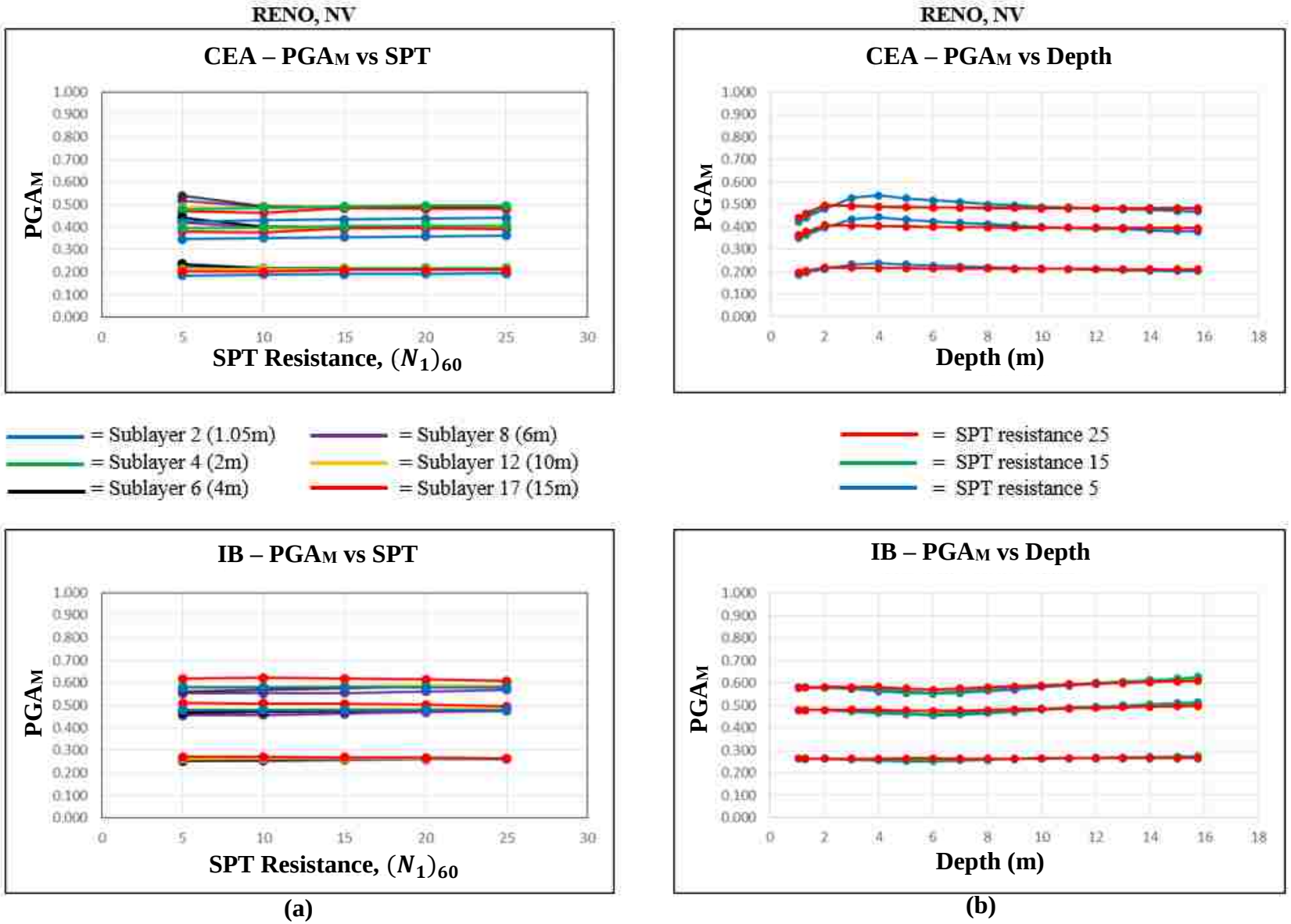

Figure A.13. Plots showing the influence of (a) $(N_1)_{60}$ on PGA_M and (b) Depth BGS on PGA_M – Reno, NV.

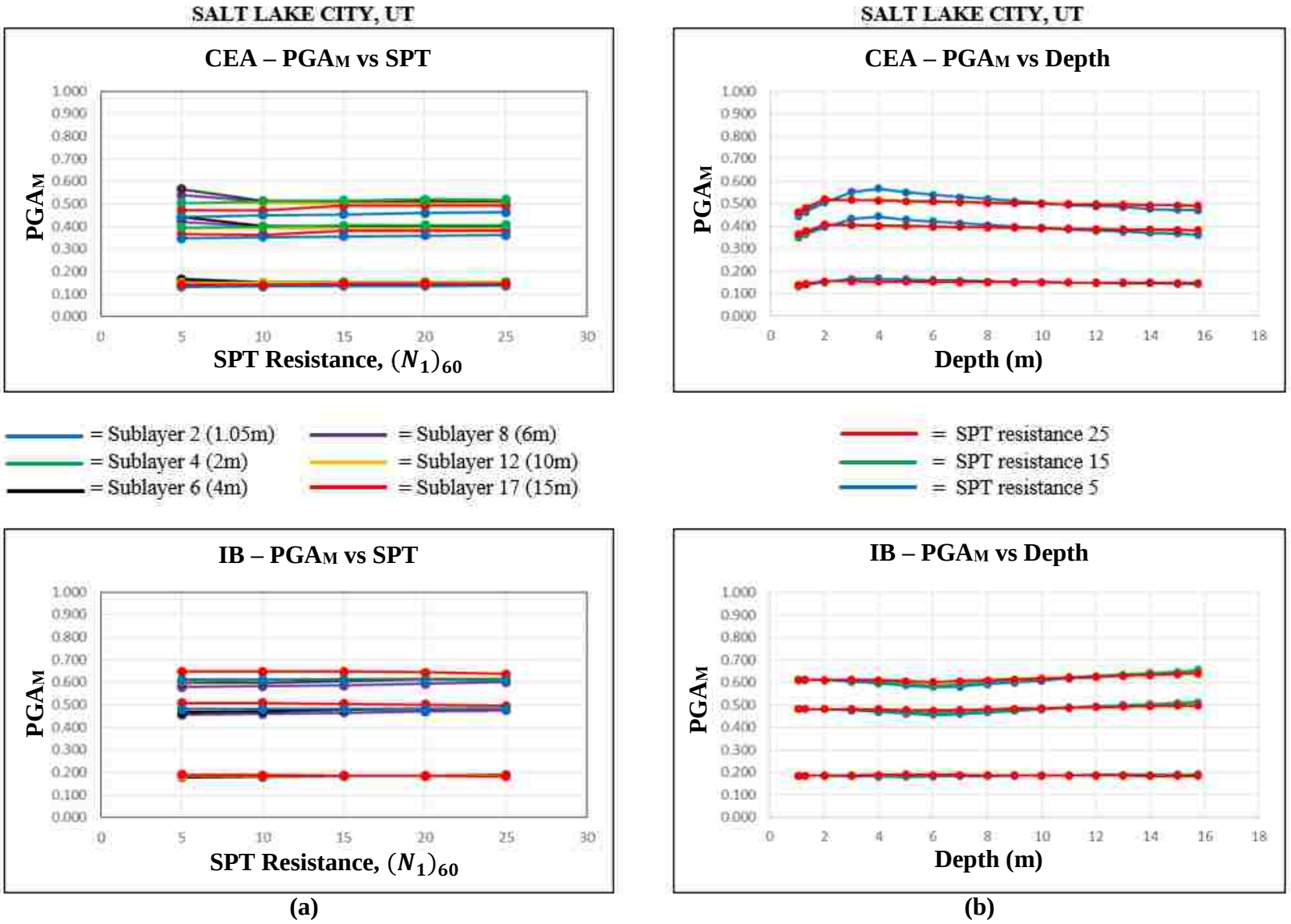

Figure A.14. Plots showing the influence of (a) $(N_1)_{60}$ on PGA_M and (b) Depth BGS on PGA_M – Salt Lake City, UT.

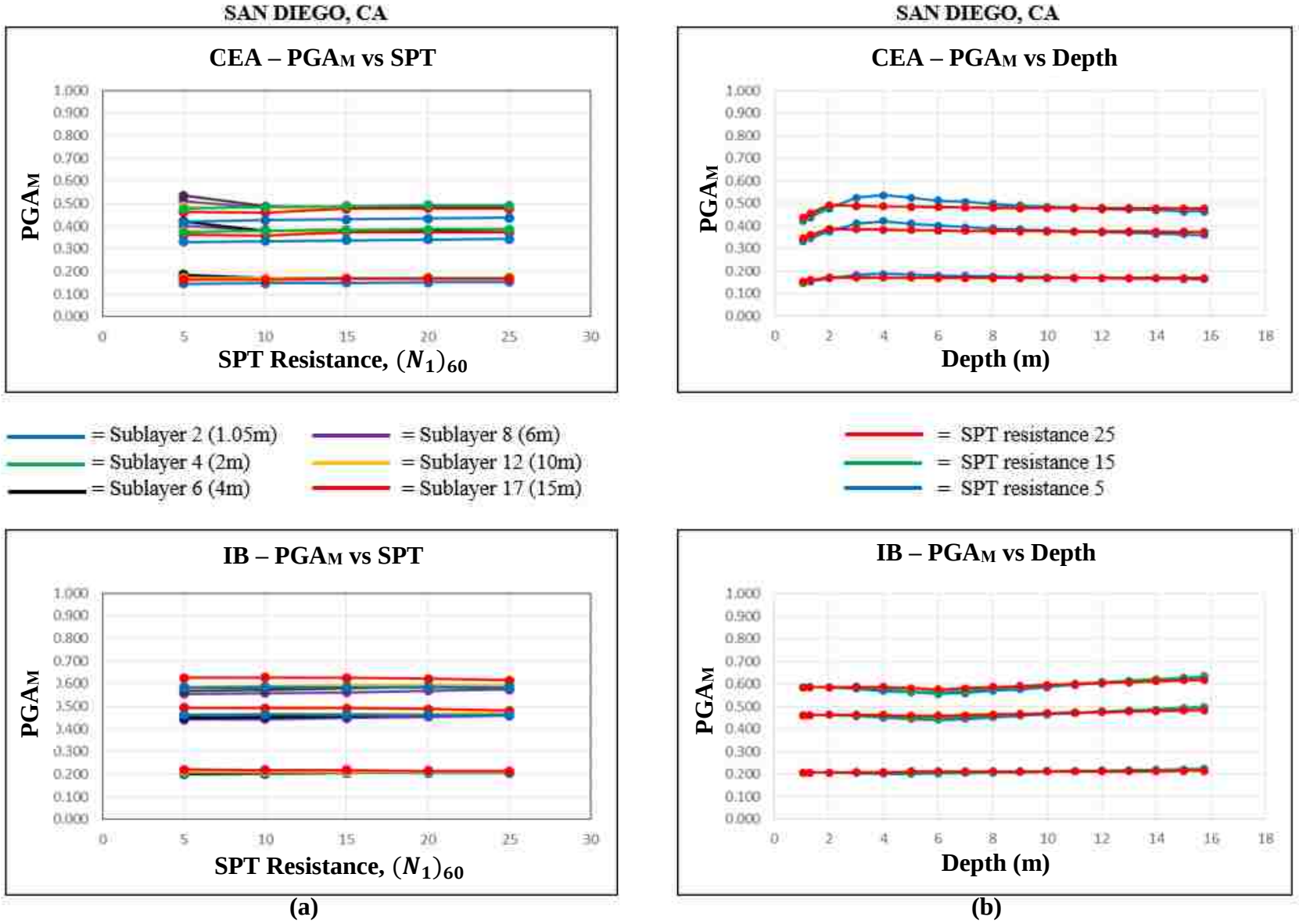

Figure A.15. Plots showing the influence of (a) $(N_1)_{60}$ on PGA_M and (b) Depth BGS on PGA_M – San Diego, CA.

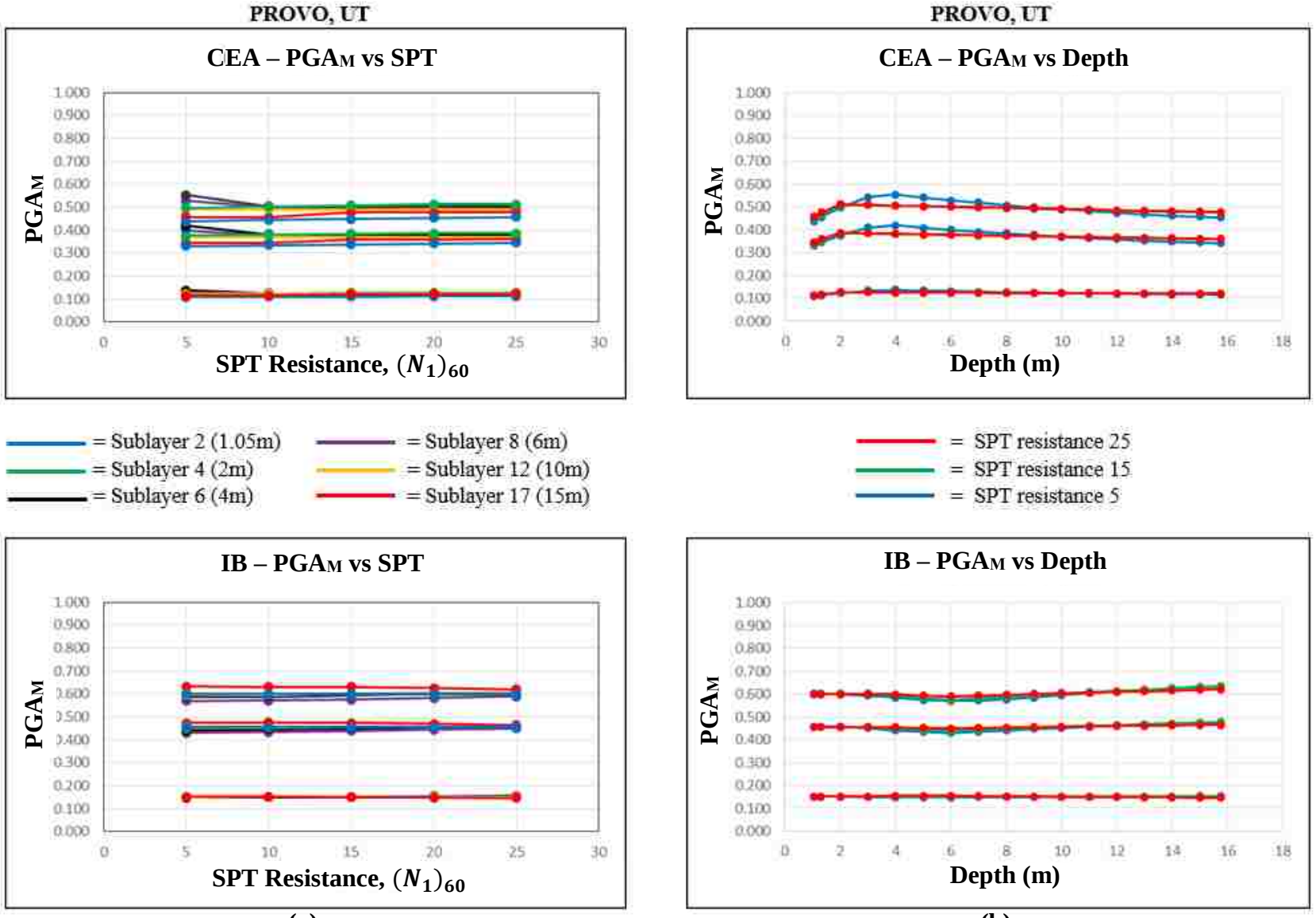

Figure A.16. Plots showing the influence of (a) $(N_1)_{60}$ on PGA_M and (b) Depth BGS on PGA_M – Provo, UT.

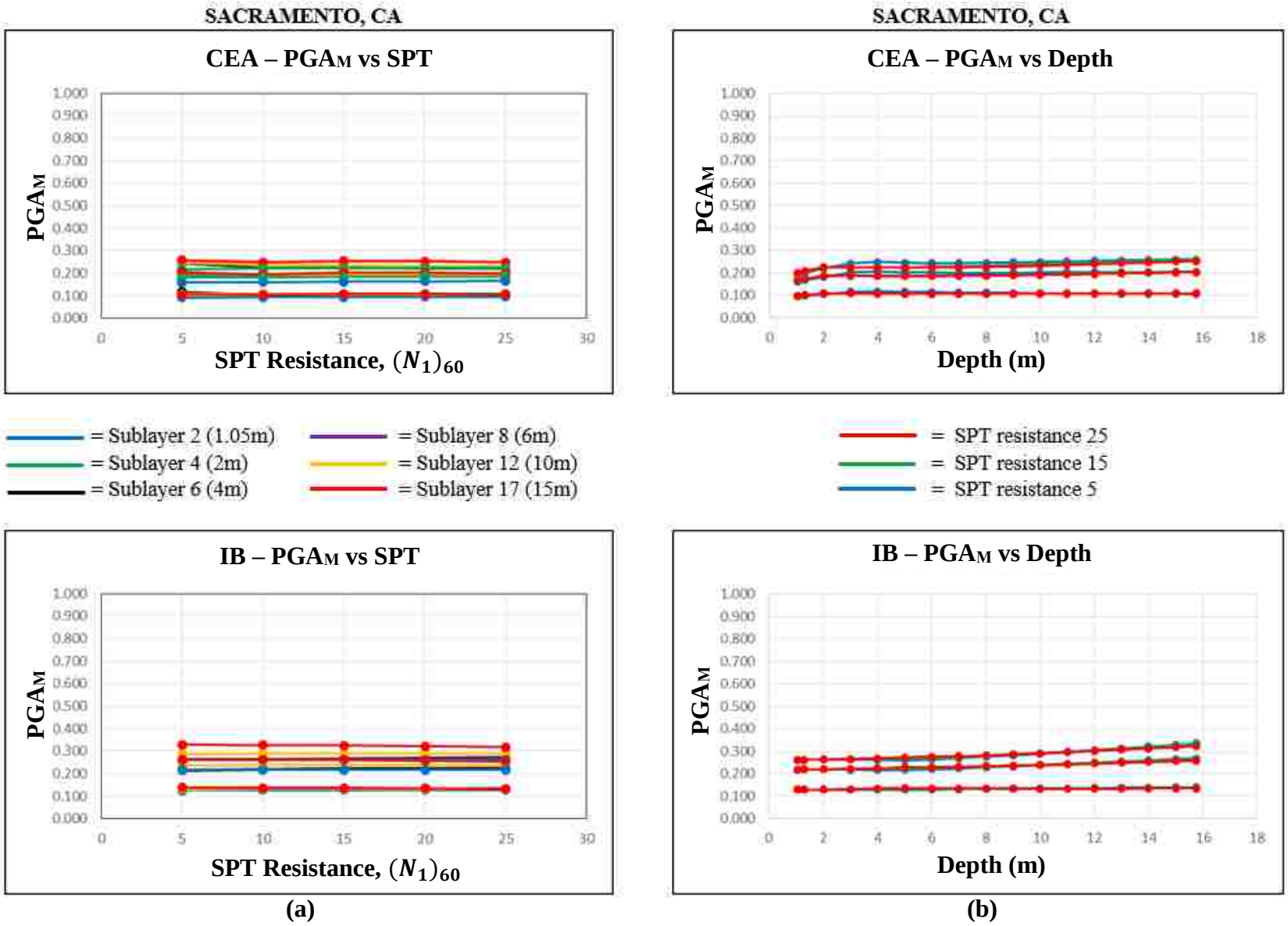

Figure A.17. Plots showing the influence of (a) $(N_1)_{60}$ on PGA_M and (b) Depth BGS on PGA_M – Sacramento, CA.

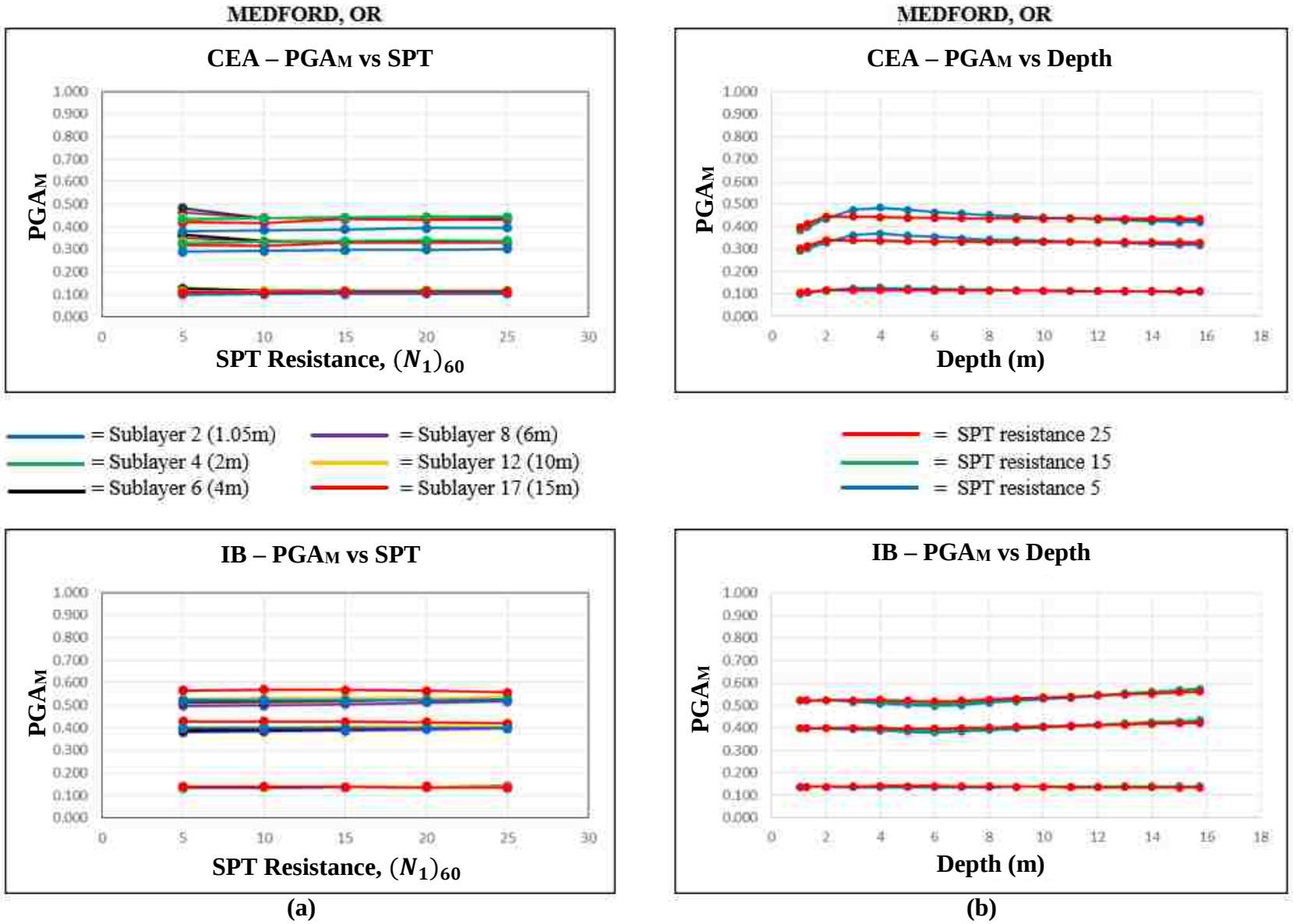

Figure A.18. Plots showing the influence of (a) $(N_1)_{60}$ on PGA_M and (b) Depth BGS on PGA_M – Medford, OR.

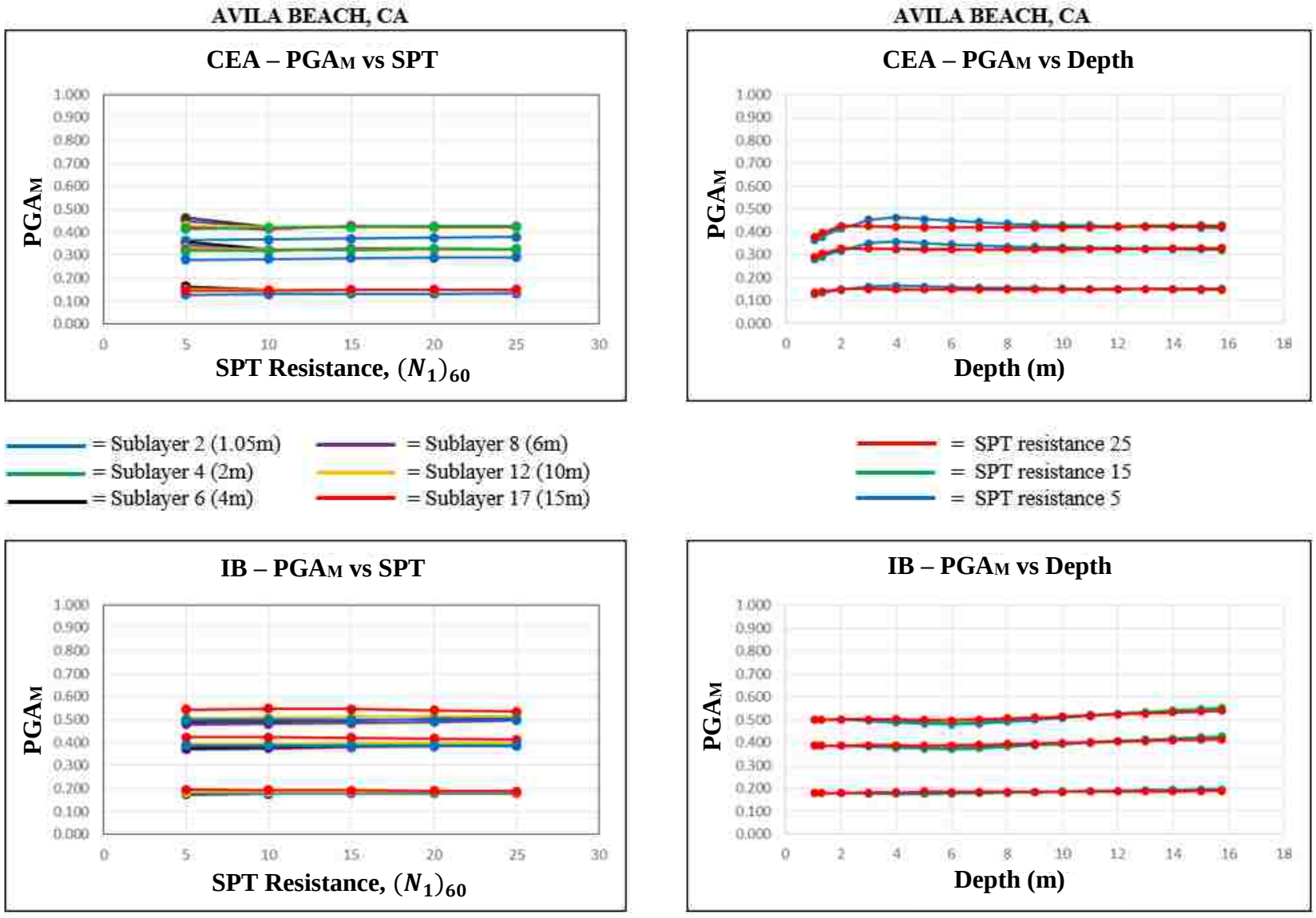

Figure A.19. Plots showing the influence of (a) $(N_1)_{60}$ on PGA_M and (b) Depth BGS on PGA_M – Avila Beach, CA.

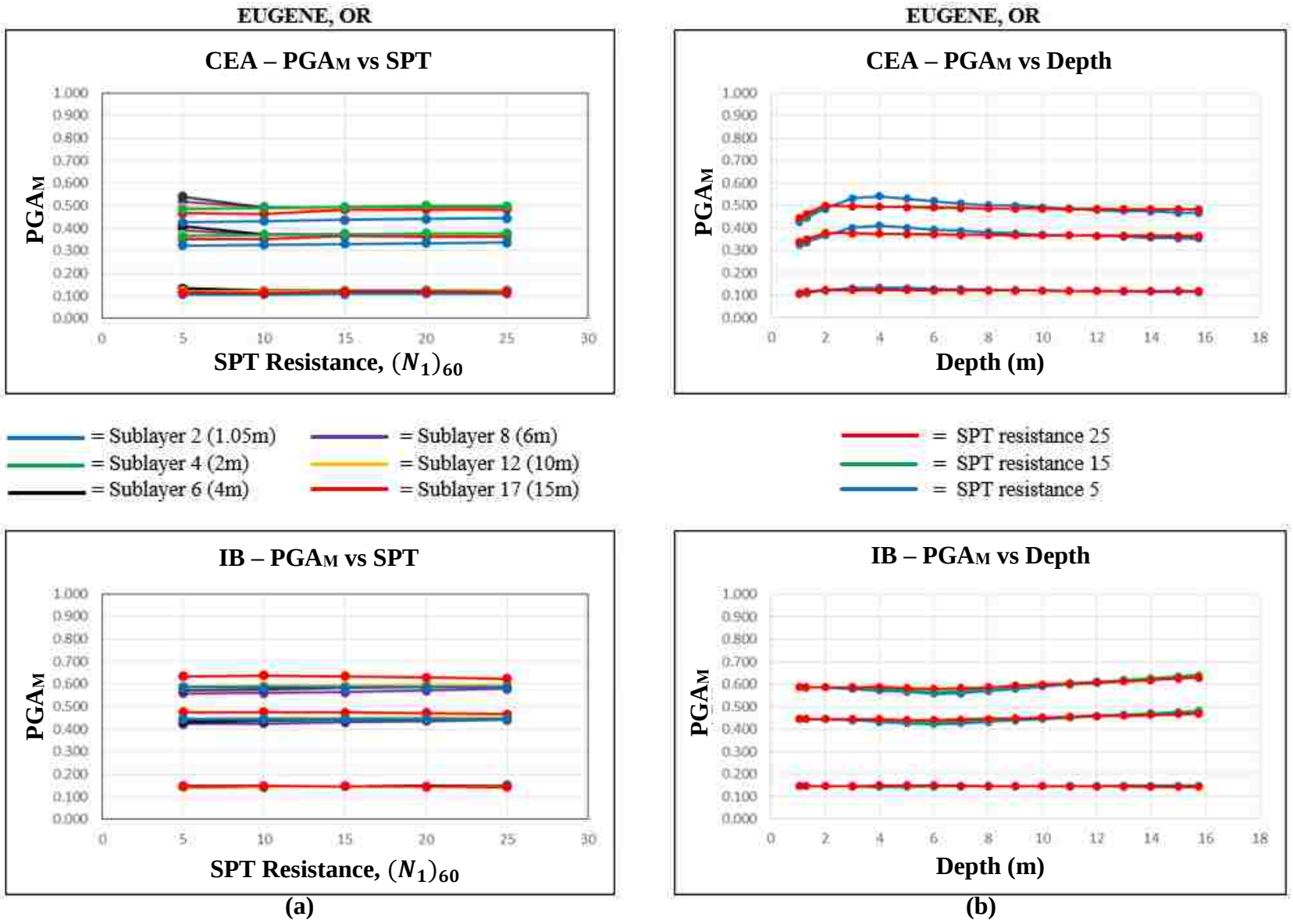

Figure A.20. Plots showing the influence of (a) $(N_1)_{60}$ on PGA_M and (b) Depth BGS on PGA_M – Eugene, OR.

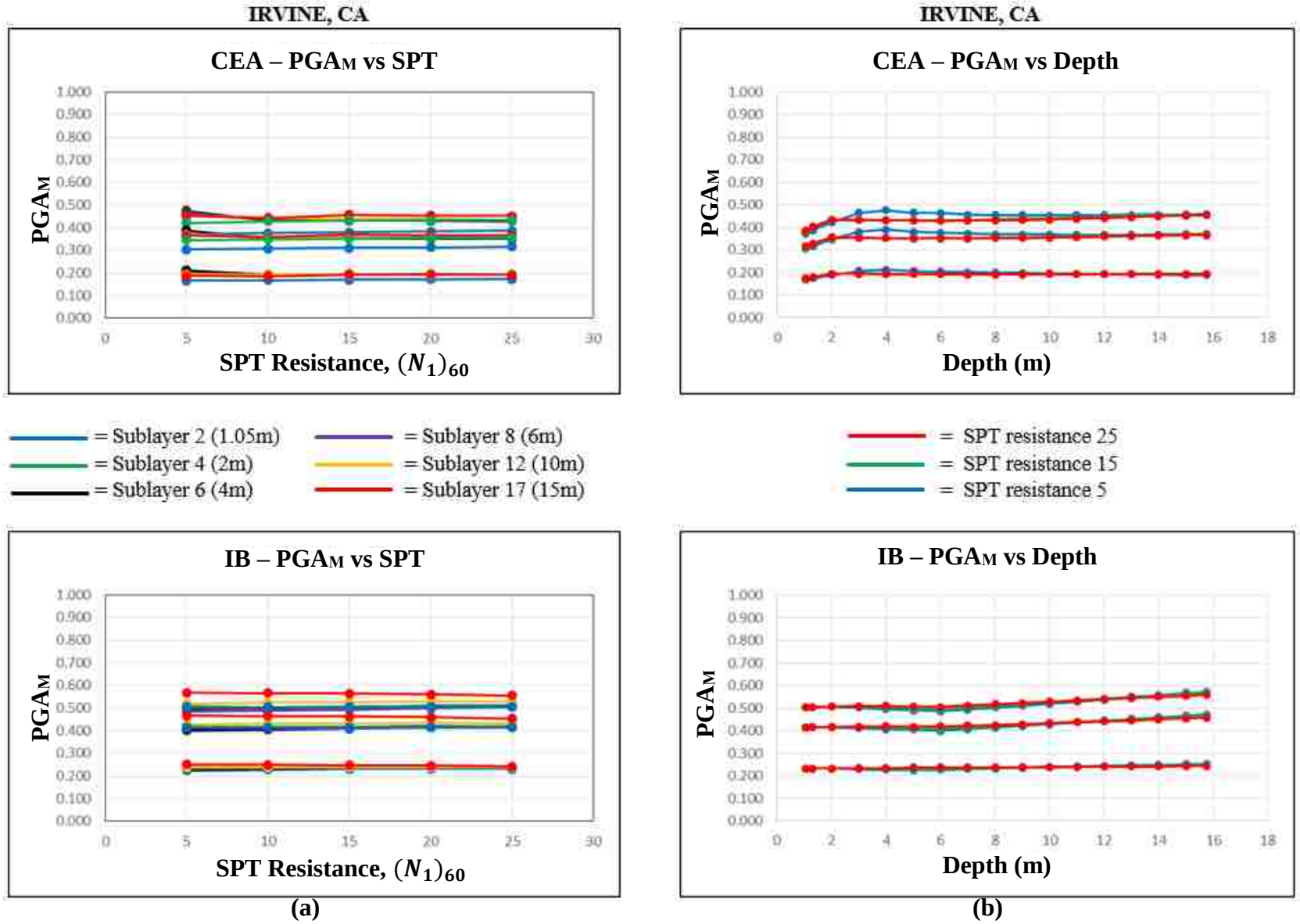

Figure A.21. Plots showing the influence of (a) $(N1)_{60}$ on PGA_M and (b) Depth BGS on PGA_M – Irvine, CA.

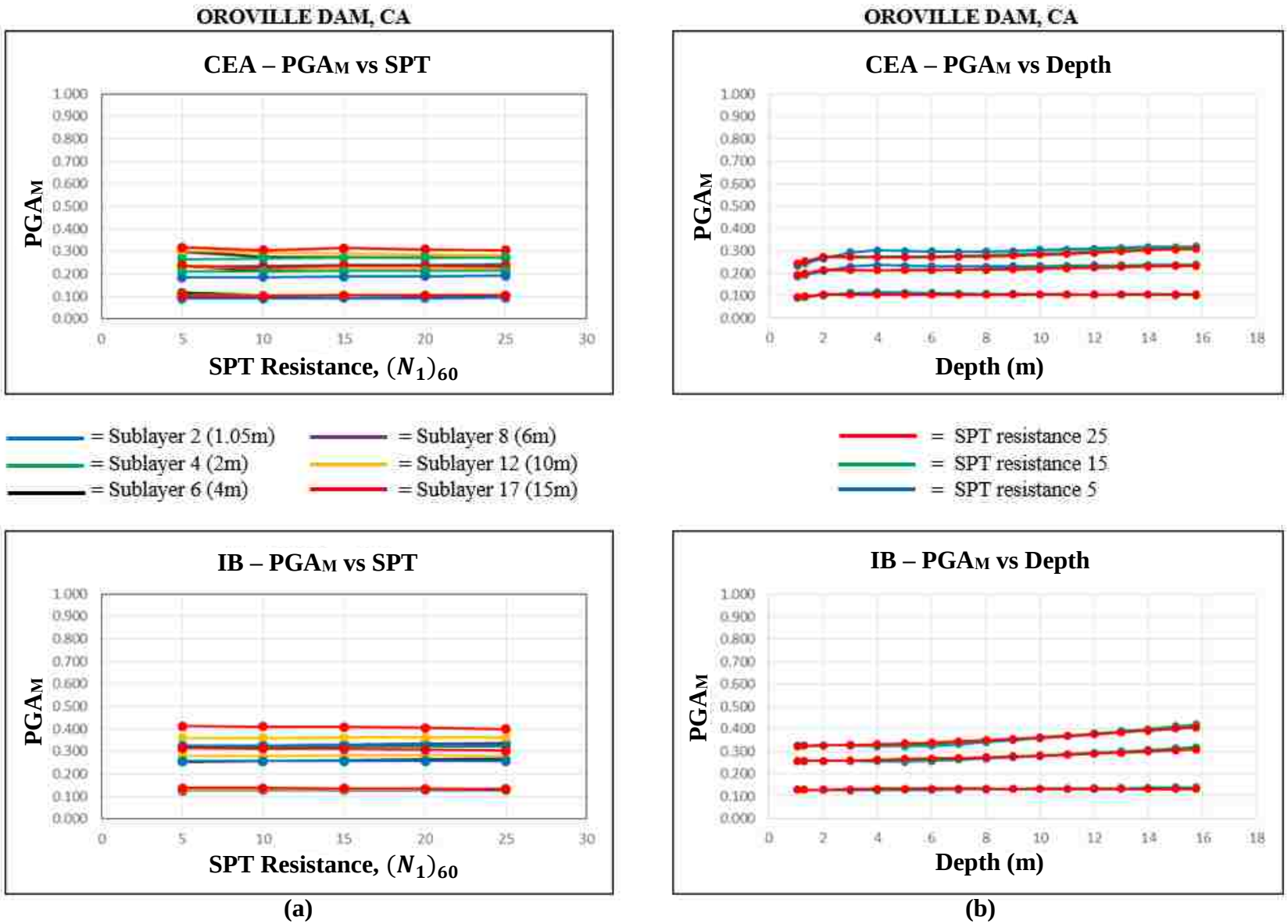

Figure A.22. Plots showing the influence of (a) $(N_1)_{60}$ on PGA_M and (b) Depth BGS on PGA_M – Oroville Dam, CA.

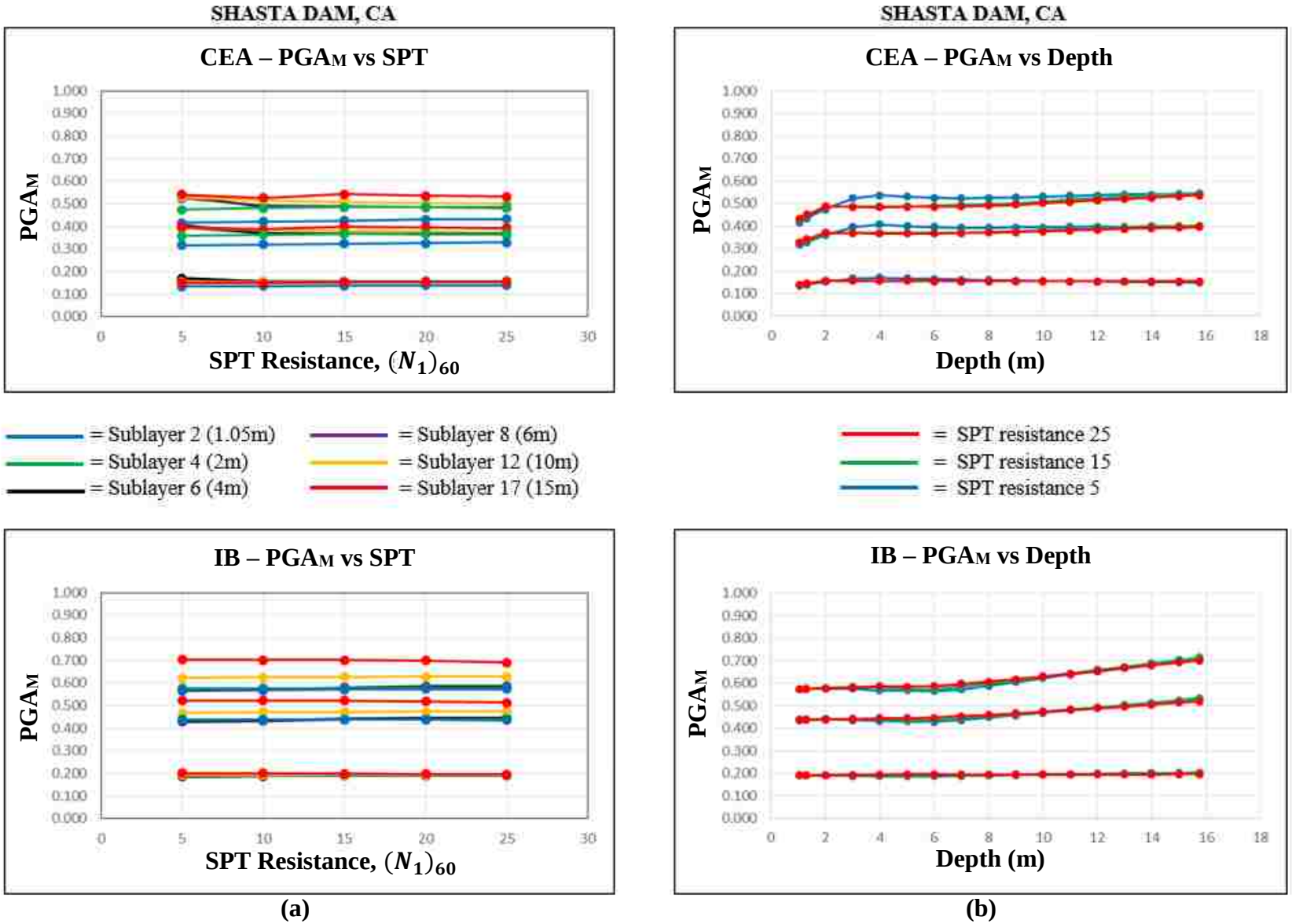

Figure A.23. Plots showing the influence of (a) $(N_1)_{60}$ on PGA_M and (b) Depth BGS on PGA_M – Shasta Dam, CA.

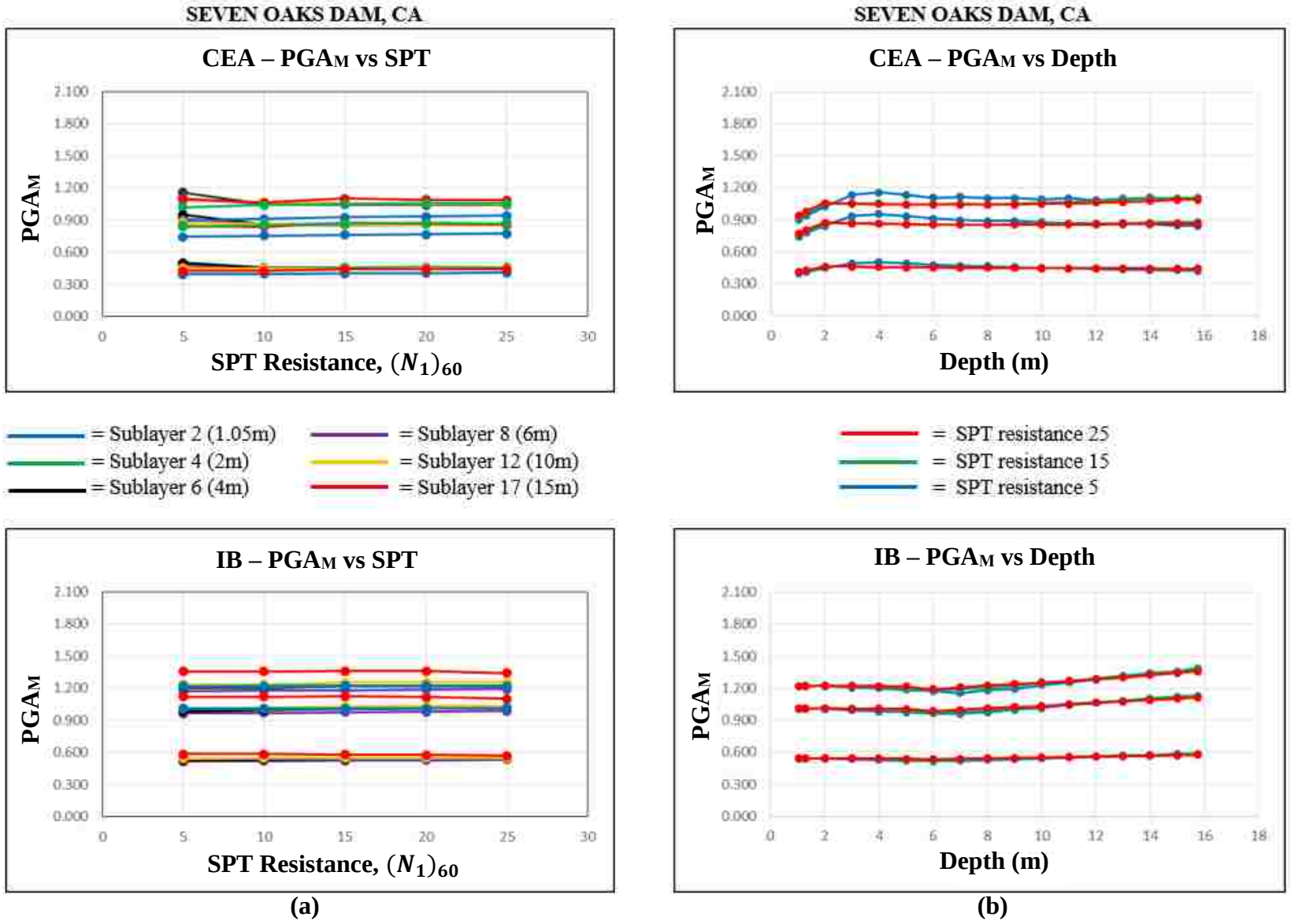

Figure A.24. Plots showing the influence of (a) $(N_1)_{60}$ on PGA_M and (b) Depth BGS on PGA_M – Seven Oaks Dam, CA.

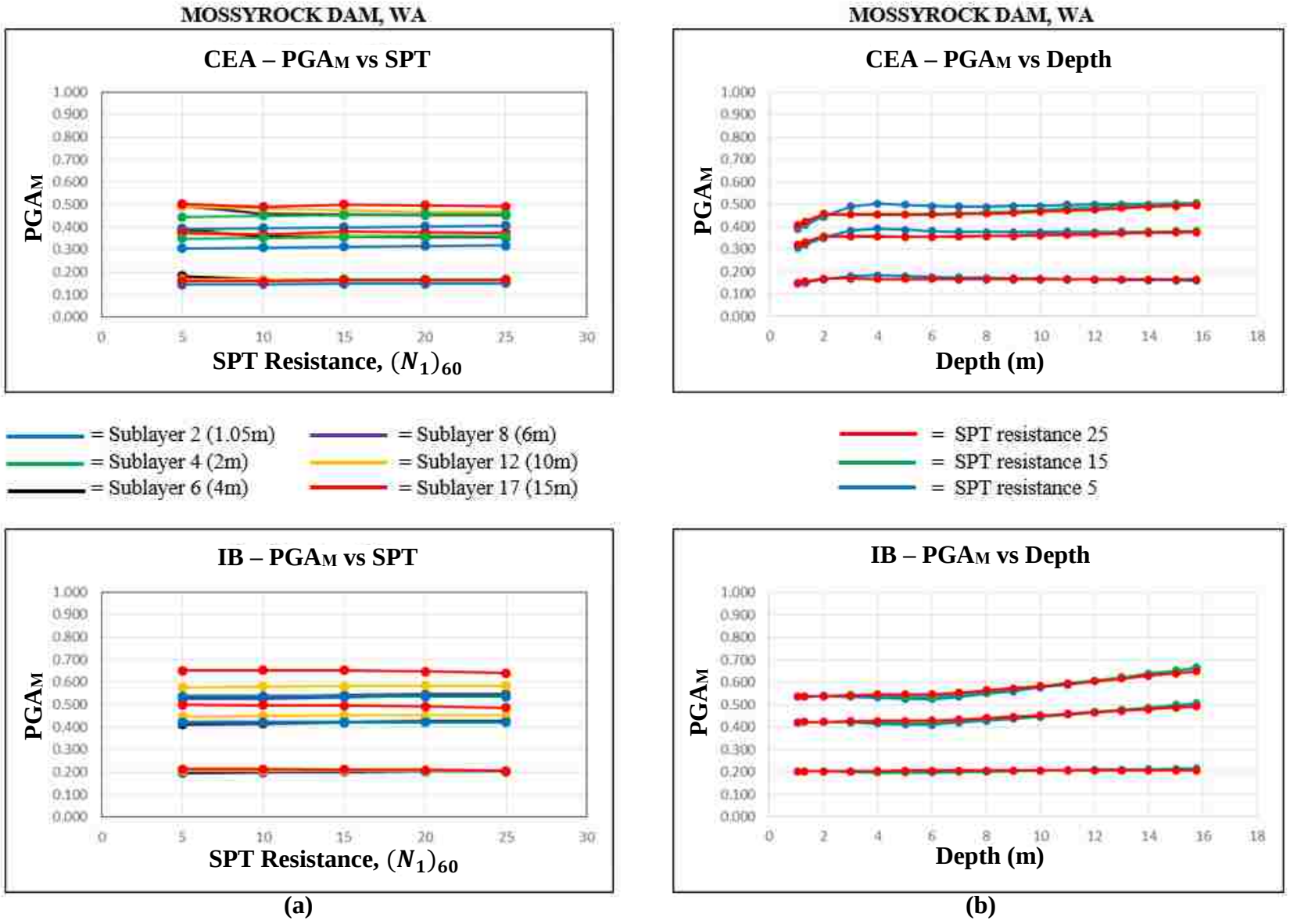

Figure A.25. Plots showing the influence of (a) $(N_1)_{60}$ on PGA_M and (b) Depth BGS on PGA_M – Mossyrock Dam, WA.

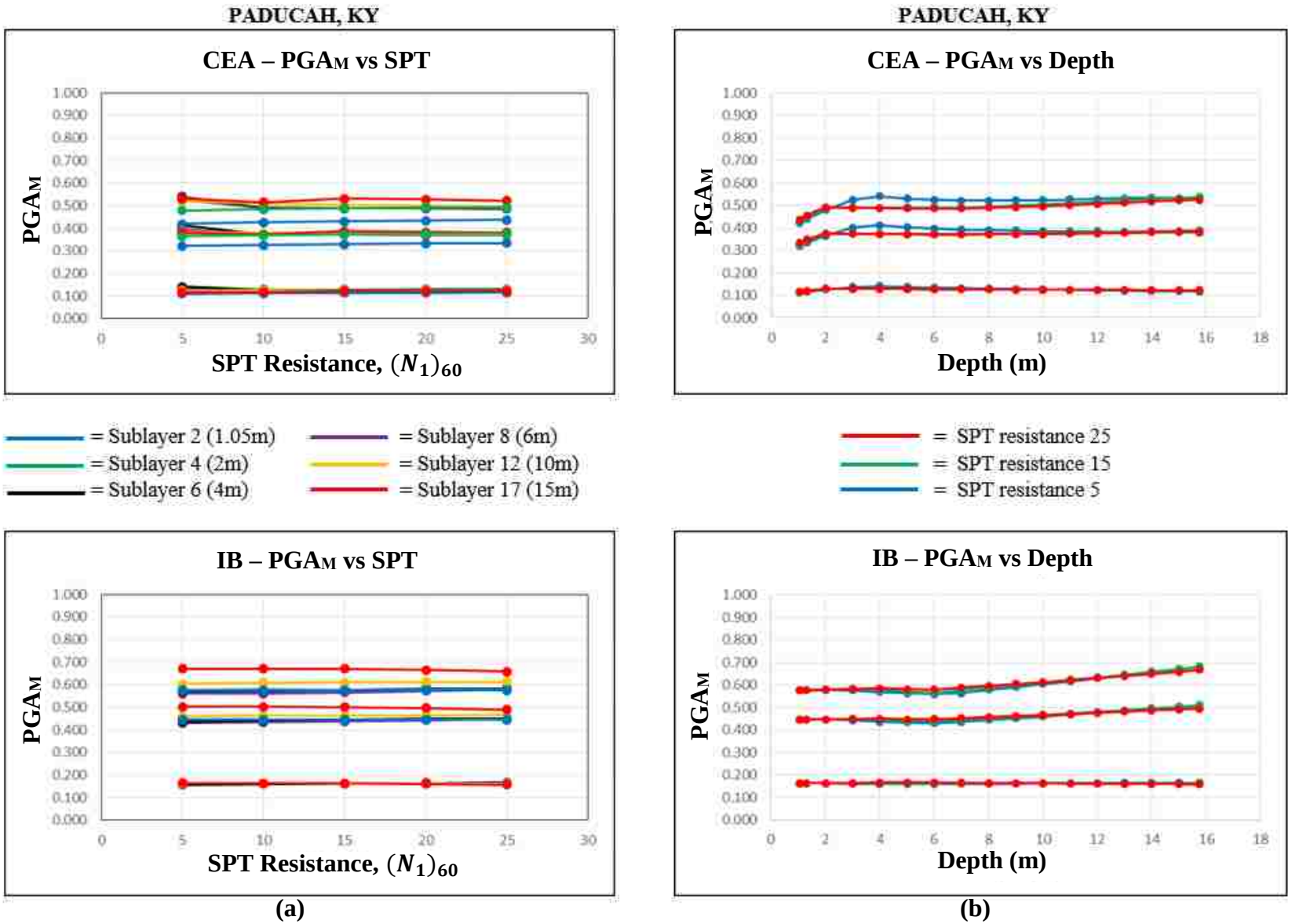

Figure A.26. Plots showing the influence of (a) $(N_1)_{60}$ on PGA_M and (b) Depth BGS on PGA_M – Paducah, KY.

APPENDIX B

LINEAR REGRESSION EQUATIONS USED TO DEVELOP NORMALIZED PGA_M AS A FUNCTION OF $(N_1)_{60}$

Table B.1. Linear Regression equations of the CEA2004 calculated PGA_M as a function of $(N_1)_{60}$ for returns periods of 475, 2475, and 4975 years at depths of 1.05 m., 2m., 4m., 6m., 10m., and 15 m. for Charleston, SC.

CEA2004	Depth					
Tr	1.05m	2m	4m	6m	10m	15m
475	y = 0.000207125x + 0.098988818	y = 0.000192489x + 0.112546953	y = -0.000431879x + 0.123745621	y = -0.000232813x + 0.118452604	y = 0.000033194x + 0.110520733	y = 0.000295851x + 0.101541119
2475	y = 0.000829883x + 0.382290240	y = 0.000698260x + 0.436640860	y = -0.001799788x + 0.482165817	y = -0.001014163x + 0.462958801	y = -0.000293033x + 0.443696727	y = 0.000925155x + 0.413852989
4975	y = 0.001185570x + 0.537233322	y = 0.001074016x + 0.611826670	y = -0.002467457x + 0.677550843	y = -0.001497980x + 0.653092213	y = -0.000430252x + 0.624068105	y = 0.001464547x + 0.578425894

Table B.2. Linear Regression equations of the CEA2004 calculated PGA_M as a function of $(N_1)_{60}$ for returns periods of 475, 2475, and 4975 years at depths of 1.05 m., 2m., 4m., 6m., 10m., and 15 m. for Eureka, CA.

CEA2004	Depth					
Tr	1.05m	2m	4m	6m	10m	15m
475	y = 0.000899702x + 0.433241303	y = 0.000812922x + 0.493015552	y = -0.001863553x + 0.541239919	y = -0.001259947x + 0.523776418	y = -0.000022948x + 0.490249387	y = 0.001286465x + 0.449769180
2475	y = 0.001829866x + 0.932891992	y = 0.001628622x + 1.065030843	y = -0.004924832x + 1.186619847	y = -0.003639497x + 1.153839508	y = -0.001339909x + 1.110904427	y = 0.001091698x + 1.081716283
4975	y = 0.002211356x + 1.166814067	y = 0.001808600x + 1.333892536	y = -0.006662863x + 1.493589735	y = 0.011706503x + 1.388198505	y = 0.016158706x + 1.291727195	y = -0.002831593x + 1.532781451

Table B.3. Linear Regression equations of the IB2012 calculated PGA_M as a function of $(N_1)_{60}$ for returns periods of 475, 2475, and 4975 years at depths of 1.05 m., 2m., 4m., 6m., 10m., and 15 m. for Charleston, SC.

IB2012	Depth					
Tr	1.05m	2m	4m	6m	10m	15m
475	y = 0.00000080x + 0.15395150	y = -0.00000091x + 0.15374382	y = 0.00036483x + 0.14788398	y = 0.00028041x + 0.14847250	y = -0.00002177x + 0.15100467	y = -0.00028440x + 0.15217557
2475	y = -0.00002571x + 0.54087651	y = -0.00002425x + 0.54138482	y = 0.00086445x + 0.52263629	y = 0.00102640x + 0.50767929	y = 0.00037790x + 0.54161305	y = -0.00055313x + 0.58380985
4975	y = -0.00003310x + 0.74891214	y = -0.00009068x + 0.75144142	y = 0.00103891x + 0.72824580	y = 0.00101258x + 0.70773497	y = 0.00070962x + 0.75140250	y = -0.00061681x + 0.82134928

Table B.4. Linear Regression equations of the IB2012 calculated PGA_M as a function of $(N_1)_{60}$ for returns periods of 475, 2475, and 4975 years at depths of 1.05 m., 2m., 4m., 6m., 10m., and 15 m. for Eureka, CA.

IB2012	Depth					
Tr	1.05m	2m	4m	6m	10m	15m
475	y = 0.00001107x + 0.60101243	y = 0.00001037x + 0.60161852	y = 0.00093968x + 0.58102815	y = 0.00098332x + 0.56494950	y = 0.00037538x + 0.60125866	y = -0.00051197x + 0.64788425
2475	y = 0.00007561x + 1.28191581	y = -0.00022922x + 1.29297426	y = 0.00190336x + 1.25472404	y = 0.00192773x + 1.21527126	y = 0.00133175x + 1.31316932	y = -0.00053500x + 1.47728215
4975	y = 0.00018541x + 1.59986016	y = -0.00013248x + 1.61362027	y = 0.00177442x + 1.58261935	y = 0.00264650x + 1.51899089	y = 0.00203577x + 1.64700606	y = -0.00019860x + 1.87290102

APPENDIX C

INFINITE SLOPE MODELS - COMPARISON OF INFINITE SLOPE EQUILIBRIUM EQUATIONS TO PLAXIS OUPUT

Soil Element 2

Soil Element 2 is located at the model coordinates (x,y) = (-384,-20) meters which corresponds to the center of an element at the ground surface (see Figure C.1) All 12 stress points for Soil Element 2 are plastic and the PLAXIS and ISEE stress results are shown in Table C.1. Examining the percent error in Table C.1, one can see the σ_{yy} values between the PLAXIS and ISEE results have a percent error of approximately 1-6%. The σ_{xy} and SSR are significantly different as indicated by percent error values ranging from over 200% to 1000%.

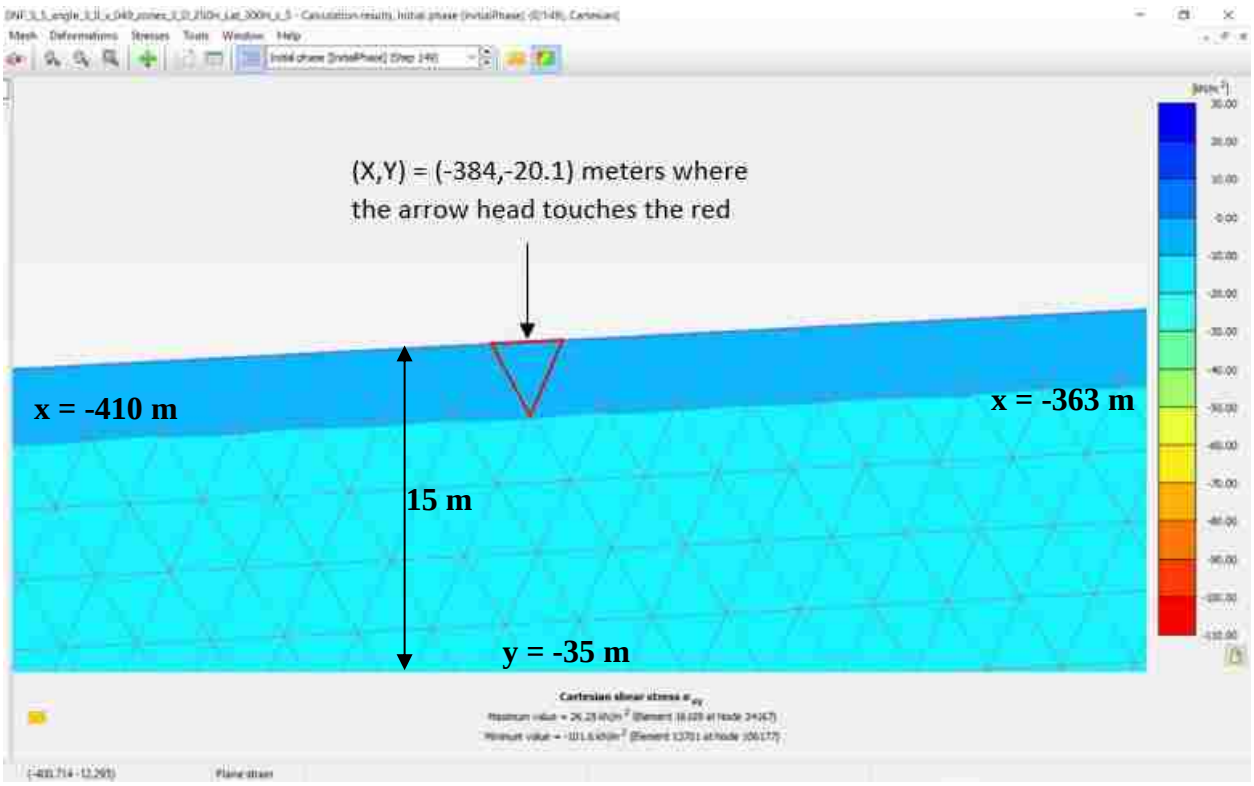

Figure C.1. Shear stress color contour for the three-degree infinite slope model in the region of Soil Element 2.

Table C.1. Comparison of PLAXIS and ISEE stresses for Soil Element 2 of the three-degree infinite slope.

Location Information					PLAXIS Output			ISEE			Percent Error		
Stress point	x (m)	y (m)	y_{GS} (m)	y_{BGS} (m)	σ_{yy} (kPa)	σ_{xy} (kPa)	SSR	σ_{yy} (kPa)	σ_{xy} (kPa)	SSR	σ_{yy}	σ_{xy}	SSR
3817	-383.769	-22.540	-20.112	-2.427	-41.645	-8.122	0.195	-41.208	-2.160	0.052	1.061%	276.097%	272.147%
3818	-382.721	-20.233	-20.058	-0.175	-3.138	-1.523	0.485	-2.977	-0.156	0.052	5.417%	876.290%	826.122%
3819	-385.079	-20.356	-20.181	-0.175	-3.017	-1.517	0.503	-2.977	-0.156	0.052	1.363%	872.511%	859.432%
3820	-383.829	-21.509	-20.116	-1.393	-23.910	-5.119	0.214	-23.647	-1.239	0.052	1.113%	313.019%	308.474%
3821	-383.503	-20.791	-20.099	-0.693	-11.934	-3.014	0.253	-11.757	-0.616	0.052	1.505%	389.227%	381.972%
3822	-384.237	-20.830	-20.137	-0.693	-11.968	-3.086	0.258	-11.757	-0.616	0.052	1.797%	400.887%	392.046%
3823	-383.434	-21.863	-20.095	-1.768	-30.315	-6.186	0.204	-30.017	-1.573	0.052	0.994%	293.262%	289.390%
3824	-383.012	-20.935	-20.073	-0.862	-14.778	-3.433	0.232	-14.637	-0.767	0.052	0.963%	347.599%	343.328%
3825	-383.428	-20.242	-20.095	-0.148	-2.651	-1.480	0.558	-2.508	-0.131	0.052	5.715%	1026.093%	965.218%
3826	-384.376	-20.292	-20.144	-0.148	-2.583	-1.454	0.563	-2.508	-0.131	0.052	3.014%	1006.174%	973.807%
3827	-384.709	-21.024	-20.162	-0.862	-14.893	-3.613	0.243	-14.637	-0.767	0.052	1.749%	370.972%	362.875%
3828	-384.182	-21.902	-20.134	-1.768	-30.305	-6.161	0.203	-30.017	-1.573	0.052	0.961%	291.658%	287.930%

Soil Element 3

Soil Element 3 is located at the model coordinates (x,y) = (343,18) meters which corresponds to the center of the element at the ground surface (see Figure C.2). Six of the 12 stress points are considered elastic and the other six considered plastic. The shear stress in Figure C.2 is "jumping" between approximately -1 kPa and 3 kPa in just Soil Element 3 which is approximately 3 meters in width at the ground surface. Plastic points are shown in Figure C.3 in the Soil Element 3 region.

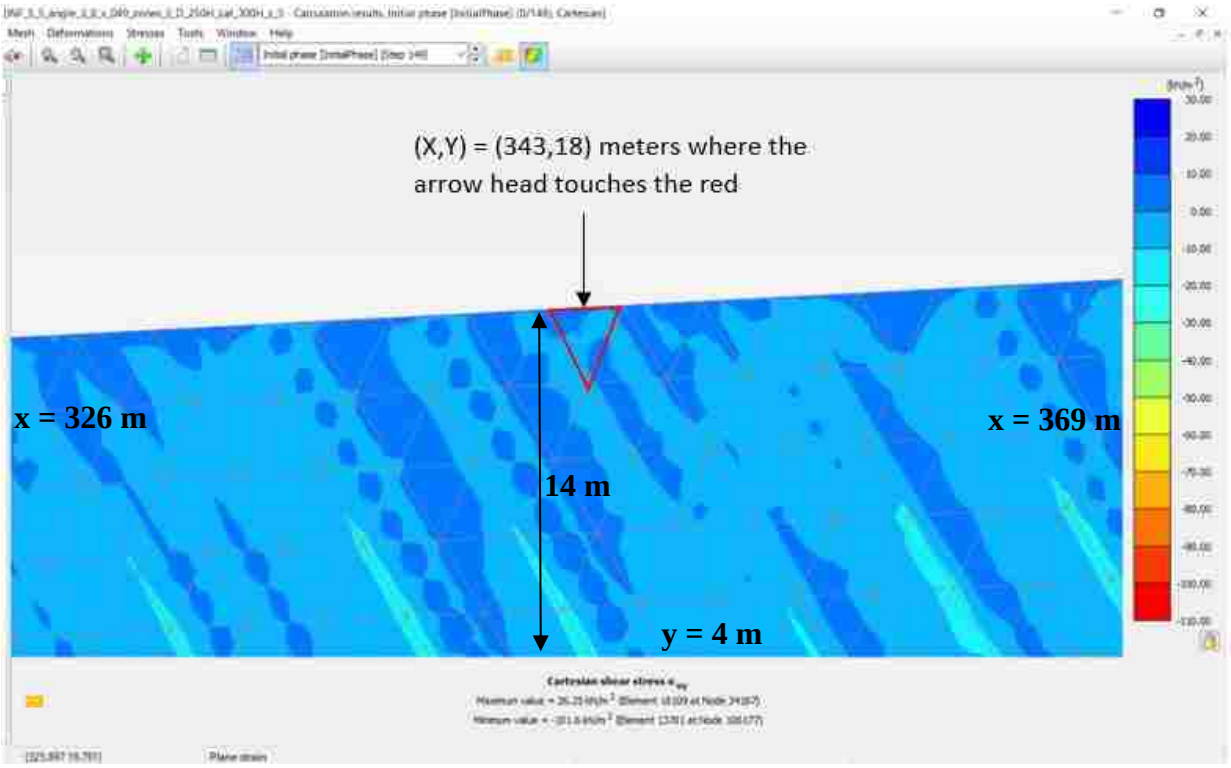

Figure C.2. Shear stress distribution for the three-degree infinite slope model in the region of Soil Element 3.

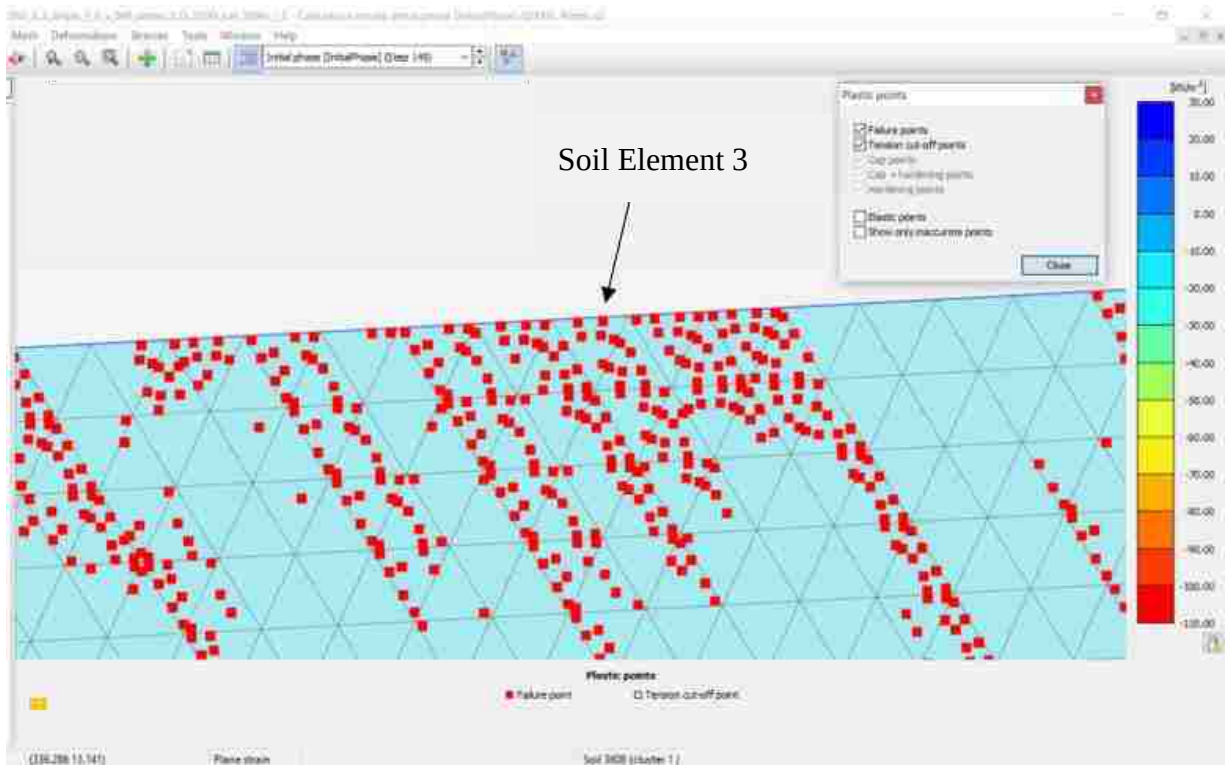

Figure C.3. Plastic points in the region of Soil Element 3 for the three-degree infinite slope.

Table C.2 shows the PLAXIS and ISEE results. Examining the percent error in Table C.2 one can see the σ_{yy} values between the PLAXIS and ISEE results have a percent error of approximately 6% to 57%. The σ_{xy} and SSR are significantly different as indicated by percent error values typical ranging in the hundreds of percent. There was no clear difference between the stress results for the six elastic and plastic stress points.

Table C.2. Comparison of PLAXIS and ISEE stresses for Soil Element 3 of the three-degree infinite slope.

Location Information					PLAXIS Output			ISEE			Percent Error		
Stress point	x (m)	y (m)	y_{GS} (m)	y_{BGS} (m)	σ_{yy} (kPa)	σ_{xy} (kPa)	SSR	σ_{yy} (kPa)	σ_{xy} (kPa)	SSR	σ_{yy}	σ_{xy}	SSR
3793	343.334	15.566	17.993	-2.427	-45.953	3.035	-0.066	-41.207	-2.160	0.052	11.518%	240.557%	226.040%
3794	344.382	17.873	18.048	-0.175	-3.499	-0.960	0.274	-2.974	-0.156	0.052	17.644%	515.892%	423.523%
3795	342.024	17.750	17.925	-0.175	-4.685	1.045	-0.223	-2.974	-0.156	0.052	57.523%	770.420%	525.601%
3796	343.274	16.597	17.990	-1.393	-25.004	-0.140	0.006	-23.645	-1.239	0.052	5.748%	88.665%	89.281%
3797	343.600	17.315	18.007	-0.692	-13.281	-0.746	0.056	-11.755	-0.616	0.052	12.987%	21.057%	7.142%
3798	342.866	17.276	17.969	-0.692	-12.583	0.133	-0.011	-11.755	-0.616	0.052	7.049%	121.574%	120.154%
3799	343.670	16.243	18.011	-1.768	-32.954	1.184	-0.036	-30.015	-1.573	0.052	9.791%	175.297%	168.583%
3800	344.091	17.171	18.033	-0.862	-13.739	-1.175	0.086	-14.634	-0.767	0.052	6.121%	53.226%	63.216%
3801	343.676	17.864	18.011	-0.148	-3.035	0.197	-0.065	-2.505	-0.131	0.052	21.169%	249.898%	223.710%
3802	342.727	17.814	17.962	-0.148	-1.095	0.203	-0.185	-2.505	-0.131	0.052	56.305%	254.347%	453.239%
3803	342.394	17.082	17.944	-0.862	-16.262	1.980	-0.122	-14.634	-0.767	0.052	11.124%	358.105%	332.267%

Soil Element 4

Soil Element 4 is located at the model coordinates (x,y) = (0,-22.23) which corresponds to the top center of the element (see Figure C.4). Because Soil Element 4 is at the center of the model it should be less likely to be influenced by boundary conditions when compared to Soil Elements 2 and 3. Soil Element 4 has all elastic stress points and Table C.3 shows the PLAXIS and ISEE results for each stress point. Examining the percent error in Table C.3, one can see the σ_{yy} values are very similar between the PLAXIS and ISEE results (just like Soil Element 1 which was also at the center of the model). The σ_{xy} and SSR values are significantly different between the PLAXIS and ISEE results as indicated by percent error values of about 63.5% for each stress point.

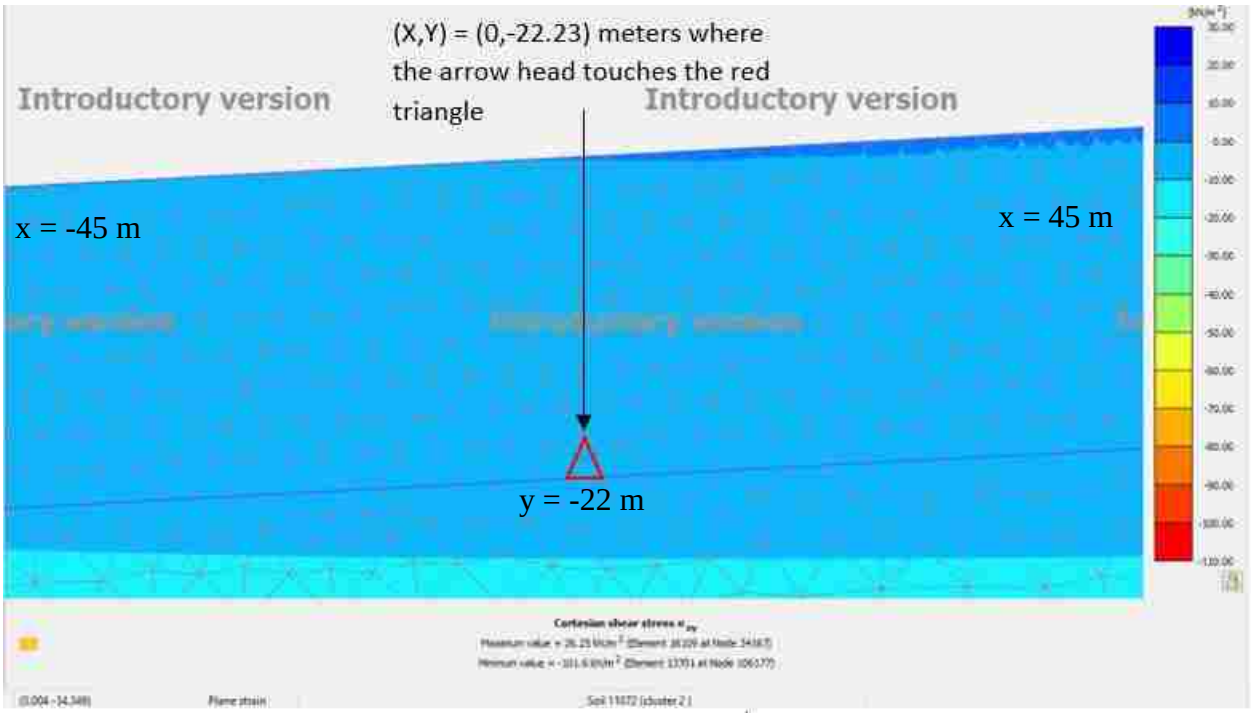

Figure C.4. Shear stress distribution for the three-degree infinite slope model in the region of Soil Element 4.

Table C.3. Comparison of PLAXIS and ISEE stresses for Soil Element 4 of the three-degree infinite slope.

Location Information					PLAXIS Output			ISEE			Percent Error		
Stress point	x (m)	y (m)	y_{GS} (m)	y_{BGS} (m)	σ_{yy} (kPa)	σ_{xy} (kPa)	SSR	σ_{yy} (kPa)	σ_{xy} (kPa)	SSR	σ_{yy}	σ_{xy}	SSR
8713	-0.141	-22.580	-0.007	-22.573	-383.702	-7.327	0.019	-383.210	-20.083	0.052	0.128%	63.516%	63.563%
8714	-1.189	-24.887	-0.062	-24.825	-421.978	-8.044	0.019	-421.442	-22.087	0.052	0.127%	63.582%	63.628%
8715	1.169	-24.763	0.061	-24.825	-421.995	-8.004	0.019	-421.442	-22.087	0.052	0.131%	63.761%	63.808%
8716	-0.081	-23.611	-0.004	-23.607	-401.287	-7.648	0.019	-400.772	-21.004	0.052	0.129%	63.588%	63.635%
8717	-0.407	-24.329	-0.021	-24.308	-413.191	-7.870	0.019	-412.662	-21.627	0.052	0.128%	63.608%	63.654%
8718	0.326	-24.290	0.017	-24.308	-413.196	-7.858	0.019	-412.662	-21.627	0.052	0.130%	63.664%	63.711%
8719	-0.477	-23.257	-0.025	-23.232	-394.906	-7.538	0.019	-394.402	-20.670	0.052	0.128%	63.531%	63.578%
8720	-0.898	-24.185	-0.047	-24.138	-410.304	-7.826	0.019	-409.782	-21.476	0.052	0.127%	63.558%	63.604%
8721	-0.483	-24.878	-0.025	-24.852	-422.452	-8.040	0.019	-421.911	-22.111	0.052	0.128%	63.638%	63.684%
8722	0.466	-24.828	0.024	-24.852	-422.459	-8.024	0.019	-421.911	-22.111	0.052	0.130%	63.709%	63.756%
8723	0.798	-24.096	0.042	-24.138	-410.316	-7.798	0.019	-409.782	-21.476	0.052	0.130%	63.690%	63.738%
8724	0.271	-23.218	0.014	-23.232	-394.911	-7.525	0.019	-394.402	-20.670	0.052	0.129%	63.592%	63.639%

APPENDIX D

CODES FOR DEVELOPMENT OF PREDICTIVE STRESS FUNCTION

Code *"load data"*

```
% Load Plaxis Output data
clc
clear all

MainDirectory='C:\Users\Ryan_\Desktop\PLHA
Kramer\Lateral_Spreading\PLAXIS2D\Calculations\Matlab_testing\Excel_Database_MC';

[~,~,Filenames]=xlsread('Filenames.xlsx');

% Filesnames is an Excel file that stores the geometry names in the form of "12.xlsx" for example.

for a=[61,62,63,64,65,66,67,68,69,70,71,72,73,74]
% "a" represents the name of each geometry, e.g., 12 is geometry 5-0-5-0
   Present_filename=Filenames{a};
   File2Read=fullfile(MainDirectory,Present_filename);
   [values, text, raw] = xlsread(File2Read,1,'D:J');
   Cell_data_table{:,:,a}=values;
% Creating multiple tables laterally stacked
end

ALL_values=Cell_data_table{:,:,61};
% all other i's except the first that are included in "a"

for i=[62,63,64,65,66,67,68,69,70,71,72,73,74]
      temp_values=Cell_data_table{:,:,i};
      ALL_values=[ALL_values;temp_values];
end

% Cell data table = each geometry individually stacked into multiple tables
% ALL_values = all of the geometires specified by "a" vertically concatenated into one table
% ALL_values=[ALL_values;temp_values]; is what stacks it vertically as indicated by the semicolon
```

Code *"Coordinate Transformation"*

```
% Calculate dimensionless coordinates and normalize stresses
clear all
clc

% If desire to vertically concatenate all PLAXIS output data from each geometry and then calculate delta, eta, norm shear stress, etc. then load "All_values.mat"

% To load all files load "All_values_ALL" instead.

% For MC
load('MC_All_values.mat');

% If desire to create plots of each geometry individually, e.g. norm. stress vs delta or eta vs norm. stress then load "Cell_data_table.mat"

% To load all files load "Cell_data_table_ALL"

% For MC
load('MC_Cell_data_table.mat');

load('geom_values.mat');
% Loads the geometry parameters for each geometry such as the height of the slope

geo=geom_values;
% change to "geo" to shorten the commands later

gamma = 17;
% Unit weight

multiple_geomrun=0;
% If only a single geometry is desired in the output "data_table" type any # but "1" below, and if it is desired to have multiple
%geometries included in the "data_table" then type 1 below
```

```
for i=[74]
   if multiple_geomrun==1
      geomdata=ALL_values;
   else
      geomdata=ALL_values(ALL_values(:,1)==i,:);
   end

   data_table = array2table(geomdata,'variablenames',{'ID','X','Y','s_xx','s_yy','s_zz','s_xy'});
   % Adding columns of new variables to table
   data_table.Y_pos = (data_table.Y*(-1));
   data_table.s_yy_pos = (data_table.s_yy*(-1));
   data_table.delta = (data_table.X.*(tand(geo(i,6)))./(geo(i,4));

   y0_1 = data_table.X.*(tand(geo(i,5)));
   % don't make -X in yo_1 since X is already negative if left of (0,0)

   y0_2 = (-1)*data_table.X.*(tand(geo(i,6)));
   y0_3 = ((-1)*(geo(i,4)))-((data_table.X-(geo(i,9))).*(tand(geo(i,7))));
   % yo_2 and yo_3 are not inherently negative because the PLAXIS does not output the negative y value so you have to add a (-1) in
%     yo_2 and yo_3

   % Using the proper eta values based on the location "x" with respect to the toe of the slope
   eta = zeros(length(y0_1),1);
   index1 = find(data_table.X <= 0);
   eta(index1) = ((data_table.Y_pos(index1))-(y0_1(index1)))./(geo(i,4));

   index2 = find((data_table.X > 0 & data_table.X <= (geo(i,9))));
   eta(index2) = ((data_table.Y_pos(index2))-(y0_2(index2)))./(geo(i,4));

   index3 = find(data_table.X > (geo(i,9)));
   eta(index3) = ((data_table.Y_pos(index3))-(y0_3(index3)))./(geo(i,4));

   data_table.eta = eta;
```

```
    % Normalizing the vertical eff. stress and shear stress by gamma*H
    data_table.s_yy_norm = data_table.s_yy_pos./((geo(i,4))*gamma);

    data_table.s_xy_norm = data_table.s_xy./((geo(i,4))*gamma);
end
```

Code *"Mapping Stresses to Regular Grid"*

```
clear all
% Important to update filename, output textfile to proper file directory, slope angles, and slope height

% Example loading of a geometry
load c:\ryan\MC\H1_a0_B25_T5.mat;

% Enter slope angles based on file names loaded theta_one = alpha, theta_two = beta, and theta_three = theta
height = 1;
theta_one = 0;
theta_two = 25;
% theta_three = 0.00000001;
% if geometry has a theta_three = 0 use 0.00000001 for computational reasons
theta_three = 5;

ryan = table2array(data_table);                    % Change .mat file to array (remove headers)

% Assign variables to columns
delta = ryan(:,10);
eta = ryan(:,11);
sig = ryan(:,12);
tau = ryan(:,13);
ratio = tau./sig;
nn = size(eta);
n = nn(1,1);                                       % length of vectors
etamin = 0;                                        % lower bound eta for grid
etamax = 3;                                        % upper bound eta for grid
deltamin = -8;                                     % lower bound delta for grid
deltamax = 8;                                      % upper bound delta for grid
n_eta = 200;                                       % number of eta subdivisions for grid
n_delta = 320;                                     % number of delta subdivisions for grid
eta_grid = (etamin:(etamax-etamin)/n_eta:etamax);  % define eta values for grid
delta_grid = (deltamin:(deltamax-deltamin)/n_delta:deltamax);   % define delta values for grid
```

```
[roww1,coll]=find(isinf(ratio));                    % Set "Inf" values to some value (Usually 0 or only a few)
ratio(roww1,1)=0;
[roww2,coll]=find(isnan(ratio));                    % Set "NaN" values to some values, e.g. 0 (Usually 0 or only a few)
ratio(roww2,1)=0;

p = 8;                                              % exponent for IDW factors
radius = 2;                                         % distance beyond which weighting factors set to zero
for i=1:n_delta                                      % loop over all delta values
   for j=1:n_eta                                    % loop over all eta values
      den = 0;                                      % set denominator of weighting factor summation to zero
      sig_grid(i,j) = 0;                            % set initial value of sigma summation to zero
      tau_grid(i,j) = 0;                            % set initial value of tau summation to zero
      ratio_grid(i,j) = 0;                          % set initial value of ratio summation to zero
      for k=1:n                                     % loop over all PLAXIS stress point values
         dist(k,1) = sqrt((eta(k,1)-eta_grid(1,j))^2+(delta(k,1)-delta_grid(1,i))^2);
% calculate distance from grid point (i,j) in delta, eta space
         if dist(k,1) < radius
            den = den + dist(k,1)^-p;               % carry out summation for denominator in IDW factor expression
         else
            den = den;
         end
      end
      for k=1:n
         if dist(k,1) < radius
            w(k,1) = dist(k,1)^-p/den;              % compute weighting factor for each PLAXIS stress point
         else
            w(k,1) = 0;
         end
      end

      for k=1:n
```

```
            sig_grid(i,j) = sig_grid(i,j)+w(k,1)*sig(k,1);          % sum up weighted vertical stress values
            tau_grid(i,j) = tau_grid(i,j)+w(k,1)*tau(k,1);          % sum up weighted shear stress values
            ratio_grid(i,j) = ratio_grid(i,j)+w(k,1)*ratio(k,1);    % sum up weighted stress ratio values
        end
        xx = [i j delta_grid(i) eta_grid(j) sig_grid(i,j) tau_grid(i,j)]   % set up array to be displayed during calculations (can be deleted)
        disp(xx)                                                    % display values during calculations (can be deleted)
    end
end

figure(1)
mesh(eta_grid(1,1:n_eta),delta_grid(1,1:n_delta),tau_grid)          % shear stress values at grid points
title('Shear stress grid')

figure(2)
mesh(eta_grid(1,1:n_eta),delta_grid(1,1:n_delta),sig_grid)          % vertical stress values at grid points
title('Vertical stress grid')

figure(3)
mesh(eta_grid(1,1:n_eta),delta_grid(1,1:n_delta),ratio_grid)        % vertical stress values at grid points
title('Stress ratio grid')

figure(4)
scatter3(eta,delta,tau,'.')                                         % shear stress values at PLAXIS stress points
ylim([deltamin deltamax])
xlim([etamin etamax])
zlim([-0.12 0.12])
title('Shear stress data')

figure(5)
scatter3(eta,delta,sig,'.')                                          % normal stress values at PLAXIS stress points
ylim([deltamin deltamax])
xlim([etamin etamax])
zlim([0 5])
```

```
title('Normal stress data')

figure(6)
scatter3(eta,delta,ratio,'.')                                   % stress ratio values at PLAXIS stress points
ylim([deltamin deltamax])
xlim([etamin etamax])
title('Stress ratio data')

figure(7)                                                       % shear stress vs delta at different shallow eta
plot(delta_grid(1,1:n_delta),tau_grid(:,1),delta_grid(1,1:n_delta),tau_grid(:,4),delta_grid(1,1:n_delta),tau_grid(:,7),delta_grid(1,1:n_de
lta),tau_grid(:,10),delta_grid(1,1:n_delta),tau_grid(:,15))

figure(8)                                                       % shear stress vs delta down to larger eta's (from eta = 0 to eta = 3)
plot(delta_grid(1,1:n_delta),tau_grid(:,1),delta_grid(1,1:n_delta),tau_grid(:,15),delta_grid(1,1:n_delta),tau_grid(:,35),delta_grid(1,1:n_
delta),tau_grid(:,68),delta_grid(1,1:n_delta),tau_grid(:,101),delta_grid(1,1:n_delta),tau_grid(:,135),delta_grid(1,1:n_delta),tau_grid(:,1
68),delta_grid(1,1:n_delta),tau_grid(:,200))

figure(9)                                                       % stress ratio vs delta at different shallow eta
plot(delta_grid(1,1:n_delta),ratio_grid(:,1),delta_grid(1,1:n_delta),ratio_grid(:,4),delta_grid(1,1:n_delta),ratio_grid(:,7),delta_grid(1,1:
n_delta),ratio_grid(:,10),delta_grid(1,1:n_delta),ratio_grid(:,15))

figure(10)                                                      % stress ratio vs delta down to larger eta's (from eta = 0 to eta = 3)
plot(delta_grid(1,1:n_delta),ratio_grid(:,1),'r',delta_grid(1,1:n_delta),ratio_grid(:,15),'g',delta_grid(1,1:n_delta),ratio_grid(:,35),'b',delta
_grid(1,1:n_delta),ratio_grid(:,68),'m',delta_grid(1,1:n_delta),ratio_grid(:,101),'k',delta_grid(1,1:n_delta),ratio_grid(:,135),'--
r',delta_grid(1,1:n_delta),ratio_grid(:,168),'--g',delta_grid(1,1:n_delta),ratio_grid(:,200),'--b')
ylim([-0.15,0.2])
xlabel('Delta')
ylabel('Stress Ratio')
legend({'eta = 0','eta = 0.21','eta = 0.51','eta = 1.005','eta = 1.5','eta = 2.01','eta = 2.505','eta = 3'},'Location','southwest')

figure(11)                                                      % stress ratio vs delta down to larger eta's (from eta = 0 to eta = 3)
plot(delta_grid(1,1:n_delta),ratio_grid(:,35),'b',delta_grid(1,1:n_delta),ratio_grid(:,68),'m',delta_grid(1,1:n_delta),ratio_grid(:,101),'k',d
elta_grid(1,1:n_delta),ratio_grid(:,135),'--r',delta_grid(1,1:n_delta),ratio_grid(:,168),'--g',delta_grid(1,1:n_delta),ratio_grid(:,200),'--b')
```

```
xlim([-1.5 1.5])
ylim([-0.08,0.05])
xlabel('Delta')
ylabel('Stress Ratio')
legend({'eta = 0.51','eta = 1.005','eta = 1.5','eta = 2.01','eta = 2.505','eta = 3'},'Location','southwest')


load c:\ryan\delta_target.txt                    % define final grid (reduced size)
load c:\ryan\eta_target.txt                      % for eta down to 3

for i = 1:length(delta_target)
   for j = 1:length(eta_target)
      sig1(i,j) = sig_grid(delta_target(i),eta_target(j));
      tau1(i,j) = tau_grid(delta_target(i),eta_target(j));
      ratio1(i,j) = ratio_grid(delta_target(i),eta_target(j));
   end
end
figure(12)
mesh(eta_target(:,1),delta_target(:,1),tau1)     % shear stress values at final grid points
title('Shear stress - reduced grid')

figure(13)
mesh(eta_target(:,1),delta_target(:,1),sig1)     % shear stress values at final grid points
title('Normal stress - reduced grid')

figure(14)
mesh(eta_target(:,1),delta_target(:,1),ratio1)   % shear stress values at final grid points
title('Stress ratio - reduced grid')

for i = 1:length(delta_target)                   % put data for optimization in array that can be written to text file
   for j = 1:length(eta_target)
      k = (i-1)*length(eta_target)+j;
      xxx(k,1) = delta_grid(delta_target(i,1));
```

```
        xxx(k,2) = eta_grid(eta_target(j,1));
        xxx(k,3) = sig1(i,j);
        xxx(k,4) = tau1(i,j);
        xxx(k,5) = ratio1(i,j);
        xxx(k,6) = theta_one;
        xxx(k,7) = theta_two;
        xxx(k,8) = theta_three;
        xxx(k,9) = height;
    end
end

fid = fopen('c:\ryan\MC\Optimization\RRresults\1_0_25_5\RRresults.txt','w');                    % write results to RRresults.txt
fprintf(fid,'%12.8f  %12.8f  %12.8f  %12.8f  %12.8f  %12.8f  %12.8f  %12.8f  %12.8f\n',xxx.');
fclose(fid);
```

Code *"Moments"*

```
clear all
close all
format long
load C:\ryan\MC\Optimization\RRresults\5_0_15_0\RRresults.txt              % Read data in original format
RRdelta = RRresults(:,1);
RReta   = RRresults(:,2);
RRratio = RRresults(:,5);
nn = length(RRdelta);
num = 0;
minval = 0.01;                          % May need to increase for theta3 > 0 geometries?
maxval = 1-minval;
delta_shift = 2;                        % Allow delta values to be shifted to reduce COV (helps with beta function fit)


for i=2:nn                              % Find number of unique delta values delta values (e.g., 1 geometry then 91)
   if RRdelta(i)-RRdelta(i-1) > 0.001
      num = num+1;
   end
end
m = num+1;                             % Number of delta values
n = nn/m;                               % Number of eta values
eta = RReta(1:n);                       % Vector of eta values

dmax_shift = 1.6;                       % Allow max bound to be shifted to right (helps with beta function fit)
dmin_shift = 1.8;                       % Allow min bound to be shifted left (helps with beta function fit)
                                        % dmax_shift and dmin_shift may be required to be functions of depth to obtain the best fit

for i=1:m
   nn=(n-1)/2+n.*(i-1);                 % nn jumps every 101 rows to find the next delta value (there are 101 of each unique delta)
   delta(i) = RRdelta(nn) + delta_shift;       % Vector of delta values (shifted)
end
```

```
count = 0;
for i=1:n
   if eta(i) < 0.5
      count = count+1;                    % Find number of eta values < 0.5 to avoid plotting
   end
end

for ii = 1:n
   for jj = 1:m
      ratio(ii,jj) = -RRratio((jj-1)*n+ii);     % Assemble ratio values in matrix form
   end                                  % Cycling through j's first to fill out first 91 values in row 1 which is the first eta, then will fill out
the 91 values of row 2
end                                     % Note, stress ratio values are made negative, thus the stress ratio's we are looking at are now
positive since PLAXIS ouputs negative values of the shear stress we were interested in

cum_ratio = zeros(n,m);                 % creating a zero's matrix the same size as the ratio matrix (n,m) = (101x91)
for i=1:n
   for j=2:m
      cum_ratio(i,j) = cum_ratio(i,j-1)+ratio(i,j);  % Cumulative ratio values (increasing left to right)
   end
end

for i=1:n
   for j=2:m
      CDF(i,j) = cum_ratio(i,j)/cum_ratio(i,m);      % Normalize to produce data-based CDF
   end                                          %(i,m) gives the last value of the row, e.g., (1,91) which is the max value of the cumsum
end

for i=1:n
   for j=2:m
      PDF(i,j) = CDF(i,j)-CDF(i,j-1);           % Normalize to produce data-based PDF
      if PDF(i,j) < 0
```

```
        PDF(i,j) = 0;                   % Eliminate negative PDF values (caused by negative CDF slopes) We no longer want
negative values since we made "-ratio" earlier to give positive values that we are interested in
      end
   end
end

subplot(2,1,1)
plot(delta,CDF(10,:),delta,CDF(20,:),delta,CDF(40,:),delta,CDF(80,:))
title('Data-based CDF')
subplot(2,1,2)
plot(delta,PDF(10,:),delta,PDF(20,:),delta,PDF(40,:),delta,PDF(80,:))
title('Data-based PDF')

figure
surf(PDF)
title('Data-based PDF')

for i=1:n                               % Find left boundary at minval by linear interpolation
   for j=2:m                            % 0.01 could cause problems later if CDF goes above 0.01 then goes back below - can
happen due to some larger positive shear stresses (and thus stress ratios) from PLAXIS
      if (CDF(i,j-1)-minval)*(CDF(i,j)-minval) < 0   % Becomes > 0 when the first j value is > 0.01 --> everything before that j will
give negative values!
         nmin(i) = j;                   % index j when CDF for a certain eta, i, is at the min bound, i.e. just greater than 0.01
         fraction(i) = (minval-CDF(i,nmin(i)-1))/(CDF(i,nmin(i)) - CDF(i,nmin(i)-1));    % part of linear interpolatiom
         dmin(i) = delta(nmin(i)-1)+fraction(i)*(delta(nmin(i))-delta(nmin(i)-1));       % the rest of the linear interpolation
         dmin_noshift(i) = dmin(i);                                    % Not shifted yet
         dmin(i) = dmin(i)-dmin_shift;
      end
   end
end

for i=1:n                           % Find right boundary at maxval (0.99 for now) by linear interpolation
   for j=2:m
```

```
        if (CDF(i,j-1)-maxval)*(CDF(i,j)-maxval) < 0
            nmax(i) = j;
            fraction(i) = (maxval-CDF(i,nmax(i)-1))/(CDF(i,nmax(i)) - CDF(i,nmax(i)-1));
            dmax(i) = delta(nmax(i)-1)+fraction(i)*(delta(nmax(i))-delta(nmax(i)-1));
            dmax_noshift(i) = dmax(i);
            dmax(i) = dmax(i)+dmax_shift;
        end
    end
end

figure
plot(dmin,eta,dmax,eta,dmin_noshift,eta,dmax_noshift,eta)
title('Lower and upper bounds')
set(gca, 'YDir','reverse')

mean1 = zeros(n,1);                     % Calculate mean value of delta based on data
stdevv1 = zeros(n,1);
for i=1:n                               % remember n = 101 and m = 91
    sum = 0;
    for j=1:m
%       if delta(j) < dmin(j)
%           value(i,j) = 0;
%           sum = sum+value(i,j);
%       elseif delta(j) > dmax(j)
%           value(i,j) = 0;
%           sum = sum+value(i,j);
%       else
        value(i,j) = PDF(i,j).*delta(j);    % Mean calculation - 1st moment
        sum = sum+value(i,j);
%       end
    end
    mean_data(i) = sum;
end
```

```
for i=1:n                                   % Calculate standard deviation of delta based on data
   sum = 0;
   for j=1:m
%        if delta(j) < dmin(j)
%            value(i,j) = 0;
%            sum = sum+value(i,j);
%        elseif delta(j) > dmax(j)
%            value(i,j) = 0;
%            sum = sum+value(i,j);
%        else
       value(i,j) = PDF(i,j).*(delta(j)-mean_data(i))^2;
       sum = sum+value(i,j);
%        end
   end
   sigma_data(i) = sqrt(sum);               % This would be the 2nd moment which is the variance, thus to get stan. dev. it needed
to have the square root taken
end

for i=1:n                                   % Calculate skewness of delta based on data - 3rd moment
   sum = 0;
   for j=1:m
      value(i,j) = PDF(i,j).*(delta(j)-mean_data(i))^3;
      sum = sum+value(i,j);                 % Third central moment
   end                                      % Pearson's moment coefficient of skewness
   skew_data(i) = sum./sigma_data(i).^3;    % Skewness coefficient based on data
end

figure
subplot(1,2,1)
plot(mean_data,eta)
title('Mean vs eta')
set(gca, 'YDir','reverse')
```

```
subplot(1,2,2)
plot(sigma_data,eta)
title('Stdev vs eta')
set(gca, 'YDir','reverse')

for i=1:n
   part1(i) = (mean_data(i)-dmin(i))/(dmax(i)-dmin(i));    % Note that the shift bounds are used to calculate alpha and beta!
   part2(i) = 1- part1(i);
   part3(i) = sigma_data(i).^2./(dmax(i)-dmin(i))^2;
   alpha(i) = part1(i).^2.*part2(i)./part3(i)-part1(i);
   beta(i) = part1(i).*part2(i)./part3(i)-alpha(i);
end

for i=1:n
   mean_pred(i) = dmin(i)+alpha(i).*(dmax(i)-dmin(i))./(alpha(i)+beta(i));     % predicted mean
   sigma_pred(i) = sqrt(alpha(i).*beta(i).*(dmax(i)-dmin(i)).^2./((alpha(i)+beta(i)).^2.*(alpha(i)+beta(i)+1)));   % predicted stan. dev.
   skew_pred(i) = 2.*(beta(i)-alpha(i))*sqrt(alpha(i)+beta(i)+1)./((alpha(i)+beta(i)+2).*sqrt(alpha(i)*beta(i)));  % predicted skewness
end

figure
subplot(1,3,1)
plot(mean_data,eta,'o',mean_pred,eta)
title('Mean vs eta')
set(gca, 'YDir','reverse')
subplot(1,3,2)
plot(sigma_data,eta,'o',sigma_pred,eta)
title('Stdev vs eta')
set(gca, 'YDir','reverse')
subplot(1,3,3)
plot(skew_data,eta,'o',skew_pred,eta)
title('Skew vs eta')
set(gca, 'YDir','reverse')
```

```
for i = 1:n
   alphabeta(i) = alpha(i)./beta(i);
end
figure
subplot(1,3,1)
plot(alpha,eta)
title('Alpha vs eta')
set(gca, 'YDir','reverse')
subplot(1,3,2)
plot(beta,eta)
title('Beta vs eta')
set(gca, 'YDir','reverse')
subplot(1,3,3)
plot(alphabeta,eta)
title('Alpha/Beta vs eta')
set(gca, 'YDir','reverse')

figure
subplot(1,3,1)
plot(alpha,eta,'o')
title('Alpha vs eta')
set(gca, 'YDir','reverse')
subplot(1,3,2)
plot(beta,eta,'o')
title('Beta vs eta')
set(gca, 'YDir','reverse')
subplot(1,3,3)
plot(alphabeta,eta,'o')
title('Alpha/Beta vs eta')
set(gca, 'YDir','reverse')

eta_fit = eta(count+1:n);
alpha_fit = alpha(count+1:n);
```

```
beta_fit = beta(count+1:n);
dmin_noshift_fit = dmin_noshift(count+1:n);
dmax_noshift_fit = dmax_noshift(count+1:n);

for i=1:n
   for j=1:m
      if delta(j) < dmin(i)
         RR(i,j) = 0;
      elseif delta(j) > dmax(i)
         RR(i,j) = 0;
      else
         RR(i,j) = (delta(j)-dmin(i))^(alpha(i)-1)*(dmax(i)-delta(j))^(beta(i)-1);   % this is betafunc w/o amplitude
      end
   end
end

r20 = ratio(20,:);                    % Create plots of normalized ratio to check shapes
r40 = ratio(40,:);
r80 = ratio(80,:);                    % r is the PLAXIS data
RR20 = RR(20,:);
RR40 = RR(40,:);                      % RR is the predicted fit to the data
RR80 = RR(80,:);

for i = 1:n
   rmax(i) = max(ratio(i,:));         % Maximum value of ratio at each eta
   RRmax(i) = max(RR(i,:));           % Maximum value of RR at each eta
end
for i = 1:n
   for j = 1:m
      rnorm(i,j) = ratio(i,j)./rmax(i);        % Normalized values of ratio
      RRnorm(i,j) = RR(i,j)./RRmax(i);         % Normalized values of RR
   end
end
```

```
rmax_fit = rmax(count+1:n);

r20norm = ratio(20,:)/max(r20);                % normalizing by the maxval
r40norm = ratio(40,:)/max(r40);
r80norm = ratio(80,:)/max(r80);
RR20norm = RR(20,:)/max(abs(RR20));
RR40norm = RR(40,:)/max(abs(RR40));
RR80norm = RR(80,:)/max(abs(RR80));

figure
plot(delta,r20norm,'o',delta,RR20norm,'r-')
figure
plot(delta,r40norm,'o',delta,RR40norm,'r-')
figure
plot(delta,r80norm,'o',delta,RR80norm,'r-')


for i=1:n                                      % Calculate error in normalized ratios (shape check)
   for j=1:m
      if delta(j) < dmin(j)
         Error(i,j) = 0;
      elseif delta(j) > dmax(j)
         Error(i,j) = 0;
      else
         if eta(i) < 0.5
            Error(i,j) = 0;                    % Don't count eta < 0.5 toward error
         else
            Error(i,j) = abs(RRnorm(i,j)-rnorm(i,j));
         end
      end
   end
end
```

```
for i = 1:n                                % Calculate errors at each eta value
   AbsError = 0;
   SquaredError = 0;
   for j = 1:m
      AbsError = AbsError+Error(i,j);
      SquaredError = SquaredError+Error(i,j)^2;
   end
   TotAbsError(i) = AbsError;
   TotSquaredError(i) = SquaredError;
end

E(1) = 0;
E(2) = 0;
for i = 1:n
   E(1) = E(1) + TotAbsError(i);           % Sum of absolute value of errors over all eta > 0.5
   E(2) = E(2) + TotSquaredError(i);       % Sum of squared errors over all eta > 0.5
end

E                                          % Display summed errors on one line

figure
subplot(1,2,1)
plot(TotAbsError,eta)
title('Abs Error (norm) vs eta')
set(gca, 'YDir','reverse')
subplot(1,2,2)
plot(TotSquaredError,eta)
title('Squared Error (norm) vs eta')
set(gca, 'YDir','reverse')
```

Code 5 *"Optimization Function"*

```
% Important to update output text file "RRParameters.txt" filepath to correct geometry folder
clear all
format long

geometry_type = 3;
% Enter 1 for theta1 > 0 and theta3 > 0
% Enter 2 for theta1 > 0 and theta3 = 0
% Enter 3 for theta1 = 0 and theta3 > 0
% Enter any number other than 1, 2, or 3 for theta1 = 0 and theta3 = 0

% Select optimization iteration tolerance - TolFun and TolX current values may not reflect values used
options = optimset('TolFun',1.e-4,'TolX',1.e-4,'Display','iter');

% Values in square brackets below are initial estimates of values to be optimized (contained in x-vector)
if geometry_type == 1
[x,out] = fminsearch('code_6',[1,2,3,4,5,6,7,8,9,10,11,12,13,14,15,16],options);

elseif geometry_type == 2
[x,out] = fminsearch('code_6',[1,2,3,4,5,6,7,8,9,10,11,12,13,14,15,16],options);

elseif geometry_type == 3
[x,out] = fminsearch('code_6',[1,2,3,4,5,6,7,8,9,10,11,12,13,14,15,16],options);

else % geometry_type == 4 or any other number
[x,out] = fminsearch('code_6',[1,2,3,4,5,6,7,8,9,10,11,12,13,14,15,16],options);
end

fid = fopen('c:\Ryan\MC\Optimization\RRresults\Combined_more\RRParameters.txt','w');
fprintf(fid,'%18.12f',x);
fclose(fid);

x
```

Code 6 "Optimizing Coefficients"

```
function f = Code_6(x)

% Important to update file path to proper geometry folder (e.g. "5_0_5_0") and update/unlock coefficients, theta1 and theta3, and each of the variables not unlocked

load c:\Ryan\MC\Optimization\RRresults\Combined_more\RRresults.txt          % Read data in original format

% if any geometries have theta1 or theta3 > 0 then insert any # other than 0 for theta1 and/or theta3
theta1 = 0.0;                       % Left slope angle
theta3 = 1.0;                       % Right slope angle

number_geometries = 19;             % MAKE SURE TO UPDATE
RRdelta = RRresults(:,1);
RReta   = RRresults(:,2);
RRratio = RRresults(:,5);
RRtheta2 = RRresults(:,7);          % Central slope angle
RRtheta3 = RRresults(:,8);          % Upper slope angle
delta_inc = 0.001;
nn = length(RRdelta);
delta_shift = 2;                    % Allow delta values to be shifted to reduce COV (helps with beta function fit)
num = 0;
for i=2:nn                          % Find number of unique delta values (e.g., 90 but if multiple geometries like 3 then 270)
   if RRdelta(i)-RRdelta(i-1) > 0.001
      num = num+1;
   end
end
m = num+number_geometries;          % Number of delta values the +# is based upon how many geometries
n = nn/m;                           % Number of eta values
eta = RReta(1:n);                   % eta values
for i=1:m
   nn=(n-1)/2+n.*(i-1);             % nn jumps every 101 rows to find the next delta value (there are 101 of each unique delta)
   delta(i) = RRdelta(nn) + delta_shift;      % Vector of delta values (shifted)
```

```
end
count = 0;
for i=1:n
   if eta(i) < 0.5
      count = count+1;                    % Find number of eta values < 0.5 to avoid plotting
   end
end

ww = length(RRtheta2)/number_geometries;   % find how many rows each geometry has
for i=1:number_geometries
   t=i*ww;
   theta2(i,1) = RRtheta2(t);              % Every geometry has rr number of rows, thus for 1 to the number of geometries
we can find each theta2 value.
end                                        % Note it does not matter if you have two different geometries with the same
theta2, it still will work as long as number_geometries is correct.

rr = length(RRtheta3)/number_geometries;   % find how many rows each geometry has
for i=1:number_geometries
   t=i*rr;
   theta3(i,1) = RRtheta3(t);              % Every geometry has rr number of rows, thus for 1 to the number of geometries
we can find each theta2 value.
end                                        % Note it does not matter if you have two different geometries with the same
theta2, it still will work as long as number_geometries is correct

for ii = 1:n
   for jj = 1:m
      ratio(ii,jj) = RRratio((jj-1)*n+ii);  % Creating ratio matrix. ii and jj = 1 gives RRratio(1) then ii = 1 and jj = 2 gives
RRratio(102), so it's filling out the first row with 101 values since 101 values is the range of eta so for that specific delta you are again
getting row 1 values
   end
end

% NOTE: The following comments up until the next %%%% %%%% are not used, but provide
```

```
% insight to a possible method to determine the min and max bounds

%%%%%%%%%%%%%%%%%%---xx(7) to xx(10) determination start---%%%%%%%%%%%%%%%%%%

% % CALCULATING MIN AND MAX BOUNDS - FF FOR CALC MAX AND MIN BOUNDS

% deltainterp = min(delta):delta_inc:max(delta);

% ratio_inc = interp2(delta,eta,ratio,deltainterp,eta);

% w = length(deltainterp);

% CDF = zeros(n,w);
% norm_CDF = zeros(n,w);

% for i=1:n
% ff_cent(i) =  0.5;
% ff_steep(i) = 20;
% index_negfour = find(deltainterp(1,:) ==-4);
% index_posfour = find(deltainterp(1,:) ==4);
% Left_Plateau(i) = sum(ratio_inc(i,1:index_negfour))/(length(ratio_inc(i,1:index_negfour)));
% Right_Plateau(i) = sum(ratio_inc(i,index_posfour:w))/(length(ratio_inc(i,index_posfour:w)));

%     for j=1:w
%         if deltainterp(j) < 0
%             ff(i,j) = Left_Plateau(i);
%         else
%             ff(i,j) = Left_Plateau(i)+(Right_Plateau(i)-Left_Plateau(i))./(1+(ff_cent(i)./deltainterp(j)).^ff_steep(i));
%         end
%     end
% end

% for i = 1:n
```

```
%     if eta(i) > 0.5
%         CDF(i,:) = cumtrapz(deltainterp,(ratio_inc(i,:)-ff(i,:)));
%         norm_CDF(i,:) = CDF(i,:)/min(CDF(i,:));
%         if i == 18
%         figure()
%         plot(deltainterp,norm_CDF(count+1,:)) % Example psuedo CDF plot for eta = 0.51
%         end
%     else
%         CDF(i,:) = zeros(1,w);
%     end
% end

% for i = (count+1):n
% ind_j_max(i) = find(norm_CDF(i,:) >.98, 1, 'first');       % find the first value of norm_CDF that is greater than 0.98
% ind_j_min(i) = find(norm_CDF(i,:) <0.02, 1, 'last');      % find the first value of norm_CDF that is greater than 0.02

% delta_max(i) = deltainterp(ind_j_max(i));
% delta_min(i) = deltainterp(ind_j_min(i));
% end

% eta_reg = eta((count+1):n);
% delta_min_reg = delta_min((count+1):n);
% delta_max_reg = delta_max((count+1):n);

% linear_regression_min = fitlm(eta_reg,delta_min_reg);
% min_coeff = linear_regression_min.Coefficients.Estimate;

% linear_regression_max = fitlm(eta_reg,delta_max_reg);
% max_coeff = linear_regression_max.Coefficients.Estimate;

%%%%%%%%%%%%%%%%---xx(7) to xx(10) determination end---%%%%%%%%%%%%%%%%
```

```
% Coefficients

% Filter Function coefficients
xx(1) =  2;                 % Center of filter function int - coeff added 2 due to shift

xx(2) = 4;                  % Steepness of filter function coeff - Not too steep to be noticeable like step function, but steep enough
to be occur between min and max bounds

% Left Plateau coefficient
xx(3) =  0;                 % Left plateau (we have found this to be constant at all eta's, i.e. no slope)

% Right Plateau coefficient
xx(4) = 0.0052;             % Right plateau coeff

% Min Bound coefficients
xx(5) = 1.33;               % Min Bound int - int
xx(6) = -0.21;              % Min Bound int - coeff
xx(7) = 0.1103;             % Min Bound coeff - int
xx(8) = -0.1198;            % Min Bound coeff - coeff

% Min Shift for geometries with theta3 for one theta2 geometry
xx(9) = 0.801928;           % Min shift coeff
xx(10) = 0.896234;          % Min shift exp

% Max Bound Coefficients
xx(11) = 2.19;              % Max Bound int - int
xx(12) = 0.2308;            % Max Bound int - coeff
xx(13) = 0.221340;          % Max Bound coeff - int
xx(14) = 0.077;             % Max Bound coeff

% Max Shift for geometries with theta3 for one theta2 geometry
xx(15) = -0.801928;         % Max shift coeff
```

```
xx(16) = 0.896234;          % Max shift exp

% Alpha coefficients
xx(17) = 11.672;            % Alpha coeff - coeff
xx(18) = 0.9729;            % Alpha coeff - exponent
xx(19) = -0.241213;         % MAKE NEGATIVE - Alpha exponent - coeff
xx(20) = 0.275908;          % Alpha exponent - exponent

% Beta coefficients
xx(21) = 2.6;               % Beta coeff - coeff
xx(22) = 1.376;             % Beta coeff - exponent
xx(23) = -0.070529;         % MAKE NEGATIVE - Beta exponent - coeff
xx(24) = 0.672342;          % Beta exponent - exponent

% Amplitude coefficients
xx(25) = 0.0273315500;      % amplitude coefficient - coefficient
xx(26) = 0.6685027450;      % amplitude coefficient - exponent
xx(27) = -0.0998010525;     % MAKE NEGATIVE - amplitude exponent - coefficient
xx(28) = 0.6305506628;      % amplitude exponent - exponent

% Amplitude reduction for geometries with theta3 for one theta2 geometry
xx(29) = -0.087171;         % Amplitude reduction coeff
xx(30) = -1.021359;         % Amplitude reduction exp

% Amplitude increase to fit all of the theta3 > 0 geometries
xx(31) = 1.760799;
xx(32) = -1.627222;

% Pseudo Kronecker Delta Function (applies approximate value of 0 if theta3 = 0 and a value of 1 is theta3 > 0
% Do not optimize the pseudo Kronecker Delta Function
xx(33) = 1.106530;
xx(34) = 0.158467;
xx(35) = 0.0767;
```

```
xx(36) = 0.05;

% Unlock and/or renumber coefficients to optimize

% xx(1) = x(1);
% xx(2) = x(2);
% xx(3) = x(3);
% xx(4) = x(4);
% xx(5) = x(5);
% xx(6) = x(6);
% xx(7) = x(7);
% xx(8) = x(8);
% xx(9) = x(9);
% xx(10) = x(10);
% xx(11) = x(11);
% xx(12) = x(12);
% xx(13) = x(13);
% xx(14) = x(14);
% xx(15) = x(15);
% xx(16) = x(16);
% xx(17) = x(17);
% xx(18) = x(18);
% xx(19) = x(19);
% xx(20) = x(20);
% xx(21) = x(21);
% xx(22) = x(22);
% xx(23) = x(23);
% xx(24) = x(24);
% xx(25) = x(25);
% xx(26) = x(26);
% xx(27) = x(27);
% xx(28) = x(28);
% xx(29) = x(29);
```

```
% xx(30) = x(30);
% xx(31) = x(31);
% xx(32) = x(32);

end

for k=1:number_geometries

for i=1:n

   c1(i,k) = xx(1);                    % FF center is constant
   c2(i,k) = xx(2);                    % FF steepness is constant
   c3(i,k) = xx(3);                    % Left Plateau = 0
   c4(i,k) = xx(4)*theta3(k);          % Right Plateau
   c5(i,k) = ((xx(5)+xx(6)*theta2(k))+(xx(7)+xx(8)*theta2(k))*eta(i))+((xx(33)*theta3(k)^xx(34))-
(xx(35)*theta3(k)+xx(36)))*((xx(9)*eta(i)^xx(10)));
   c6(i,k) = ((xx(11)+xx(12)*theta2(k))+(xx(13)+xx(14)*theta2(k))*eta(i))+((xx(33)*theta3(k)^xx(34))-
(xx(35)*theta3(k)+xx(36)))*((xx(15)*eta(i)^xx(16)));
   c7(i,k) = ((xx(17)*theta2(k)^xx(18))*exp((xx(19)*theta2(k)^xx(20))*eta(i)));
   c8(i,k) = ((xx(21)*theta2(k)^xx(22))*exp((xx(23)*theta2(k)^xx(24))*eta(i)));
   c9(i,k) = ((xx(25)*theta2(k)^xx(26))*eta(i)^(xx(27)*theta2(k)^xx(28)))+(((xx(33)*theta3(k)^xx(34))-
(xx(35)*theta3(k)+xx(36)))*(((xx(29)*eta(i)^xx(30)))+(xx(31)*theta2(k)^xx(32))*(0.24/(eta(i)^2))));

   maxval(i) = (((c7(i)-1)/(c7(i)+c8(i)-2))*(c6(i)-c5(i)))^(c7(i)-1)*(c6(i)-c5(i)-((c7(i)-1)/(c7(i)+c8(i)-2))*(c6(i)-c5(i)))^(c8(i)-1);
 % peak amplitude of beta function

   for j=1:m                           % Compute filter function (adjusted for negative delta)
      if delta(j) < 0
         filterfunc(i,j) = c3(i);
      else
         filterfunc(i,j) = c3(i)+(c4(i)-c3(i))./(1+(c1(i)./delta(j)).^c2(i));
      end
   end
```

```
   for j=1:m                          % Compute beta function
      if delta(j) < c5(i)
         betafunc(i,j) = c3(i);
      elseif delta(j) > c6(i)
         betafunc(i,j) = c4(i);
      else
         betafunc(i,j) = (delta(j)-c5(i)).^(c7(i)-1).*(c6(i)-delta(j)).^(c8(i)-1);
      end
      betafuncnorm(i,j) = betafunc(i,j)./maxval(i);          % Normalize beta function so that all have the same peak amplitude
      pred(i,j) = -(filterfunc(i,j)+c9(i).*betafuncnorm(i,j)); % Predicted stress ratio

   end
end
end

Error = 0;
E = zeros(n,m);
for k=1:number_geometries
   for i = 1:n
      for j = ((k-1)*91)+1 : k*91
         if eta(i) > 0.5                                     % Don't count eta < 0.5 toward error
            E(i,j) = (pred(i,j)-ratio(i,j))^2;               % Matrix of error values
%              E(i,j) = ((pred(i,j)-ratio(i,j))./(ratio(i,j))).^2;   % Matrix of normalized error values
         end
            Error = Error+E(i,j);                            % Sum to obtain total error
      end
%       Error = Error*(1+50/((1+(c7(i))^40)*(1+(c8(i))^40)));   % Inflate error if c7 or c8 approach 0
   end
end

Error                                                        % Let Error value be written to screen during optimization

f = Error;
```

Code "*Optimization Plotting*"

```
clear all
load c:\Ryan\MC\Optimization\RRresults\Combined_more\RRresults.txt          % Read data in original format

% Note: You may see Nan and -Inf values for the predicted function when
% eta = 0, however, we are only concerned with eta >= 0.51 to 3.

theta1 = 0.0;                                % Left slope angle
theta3 = 1;                                  % Right slope angle
number_geometries = 19;                      % MAKE SURE TO UPDATE THIS
RRdelta = RRresults(:,1);
RReta   = RRresults(:,2);
RRratio = RRresults(:,5);
RRtheta2 = RRresults(:,7);                   % Central slope angle
RRtheta3 = RRresults(:,8);                   % Upper slope angle
delta_inc = 0.001;
nn = length(RRdelta);
delta_shift = 2;                             % Allow delta values to be shifted to reduce COV (helps with beta function fit)
num = 0;
for i=2:nn                                   % Find number of unique delta values (e.g., 90 but if multiple geometries like 3 then 270)
   if RRdelta(i)-RRdelta(i-1) > 0.001
      num = num+1;
   end
end
m = num+number_geometries;                   % Number of delta values the +# is based upon how many geometries
n = nn/m;                                    % Number of eta values
eta = RReta(1:n);                            % eta values
for i=1:m
   nn=(n-1)/2+n.*(i-1);                % nn jumps every 101 rows to find the next delta value (there are 101 of each unique delta)
   delta(i) = RRdelta(nn) + delta_shift;     % Vector of delta values (shifted)
end
count = 0;
for i=1:n
```

```
    if eta(i) < 0.5
        count = count+1;                    % Find number of eta values < 0.5 to avoid plotting
    end
end

ww = length(RRtheta2)/number_geometries;    % find how many rows each geometry has
for i=1:number_geometries
    t=i*ww;
    theta2(i,1) = RRtheta2(t);              % Every geometry has rr number of rows, thus for 1 to the number of geometries
we can find each theta2 value.
end                                         % Note it does not matter if you have two different geometries with the same
theta2, it still will work as long as number_geometries is correct

rr = length(RRtheta3)/number_geometries;    % find how many rows each geometry has
for i=1:number_geometries
    t=i*rr;
    theta3(i,1) = RRtheta3(t);              % Every geometry has rr number of rows, thus for 1 to the number of geometries
we can find each theta2 value
end                                         % Note it does not matter if you have two different geometries with the same
theta2, it still will work as long as number_geometries is correct

for ii = 1:n
    for jj = 1:m
        ratio(ii,jj) = RRratio((jj-1)*n+ii);    % Creating ratio matrix. ii and jj = 1 gives RRratio(1) then ii = 1 and jj = 2 gives
RRratio(102), so it's filling out the first row with 101 values since 101 values is the range of eta so for that specific delta you are again
getting row 1 values
    end
end


% NOTE: The following comments up until the next %%%% %%%% are not used, but provide
% insight to a possible method to determine the min and max bounds
```

```
%%%%%%%%%%%%%%%%%%---xx(7) to xx(10) determination start---%%%%%%%%%%%%%%%%%%

% % CALCULATING MIN AND MAX BOUNDS - FF FOR CALC MAX AND MIN BOUNDS

% deltainterp = min(delta):delta_inc:max(delta);

% ratio_inc = interp2(delta,eta,ratio,deltainterp,eta);

% w = length(deltainterp);

% CDF = zeros(n,w);
% norm_CDF = zeros(n,w);

% for i=1:n
% ff_cent(i) =  0.5;
% ff_steep(i) = 20;
% index_negfour = find(deltainterp(1,:) ==-4);
% index_posfour = find(deltainterp(1,:) ==4);
% Left_Plateau(i) = sum(ratio_inc(i,1:index_negfour))/(length(ratio_inc(i,1:index_negfour)));
% Right_Plateau(i) = sum(ratio_inc(i,index_posfour:w))/(length(ratio_inc(i,index_posfour:w)));

%     for j=1:w
%         if deltainterp(j) < 0
%             ff(i,j) = Left_Plateau(i);
%         else
%             ff(i,j) = Left_Plateau(i)+(Right_Plateau(i)-Left_Plateau(i))./(1+(ff_cent(i)./deltainterp(j)).^ff_steep(i));
%         end
%     end
% end

% for i = 1:n
%     if eta(i) > 0.5
%         CDF(i,:) = cumtrapz(deltainterp,(ratio_inc(i,:)-ff(i,:)));
```

```
%         norm_CDF(i,:) = CDF(i,:)/min(CDF(i,:));
%         if i == 18
%         figure()
%         plot(deltainterp,norm_CDF(count+1,:)) % Example psuedo CDF plot for eta = 0.51
%         end
%     else
%         CDF(i,:) = zeros(1,w);
%     end
% end

% for i = (count+1):n
% ind_j_max(i) = find(norm_CDF(i,:) >.98, 1, 'first');       % find the first value of norm_CDF that is greater than 0.98
% ind_j_min(i) = find(norm_CDF(i,:) <0.02, 1, 'last');      % find the first value of norm_CDF that is greater than 0.02

% delta_max(i) = deltainterp(ind_j_max(i));
% delta_min(i) = deltainterp(ind_j_min(i));
% end

% eta_reg = eta((count+1):n);
% delta_min_reg = delta_min((count+1):n);
% delta_max_reg = delta_max((count+1):n);

% linear_regression_min = fitlm(eta_reg,delta_min_reg);
% min_coeff = linear_regression_min.Coefficients.Estimate;

% linear_regression_max = fitlm(eta_reg,delta_max_reg);
% max_coeff = linear_regression_max.Coefficients.Estimate;

%%%%%%%%%%%%%%%%%---xx(7) to xx(10) determination end---%%%%%%%%%%%%%%%%%
```

```
% Filter Function coefficients
xx(1) =  2;                 % Center of filter function int - coeff added 2 due to shift

xx(2) = 4;                  % Steepness of filter function coeff - Not too steep to be noticeable like step function, but steep enough
to be occur between min and max bounds

% Left Plateau coefficient
xx(3) =  0;                 % Left plateau (we have found this to be constant at all eta's, i.e. no slope)

% Right Plateau coefficient
xx(4) = 0.0052;             % Right plateau coeff

% Min Bound coefficients
xx(5) = 1.33;               % Min Bound int - int
xx(6) = -0.21;              % Min Bound int - coeff
xx(7) = 0.1103;             % Min Bound coeff - int
xx(8) = -0.1198;            % Min Bound coeff - coeff

% Min Shift for geometries with theta3 for one theta2 geometry
xx(9) = 0.801928;           % Min shift coeff
xx(10) = 0.896234;          % Min shift exp

% Max Bound Coefficients
xx(11) = 2.19;              % Max Bound int - int
xx(12) = 0.2308;            % Max Bound int - coeff
xx(13) = 0.221340;          % Max Bound coeff - int
xx(14) = 0.077;             % Max Bound coeff - coeff

% Max Shift for geometries with theta3 for one theta2 geometry
xx(15) = -0.801928;         % Max shift coeff
xx(16) = 0.896234;          % Max shift exp

% Alpha coefficients
```

```
xx(17) = 11.672;          % Alpha coeff - coeff
xx(18) = 0.9729;          % Alpha coeff - exponent
xx(19) = -0.241213;       % MAKE NEGATIVE - Alpha exponent - coeff
xx(20) = 0.275908;        % Alpha exponent - exponent

% Beta coefficients
xx(21) = 2.6;             % Beta coeff - coeff
xx(22) = 1.376;           % Beta coeff - exponent
xx(23) = -0.070529;       % MAKE NEGATIVE - Beta exponent - coeff
xx(24) = 0.672342;        % Beta exponent - exponent

% Amplitude coefficients
xx(25) = 0.0273315500;    % amplitude coefficient - coefficient
xx(26) = 0.6685027450;    % amplitude coefficient - exponent
xx(27) = -0.0998010525;   % MAKE NEGATIVE - amplitude exponent - coefficient
xx(28) = 0.6305506628;    % amplitude exponent - exponent

% Amplitude reduction for geometries with theta3 for one theta2 geometry
xx(29) = -0.087171;       % Amplitude reduction coeff
xx(30) = -1.021359;       % Amplitude reduction exp

% Amplitude increase to fit all of the theta3 > 0 geometries
xx(31) = 1.760799;
xx(32) = -1.627222;

% Pseudo Kronecker Delta Function (applies an approximate value of 0 if theta3 = 0 and a value of 1 is theta3 > 0
xx(33) = 1.106530;
xx(34) = 0.158467;
xx(35) = 0.0767;
xx(36) = 0.05;

for k=1:number_geometries
```

```
for i=1:n                                   % Compute actual coefficients

   c1(i,k) = xx(1);                         % FF center is constant
   c2(i,k) = xx(2);                         % FF steepness is constant
   c3(i,k) = xx(3);                         % Left Plateau = 0
   c4(i,k) = xx(4)*theta3(k);               % Right Plateau
   c5(i,k) = ((xx(5)+xx(6)*theta2(k))+(xx(7)+xx(8)*theta2(k))*eta(i))+((xx(33)*theta3(k)^xx(34))-
(xx(35)*theta3(k)+xx(36)))*((xx(9)*eta(i)^xx(10)));
   c6(i,k) = ((xx(11)+xx(12)*theta2(k))+(xx(13)+xx(14)*theta2(k))*eta(i))+((xx(33)*theta3(k)^xx(34))-
(xx(35)*theta3(k)+xx(36)))*((xx(15)*eta(i)^xx(16)));
   c7(i,k) = ((xx(17)*theta2(k)^xx(18))*exp((xx(19)*theta2(k)^xx(20))*eta(i)));
   c8(i,k) = ((xx(21)*theta2(k)^xx(22))*exp((xx(23)*theta2(k)^xx(24))*eta(i)));
   c9(i,k) = ((xx(25)*theta2(k)^xx(26))*eta(i)^(xx(27)*theta2(k)^xx(28)))+(((xx(33)*theta3(k)^xx(34))-
(xx(35)*theta3(k)+xx(36)))*(((xx(29)*eta(i)^xx(30)))+(xx(31)*theta2(k)^xx(32))*(0.24/(eta(i)^2))));

   maxval(i,k) = (((c7(i,k)-1)/(c7(i,k)+c8(i,k)-2))*(c6(i,k)-c5(i,k)))^(c7(i,k)-1)*(c6(i,k)-c5(i,k)-((c7(i,k)-1)/(c7(i,k)+c8(i,k)-
2))*(c6(i,k)-c5(i,k)))^(c8(i,k)-1);  % peak amplitude of beta function

   for j=1:m                                % Compute filter function (adjusted for negative delta)
      if delta(j) < 0
         filterfunc(i,j,k) = c3(i,k);
      else
         filterfunc(i,j,k) = c3(i,k)+(c4(i,k)-c3(i,k))./(1+(c1(i,k)./delta(j)).^c2(i,k));
      end
   end
   for j=1:m                                % Compute beta function
      if delta(j) < c5(i,k)
         betafunc(i,j,k) = c3(i,k);         % Set to zero outside left bound
      elseif delta(j) > c6(i,k)
         betafunc(i,j,k) = c4(i,k);         % Set to right plateau outside right bound
      else
         betafunc(i,j,k) = (delta(j)-c5(i,k)).^(c7(i,k)-1).*(c6(i,k)-delta(j)).^(c8(i,k)-1);
      end
```

```
        betafuncnorm(i,j,k) = betafunc(i,j,k)./maxval(i,k);          % Normalize beta function so that all have the same peak amplitude

        pred(i,j,k) = -(filterfunc(i,j,k)+c9(i,k).*betafuncnorm(i,j,k));          % Predicted value - sum of filter and betafunc

    end
end
end
Error = 0;
E = zeros(n,m,k);
for k = 1:number_geometries
    for i = 1:n
        for j = ((k-1)*91)+1 : k*91
            if eta(i) > 0.5
                E(i,j,k) = (pred(i,j,k)-ratio(i,j))^2;                    % SSE
%                   E(i,j,k) = ((pred(i,j,k)-ratio(i,j))./(ratio(i,j))).^2;          % Normalized Error
            else
                E(i,j,k) = 0;
            end
            Error = Error+E(i,j,k);
        end
%       Error = Error*(1+50/((1+(c7(i,k))^40)*(1+(c8(i,k))^40)));          % Inflate error if c7 or c8 approach 0
    end
end
```

```
%%%%% IMPORTANT %%%%%
% When plotting pred(i,j,k) or any 3 dimensional array you need to make sure you select the proper "j" columns. Geometry #1 will be from J = 1:91, #2 from J = 92:182, #3 from J = 183:273 and so on


% 2D SUBPLOTS STRESS RATIO VS DELTA FOR DIFFERENT ETA'S

% Only showing one subplot figure for brevity
figure(13)
subplot(2,3,1);
plot(delta(1,1:91),pred(18,1:91,1))
hold
scatter(delta(1,1:91),ratio(18,1:91))
xlim([-6,10])
ylim([-.35,0.05])
xlabel('Delta')
ylabel('Stress Ratio')
title('5-0-5-0, Pred. function with FEM data at eta = 0.51')
legend({'Predicted','PLAXIS'},'Location','southwest','Box','off')

subplot(2,3,2);
plot(delta(1,1:91),pred(35,1:91,1))
hold
scatter(delta(1,1:91),ratio(35,1:91))
xlim([-6,10])
ylim([-.35,0.05])
xlabel('Delta')
ylabel('Stress Ratio')
title('5-0-5-0, Pred. function with FEM data at eta = 1.0')
legend({'Predicted','PLAXIS'},'Location','southwest','Box','off')

subplot(2,3,3);
plot(delta(1,1:91),pred(51,1:91,1))
```

```
hold
scatter(delta(1,1:91),ratio(51,1:91))
xlim([-6,10])
ylim([-.35,0.05])
xlabel('Delta')
ylabel('Stress Ratio')
title('5-0-5-0, Pred. function with FEM data at eta = 1.5')
legend({'Predicted','PLAXIS'},'Location','southwest','Box','off')

subplot(2,3,4);
plot(delta(1,1:91),pred(68,1:91,1))
hold
scatter(delta(1,1:91),ratio(68,1:91))
xlim([-6,10])
ylim([-.35,0.05])
xlabel('Delta')
ylabel('Stress Ratio')
title('5-0-5-0, Pred. function with FEM data at eta = 2.0')
legend({'Predicted','PLAXIS'},'Location','southwest','Box','off')

subplot(2,3,5);
plot(delta(1,1:91),pred(84,1:91,1))
hold
scatter(delta(1,1:91),ratio(84,1:91))
xlim([-6,10])
ylim([-.35,0.05])
xlabel('Delta')
ylabel('Stress Ratio')
title('5-0-5-0, Pred. function with FEM data at eta = 2.5')
legend({'Predicted','PLAXIS'},'Location','southwest','Box','off')

subplot(2,3,6);
plot(delta(1,1:91),pred(101,1:91,1))
```

```
hold
scatter(delta(1,1:91),ratio(101,1:91))
xlim([-6,10])
ylim([-.35,0.05])
xlabel('Delta')
ylabel('Stress Ratio')
title('5-0-5-0, Pred. function with FEM data at eta = 3.0')
legend({'Predicted','PLAXIS'},'Location','southwest','Box','off')
```

APPENDIX E

COMPARISON OF PREDICTED FUNCTION AND PLAXIS *SSR*

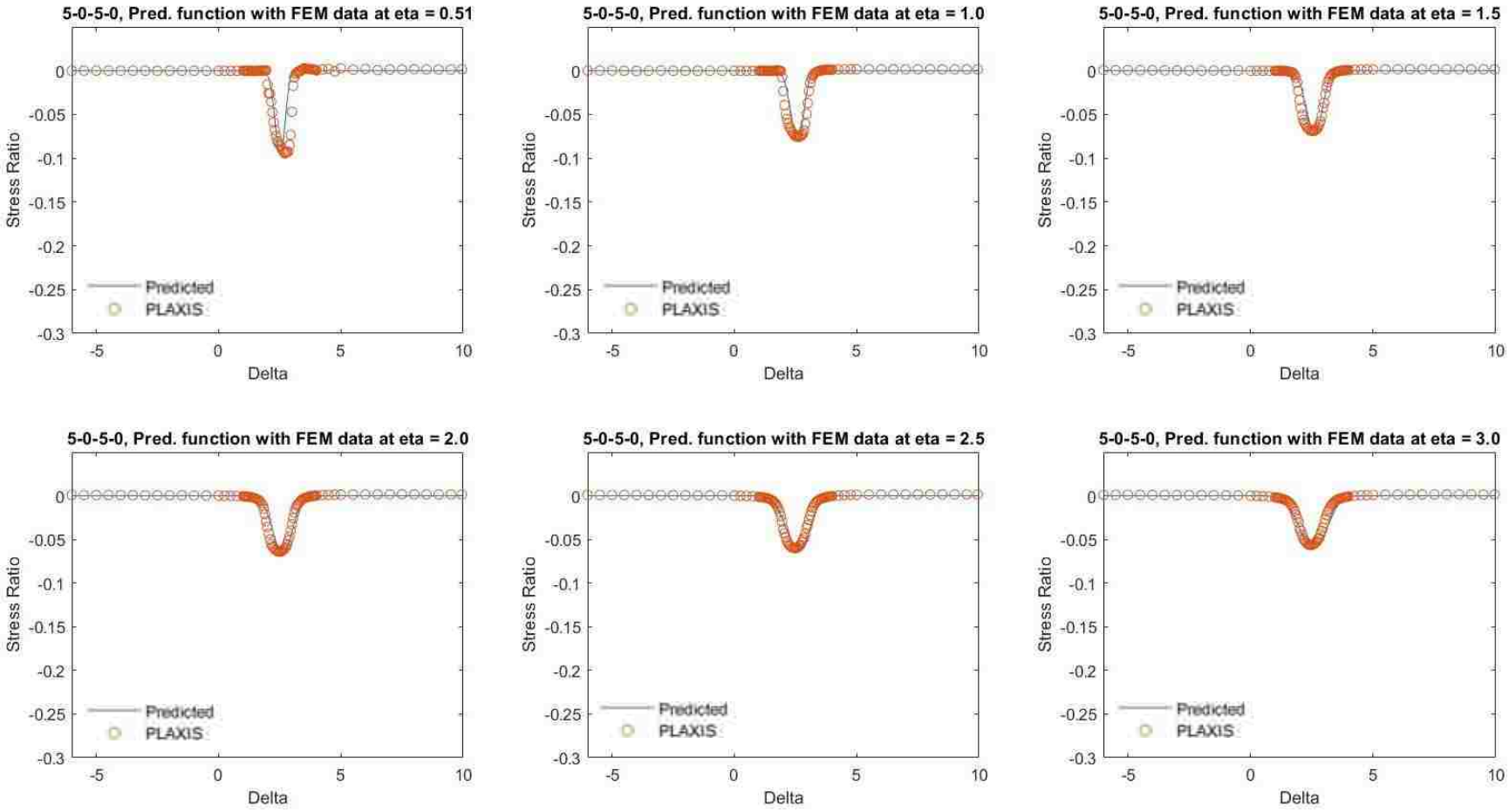

Figure E.1. Predicted function using the B_D compared to the PLAXIS stress ratio data for geometry 5-0-5-0.

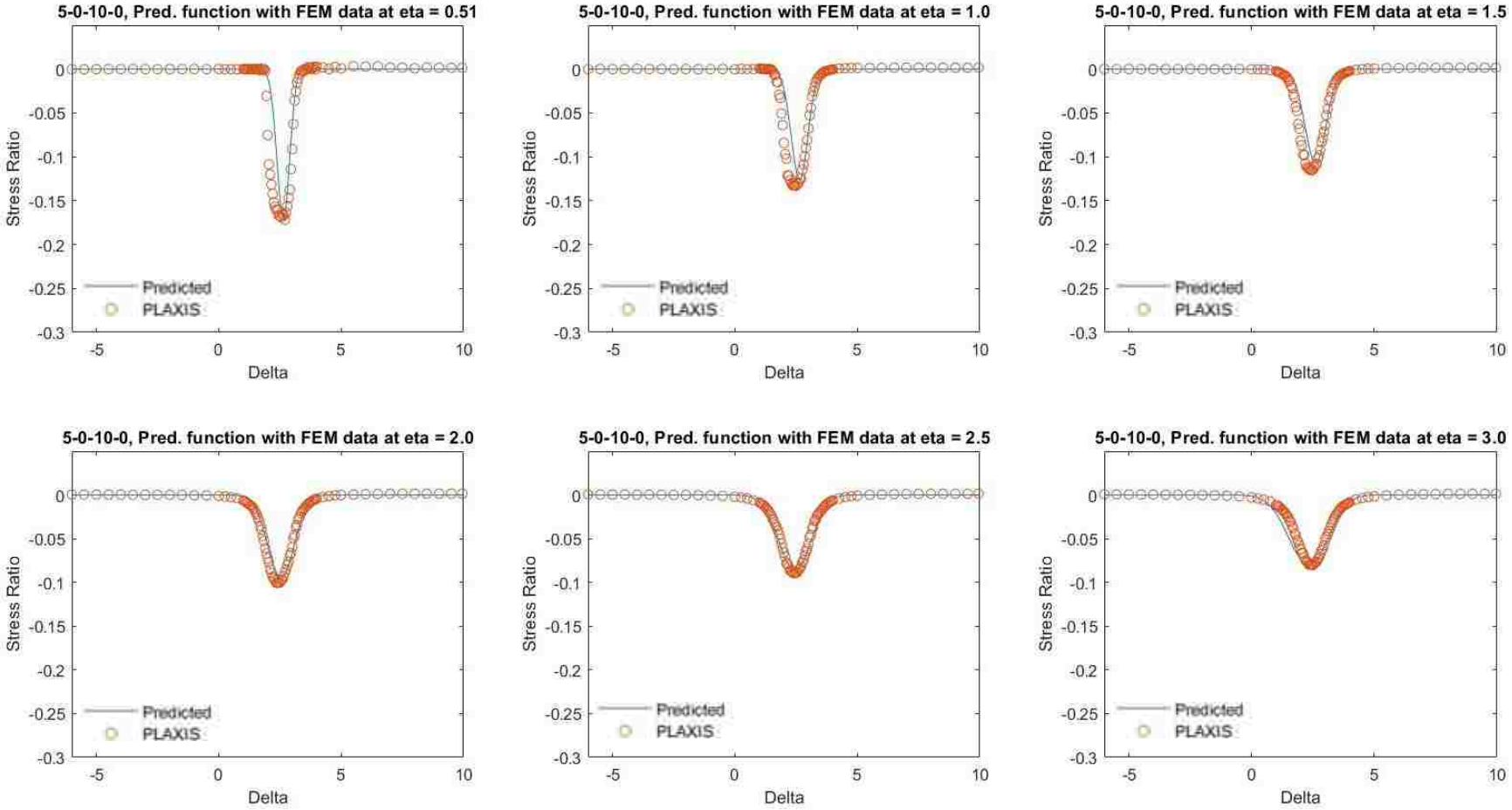

Figure E.2. Predicted function using the B_D compared to the PLAXIS stress ratio data for geometry 5-0-10-0.

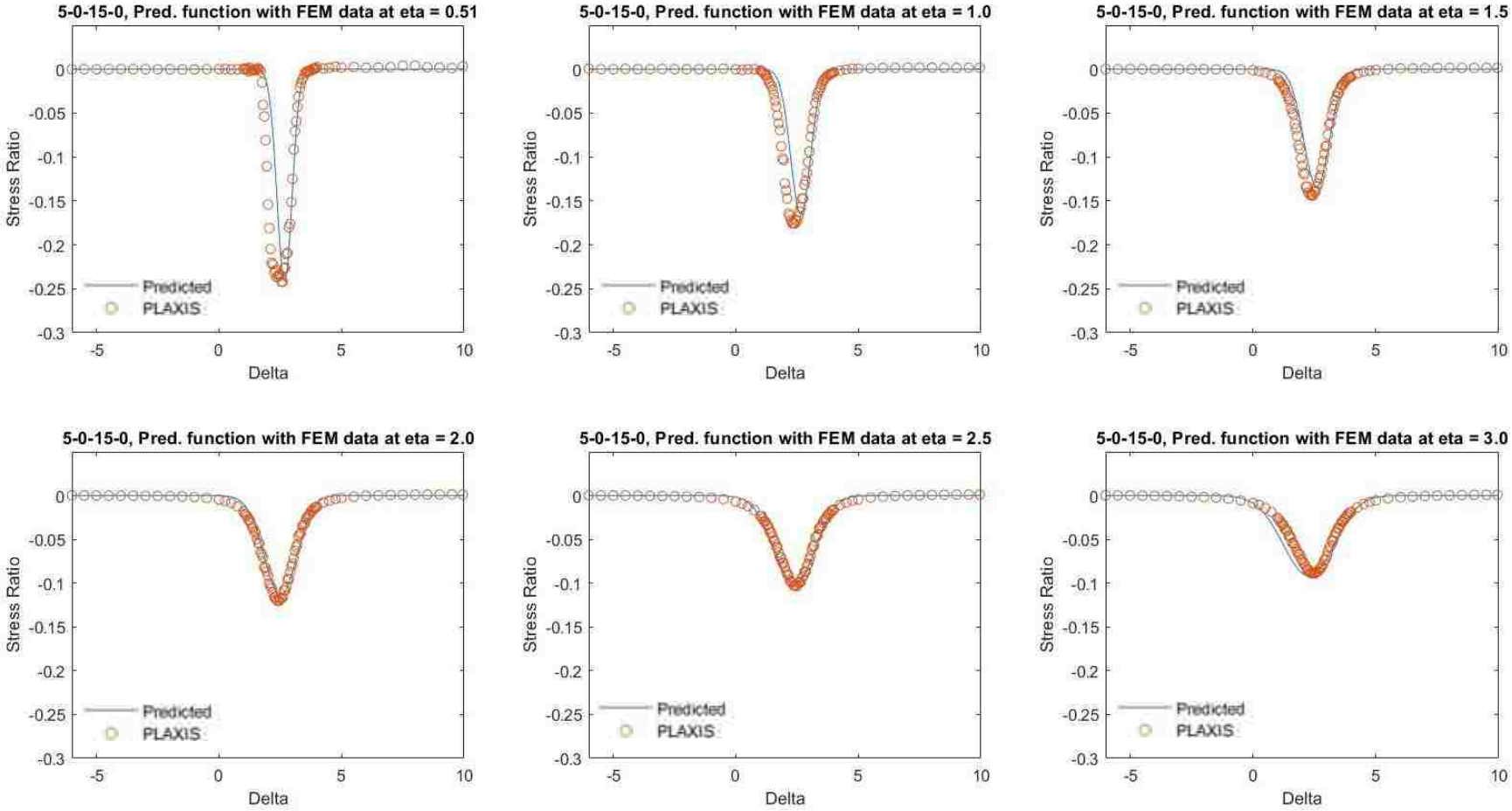

Figure E.3. Predicted function using the B_D compared to the PLAXIS stress ratio data for geometry 5-0-15-0.

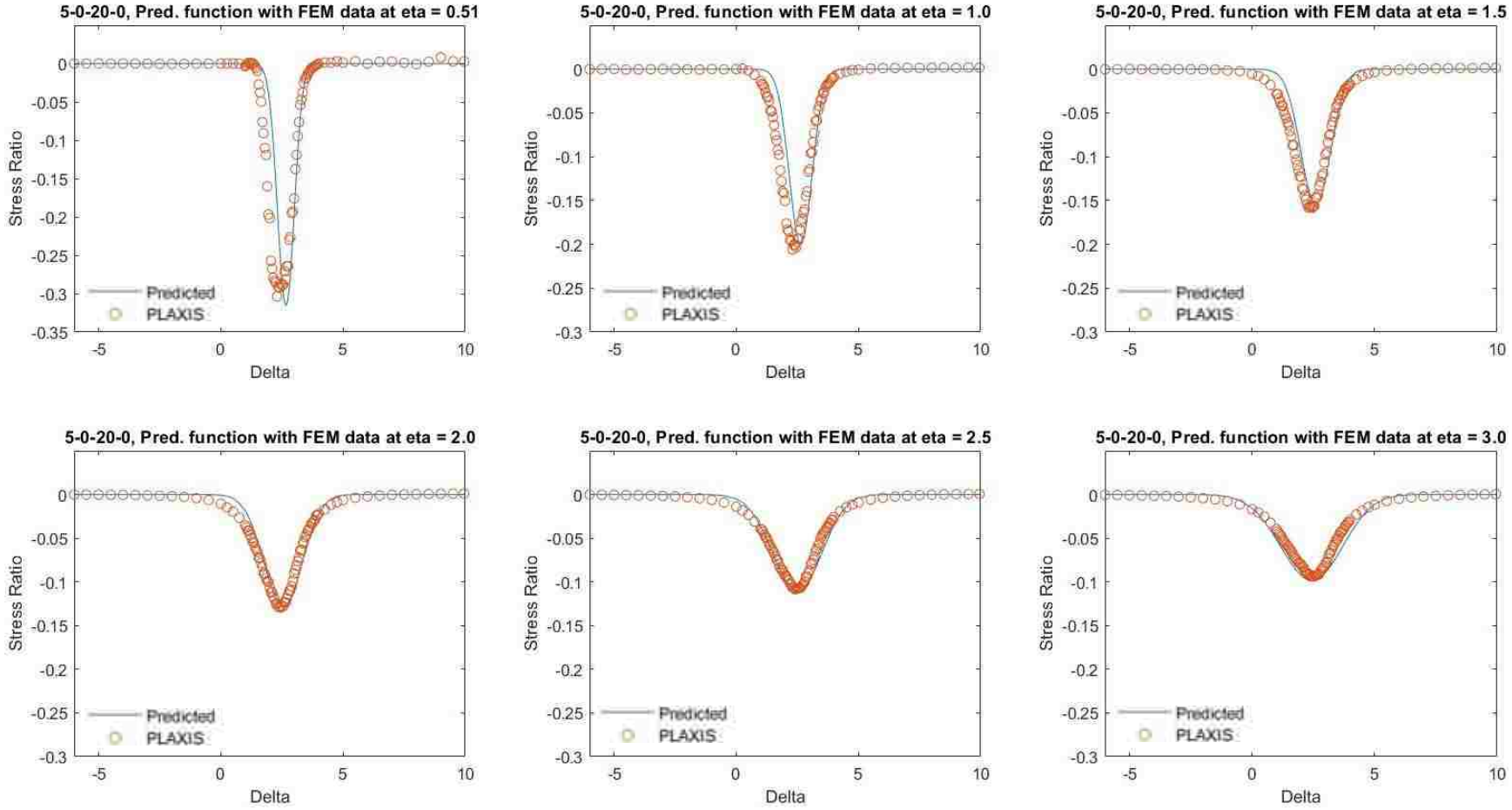

Figure E.4. Predicted function using the B_D compared to the PLAXIS stress ratio data for geometry 5-0-20-0.

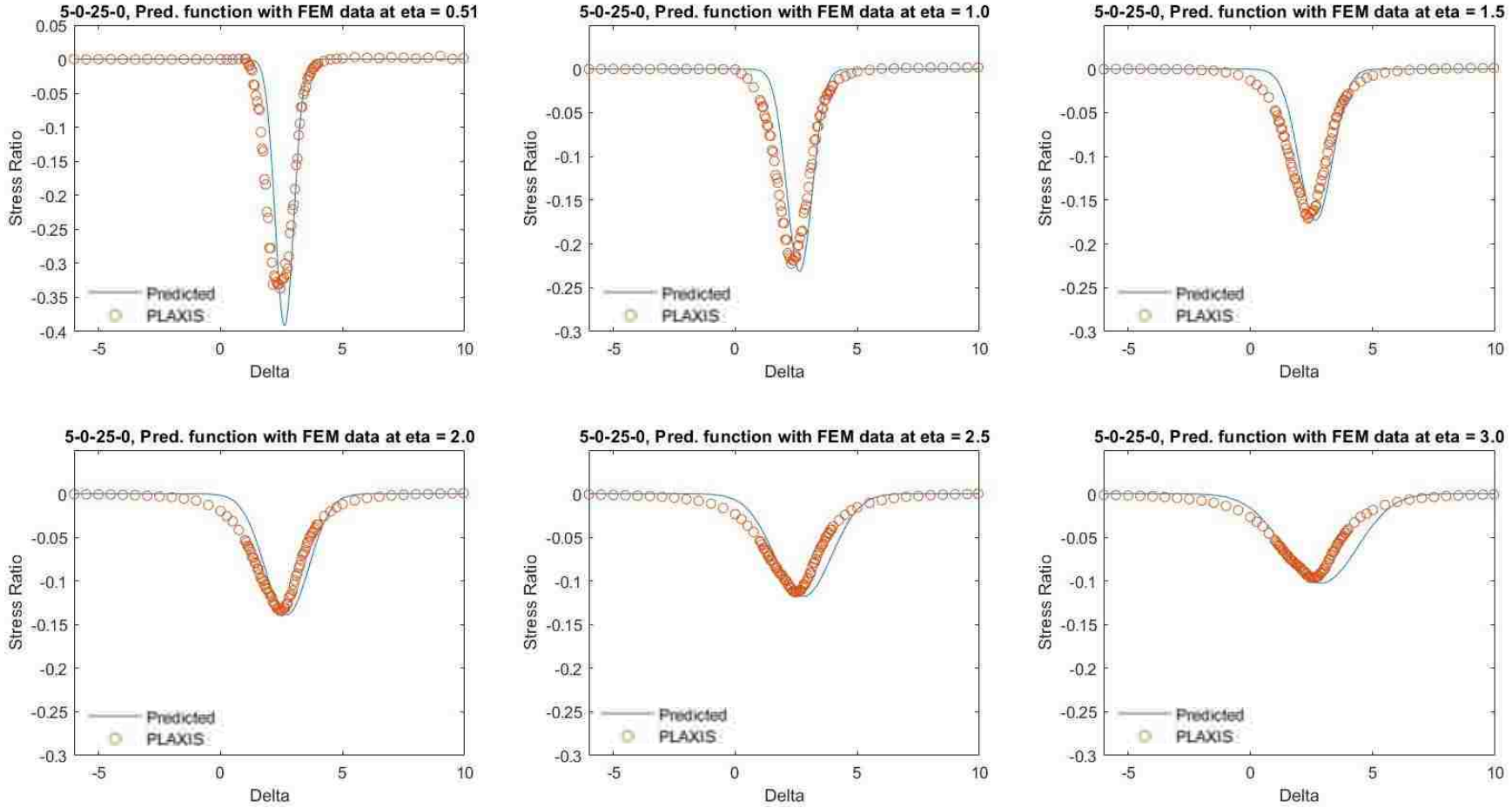

Figure E.5. Predicted function using the B_D compared to the PLAXIS stress ratio data for geometry 5-0-25-0.

VITA

The author was born on April 23, 1992 in Seattle, Washington. His family moved for work to beautiful, although at times frozen, Minot, North Dakota where he grew up and then attended college at the University of North Dakota in Grand Forks, North Dakota – the coldest city in contiguous United States. The author started his career with a 4.0 GPA and degree in Geological Engineering from the University of North Dakota. After graduation, he found his way back to the PNW, gaining experience as a rock-mechanics engineer at Golder Associates in Portland, Oregon. While there, he specialized in landslide hazard analysis and developed training presentations on the derivations, applications, and benefits of different slope-stability models. He also analyzed laboratory test results in accordance with American Society of Testing (ASTM) standards to develop material parameters for slope-stability models. Recognizing that he desired a deeper understanding of soil mechanics, the author moved to GeoDesign, Inc. in Portland, Oregon. While working on large infrastructure projects, he performed exploratory drilling, in-situ and laboratory soil testing, and foundation installation. This gave him the critical hands-on experience to relate field investigations and measurements to engineering analyses.

After gaining two years of experience in the mechanics and testing of geomaterials, the author enrolled at the University of Washington (UW) to pursue an M.S. degree in Geotechnical Engineering. While at UW, he sought out research with Professor Steven Kramer on probabilistic liquefaction modelling. Through this experience, he has studied the body of knowledge on liquefaction susceptibility, triggering, and effects. He also has conducted sensitivity analyses on the leading probabilistic liquefaction models to analyze their performance for differing site conditions, with the ultimate goal of formulating an improved model. This knowledge of

probabilistic liquefaction triggering models will be essential for formulating the mathematical tools to perform inverse-analysis of ancient liquefaction evidence, which is the topic of the authors future PhD research. The author has also developed new functions via optimization-analysis for computing the driving stress within a slope which is planned to be used in the future to develop an improved model to predict lateral spread displacements. The author graduated with a M.S. degree in Geotechnical Engineering in June 2019.

The authors future goals include: graduating with a PhD from the University of Washington; promoting STEM education and STEM careers to younger students, particularly those less represented in science and engineering; working at the USGS to characterize the hazards and risks communities face across the country; becoming a professional engineer (EIT certification No. 13469); and becoming a leader in the ASCE Geo-Institute community. The author has progressed towards achieving these goals by serving as President of the Geo-Institute Student Society at the University of Washington. In this leadership role, he has:

- Organized a regional Graduate Student conference where geotechnical engineering students from UW, Washington State University, Oregon State University, and the University of British Columbia presented their research and collaborated on engineering outreach programs.
- Raised funds to send fellow students to national and international conferences so that they can grow connections in the scientific and engineering communities.
- Established a monthly lecture series where practicing professionals from local geotechnical firms present their work in the community and form connections with graduate students.
- Planned and hosted a Seattle-section ASCE research symposium attended by academics and practitioners and highlighted by an internationally-renowned keynote lecturer.

- Participated in Engineering Discovery Days and other events that facilitate K-12 outreach and mentorship, promoting STEM education and careers, and conveying the importance of natural-hazards engineering to society and the environment.

The author has also made progress towards his PhD work and forming relationships with the USGS by having performed paleoliquefaction site investigations which included canoeing across the Columbia and Duwamish Rivers with Dr. Brian Atwater, an emeritus USGS scientist and member of the National Academy of Sciences. The author looks forward to continuing his research with Dr. Brian Atwater and his future PhD advisor Dr. Brett Maurer, who in an expert in liquefaction analytics. The authors future PhD research will be involved with decoding seismic hazard enigmas via next-generation paleoliquefaction analytics. The author was awarded the National Science Foundation Graduate Research Fellowship in 2019, which provides him funding for his PhD research over the next 3 years. The author is specifically interested in decoding the enigmas of the Cascadia Subduction Zone, and applying the research developed to other seismic hazard zones across the United States.